Multi-proxy approach (Thorium-234, excess Barium) of export and remineralization fluxes of carbon and biogenic elements associated with the oceanic biological pump

Nolwenn Lemaitre

UNIVERSITE BRETAGNE LOIRE

THÈSE / UNIVERSITÉ DE BRETAGNE OCCIDENTALE

sous le sceau de l'Université Bretagne Loire

pour obtenir le titre de

DOCTEUR DE L'UNIVERSITÉ DE BRETAGNE OCCIDENTALE

Mention : Chimie Marine

École Doctorale des Sciences de la Mer

présentée par

Nolwenn LEMAITRE

Préparée à l'Institut Universitaire Européen de la Mer (IUEM) en cotutelle avec la Vrije Universiteit Brussel (VUB).
Au sein du laboratoire des sciences de l'environnement marin (LEMAR) et du laboratoire Analytical, Environmental and Geo-Chemistry (AMGC).

Multi-proxy approach (^{234}Th, Ba_{xs}) of export and remineralization fluxes of carbon and biogenic elements associated with the oceanic biological pump

Thèse soutenue le 20 Janvier 2017
devant le jury composé de:

Ian SALTER
Docteur, Alfred Wegener Institute (AWI)
Bremerhaven - Allemagne / Rapporteur

Frédéric LE MOIGNE
Docteur, GEOMAR Helmholtz Centre for Ocean Research
Kiel - Allemagne / Rapporteur

Stéphane BLAIN
Professeur, Laboratoire d'Océanographie Microbienne (LOMIC)
Banyuls sur Mer - France / Examinateur

Lionel GUIDI
Docteur, Observatoire Océanologique de Villefranche/Mer (LOV)
Villefranche sur Mer - France / Examinateur

Filip MEYSMAN
Professeur, Vrije Universiteit Brussel (VUB)
Bruxelles - Belgique / Examinateur

Frank DEHAIRS
Professeur, Vrije Universiteit Brussel (VUB)
Bruxelles - Belgique / Directeur de thèse

Géraldine SARTHOU
Docteur, Laboratoire des sciences de l'environnement marin (LEMAR)
Brest - France / Directeur de thèse

Hélène PLANQUETTE
Docteur, Laboratoire des sciences de l'environnement marin (LEMAR)
Brest - France / Encadrante

Frédéric PLANCHON
Docteur, Laboratoire des sciences de l'environnement marin (LEMAR)
Brest - France / Encadrant

Contents

Acknowledgements 13
Abstract 17
Résumé 18
Samenvatting 19

Chapter 1: General Introduction 23
1.1. The Carbon cycle 24
1.2. The biological carbon pump 32
1.3. The different approaches to study the biological carbon pump 46
1.4. Study areas, objectives and thesis outline 50

Chapter 2: Material and Methods 57
2.1. Sample collection, chemical processing and analyses 58
2.2. ^{234}Th Export determination 76
2.3. Elemental export fluxes 80
2.4. Carbon remineralization fluxes determined from Ba_{xs} distributions 84

Chapter 3: High variability of particulate organic carbon export fluxes in the North Atlantic Ocean 91
Abstract 92
3.1. Introduction 93
3.2. Methods 95
3.3. Results 103
3.4. Discussion 121
3.5. Conclusion 133
Acknowledgements 134

Chapter 4: Particulate barium tracing significant mesopelagic carbon remineralization in the North Atlantic Ocean 143
Abstract 144
4.1. Introduction 145
4.2. Methods 146
4.3. Results 153
4.4. Discussion 166
4.5. Conclusion 177
Acknowledgements 178

Chapter 5: Biogenic trace element export fluxes in the North Atlantic Ocean 181
Abstract 182
5.1. Introduction 183
5.2. Methods 185
5.3. Results 191
5.4. Discussion 203
5.5. Conclusion 221
Acknowledgements 221

Chapter 6: Impact of the natural Fe-fertilization on the magnitude, stoichiometry and efficiency of particulate biogenic silica, nitrogen and iron export fluxes 229
Abstract 230
6.1. Introduction 231
6.2. Methods 233
6.3. Results 242
6.4. Discussion 253
6.5. Conclusion 265
Acknowledgments 266

Chapter 7: General conclusions and future directions 271
7.1. Major findings 272
7.2. Comparison of the two study areas 275
7.3. Perspectives 279
7.4. The fate of the BCP with global warming 282

References 287

Table of figures

Chapter 1:

Figure 1.1: The global carbon cycle. Arrows represent the fluxes in gigatons of carbon per year and the boxes represent the reservoirs in gigatons of carbon. Black values are natural fluxes and red are anthropogenic contributions (Diagram from http://www.ipcc.ch/, modified from (Sabine et al., 2004; Sarmiento, 2002). 24
Figure 1.2: The marine carbon cycle including the solubility and biological pumps with the pre-industrial fluxes and average values for the 1980-1990s (in brown box). Fluxes are represented by arrows and are in Pg C/year. Reservoir sizes are represented by the numbers in brackets and are expressed in Pg C. NPP is the net primary productivity (Modified from Sabine and Feely, 2007). 27
Figure 1.3: Global map of annual sea to air CO_2 exchanges (in µatm; Sarmiento and Gruber, 2006).28
Figure 1.4: Simplified view of the biological carbon pump (S. Hervé, IUEM).....29
Figure 1.5: Contribution of the different carbon pump components (the solubility pump $\Delta C_{gas\text{-}ex}$; the carbonate counter pump ΔC_{carb}; and the biological carbon pump ΔC_{soft}) to DIC increase in the deep ocean (Gruber and Sarmiento, 2006).....31
Figure 1.6: Schematic view of the decrease of the downward POC flux with depth (Lampitt et al., 2008).. 34
Figure 1.7: Patterns of nutrient limitation. Backgrounds indicate annual average surface concentrations of nitrate (a) and phosphate (b) in µmol.kg^{-1}.To assist comparison, nitrate is scaled by the mean N:P ratio of organic matter (that is divided by 16). Symbols indicate the primary (central circles) and secondary (outer circles) limiting nutrients as inferred from chlorophyll and/or primary productivity increases following artificial amendment of: N (green), P (black), Fe (red), Si (orange), Co (yellow), Zn (cyan) and vitamin B12 (purple). Divided circles indicate potentially co-limiting elements. White outer circles indicate that no secondary limiting nutrient was identified, which will be because of the lack of a test (from Moore et al., 2013). 39
Figure 1.8: Correlations between POC and mineral fluxes collected in 52 sediment traps below 1000 m and around the world ocean (Klaas and Archer, 2002).....40
Figure 1.9: Attenuation of the carbon export flux from the mixed layer into the mesopelagic zone by the microbial and zooplankton metabolisms (Steinberg et al., 2008).....43
Figure 1.10: SeaWIFS Chlorophyll-*a* concentrations averaged over boreal spring (http://oceancolor.gsfc.nasa.gov/cgi/biosphere_globes). The red line indicates the GEOVIDE transect. 51
Figure 1.11: SeaWIFS mean Chlorophyll-*a* concentrations averaged over austral spring (http://oceancolor.gsfc.nasa.gov/cgi/biosphere_globes). The red arrow indicates the Kerguelen Island position. 52

Chapter 2:

Figure 2.1: Summary of the different sampling and analytical steps on samples collected during the GEOVIDE cruise.....69
Figure 2.2: Perspex filtrations units used for the determination of Ba_{xs} concentrations during the GEOVIDE cruise.....70
Figure 2.3: $CaCO_3$ (a) pAl (b) and pBa (c) concentrations determined on samples collected with Niskin bottles and *in-situ* pumps. The black lines represent the 1:1 slopes. 73
Figure 2.4: Depth profiles at Station 32 of particulate trace elements as determined using GO-FLO bottles (blue diamond) and *in-situ* pumps (red triangles). 75
Figure 2.5: Radioactive decay chain of ^{238}U (a=years; d=days; h= hours; m=minutes; s=seconds)....77
Figure 2.6: Typical profile of the $^{234}Th/^{238}U$ ratio in seawater.....77
Figure 2.7: Mesopelagic particulate biogenic Ba (Ba_{xs}) versus calculated oxygen consumption rate (JO_2) for stations within the Southern Antarctic Circumpolar Current region (Dehairs et al., 1997). 85
Figure 2.8: Typical Ba_{xs} profile in seawater, adapted from Jacquet, 2007.....86
Figure 2.9: Example of a barite crystal (indicated with the red arrow) obtained by scanning electron microscopy, on the filter sampled at 600 m of Station 69 during the GEOVIDE cruise, and the corresponding energy-dispersive spectra. 87

Chapter 3:

Figure 3.1: Simplified schematic of the water mass circulation in the North Atlantic (adapted from Garcia-Ibanez et al., 2015) superimposed with the GEOVIDE cruise track (thick grey line) and stations (colored diamonds). Surface currents are represented.....96
Figure 3.2: Chlorophyll-a (Chl-a) concentrations in mg.m-3 (closed symbols) and total phaeopigment over Chl-a ratios (TPhaeo/Chl-a; open symbols) in the upper 200 m. 104
Figure 3.3: Main phytoplankton size groups and chloropigments (from the GEOVIDE database). a) Relative abundance of microphytoplankton (black line, circles), nanophytoplankton (dark green line, squares), picophytoplankton (light green line, triangles). b) Relative abundance of Fucoxanthin (black), 19'-HF (light grey), Zeaxanthin (dark grey), and peridinin (white) pigments 105
Figure 3.4: Particulate ^{234}Th activities for the small size fraction (SSF; 1-53 µm; open diamonds) and for the large size fraction (LSF; >53 µm; open triangles); Total ^{234}Th (closed blue circles) and ^{238}U (thick grey vertical line); all activities expressed in dpm.L^{-1}. The horizontal black line is the Eq depth (depth where ^{234}Th returns to equilibrium with ^{238}U) used for estimating the export fluxes, and the horizontal green line is the calculated PPZ depth (primary production zone). Error bars are hidden by the symbols 108
Figure 3.5: ^{234}Th flux attenuation between Eq and 400 m (in dpm.m^{-2}.d^{-1}). Negative values indicate an attenuation of the ^{234}Th flux between Eq and 400 m while positive values denote an increase of the ^{234}Th flux between both depths. The error bars are calculated using the error propagation laws. 111
Figure 3.6: POC:^{234}Th ratios (µmol.dpm^{-1}) in the SSF (open symbols) and LSF (closed symbols). The Eq depth (depth where ^{234}Th is back to equilibrium with ^{238}U) is indicated with the grey line except for Stations 26, 44 and 69 where the Eq depths are represented by green, pink and purple lines, respectively. The thin black line represents the power law fits (POC:^{234}Th=a×Z-b) of each province or basin. 114
Figure 3.7: POC:^{234}Th ratios (µmol.dpm^{-1}) between the small size fraction (SSF) and large size fraction (LSF) at Eq (left) and at 400 m (right). The diagonal black line represents the 1:1 ratio. For the readability of the figure, the error bars of Station 1 are not indicated (errors: LSF=17.2 µmol.dpm^{-1} and SSF=13.8 µmol.dpm^{-1})..... 115
Figure 3.8: Export fluxes of particulate organic carbon (POC), calcium carbonate ($CaCO_3$), biogenic silica (BSi) and particulate aluminum (pAl) at Eq (solid fill) and at 400 m (dashed), from the Iberian Margin (Station 1) to the Newfoundland Margin (Station 77). 118
Figure 3.9: Upper 20 m integrated satellite-derived Chl-a concentrations (black line) from http://giovanni.sci.gsfc.nasa.gov/giovanni/. The pink line represents the sampling period during GEOVIDE and the black stars represent the Chl-a concentration measured in-situ. 124
Figure 3.10: a) POC export fluxes at Eq versus daily primary production (PP) and b) POC export fluxes at Eq versus POC export fluxes at 400 m. For the readability of the figure, the error bars for the POC export fluxes of Station 1 are not indicated (error at Eq=22 mmol.m^{-2}.d^{-1} and at 400 m=10 mmol.m^{-2}.d^{-1}) and Station 26 (error at Eq=6.7 mmol.m^{-2}.d^{-1} and at 400 m=7.3 mmol.m^{-2}.d^{-1}). 130

Chapter 4:

Figure 4.1: Satellite Chlorophyll-a concentrations (MODIS Aqua from http://oceancolor.gsfc.nasa.gov), in mg.m-3 during the GEOVIDE cruise (May and June 2014). Stations are indicated by the diamonds. Colored diamonds indicate the approximate time of sampling..... 147
Figure 4.2: a) Schematic of the circulation features, adapted from Garcia-Ibanez et al., 2015. b) Salinity along the GEOVIDE section, and associated water masses: LSW: Labrador Seawater; ISOW: Iceland Scotland Overflow Water; IcSPMW: Iceland Subpolar Mode Water; SAIW: Sub Arctic Intermediate Water; NACW: North Atlantic Central Waters; MW: Mediterranean Water; DSOW: Danmark Strait Water; NEADW: North East Atlantic Deep Water. Stations in bold correspond to stations where detailed vertical Niskin profiles were collected. 149
Figure 4.3: Barite particles observed by FE-SEM at a) Station 38 (300 m); b) Station 44 (700 m); c and d) Station 69 (600 m). The white arrows indicate the position of barite crystals. 155
Figure 4.4: Section of the particulate biogenic barium (Baxs) in pmol.L^{-1} determined in samples collected with the Go-Flo bottles. Niskin detailed vertical profiles were determined at stations in bold. 157
Figure 4.5: Individual profiles of Baxs concentrations (in pmol.L^{-1}) determined using Niskin bottles from GEOVIDE (squares) and GEOSECS (circles) cruises. 158
Figure 4.6: Total bacterial abundance (cells.µL^{-1}) measured by flow cytometry (J. Laroche, J. Ratten and R. Barkhouse, personal communication). 160
Figure 4.7: Regression of the 100-500 m integrated total bacterial abundance (events.µL^{-1}) versus the 100-500 m DWA Baxs values (pmol.L-1). 161

Figure 4.8: Carbon mesopelagic remineralization fluxes (in mmol $C.m^{-2}.d^{-1}$) at all stations sampled with Niskin bottles, between 100 - 1000 m. Provinces are indicated below the x-axis..... 163
Figure 4.9: Comparison of POC remineralization fluxes from this study (circles lined in black) to remineralization fluxes from literature in the North Atlantic. Note that these studies used different methods for determining remineralization fluxes: moored sediment traps (# symbols, Honjo et al., 2008), onboard incubations (° symbols, Giering et al., 2014; Collins et al., 2015); excess barium proxy (* symbols, Brewer et al., unpublished results)..... 168
Figure 4.10: Time averaged map of Chlorophyll-a concentrations (mg.m-3) over January – June 2014 (monthly 4 km MODIS Aqua model; http://giovanni.sci.gsfc.nasa.gov/). 169
Figure 4.11: Mesopelagic remineralization fluxes (mmol.m-2.d-1) plotted as a function of the corresponding fractions of micro-, nano- and pico-phytoplankton. The black line corresponds to the linear regression between both parameters for all stations except Station 51 (pink triangle)..... 171
Figure 4.12: Bubble plot showing the mesopelagic remineralization flux (mmol.m-2.d-1) and the abundance of the two main phytoplankton communities (diatoms and coccolithophorids, in %) along the GEOVIDE transect. The size of the bubble is proportional to the magnitude of the flux. 173
Figure 4.13: Potential temperature θ - salinity S plots and isopycnals for the Stations a) #44 and #69 and b) #32 and #38 of the GEOVIDE cruise focus on the 50-2000 m depth interval. The concentrations of Baxs are shown by the colored points. LSW: Labrador Sea water; SAIW: Subarctic Intermediate water. 174
Figure 4.14: Global schematic of the biological carbon pump during GEOVIDE in the NAST, NADR and ARCT provinces. Primary production (PP) data from A. Roukaerts and D. Fonseca Batista; particulate organic carbon (POC) export fluxes from Lemaitre et al., in prep.; and POC remineralization fluxes from this study. The dominating phytoplanplankton communities and the stage of the bloom are also indicated. The red numbers are the ratio between PP and mesopelagic remineralization fluxes and indicate the proportion of PP remineralized through the mesopelagic layer..... 177

Chapter 5:

Figure 5.1: Map of the GEOVIDE section in the North Atlantic with the stations (stars) investigated within the North Atlantic Subtropical gyre (NAST) province, the North Atlantic Drift (NADR) province and the Arctic (ARCT) province (Longhurst, 1995). 187
Figure 5.2: Particulate aluminum (pAl) (a); particulate iron (pFe) (b); particulate phosphorus (pP) (c); particulate manganese (pMn) (d); particulate zinc (pZn) (e); particulate cobalt (pCo) (f); particulate cadmium (pCd) (g); particulate cupper (pCu) (h); and particulate nickel (pNi) (i) to ^{234}Th ratios ($nmol.dpm^{-1}$) in the large size fraction (LSF; > 53 µm) along the GEOVIDE transect. 195
Figure 5.3: Particulate trace element export fluxes in $\mu mol.m^{-2}.L^{-1}$ estimated in the large size fraction at the Eq depth (black bars) and at 400 m (grey line). Note the different y-axis scales..... 199
Figure 5.4: Variance of thirteen elemental fluxes determined at Eq at all stations (Test 1), at all stations except Station 1 (Test 2). The description of the components is provided in the text. 202
Figure 5.5: Molar ratios of the trace element over Al fluxes along the GEOVIDE transect determined at Eq. The brown horizontal dashed line represents the ratios determined in the upper continental crust (UCC) by Taylor and Mclennan (1985). Note that the y axis represents the values of the ratios in a logarithmic scale ($mol.mol^{-1}$)..... 204
Figure 5.6: Export fluxes of lithogenic materials (Litho in $mg.m^{-2}.d^{-1}$), Mn oxides (MnO_2 in $mg.m^{-2}.d^{-1}$) and Fe oxides ($Fe(OH)_3$ in $mg.m^{-2}.d^{-1}$) determined at a) Eq and b) 400 m. Negative values have been set to zero..... 206
Figure 5.7: Beam attenuation (%; in blue) and fluorescence (µg/L; in green) profiles of Stations 1 and 64, located near the Iberian and Greenland margins, respectively..... 207
Figure 5.8: (left) Relationships between pCo, pNi,and pCu fluxes versus pMn oxides fluxes ($\mu mol.m^{-2}.d^{-1}$), and (right) relationships between pCo, pNi and pZn fluxes versus pFe oxides fluxes.The grey circles and the black diamonds represent respectively the fluxes estimated at Eq and 400 m. 210
Figure 5.9: Carbon normalized Fe, Mn, Zn, Co, Cu, Cd and Ni molar ratios for export fluxes determined at Eq, from Station 1 (Iberian Margin; right) to Station 77 (Newfoundland Margin; left). The green rectangles indicate the range of intracellular metal stoichiometries presented by Twining et al. (2015), Muggli et al. (1996), Muggli and Harrison (1996) and Sunda and Huntsman (1995 a and b). 213
Figure 5.10: Phosphorus normalized Fe, Mn, Zn, Co, Cu, Cd and Ni molar ratios for export fluxes determined at Eq, from Station 1 (Iberian Margin; right) to Station 77 (Newfoundland Margin; left). The green rectangles indicate the range of intracellular metal stoichiometries presented by Twining and Baines (2013). 214

Figure 5.11: Relationships between pZn, pMn, pFe, pCu, pCo and BSi export fluxes at Eq. In the graph showing pZn and BSi exports, the green dashed line represents the averaged Zn/Si ratio measured in diatom phytoplankton cells (i.e. 2×10^{-4} mol.mol^{-1}; Twining et al., 2004). 217
Figure 5.12: Relationship between pFe, pCo, pMn, pZn and $CaCO_3$ export fluxes at Eq. 220

Chapter 6:

Figure 6.1: Surface Chlorophyll-a concentrations (mg.m^{-3}) at the beginning (19/10/2011) and at the end (17/11/2011) of the KEOPS2 cruise. Filled circles represent the location of stations. The station F-L, represented by a dotted circle, was sampled between these two dates (06/11/2011). The thick dotted line represents the approximate location of the Polar Front while the thick black arrows indicating the Antarctic Circumpolar Current (ACC) and the Fawn Trough Current (FTC; adapted from Park et al., 2008)..... 234
Figure 6.2: Vertical profiles of BSi, PN (µmol.L^{-1}) and PFe (nmol.L^{-1}) concentrations for the different stations. 244
Figure 6.3: Vertical profiles of elemental ratios of a) BSi:^{234}Th, b) PN:^{234}Th, c) PFe:^{234}Th. Large (> 53 µm) particles are represented by filled symbols while small particles (1-53 µm) are represented by open symbols. PFe concentrations for small particles are discussed in van der Merwe et al. (2015), PN concentrations for small particles can be found in Table S2. Sediment trap ratios (from Laurenceau et al., 2015; Bowie et al., 2015) at 200 m are represented by thick black surrounded symbols. Bottom depths are indicated by the zebra lines and Eq depths are indicated by the light green lines. 246
Figure 6.4: Elemental ratios of PN, BSi and PFe to ^{234}Th for the >53 µm size fraction calculated at the Eq depth using different interpolation/averaging methods being: linear interpolation; average around Eq; power interpolation; depth-weighted average. The ratios obtained from sediment traps are also indicated with the BSi:^{234}Th and PN:^{234}Th ratios from Laurenceau et al. (2015) and the PFe:^{234}Th ratios from Bowie et al. (2015). 249
Figure 6.5: Range of calculated PN, BSi (mmol.m^{-2}.d^{-1}) and PFe (µmol.m^{-2}.d^{-1}) export fluxes at the Eq depth from in-situ pumps (box plots) and export fluxes obtained by sediment traps at 200 m (circles; Laurenceau et al., 2015 and Bowie et al., 2015) during KEOPS2. The heights of the boxes correspond to the lowest and the highest values determined by the 4 different interpolation/averaging methods. The plain line inside the box represents the median value. 252
Figure 6.6: Vertical profiles of BSi:POC, BSi:PN, BSi:PFe and POC:PN molar ratios in large particles (> 53 µm) collected in the Kerguelen area. Close to the surface, green surrounded symbols represent Si:C ratios specific to diatoms as reported by Lasbleiz (2014). These ratios were obtained from the carbon biomass and the BSi concentration. The latter may be overestimated by taking into account the living and dead cells. At 200 m, ratios measured in sediment traps by Laurenceau et al. (2015) and Bowie et al. (2015) are represented by the black surrounded symbols. The dashed line represents the typical value of the C:N ratio (6.6) reported by Redfield et al. (1963). 260
Figure 6.7: POC versus PN fluxes (mmol.m^{-2}.d^{-1}) for all stations..... 262
Figure 6.8: Schematic of the main variations of export fluxes determined in this study, in line with other parameters studied during KEOPS2 cruise, including ThE_{PN} , ThE_{BSi}, estimated POC (grey circles), PN (white squares), BSi (grey stars; mmol.m^{-2}.d^{-1}), and PFe (orange triangles; µmol.m^{-2}.d^{-1}) export fluxes. PN export fluxes are multiplied by 6.6 to examine directly the variations of the C:N Redfield ratio. [a] primary production data (mmol C.m^{-2}.d^{-1}) from Cavagna et al. (2015). [b] dFe concentrations (nmol.L^{-1}) from Quéroué et al. (2015). [c] N uptake data (mmol N.m^{-2}.d^{-1}) from Cavagna et al. (2015). [d] Si uptake data (mmol Si.m^{-2}.d^{-1}) from Closset et al. (2014). [e] total mesozooplankton biomass data (g C.m^{-2}) from Carlotti et al. (2015). [f] bacterial respiration rates (µmol C.L^{-1}.d^{-1}) from Christaki et al. (2014). [g] taxonomic data from Lasbleiz et al. (2016). [h] POC export fluxes (mmol.m^{-2}.d^{-1}) from Planchon et al. (2015). 264

Table of tables

Chapter 1:

Table 1.1: Common metalloproteins present within marine phytoplankton and associated functions (from Twining and Baines, 2013). 38

Chapter 2:

Table 2.1: Ranges, blanks and detection limits of POC (µmol) during GEOVIDE sample runs.....63
Table 2.2: Determined concentrations (mg.kg^{-1}) and resulting recoveries (%) of the Certified Reference Material plankton BCR-414, compared to certified or indicative (*) values, analyzed by HR-ICP-MS. .66
Table 2.3: Determined concentrations (µg.g^{-1}) and resulting recoveries (%) of the Certified Reference Material plankton BCR-414, compared to indicative values, analyzed by ICP-AES.....66
Table 2.4: Ranges, blanks and detection limits of BSi (µmol) in large and small particles collected during GEOVIDE. 68
Table 2.5: Determined concentrations and resulting recoveries of the certified reference materials SLRS-5 (river water), BHVO-1 (basalt powder), JB-3 (basalt powder) and JGb-1 (gabbro powder) 71

Chapter 3:

Table 3.1: Determined concentrations (µg.g-1) and resulting recoveries (%) of the Certified Reference Material plankton BCR-414, compared to indicative values (n=5). 101
Table 3.2: Comparison of the POC export fluxes as determined using the POC:^{234}Th ratios in large (> 53 µm) and small particles (1-53 µm)..... 116
Table 3.3: POC (particulate organic carbon), BSi (biogenic silica), $CaCO_3$ (calcium carbonate) and pAl (particulate aluminum) export fluxes (in mmol.m^{-2}.d^{-1} or µmol.m^{-2}.d^{-1}) obtained by multiplying the ^{234}Th export flux with the Element to ^{234}Th ratio of large (>53 µm) particles (see text for details). These fluxes were integrated between surface and Eq, where total ^{234}Th returns to equilibrium with ^{238}U, and at 400 m..... 120
Table 3.4: Comparison of POC export flux, POC export efficiency (POC flux at Eq / PP) and transfer efficiency (POC flux at 400 m / POC flux at Eq) in the North Atlantic with literature data. 123

Chapter 4:

Table 4.1: Particulate barium (Ba) and aluminum (Al) concentrations and resulting recoveries (the bold and italic percentages) of the certified reference materials SLRS-5 (river water), BHVO-1 (basalt powder), JB-3 (basalt powder) and JGb-1 (gabbro powder)..... 151
Table 4.2: Depth-weighted average (DWA) values of mesopelagic Baxs (pmol.L^{-1}) and resulting Baxs-based mesopelagic POC remineralization rates (mmol C.m^{-2}.d^{-1}) integrated between 100-500 m and 100-1000 m depths. The biogeochemical provinces defined by Longhurst et al. (1995) are also indicated: NAST: North Atlantic subtropical gyre; NADR: North Atlantic drift; ARCT: Atlantic Arctic. 162
Table 4.3: Comparison of the Baxs inventory (pmol.L^{-1}) and related-carbon mesopelagic remineralization fluxes (mmol.m^{-2}.d^{-1}) obtained in the world's ocean. 165
Table 4.4: Comparison of the mesopelagic POC remineralization fluxes (Remineralization) with primary production (PP) and POC export fluxes in the upper water column (Export). All fluxes are expressed in mmol C.m^{-2}.d^{-1}. [1] PP data from A. Roukaerts, D. Fonseca Batista and F. Deman (unpublished data); [2] EP data from Lemaitre et al., in prep..... 175

Chapter 5:

Table 5.1: Measured particulate trace element concentrations (in mg.kg^{-1}) and resulting recoveries (in %) of the certified reference material plankton BCR-414 compared to the certified or indicative (*) values (n=5). 190
Table 5.2: pFe, pMn, pCo, pNi, pCu, pZn, pCd, pAl and pP export fluxes (in µmol.m^{-2}.d^{-1} or nmol.m^{-2}.d^{-1}) obtained by multiplying the ^{234}Th export flux with the Element to ^{234}Th ratio of large (>53 µm) particles. These fluxes were integrated between surface and Eq, where total ^{234}Th returns to equilibrium with ^{238}U, and at 400 m using a linear interpolation (see text for details)..... 200

Chapter 6:

Table 6.1: Determined concentrations (µg.g-1) and resulting recoveries (%) of the Certified Reference Material plankton BCR-414, compared to certified or indicative (*) values. Three replicates of BCR-414 were digested then analyzed during different ICP-MS sessions. 238
Table 6.2: Mixed layer depth (MLD), depth of the maximal ^{234}Th export (i.e., "Eq"; Planchon et al., 2015), range of Element:^{234}Th ratios calculated with the different interpolation methods (µmol.dpm^{-1} for PN and BSi:^{234}Th; nmol.dpm^{-1} for PFe:^{234}Th) and corresponding ranges of elemental export fluxes estimated at Eq (mmol.m^{-2}.d^{-1} for PN and BSi fluxes; µmol.m^{-2}.d^{-1} for PFe fluxes). The median value (med.) is also indicated. Determination of BSi and PN export efficiencies were based on Si-uptake (Closset et al., 2014) and total N-uptake rates (Cavagna et al., 2015) in water column integrated from surface to 1% of surface Photosynthetically Active Radiation. Whenever possible, element:^{234}Th ratios and export fluxes are compared to fluxes estimated from sediment traps (P-trap; Laurenceau et al., 2015; Bowie et al., 2015). POC:^{234}Th ratios, POC export fluxes and efficiencies (from Planchon et al., 2015) are also indicated. 250
Table 6.3: Comparison of reported ranges for particulate POC, PN, BSi, PFe concentrations and export fluxes in the Southern Ocean. 255

Chapter 7:

Table 7.1: POC export fluxes and efficiencies (ThE POC), BSi and pFe export fluxes, primary production (PP), POC mesopelagic remineralization and the main biogeochemical features (bloom stage, limitation, phytoplankton communities) observed during KEOPS1 (Kerguelen Island, austral summer), KEOPS2 (Kerguelen Island, austral spring) and GEOVIDE (North Atlantic, boreal spring). Data from (Cavagna et al., 2015; Jacquet et al., 2015, 2008; Planchon et al., 2015; Savoye et al., 2008; A. Roukaerts, D. Fonseca Batista and F. Deman (unpublished data). 278

Abbreviations

ARCT: Arctic province

Ba_{xs}: particulate biogenic barium, also called excess barium

BSi: Biogenic silica

$CaCO_3$: calcium carbonate

cpm: Counts per minute

dpm: Disintegration per minute

DIC: Dissolved inorganic carbon

DOC: Dissolved organic carbon

EP: Export production

Eq: Equilibrium depth corresponding to the depth where total ^{234}Th returns to equilibrium with ^{238}U

Ez: Euphotic zone

HNLC: High nutrient – low chlorophyll

ICP-AES: Inductively-coupled plasma atomic emission spectroscopy

ICP-MS: Inductively-coupled plasma mass spectrometer

ISP: *In-situ* pump

LSi: Lithogenic silica

Milli-Q water: Ultra-pure deionized water with conductivity of 18.2 $M\Omega.cm^{-1}$

MR: Mesopelagic remineralization

NADR: North Atlantic Drift province

NAST province: North Atlantic Subtropical province

PAR: Photosynthetically active radiation

ppm: part per million

PPZ: Primary production zone

P-trap: sediment trap

PN: Particulate nitrogen

POC: Particulate organic carbon

PP: Primary production

pTEs: Particulate trace elements

pAl: particulate aluminium

pCd: particulate cadmium

pCo: particulate cobalt

pCu: particulate cupper

pMn: particulate manganese

pNi: particulate nickel

pP: Particulate phosphorus

pZn: particulate zinc

RSD: Relative standard deviation (standard deviation / average)

TEP: Transparent exopolymer particles

^{234}Th: Naturally-occurring isotope of thorium, produced in-situ from ^{238}U

^{238}U: the most abundant isotope of uranium

Acknowledgements

J’ai entendu parler pour la première fois de chimie marine sur le marché de Locquirec. Catherine, tu as réussi à me transmettre ta passion, merci ! Mon intérêt pour la chimie marine a ensuite été confirmé pendant mes stages avec Emilie, Germain, et Catherine, qui par leur optimisme et leur pédagogie, m’ont décidé à me lancer dans cette voie. Toutes ces expériences m’ont donné l’envie, la motivation et la curiosité de m’intéresser scientifiquement à l’océan : Merci à vous !!

Aujourd’hui, après trois ans et quelques mois de thèse, je suis toujours passionnée par l’océan et curieuse par tout ce qu’il y a encore à apprendre et comprendre ! Je pense qu’une partie de cet enthousiasme vient de l’énergie et de l’état d’esprit de mes superviseurs, Hélène, Fred, Frank et Géraldine, qui sont passionnés et extrêmement actifs dans un large domaine de l’océanographie. Je vous remercie énormément pour vos encouragements, vos nombreux conseils (professionnels mais aussi personnels), votre sympathie et votre enthousiasme tout au long de cette thèse. Merci d’avoir cru en moi, de m’avoir fait partager toutes vos connaissances, de m’avoir aidée du début à la fin, de m’avoir remotivée et donné confiance quand ça n’allait pas trop et d’avoir, avec une grande patience, répondu à toutes mes questions même quand la même question revenait à quelques jours/mois d’intervalle ! J’ai vraiment apprécié travailler avec vous et j’espère que cette fin de thèse n’est que le début de nombreuses futures collaborations.

Je tiens à remercier les membres de mon jury : Frédéric Le Moigne et Ian Salter, mes rapporteurs, pour avoir lu mon manuscrit avec intérêt et pour m’avoir donné de précieux conseils tant après la lecture du manuscrit qu’au travers des discussions pendant la

soutenance ; Lionel Guidi, Filip Meysman et Stéphane Blain, mes examinateurs, pour les discussions, commentaires et conseils qu'ils ont apportés le jour de la soutenance.

Ces trois années et quelques mois de thèse ont été le résultat d'un travail que j'ai adoré mais aussi de superbes rencontres, d'apprentissage, de partage et de découvertes. La thèse ça a aussi été du stress, puis du soulagement, quelques larmes et d'énormes fous rires, des remises en questions et des moments d'excitation en acquérant les données. Ça a aussi été des voyages, entre la Bretagne, la Belgique, les iles Hawaïennes, Lisbonne, le Groenland, Terre Neuve, Prague, Londres, la Nouvelle-Orléans… Un immense merci à toutes celles et ceux qui de près ou de loin ont partagé tous ces moments avec moi.

Je commencerais par les bretons. Tout d'abord, je voudrais remercier l'équipe du LEMAR à l'IUEM pour m'avoir donné les moyens de réaliser mon travail. Je remercie les secrétaires du LEMAR Gene, Anne-So et Yves, les secrétaires du Labex-Mer Nadine et Céline et la secrétaire de l'EDSM Elisabeth, pour leur grande aide toujours avec un grand sourire et dans la bonne humeur. Merci à Manon, Emilie et Morgane pour m'avoir aidée dans les labos, et pour avoir toujours fait marcher le Technicon ! Merci aussi à l'équipe du PSO : Claire, Céline, Marie-Laure, Philippe, Kévin et aussi Manu et Yohan pour m'avoir laissée travailler dans les salles blanches, et pour m'avoir appris à comment acquérir de belles données par ICP-MS/AES ! Merci à mes coloc et amis de bureau: Coraline, Aurélie, Romain, Pierre-Amaël et Guillaume pour m'avoir appris plein de choses sur la vie après-thèse, m'avoir fait relativiser les choses et pour les gros papotages et rigolades qui font du bien ! Un grand merci à tous les copains du LEMAR et en particulier à Manon, Julia (aussi surnommées les Shakira bombass), Thomas et Gaspard pour leur aide et toutes ces discussions sur le travail, la vie, Kelly Slater, le yoga (que je ne comprenais pas encore à l'époque où je vous entendais en parler) mais aussi pour avoir supporté l'En Avant Guingamp au moins une fois, la découverte du citrate de bétaïne (accompagné de pain beurre pour encore mieux récupérer), pour ce voyage incroyable à Hawaii avec le Aloha spirit (ou celui de Sean Paul) mais aussi pour avoir toujours été là pour

m'accueillir à Brest ou à Locmaria ; Marie Cheize pour m'avoir remonté le moral quelques fois, m'avoir donné plein de conseils et pour toutes ces discussions en salle blanche ; et j'ai aussi une grosse pensée pour Fabien, Violette, Rachel, Jill, Nathalie, Malwenn, Camille, Manon T., Arthur, Aridane, Jorge, Nina, Lucille, Lauriane, Ewan, Marie Czam, Seb.

Dank U wel aan iedereen in België! I did not learn much about Flamish and I am still mixing «Smakelijk» and «Alsjeblieft», so I will continue in English (but with my French accent, of course!). First, I would like to thank the AMGC team, at the VUB, for their support and their hospitality. Thanks to David (Allez Anderlecht!), Claire and Martine for their great help and explanations in the lab and with the analytical machines. Thanks also to my work mates, Emilie and Audrey who welcomed me with lots of energy and who taught me the belgium style ; Christina who explained many many things to me, who always adviced me and often helped me to improve my English!

Special thanks to my friends of the « seawater group »: Debany, Arnout, Florian, François and Natacha. It was great to work but also to share these moments with all of you. Thank you for welcoming me at the middle of my PhD, for the help with the administration (even when I was super stressed because I lost some papers), to have discovered me the best beers and meals. I would like also to thank the geologists, the people of the 7th floor, and also my great flatmates. I really liked my Belgium life thanks to all of you!

Toujours en Belgique, j'aimerais remercier Luc André et plus particulièrement Laurence Monin au Musée Royal d'Afrique Centrale de Tervuren, pour m'avoir accueillie dans leur laboratoire pendant quelques mois et m'avoir fourni tout le matériel et l'aide dont j'avais besoin.

J'aimerais aussi remercier l'ensemble de la GEOVIDE team ! Ma première campagne a tout simplement été géniale sur le plan scientifique avec tous ces beaux résultats, mais aussi sur le plan humain avec de belles amitiés et de très (très !) belles rencontres.

Eskerrik asko Maxi ! Tu as dû te faire au pain beurre demi-sel, aux pauses BD où je voulais rester seule et à mes moments ronchons lorsque je ne dormais pas assez, mais tu n'as pas lâché et nous voilà maintenant ensemble en Suisse ! Merci de m'avoir toujours chouchoutée, soutenue, aidée et de m'avoir fait devenir un peu plus « sudiste » !

Un immense merci à ma famille qui m'a toujours soutenue ! Papa, Maman et Maëlenn, vous m'avez toujours écoutée et vous avez toujours trouvé les mots pour me redonner confiance !

Et pour tellement plus, merci !

Abstract

The main objective of this thesis is to improve our understanding of the different controls that affect the oceanic biological carbon pump. Particulate export and remineralization fluxes were investigated using the thorium-234 (^{234}Th) and biogenic barium (Ba_{xs}) proxies.

In the North Atlantic, the highest particulate organic carbon (POC) export fluxes were associated to biogenic (biogenic silica or calcium carbonate) and lithogenic minerals, ballasting the particles. Export efficiency was generally low (< 10%) and inversely related to primary production, highlighting a phase lag between production and export. The highest transfer efficiencies, i.e. the fraction of POC that reached 400m, were driven by sinking particles ballasted by calcite or lithogenic minerals.

The regional variation of mesopelagic remineralization was attributed to changes in bloom intensity, phytoplankton cell size, community structure and physical forcing (downwelling). Carbon remineralization balanced, or even exceeded, POC export, highlighting the impact of mesopelagic remineralization on the biological pump with a near-zero, deep carbon sequestration for spring 2014.

Export of trace metals appeared strongly influenced by lithogenic material advected from the margins. However, at open ocean stations not influenced by lithogenic matter, trace metal export rather depended on phytoplankton activity and biomass.

A last part of this work focused on export of biogenic silica, particulate nitrogen and iron near the Kerguelen Island. This area is characterized by a natural iron-fertilization that increases export fluxes. Inside the fertilized area, flux variability is related to phytoplankton community composition.

Key words: oceanic biological pump, export, remineralization, carbon, trace elements, biogenic silica, calcium carbonate

Résumé

L'objectif principal de cette thèse est de mieux comprendre les différents facteurs contrôlant la pompe biologique de carbone en Atlantique Nord et dans l'Océan Austral, à proximité des îles Kerguelen, en utilisant notamment deux approches: le Thorium-234 (^{234}Th) et le baryum biogénique (Ba_{xs}).

En Atlantique Nord, les flux d'export de carbone organique particulaire (POC) augmentent lorsqu'ils sont associés à des minéraux biogéniques (silice biogénique et carbonate de calcium) et lithogènes, capable de lester les particules. L'efficacité d'export, généralement plus faible que précédemment supposé (< 10%), est inversement corrélée à la production, soulignant un décalage temporel entre production et export. La plus forte efficacité de transfert, i.e. la fraction de POC atteignant 400m, est reliée à des particules lestées par du carbonate de calcium ou des minéraux lithogènes.

Les flux de reminéralisation mésopélagique sont similaires ou parfois supérieurs aux flux d'exports et dépendent de l'intensité du développement phytoplanctonique, de la structure en taille, des communautés phytoplanctoniques et des processus physiques (advection verticale).

Comme observé pour le POC, l'export des éléments traces est influencé par les particules lithogènes provenant des marges océaniques, mais aussi des différentes espèces phytoplanctoniques.

Dans l'Océan Austral, la zone à proximité de l'île de Kerguelen est naturellement fertilisée en fer, augmentant les flux d'export de fer, d'azote et de silice biogénique. Il a été démontré que la variabilité des flux dépendait des communautés phytoplanctoniques dans la zone fertilisée.

Mots clés: pompe biologique océanique, export, reminéralisation, carbone, éléments traces, silice biogénique, carbonate de calcium

Samenvatting

De werking van de biologische koolstofpomp in de noordelijke Noord Atlantische Oceaan en in de zone aangrenzend aan Kerguelen eiland in de Sub-Antarctische Zuidelijke Oceaan werd bestudeerd.

Er werd deelgenomen aan een campagne in de Noord Atlantische Oceaan waarbij een transect tussen Portugal en Newfoundland bemonsterd werd (GEOTRACES GA01; GEOVIDE, Mei-Juni 2014). Dit terreinwerk bood een ideale gelegenheid om de export van fotosynthetisch aangemaakt organisch koolstof, stikstof, silicium en een aantal sporeëlementen uit de oppervlakte oceaan naar de diepzee, alsook het heroplossen van deze elementen, te bestuderen door gebruik van de thorium-234 en biogeen barium proxies.

De Noord Atlantische Oceaan wordt gekenmerkt door een recurrente algenbloei die een flux van biogene deeltjes naar de diepzee ondersteunt. De export van particulair organisch koolstof (POC) was het grootst in het westelijke Europese bekken en in de Labrador Zee, en bleek gerelateerd aan de aanwezigheid van biogene deeltjes zoals opaal en calcium carbonaat, maar ook van lithogene deeltjes, componenten die een ballast effect uitoefenen tijdens de bezinking van partikels. Daar dit ballast effect kleiner is voor opaal dan voor calcium carbonaat wordt de exportefficiëntie van POC naar de diepzee mede bepaald door de samenstelling van het fytoplankton. De export uit de eufotische zone bleef algemeen echter vrij laag (<10% van de primaire productie) en bleek zelf geanticorreleerd met lokale primaire productie, wat niet enkel duidt op een fase-shift van koolstofproductie en -export, maar eveneens op het feit dat de biopomp in de Noord Atlantische Oceaan niet zo efficiënt werkt als eerder gedacht. De grootste POC transfer efficiënties naar dieptes > 400m werden waargenomen met calcium carbonaat en lithogeen materiaal als ballast. Export van sporemetalen (Fe, Zn, Mn) bleek, zoals vastgesteld voor POC, sterk beïnvloed door de aanwezigheid van lithogeen materiaal aangevoerd vanaf kontinentale hellingen. Voor open oceaan sites echter, is de activiteit en biomassa van fytoplankton een belangrijke factor die de export van sporemetalen stuurt. Remineralisatie in de mesopelagische waterkolom varieerde aanzienlijk, te wijten aan

intensiteit van de bloei, samenstelling van de fytoplanktongemeenschap en cel grootte, alsook heersende hydrodynamische condities. Mesopelagische remineralisatie van POC bleek, in tegenstelling tot de verwachting, even groot en in sommige gevallen zelfs groter dan de POC export flux. Dit kan verklaard worden door het feit dat bij de bepalingen van primaire productie en remineralisatie, deze processen over verschillende tijdsschalen geïntegreerd worden. Algemeen echter duiden onze waarnemingen op het grote belang van het remineralisatieproces als onderdeel van de biopomp, waarbij blijkt dat tijdens de lente 2014 haast geen organisch koolstof uitgevoerd werd naar de diepzee.

Eveneens werd de werking van de biopomp in de nabijheid van Kerguelen eiland bestudeerd, een gebied dat op natuurlijke wijze gefertiliseerd wordt met ijzer (Zuidelijke Oceaan; KEOPS2 expeditie; zuidelijke hemisfeer lente 2011). Deze natuurlijke fertilisatie ondersteunt een recurrente algenbloei die zich tot 1000 km stroomafwaarts van het eiland uitstrekt. Fe-fertilisatie leidt tot verhoogde export van POC, particulair stikstof, opaal, en particulair Fe, waarbij de samenstelling van de fytoplanktongemeenschap een belangrijke sturende factor is.

Dit werk is één van de eerste waarbij zowel export als remineralisatie bestudeerd werden in de Noord Atlantische Oceaan. Hierdoor vormt het een referentie voor toekomstige studies van de biologische pomp in dit gebied. Een bijkomende originaliteit van het werk betreft de vergelijkende studie van de biopomp werking in een Sub-Arctisch en een Sub-Antarctisch system

Sleutelwoorden: biologische koolstofpomp, export, remineralisatie, koolstof, sporeëlementen, biogeen silicium, calcium carbonaat

Chapter 1

General Introduction

1.1. The Carbon cycle

1.1.1. Global carbon cycle

The global carbon cycle is a biogeochemical cycle involving carbon exchanges between land, atmosphere, and ocean (Figure 1.1). These reservoirs are characterized as sources or sinks for atmospheric CO_2 and any shifts in the cycle can result in temperature changes on Earth (e.g. Cox et al., 2000).

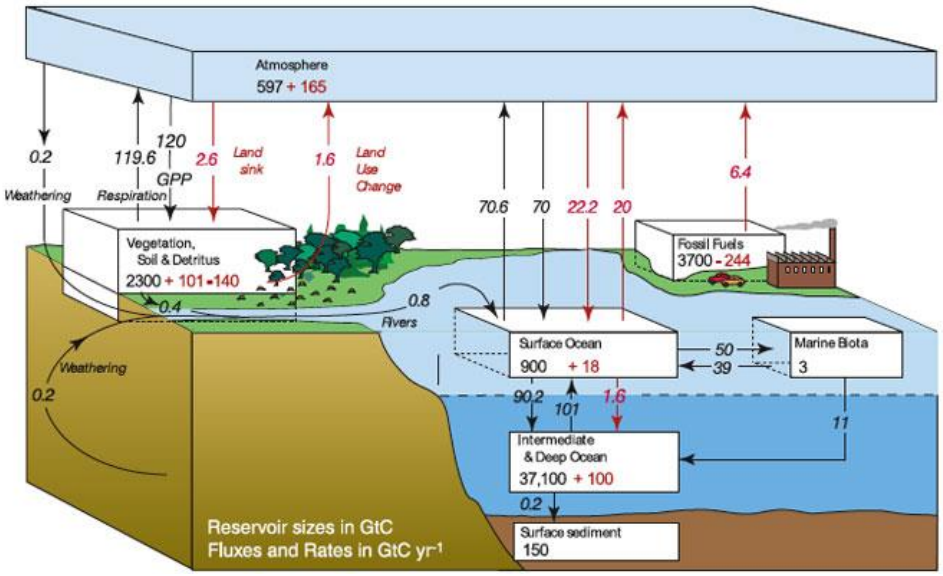

Figure 1.1: The global carbon cycle. Arrows represent the fluxes in gigatons of carbon per year and the boxes represent the reservoirs in gigatons of carbon. Black values are natural fluxes and red are anthropogenic contributions (Diagram from http://www.ipcc.ch/, modified from (Sabine et al., 2004; Sarmiento, 2002).

Since the beginning of the industrial revolution in the 19th century, CO_2 concentrations in the atmosphere have dramatically increased from 277 ppm (Joos and Spahni, 2008) to 404 ppm in November 2016, recently recorded at Mauna Loa station (Hawaii, USA; https://www.co2.earth/). This increase is mainly caused by fossil fuel combustion, cement manufacturing and changes in land use (Crowley, 2010). About 29% of this anthropogenic CO_2 emission is absorbed by terrestrial biosphere and 26% by ocean (Le Quéré et al., 2015, 2009). The ocean's heat capacity is about 1,000 times larger than that of the atmosphere, and the oceans net heat uptake since 1960 is around 20 times greater than that of the atmosphere

(Levitus et al., 2005). This large amount of heat, which is mainly stored in the upper layers of the ocean, can be transported by ocean currents inducing an important effect on regional climates. At a global scale, the large-scale Meridional Overturning Circulation (MOC; also referred to as thermohaline circulation) induces variations at seasonal to decadal time scales (e.g., Vellinga and Wood, 2002). Life in the sea is dependent on the biogeochemical status of the ocean and is also influenced by changes in the physical state and circulation. Changes in ocean biogeochemistry can directly feed back to the climate system, for example, through changes in the uptake or release of radiatively active gases such as carbon dioxide. The ocean is thus a primordial reservoir to investigate in order to better understand the global carbon cycle (Figure 1.1) as it strongly participates to the CO_2 regulation.

1.1.2. Marine carbon cycle

The ocean is the major carbon reservoir (Figure 1.1), storing ~ 38 Teratones of carbon, under four chemical forms, namely dissolved inorganic carbon (DIC), dissolved organic carbon (DOC), particulate inorganic carbon (PIC) and particulate organic carbon (POC) resulting in a complex internal cycle as shown in Figure 1.2. Exchanges with the atmosphere are a key component of the marine carbon cycle and are promoted by the high solubility of gaseous CO_2 in the surface ocean. This gas exchange depends on many factors such as biology, temperature, wind speed, precipitation, waves or sea-ice cover (Nightingale et al., 2000; Shutler et al., 2016; Wanninkhof and McGillis, 1999; http://www.esa.int/spaceinvideos/Videos/2016/02/Carbon_flux) and aqueous CO_2 in the surface ocean can exchange back to the atmosphere. More importantly, aqueous CO_2 can also undergo various transformations that contribute to its redistribution into the ocean interior.

This carbon redistribution occurs on different timescales.

The fast marine carbon cycle represents a rapid CO_2 interchange between the surface ocean and the atmosphere (time scales of days; Heinze et al., 2015), and is mediated through phytoplankton photosynthesis. A fraction of the organic matter produced by this process can

be then consumed by zooplankton or bacteria and the respired carbon can return to the atmosphere. Another short term exchange of carbon between ocean and atmosphere results from the diffusion of CO_2 across the air-sea interface, in both directions (timescale of minuts)

The thermohaline circulation, can store carbon for centuries (Kuhlbrodt et al., 2007; IPCC Report, 2007) as dissolved CO_2 in the surface ocean is transferred to the deep ocean via the subduction of dense water masses in high latitudes and stays in the deep ocean for years to centuries before the water is mixed back to the surface where warmer waters release the CO_2 back to the atmosphere.

Finally, the long-term marine carbon cycle is regulated by the quantity of particulate organic carbon reaching the sediments. Only a minor fraction of this organic matter, produced in surface waters, is buried in the deep-sea sediments over geological timescales (million years; IPCC Report, 2007; Heinze et al., 2015).

Four ocean carbon pumps are recognized to deplete the ocean surface of carbon relative to the deep ocean: the solubility pump, the biological pump, the carbonate pump and the recently proposed microbial pump (Honjo et al., 2014; Jiao et al., 2010; Legendre et al., 2015; Sarmiento, 2002; Sigman and Boyle, 2000; Turner, 2015; Volk and Hoffert, 1985).

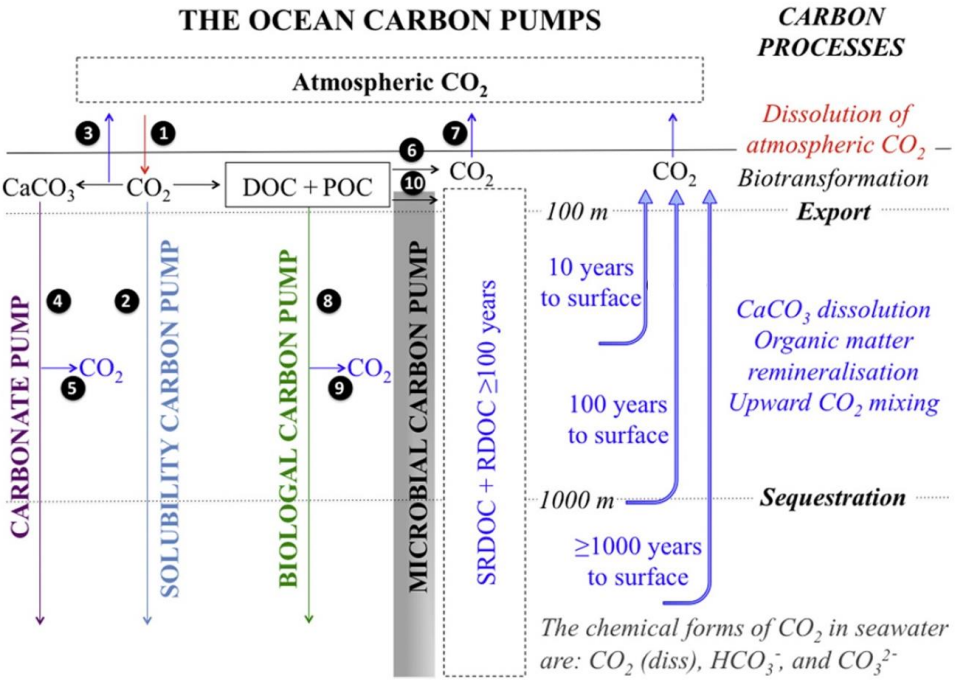

Figure 1.2: The four ocean carbon pumps: The solubility pump, i.e., the dissolution of atmospheric CO_2 in surface waters (**1**), followed by deep mixing of the CO_2-rich water and sequestration (**2**); The carbonate pump, i.e., the bio-precipitation of $CaCO_3$ (or PIC) in the upper water column which is accompanied by the release of CO_2 (**3**), followed by the sinking of bio-mineral particles to depth where their carbon is sequestered (**4**); The biological pump, i.e., the photosynthetic uptake of carbon by phytoplankton and its transformation by the food web in the euphotic zone, including respiration (6) and loss to the atmosphere (**7**), followed by transfer of particulate organic carbon (POC) into deep waters where it is sequestered (**8**). During the downward transit from 100 to 1000m, CO2 is released in the water column by dissolution of part of sinking $CaCO_3$ (**5**) and remineralization of part of the POC that is transferred to depth (**9**). The production of recalcitrant DOC (RDOC) and semi-refractory DOC (SRDOC) with a life time ≥ 100 years (i.e., $DOC_{>100}$) presumably by microbial activity, will sequester ocean carbon because their lifetimes are ≥ 100 years (**10**). The small numbers in full circles identify arrows in the figure. (Modified from Legendre et al., 2015).

1.1.2.1. The solubility pump

The solubility pump starts with the dissolution of atmospheric CO_2 into seawater which is the difference between the fugacity of CO_2 in the seawater and the atmosphere. The disequilibrium between oceanic and atmospheric CO_2 is shown in Figure 1.3 representing the CO_2 partial pressure difference across the air-sea interface (ΔpCO_2). ΔpCO_2 indicates if CO_2 is absorbed into the ocean from the atmosphere (under-saturation, negative values) or if CO_2 is released from the ocean to the atmosphere (over-saturation, positive values).

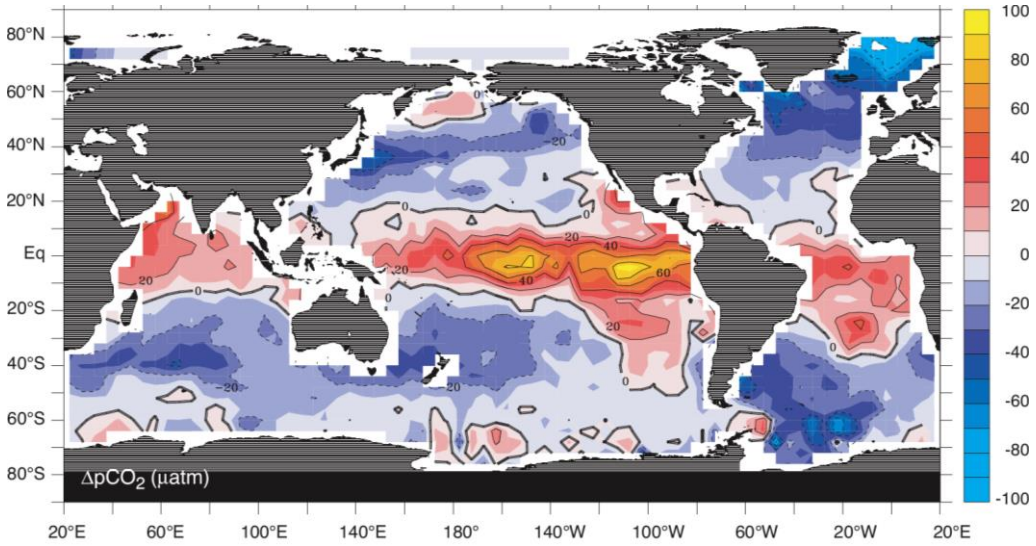

Figure 1.3: Global map of annual sea to air CO_2 exchanges (in µatm; Sarmiento and Gruber, 2006).

The atmospheric gaseous CO_2 is dissolved and transformed into DIC within the surface ocean (right part of Figure 1.2): it becomes aqueous and is transformed in carbonic acid (H_2CO_3), itself in equilibrium with carbonate (CO_3^{2-}) and bicarbonate (HCO_3^-) ions (Equation 1.1). This last form is the most abundant in seawater, representing more than 94% of total DIC (Equation 1.2). In parallel, we can note that CO_2 absorption increases the ocean acidity by adding H^+ ions in solution. Indeed, sea surface pH increased by about 0.1 pH units since the beginning of the industrial revolution (Caldeira and Wickett, 2003).

$$CO_2\,(g) + H_2O \leftrightarrow CO_2\,(aq) + H_2O \leftrightarrow H_2CO_3 \leftrightarrow H^+ + HCO_3^- \leftrightarrow 2H^+ + CO_3^{2-} \quad \text{(Equation 1.1)}$$

$$CO_2\,(aq) + H_2O + CO_3^{2-} \rightarrow 2\,HCO_3^- \quad \text{(Equation 1.2)}$$

At high latitudes, where temperature is low and CO_2 is more soluble (Figure 1.3), the DIC can be transferred to the deep ocean through deep water formation. The depth at which DIC is transported via the circulation is important as the DIC can be sequestered by ocean, i.e. not exchangeable with atmosphere, for longer time scales, from weeks in surface to centuries at 3000 m depth.

1.1.2.2. The biological pump

In 1934, Redfield noticed that the growth, sinking and remineralization of phytoplankton generate a difference of carbon concentrations between surface and deep waters. This difference was named “soft-tissue carbon pump” by Volk and Hoffert (1985) better known nowadays as the biological carbon pump (BCP). The biological pump is a suite of biologically mediated processes (left part of Figure 1.2) that consist of surface production and subsequent sinking and remineralization of organic matter (Figure 1.4). These steps are described in details in section 1.2.1.

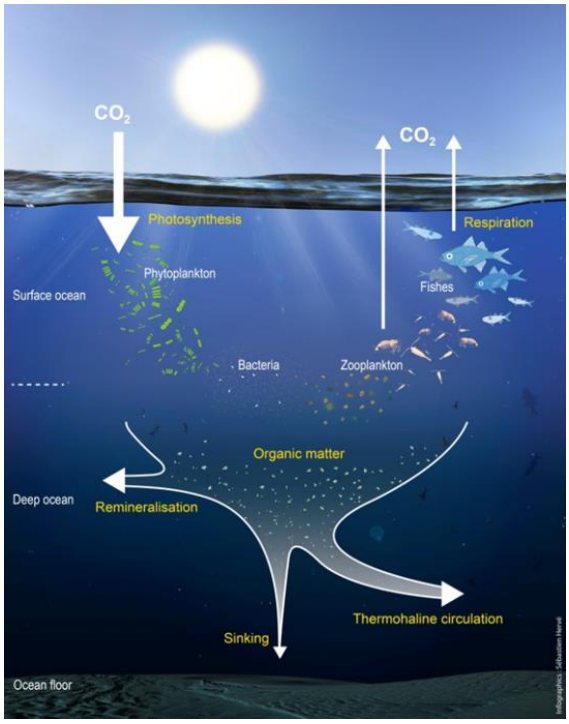

Figure 1.4: Simplified view of the biological carbon pump (S. Hervé, IUEM).

In surface waters, phytoplankton assemblages take up nutrients and DIC during photosynthesis and convert it into particulate organic matter (POM) and biomineral compounds (calcium carbonate, also named calcite - $CaCO_3$, for coccolithophores or biogenic silica, also named opal – BSi, for diatoms). Photosynthesis is a reductive chemical reaction transforming CO_2 and H_2O into organic molecules (e.g. sugars; Equation 1.3).

$$6CO_2 + 6H_2O + \text{light} \rightarrow C_6H_{12}O_6 + 6O_2 \quad \text{(Equation 1.3)}$$

This carbon fixation, also defined as primary production (PP) in surface waters, produces particulate organic carbon (POC) which can then be exported to the deep ocean through the sinking of organic particles.

This organic matter can be consumed by zooplankton through grazing, which then excretes fecal pellets and DOC. POC can also be remineralized from the particulate to the dissolved phase, and oxidized from the organic to the inorganic form (DIC) through bacterial activity or zooplankton respiration. If this remineralization occurs in the surface ocean, the released CO_2 can be then transferred back to the atmosphere.

As a result, only a small fraction of POC (< 0.1 Pg C.year^{-1}) reaches the seabed, trapping the carbon for thousands to hundreds of thousand years (Sabine and Feely, 2007).

1.1.2.3. The carbonate pump

Another important part of the biological pump involves the formation of PIC via the precipitation of calcium carbonate by specific plankton species such as coccolithophores, foraminifera and pteropods (e.g. Emilio et al., 1993). These calcifying species directly use DIC to synthesize their carbonate shell, thereby releasing CO_2 (Equation 1.4). This process is known as the carbonate counter pump (left part of Figure 1.2).

$$Ca^{2+} + 2HCO_3^- \leftrightarrow CaCO_3 + CO_2 + H_2O \qquad \text{(Equation 1.4)}$$

The precipitation of carbonates results in an increase of the surface ocean pCO_2 (Frankignoulle et al., 1993) on timescales of 100-1000 years (Zeebe, 2012). However, an opposite effect of the carbonate counter pump is the increased organic carbon export flux to the deep ocean (0.1 Pg C.year^{-1}; Sabine and Feely, 2007), ballasted by the calcium carbonate (Francois et al., 2002).

1.1.2.4. The microbial pump

The majority of the organic matter is remineralized by respiration, releasing CO_2 back to the atmosphere. However, a large reservoir of dissolved organic carbon (DOC) exists, in which 95% is recalcitrant DOC (RDOC). Being resistant to biological decomposition, the RDOC can persist in the ocean for at least 100 years and represents thus a reservoir for carbon. The

origin of this RDOC is still misunderstood but some authors have suggested that RDOC may be formed by the microbes 'pumping' the bioavailable DOC into this RDOC (Jiao et al., 2010; Legendre et al., 2015).

Physical transfers of carbon via the solubility pump are one order larger in magnitude than the carbon export via the biological pump (265 Pg C.yr^{-1} compared to 11 Pg C.yr^{-1}) but in obduction regions, the carbon related to the solubility pump is released back to the atmosphere (276 Pg C.yr^{-1}; Levy et al., 2013).

Sarmiento and Gruber (2006) have compared the impact of the oceanic pumps on the surface-to-deep gradient of DIC concentrations (ΔsDIC; Figure 1.5). The authors have estimated that the biological carbon pump (ΔC_{soft}) is responsible for 70% of the DIC increase in the deep-waters whereas the solubility pump ($\Delta C_{gas\text{-}ex}$) and the carbonate counter pump (ΔC_{carb}) account for 10 and 20% respectively of the observed gradient. This finding clearly highlights that the biological carbon pump is the most important process controlling the distribution of DIC in ocean and therefore the atmospheric CO_2 concentrations.

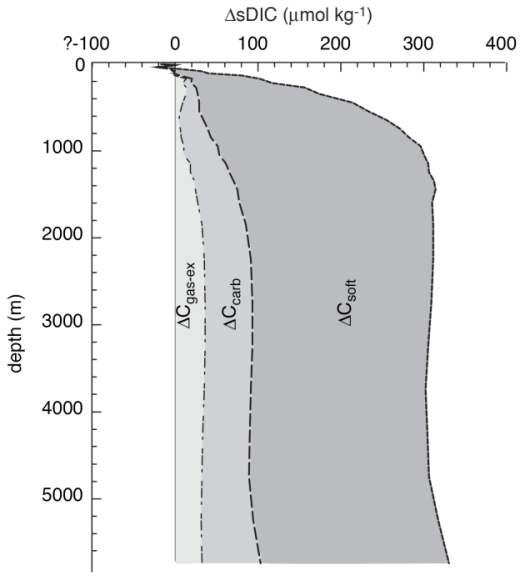

Figure 1.5: Contribution of the different carbon pump components (the solubility pump $\Delta C_{gas\text{-}ex}$; the carbonate counter pump ΔC_{carb}; and the biological carbon pump ΔC_{soft}) to DIC increase in the deep ocean (Gruber and Sarmiento, 2006).

In the following section, the biological pump will be at the core of the different chapters.

1.2. The biological carbon pump

1.2.1. General view

The first step of the BCP occurs in the surface ocean, where phytoplankton species, which are photoautotrophic organisms, use energy from sunlight to synthesize complex organic compounds such as carbohydrates, lipids and proteins. This is known as primary production. Phytoplankton can be eukaryotes (the cell contains a nucleus and other organelles enclosed within membranes) such as the opal-secreting diatoms, prymnesiophytes (including the $CaCO_3$-secreting coccolithophores) and dinoflagellates; or prokaryotes (the cell lacks a distinct nucleus and membrane bound organelles) such as cyanobacteria (Sigman and Hain, 2012). In addition to carbon, phytoplankton require a wide range of nutrients, many of which become limiting in certain regions of the ocean, exerting a significant control on surface ocean production and ultimately the efficiency of the BCP (Moore et al., 2013). These elements are presented in section 1.2.2.1. Other controls of the primary production in surface waters include the dissolved CO_2 concentrations, temperature, stratification of the water column, and grazing.

The second step of the BCP is the export of organic matter from the sunlit surface ocean to depth through different types of vertical transfer: 1) the passive sinking of particles and aggregates, 2) the physical advection and diffusion between the surface and the deep ocean and 3) the daily vertical migration of zooplankton, grazing phytoplankton, ingesting thus the associated-chemical elements in the surface ocean and then excreting fecal pellets after their descent to mesopelagic depths (100-1000 m). Sinking particles transport carbon but also all the other elements composing POM, previously incorporated as nutrients by phytoplankton. The export occurs when there is an excess density of the POM, i.e. when the density of the POM is greater than the density of seawater. This generally occurs at the death of organisms but most phytoplankton cells are too small to sink individually, so sinking occurs once they aggregate into larger particles or are repackaged into fecal pellets by zooplankton. The biogenic minerals (BSi and $CaCO_3$), as well as the lithogenic minerals (dust, clay particles), can be incorporated into aggregates, thereby increasing the excess density of settling particles

and inducing an increase of the settling velocity (De La Rocha and Passow, 2007; Honjo, 1996, see in section 1.2.2.1).

Once formed, settling particles also face the possibility of decomposition through consumption and respiration by herbivorous zooplankton and degradation by bacteria: it is the third component of the BCP. Most of these recycling processes take place within the upper 500m of the water column (Guidi et al., 2009). The remineralization rates of the different elements composing the particles can be influenced by a wide range of processes (e.g. Boyd et al., 2010; Twining et al., 2014). For example, carbon (C), nitrogen (N) and phosphorous (P) are remineralized faster and hence at shallower depths than the biomineral silicon (Si) (Boyd et al., 2010; Boyd and Trull, 2007; Twining et al., 2014). This can be explained by the presence of Si in opal frustule of diatoms that are protected of the degradation by an organic coating (Bidle and Azam, 1999) whereas P, N or C are associated to the organic matter. The different remineralization length scales are thus regulated by the lability of the material, which likely depends on the chemical composition of the sinking particles, with lithogenic, opal or calcareous materials more resistant to the degradation (Boyd et al., 2010). Moreover, sinking particles can be progressively enriched in trace elements such as iron (Fe) relative to C, N or P with depth (Boyd et al. 2010; Twinning et al. 2014) due to scavenging of any freshly released Fe back onto particles (Boyd et al. 2010). Such mechanisms induce different remineralization rates that can have a strong feedback on surface processes, in particular influencing the concentrations of micro- and macronutrients, locally or, through interactions with the large scale oceanic circulation.

The net result of these three components of the BCP is that a relatively small fraction (1%, Martin et al., 1987, Figures 1.3 and 1.6) of the primary production is exported to deep waters or even to sediments. As shown on Figure 1.6, the POC flux generally decreases exponentially with depth as more than 50% of the primary production in the euphotic zone is grazed or degraded by microbes and bacteria.

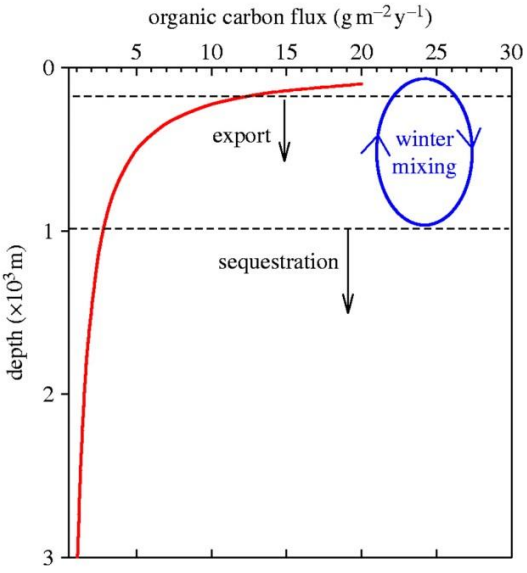

Figure 1.6: Schematic view of the decrease of the downward POC flux with depth (Lampitt et al., 2008).

Therefore, it is important to determine POC fluxes from the surface to the deep sea in order to assess the efficiency of the BCP. This efficiency will depend on the amount of primary production in surface waters, itself depending on nutrient and light availability; the rate at which the particles sink, depending on their size and density; and the degradation rate of organic C and other elements composing the particles, following grazing and remineralisation.

1.2.2. Influencing factors

1.2.2.1. Chemical controls

- *Macro- and micro-nutrients availability*

To grow, phytoplankton requires chemical elements, which are typically identified as nutrients (Sigman and Hain, 2012). Nutrients can be divided in two categories: macro- and micro-nutrients, this distinction being made by their concentration in seawater (µmol.L^{-1} and nmol.L^{-1} to pmol.L-^{1}, respectively). In the following, the cycle of the elements of interest are briefly described.

Macronutrients

Redfield et al. (1963) discovered that relatively invariant elemental ratios of C, N, and P found in marine organisms are intimately entwined with the co-variation (106C:16N:1P) of these elements in the ocean.

Dissolved phosphorous is present in seawater under the phosphate form (PO_4^{3-}; < 0.1 – 3.0 µmol.L^{-1}). Important inputs of PO_4^{3-} are delivered through riverine runoff, atmospheric deposition and submarine groundwater discharge (e.g. Paytan and McLaughlin, 2007). In polar areas, ice sheets could also bring large quantities of P in solution (Hawkings et al., 2016). These PO_4^{3-} sources fuel phytoplankton blooms in surface waters but in some regions, like in the subtropical Sargasso Sea, P has been reported to limit the phytoplankton developments (Wu et al., 2000). Phosphorus is easily remineralized in the water column (Clark and Ingall, 1998), and its preferential remineralization compared to C is explained by the more labile nature of organic compounds containing P (Berner, 1980).

Inorganic nitrogen is mainly present in the marine system as nitrate (NO_3^-) but also under other forms such as ammonium (NH_4^+), nitrite (NO_2^-), nitrous oxide (N_2O), nitric oxide (NO) and dinitrogen (N_2) and is brought through the rivers, the atmospheric depositions or the N_2 fixation (Capone et al., 2005; Gruber, 2008). Ammonium (< 0.3 – 1.2 µmol.L^{-1}) is the preferred source of nitrogen for phytoplankton because its assimilation requires less energy (Zehr and Ward, 2002). Nitrate uptake requires more energy but since nitrate concentrations are more abundant in the ocean (< 1 - 35 µmol.L^{-1}), most phytoplankton have the enzymes to initiate the reduction of NO_3^- in order to grow (nitrate reductase), with the exception of prokaryote species such as *Synechococcus* (Moore et al., 2002). Phytoplankton can also use NO_2^- as a nitrogen source but its concentration in the ocean is usually low (< 0.2 – 1.5 µmol.L^{-1}). Another important source of N, when the other forms are exhausted or when the N/P ratio is not “Redfieldian”, (with P being in excess compared to N in Redfield stoichometry) is via the biological N_2 fixation which transforms N_2 into PON. Organisms able to fix dissolved N_2, called diazotrophs, are found among free and/or symbiotic cyanobacteria some filamentous such as bloom forming

Trichodesmium spp. (Capone et al., 1997; Carpenter et al., 1999), Richelia (Foster et al., 2007; Foster and Zehr, 2006) and others unicellullar diazotrophic cyanobacteria (Zehr et al., 2001) as well as heterotrophic bacteria (Zehr et al., 1998). Once phytoplankton has satisfied its nitrogen demand for growth, the different dissolved nitrogen forms are transformed in PON. Most of the PON is returned back to dissolved inorganic nitrogen by remineralization processes generated by bacteria: ammonification transforming PON to NH_4^+, nitrification transforming NH_4^+ to NO_2^- (ammonium oxidation) and then NO_2^- to NO_3^- (nitrite oxidation or true nitrification). In the ocean, the fluxes of PON to the seabed are small. The major sink for nitrogen is the denitrification transforming the NO_3^- into N_2 in low oxygen environment (oxygen minimum zones, shelf or margin sediments), leading to a nitrogen loss through the atmosphere (Galloway et al., 2004; Gruber, 2004). In addition, nitrogen is also lost as N_2O produced during the nitrification as well as during denitrification.

Silicic acid (H_4SiO_4 or dSi) is also considered as a macronutrient and is particularly essential for some plankton taxa known as silicifiers such as diatoms (autotrophic phytoplankton), silicoflagellates and radiolarians (heterotrophic zooplankton), as they use it to build their shells which is then referred as biogenic silica (BSi or $bSiO_2$). Silicic acid is brought to the ocean essentially via the rivers (about 66% of the total net inputs, Tréguer and De La Rocha, 2013) and its concentrations vary from < 0.2 to 170 $\mu mol.L^{-1}$. In the world ocean, 56% of BSi is recycled in the upper 100m and the remaining fraction is transported to the deep ocean where BSi can also undergo dissolution. Only 3% of BSi is estimated to reach the seafloor (Tréguer and De La Rocha, 2013).

Micronutrients

Other elements, such as the following metals: Fe, Zn, Mn, Ni, Cu, Co, Cd, Mo that are present at subnanomolar concentrations in seawater exert a key role in many metabolic processes (Table 1.1) and are referred as key micronutrients. As a result, the oceanic trace element biogeochemical cycles have been intensely studied over the past decade (e.g. see review in SCOR working group, 2007). Their sources are very diverse being atmospheric (e.g. Jickells

et al., 2005; Shelley et al., 2015), riverine (e.g. de Baar and Jong, 2001), sedimentary (e.g. Bruland and Lohan, 2008), hydrothermal (e.g. Tagliabue et al., 2010), cold seep vents (e.g. Lemaitre et al., 2014), ice melting (e.g. Lannuzel et al., 2011), anthropogenic (e.g. Gao et al., 2014), groundwater discharge (e.g. Trezzi et al., 2016), extraterrestrial (e.g. Johnson, 2001) or volcanic activity (e.g. Achterberg et al., 2013), shelves (Elrod et al., 2004). However, only a small fraction of trace metals originating from these sources is soluble in seawater and accessible to the phytoplankton. In the surface, a significant fraction of trace metals is bound to strong organic complexes, that increase their solubility and can favor their bioavailability (e.g. Gledhill and Buck, 2012; Rue and Bruland, 1995). Some trace metals are easily scavenged onto particles and are subsequently removed from the surface waters when particles sink. In the mesopelagic layer, trace metals are also affected by bacterial activity, at different remineralization rates. For example, Twining et al. (2014) have shown that Ni or Zn were remineralized faster than Fe.

Metal	Protein(s)	Function(s)
Fe	Cytochromes	Electron transport in photosynthesis and respiration
	Ferredoxin	Electron transport in photosynthesis and N fixation
	Other Fe-S proteins	Electron transport in photosynthesis and respiration
	Nitrate and nitrite reductase	Conversion of nitrate to ammonia
	Chelatase	Porphyrin and phycobiliprotein synthesis
	Nitrogenase	N fixation
	Catalase	Conversion of hydrogen peroxide to water
	Peroxidase	Reduction of reactive oxygen species
	Superoxide dismutase	Disproportionation of superoxide to hydrogen peroxide and O_2
Zn	Carbonic anhydrase	Hydration and dehydration of carbon dioxide
	Alkaline phosphatase	Hydrolysis of phosphate esters
	RNA polymerase	Nucleic acid replication and transcription
	tRNA synthetase	Synthesis of tRNA
	Reverse transcriptase	Synthesis of single-stranded DNA from RNA
	Carboxypeptidase	Hydrolysis of peptide bonds
	Superoxide dismutase	Disproportionation of superoxide to hydrogen peroxide and O_2

Metal	Protein(s)	Function(s)
Mn	O2-evolving enzyme	Oxidation of water during photosynthesis
	Superoxide dismutase	Disproportionation of superoxide to hydrogen peroxide and O_2
	Arginase	Hydrolysis of arginine to ornithine and urea
	Phosphotransferases	Phosphorylation reactions
Ni	Urease	Hydrolysis of urea
	Superoxide dismutase	Disproportionation of superoxide to hydrogen peroxide and O_2
Cu	Plastocyanin	Photosynthesis electron transport
	Cytochrome oxidase	Mitochondrial electron transport
	Ascorbate oxidase	Ascorbic acid oxidation and reduction
	Superoxide dismutase	Disproportionation of superoxide to hydrogen peroxide and O_2
	Multicopper ferroxidase	High-affinity transmembrane Fe transport
Co	Vitamin B12	C and H transfer reactions
Cd	Carbonic anhydrase	Hydration and dehydration of carbon dioxide
Mo	Nitrate reductase	Conversion of nitrate to ammonia
	Nitrogenase	N fixation

Table 1.1: Common metalloproteins present within marine phytoplankton and associated functions (from Twining and Baines, 2013).

Some oceanic areas are particularly productive owing to the availability of all essential elements described above due to their close vicinity to the sources (e.g. estuaries, coastal areas) or favored by physical processes (e.g. coastal upwelling, mixing of nutrient-rich water masses).

However, two broad regimes of phytoplankton nutrient limitations exist in the upper ocean (Figure 1.7). The first one is dependent on nitrogen and phosphorus availability, which mainly occurs at low latitudes characterized by a slow supply of nutrients from the sub-surface. These areas are defined as low nutrient low chlorophyll (LNLC). The second one is intimately linked to iron availability, which is limiting in vast regions of Southern Ocean, Eastern Equatorial Pacific, North Pacific and North Atlantic, where in contrast to Fe, N and P nutrients are not limiting. These areas are defined as high nutrient low chlorophyll (HNLC).

Vitamins and other micro nutrients can also limit marine phytoplankton (Moore et al., 2013; Morel, 2003; Swift, 1981; Wu et al., 2000; Figure 1.7).

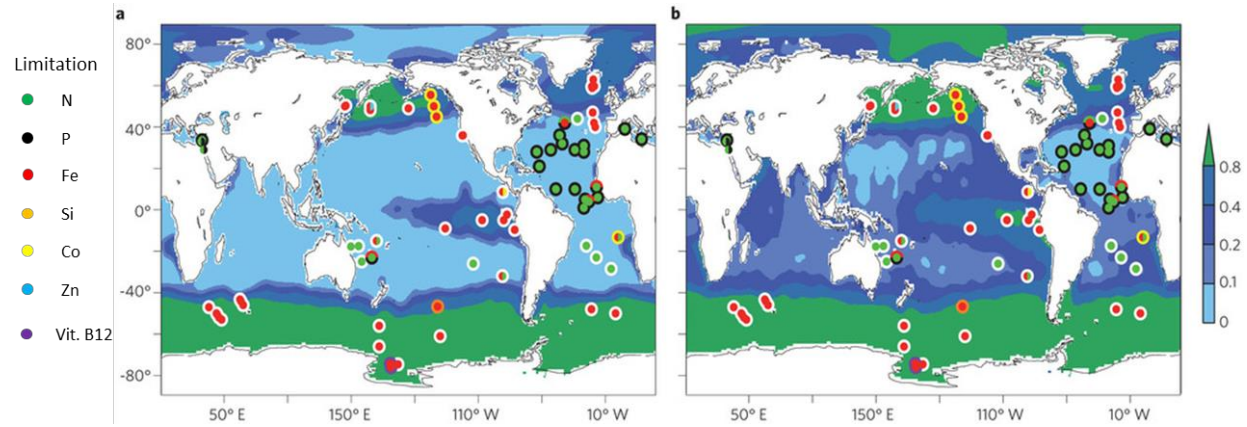

Figure 1.7: Patterns of nutrient limitation. Backgrounds indicate annual average surface concentrations of nitrate (a) and phosphate (b) in µmol.kg^{-1}.To assist comparison, nitrate is scaled by the mean N:P ratio of organic matter (that is divided by 16). Symbols indicate the primary (central circles) and secondary (outer circles) limiting nutrients as inferred from chlorophyll and/or primary productivity increases following artificial amendment of: N (green), P (black), Fe (red), Si (orange), Co (yellow), Zn (cyan) and vitamin B12 (purple). Divided circles indicate potentially co-limiting elements. White outer circles indicate that no secondary limiting nutrient was identified, which will be because of the lack of a test (from Moore et al., 2013).

These nutrient limitations directly impact the phytoplankton development and more generally, the ecosystem structures, resulting in a change of the 106C:16N:1P Redfield ratio. Indeed, spatial variations in the elemental stoichiometry of phytoplankton have been observed due to supply and limitation of nutrients but also due to specific uptake by the different phytoplankton communities (Hagstrom et al., 2016; Martiny et al., 2013; Rembauville et al., 2016a; Teng et al., 2014; Weber and Deutsch, 2010).

It is typically the case for the Southern Ocean which is isolated from any major iron sources, inducing a limited primary production (Martin, 1990). However, in this HNLC Southern Ocean, diatoms (the major phytoplankton group in this region) can develop important adaptive strategies to these particular conditions (Boyd et al., 2007; de Baar, 2005), such as a heavily silicified and thick shell, a slower growth rate and a high iron storage capacity (Boyd, 2013).

A nutrient limitation, as seen above, drives the succession of the phytoplankton communities. In the North Atlantic, for example, a strong diatom bloom usually thrives during spring, consuming the available nutrients. When silicic acid levels are depleted, there is then a transition from diatoms to coccolithophores (Henson et al., 2006; Sanders et al., 2014). Moreover, at the end of the productive period, a Fe limitation or co-limitation with silicic acid

has also been reported (Nielsdottir et al., 2009) inducing seasonal HNLC conditions in this area.

These different limitations have broad implications for the oceanic 'biological pump' that links nutrient and carbon cycling.

- *Suspended "ballast" mineral*

Ballast minerals, including lithogenic minerals (e.g. dust, clays) and biogenic minerals (BSi and $CaCO_3$), are important for the settling of POM to depth. Indeed, the density of the organic matter (≈ 1.05 $g.cm^{-3}$) is almost the same as seawater (≈ 1.03 $g.cm^{-3}$) and thus particles require a "ballast" effect to sink. Biogenic mineral ballast are mainly calcium carbonate ($CaCO_3$) and biogenic silica ($bSiO_2$) that form the shells of coccolithophores, pteropods, foraminifers for the former, and of diatoms and radiolarians respectively (Lam and Bishop, 2007). Calcite density is 2.71 $g.cm^{-3}$, opal density is 2.1 $g.cm^{-3}$ and lithogenic material density can reach 2.65 $g.cm^{-3}$ (e.g. quartz; Klaas and Archer, 2002). Some authors have proposed a relationship between the POC flux and the flux of ballast minerals in deep sediment traps (Armstrong et al., 2002; Francois et al., 2002; Klaas and Archer, 2002; Figure 1.8) as well as in the upper water column (Sanders et al., 2010; Thomalla et al., 2008).

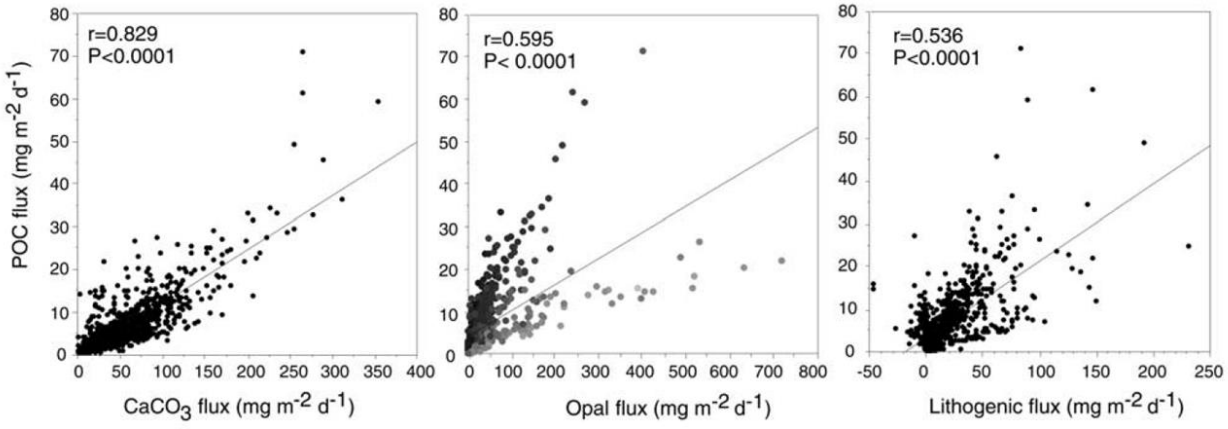

Figure 1.8: Correlations between POC and mineral fluxes collected in 52 sediment traps below 1000 m and around the world ocean (Klaas and Archer, 2002).

The biogenic and lithogenic minerals have the potential to control the fraction of primary production that reaches the seabed by protecting the organic matter from oxidation, by initiating

a more rapid aggregation or by increasing density and in fine, sinking velocity (Armstrong et al., 2002; Le Moigne et al., 2013b). The transfer efficiency of POC to the deep ocean has been strongly related to the calcite flux (François et al., 2002) because calcite is denser, more abundant than opal and clays (Klass and Archer, 2002) and is susceptible to dissolve less than opal in the upper water column (Nelson and Brzezinski, 1997). A recent study has also highlighted the importance of calcium carbonate to export POC in the Southern Ocean (Salter et al., 2014), where the carbon export has usually been attributed to large and heavily silicified diatoms. Nonetheless, diatoms represent an important vector of carbon export as they carry out half of the primary production in the world ocean (Buesseler, 1998; De La Rocha and Passow, 2007; Tréguer et al., 1995).

Finally, recent studies have demonstrated that the effect of ballast minerals on the POC flux varies regionally (Frédéric A C Le Moigne et al., 2014; Le Moigne et al., 2012). In the high-latitude North Atlantic, mineral ballasting seems to be important with 60% of the POC flux associated with minerals (on average, mostly $CaCO_3$ and BSi) whereas this fraction is only about 40% in Southern Ocean (on average, mostly BSi). The remainder of the export flux is unballasted, suggesting that the association between POC and minerals is not always necessary to promote the export of organic matter. In this case, low export efficiencies due to the easier degradation of the unballasted POC have been reported (e.g. Le Moigne et al., 2012). However, some discrepancies have been observed, indicating that other parameters such as low microbial activity or large zooplankton migration can impact the magnitude of surface export (Le Moigne et al., 2016).

1.2.2.2. Biological controls

Spatial variations in phytoplankton size structure are known to exert a control on the magnitude of the POC export flux (Boyd and Newton, 1999) and high POC exports are usually related to a greater size of the sinking phytoplankton cells (Alldredge and Silver, 1988; Guidi et al., 2009). In addition to the size structure, the composition of the phytoplankton community has been

shown to influence the magnitude of the biogeochemical export fluxes. As seen in the previous section, diatoms and calcifying species are important vectors of carbon export, as their 'hard parts' (BSi and $CaCO_3$, respectively) can be incorporated into aggregates and increase the excess density of suspended particles provoking an increase of the sinking velocity (Honjo, 1996). The life stage of the certain phytoplankton communities can also influence the magnitude of the export fluxes. For example, the formation of diatom resting spores has been shown to strongly enhance the deep carbon export (Rembauville et al., 2016b, 2015a; Rynearson et al., 2013; Salter et al., 2012). The succession of the different phytoplankton communities as well as the succession of the different life stages can be triggered by a nutrient limitation (see section 1.2.2.1; Sugie and Kuma, 2008) but also by turbulence (Margalef, 1978) or light changes (Lasbleiz et al., 2016).

The magnitude and the fate of the primary production exported from surface waters to deeper depths are also related to remineralization processes that are led by zooplankton and bacteria activities in the euphotic zone but also in the mesopelagic zone to support their metabolic demands (Figure 1.9). Modest variations of the remineralization depth have been shown to impact strongly the air-sea carbon balance. For example, a remineralization depth increasing by only 24 m would induce a decrease in atmospheric CO_2 concentrations from 10 to 30 ppm, i.e., ~3 to 9% of the present atmospheric pCO_2 (Kwon et al., 2009).

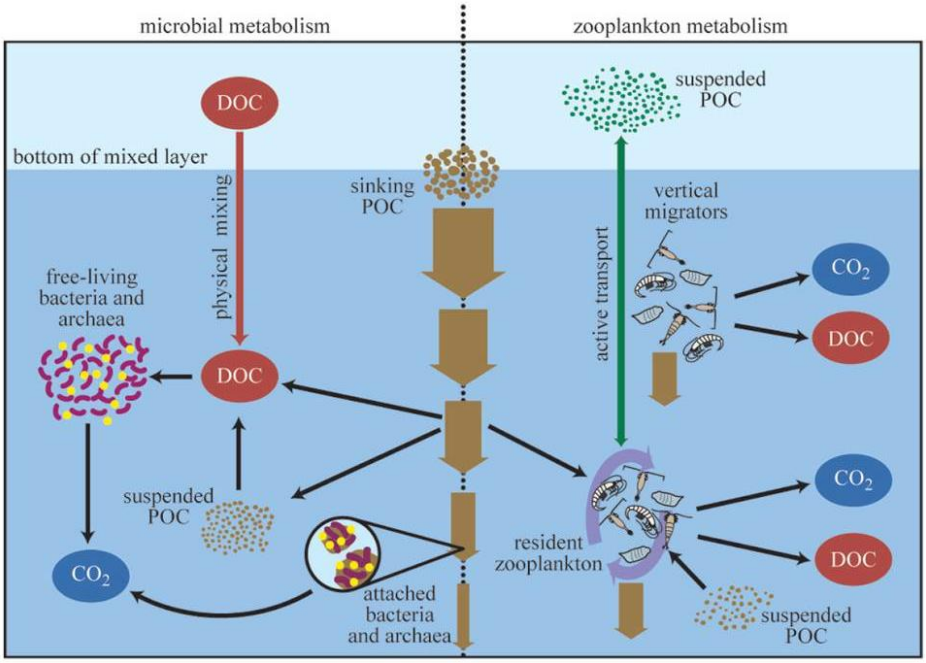

Figure 1.9: Attenuation of the carbon export flux from the mixed layer into the mesopelagic zone by the microbial and zooplankton metabolisms (Steinberg et al., 2008).

- *Grazing and fecal pellets production by zooplankton*

Food sources for micro- and meso-zooplankton are phytoplankton and sinking phytodetrital aggregates (also known as “marine snow”). Zooplankton communities can fragment large sinking particles into smaller less-sinking particles, leading to a POC flux decrease (Steinberg et al., 2008). Once consumed, a fraction of carbon is respired back into DIC or released as DOC (Allredge and Jackson, 1995). Similarly, nutrients such as N or Fe are released to the water column after zooplankton regeneration (e.g. Giering et al., 2012). This process can account for 30 to 100% of total Fe supplied to the euphotic zone (Bowie et al., 2001; Sarthou et al., 2008; Strzepek et al., 2005) and is also a significant source of bioavailable Fe (Dalbec and Twining, 2009; Nuester et al., 2014). Zooplankton respiration has been estimated to account for 7-66% of the loss of sinking POC flux in the bathypelagic (> 1000 m), depending on region and season (Burd et al., 2010). Another fraction of the carbon consumed by zooplankton is exported as sinking fecal pellets, packing the phytoplankton cells and increasing the downward flux (Silver and Gowing, 1991). The fecal pellets can be dense and fast sinking in the water column and many studies have considered them as a major constituent

of the downward flux with the large organic aggregates (De La Rocha and Passow, 2007; Ebersbach and Trull, 2008; Laurenceau-Cornec et al., 2015a; Turner, 2015). However, zooplankton itself can cause the degradation of the downward flux of fecal pellets through coprophagy (ingestion of fecal pellets), coprorhexy (fragmentation of fecal pellets), and coprochaly (removal of fecal pellets membrane; Belcher et al., 2016).

Generally, zooplankton communities consume organic particles in surface waters during the night and produce fecal pellets at depth during the day (Longhurst and Glen Harrison, 1988). This vertical migration contributes from a few to 70% of POC flux depending on the season, the region and the species composition (Steinberg et al., 2000). For example, in the Southern Ocean, recent studies indicate that despite the low primary production, high zooplankton-mediated export and low microbial abundance could explain the high export efficiency (Cavan et al., 2015; Le Moigne et al., 2016).

Finally, under high grazing pressure and in order to avoid predation, diatoms are able to change their density, by increasing their silica content (Pondaven et al., 2007). The cell wall silicification directly impacts the efficiency of the export by promoting resistance to grazing and the subsequent remineralization and by increasing the export fluxes through fast-sinking diatoms (Quéguiner, 2013).

- *Microbial activity*

Bacterial remineralization is the main mechanism of particle degradation in seawater (Herndl and Reinthaler, 2013), in particular within the mesopelagic zone, where microbes are responsible for 70 to 92% of the remineralization (Giering et al., 2014). This microbial loop can be stimulated by the release of DOC from zooplankton activities, enzymatic solubilization or mechanical disaggregation (Collins et al., 2015; Giering et al., 2014; Steinberg et al., 2008). Temperature seems to also regulate the heterotrophic respiration with shallower remineralization in warm waters (Belcher et al., 2016; Laws et al., 2000; Marsay et al., 2015). Bacteria associated to particles solubilize POC into DOC which is respired directly or used and respired by free-living bacteria in the mesopelagic zone (Figure 1.9).

Microbial processes can also generate transparent exopolymer particles (TEP) when bacteria are attached to surface like biofilms or macroaggregates but also when they are freely suspended under non-bloom conditions of phytoplankton (Simon et al., 2002). TEP are a class of acidic polysaccharides and their stickiness appear to promote the aggregation of particles and thereby affect the export (Burd et al., 2016; Passow, 2002).

1.2.2.3. Physical controls

Physical dynamics influence the various components of the biological carbon pump. Indeed, mixing and diffusion can transport the dissolved and suspended particulate organic matter to the deep ocean (Figure 1.9; Burd et al., 2010). For example, convective mixing can represent ~20% of the global carbon export (mainly as DOC, (Carlson et al., 2010; Hansell et al., 2009). Diffusion and advection can also reintroduce nutrients in the euphotic zone and fuel the primary production (Benitez-Nelson et al., 2000). Similarly, at larger scales, eddies, upwellings and fronts can bring pulses of new nutrients into the euphotic zone or initiate the spring stratification, both enhancing the biological activity (Mahadevan et al., 2012; McGillicuddy and Robinson, 1997).

These physical processes can also increase the particulate export and eddies, for instance, could contribute half of the spring POC export in the highly productive subpolar zones (Benitez-Nelson et al., 2007; Bidigare et al., 2003; Omand et al., 2015; van Weering et al., 2002; Waite et al., 2016). Regional subduction and the formation of deep and mode water masses, can directly lead to export a fraction of the primary production to deeper depths (Dall'Olmo et al., 2016; Guieu et al., 2005).

1.3. The different approaches to study the biological carbon pump

1.3.1. Particle export measurement

There are several methods to estimate the export fluxes. Eppley (1989) described four major approaches: nutrient uptakes, geochemical budgets, sediment traps and naturally occurring particle-reactive radionuclides. The measurement of nutrient uptake rates using ^{15}N in bottle incubation experiments allow the estimation of the new production via the *f*-ratio concept (Dugdale and Goering, 1967; Eppley and Peterson, 1979). The geochemical budgets (of nutrient or oxygen) is based on the fact that the nutrient supply in the euphotic zone is balanced by the downward export of organic matter (Eppley and Peterson, 1979). The naturally occurring particle-reactive radionuclides and the sediment traps methods are broadly used and are explained in more details thereafter. Other approaches, recently developed thanks to technological advances, can be used: *in-situ* optical methods allowing the measurement of the particle size distribution and abundance (Boss et al., 2015); satellite-based models (Siegel et al., 2014).

- *The naturally occurring particle-reactive radionuclides*

The naturally occurring particle-reactive radionuclides are tracers for particle sinking and are of specific interest to the present work. This method uses the different properties in seawater and the different half-lives of a radioisotope pair to estimate the export fluxes. The ^{234}Th:^{238}U pair is well-known and has been used extensively to study the particle export fluxes in the upper ocean (e.g., Buesseler et al., 1992; Coale and Bruland, 1985; Cochran and Masqué, 2003). Besides, the ^{210}Pb:^{210}Po pair has been also used to determine export fluxes but in a more limited number of studies (e.g., Le Moigne et al., 2013; Roca-Marti et al., 2016b; Stewart et al., 2007).

In order to quantify elemental export fluxes, these indirect methods need to determine the ratio of the element of interest to ^{234}Th or ^{210}Po in sinking particles that are usually collected with *in-situ* pumps (ISP). ISP are large volume filtration systems, that allow the collection of adequate

quantities of size fractionated particles (see GEOTRACES cookbook[1] and McDonnell et al., 2015). They can operate at any depth and, at a same station many ISP can be deployed along a cable off the side of the ship. The pumping time is typically 2-4 hours and 1000-2000 L of seawater can be filtered depending on particle concentration. The two commercial systems used in the present work are Challenger and McLane and the latter can be configured with two pump heads equipped with different filters that can be subsampled for multiple measurements. It is important to note that suspended particles sampled with ISP are not necessarily the ones that sink and can lead to substantial biases in estimates of export flux. Moreover, the size is not always related to density and ISP sampling can include living and non-sinking phytoplankton or micro-zooplankton (Lalande et al., 2008; Puigcorbé et al., 2015). Other methodological issues are the high pressure differential created within ISP that may cause a rupture of aggregates (Gardner et al., 2003) and the adsorption of dissolved matter onto the membranes filters (Zhou et al., 2016) which both can bias the size structure of particles and their elemental concentrations.

After ISP collection, particle concentrations can be measured and combined with the ^{210}Po or ^{234}Th export flux in order to deduce a particulate elemental export flux. This latter method is used and described in this thesis (see section 2.2.1).

- *Sediment traps*

Sediment trap collect directly sinking particles during their transit to depth, into successive cups placed into a carousel hermetically sealed from ambient water. The cup position switches in order to collect a time series or to separate the sampling between the elements of interest (POC versus trace elements for example). Often, poison (formalin or mercury) is added to the cups in order to stop the bacterial activity or to kill zooplankton swimmers that enter in the cups (Lee and Fisher, 1992; Lee et al., 1992). However, this poison can change qualitatively the trapped organic matter (Liu et al., 2006) or contaminate for trace element determinations

[1] http://www.geotraces.org/science/intercalibration/222-sampling-and-sample-handling-protocols-for-geotraces-cruises

(McDonnell et al., 2015). Different types of traps can be deployed: moored traps, usually deployed in the deep sea and used for time series (Antia et al., 2001; Honjo et al., 2008; Rembauville et al., 2015a, 2015b); drifting traps usually deployed in the upper water column (Laurenceau-Cornec et al., 2015a); free-drifting traps that are able to sample at a density horizon (Buesseler et al., 2007; Lampitt et al., 2008); polyacrylamide gel-filled sediment traps to examine sinking flux characteristics (particle type, number, size; Ebersbach and Trull, 2008; Laurenceau-Cornec et al., 2015a). Sediment traps allow the direct quantification of export fluxes but they tend to undercollect slower sinking particles due to physical advection, in particular the moored sediment traps. Also, the sampling of swimmers, even when killed by poison, can alter the particle composition and the related flux (McDonnel et al., 2015; Buesseler et al., 2007).

To sum up, the collection of the sinking material by sediment traps or ISP is not without difficulties knowing the contamination sources of each element of interest (specifically in this study: POC, PN, BSi, and particulate trace metals), the physical processes as the lateral advection perturbing the particle trajectories or the inclination of the particle collector, the solubilization or the loss of material during collection or recovery, and the biological interactions such as zooplankton grazing, migration and excretion which can remove or add to the particulate flux instantly and locally.

1.3.2. Determination of remineralization fluxes

The attenuation of the particulate organic matter concentration with depth can be observed using sediment traps, *in-situ* pumps or the ^{234}Th deficit method between the surface and the mesopelagic layers (Marsay et al., 2015; Usbeck, 2002) but other tools can estimate the oxygen consumption and thus quantify the remineralization fluxes:

- *Bacterial respiration*

The bacterial respiration can be determined from dissolved oxygen consumption in dark seawater incubations. The dissolved oxygen consumption is determined by Winkler titration

(Christaki et al., 2014; Lefèvre et al., 2008), then the oxygen consumption rate can be estimated by integrating the bacterial respiration in a set depth layer. However, the determination of the bacterial respiration is mostly limited to the upper 200 m of depth because of sensitivity issues (detection limit varying from 0.06 to 0.5 µmol $O_2.L^{-1}.d^{-1}$; Arístegui et al., 2005; Robert, 2012).

- *Oxygen Utilization Rate (OUR)*

Surface oxygen concentrations are close to saturation with atmosphere and oxygen can be supplied to the water column by the physical transport of oxygenated surface waters to depth. The OUR can be estimated by dividing the apparent oxygen utilization (AOU) by the age of the water mass, i.e. the elapsed time since the water mass was in contact with atmosphere (Jenkins, 1982). The AOU provides a measure of the oxygen undersaturation, due to the remineralization, and is calculated by subtracting the observed oxygen concentration to the preformed (or saturated) oxygen concentration (Broecker and Peng, 1982). The integrated OUR can then be converted into a carbon remineralization flux using the Redfield molar ratio C/O_2 (127/175; Feely et al., 2004; Sonnerup et al., 2014).

- *Other tracers*

Remineralization processes are a source of changes in the elemental concentrations and isotopic compositions. For example, ammonium is produced during remineralization and is, in general, rapidly transformed into nitrate (nitrification) but an ammonium accumulation indicates an imbalance between the two processes and thus an important remineralization (Sigman et al., 2009). Stable isotopes provide information on the relationship between the dissolved and particulate phases such as uptake, scavenging and remineralization. In surface waters, the increase of the isotopic signatures of dissolved compounds (NO_3^-, trace metals) can be related to the biological uptake of lighter isotopes while below the surface, the remineralization contributes to the lower isotopic signatures by releasing the lighter isotopes in solution (Hoefs, 2010).

The distribution of particulate biogenic barium in the ocean can also give information on the remineralization processes and its integrated content in the mesopelagic layer can be converted into an oxygen consumption and then into a carbon remineralization flux (Dehairs et al., 1997, 1991; Shopova et al., 1995). This last tracer is used in this thesis and thus is described in more detail in Chapter 2 (section 2.4).

1.4. Study areas, objectives and thesis outline

1.4.1. Study areas

In this thesis, two areas are considered: the Kerguelen Island located in the Southern Ocean, and the North Atlantic. A general overview of these two areas is given below, but detailed description of each study area is provided in Chapters 3, 4 and 5 (North Atlantic) and 6 (Kerguelen).

- The North Atlantic

The North Atlantic is an important zone for the Earth climate and the thermohaline circulation (Seager et al., 2002). It represents a major area of the meridional overturning circulation (MOC), which transports warm waters to the northern North Atlantic where the deep convection occurs and contributes to southward transport by mode and deep waters (Dickson et al., 2002; Pickart et al., 2002). For example, the Labrador Sea Water (LSW) sinks from the surface to 2000 m due to its density sets by salinity (34.8 – 34.9 ‰) and temperature (3.3 – 3.6 °C) characteristics. The subduction of these waters increases significantly the carbon sink but the declining rate of wintertime mixing and ventilation between surface and subsurface waters observed from 1990 caused a decrease of this carbon sink in North Atlantic (Pérez et al., 2013; Schuster and Watson, 2007; Watson et al., 2009). Located between North America and Europe, the North Atlantic is known to be an important anthropogenic CO_2 sink of the global ocean (Sabine et al., 2004a; Sarmiento and Gruber, 2002). The North Atlantic represents also

one of the most productive spring phytoplankton bloom of the world's ocean (Figure 1.10; Esaias et al., 1986; Longhurst, 2010), that can be iron limited (Blain et al., 2004; Nielsdottir et al., 2009; Achterberg et al., 2013).

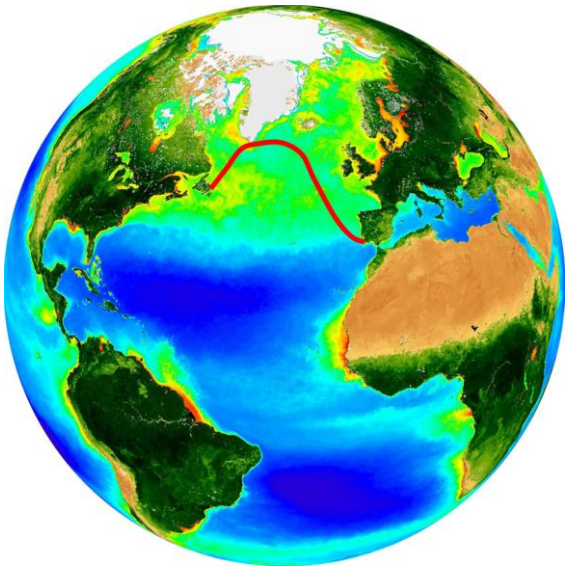

Figure 1.10: SeaWIFS Chlorophyll-*a* concentrations averaged over boreal spring (http://oceancolor.gsfc.nasa.gov/cgi/biosphere_globes). The red line indicates the GEOVIDE transect.

- Kerguelen Island

The Southern Ocean is a key area in the global carbon cycle because of its important capacity to store CO_2 (Gruber et al., 2009; Lenton et al., 2013). There, deep convection controls the air-sea balance of CO_2 (Marinov et al., 2006), especially with the production of the Antarctic Bottom Water (AABW) which is the coldest, densest and most voluminous water mass of the world ocean (Johnson, 2008). AABW feeds the Meridional Overturning Circulation (MOC) by being exported northward and by covering much of the world ocean floor, except in Arctic and some parts of North Atlantic (Orsi et al., 2001). However, recent studies highlighted the weakening of the deep convection in Southern Ocean and thus a decrease of the Southern Ocean CO_2 sink (de Lavergne et al., 2014; Le Quéré et al., 2007). Another important point is that the Southern Ocean is also the largest HNLC region of the global ocean and its potential to transfer carbon and other elements via the biological carbon pump is limited by a lack of micro-nutrients and in particular by a lack of iron (Martin, 1990). Natural phytoplankton blooms occur close to Southern Ocean islands (Morris and Charette, 2013) and the largest blooms are

observed around the sub-Antarctic islands such as the Crozet (Pollard et al., 2007), South Georgia (Tarling et al., 2012) or Kerguelen Islands (Blain et al., 2007; Figure 1.11). These large phytoplankton blooms are sustained by the supply of iron and major nutrients to surface waters from iron-rich deep water (Blain et al., 2007; Pollard et al., 2009) and can trigger large carbon export fluxes (Le Moigne et al., 2016; Morris et al., 2007; Planchon et al., 2015; Salter et al., 2007; Savoye et al., 2008).

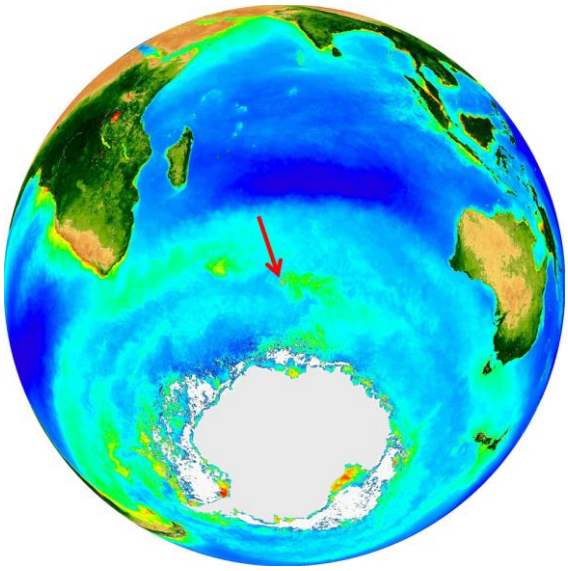

Figure 1.11: SeaWIFS mean Chlorophyll-*a* concentrations averaged over austral spring (http://oceancolor.gsfc.nasa.gov/cgi/biosphere_globes). The red arrow indicates the Kerguelen Island position.

1.4.2. Objective and thesis outline

The biological carbon pump plays a major role on the sequestration of carbon-rich particles in the ocean interior but its functioning remains misunderstood.

Indeed, the ocean is still under-observed and the study of the biological carbon pump is limited by the challenging measurements of the export and remineralization fluxes in the water column requiring different instruments and/or proxies. Moreover, most studies focused on the upper water column while an important fraction of the POC is remineralized in the mesopelagic zone, and the magnitude of these fluxes remain poorly constrained.

Nutrients are essential in the regulation of the marine primary productivity and their availability can thus strongly perturb the marine carbon cycle. However, the export of these essential biogenic elements is poorly studied too.

The general objective of this work tends to reduce the above gaps by improving our understanding on the export and remineralization fluxes of carbon and nutrients (N, Si, trace elements) by using a multi-proxy approach in the upper and mesopelagic zones in two contrasting environments in terms of ecosystem, water masses, temperature and nutrient sources.

Chapter two provides a complete description of the methods used during this work, from sample collection to analyses, including an overview of the ^{234}Th and particulate biogenic barium proxies. Main issues to estimate elemental export fluxes and especially the determination of the ratio Element to ^{234}Th are also discussed.

The objective of **Chapter three** is to investigate the distribution of POC export fluxes in the North Atlantic Ocean within the framework of the GEOVIDE cruise (GA01 GEOTRACES section). Particular emphasis has been placed on the different controls, in particular the stage and intensity of the bloom, the phytoplankton size structure, and the composition in biogenic and lithogenic minerals that can play a role of ballast for POC. Also, using *in-situ* primary production data and deep carbon export fluxes, we investigate the efficiency of the biological carbon pump in the North Atlantic. I participated to the cruise and this work has been done in collaboration with D. Fonseca Batista, A. Roukaerts and F. Deman (VUB) for the primary production data, M. Tonnard (LEMAR-ACE CRC) for the dFe data, H. Claustre and J. Ras (LOV) for the pigment data.

Chapter four presents for the first time the Ba_{xs} distributions in the North Atlantic, with the main objective of estimating carbon remineralization fluxes. Similarly to Chapter 3, these fluxes are discussed regarding to the stage and intensity of the bloom, phytoplankton size and community structure and physical forcing. This, in combination with surface primary production (PP) and POC export estimates allow the investigation of the fate of POC to the deep ocean.

This work has been carried out in collaboration with S. Jacquet (MIO) for the dissolved barium data, P. Laha (VUB) for the SEM analyses, A. Gourain and M. Cheize (LEMAR) for the particulate barium data from GO-FLO bottles.

The third objective was to look into the variability of particulate trace elements (Fe, Zn, Mn, Al, P, Co, Cd, Cu, Ni) export fluxes that are presented in **Chapter five.** Vertical export fluxes of the trace elements along the GEOVIDE transect in the North Atlantic are presented and discussed. A principal component analysis is used to regroup elemental fluxes before investigating the lithogenic, anthropogenic and biogenic influence on these fluxes. The preferential remineralization with depth of the different trace elements is then discussed.

Chapter six examines the biogeochemical export fluxes obtained in HNLC and Fe-enriched waters around the Kerguelen Island in order to assess the impact of the natural Fe-fertilization on the vertical transfer of PN, BSi and PFe. We further investigate how phytoplankton community composition, lithogenic contribution and degradation of particles, influence the magnitude, efficiency and stoichiometry of the export fluxes. This work has been done in collaboration with P. van der Merwe, A. Bowie, T. Trull, E. Laurenceau-Cornec and D. Davies (IMAS, ACE, CRC).

Finally, the main findings of this work, as well as the conclusions in a broader context, are summarized in **Chapter 7** and some suggestions for future work are listed.

Chapter 2

Material and Methods

This chapter gives an overview of the different steps undertaken on samples collected during the GEOTRACES GA01 (GEOVIDE) cruise in the North Atlantic, including sample collection, chemical processing, analytical protocols and mathematical determination of the fluxes.

I have participated to the GEOVIDE cruise during which I was in charge of the excess barium sampling and where I substantially contributed to the *in-situ* pump sampling (preparation and recovery of the pumps, filter handling in the clean bubble). Back in the lab, I have determined the ^{234}Th recovery (MRAC, Tervuren), the POC and PN concentrations (VUB, Brussels), the trace element concentrations (IUEM, Brest) and the excess barium concentrations (MRAC, Tervuren). The sampling, preparation and Beta counting of the samples dedicated to ^{234}Th were made by F. Planchon at sea; the Beta counting of the ^{234}Th residual activities were determined by A. Plante, E. Le Roy (Master students, VUB), F. Planchon and myself (VUB and IUEM); the BSi concentrations were determined by S. Roig (Master student, IUEM); and replicates of POC and PN concentrations were determined by C. Mariez (Master student, IUEM).

2.1. Sample collection, chemical processing and analyses

2.1.1. Total Thorium-234: ^{234}Th

2.1.1.1. Sampling

Total ^{234}Th activities were determined on 4L seawater samples collected with 12L Niskin bottles (Pike et al., 2005) triggered at 18 depths in the upper 1000m. Using a silicone tube, seawater was transferred from the 12L Niskin bottle to a 4L polypropylene bottle (Nalgene). Before the sampling, the 4L-bottles were cleaned with a solution of 7M HNO_3/1M H_2O_2 (suprapur grade, Merck) at ambient temperature, to avoid memory effects on ^{234}Th and to remove MnO_2 impurities, they were then rinsed three times with Milli-Q water and finally with the sampled seawater.

Immediately after sampling, samples were acidified to pH 2 using concentrated HNO_3 (suprapur grade, Merck) and spiked with 1 mL of ^{230}Th (5.2 ng.g^{-1}) in order to monitor the

recovery. The 4L-bottles were shaken manually and allowed to equilibrate for 12 hours. Concentrated NH_4OH (suprapur grade, Merck) was added to increase the pH above 8.5, and 100 µl of $KMnO_4$ solution (0.2 M, analytical grade, Merck) and $MnCl_2$ (0.1M, analytical grade, Merck) were added to co-precipitate the Th with the MnO_2 precipitate. Samples were shaken again and allowed to grow for 12 hours before filtration through quartz-microfiber discs (QMA, Sartorius, nominal porosity=1 µm, diameter=25 mm).

2.1.1.2. Analyses

After drying (50°C overnight), filters were mounted on nylon holders, covered with Mylar and aluminum foil and finally counted on board using low level beta counters (RISØ, Denmark) until the counting uncertainty was below 2% RSD (between 1 and 6 counts per minute). The samples were counted twice on board in order to eliminate the shorter-lived Beta emitters and a final counting was performed after a delay of six ^{234}Th half-lives (~6 months) at VUB and LEMAR to determine the residual activity associated to longer-lived Beta emitters. This residual activity was then subtracted from the gross counts obtained on board.

Calibration for the relative efficiency of the low level Beta counting equipment was carried out with certified ^{99}Tc standards, and verified with the home-made ^{238}U standards and deep ocean samples (2000 – 3000 m, van der Loeff et al., 2006). The values obtained with the ^{99}Tc and ^{238}U standards were constant along the GEOVIDE cruise, with deviations lower than 1 and 5% respectively, reflecting good stability of the low level Beta counters. Deep ocean samples were used to calibrate the ^{234}Th measurements, as in open ocean the ^{234}Th is in secular equilibrium with ^{238}U at great depths (2000 – 3000 m), which is assumed conservative and predictable from salinity. However, Owens et al. (2015) observed that this assumption may not always be valid due to Th scavenging at depth and also due to non-conservative behavior of ^{238}U. During GEOVIDE, the $^{234}Th/^{238}U$ ratios of the deep samples (between 1000 and 3500 m) averaged 1.00 ± 0.02 (n=15).

After background counting all samples were processed for ^{234}Th recovery using the ^{229}Th as a second spike, following a procedure from Pike et al (2005) that was recommended by Rutgers

van der Loeff and included in the GEOTRACES cookbook. This method was modified following Planchon et al. (2013).

Briefly, filters were dismounted from the filter holder and inserted into 30 mL Teflon vials (Savillex), previously cleaned by submersion in distilled concentrated HNO_3 kept overnight at 130°C on a heating plate. Then, samples were spiked with 50 µl of ^{229}Th (7.55 $Bq.g^{-1}$), dissolved in 10 mL of 7M HNO_3/1M H_2O_2 (suprapur grade, Merck) solution and heated overnight at 60°C. Then, samples were filtered through Acrodisc® syringe filters (Pall, Nylon membrane, nominal porosity=0.2 µm, diameter=25 mm) to get rid of residual particles (essentially QMA broken pieces) and stored in new 30 mL HDPE (high-density polyethylene) bottles (VWR). In order to increase concentrations and to improve the RSD during the analyses, a pre-concentration step was necessary: to this aim, 2 mL of the filtered solution was transferred into a 30 mL clean Teflon vial and evaporated at 100°C on a hotplate, placed under a clean fume hood. The residue was dissolved in 6 mL of 1.4M HNO_3 (suprapur grade, Merck), refluxed overnight at 60°C and stored in new 15mL centrifuge tubes (VWR) until analysis. Three different types of standard were also prepared following the same procedure as for the samples:

- with only ^{229}Th and ^{230}Th spikes
- with ^{229}Th and ^{230}Th spikes and a new QMA filter
- with ^{229}Th and ^{230}Th spikes, a new QMA filter and 100 µl of $KMnO_4$ and $MnCl_2$ solutions

All ^{230}Th and ^{229}Th measurements were performed on a SF-ICP-MS (Element 2, Thermo Scientific) in low resolution mode. Each sample and standard was analyzed 3 times and the RSD of the $^{230}Th/^{229}Th$ ranged between 0.03 and 1.2% (n=3 replicates for each sample or standard). The reproducibility of the method, evaluated by analyzing 43 standard solutions prepared separately and determined over different analytical sessions (typically 6 to 7 standards analyzed per session) ranged between 0.1 and 2.2%. Th recovery was estimated for every sample and was on average 91 ± 14 % (n=200), with an average precision of ^{230}Th:^{229}Th ratios of 1.2% which was lower than the 2% precision recommended by Pikes et al. (2005).

2.1.2. Particulate $^{234}Th_p$ and POC

2.1.2.1. Sample collection

Two particle size classes (> 53 µm and 1-53 µm) were collected using *in-situ* large-volume filtration systems (Challenger Oceanics and McLane pumps; hereafter referred to as ISP) equipped with 142 mm diameter filter holders.

The large particles were collected on a 53 µm mesh nylon screen (SEFAR-PETEX®; polyester) whereas the small particles were collected on a 1 µm pore size quartz-microfiber filter (QMA, Sartorius). Indeed, QMA filters are the best suited for carbon and nitrogen analyses while Supor membranes are best for trace elements (GEOTRACES cookbook; Planquette and Sherrell, 2012). Before being used for sampling, filters were preconditioned as follows: PETEX screens were soaked in 0.6M HCl (Normapur, Merck), then rinsed with ultrapure water (18.2 $M\Omega.cm^{-1}$, Milli-Q), dried at ambient temperature in a laminar flow hood and finally stored in clean plastic bags. QMA filters were precombusted at 450°C for 4h and stored in aluminum foils.

Prior to deployment, filters were mounted on each pump head within a clean room environment using plastic tweezers. Pump heads were covered on deck with plastic bags until deployment in order to minimize contamination. *In-Situ* Pumps were deployed using a stainless steel cable during approximatively 6 hours at depths ranging between 15 and 5300 m (see Chapter 2 and 5 for GEOVIDE samples, and Chapter 6 for KEOPS 2 samples). Immediately after ISP recoveries on deck, pump heads were covered with a plastic bag then transferred into a clean lab where filters were sub-sampled for different analyses.

2.1.2.2. Subsampling at sea

The 142 mm nylon screen (Petex) was cut in four parts, using a scalpel cleaned with ethanol (between 97 and 1626 L of filtered seawater on one quarter). Particles were rinsed off one quarter of the Petex using 30-100 mL of 0.45 µm filtered seawater collected during the cruise (filtered through a Supor filter in clean conditions) and particles were recollected on Ag filters (SterlilTech®, porosity=0.45 µm, diameter=25 mm) under a laminar flow hood. The particles

of a second quarter of the Petex were also washed off the filter and collected on a GFF filter (Whatman®, porosity=0.7 µm, diameter=25 mm) mounted on a vacuum filtration manifold (Millipore). The Ag and GFF filters were dedicated to the same analyses: ^{234}Th activities, POC and PN concentrations and isotopic signatures. In this study we focus on POC concentrations while PN concentrations and the isotopic signatures will be discussed by other GEOVIDE participants. One quarter of each nylon screen was stored in a Petri dish at -80°C, and saved for other analyses (e.g. biomarkers, to be processed by other teams). QMA filters were subsampled using a plexiglas punch of 25 mm diameter (representing between 4 and 82 L of filtered seawater) and one punch was then dried at 50°C, mounted on sample holders as explained above and Beta counted for the determination of ^{234}Th activities. Thereafter, the samples were stored in Petri dishes at ambient temperature until further analyses of POC, PN concentrations and isotopic signatures at VUB and at LEMAR (Figure 2.1).

2.1.2.3. Analyses

- Particulate $^{234}Th_p$

The 4 aliquots containing large particles (particles from the Petex screen resuspended and refiltered on 25 mm Ag, GFF, PC and Supor filters) and 1 aliquot containing small particles (particles from the QMA filter) were dried overnight (50°C), and prepared for beta counting, as explained for total ^{234}Th samples (see section 2.1.1.2).

- Carbon

After counting of the residual Beta activity, Ag and QMA filters were carefully dismounted from their filter holders and fumed with HCl vapor overnight inside a glass desiccator, in order to remove the carbonate phase. After this step, samples were dried overnight (50°C), then packed in precombusted (450°C overnight) silver cups and analyzed with an elemental analyzer – isotope ratio mass spectrometer (EA-IRMS, Delta V Plus, Thermo Scientific) at VUB. Acetanilide standards were used for the calibration. The ranges of POC concentrations measured for all GEOVIDE samples, the blanks and the detection limits, defined as three times the standard deviation of the blank, are shown in Table 1. The median uncertainty of the values

obtained during 3 different instrumental sessions accounted for 5% in >53 µm particles (n=59), and 4% in 1-53 µm (n=61).

µmol	**1-53 µm POC**		**> 53 µm POC**
range (n=64)	0.77 - 78	range (n=63)	2.42 - 372
blank (n=13)	1.52	blank (n=11)	0.8
detection limit	0.49	detection limit	0.63

Table 2.1: Ranges, blanks and detection limits of POC (µmol) during GEOVIDE sample runs.

Along the GEOVIDE transect, POC concentrations ranged from 0.02 ± 0.01 µmol.L^{-1} to 4.75 ± 0.02 µmol.L^{-1} in the large size fraction and from 0.03 ± 0.03 µmol.L^{-1} to 16.7 ± 0.1 µmol.L^{-1} in the small size fraction.

2.1.3. Trace elements, BSi and major elements

2.1.3.1. Sample collection

The large particles were collected on a 53 µm mesh nylon screen (SEFAR-PETEX®; polyester) whereas the small particles were collected on a 0.8 µm pore size polyestersulfone filter (Supor). Before being used for sampling, filters were preconditioned as follows: filters were placed in an acid cleaned container (PETEX) or 1L-LDPE bottle (Supor) containing 1.2M HCl (Suprapur grade, Merck). The containers were then double bagged in Ziploc bags and placed in an oven at 60°C overnight. After cooling, the acid solution was removed and filters were thoroughly rinsed with Milli-Q water. Due to the slow release of acid from the filters, this rinsing step took days in order to reach a pH value slightly inferior to 7. Filters were then kept in Milli-Q until use.

2.1.3.2. Subsampling at sea

Before deployment and after recovery, pump heads were covered with plastic bags to minimize contamination. Aliquots for sensitive elements were processed on board under a laminar flow unit in a clean lab. Large particles were collected on a 142 mm nylon screen (Petex) which was cut in four parts using a clean ceramic scalpel. One quarter (between 10 and 794 L of filtered seawater) of the Petex was dedicated to ^{234}Th and BSi analyses (described below in section 2.1.3.3): particles were rinsed off the filter using approximately 50 mL of 0.45 µm filtered seawater collected during the cruise (filtered through a Supor filter in clean conditions) and collected onto Polycarbonate filters (Nuclepore®, porosity=0.4 µm, diameter=25 mm) mounted on polysulfone filtration units (Pall). A second quarter of the Petex was dedicated to ^{234}Th only: particles were washed off using approximately 50 mL of 0.45 µm filtered seawater collected during the cruise (filtered through a Supor filter in clean conditions) and collected on a polyestersulfone filter (Supor®, porosity=0.45 µm, diameter=25 mm) mounted on a Nalgene filtration unit. The two remaining Petex quarters were stored in clean Petri slides (Millipore) at -20°C for further analysis (TEs and major elements, described below in section 2.1.3.3). Because the mounting of samples on nylon holders, covered with Mylar and aluminum foil (for the Beta counting) is probably incompatible with trace metal clean stringent conditions, TE concentrations in large particles were only measured on the non-counted filters.

Supor membranes (0.8 µm porosity) were sub-sampled for TEs, major elements and BSi analyses, using a 13 mm diameter disposable skin biopsy Acupunch, each punch corresponding between 1 and 28 L of seawater. These punches were not Beta counted and were directly stored in clean Petri dishes (Petrislide, Millipore), double bagged in Ziploc bags and stored at -20°C until analysis at LEMAR (Figure 2.1).

2.1.3.3. Sample handling and analyses in the home laboratory

- Trace elements

Sample handling, processing and preparation were performed in accordance with GEOTRACES recommendations

(http://geotraces.org/images/stories/documents/intercalibration/Cookbook.pdf). One of the remaining PETEX quarter was used for the analyses of trace and major elements of the large particles. It was decided to remove the particles from the nylon screen for two main reasons: (i) high blanks for TEs have been reported from nylon screens (Weinstein and Moran, 2004), (ii) it is not possible to fully acid-digest the nylon screen. Therefore, the particles on the nylon screen were washed off with 50 mL of 0.45 µm filtered surface seawater collected during the GEOVIDE cruise (Station 77, 40m, filtered through a Supor filter) on acid cleaned 47 mm diameter mixed cellulose esters filters (MF-Millipore® filters, 0.8 µm), mounted on acid cleaned polysulfone filtration units (Nalgene®). This seawater has a dissolved iron (dFe) concentration of 0.102 ± 0.019 nmol.L^{-1} (Tonnard et al., in prep), which should have minimized the effect of trace metal adsorption on the filter. The MF filter was then cut in two equal parts using an acid clean ceramic scalpel in order to digest totally the first half and to leach the second half (see below).

Under a Class-100 clean fume hood at the Pôle Spectrométrie Océans (PSO), one 13mm punch of the Supor filter (1-53 µm particle size) or one half of the 47 mm MF filter (>53 µm particle size) was placed along the wall of a 15 mL acid cleaned Teflon vial (Savillex). Then, 2 mL of 8M HNO_3 (Ultrapur grade, Merck) and 2.3M HF (Suprapur grade, Merck) solution was added. Vials were then refluxed at 130°C on a hotplate during 4h. After gentle evaporation, 200 µL of concentrated HNO_3 (Ultrapur grade, Merck) was added in order to drive off the fluorides. The residue was brought back into solution with 3% HNO_3 spiked with 1 µg.L^{-1} of Indium and stored in acid cleaned 15 mL centrifuge tubes until analysis for estimating the total particulate trace elements concentrations (Planquette and Sherrell, 2012).

All measurements for trace elements were performed using a SF-ICP-MS (Element 2, Thermo) at the Pôle Spectrométrie Océans following the method of Planquette and Sherrell (2012). Sample introduction system consisted of a FAST valve, a PFA nebulizer and a double stage spray chamber. Every 11 samples, a replicate analysis of a selected sample digest solution

was made. The precision and the accuracy of our analyses were assessed by measuring replicates and the Certified Reference Materials (CRM) BCR-414, respectively.

	Certified/indicative* value (mg/kg)	Measured value (n=5; mg/kg)	Recovery (%)
Cd	0.383 ± 0.014	0.385 ± 0.020	101%
Pb	3.97 ± 0.19	2.95 ± 0.11	74%
Al*	2154 ± 803 *	3112 ± 464	144%
P*	12840 ± 4978 *	15541 ± 3732	121%
Ti*	105 ± 25 *	95 ± 8	90%
V	8 ± 0.2	9 ± 1	111%
Cr	23.8 ± 1.2	24.8 ± 3.07	104%
Mn	299 ± 13	301 ± 42	101%
Fe*	1850 ± 190 *	1860 ± 230	101%
Co*	1.43 ± 0.06 *	1.44 ± 0.21	101%
Ni	18.8 ± 0.8	17.8 ± 2.91	95%
Cu	29.5 ± 1.3	29.7 ± 3.8	101%
Zn	111.6 ± 2.5	112.4 ± 18.8	101%
Mo*	1.35 ± 0.2 *	1.37 ± 0.28	101%
Ba*	29.5 ± 3.9 *	32.7 ± 5.15	111%

Table 2.2: Determined concentrations ($mg.kg^{-1}$) and resulting recoveries (%) of the Certified Reference Material plankton BCR-414, compared to certified or indicative (*) values, analyzed by HR-ICP-MS.

External calibration curves were ran at the beginning, middle and end of the run. Data processing included drift correction through ^{115}In monitoring, Cd-Mo oxides correction, and blank correction.

- Major elements

The measurements of major elements (Ca, K, Mg, Na, Sr) were performed using an ICP-AES (ULTIMA 2) at the PSO using the archive 3% HNO_3 solutions that were prepared for the totally digested trace element concentrations. The precision and the accuracy of our analyses were assessed by measuring replicates and the Certified Reference Materials (CRM) BCR-414.

	Ba	Ca	K	Mg	Na	P	Sr
Indicative value ($\mu g.g^{-1}$)	30	65955	6850			12840	220
Determined concentration (n=2; $\mu g.g^{-1}$)	28 ± 1	51133 ± 1057	5887 ± 165	2053 ± 78	6601 ± 13	10910 ± 275	188 ± 2
Recovery (%)	95	78	86			85	85

Table 2.3: Determined concentrations ($\mu g.g^{-1}$) and resulting recoveries (%) of the Certified Reference Material plankton BCR-414, compared to indicative values, analyzed by ICP-AES.

It was then possible to estimate the calcium carbonate concentration, assuming that all Ca comes from the carbonate ($CaCO_3$) and the seawater, following this equation:

$$[Ca]_{CaCO3} = Ca - [(Ca/Na)_{SW} \times Na] \quad \text{(Equation 2.1)}$$

where $[Ca]_{CaCO3}$ is the estimated concentration of calcium carbonate in $\mu mol.L^{-1}$; *Ca* and *Na* are respectively the calcium and sodium concentrations analyzed in $\mu mol.L^{-1}$; $(Ca/Na)_{SW}$ is equal to 0.022 $mol.L^{-1}$ and represents the mean ratio determined in seawater by Copin-Montégut (1996).

The $CaCO_3$ concentrations ranged from 0.002 ± 0.0001 $\mu mol.L^{-1}$ to 0.139 ± 0.0003 $\mu mol.L^{-1}$ in the large size fraction and from 0.006 ± 0.0002 $nmol.L^{-1}$ to 1.54 ± 0.01 $\mu mol.L^{-1}$ in the small size fraction. The median errors accounted for 1.2% (n=51) and 0.5% (n=76) of the concentration for the large and small size fractions, respectively.

- Biogenic Silica

Following the method of Ragueneau et al. (2005), BSi was estimated after alkaline digestions allowing the correction of the LSi that can represent up to 90% of the total particulate silica in coastal waters. All experiments using clean polymethylpentene and polypropylene (VWR) centrifuge tubes. One Supor punch (1-53 µm particle size), or a 25 mm diameter Nuclepore filter previously Beta counted (>53 µm particle size), was placed in a centrifuge tube and digested with 8 mL of a 0.2 M NaOH solution (pellets for analysis, Merck) at 95°C during 1h in a hot bath. After cooling, the pH was neutralized by adding 2 mL of 1M HCl (Analar Normapur, Merck). Tubes were then centrifuged at ambient temperature for 10 min at 4000 rpm (Thermo Scientific Multifuge 3S+/3SR+) and the supernatant was separated from the remaining suspended material. Finally, 1 mL of supernatant was diluted 10 times with Milli-Q water for the silicic acid analyses, and similarly, 1 mL of supernatant was diluted 10 times with Milli-Q water for the aluminium analyses. At the end of the first digestion, all the BSi should be converted into silicic acid. However, it is possible that a part of LSi is dissolved during this first digestion involving a bias for the determination of BSi concentration. This bias is resolved with

a second digestion, equivalent to the first one, allowing the determination of a ratio (Si/Al) characteristic of the minerals. The corrected BSi concentration is then deduced using the following equation:

$$BSi = [Si_1] - [Al_1] \times (Si/Al)_2 \qquad \text{(Equation 2.2)}$$

where *BSi* is the final concentration of biogenic silica in µmol.L^{-1}; *$[Si_1]$* and *$[Al_1]$* are the concentrations of silicic acid and aluminium determined during the first digestion in µmol.L^{-1}; *$(Si/Al)_2$* is the ratio of the concentrations of silicic acid and aluminium determined during the second digestion.

After each alkaline digestion of the filter, silicic acid concentrations were determined following the automated acid/molybdate colorimetric method (Aminot and Kérouel, 2007), using an AutoAnalyzer3 Bran&Luebbe (detection limit: 0.07 µmol.L^{-1}). Dissolved aluminium concentrations were determined by a fluorimetric method (fluorimeter MITHRAS LB 940) detecting a complex Aluminium-Lumogallion developed by Hydes and Liss (1976; detection limit: 0.05 µmol.L^{-1}). The median precision of the values obtained during 4 different instrumental sessions reached 0.25% in >53 µm particles, and 7.1% in 1-53 µm.

µmol	**BSi 1-53 µm**	**BSi >53 µm**
range (n=60)	0.02 - 2.2	0.02 - 48
blank (n=9)	0.001	0.02
detection limit	0.003	0.002

Table 2.4: Ranges, blanks and detection limits of BSi (µmol) in large and small particles collected during GEOVIDE.

The BSi concentrations ranged from 0.0009 ± 0.0006 µmol.L^{-1} to 1.414 ± 0.004 µmol.L^{-1} in the large size fraction and from 0.005 ± 0.002 µmol.L^{-1} to 0.871 ± 0.012 µmol.L^{-1} in the small size fraction. The median errors accounted for 1.8% (n=57) and 9.1% (n=55) of the concentration for the large and small size fractions, respectively.

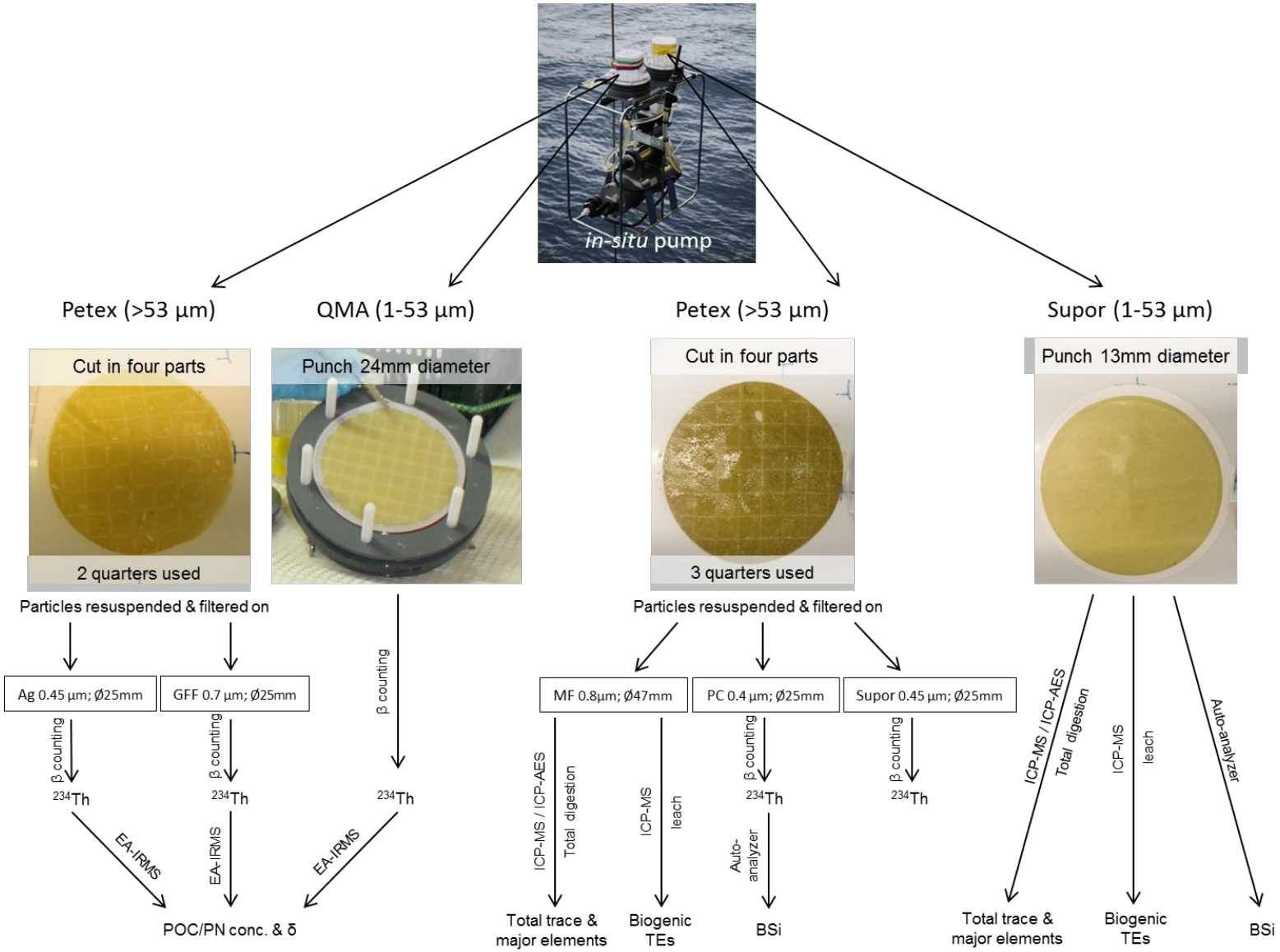

Figure 2.1: Summary of the different sampling and analytical steps on samples collected during the GEOVIDE cruise

2.1.4. Excess Barium

2.1.4.1. Sampling

During the GEOVIDE cruise, samples for excess Barium (Ba_{xs}) were collected at 18 depths between surface and 1500m in order to get a high resolution of the Ba_{xs} signal at each station. Seawater was sampled using a standard CTD Rosette equipped with 12L Niskin bottles. Typically, 4 to 8 L of seawater were sampled in polyethylene jerrycans and then transferred to 10 L custom made Perspex filtrations units (Figure 2.2) where particles were collected on acid-cleaned polycarbonate membranes of 0.4 µm porosity (Nuclepore®, 47 or 90 mm diameter).

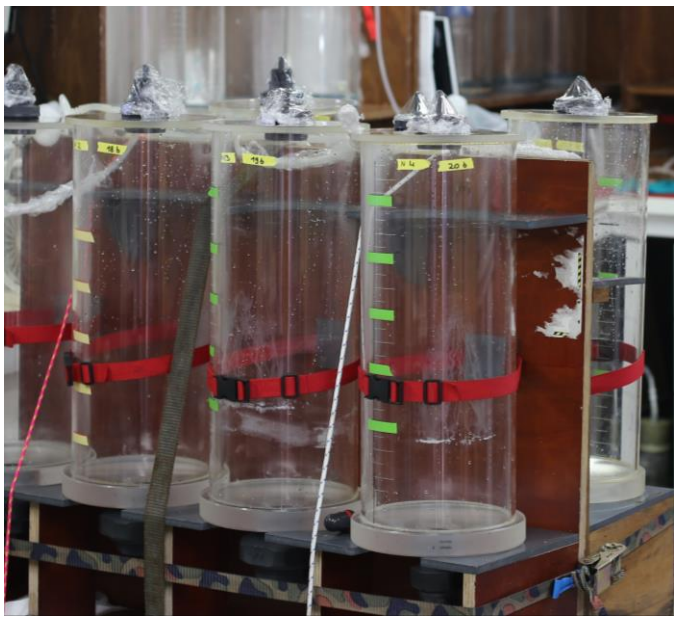

Figure 2.2: Perspex filtrations units used for the determination of Ba_{xs} concentrations during the GEOVIDE cruise

After particle collection, filters were rinsed with ~ 5 mL of Milli-Q water to remove sea-salt, dried at ambient temperature under a laminar flow hood and finally stored at ambient temperature in clean petrislides (Millipore) until analysis (Jacquet et al., 2015).

2.1.4.2. Analyses

Back to the clean laboratory at the Royal Museum for Central Africa (Tervuren, Belgium), filters were cut with clean ceramic scissors in two equal parts. One half was totally digested using a

concentrated tri-acid mixture (1.5 mL HCl – 1 mL HNO_3 – 0.5 mL HF; all Merck suprapur grade) in cleaned 30 mL Teflon vials (Savillex®). Vials were then refluxed at 90°C on a hotplate overnight. After evaporation, the residue was brought back into solution with 0.32M HNO_3. The solutions were then analyzed for Ba and other major and minor elements using an ICP-QMS (inductively coupled plasma-quadrupole mass spectrometer; X Series 2 Thermo Fisher) equipped with collision cell technology (CCT).

Internal standards (Ru, In, Re and Bi) were added directly during the analysis in order to correct for drift and matrix-dependent sensitivity variations.

Two multi-element artificial standard solutions were prepared for external calibration. The first contained major elements (Na, Mg, Al, Ca and Ti) and the second was prepared with minor elements (Sr, Ba, REEs, Th and U). The external standard curves were prepared by dilutions of the multi-element mixed standard stock solution to span the expected range of sample concentrations, with concentrations in the standard curve spaced to cover potential sample variations.

The accuracy and precision of our analyses were assessed using the following Certified Reference Materials (CRM): SLRS-5; BHVO, JB-3 and JGb-1 (Table 2.5).

		Ba	Al
SLRS-5	Certified value ($\mu g.kg^{-1}$)	14 ± 0.5	49.5 ± 5
	Determined concentration (n=4; $\mu g.kg^{-1}$)	13 ± 1	47 ± 2
	Recovery (%)	95%	95%
BHVO-1	Certified value ($\mu g.g^{-1}$)	139 ± 14	73037 ± 1111
	Determined concentration (n=4; $\mu g.g^{-1}$)	129 ± 1	70118 ± 984
	Recovery (%)	93%	96%
JB-3	Certified value ($\mu g.g^{-1}$)	244 ± 10	90819 ± 70
	Determined concentration (n=4; $\mu g.g^{-1}$)	229 ± 13	92144 ± 1620
	Recovery (%)	94%	101%
JGb-1	Certified value ($\mu g.g^{-1}$)	64 ± 5	92566 ± 582
	Determined concentration (n=4; $\mu g.g^{-1}$)	68 ± 15	91491 ± 732
	Recovery (%)	106%	99%

Table 2.5: Determined concentrations and resulting recoveries of the certified reference materials SLRS-5 (river water), BHVO-1 (basalt powder), JB-3 (basalt powder) and JGb-1 (gabbro powder)

The detailed procedure for sample preparation and analysis is given in Cardinal et al. (2001). Particulate biogenic Ba (Ba_{xs}) was estimated by subtracting the lithogenic barium from the total barium. Lithogenic Ba was calculated by multiplying the Al concentration of the sample by the molar crustal Ba/Al ratio of the upper continental crust (UCC; 0.00135 $mol.mol^{-1}$; Taylor and Mclennan, 1985).

$$Ba_{xs} = [Ba] - [Al] \times (Ba/Al)_{UCC} \quad \text{(Equation 2.3)}$$

During GEOVIDE, lithogenic barium represented less than 7% of the total barium, except at stations located close to the Iberian shelf (station 1; 4 - 28%) and in the vicinity of the Greenland shelf (station 53; 19 - 44%; see section IV). The Ba_{xs} concentrations ranged from 58 ± 9 $pmol.L^{-1}$ to 1888 ± 311 $pmol.L^{-1}$ along the transect and the median error accounted for 15% of the concentration (n=199).

2.1.5. Agreement between analytical methods

As described previously, particles can be collected by several methods, including in-line filtration from sample bottles (Niskin or GO-FLO bottles) and *in-situ* pumping. Both approaches were used during GEOVIDE allowing a comparison for some particulate elemental concentrations. The comparison was carried out on samples collected at matching stations and depths. As the Niskin or GO-FLO bottles do not sample efficiently the large particulate fraction (GEOTRACES S&I Committee, personal communication), a meaningful comparison is to compare concentrations from the small size fraction sampled by ISP (1-53 µm) with total concentrations on particles collected with bottles.

2.1.5.1. Between Niskin bottles and *in-situ* pumps

The calcium carbonate ($CaCO_3$), particulate barium (pBa) and particulate aluminum (pAl) concentrations were obtained following two methods: 1) using Niskin bottles followed by a tri-acid digestion (HCl-HF-HNO_3) and analyzed by Quadrupole ICP-MS (see section 1.d) and 2)

using *in-situ* pumps followed by an acid digestion (HF-HNO_3) and analyzed by HR-ICP-MS (see sections 2.1.3 and 2.1.4).

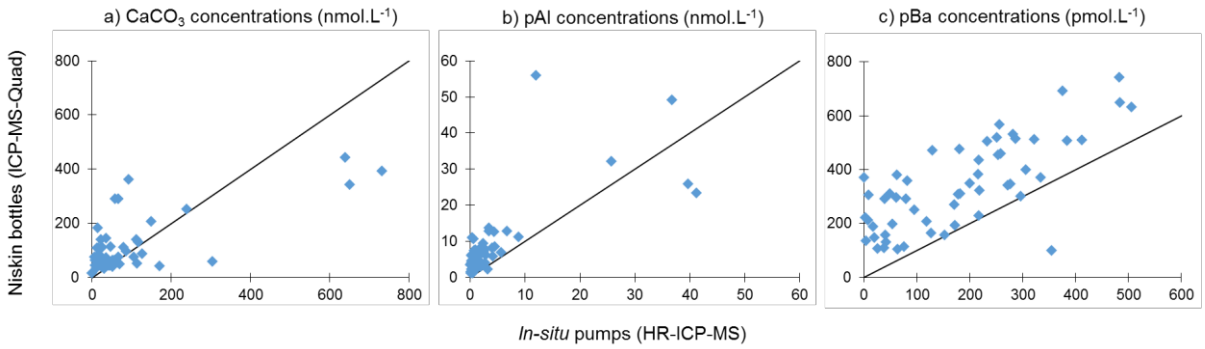

Figure 2.3: $CaCO_3$ (a) pAl (b) and pBa (c) concentrations determined on samples collected with Niskin bottles and *in-situ* pumps. The black lines represent the 1:1 slopes.

$CaCO_3$, pAl and pBa concentrations were 1.5, 3.1 and 1.8 higher in Niskin samples compared to ISP samples (median values, n=52; Figure 2.3). Nevertheless, we can also observe that some data do not follow the same trend, with higher concentrations measured in ISP samples compared to Niskin samples (Figure 2.3).

A greater difference was observed for pAl concentrations and may be explained by the difference of pore size of the different filters. Indeed, particles were collected through paired 142 mm-diameter 53 µm mesh nylon screen (Petex; polyester) and a 0.8 µm polyestersulfone filter (Supor) for the ISP sampling and through a 47 or 90mm-diameter 0.4 µm polycarbonate filter (Nuclepore). The aluminium bearing particles, such as the aluminosilicate minerals, are small particles (ranging from the subnanometer to the micromiter scale; Arrhenius, 1954) and may have been under-sampled by the pair Petex-Supor filter (pore sizes=53 and 0.8 µm, respectively) compared to the Nuclepore filter (pore size=0.4 µm).

Second, a potential bias might also originate from particle washout from filter holders during recovery, as the ISPs were not systematically equipped with anti-washout systems, thus possibly inducing some loss of particles during handling filter. ISP samples were also resuspended and recollected onto other filters, probably inducing some loss too.

Fourth, samples were digested using different techniques. The Niskin samples were digested using a tri-acid mix (50% HCl, 33% HNO_3 and 17% HF) while the ISP samples were digested

using a 50% HNO_3/10% HF acid mix. Addition of HCl has been shown not to improve elemental recoveries of marine particles (Ohnemus and Lam, 2014) but the higher HF contents for the tri-acid mix, perhaps dissolved more the refractory particles, explaining the higher concentrations obtained in Niskin samples.

Finally, the concentrations determined by small-volume bottle filtration may be higher than those determined by large-volume ISP because of the adsorption effect of dissolved elements on the filter (Liu et al., 2005; Moran et al., 1999; Zhou et al., 2016).

Three points were characterized by high pAl concentrations in ISP samples (Figure 2.3). These samples were collected at Station 1, near the Iberian Margin, where high lithogenic inputs occurred (see Chapters 3 and 5). A similar difference has been observed by Twining et al. (2015) in the North Atlantic, suggesting that large lithogenic particles may be undersampled by bottles in near-shelf environments, such as the Iberian Margin.

A complete removal of sea-salt is not possible for samples collected with ISPs which tend to retain excess seawater. This can affect the particulate concentrations of sea-salt derived elements, such as Ca. The sea-salt correction to determine the $CaCO_3$ concentrations (Equation 2.1) may involve some bias. This could explain the higher $CaCO_3$ concentrations in some ISP samples compared to Niskin samples. The higher $CaCO_3$ concentrations in ISP samples could also result from the sampling of larger phytoplankton species, such as pteropods or foraminifers, compared to Niskin samples.

2.1.5.2. Between GO-FLO bottles and *in-situ* pumps

Trace element concentrations were determined on samples collected by two methods: 1) using GO-FLO bottles (Gourain et al., in prep.) 2) using *in-situ* pumps (see Chapter 5). Then, collected samples were treated using the same chemical and analytical procedures: acid digestion (2.3M HF-8M HNO_3) and SF-ICP-MS analysis (see section 2.1.3.3).

The comparison of particulate trace element concentrations between bottles and *in-situ* pumps has been shown to agree well when contamination is avoided and when similar sample

digestion is used (Bishop et al., 2012; Planquette and Sherrell, 2012). In this study, the two particle sampling approaches produced similar element profiles confirming the good quality of our data (Figure 2.4).

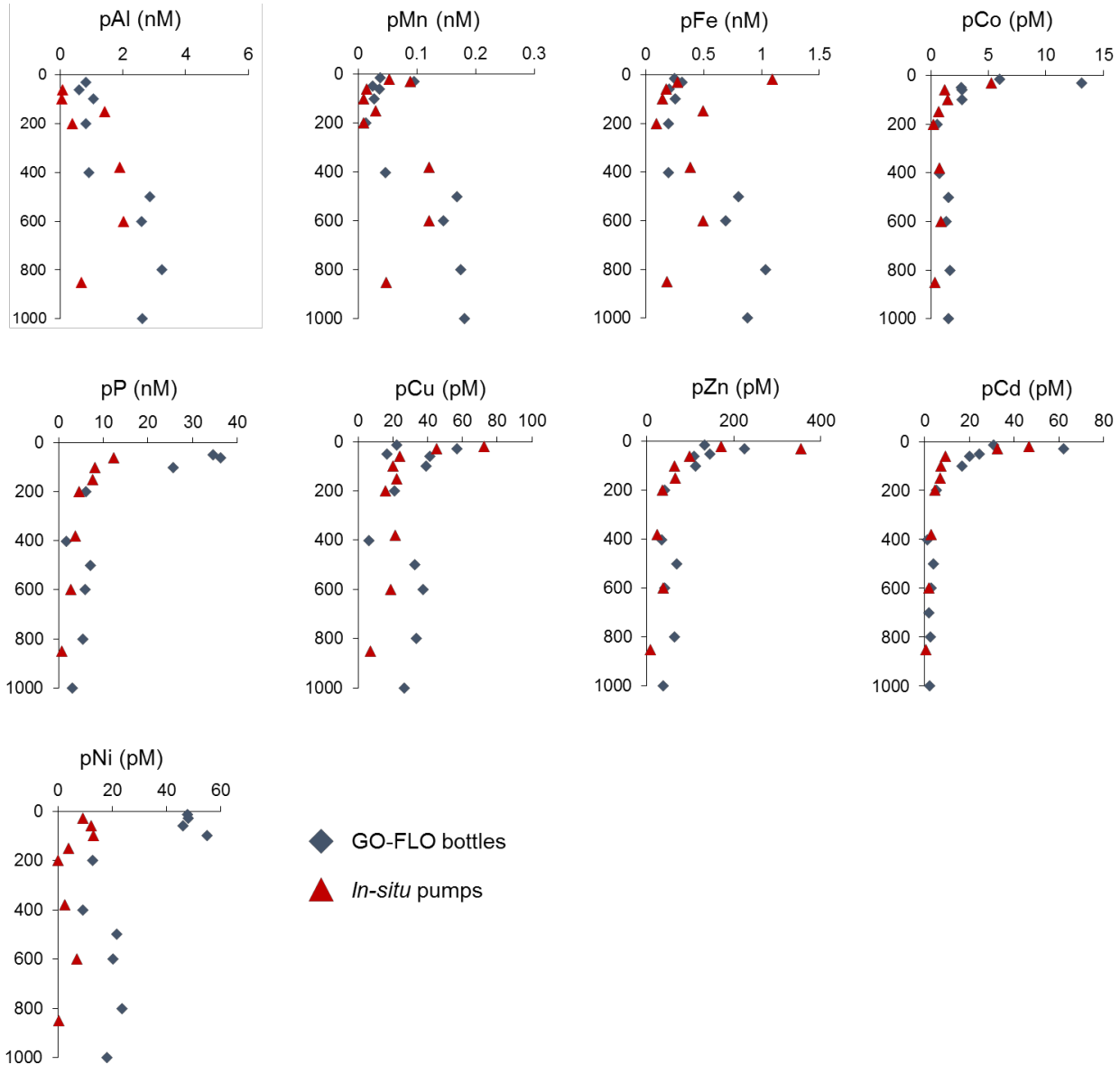

Figure 2.4: Depth profiles at Station 32 of particulate trace elements as determined using GO-FLO bottles (blue diamond) and *in-situ* pumps (red triangles).

Nevertheless, the particulate trace element concentrations determined by ISP were generally lower than the concentrations determined by GO-FLO bottles. This potential bias might originate from particle washout from filter holders during recovery, as our ISP were not systematically equipped with anti-washout systems, as well as the resuspension and recollection of particles onto other filters, as already mentioned above.

Overall, the comparison of the depth profiles highlights the data quality obtained during GEOVIDE but the trace element concentrations across the section were lower for particles sampled by ISP than GO-FLO bottles. In the North Atlantic, Twining et al. (2014) also observed higher pCd, pMn, pCo and pP concentrations in bottle samples compared to ISP samples. However, the authors determined lower pFe and pAl concentrations in bottle samples, which is the case for pFe in the upper 200 m in this study. To limit these effects, we focus on elemental ratios and element to ^{234}Th ratios, rather than on concentrations and activities.

2.2. ^{234}Th Export determination

2.2.1. Principle

The radioisotope ^{234}Th is naturally produced from the alpha decay of ^{238}U (Figure 2.5) and is characterized by a short half-life ($t_{1/2}$ = 24.1 days). On the contrary, ^{238}U is a soluble element which has a conservative behavior ($t_{1/2}$ = 4.47×10^9 years) in the open ocean (Chen et al., 1986; Figure 2.5). The radioactive pair achieves conditions of secular equilibrium (for t > 6 × $t_{1/2}$ of daughter, 145 days) when the radioactive production and decay are equal (Bourdon et al., 2003). Due to its strong affinity for particles (Kd of 10^6-10^7, IAEA, 1985) compared to ^{238}U, ^{234}Th is rapidly adsorbed onto all types of particles and can be rapidly scavenged in the water column when particles sink inducing disequilibrium between daughter (^{234}Th) and parent (^{238}U).

This was first observed during a cruise in 1967 in the Arabian Sea (Bhat et al., 1969). The disequilibrium between ^{234}Th and ^{238}U has thus been used to examine the sinking particle flux to the mesopelagic depth (Bacon and Anderson, 1982; Kaufman et al., 1981; Santschi et al., 1979). Later, a link between the biological processes and the ^{234}Th deficit was proposed by Coale and Bruland (1985; 1987) as ^{234}Th/^{238}U ratios are suitable for tracing events occurring over short time scales ranging from days to weeks, which is a similar period to the development of a phytoplankton bloom and its subsequent particulate export (Cochran and Masqué, 2003; Savoye et al., 2006; Waples et al., 2006).

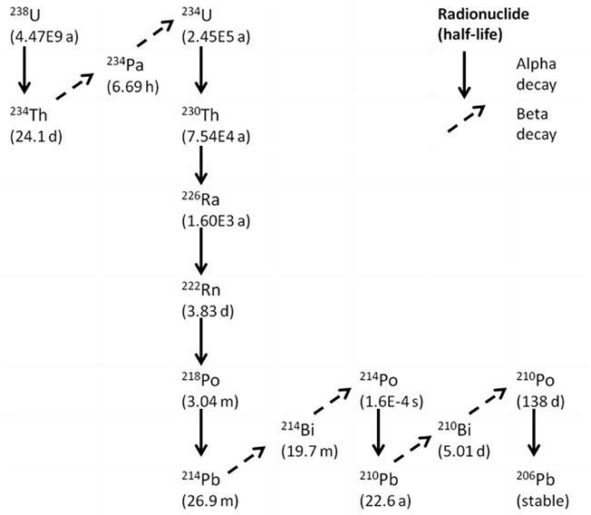

Figure 2.5: Radioactive decay chain of ^{238}U (a=years; d=days; h= hours; m=minutes; s=seconds)

The ^{234}Th deficit with respect to ^{238}U, reflected by $^{234}Th/^{238}U$ ratios less than 1, is attributed to particle export/aggregation while an excess of ^{234}Th compared to ^{238}U (ratio $^{234}Th/^{238}U$ ratios greater than 1, points to an accumulation of ^{234}Th that can be attributed to a remineralization/disaggregation of ^{234}Th-bearing particles (Figure 2.6).

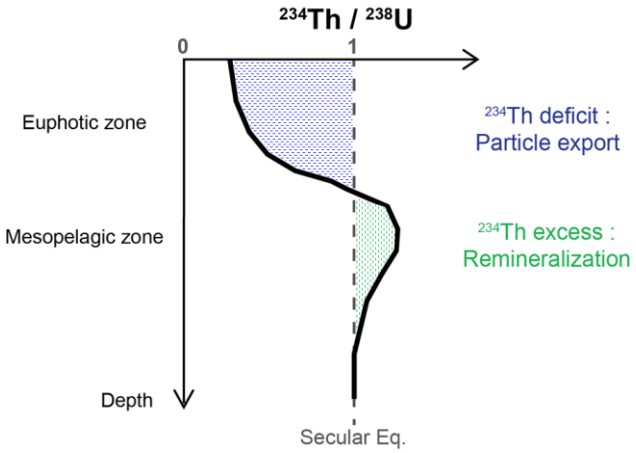

Figure 2.6: Typical profile of the $^{234}Th/^{238}U$ ratio in seawater

The ^{234}Th deficit relative to ^{238}U can be integrated over the upper column yielding to the determination of a ^{234}Th flux. Subsequently, the ^{234}Th flux can be converted into an elemental flux by using the element:^{234}Th ratio of sinking particles (Equation 2.4). In 1992, Buesseler et al. estimate the first POC and PON export fluxes and since then, the ^{234}Th approach has been

extended to numerous elements such as PIC (Bacon et al., 1996), BSi (Buesseler et al., 2001; Rutgers van der Loeff et al., 2002) or trace metals (Weinstein and Moran, 2005).

$$\text{Elemental export flux} = (\text{Element} : {}^{234}\text{Th})_{particulate} \times {}^{234}\text{Th flux} \quad \text{(Equation 2.4)}$$

where *Elemental export flux* is expressed in $mmol.m^{-2}.d^{-1}$ or $\mu mol.m^{-2}.d^{-1}$ and calculated at a specific depth z; $(Element : {}^{234}Th)_{particulate}$ is the ratio of the studied element to ^{234}Th on sinking particles calculated at z (expressed in $\mu mol.dpm^{-1}$ or $nmol.dpm^{-1}$); and $^{234}Th\ flux$ is the integrated ^{234}Th flux ($dpm.m^{-2}.d^{-1}$) at z.

2.2.2. Determination of the ^{238}U and ^{234}Th activities

Uranium is characterized by a conservative behavior with respect to salinity in the open ocean where waters are well oxygenated, as evidenced from the linear relationship established by Chen et al. (1986) using samples from the Atlantic and Pacific oceans. The relationship was re-evaluated by Owens et al. (2011) using a larger sample set and a wider salinity range:

$$^{238}\text{U} = 0.0786 \times S - 0.315 \quad \text{(Equation 2.5)}$$

where ^{238}U is the ^{238}U activity expressed in $dpm.L^{-1}$; S is the salinity expressed in PSU.

The total ^{234}Th activities are calculated considering the equations 4 and 5:

$$^{234}\text{Th}_{\text{ at counting}} = (cpm_0 - cpm_r) / (Y \times \varepsilon \times V) \quad \text{(Equation 2.6)}$$

where $^{234}\text{Th}_{\text{ at counting}}$ is the ^{234}Th activity at the counting data, expressed in $dpm.L^{-1}$; cpm_0 are the raw ^{234}Th counts detected onboard, expressed in cpm; cpm_r are the residual counts measured after a delay of ^{234}Th half-lives (~ 6 months), expressed in cpm; Y is the recovery factor determined from the ^{230}Th:^{229}Th ratio; ε is the efficiency of the Beta counter estimated with the ^{99}Tc and checked against the home-made ^{238}U standards and with the deep samples; V is the volume of seawater filtered expressed in L. It is important to note that during GEOVIDE, the temporal variations of the ^{99}Tc standards measurements were less than 1% indicating a stable Beta counting along the cruise. The ^{234}Th activities were calculated at the sampling time

by correcting from ^{234}Th decay and from ^{238}U in-growth over the period of sample treatment (Rutgers van der Loeff et al., 2006):

$$^{234}Th = {}^{234}Th_{\text{ at counting}} \times e^{(\lambda \times \Delta t2)} - {}^{238}U \times e^{(\lambda \times \Delta t1)} - 1 \quad \text{(Equation 2.7)}$$

where ^{234}Th is the final ^{234}Th activity expressed in dpm.L^{-1}; $^{234}Th_{\text{ at counting}}$ is given by (Eq 4) expressed in dpm.L^{-1}; λ is the ^{234}Th decay constant and is equal to 0.0288 day^{-1}; $\Delta t2$ is the elapsed time between the sampling date and the counting date, in days; ^{238}U is the uranium activity given by (Eq 3) expressed in dpm.L^{-1}; $\Delta t1$ is the elapsed time between the sampling date and the filtration date, in days.

Uncertainties on total ^{234}Th activities are estimated using an error propagation law (and considering the different sources of error, initial and final counting, counter efficiency, recovery; Rutgers van der Loeff et al., 2006) and represent 0.07 dpm.L^{-1}.

2.2.3. Determination of the ^{234}Th export flux

The ^{234}Th flux is calculated from ^{234}Th and ^{238}U activities using the mass balance equation established for a 1-D box model (Savoye et al., 2006):

$$\delta^{234}Th / \delta t = \lambda \times (^{238}U - {}^{234}Th) - P + V \quad \text{(Equation 2.8)}$$

where λ is the ^{234}Th decay constant (0.0288 d^{-1}); ^{238}U and ^{234}Th are the activities of ^{238}U and ^{234}Th, respectively; P is the export of ^{234}Th on sinking particles; V is the sum of advective and diffusive fluxes of ^{234}Th and can be modeled by the equation:

$$V = u \times (\delta^{234}Th / \delta x) + v \times (\delta^{234}Th / \delta y) + w \times (\delta^{234}Th / \delta z) + Kx \times [\delta^2 (^{234}Th) / \delta x^2]$$
$$+ Kv \times [\delta^2 (^{234}Th) / \delta y^2] + Kz \times [\delta^2 (^{234}Th) / \delta^2 z] \quad \text{(Equation 2.9)}$$

where velocities are denoted u, v and w; $(\delta^{234}Th / \delta x)$, $(\delta^{234}Th / \delta y)$ and $(\delta^{234}Th / \delta z)$ are the ^{234}Th activity gradients; K_x, K_y and K_z are the diffusion coefficients.

The vertical advection has been shown to be an important process in areas where intense upwelling or downwelling occur (see Buesseler et al., 1995), which is the case close to the Iberian margin (http://marine.copernicus.eu/) or within the Labrador Sea (Kieke and

Yashayaev, 2015). Lateral transport of ^{234}Th can also be important close to ocean margins or in areas where currents are strong (Benitez-Nelson et al., 2000; Resplandy et al., 2012; Savoye et al., 2006). The impact of physics during GEOVIDE is discussed in Chapter 3.

During GEOVIDE, we assume that $(\delta^{234}Th / \delta t) = 0$ or that the system is in steady state (SS). Indeed, a non-steady state (NSS) study implies to sample a station twice minimum, which was impossible during the transect of the GEOVIDE cruise. However, during KEOPS2 cruise, around Kerguelen Island in the Southern Ocean, a NSS model has been used at two stations and the comparison with the SS model did not reveal significant differences (Planchon et al., 2015).

The ^{234}Th flux is calculated by integrating the ^{234}Th activity deficit (relative to ^{238}U) at a specific depth, using a midpoint integration method. Briefly, the water column is divided in layers where a ^{234}Th export flux is calculated by multiplying the thickness of the layer using equation 2.8. The ^{234}Th export flux at the specific depth represents the cumulative ^{234}Th export fluxes deduced from the upper layers.

2.3. Elemental export fluxes

Biogeochemical (POC, BSi, major or trace elements) export fluxes can be determined using the ^{234}Th-based approach by multiplying the ratio of the element of interest to ^{234}Th in particles with the total ^{234}Th export flux (Equation 2.4). This approach assumes that the deficiency in total ^{234}Th with respect to ^{238}U reveals a ^{234}Th flux associated with particles sinking from the euphotic zone to deeper depths (Buesseler et al., 1992). The selection of the Element:^{234}Th ratio representative of sinking particles exiting the surface waters is decisive for the ^{234}Th proxy method. In fact, this ratio can vary spatially and temporally and is dependent on the kind of particles, particle-size, plankton communities, food web dynamics, aggregation-disaggregation processes or sampling methods (Benitez-Nelson and Charette, 2004; Buesseler, 1991; Buesseler et al., 2006; Moran et al., 2003). In order to estimate the most representative export

flux, the two following sub-sections discuss about the choice of the depth to estimate the Element:^{234}Th ratio and thus the elemental export flux, as well as the different mathematical fits to estimate the Element:^{234}Th at the specific depth. In general, larger particles (> 53 µm) are considered as the sinking particles and thus responsible of the particulate export flux (Michaels and Silver, 1988). The particulate ratio Element to ^{234}Th in this > 53 µm size fraction is usually used to convert the ^{234}Th flux into the elemental flux (Buesseler et al., 2006). However, recent studies have shown that smaller particles (1-53 µm) also contribute to the export flux (Puigcorbé et al., 2015). Therefore, for samples where ^{234}Th analysis have been performed (POC, PN), the Element:^{234}Th ratios were also determined for the small size fraction (1-53 µm) in order to compare both size fractions individually. Despite the different timescales integrated and the problems of each sampling method, a comparison of the element to ^{234}Th ratio in particles between ISP and sediment traps is a good indicator of the particles reaching the sediment traps. A good agreement would confirm the estimations of the ratio as well as the export flux. However, several authors have documented problems from methodological issues (angle of the P-trap, swimmers in P-trap, rupture of aggregates by ISP filtration) or the sampling of different particle pools (P-trap particles represent the sinking particles whereas ISP particles represent the standing stock; Buesseler et al., 2006; Benitez-Nelson and Charette, 2004; Moran et al., 2003) which can cause discrepancies between the Element/^{234}Th ratios. During GEOVIDE, no sediment traps were deployed, while during KEOPS2, the comparison between ISP and trap was possible.

2.3.1. Integration depth for export calculations

The Element/^{234}Th ratio varies vertically and, in order to use it as a factor of conversion to estimate the corresponding elemental export, the ratio needs to be determined at the depth of export (Buesseler et al., 2006) and has to represent the sinking particles exiting the surface waters. In this context, the choice of the depth for export calculations is crucial. Many former studies have used a fixed depth for convenience, because of limited sampling resolution or

ease of comparison with literature. However, Buesseler and Boyd (2009) have shown that the use of a single depth could bias temporal and spatial comparisons of particle export fluxes. They proposed to estimate the elemental fluxes, by integrating the ^{234}Th export flux as well as to determine the ratio of the element to ^{234}Th in particles, to the depth where the net primary production (NPP = GPP – R, where *GPP* is the gross primary production and *R* the respiration) goes to zero. In practice, this depth usually corresponds to the base of the euphotic zone (Ez; depth of the 1% light level; Jerlov, 1968), determined from the profile of PAR (photosynthetically active radiation). This standardization allows the assessment of the strength of the biological pump in different regions of the upper ocean across seasons and regions. Indeed, the layer above Ez is a particulate production layer, not representing necessarily the sinking particles whereas below Ez the particles undergo degradation by heterotrophic bacteria or zooplankton which will attenuate the export flux. However, Marra et al. (2014) pointed that the depth where NPP goes to zero is often deeper than the 1% light level, indicating that Ez is maybe not the most appropriate depth to choose the Element/^{234}Th for the calculation of the elemental export fluxes. Other parameters than light can give information on the layer where primary production is occurring. The transmissiometry data designate the particle-rich surface zone but lateral inputs of particles can alter the choice of the depth, especially in the vicinity of margins. Fluorescence allows the determination of the primary production zone (PPZ) depth and was defined by Owens et al. (2014) as the region from 0 m to the depth at which the fluorescence reaches 10% of its maximum value. Considering that there can be export (or remineralization) below or above these previous depths, another alternative is the choice of the ^{234}Th – ^{238}U equilibrium depth (Eq) representing the fully-integrated depletion of total ^{234}Th in the upper waters and thus the maximal export. However, this depth can be used only when the vertical sampling resolution of the total ^{234}Th is sufficient to constrain the exact equilibrium depth. This approach is the one that was possible to undertake for the GEOVIDE and KEOPS 2 samples.

2.3.2. Mathematical fitting of the particulate ratio Element/^{234}Th

Often, the ratio Element/^{234}Th at the specific depth (Eq or other depths) is not available. It is thus necessary to estimate it using a mathematical fitting with the ratios obtained at surrounding sampling depths. Buesseler and Boyd (2009) pointed that the conventional power law fitting of particle flux (Martin et al., 1987) could alter the Element to ^{234}Th ratio and thus the magnitude of the elemental flux. Indeed, as the power function is characterized by a curve approaching zero at infinite depth, the constraint of the curve fit could bias the real value, particularly at shallow depths. In order to account for the site-depending characteristics and the depth-related variations of element to ^{234}Th ratios, different interpolation/averaging methods can be used to obtain different estimates of this conversion factor at the specific depth, defined below by Z:

- the linear interpolation:

  $$\text{Element}/^{234}\text{Th} = a \times Z + b \qquad \text{(Equation 2.10)}$$

  where *Z* is the depth; *a* and *b* are the parameters obtained by a straight line fit between the upper and the lower data point relative to the target depth

- the power law interpolation:

  $$\text{Element}/^{234}\text{Th} = a \times Z^{-b} \qquad \text{(Equation 2.11)}$$

  where *Z* is the depth; *a* and *b* are the parameters obtained by an exponential fit

- the average of the two ratios bracketing the specific depth:

  $$\text{Element}/^{234}\text{Th} = [(\text{Element}/^{234}\text{Th})_{z-1} + (\text{Element}/^{234}\text{Th})_{z+1}] / 2 \qquad \text{(Equation 2.12)}$$

  where Z_{-1} and Z_{+1} are the depths immediately below and above the specific depth, *Z*

- the depth-weighted average Element:^{234}Th ratios in the water layer extending above Z:

  $$\text{Element}/^{234}\text{Th} = [\Sigma(\text{Element}/^{234}\text{Th} \times Z^*)] / [\Sigma Z^*] \qquad \text{(Equation 2.13)}$$

  where Z^* is the depth layer considered

The choice of the interpolation method depends on how processes affect the Element:^{234}Th ratio profiles.

The linear interpolation between depths bracketing Z, as well as taking the average of these depths, are appropriate calculations when the curve is monotonic but it can also yield to over- or under-estimates if there is an important fluctuation at one of the depths bracketing Z. The power law interpolation fits well the vertical evolution of labile element (C, N, P) to ^{234}Th ratios. The depth-weighted average approach yields to a ratio of all particles in the layer between surface and Z thus potentially including living and non-sinking plankton cells which can affect the Element/^{234}Th ratio. However, this calculation seems particularly appropriate for the metals/^{234}Th ratios increasing with depth.

2.4. Carbon remineralization fluxes determined from Ba_{xs} distributions

2.4.1. Principle

Originally, the presence of Ba in biogenic particles has been deduced from the important presence of Ba in sediments located under highly productive surface waters (Church, 1970; Turekian and Tausch, 1964). Later, Dehairs et al. (1980) highlighted that barite crystals ($BaSO_4$) were the main carrier of this particulate biogenic barium, also called excess barium (Ba_{xs}) in intermediate and deep waters. These different authors, as well as Bishop (1988), confirmed that the formation of these barite crystals was controlled by biota in surface waters. Then, the formation of barite crystals in sediment traps has been shown to be strongly related to POC export fluxes (Bishop, 1988; Dymond and Collier, 1996; Francois et al., 1995; Jeandel et al., 2000) and consequently, Ba_{xs} accumulation in sediments has been used to reconstruct paleo-productivity (Eagle et al., 2003; Paytan et al., 1996; Paytan and Griffith, 2007).

In the Southern Ocean, a good agreement between the Ba_{xs} content in the mesopelagic zone and the oxygen consumption rate has been demonstrated (Figure 2.7; Dehairs et al., 1997, 1991; Shopova et al., 1995), with the O_2 consumption rate deduced from the dissolved oxygen profiles using a one-dimensional inverse model. Ba_{xs}, associated with barite crystals, were thus used as a proxy to determine mesopelagic remineralization fluxes of exported biogenic

material (Dehairs et al., 1997). This proxy was then used in the Southern and North Pacific oceans (Cardinal et al., 2005; Dehairs et al., 2008; Jacquet et al., 2015, 2011; Jacquet et al., 2008; Jacquet et al., 2008; Planchon et al., 2013).

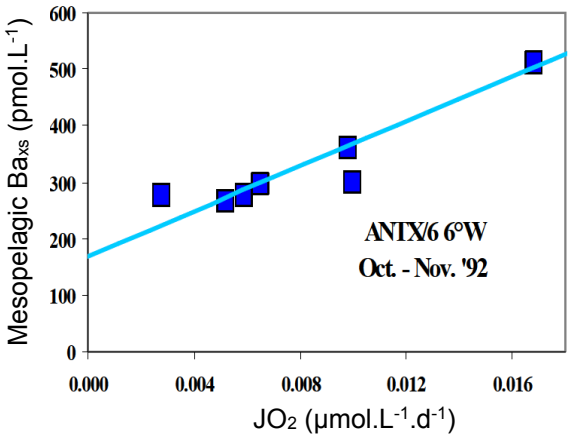

Figure 2.7: Mesopelagic particulate biogenic Ba (Ba_{xs}) versus calculated oxygen consumption rate (JO_2) for stations within the Southern Antarctic Circumpolar Current region (Dehairs et al., 1997).

Despite the lack of understanding on the barite formation, results support the idea that the barite crystals precipitate inside oversaturated micro-environments, mostly aggregates of organic material where bacterial activity is intense (Bishop, 1988; Collier and Edmond, 1984; Dehairs et al., 1980; Ganeshram et al., 2003). When these aggregates are remineralized due to heterotrophic bacterial activity, barite crystals are released over the mesopelagic layer as micro-sized particles (≈ 1 µm; Ganeshram et al., 2003, Figure 2.9).

Usually, Ba_{xs} distributions display maximum concentrations in the mesopelagic layer (100-1000m) reflecting the release of barite crystals during remineralization of organic matter (Figure 2.8). At greater depths, usually below 1000 m, Ba_{xs} concentrations decrease to a background level (around 180 pM, Dehairs et al., 1997). In surface waters, a peak of Ba_{xs} can sometimes be observed, which is probably not related to remineralization, but rather to Ba absorption by phytoplankton. Indeed, barite crystals are not observed in the surface samples (Ganeshram et al., 2003). Between the surface water Ba_{xs} peak and the increased Ba_{xs} contents in the mesopelagic layer, the signal returns to the background level, which also suggests a different process between surface and mesopelagic layers.

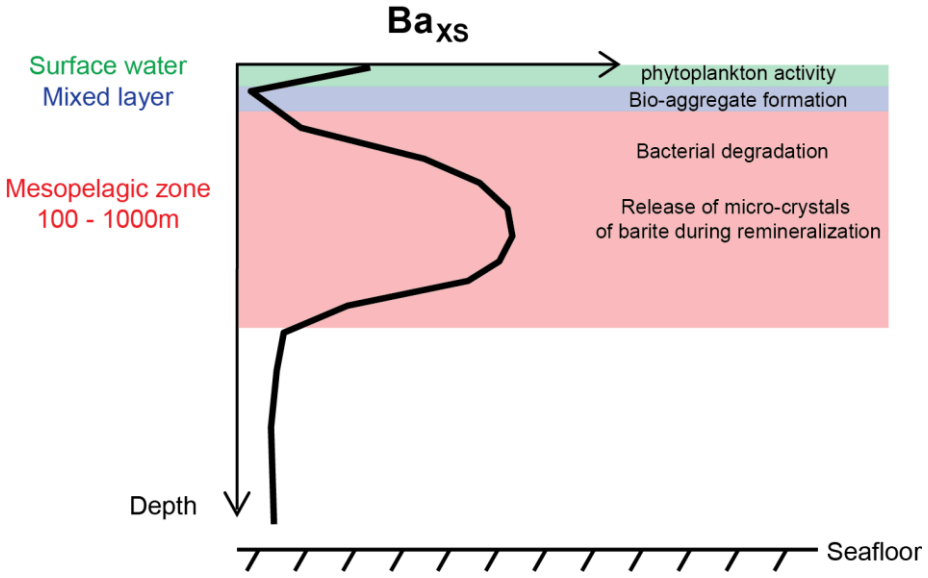

Figure 2.8: Typical Ba_{xs} profile in seawater, adapted from Jacquet, 2007.

In order to verify that the concentrations of Ba_{xs} (analyzed by ICP-MS, see section II.1.d of this chapter) are related to the presence of barite crystals, I estimated the quantity of Ba_{xs} associated with barite crystals detected with scanning electron microscopy- Electron Microprobe (SEM-EMP). At VUB metallurgy laboratory, I used a field emission scanning electron microscope (JSM-7100F, JEOL) to scan fractions (0.5/0.8 cm² from a total surface of 15 cm²). As the barite is a dense mineral (density 4.45 $g.cm^{-3}$), they are brighter than less dense particles (salt, lithogenic particles, biogenic shells). For these particles, we then verified the energy-dispersive spectrum. The identification of barite crystals was confirmed if three Barium-L_α and one Sulfur-K_α spectral lines were present as principal components (Figure 2.9).

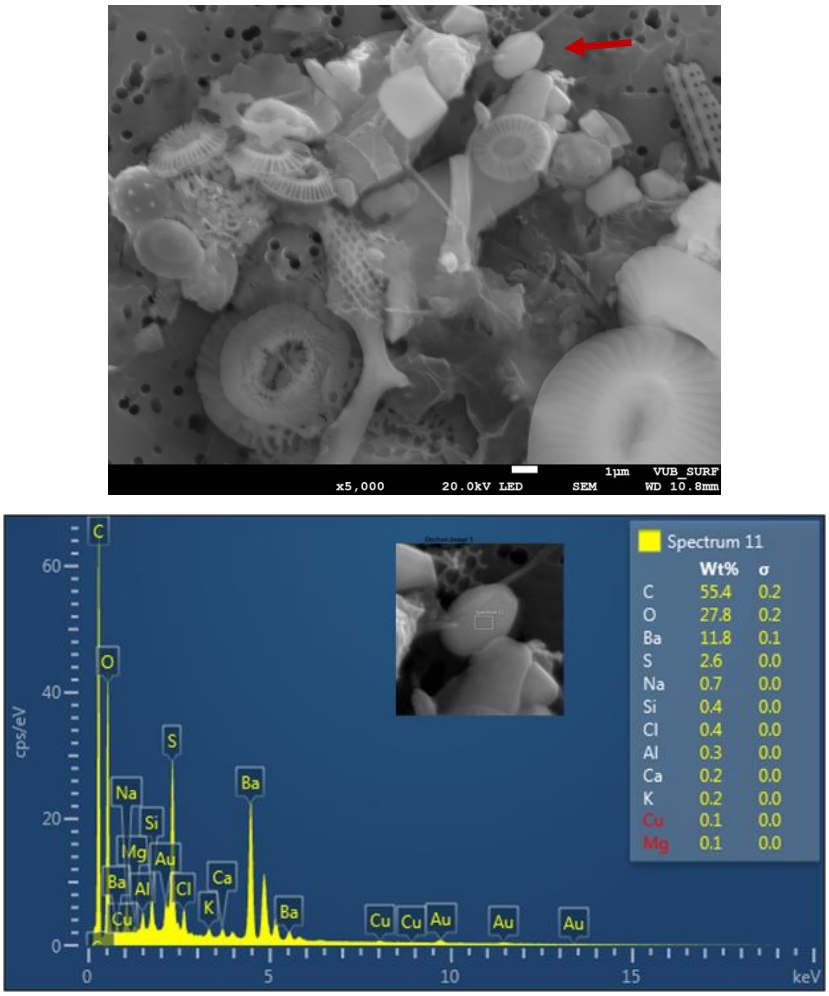

Figure 2.9: Example of a barite crystal (indicated with the red arrow) obtained by scanning electron microscopy, on the filter sampled at 600 m of Station 69 during the GEOVIDE cruise, and the corresponding energy-dispersive spectra.

Seven samples from the GEOVIDE cruise (Stations 13, 26, 38, 44, 69 and 77), including six samples collected between 300 and 700 m and one at 50 m, were analyzed. In the latter sample, no barite crystals were found, but for the other samples several barite crystals were observed close to biogenic aggregates.

A small part of one filter sampled at 600 m (0.003% of the total surface) was carefully analyzed in order to deduce the concentration of barium originating from barite crystals, using the following equation:

$$pBa\ in\ barite = \frac{V \times \mu_{BaSO_4} \times \frac{M(Ba)}{M(BaSO_4)}}{V_{SW\ filtered}} \qquad \text{(Equation 2.14)}$$

where pBa is the concentration of barium deduced from the SEM analysis, V is the volume of each crystal calculated using the largest and smallest axes of the projected particle surface (assimilated to the projection of an ellipse or a sphere with the Image J software, μ_{BaSO4} is the density of barite (4.5), $\frac{M(Ba)}{M(BaSO4)}$ is the molar fraction of Ba in $BaSO_4$ and V_{SW} is the volume of seawater filtered through this part of the filter.

Finally, the Ba concentration based on the analysis of discrete barite particles (1260 pmol.L^{-1}) compared well with the concentration of total Ba_{xs} analyzed by ICP-MS (831 pmol.L^{-1}). These values are of the same order of magnitude (but with Ba from discrete barite being 1.5 times larger than Ba from total analysis), confirming that the total particulate biogenic barium is mainly carried by barite crystals and that the barium concentration in the mesopelagic layer can be related to the oxygen consumption.

2.4.2. Determination of the carbon remineralization flux

The mesopelagic carbon remineralization was estimated using an empiric algorithm relating the Ba_{xs} content to the rate of oxygen consumption (Shopova et al., 1995; Dehairs et al., 1997):

$$JO_2 = (\text{meso } Ba_{xs} - Ba_{\ residual}) / 17200 \qquad \text{(Equation 2.15)}$$

where JO_2 is the rate of oxygen consumption (µmol.L^{-1}.d^{-1}), *meso* Ba_{xs} is the depth-weighted average concentration of biogenic barium (DWA; pmol.L^{-1}), $Ba_{residual}$ is the deep ocean Ba_{xs} value (or Ba_{xs} background signal, pmol.L^{-1}).

The depth-weighted average of meso Ba_{xs} was performed between 100 and 500 m, and between 100 and 1000 m in order to compare the carbon remineralization rate in the top and in the whole mesopelagic layer, in order to determine where is the most important zone for remineralization.

In the Southern Ocean, the residual Ba_{xs} value was observed at zero oxygen consumption and reached 180 $pmol.L^{-1}$ (Dehairs et al., 1997). A similar residual Ba_{xs} value was observed in the North Atlantic (see Chapter 4).

Then, the oxygen consumption JO_2 can be converted into a C remineralized flux using this relationship:

$$\text{POC Mesopelagic Remineralization} = Z \times JO_2 \times (C/O_2)_{\text{Redfield Ratio}} \qquad \text{(Equation 2.16)}$$

where *MR* is the mesopelagic remineralization rate of organic carbon (mg $C.m^{-2}.d^{-1}$), *Z* is the thickness of the depth layer in which meso Ba_{xs} is calculated, JO_2 is given by the Equation 9 and $(C/O_2)_{Redfield\ Ratio}$ is the stoichiometric molar C to O_2 ratio (127/175).

Chapter 3

High variability of particulate organic carbon export fluxes in the North Atlantic Ocean

This manuscript will be submitted in January 2017 to Biogeosciences (GEOVIDE special issue)

Abstract

In this study, we report Particulate Organic Carbon (POC) export fluxes estimated using the ^{234}Th-based approach in different biogeochemical provinces of the North Atlantic, as part of the GEOTRACES GA01 expedition (GEOVIDE, 15th May-30th June 2014). Surface and deep POC export fluxes were deduced by combining export fluxes of ^{234}Th with the POC/^{234}Th ratio of sinking particles at the depth of export. Particles were collected in two size classes (>53 µm and 1-53 µm) using *in-situ* pumps, considering the large size fraction as representative of sinking material. Surface POC export fluxes revealed latitudinal variations between provinces ranging from 1.4 mmol C.m^{-2}.d^{-1} in the Irminger Sea where the bloom was on this way down but close to its maximum peak, to 12 mmol C.m^{-2}.d^{-1} near the Iberian Margin where the bloom had already declined. In addition to the bloom staging, the variations of POC export fluxes were also related to the presence of biogenic (biogenic silica or calcium carbonate) and lithogenic (aluminum) minerals, able to ballast the POC. Indeed, the comparison between the POC export fluxes with those of biogenic silica (BSi) related to the presence of diatoms, calcium carbonate ($CaCO_3$) related to the presence of coccolithophorids and particulate aluminum (pAl) as a tracer of lithogenic particles, highlighted a direct influence of these minerals on the magnitude of POC export fluxes. The density of the particles, controlled by these minerals, appeared to contribute more to the POC export flux than the phytoplankton size structure. The surface POC export fluxes were then compared to primary production (PP) in order to assess the export efficiency, defined as the ThE ratio. This ratio strongly varied regionally and was generally low (≤ 12%), except at two stations located near the Iberian margin (35%) and within the Labrador Sea (34%), which were characterized by the lowest PP. We thus conclude that the North Atlantic during this period was not as efficient in transferring carbon to depth as described in previous studies. Finally, we compare the surface and deep POC export fluxes to investigate the transfer efficiency (T_{eff}) of the North Atlantic biological pump. This parameter was also highly variable regionally and appeared to be driven by sinking

particles ballasted by calcite or lithogenic minerals, but also by sub-mesoscale features such as the sub-arctic front.

3.1. Introduction

The North Atlantic represents one of the most productive spring phytoplankton bloom of the world‘s ocean (Esaias et al., 1986; Longhurst, 2010), starting first within the European basin in March and propagating northwards within the subpolar region in April and May (Henson et al., 2009; Pommier et al., 2009). This strong bloom generates an important pulse of biogenic sinking particles (Buesseler et al., 1992; Honjo and Manganini, 1993; Le Moigne et al., 2013b) which accounts for up to 18% of the global biological carbon pump (Sanders et al., 2014). As a consequence, the North Atlantic has been identified as an efficient ocean to export carbon to depth (Buesseler and Boyd, 2009; Herndl and Reinthaler, 2013).

The North Atlantic consist of several provinces (sensu Longhurst, 1995) characterized by distinct biogeochemical and physical characteristics which influence the magnitude of the particle export fluxes. For example, the low nutrient availabilities in the North Atlantic subtropical gyre (NAST) province limits the biomass development (Moore et al., 2008), dominated by pico-phytoplankton such as cyanobacteria (Zehr and Ward, 2002). Northward, in the Atlantic Arctic (ARCT) province, the phytoplankton growth is strongly seasonally light-limited (Riley, 1957) and the key parameter for alleviating these limitations is the progressive shoaling of the mixed layer. There, diatoms dominate the phytoplankton bloom until the exhaustion of the silicic acid stock (Martin et al., 2011). Then, an intense bloom of coccolithophorids develops (Poulton et al., 2010; Raitsos et al., 2006). Between these provinces, a third area called the North Atlantic Drift (NADR) province is a transition zone where nutrients and/or light can limit the primary production (Henson et al., 2009). In summer, at the end of the bloom, this province can be iron-limited, and become “High Nutrient Low Chlorophyll” (HNLC) regions (Moore et al., 2006; Nielsdottir et al., 2009; Sanders et al., 2005).

The North Atlantic is thus a heterogeneous basin in terms of limitations and phytoplankton communities.

According to these contrasted biogeochemical regimes, carbon export fluxes in the North Atlantic are highly variable spatially (Jickells et al., 1996; Thomalla et al., 2006). Furthermore, studies using fixed sediment traps demonstrated that pulsed exports were neither necessarily recurrent over years nor associated to unused patterns of mixing and productivity (Antia et al., 2001; Billet et al., 1983; Lampitt et al., 2010; Peinert et al., 2001), indicating that carbon export fluxes in North Atlantic are also variable temporally.

The strong regional and temporal variation of the biogeochemical characteristics highlights the complexity to determine carbon export fluxes and to define a basin such as the North Atlantic as an efficient ocean to export carbon.

In this context, we investigated the carbon export fluxes derived using the Thorium-234 approach, along the GA01 GEOTRACES section (GEOVIDE cruise, 15 May - 30 June, 2014; R/V Pourquoi Pas?), crossing the three main biogeochemical provinces described above. ^{234}Th is a highly particle reactive element, with a short half-life (24.1 days), which is widely used to explore particle export over short events such as phytoplankton blooms. A deficit of ^{234}Th with respect to its parent ^{238}U (conservative in seawater) is usually observed in the upper water column where particles sink. A ^{234}Th flux can be quantified and then converted into a particulate organic carbon (POC) flux by using the POC:^{234}Th of sinking particles at the depth of export (Buesseler et al., 2006).

In this paper, we first explore ^{234}Th distributions in the upper waters to estimate surface export fluxes and in the mesopelagic waters to investigate the flux attenuation due to degradation processes. These export fluxes are discussed with regards to the stage and intensity of the bloom, the phytoplankton size structure, and the composition in biogenic and lithogenic minerals that can play a role of ballast for POC. Then, using *in-situ* primary production data and deep carbon export fluxes, we investigate the export and transfer efficiencies of the biological carbon pump in the North Atlantic.

3.2. Methods

3.2.1. Study area

For the purpose of this work, 11 stations were investigated in three different biogeochemical provinces (Figure 3.1):

- the NAST (North Atlantic Subtropical) province (Stations 1 and 13) was sampled at the beginning of the cruise (19 and 24 of May, respectively). Nitrate (NO_3^-) and silicic acid ($Si(OH)_4$) concentrations were under 1 $\mu mol.L^{-1}$ in the upper 40m, despite the proximity of the Iberian margin, where sits a natural upwelling (Costa Goela et al., 2016; Zúñiga et al., 2016; http://marine.copernicus.eu/), that potentially fuels the area with vast amounts of macronutrients. In this province, dissolved iron (dFe) concentrations were non-limiting, with concentrations in surface waters varying between 0.15 and 1.08 $nmol.L^{-1}$ (Tonnard et al., in prep.).

- the NADR (North Atlantic Drift) province, including the western European basin (Stations 21 and 26) and the Icelandic basin (Stations 32 and 38), was sampled from the 31st of May to the 10th of June. The two basins are separated by the sub-arctic front (SAF) located near Station 26. The surface waters had low $Si(OH)_4$ concentrations (≤ 1 $\mu mol.L^{-1}$), moderate dFe concentrations (0.40 $nmol.L^{-1}$; Tonnard et al., in prep.) and high NO_3^- concentrations (> 5 $\mu mol.L^{-1}$) except at Station 21, located south of the SAF, where nitrate concentrations were below 1 $\mu mol.L^{-1}$ in surface waters.

- the ARCT (Atlantic Arctic) province, including the Irminger Sea basin (Stations 44 and 51) and the Labrador Sea basin (Stations 64, 69 and 77) were sampled on the 13th and 16th of June and at the end of the cruise (19th, 22th and 26th of June), respectively. The Irminger Sea basin was characterized by high surface $Si(OH)_4$ and NO_3^- concentrations (> 6 $\mu mol.L^{-1}$) and moderate dFe concentrations (0.23-0.78 $nmol\ L^{-1}$; Tonnard et al., in prep.). The surface waters of the Labrador Sea basin was characterized by a north to south gradient in macronutrients, with high NO_3^- and $Si(OH)_4$ concentrations at Station 64 (> 3.6 $\mu mol.L^{-1}$ and 4.6 $\mu mol.L^{-1}$, respectively), decreasing gradually to the south with low concentrations at Station 77 (~1

µmol.L^{-1} and < 1 µmol.L^{-1}, respectively) . Moderate to high dFe concentrations were observed in this area (from 0.75 nmol.L^{-1} at Station 64 to 2.5 nmol.L^{-1} above the Newfoundland Plateau; Tonnard et al., in prep.). This basin is also characterized by the subduction of the Labrador Seawater (LSW; Kieke and Yashayaev, 2015) which was particularly intense (1500m-deep convection) during the winter 2013-2014 (Lherminier, personal communication).

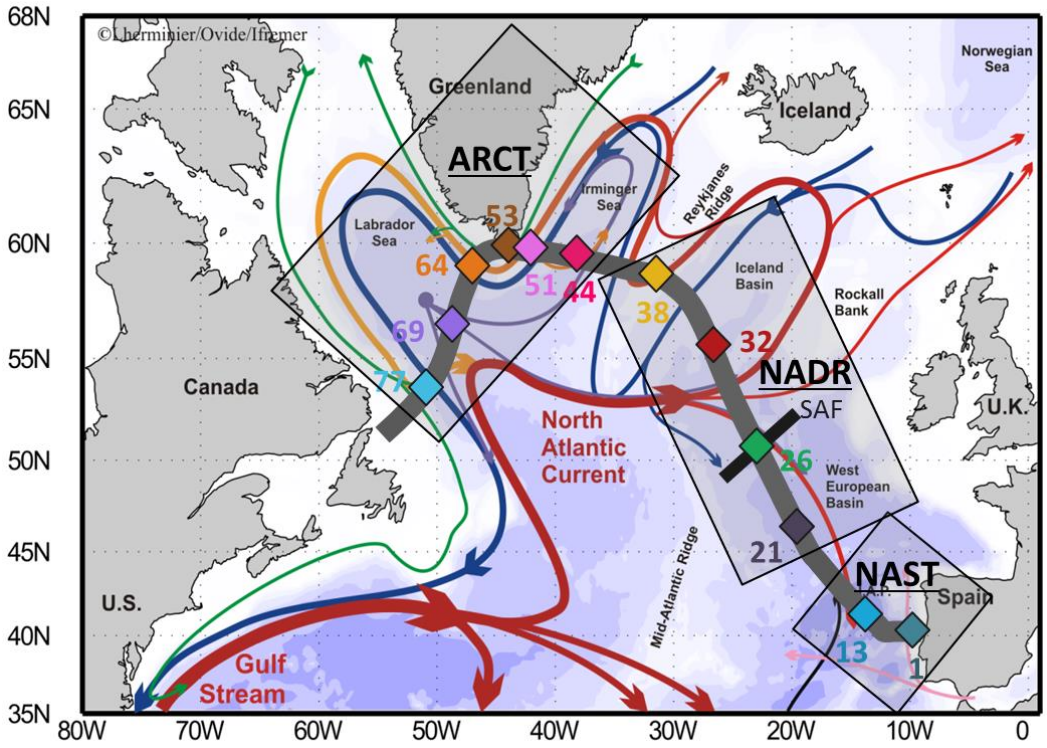

Figure 3.1: Simplified schematic of the water mass circulation in the North Atlantic (adapted from Garcia-Ibanez et al., 2015) superimposed with the GEOVIDE cruise track (thick grey line) and stations (colored diamonds). Surface currents are represented

3.2.2. Total ^{234}Th and ^{238}U

Total ^{234}Th activities were determined from 4L unfiltered seawater samples collected with Niskin bottles and stored in 4L polypropylene Nalgene bottles. Usually, 17 or 18 depths were sampled between the surface and 1000-1500m, except at Stations 26 and 77 where only 9 and 15 depths were sampled, respectively (Table S3.1). In addition, deep samples (n=15; between 1000 and 3500m) were taken for the calibration of low level beta counting (van der Loeff et al., 2006), as in open ocean studies, deep water samples (2000 – 3000 m) are generally assumed to be in secular equilibrium regarding the ^{234}Th-^{238}U pair. Seawater

samples were processed following the method developed by Pike et al. (2005). Briefly, samples were acidified at pH 2 using concentrated HNO_3 (suprapur grade, Merck), spiked with 1 mL of ^{230}Th yield monitor to estimate the ^{234}Th recovery after the Mn precipitation. After 12 hours of equilibration, pH was increased to 8.5 using concentrated NH_4OH (suprapur grade, Merck). One hundred micro-liters of $KMnO_4$ and $MnCl_2$ (analytical grade, Merck) were added to form a Mn precipitate and, after 12 hours of equilibration, samples were filtrated on quartz-microfiber discs (QMA, Sartorius, nominal porosity=1 µm, diameter=25 mm). Filters were then dried at 50°C overnight, mounted on nylon holders, covered with Mylar and aluminum foil and counted on board using low level beta counters (RISØ, Denmark) until the counting relative standard deviation (RSD) was below 2%. At the home-laboratory, residual beta activity was measured for each sample after a delay of six ^{234}Th half-lives (~6 months) and was subtracted from the gross counts obtained on-board. All samples were then processed for Th recovery using the ^{229}Th as a second yield tracer. Briefly, each filter was dismounted of nylon holder and placed into a clean 30 mL vial (Savillex). All samples were spiked with 50 µl of ^{229}Th, dissolved in 10 mL mix of 8M HNO_3/1M H_2O_2 (suprapur grade, Merck), heated overnight at 60°C and filtered through Acrodisc® syringe filters (Pall, Nylon membrane, nominal porosity=0.2 µm, diameter=25 mm). The column purification, recommended by Pike et al. (2005) was not applied, because Planchon et al., (2013) showed this was not necessary to obtain accurate measurements. In order to increase concentrations during the analyses, samples were pre-concentrated by evaporating 2 mL of the filtered solution. The residue was then diluted in 6 mL of 1.4M HNO_3 (suprapur grade, Merck) and ^{230}Th and ^{229}Th were measured by SF-ICP-MS (Element 2, Thermo Scientific) in low resolution mode. Each sample was analyzed 3 times. The chemical recovery of the analytical process was 91 ± 14 % (n=200), and the precision of ^{230}Th:^{229}Th ratios averaged 1.2% (RSD), which is within the range indicated by Pike et al. (2005). Uncertainties on total ^{234}Th activity were estimated using the error propagation and accounted to 0.07 $dpm.L^{-1}$.

The ^{238}U activity was deduced from salinity using the relationship given by Owens et al. (2011):

$$^{238}U = 0.0786 \times S - 0.315 \qquad \text{(Equation 3.1)}$$

where ^{238}U is the ^{238}U activity in dpm.L^{-1} and S is the salinity in psu.

For the deep samples, the RSD of the $^{234}Th/^{238}U$ ratios averaged 0.02 (n= 15) and was used for the calibration of low level beta counting.

3.2.3. Particulate ^{234}Th and POC sampling and analysis

Suspended particles were collected using *in-situ* large-volume filtration (100-1600 L) systems (McLane pumps, deployed in the upper 500 m, and Challenger Oceanics pumps deployed below 500 m generally; ISP hereafter) through paired 142mm-diameter filters: a 53 µm mesh nylon screen (SEFAR-PETEX®; polyester) and a 1 µm pore size quartz-microfiber filter (QMA, Sartorius), respectively. Therefore, two size fractions of particles were collected: the small size fraction (referred to SSF hereafter, 1-53 µm) and the large size fraction (referred to LSF hereafter, >53 µm). Filters were cleaned as follows: PETEX screens were soaked in 0.6M HCl, (Normapur, Merck) rinsed with Milli-Q water, dried at ambient temperature in a laminar flow hood and stored in clean plastic bags; QMA filters were precombusted at 450°C during 4h and stored in aluminum foils until use. *In-situ* pumps were deployed on a stainless steel cable between 15 and 800 m and the pumping time was approximately 2-3 hours (Table S3.2).

After collection, filters were processed on board. The 142 mm nylon screen was cut into quarters using a clean scalpel. The large particles were then rinsed off the quarter of the screen using 0.45 µm filtered seawater collected along the transect and refiltered on a silver filter (SterliTech, porosity=0.45 µm, diameter=25 mm) under a laminar flow hood using filtration units. This operation was carry out a second time by resuspending and refiltering the large particles from another 142 mm nylon quarter on a GF/F filter (Whatman®, porosity=0.7 µm, diameter=25 mm) in order to have a replicate.

Punches of the QMA filter were sampled using a plexiglas punch of 25 mm diameter.

Then, subsamples of silver, GF/F and QMA filters were dried overnight (50°C), and prepared for beta counting, as explained for total ^{234}Th samples. After the counting of the residual beta activity, samples were prepared for POC, PN analyses along with their ^{13}C and ^{15}N

abundances measurements, but, in this study, only POC data will be presented (as PN concentrations and ^{13}C and ^{15}N abundances data will be published in a separate manuscript). In brief, filters were dismounted from filter holders and fumed under HCl vapor overnight inside a glass desiccator to remove the carbonate phase. After a drying step at 50°C, samples were packed in precombusted (450°C overnight) silver cups and analyzed with an elemental analyzer – isotope ratio mass spectrometer (EA-IRMS, Delta V Plus, Thermo Scientific). Acetanilide standards were used for the calibration. The detection limits and C blanks were respectively 0.59 and 0.80 µmol for Ag filters (n=11) and were 0.49 and 1.52 µmol for QMA filters (n=13).

3.2.4. Mineral composition of particles

The concentrations of biogenic silica (BSi), non-sea salt calcium assimilated to calcium carbonate ($CaCO_3$) and particulate aluminum (pAl) were also determined from ISP filters, but from a different pump head than POC and particulate ^{234}Th, dedicated to trace elements. In this second pump head, particles were collected through paired 142 mm-diameter filters: a 53 µm mesh nylon screen (Petex; polyester) and a 0.8 µm polyestersulfone filter (Supor). Before use, filters were cleaned in Low Density PolyEthylene (LDPE) containers containing 1.2M HCl (Suprapur grade, Merck), heated at 60°C and rinsed with Milli-Q water. On board, filters were processed under a laminar flow unit located in a customized clean “bubble”. Before and after the ISP recoveries, pump heads were also covered with plastic bags to minimize contamination. The 142 mm filters were subsampled as follows: using a clean ceramic scalpel, one quarter of the Petex, dedicated to ^{234}Th and BSi analyses in the large size fraction (LSF, >53 µm), was cut out. Then, particles were washed off this Petex using 0.45 µm filtered seawater collected during the GEOVIDE cruise (filtered through a Supor filter in clean conditions) and collected on Polycarbonate filters (Nuclepore®, porosity=0.4 µm, diameter=25 mm) mounted on a polysulfone filtration units (Pall). Filters were then dried under the laminar flow unit and prepared for Beta counting. A second quarter of the Petex which was dedicated to trace element (TE, including pAl) and major element (including particulate calcium and

sodium; pCa and pNa) analyses in the LSF was kept in a clean petrislide (Millipore) at -20°C until sample processing and subsequent analysis in the home laboratory. The 142 mm Supor filter was also subsampled for TE, major element and BSi analyses in the small size fraction (SSF; 1-53 µm), using a 13 mm diameter disposable skin biopsy Acupunch. These punches were not Beta counted and were directly stored in clean Petri slide double bagged in Ziploc bags and stored at -20°C until analysis. TE export fluxes will be published separately (Lemaitre et al., in prep.).

Back in the home laboratory, the large particles of the remaining PETEX quarter dedicated to trace and major element analyses were washed off with 0.45 µm filtered surface seawater collected during the GEOVIDE cruise (Station 77, 40m, filtered through a Supor filter) and collected on acid cleaned 47 mm diameter mixed cellulose esters filters (MF-Millipore® filters, 0.8 µm), using Nalgene filtration units. Then, one half of the 47 mm MF, or one 13 mm punch of the Supor filter (SSF), was placed along the wall of a 15 mL acid cleaned Teflon vial (Savillex) and digested with a HNO_3 8M-HF 2.3M mix solution (Ultrapur and Suprapur grades, Merck), refluxing at 130°C during 4h. After gentle evaporation close to near dryness, 200 µL of concentrated HNO_3 (Ultrapur grade, Merck) was added in order to drive off the fluorides. The residue was brought back into solution with 3% HNO_3 spiked with 1 $\mu g.L^{-1}$ of Indium and stored in acid cleaned 15 mL centrifuge tubes (Corning) until analysis for estimating the total particulate trace elements concentrations (Planquette and Sherrell, 2012). The measurements were performed using a SF-ICP-MS (Element 2, Thermo) following the method of Planquette and Sherrell (2012). External calibration curves were ran at the beginning, middle and end of the run. The precision and the accuracy of our analyses were assessed by measuring replicates and the Certified Reference Materials (CRM) BCR-414, respectively (Table 3.1).

Using the same 3% HNO_3 archive solutions, major elements (Ca, K, Mg, Na, Sr) were analyzed using an ICP-AES (ULTIMA 2). The precision and the accuracy of our analyses were assessed by measuring replicates and the Certified Reference Materials (CRM) BCR-414 (Table 3.1). It

was then possible to estimate the calcium carbonate ($CaCO_3$) concentrations, assuming that non-sea salt Ca comes from the calcium carbonate:

$$[Ca]_{CaCO3} = Ca - [(Ca/Na)_{SW} \times Na] \quad \text{(Equation 3.2)}$$

where $[Ca]_{CaCO3}$ is the estimated concentration of calcium carbonate in $\mu mol.L^{-1}$; Ca and Na are respectively the particulate calcium and sodium concentrations in $\mu mol.L^{-1}$; $(Ca/Na)_{SW}$ is equal to 0.022 $mol.mol^{-1}$ and represents the mean ratio determined in seawater by Copin-Montégut (1996).

	Al	Ca	Na
Indicative value ($\mu g.g^{-1}$)	2154 ± 803	65955 ± 2893	
Determined Concentration ($\mu g.g^{-1}$)	3112 ± 464	51133 ± 1057	6601 ± 13
Recovery (%)	144	78	

Table 3.1: Determined concentrations (µg.g-1) and resulting recoveries (%) of the Certified Reference Material plankton BCR-414, compared to indicative values (n=5).

Following the method of Ragueneau et al. (2005), biogenic silica (BSi) concentrations were estimated using an alkaline digestion with correction of the lithogenic silica (LSi). All experiments were made using clean polymethylpentene and polypropylene (VWR) centrifuge tubes. A 25 mm diameter Nuclepore filter previously Beta counted (LSF), or a Supor punch (SSF), was placed in a centrifuge tube and digested with 8 mL of a 0.2 M NaOH solution (pellets for analysis, Merck) at 95°C during 1h in a hot bath. After cooling, the pH was neutralized by adding 2 mL of 1M HCl (Analar Normapur, Merck) and the supernatant was separated from the remaining suspended material. Silicic acid concentrations were determined following the automated acid/molybdate colorimetric method (Aminot and Kérouel, 2007), using an AutoAnalyzer3 Bran&Luebbe (detection limit: 0.18 $\mu mol.L^{-1}$). Dissolved aluminum concentrations were determined by a fluorimetric method (fluorimeter MITHRAS LB 940) detecting a complex Aluminum-Lumogallion developed by Hydes and Liss (1976; detection limit: 0.14 $\mu mol.L^{-1}$). At the end of the first digestion, all the BSi is converted into silicic acid,

but LSi can also be dissolved during this first digestion involving a bias for the determination of BSi concentration. This bias was resolved with a second digestion, equivalent to the first one, allowing the determination of a ratio (Si/Al) characteristic of the minerals. The corrected BSi concentration was obtained using the following equation:

$$BSi = [Si_1] - [Al_1] \times (Si/Al)_2 \qquad \text{(Equation 3.3)}$$

where *BSi* is the final concentration of biogenic silica in µmol.L^{-1}; *$[Si_1]$* and *$[Al_1]$* are the concentrations of silicic acid and aluminum determined during the first digestion in µmol.L^{-1}; *$(Si/Al)_2$* is the ratio of the concentrations of silicic acid and aluminum determined during the second digestion.

3.2.5. Pigments

Pigments were determined at 10 depths per station in samples collected between the surface and 200 m depth, using Niskin bottles. Typically, 2L of seawater were filtered through a 25 mm diameter GF/F (0.7 µm porosity, Whatman) and filters were immediately frozen in liquid nitrogen and stored at -80°C until analysis. At the home-laboratory, filters were extracted in 100% methanol, disrupted by sonication and clarified by filtration through a GF/F filter. The same day, the samples were analyzed by high-performance liquid chromatography (HPLC, Agilent Technologies 1200). The complete procedure can be found in Ras et al. (2008). These pigments are specific of individual phytoplanktonic taxa or groups and can thus be used as biomarker of various phytoplankton communities such as dinoflagellates (Peridin pigment) diatoms (Fucoxanthin pigment), prymnesiophytes including the coccolithophorids (19'-Hexanoyloxyfucoxanthin pigment) and cyanobacteria (Zeaxanthin pigment; (Ras et al., 2008; Uitz et al., 2006). These taxa are then gathered into three phytoplankton size classes (micro-, nano- and pico-phytoplankton) according to the fraction of each pigment-based size class with respect to the total phytoplankton biomass (Ras et al., 2008). Micro-phytoplankton corresponds to phytoplankton with size greater than 20 µm, nano-phytoplankton with sizes ranging between 2 and 20 µm and pico-phytoplankton relates to a size smaller than 2 µm.

3.2.6. Primary production

In order to determine the *in-situ* daily primary production (PP), incubation experiments were conducted using stable isotope enrichment techniques ($H^{13}CO_3^-$) from the surface to 0.2% Photosynthetically Active Radiation (PAR) depth level and will be described elsewhere (A. Roukaerts, D. Fonseca Batista and F. Deman, unpublished data). Briefly, at each station, seawater was sampled at 3 to 6 depths and incubated on deck with a $H^{13}CO_3^-$ enriched substrate. All on-board incubations were sampled at the initial state and after 24h of experiment, seawater was then filtered through glass fiber filters (MGF, 0.7 µm porosity, Sartorius). At the home-laboratory, POC concentrations and ^{13}C abundances were analyzed by EA-IRMS and uptake rates were deduced following the Hama et al. (1983) method. The daily primary production was then estimated by depth-integrating the uptake rates per station as a function of depth from 54 to 0.2% of PAR.

3.3. Results

3.3.1. Biological features of the study area

3.3.1.1. Pigments

Along the transect, the Chl-*a* concentrations ranged between 0.16 (Station 1) to 2.48 (Station 77) $mg.m^{-3}$ with a chlorophyll maximum always located within the upper 20 m, except at Station 1 where the highest concentrations were measured between 50 and 65 m (Figure 3.2).

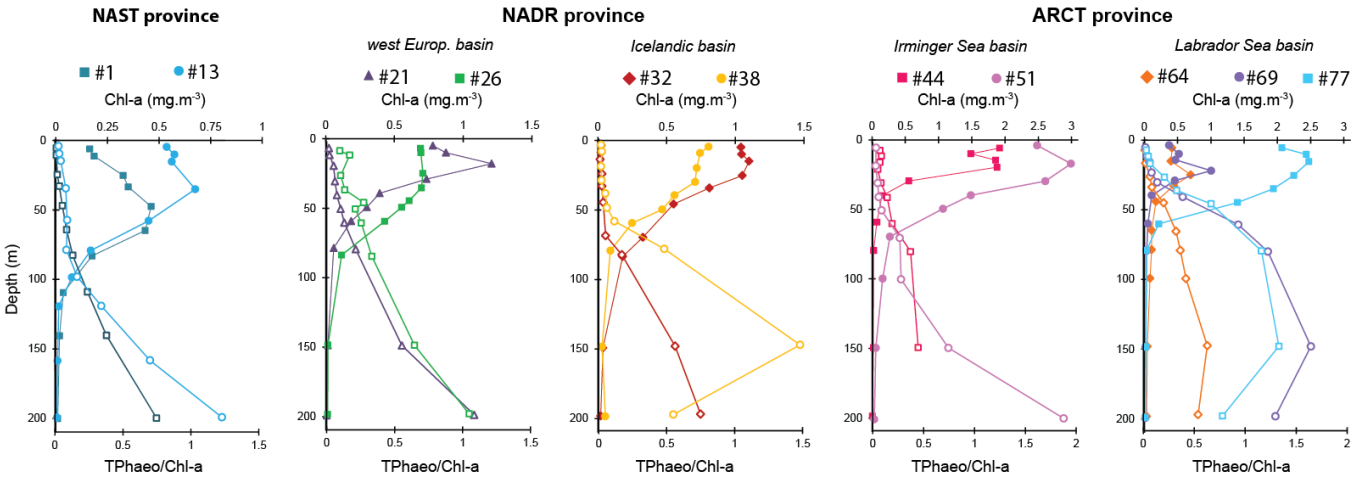

Figure 3.2: Chlorophyll-a (Chl-a) concentrations in mg.m-3 (closed symbols) and total phaeopigment over Chl-a ratios (TPhaeo/Chl-a; open symbols) in the upper 200 m.

The deep Chl-*a* maximum at Station 1 was nevertheless low (~0.45 mg.m^{-3}). In general, the lowest Chl-*a* concentrations were determined in the NAST province with a maximum of 0.68 mg.m^{-3} at 35 m. Moderate Chl-*a* concentrations were measured in the NADR province and in the Labrador sea basin, reaching respectively 1.21 and 1.00 mg.m^{-3} at ~20 m, except at Station 77 where Chl-a concentrations were higher, reaching 2.47 mg.m^{-3} at 15 m. Finally, the highest Chl-*a* concentrations were measured in the Irminger sea basin, with a maximum of 2.99 mg.m^{-3} at ~20 m (Station 51). Except for Station 1 located close to the Iberian shelf, the stations located in proximity of the shelves were characterized by the highest surface Chl-*a* concentrations reaching 2.99 and 2.47 mg.m^{-3} near the Greenland (Station 51) and Newfoundland (Station 77) shelves, respectively.

The concentrations of total phaeopigments (TPhaeo, i.e., the sum of Phaeophytin-a and Phaephorbide-a pigments) that are degraded Chl-*a* products associated with grazing activity and phytoplankton senescence (Wright et al., 2010; Ras et al., 2008) were also determined. This allowed the deduction determinaton of the ratios TPheo/Chl-a for all stations (Figure 3.2). A ratio TPaeo/Chl-a above 1 indicates a larger proportion of degraded organic matter than fresh organic matter. TPhaeo/Chl-a ratios > 1 were determined between 50 m and 200 m for Stations 69 and 77 and below 150 m for the Stations 13, 38, 21, 26 and 51.

Regional differences were also observed between phytoplankton pigments. These several pigments (described in section 3.2.5) were used as biomarkers of several phytoplankton taxa (Figure 3.3.b) and then gathered into three size classes (Figure 3.3.a).

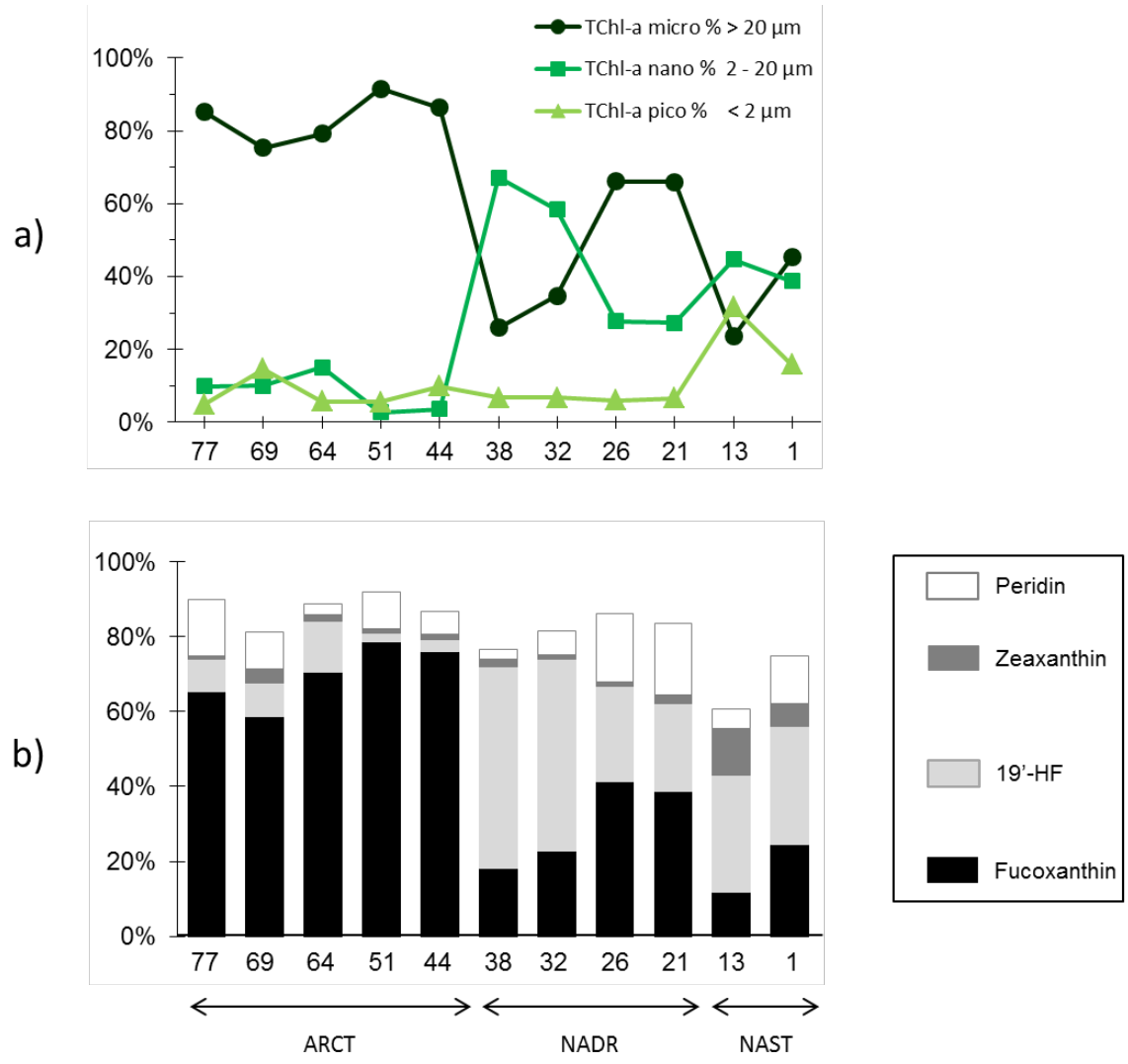

Figure 3.3: Main phytoplankton size groups and chloropigments (from the GEOVIDE database). a) Relative abundance of microphytoplankton (black line, circles), nanophytoplankton (dark green line, squares), picophytoplankton (light green line, triangles). b) Relative abundance of Fucoxanthin (black), 19'-HF (light grey), Zeaxanthin (dark grey), and peridinin (white) pigments

The NAST province was characterized by a mixed proportion of micro-, nano- and pico-phytoplanktonic species with a similar percentage of micro- and nano-phytoplanktonic species at Station 1 (38 and 45% respectively) and the highest proportion of pico-phytoplanktonic species (32% of the total Chl-*a*) at Station 13. Nevertheless, both stations were dominated by

nano-phytoplanktonic species. In this province, 19'-Hexanoyloxyfucoxanthin pigment, representative of prymnesiophytes, accounted for the highest proportion of the seven pigments (31 ± 0.3%). Coccolithophorids are part of the prymnesiophyte family and their dominance was confirmed by visual observations on filters (surface down to 400 m) by scanning electron microscopy and by the high $CaCO_3$ concentrations and export fluxes (Figure 3.8) at these stations. In the following text, we assume the 19'-Hexanoyloxyfucoxanthin pigment to be characteristic of coccolithophorids presence.

At Station 13, a significant proportion of Zeaxanthin pigment was measured, indicating the presence of cyanobacteria (12% of the total taxonomic pigments).

Within the NADR province, micro-phytoplanktonic species dominated in the Western European basin (Stations 21 and 26: > 66% of the total Chl-*a*) while nano-phytoplanktonic species dominated in the Icelandic basin (Stations 32 and 38: > 60% of the total Chl-*a*). Fucoxanthin and Peridin pigments, tracers of diatoms and dinoflagellates respectively, were found in high amounts at Stations 21 and 26 (20% peridinin; 43% fucoxanthin). At Stations 32 and 38, the 19'-Hexanoyloxyfucoxanthin pigment, found in coccolithophorids, showed high values and represented up to 54% of the total taxonomic pigments.

Finally, the ARCT province was dominated by micro-phytoplanktonic species (Stations 44, 51, 64, 69 and 77: > 75% of the total Chl-*a*) and significant concentrations of the fucoxanthin pigment were measured indicating the presence of diatoms. The fucoxanthin pigment represented 77±8% of the total taxonomic pigments.

3.3.1.2. Primary production

Along the transect, the integrated daily primary production (PP) in the euphotic zone varied by a factor of 6, ranging from 31 ± 2 at Station 69 to 174 ± 6 mmol $C.m^{-2}.d^{-1}$ at Station 26 (A. Roukaerts and D. Fonseca Batista, unpublished data; Table 3.3). The NAST province was characterized by low PP with one of the lowest values measured at Station 1 (33 mmol $C.m^{-2}.d^{-1}$) and a moderate PP at Station 13 (80 mmol $C.m^{-2}.d^{-1}$). The NADR province was highly productive with PP ranging from 135 to 174 mmol $C.m^{-2}.d^{-1}$, excluding Station 38 where a lower PP was determined (68 mmol $C.m^{-2}.d^{-1}$). Within the ARCT province, PP in the Irminger Sea

basin was high, ranging from 137 to 165 mmol $C.m^{-2}.d^{-1}$ and was lower in the Labrador Sea basin, ranging from 31 to 95 mmol $C.m^{-2}.d^{-1}$.

3.3.2. ^{234}Th activities and fluxes

3.3.2.1. Particulate ^{234}Th activities

Particulate ^{234}Th activities ($p^{234}Th$) for the small size fraction (SSF; 1-53 µm) and the large size fraction (LSF; >53 µm) are presented in Table S3.2 and Figure 3.4.

Along the transect, the particulate ^{234}Th activity was predominantly present in small particles (SSF) with the $p^{234}Th$ in the LSF accounting for 13% (median value; n=61) of the total particulate ^{234}Th. In the NAST province, this phenomena was accented, especially at Station 13 where $p^{234}Th$ in the LSF was the lowest fraction of the transect, averaging 6.6 ± 1.3 (median ± 1 s.d.; n=5). This size partitioning of $p^{234}Th$ is in line with the presence of pico-phytoplankton at this station. In the NADR province, the two basins were decoupled with higher $p^{234}Th$ in the LSF in the western European basin (22 and 30% at Stations 21 and 26) than in the Icelandic basin (16 and 13% at Stations 32 and 38). Once again, this partitioning coincided with the increasing dominance of micro- and nano-phytoplankton observed in the western European and in the Icelandic basins, respectively. In the ARCT province, the median $p^{234}Th$ in the LSF reached only 13 ± 14% (median ± 1 s.d.; n=27) in the water column which is relatively limited taking into account the dominance of micro-phytoplankton in this province. However, the fraction of $p^{234}Th$ in the LSF in surface waters was the highest in the ARCT province (median value=40%), reaching 56 and 52% at Stations 51 and 64 respectively.

Then, we compared the total particulate ^{234}Th activity (total $p^{234}Th$; sum of the LSF and SSF) to the total ^{234}Th activity. Large variations were observed along the transect, with fractions of total $p^{234}Th$ accounting from 9% (Station 1) to 94% (Station 44) of the total ^{234}Th activity. The median value was 26% (n=11) but four stations were characterized by different partitioning compared to the general trend. Stations 1, 64 and 69 were characterized by a low $p^{234}Th$ accounting for 9, 10 and 15% of the total ^{234}Th activity in agreement with the low particle concentrations and the lowest PP observed at these stations. Conversely, Station 44 was

characterized by the highest fraction of p^{234}Th (94%) and one of the highest PP. This very high particulate proportion corresponded to a high particle concentration in surface waters.

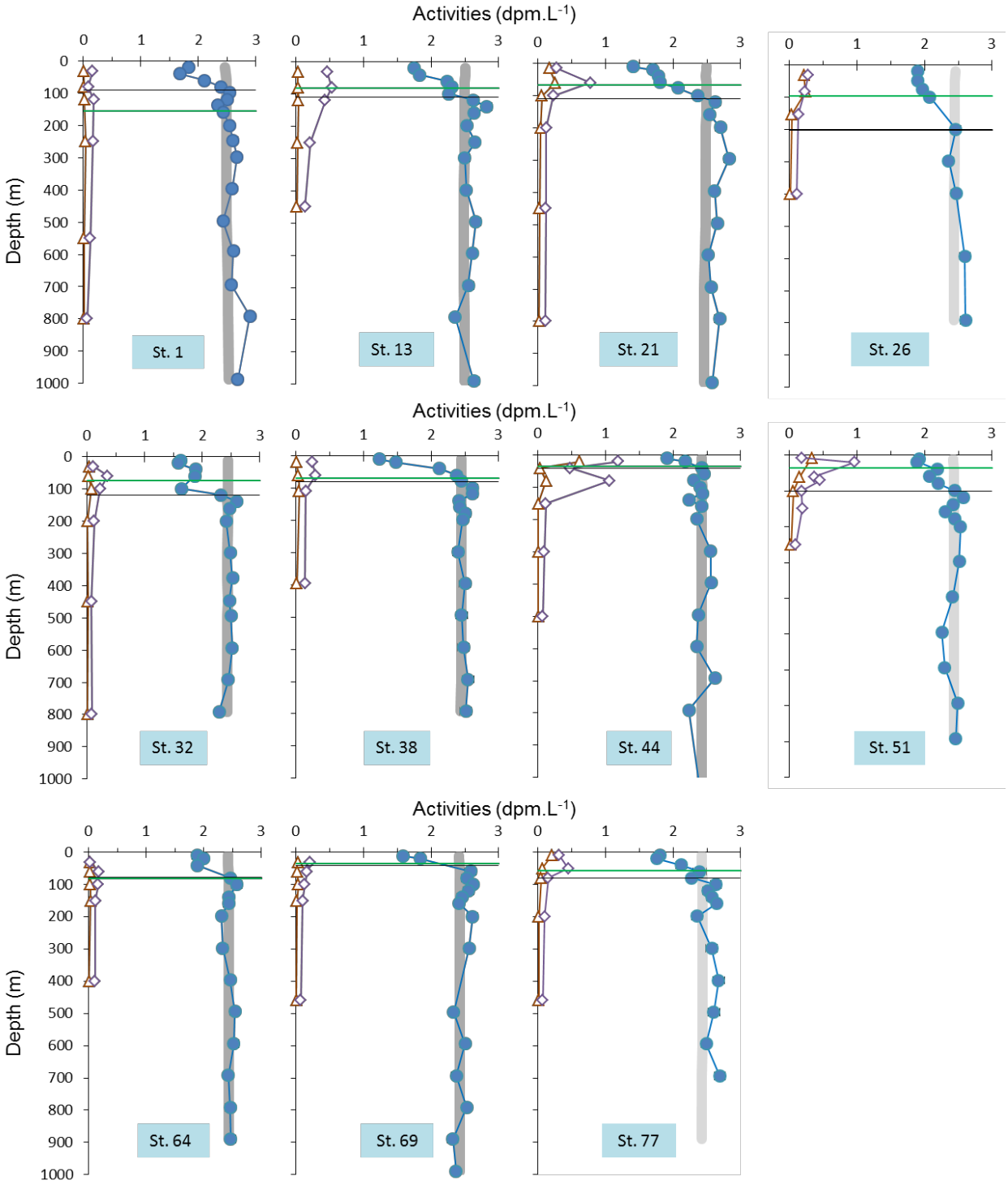

Figure 3.4: Particulate ^{234}Th activities for the small size fraction (SSF; 1-53 µm; open diamonds) and for the large size fraction (LSF; >53 µm; open triangles); Total ^{234}Th (closed blue circles) and ^{238}U (thick grey vertical line); all activities expressed in dpm.L^{-1}. The horizontal black line is the Eq depth (depth where ^{234}Th returns to equilibrium with ^{238}U) used for estimating the export fluxes, and the horizontal green line is the calculated PPZ depth (primary production zone). Error bars are hidden by the symbols

3.3.2.2. Total ^{234}Th activities

The complete dataset of total ^{234}Th, ^{238}U activities and the corresponding ^{234}Th/^{238}U ratios are presented in Table S3.1, while Figure 3.4 shows the depth profiles of total ^{234}Th and ^{238}U activities. A deficit of ^{234}Th relative to ^{238}U ratio indicates ^{234}Th scavenging by particles which can be converted into a ^{234}Th export flux (Buesseler et al., 1992; Cochran and Masqué, 2003). Conversely, excess of ^{234}Th relative to ^{238}U implies ^{234}Th accumulation which can be related to particle remineralization, releasing ^{234}Th in the dissolved phase (Waples et al., 2006). ^{234}Th activities ranged between 1.23 and 2.90 dpm.L^{-1}, while ^{238}U activities ranged from 2.19 to 2.53 dpm.L^{-1}.

At all stations, deficits of ^{234}Th relative to ^{238}U were observed in the upper 100m with the lowest ^{234}Th/^{238}U ratios measured in the upper 40 m. In the upper 40 m, ^{234}Th/^{238}U ratios ranged between 0.50 (Station 38) to 0.90 (Station 44). Generally, the lowest ratios were observed in the NADR province (median 0.61 ± 0.12, n=4), while in the other provinces, surface ^{234}Th/^{238}U ratios were 0.74 ± 0.06 (median, n=8). Moreover, at Stations 21, 26 and 32 located in the NADR province, ratios below 0.8 deepened further than the other stations (91 ± 14 m compared to 33 ± 16 m, n=8). Total ^{234}Th activities increased progressively with depth and were back to equilibrium with ^{238}U at different depths between stations: Eq reached 100 ± 10 m (n=2) in the NAST province, increased to 128 ± 51 m (n=4) in the NADR province and finally decreased to 68 ± 27 m in the ARCT province (n=5).

This equilibrium depth matched well (median of all stations: 26 m of difference, Figure 3.4) with the base of the particle production zone (PPZ) defined as the depth at which the fluorescence reaches 10% of its maximum value (Marra et al., 2014). The PPZ depth was used in different studies as the integration depth for ^{234}Th deficits (Owens et al., 2014; Roca-Marti et al., 2016a) but the good correspondence between Eq and PPZ confirms that the Eq depth is appropriate to calculate export.

Below Eq, excess of ^{234}Th relative to ^{238}U (i.e., ^{234}Th/^{238}U ratio > 1) was observed at all stations, but significant ^{234}Th excess (ratio > 1.1) was observed at Station 1 (800 m), Station 13 (140 m), Station 21 (300 m) and Station 77 (400 and 700 m).

Below Eq, small but significant ^{234}Th deficits were also observed at Station 44 at 140 m and 800 m and at Station 51 between 400 and 700 m (Figure 3.4).

3.3.2.3. ^{234}Th export fluxes

At all stations, ^{234}Th fluxes were derived from ^{234}Th and ^{238}U activities using the following mass balance equation (Savoye et al., 2006):

$$\frac{\partial A_{Th}}{\partial t} = \lambda \left(A_U - A_{Th}\right) - P + V \quad \text{(Equation 3.4)}$$

where λ is the ^{234}Th decay constant (0.0288 d^{-1}); A_U and A_{Th} are the activities of total ^{238}U and ^{234}Th, respectively; P is the export of ^{234}Th on sinking particles; V is the sum of advective and diffusive fluxes of ^{234}Th and can be expressed with the following equation:

$$V = u\frac{\delta A_{Th}}{\delta x} + v\frac{\delta A_{Th}}{\delta y} + w\frac{\delta A_{Th}}{\delta z} + Kx\frac{\delta^2 A_{Th}}{\delta x^2} + Ky\frac{\delta^2 A_{Th}}{\delta y^2} + Kz\frac{\delta^2 A_{Th}}{\delta z^2} \quad \text{(Equation 3.5)}$$

where horizontal and vertical velocities are denoted u, v and w; $\frac{\delta A_{Th}}{\delta x}$, $\frac{\delta A_{Th}}{\delta y}$ and $\frac{\delta A_{Th}}{\delta z}$ are the ^{234}Th activity gradients; K_x, K_y and K_z are the diffusion coefficients.

During GEOVIDE, we assume that $\frac{\partial A_{Th}}{\partial t}$ equals 0 meaning that the system is in steady state (SS). A non-steady state (NSS) calculation was not possible for the GEOVIDE cruise since this approach implies the same water mass to be sampled at least twice (Savoye et al., 2006). The ^{234}Th flux is calculated by integrating the ^{234}Th activity deficit (relative to ^{238}U) between the surface and the depth of export, defined here as Eq (the depth where ^{234}Th activities are back to the equilibrium with ^{238}U activities).

The highest ^{234}Th fluxes at Eq were observed in the NADR province, reaching 2252 ± 119 dpm.m^{-2}.d^{-1} at Station 32, while the lowest flux was determined in the Irminger Sea basin (321 ± 66 dpm.m^{-2}.d^{-1} at Station 44). In order to evaluate the attenuation of the export flux with depth, we also calculated the ^{234}Th flux at 400 m. The ^{234}Th flux was not estimated below 400 m because of the increase of the uncertainty with depth. Nevertheless, it is important to note that the estimation of fluxes at 400 m remains relatively imprecise because of the large uncertainties, reaching a median of 411 dpm.m^{-2}.d^{-1} compared to 104 dpm.m^{-2}.d^{-1} at Eq. The

fluxes at 400 m should thus be considered with great care. These fluxes ranged from 573 ± 473 dpm.m^{-2}.d^{-1} at Station 69 to 2171 ± 408 dpm.m^{-2}.d^{-1} at Station 26. The ^{234}Th flux attenuation between Eq and 400 m was then calculated by subtracting the ^{234}Th flux at 400 m by the flux at Eq (Figure 3.5).

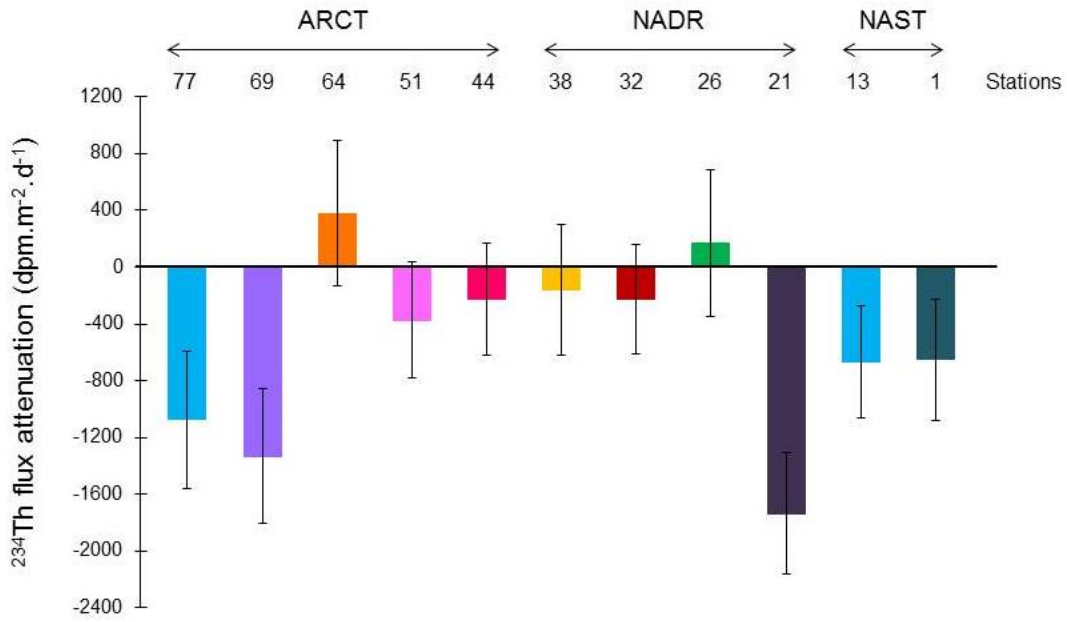

Figure 3.5: ^{234}Th flux attenuation between Eq and 400 m (in dpm.m^{-2}.d^{-1}). Negative values indicate an attenuation of the ^{234}Th flux between Eq and 400 m while positive values denote an increase of the ^{234}Th flux between both depths. The error bars are calculated using the error propagation laws.

Considering the precision of the approach, no significant differences were observed at Stations 26, 32, 38, 44, 51 and 64 but significant flux attenuations were determined at Stations 1, 13, 21, 69 and 77. The highest ^{234}Th flux attenuation was estimated at Station 21 where the flux at 400 m represented only 5% of the flux at Eq.

3.3.2.4. Influence of physical transport on the flux estimation

The North Atlantic is known to be a very dynamical area, where zonal surface currents can be strong (up to 1 m.sec^{-1}; Mercier et al., 2015; Reverdin et al., 2003). However, the longitudinal and latitudinal sampling resolution during GEOVIDE did not allow the es timation of horizontal

^{234}Th gradients. It was thus not possible to evaluate the V term (Equation 3.5) but potential errors introduced by this term on the ^{234}Th flux calculation were qualitatively considered.

Lateral transport of ^{234}Th has been shown to be important at ocean margins or in areas where currents are strong (Benitez-Nelson et al., 2000; Resplandy et al., 2012; Savoye et al., 2006)Roca-Marti et al., 2016). During GEOVIDE, the most dynamical area was encountered in the surrounding of the Greenland Margin subjected to the powerful East and West Greenland currents. For this areas, one way to characterize the potential role of advection is to compare stations close to each other, as for instance, the Stations 44 and 51 both located in the Irminger Basin. ^{234}Th fluxes showed relatively high variability at these two stations, suggesting that lateral advection was likely important in this area, but this contribution cannot be evaluated here. The NADR is also a dynamical area where lateral advection can represent up to 20% of the export flux at PAP site (Resplandy et al., 2012) but variations of ^{234}Th fluxes were less pronounced in this province.

Similarly, vertical advection has been shown to be an important process (Buesseler, 1998; Buesseler et al., 1995). In the North Atlantic, a local upwelling takes place near the Portuguese coasts in the Iberian margin (Costa Goela et al., 2016; Zúñiga et al., 2016; http://marine.copernicus.eu/) and an intense convection occurs in the Labrador Sea basin (Kieke and Yashayaev, 2015). However, strong vertical advections which mixes the water column, would homogenize the ^{234}Th activities in the water column, which is not the case during our study (Figure 3.4). Indeed, the greatest mixed layer depth during GEOVIDE reached 40 m along the transect and significant ^{234}Th deficits relative to ^{238}U were observed in surface waters compared to deeper depths. Therefore, the influence of vertical advection on ^{234}Th export fluxes was neglected.

The influence of vertical diffusion on ^{234}Th export fluxes was also tested using a Kz value ranging between 10^{-4} and 10^{-5} $m^2.s^{-1}$, as observed in the upper 1000 m between Portugal and Greenland along the OVIDE transect (Ferron et al., 2014). The highest value of vertical diffusion to the estimation of the ^{234}Th flux was about 181 $dpm.m^{-2}.d^{-1}$ at Station 69, which is in

the range of ^{234}Th flux uncertainties. Therefore, the impact of the vertical diffusion on our calculations is negligible.

As a conclusion, these physical processes, even if not quantified, should be kept in mind when interpreting reported estimates of export flux of ^{234}Th.

3.3.3. POC:^{234}Th ratios in particles

Profiles of POC:^{234}Th ratios for the small size fraction (SSF) and the large size fraction (LSF) particles are shown in Figure 3.6. POC:^{234}Th ratios spanned two orders of magnitude, ranging between 0.51 (Station 1, 800 m) to 53.7 (station 32, 30 m) μmol.dpm^{-1} in the SSF particles and from 1.05 (station 21, 400 m) to 30.6 (station 1, 30 m) μmol.dpm^{-1} in the LSF particles.

The highest and most variable ratios were observed in the upper water column (~30 m) with values ranging from 4.73 μmol.dpm^{-1} at Station 13 to 53.7 μmol.dpm^{-1} at Station 32 for the SSF, and from 5.6 μmol.dpm^{-1} at Station 38 to 30.6 μmol.dpm^{-1} at Station 1 for the LSF. Then, the ratios decreased with depth, in both size fractions, down to 100m. Below 100 m, the ratios remained relatively constant in both size fractions with median values of 1.8 ± 1.1 μmol.dpm^{-1} in the NAST province (n=13; Stations 1 and 13), 3.0 ± 1.3 μmol.dpm^{-1} in the NADR province (n=24; Stations 21, 26, 32 and 38), 3.7 ± 0.9 μmol.dpm^{-1} in the Irminger Sea basin (n=10; Stations 44 and 51) and 7.0 ± 3.8 μmol.dpm^{-1} in the Labrador Sea basin (n=16; Stations 64, 69 and 77). The decrease of the POC:^{234}Th ratio with depth illustrated the preferential degradation of carbon relative to ^{234}Th. The spatial variations of this degradation was investigated by comparing the b term of the power law regressions of POC:^{234}Th ratios versus depth (Martin et al., 1987; Puigcorbé et al., 2015):

$$POC:^{234}Th = a \times Z^{-b} \qquad \text{(Equation 3.6)}$$

where a and b are the terms obtained from the exponential fitting and Z is the depth.

In particular for the LSF particles, the median b term decreases northwards from 0.71 ± 0.30 in the NAST province to 0.34 ± 0.12 in the ARCT province, indicating a lower attenuation of POC relative to ^{234}Th with depth northwards.

At Stations 1, 13 and 21, POC in large particles was attenuated at a stronger rate relative to ^{234}Th with depth as b terms for large particles were equal to 0.92, 0.50 and 0.83 compared to 0.81, 0.32 and 0.63 for small particles. On the contrary, at the other stations, POC in small particles was attenuated at a stronger rate compared to large particles, this point being discussed in section 3.4.4.

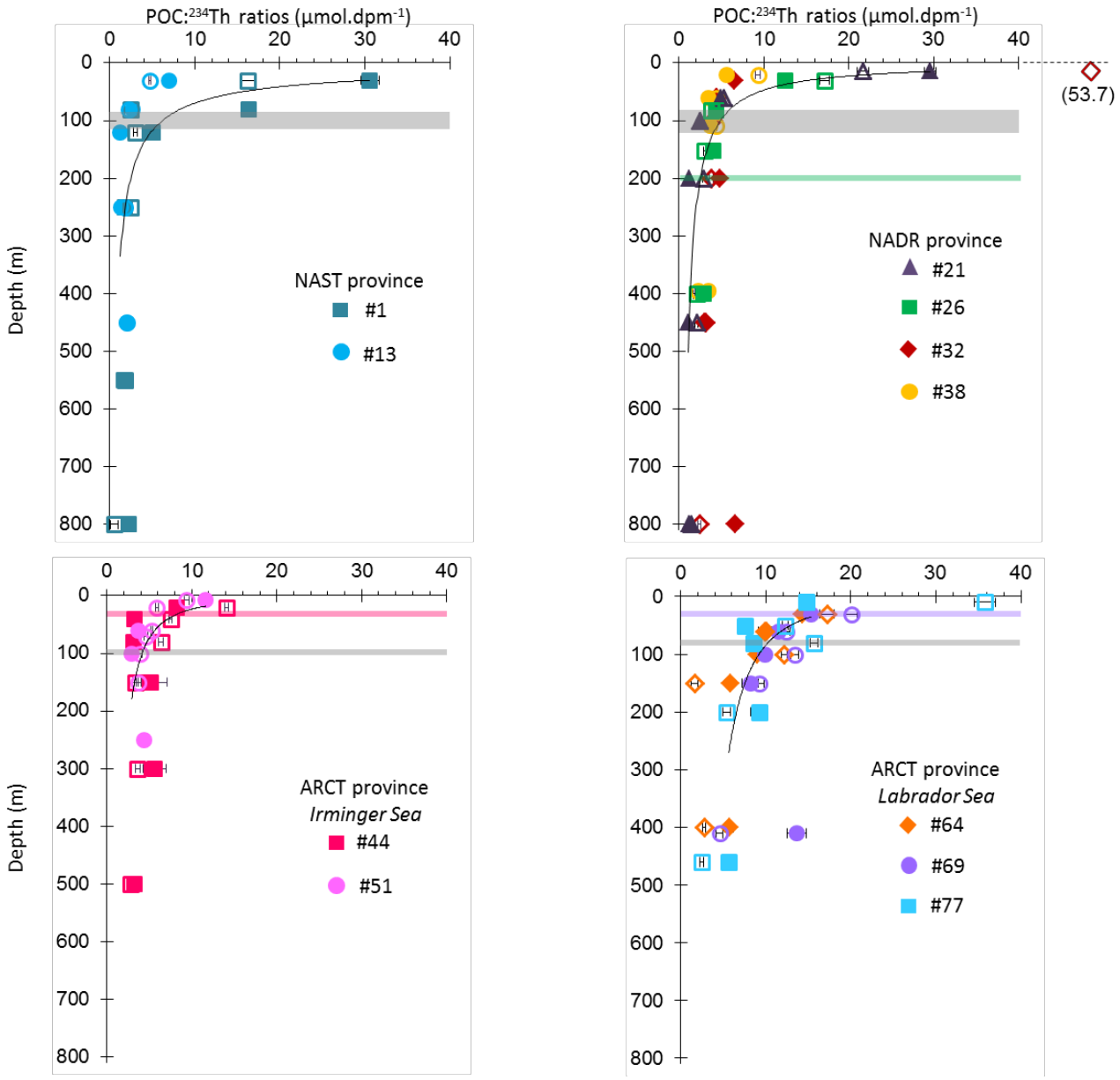

Figure 3.6: POC:^{234}Th ratios (µmol.dpm^{-1}) in the SSF (open symbols) and LSF (closed symbols). The Eq depth (depth where ^{234}Th is back to equilibrium with ^{238}U) is indicated with the grey line except for Stations 26, 44 and 69 where the Eq depths are represented by green, pink and purple lines, respectively. The thin black line represents the power law fits (POC:$^{234}Th=a\times Z^{-b}$) of each province or basin.

Because the POC to ^{234}Th ratio has to be determined at the export depth for the conversion of ^{234}Th flux into POC export flux (Buesseler et al., 2006), the POC:^{234}Th ratios in the LSF and SSF were estimated at this specific depth (Eq in the present study) using the power law interpolation of the measured ratios. At most stations, the POC:^{234}Th ratios at Eq were comparable for both size fractions with differences smaller than a factor 1.4, except at Stations 1, 26 and 44 (Figure 3.7).

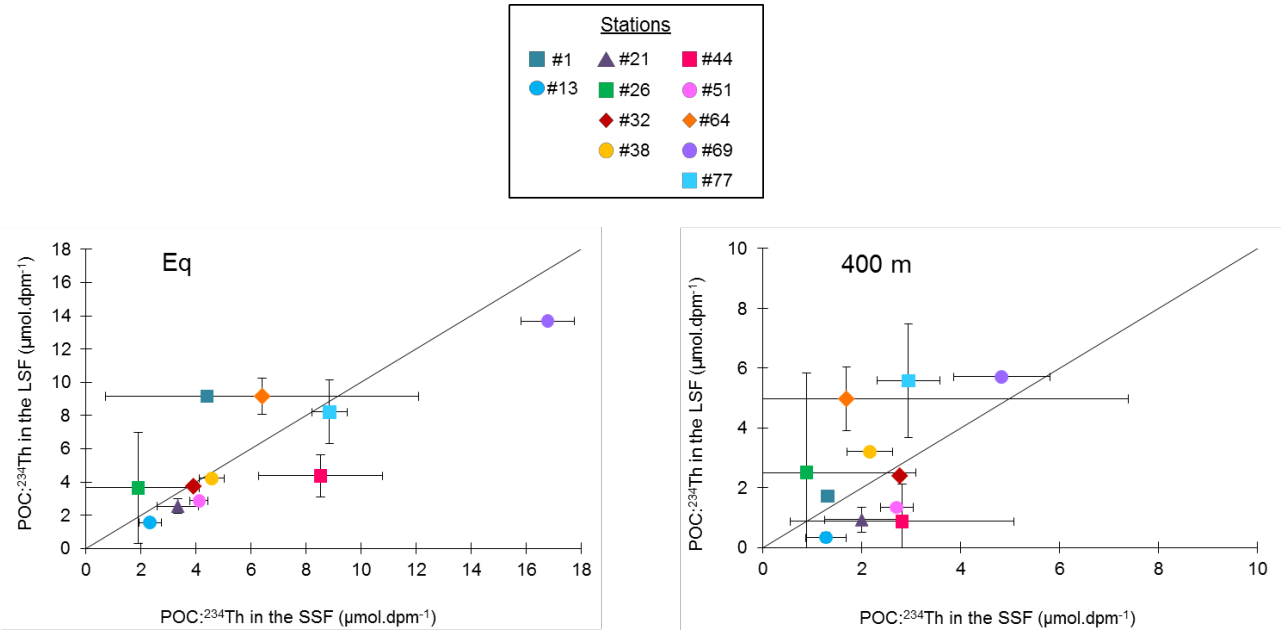

Figure 3.7: POC:^{234}Th ratios (µmol.dpm^{-1}) between the small size fraction (SSF) and large size fraction (LSF) at Eq (left) and at 400 m (right). The diagonal black line represents the 1:1 ratio. For the readability of the figure, the error bars of Station 1 are not indicated (errors: LSF=17.2 µmol.dpm^{-1} and SSF=13.8 µmol.dpm^{-1}).

At Stations 1 and 26, the POC:^{234}Th ratios of LSF particles were ~2 fold higher than those of SSF particles. Conversely, the POC:^{234}Th ratio at Station 44 was 2 fold higher in the SSF than in the LSF particles. The highest POC:^{234}Th ratios at Eq in the LSF were determined in the ARCT province reaching 13.69 ± 0.04 µmol.dpm^{-1} at Station 69.

The POC:^{234}Th ratios in the LSF and SSF were also estimated at 400 m, using the same power law function and were not significantly different between LSF and SSF for Stations 1, 21, 26, 32, 64. The highest POC:^{234}Th ratios at 400 m in LSF was determined in the ARCT province reaching 5.71 ± 0.04 µmol.dpm^{-1} at Station 69 (Figure 3.7). However, Stations 38, 69 and 77

were characterized by 1.2 to 1.9 folds higher ratios in the LSF than in the SSF, unlike Stations 13, 44 and 51 that are characterized by 2.0 to 3.9 folds lower ratios in the LSF than in the SSF, showing that small particles may contribute to export.

These results are in line with many studies (Dall'Olmo and Mork, 2014; Durkin et al., 2015; Giering et al., 2016; Puigcorbé et al., 2015), that are challenging the traditional view which considers that larger particles mainly drive the export flux (Buesseler et al., 2006).

3.3.4. POC export fluxes

We estimated the POC export fluxes by multiplying the ^{234}Th export flux with the POC:^{234}Th ratio at the same depth.

POC fluxes were determined by using the POC:^{234}Th ratios of the LSF (>53 µm) and the SSF (1-53 µm; Table 3.2) in order to compare both estimations.

Province	Station #	POC flux (>53 µm) mmol.m^{-2}.d^{-1}	sd	POC flux (1-53 µm) mmol.m^{-2}.d^{-1}	sd
NAST	1	12	22	5.6	17
	13	2.2	0.3	3.3	0.6
NADR	21	4.8	0.8	6.3	1.4
	26	7.3	6.7	3.8	4.4
	32	8.4	0.5	8.8	0.5
	38	4.8	0.4	5.2	0.7
ARCT	44	1.4	0.5	2.7	0.8
	51	2.7	0.3	3.8	0.5
	64	7.8	1.5	5.5	4.9
	69	10	1	13	1
	77	6.1	1.7	6.6	1.1

Table 3.2: Comparison of the POC export fluxes as determined using the POC:^{234}Th ratios in large (> 53 µm) and small particles (1-53 µm).

Except at Stations 1, 26 and 64, the POC fluxes were between 1.04 and 2 folds higher in the SSF than in the LSF, suggesting that small particles could contribute to export POC. However, when considering the uncertainties, POC fluxes determined with the POC:^{234}Th ratios in SSF and LSF were not significantly different. Moreover, as we did not have the possibility to compare the ratios with those from sediment traps, we cannot affirm that the small particles

participated to the export. Indeed, one problem emerging when taking the 1-53 µm in consideration is that their density, hence their sinking speed is not constrained. Therefore, in the following, we decided to discuss about the POC fluxes determined with the POC:^{234}Th ratios of the large >53 µm particles (Table 3.3; Figure 3.8). This assumption has been used in most of the studies dedicated to POC export fluxes in the North Atlantic (Ceballos-romero et al., 2016; Le Moigne et al., 2013b; Moran et al., 2003; Owens et al., 2014; Sanders et al., 2010; Thomalla et al., 2008).

The POC export fluxes at Eq in the LSF ranged from 1.4 ± 0.5 mmol.m^{-2}.d^{-1} at Station 44 to 12 ± 22 mmol.m^{-2}.d^{-1} at Station 1 and the median was 6.1 ± 3.3 mmol.m^{-2}.d^{-1} (n=11). In addition to Station 1, which is probably influenced by lithogenic inputs from the Iberian margin and where the POC flux reached 12 ± 22 mmol.m^{-2}.d^{-1} (see below, section IV.2.c), two main open-ocean areas were characterized by high POC export fluxes: 1) the NADR province and in particular Stations 26 and 32 where POC export fluxes reached 6.0 ± 1.8 mmol.m^{-2}.d^{-1} and 2) the Labrador Sea basin and in particular Station 69 where POC export flux reached 10 ± 1 mmol.m^{-2}.d^{-1}.

POC export fluxes were also estimated at 400 m, by multiplying the ^{234}Th export flux with the POC:^{234}Th ratio of the >53 µm particles at 400 m, in order to quantify the impact of remineralization on the POC export fluxes in the upper mesopelagic (Figure 3.8).

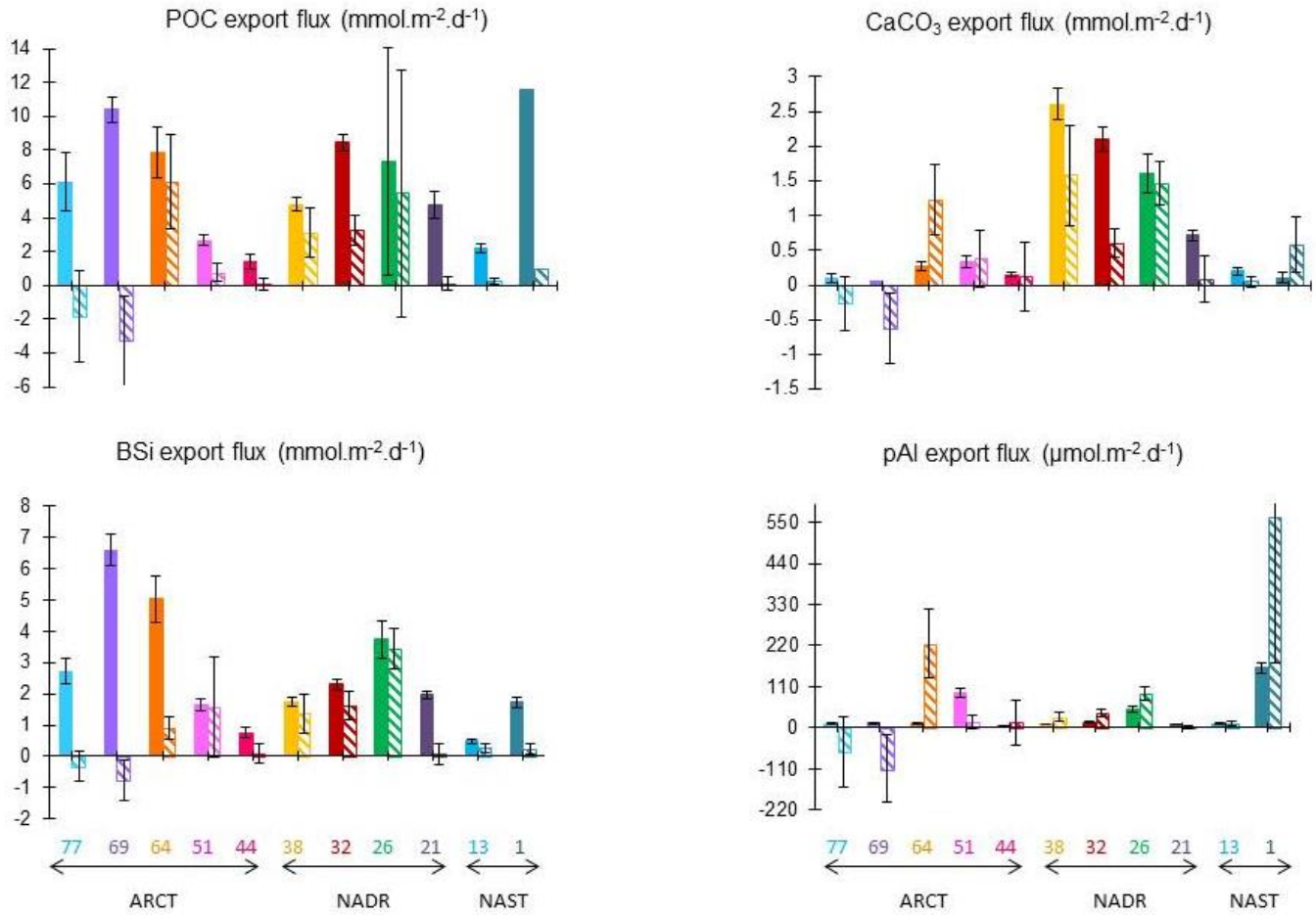

Figure 3.8: Export fluxes of particulate organic carbon (POC), calcium carbonate ($CaCO_3$), biogenic silica (BSi) and particulate aluminum (pAl) at Eq (solid fill) and at 400 m (dashed), from the Iberian Margin (Station 1) to the Newfoundland Margin (Station 77).

At all stations, POC export fluxes were lower at 400 m than at Eq, likely indicating a POC remineralization in this depth interval (see discussion below). The reduction of the POC export flux was limited at Stations 26, 38 and 64 where the fluxes were 25, 35 and 22% lower at 400m than at Eq. By contrast, at other stations, the mean flux reduction was more important and reached 84 ± 14%. This was especially the case in the Labrador Sea basin where similarly to ^{234}Th export fluxes, negative POC export fluxes were estimated at 400 m.

3.3.5. BSi, $CaCO_3$ and pAl export fluxes

BSi, $CaCO_3$ and pAl concentrations were determined on different filters than those dedicated to POC. Particulate ^{234}Th was analyzed on the LSF but not on the SSF, and thus the Element

to ^{234}Th ratios were determined only for the LSF. At most stations, biogenic elements (BSi, $CaCO_3$) to ^{234}Th ratios decreased with depth, as observed for POC:^{234}Th ratios, whereas the pAl to ^{234}Th ratios tend to increase. However, these trends were not always observed and we decided to use a linear interpolation to estimate the appropriate element:^{234}Th ratio at Eq and at 400 m. The range of the calculated ratios can be found in Table 3.3.

The elemental export fluxes can be found in Table 3.3 and Figure 3.8.

In the NAST province, high pAl export fluxes were determined at Station 1, indicating an important contribution of lithogenic material to the particulate export. At 400 m, the pAl flux reached 565 $\mu mol.m^{-2}.d^{-1}$, which is the maximum value determined during the cruise. The median value of other stations was 11 $\mu mol.m^{-2}.d^{-1}$. Station 13 was characterized by the lowest export fluxes of respectively 0.48 $mmol.m^{-2}.d^{-1}$, 0.20 $mmol.m^{-2}.d^{-1}$, 11 $\mu mol.m^{-2}.d^{-1}$ for BSi, $CaCO_3$ and pAl, which is typical of oligotrophic conditions.

The NADR province was characterized by high biogenic export fluxes of 2.1 ± 0.9 and 1.9 ± 0.8 $mmol.m^{-2}.d^{-1}$ for BSi and $CaCO_3$, respectively (n=4). Interestingly, the province can be divided in two sub-provinces, the west European basin which displayed high BSi export fluxes (reaching 3.8 $mmol\ .m^{-2}.d^{-1}$ at Station 26) and the Icelandic basin, characterized by high $CaCO_3$ (reaching 2.6 $mmol\ .m^{-2}.d^{-1}$ at Station 38) export fluxes. The pAl fluxes were relatively low compared to the Iberian Margin (median value: 13 $\mu mol.m^{-2}.d^{-1}$, n=4) but yet reached 49 $\mu mol.m^{-2}.d^{-1}$ at Station 26.

In the ARCT province, important pAl export fluxes were estimated near the Greenland Margin with a flux reaching 94 $\mu mol.m^{-2}.d^{-1}$ at Eq of Station 51 and 225 $\mu mol.m^{-2}.d^{-1}$ at 400 m of Station 64. In the latter case, this suggests an important deep advection of lithogenic particles (see below in the discussion IV.2.c). The highest BSi export fluxes at Eq were determined in the Labrador Sea basin reaching 6.6 $mmol.m^{-2}.d^{-1}$ at Station 69. The $CaCO_3$ fluxes were very low at Eq with a median value of 0.15 $mmol.m^{-2}.d^{-1}$. At 400 m, the flux reached 1.2 $mmol.m^{-2}.d^{-1}$ at Station 64, which is comparable to fluxes observed in the NADR province.

Station	Date	Lat	Long	PP	Eq	Depth	^{234}Th flux	POC/^{234}Th	POC flux	BSi/^{234}Th	BSi flux	$CaCO_3$/^{234}Th	$CaCO_3$ flux	pAl/^{234}Th	pAl flux
#		°N	°E	mmol.m^{-2}.d^{-1}	m	m	dpm.m^{-2}.d^{-1}	µmol.dpm^{-1}	mmol.m^{-2}.d^{-1}	µmol.dpm^{-1}	mmol.m^{-2}.d^{-1}	µmol.dpm^{-1}	mmol.m^{-2}.d^{-1}	nmol.dpm^{-1}	µmol.m^{-2}.d^{-1}
1	19 May	40.33	-10.04	33 ± 2	90	Eq	1264 ± 104	9.2	6.6 ± 4.4	1.4	1.7 ± 0.2	0.08	0.10 ± 0.08	127	160 ± 13
						400	593 ± 411	1.7	0.7 ± 2.1	0.42	0.25 ± 0.18	0.98	0.58 ± 0.40	952	565 ± 391
13	24 May	41.38	-13.89	80 ± 3	110	Eq	1418 ± 111	1.6	3.7 ± 0.7	0.34	0.48 ± 0.07	0.14	0.20 ± 0.05	8.0	11 ± 1
						400	690 ± 380	0.3	1.2 ± 0.7	0.39	0.27 ± 0.15	0.08	0.05 ± 0.07	15	11 ± 6
21	31 May	46.54	-19.67	135 ± 2	110	Eq	1873 ± 69	2.6	4.3 ± 0.3	1.0	2.0 ± 0.1	0.38	0.71 ± 0.08	5.8	11 ± 1
						400	103 ± 423	0.9	0.05 ± 0.20	0.80	0.08 ± 0.34	0.79	0.08 ± 0.33	12	1.2 ± 5
26	4 June	50.28	-22.60	174 ± 6	200	Eq	2001 ± 319	3.6	5.8 ± 0.6	1.9	3.8 ± 0.6	0.80	1.6 ± 0.3	24	49 ± 8
						400	2171 ± 408	2.5	3.2 ± 0.3	1.6	3.5 ± 0.7	0.68	1.5 ± 0.3	42	92 ± 17
32	7 June	55.51	-26.71	142 ± 6	120	Eq	2252 ± 119	3.8	8.9 ± 0.5	1	2.3 ± 0.2	0.93	2.1 ± 0.2	7	15 ± 1
						400	1370 ± 365	2.4	4.4 ± 1.2	1.2	1.6 ± 0.4	0.44	0.60 ± 0.20	27	39 ± 10
38	10 June	58.84	-31.27	68 ± 2	80	Eq	1135 ± 95	4.2	5.1 ± 0.7	1.6	1.8 ± 0.2	2.3	2.6 ± 0.2	8	9 ± 1
						400	975 ± 449	3.2	2.1 ± 1.1	1.4	1.4 ± 0.6	1.6	1.6 ± 0.7	30	29 ± 14
44	13 June	59.62	-38.95	137 ± 2	40	Eq	321 ± 47	4.4	2.5 ± 0.6	2.4	0.76 ± 0.16	0.47	0.15 ± 0.04	17	6 ± 1
						400	98 ± 388	0.9	0.3 ± 1.1	0.78	0.08 ± 0.30	1.3	0.13 ± 0.50	154	15 ± 60
51	16 June	59.80	-42.00	165 ± 32	100	Eq	922 ± 103	2.9	3.9 ± 0.4	1.8	1.6 ± 0.2	0.37	0.34 ± 0.08	102	94 ± 11
						400	550 ± 398	1.3	1.1 ± 0.8	4.0	1.6 ± 1.6	1.0	0.38 ± 0.41	4	16 ± 2
64	19 June	59.07	-46.08	67 ± 2	80	Eq	855 ± 95	9.2	6.0 ± 2.4	5.9	5.0 ± 0.8	0.33	0.28 ± 0.06	12	10 ± 2
						400	1236 ± 497	5.0	2.7 ± 3.4	0.72	0.89 ± 0.37	1.0	1.2 ± 0.5	182	225 ± 91
69	22 June	55.84	-48.09	31 ± 2	40	Eq	758 ± 57	14	13 ± 1.8	8.7	6.6 ± 0.5	0.09	0.07 ± 0.03	16	12 ± 1
						400	-573 ± 468	6	-3.3 ± -2.9	1.4	-0.79 ± -0.65	1.1	-0.62 ± -0.50	192	-110 ± -90
77	26 June	52.99	-51.10	95 ± 2	80	Eq	745 ± 77	8.2	6.3 ± 1.1	3.7	2.7 ± 0.4	0.13	0.10 ± 0.06	14	11 ± 2
						400	-327 ± 471	5.6	-1.1 ± -1.6	1.0	-0.33 ± -0.47	0.81	-0.26 ± -0.38	199	-65 ± -94

Table 3.3: Primary production (PP, in mmol.m^{-2}.d^{-1}; A. Roukaerts, D. Fonseca Batista and F. Deman, unpublished data), ^{234}Th (in dpm.m^{-2}.d^{-1}), POC (particulate organic carbon, in mmol.m^{-2}.d^{-1}), BSi (biogenic silica, in mmol.m^{-2}.d^{-1}), $CaCO_3$ (calcium carbonate, in mmol.m^{-2}.d^{-1}) and pAl (particulate aluminum, in µmol.m^{-2}.d^{-1}) export fluxes obtained by multiplying the ^{234}Th export flux with the Element to ^{234}Th ratio (in µmol.dpm^{-1} or nmol.dpm^{-1}) of large (>53 µm) particles (see text for details). These fluxes were integrated between surface and Eq, where total ^{234}Th returns to equilibrium with ^{238}U, and at 400 m.

3.4. Discussion

This dataset is first compared to published studies in the North Atlantic and is then discussed with regards to the intensity and the stage of the bloom, the phytoplankton size structure and the ballast effect of biogenic and lithogenic minerals. Grazing impact could not be assessed, as no dedicated sampling was performed during this cruise. Temporal and regional variations of the carbon export fluxes are examined within this context, and finally, the export production and the attenuation of the POC export flux with depth are discussed using the export and transfer efficiencies.

3.4.1. Comparison with literature

Overall, the POC export fluxes from this dataset are in line with the lower end of the ranges determined in previous studies in the North Atlantic that are reported in Table 3.4. At Station 13, in the NAST province, the carbon export fluxes compared well with those measured by Owens et al. (2014) in the same area, confirming the lower carbon export fluxes in these oligotrophic regions. In the NADR province, some studies, conducted either before or after the period of the year of our study, reported POC export fluxes up to 11 fold higher than this study (Buesseler et al., 1992; Ceballos-romero et al., 2016; Giering et al., 2016; Martin et al., 2011; Sanders et al., 2010). Other studies in the NADR province and in particular in the western European basin at the Porcupine abyssal plain time series site (PAP site) estimated similar POC export fluxes during (Thomalla et al., 2008) or just after (Lampitt et al., 2008; Le Moigne et al., 2013b) our sampling period. In the ARCT province, published data are all higher than those measured during the present study with differences reaching factors of 27 and 8 in the Irminger Sea (Ceballos-Romero et al., 2016) and Labrador Sea (Moran et al., 2003) basins, respectively.

The differences between our POC export flux estimates (factor 8.6 between the highest and the lowest POC export flux) and with the literature (up to a factor 27 in only 1 month time lag;

Ceballos-Romero et al., 2016) confirm the important spatial and temporal variation of the parameters controlling the sinking particles and thus the export fluxes.

Province	Season	Method	Particle size	Integration depth	POC export flux	POC export efficiency	POC transfer efficiency	Reference
			µm	m	$mmol.m^{-2}.d^{-1}$	%	%	
NAST	May 2014	ISP	>53	90	11.6	35	8.8	# 1, this study
				110	2.2	2.8	10	# 13, this study
	October 2010	ISP	>51	113	4.2			Owens et al., 2014
NADR *Western European basin*	April-May 1989	P-trap		35	5 - 41	5 - 42		Buesseler et al., 1992
	May 2004	ISP	>50	30	2.8	11		Thomalla et al., 2008
	May 2014	ISP	>53	110	4.8	3.5	2.0	# 21, this study
	June 2014			200	7.3	4.2	75	# 26, this study
	July 2005/06	P-trap		120-150	1.3 - 8.1	1.0 - 14		Lampitt et al., 2008
	July-August 2009	ISP	>53	150	2.3 - 7.9			Le Moigne et al., 2013
NADR *Icelandic basin*	March-April 2012	P-trap	<100	50	6.8 - 15			Giering et al., 2016
	May 2008	P-trap		100	0.8 - 52		25 - 43	Martin et al., 2011
	May 2010	ISP	>53	150	14 - 32			Ceballos-Romero et al., 2016
	June 2014	ISP	>53	120	8.4	5.9	39	# 32, this study
				80	4.8	7.0	65	# 38, this study
	July-August 2010	ISP	>53	150	6.3 - 12	5.3 - 8.3		Ceballos-Romero et al., 2016
	August 2007	ISP	>53	100	4.5 - 38			Sanders et al., 2010
ARCT *Irminger Sea*	May 2010	ISP	>53	150	9 - 38			Ceballos-Romero et al., 2016
	June 2014	ISP	>53	40	1.4	1.0	6.1	# 44, this study
				100	2.7	1.6	28	# 51, this study
	July-August 2010	ISP	>53	150	5.0 - 26	4.3 - 16		Ceballos-Romero et al., 2016
ARCT *Labrador Sea*	June 2014	ISP	>53	80	7.8	12	78	# 64, this study
				40	10.4	34	-32	# 69, this study
				80	6.1	6.4	-30	# 77, this study
	July 1999	ISP	>53	50-100	3.7 - 47	4 - 111		Moran et al., 2003

Table 3.4: Comparison of POC export flux, POC export efficiency (POC flux at Eq / PP) and transfer efficiency (POC flux at 400 m / POC flux at Eq) in the North Atlantic with literature data.

3.4.2. POC export flux variations

3.4.2.1. Influence of the intensity and stage of the bloom

The GEOVIDE cruise was carried out in late spring (May-June), a period during which POC export fluxes may be important (Sanders et al., 2014). As the ^{234}Th proxy integrates the activity deficits over a timescale of 2-3 weeks preceding the sampling, we investigate the sampling time in light of the bloom development using satellite-derived Chl-*a* concentrations (http://giovanni.sci.gsfc.nasa.gov/giovanni/; Figure 3.9).

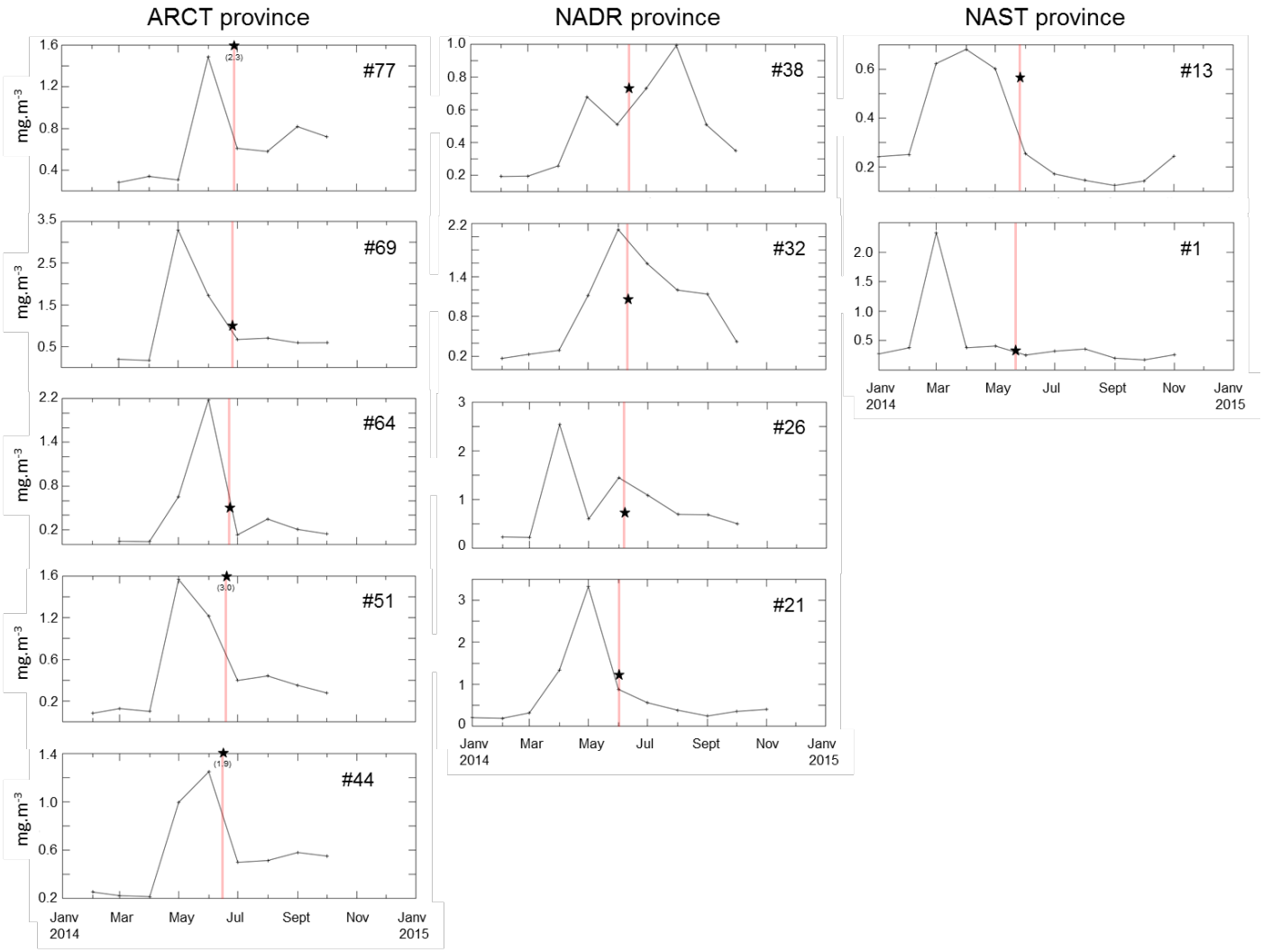

Figure 3.9: Upper 20 m integrated satellite-derived Chl-a concentrations (black line) from http://giovanni.sci.gsfc.nasa.gov/giovanni/. The pink line represents the sampling period during GEOVIDE and the black stars represent the Chl-a concentration measured in-situ.

Apart from Station 1 which was sampled after the bloom, the different provinces were sampled during the bloom, yet at different stages. One of the lowest POC export flux was determined at Station 13, in the NAST province, where the Chl-*a* biomass development remained rather low along the season (< 0.7 $mg.m^{-3}$) due to oligotrophic conditions (depleted nutrients). However, the highest POC export flux was determined at Station 1, also in the NAST province. This station was characterized by high biomass in the early spring (2.5 mg Chl-$a.m^{-3}$ in March) but was sampled after the bloom period. Interestingly, this station was also characterized by a deep Chl-*a* maximum (DCM) located below the euphotic zone (~65 m) and coinciding with higher NO_3^- and $Si(OH)_4$ concentrations (4.1 and 1.1 $\mu mol.L^{-1}$, respectively) compared to surface waters (0.02 and 0.6 $\mu mol.L^{-1}$, respectively). Within the DCM, Chl-*a* concentrations were low, indicating the decline of the DCM, generally composed by slowly growing but large and fast-sinking phytoplankton cells (Pommier et al., 2009), that are able to enhance the POC export flux.

High POC export fluxes were also estimated within the NADR province (Stations 21, 26, 32 and 38), a province in which the sampling was performed during the bloom. This province has been previously characterized by fast-sinking particles during the bloom (data from cruises in Spring 2012 and Summer 2009; Villa-Alfageme et al., 2016) promoting the high POC export fluxes.

Within the ARCT province, the Irminger Sea basin (Stations 44 and 51) was sampled close to the bloom maximum while the Labrador Sea basin (Stations 64, 69 and 77) was sampled during the decline of the bloom. The low POC export fluxes in the Irminger Sea basin were probably reflecting an accumulation phase of biomass rather than an export phase. Indeed, this area was characterized by a high proportion of particulate ^{234}Th in surface waters (reaching 94% of the total ^{234}Th activity at Station 44) confirming the accumulation phase. Interestingly, an important remineralization event in the mesopelagic layer was evidenced in this basin based on the excess particulate biogenic barium (Ba_{xs} proxy), which indicate a past production and export event (Lemaitre et al., in prep., Chapter 5). These results suggest that this basin may work as a pulsed system with high and sudden export events and fast renewal of the bloom

conditions such as nutrient concentrations, maybe due to the proximity of the Greenland ice sheets, releasing important quantities of nutrients (Hawkings et al., 2016; Meire et al., 2016), through advective supply.

The Labrador Sea basin was characterized by low PP (31 mmol $C.m^{-2}.d^{-1}$ at Station 69), low NO_3^- (0.07 $\mu mol.L^{-1}$ at Station 69) and moderate $Si(OH)_4$ (3.6 $\mu mol.L^{-1}$ at Station 69) concentrations, indicating the decline of the bloom triggering high POC export fluxes. The decline of the bloom in this basin was also supported by satellite data as the peak of the bloom was 1-2 months before our sampling (Figure 3.9).

Overall, the magnitudes of the POC export seem to be dependent of the evolution of the bloom, with high exports in post bloom periods, as observed in deep sediment traps (Lampitt et al., 2010), driven by large and rapidly sinking aggregates (Lampitt et al., 2001; Turner and Millward, 2002)

3.4.2.2. Influence of the phytoplankton size structure

In the North Atlantic, the phytoplankton composition significantly varies, depending on the bloom evolution and on any modification of environmental parameters such as micro- and macro-nutrient concentrations or stratification depth (Moore et al., 2005). Spatial variations in phytoplankton size structure are known to exert a control on the magnitude of the POC export flux (Boyd and Newton, 1999) and high POC exports are usually related to a greater size of the sinking phytoplankton cells (Alldredge and Silver, 1988; Guidi et al., 2009).

Within the NAST area, the low POC export flux determined at the subtropical Station 13 was related to the presence of pico-phytoplankton (32% of the total Chl-*a*; Figure 3.3), typical of oligotrophic waters (Dortch and Packard, 1989; Steinberg et al., 2001). Villa-Alfageme et al. (2016) highlighted that small cells are usually slow-sinking particles that can be easily remineralized in shallow waters, as a small sinking velocity (<100 $m.d^{-1}$) allows time for bacteria and zooplankton to degrade these particles, thus reducing the export flux.

At higher latitudes, the sinking velocity of the organic matter is considered to be high (>100 $m.d^{-1}$; Villa-Alfageme et al., 2016), as cells are of larger size. Indeed, in the ARCT province and in the Western European basin, micro-phytoplankton communities represented between

66 and 92% of the total Chl-*a* (Figure 3.3), which could explain the moderate to high POC fluxes. However, in the NADR province and in particular in the Icelandic basin, nano-phytoplankton communities represented up to 67% of the total Chl-*a* (Station 38, Figure 3.3) while this area was characterized by relatively high POC exports.

Our results, alongside with other recent studies in the North Atlantic (Brew et al., 2009; Durkin et al., 2015; Giering et al., 2016) suggest that high POC export fluxes can also be mediated through small particles (Giering et al., 2016; Brew et al., 2009), highlighting that sinking velocity is influenced by other parameters than the size, likely their composition and density, this point being discussed hereafter.

3.4.2.3. Influence of the biogenic and lithogenic minerals

Some phytoplankton communities are composed by “hard” parts such as biogenic silica (BSi) frustules of diatoms and calcium carbonate ($CaCO_3$) shells of coccolithophorids. These biogenic minerals, as well as the lithogenic minerals (dust, clay particles) can be incorporated into aggregates, protecting the organic matter from oxidation and increasing the excess density of suspended particles and thus the sinking velocity (Honjo, 1996). It is thus important to investigate their fluxes (Figure 3.8) in order to better understand their effect on the magnitude of the POC export fluxes.

In the NAST province, Station 1 was strongly influenced by lithogenic inputs as illustrated by the highest particulate aluminum (pAl) export at Eq and at 400 m. Station 1 was also characterized by one of the highest POC export flux at Eq, suggesting that lithogenic particles may play a role in the magnitude of the POC export flux, as the aggregation of lithogenic particles with particulate organic matter has been demonstrated to strongly enhance the POC export flux by acting as a mineral ballast (Bressac et al., 2012; Salter et al., 2010; Ye et al., 2011).

In the NADR, high BSi export fluxes were measured, especially at Station 26, which is consistent with the prevalence of diatoms in the western European basin (Figure 3.3.b). With their high Si content, diatoms are known to ballast the POC vertical export fluxes (Buesseler, 1998), probably leading to the high POC export fluxes determined in this region

In the NADR province, high $CaCO_3$ export fluxes were also observed in the NADR province and in particular in the Icelandic basin where coccolithophorids, traced by the 19'-Hexanoyloxyfucoxanthin pigment, dominated (54% of the total taxonomic pigments; Figure 3.3.b). This phytoplankton community is known to ballast strongly the POC export flux with their dense calcite shells (Francois et al., 2002).

In the ARCT province, the BSi export fluxes were the highest at Eq, reaching 6.60 $mmol.m^{-2}.d^{-1}$, which is in agreement with the dominance of diatoms in this province (fucoxanthin > 60% of the total taxonomic pigments; Figure 3.3.b). This high contribution of sinking diatoms is also suggested by the high POC:^{234}Th ratios observed at Eq in the Labrador basin, explained by the fact that diatoms have a high volume to surface area ratio (Buesseler et al., 2006). Using the cellular BSi/POC ratios of diatoms (0.6 $mol.mol^{-1}$; Baines et al., 2010), we estimated that 90 to 103% of the POC fluxes in the Irminger Sea basin (Stations 44 and 51) and 74 to 107% of the POC fluxes in the Labrador Sea basin (Stations 64, 69 and 77) were carried by the diatoms. The considerable contribution determined in the ARCT province could be caused by a strong silicification of the diatoms, increasing the cellular BSi/POC ratio. Some authors have reported an increase of the BSi/POC ratio under nutrient limitation (Claquin et al., 2002; Marchetti and Cassar, 2009) which may be in line with the post-bloom conditions in the Labrador Sea basin.

The ARCT province was also characterized by high lithogenic inputs near the Greenland Margin. As shown in Figure 3.8, pAl export fluxes were strongly enhanced at 400 m of Station 64, similarly to the POC export flux. Station 64 was affected by the West Greenland Current (WGC) carrying fresh waters produced by runoff and ice melting (Mertz et al., 1993). This current might have transported lithogenic particles to Station 64 between Eq and 400 m which may possibly have ballasted the POC export flux

3.4.3. Export efficiency

The export efficiency (ThE) is a key parameter to illustrate the strength of the biological carbon pump. It is calculated by dividing the POC export flux by the primary production (Buesseler,

1998). However, this calculation is based on two parameters that are integrating processes over different time scales: 24h for PP and 2-3 weeks for export. As a result of this temporal mismatch and due to the strong variability in PP, the ThE ratio has to be addressed carefully (Henson et al., 2015).

During GEOVIDE, ThE values ranged from 1 (Station 44) to 35% (Station 1) with a median value of 6% along the transect (Figure 3.10.a). The highest export efficiencies were determined at Stations 1 and 69 where ThE reached 35 and 34%, respectively. Other stations were characterized by ThE ≤ 12% with a higher range (6 - 12%) at Stations 32, 38, 64 and 77. Export efficiencies around 10% are common in the open ocean (Buesseler, 1998). Lower export efficiency can be related to important microbial and zooplankton grazing activities as well as to biomass accumulation in surface waters (Planchon et al., 2015, 2013). On the contrary, ratios greater than 10% highlight an efficient biological pump. High ThE can be caused by numerous processes such as the presence of large and/or dense and fast sinking particles, low surface remineralization or active zooplankton migration and also nutrient stress (Ceballos-romero et al., 2016; Le Moigne et al., 2016; Planchon et al., 2015).

Interestingly, the stations with the highest ThE were also characterized by the lowest PP (Stations 1 and 69) while the stations with lowest ThE were characterized by the highest PP (Stations 44 and 51). This inverse relationship between PP and ThE was significant for all stations of the GEOVIDE cruise (regression slope: -0.15; r^2: 65%; $p<0.01$; n=11) and has been explained in the Southern Ocean by the temporal decoupling between PP and export (Henson et al., 2015), biomass accumulation in surface waters (Planchon et al., 2013), or other processes such as zooplankton grazing and bacterial activities (Le Moigne et al., 2016; Maiti et al., 2013; Roca-Marti et al., 2016a). Indeed, efficient recycling of particles in the upper waters has been observed in the North Atlantic due to high microbial or grazing activities (Collins et al., 2015; Giering et al., 2014; Marsay et al., 2015) limiting the POC export to the deep ocean. In this study, the extent of heterotrophic degradation can be illustrated from the TPhaeo/Chl-*a* ratio (Ras et al., 2008; Wright et al., 2010). Stations 1 and 69 were characterized by TPhaeo/Chl-*a* ratios below and above 1, respectively, suggesting that this factor did not control

the variation of the ThE. A recent study in the Iceland and Irminger basins highlighted the importance of the bloom dynamic on the particle export efficiency suggesting a strong seasonal variability of the ThE (Ceballos-Romero et al., 2016). Our estimates are in the lower range of export efficiencies reported for the North Atlantic (Table 3.4; Buesseler et al., 1992; Moran et al., 2003; Thomalla et al., 2008; Lampitt et al., 2008) confirming that export efficiencies are highly variable in time. This is a key result because the North Atlantic is generally assumed to be efficient in exporting carbon, but, in fact, the North Atlantic during the period of our study seems to behave like most of the highly productive areas of the world's oceans, with a low export efficiency.

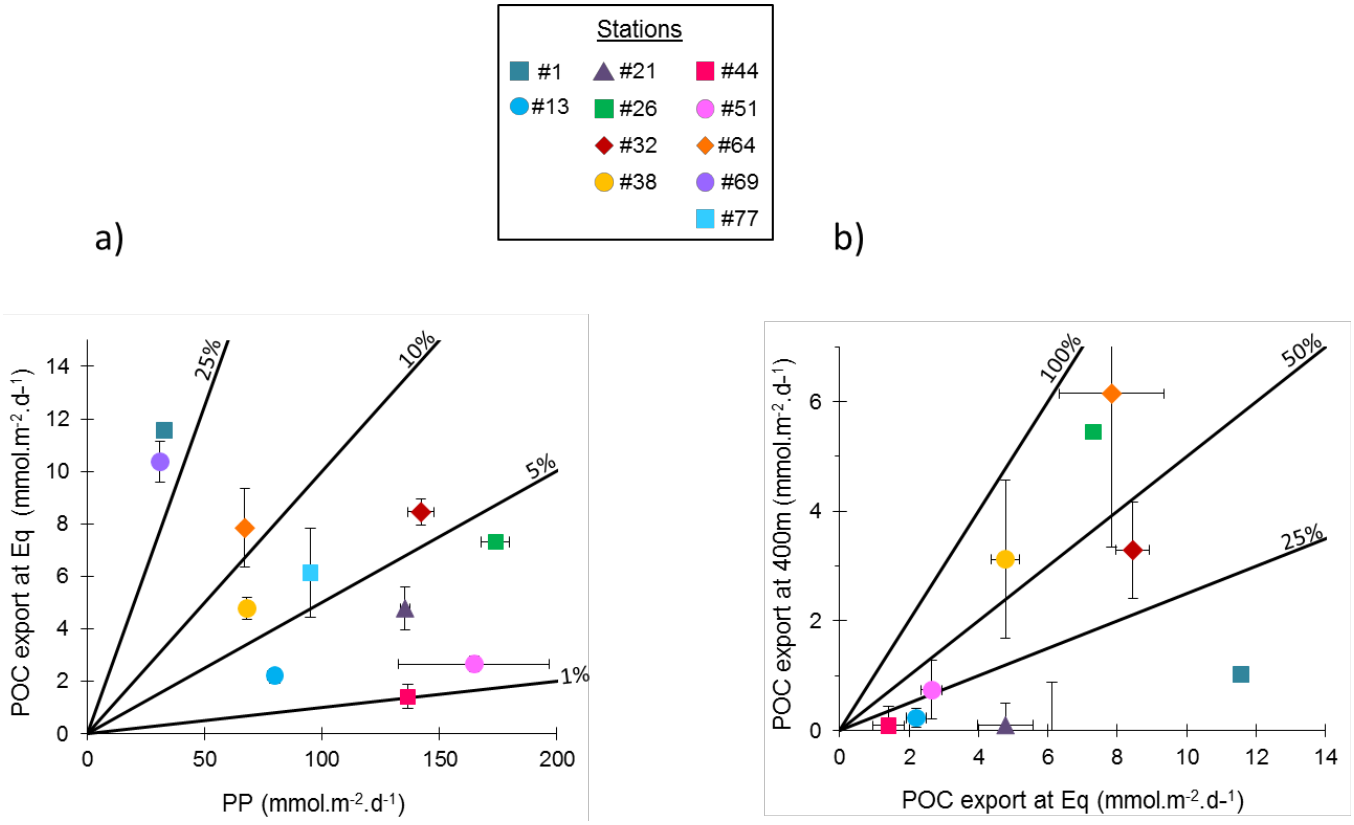

Figure 3.10: a) POC export fluxes at Eq versus daily primary production (PP) and b) POC export fluxes at Eq versus POC export fluxes at 400 m. For the readability of the figure, the error bars for the POC export fluxes of Station 1 are not indicated (error at Eq=22 mmol.m^{-2}.d^{-1} and at 400 m=10 mmol.m^{-2}.d^{-1}) and Station 26 (error at Eq=6.7 mmol.m^{-2}.d^{-1} and at 400 m=7.3 mmol.m^{-2}.d^{-1}).

3.4.4. Transfer efficiency

The major transformation of the sinking particle-size occurs in the upper 300 m where the downward particulate flux is strongly modified due to physical and biological processes, such as microbial degradation, zooplankton fragmentation, disaggregation from turbulence or coagulation (Ken O Buesseler et al., 2007; Guidi et al., 2009). To consider these changes, we have estimated the transfer efficiency (T_{eff}) by dividing the POC export at 400 m by the one at Eq (Figure 3.10.b). However, the calculation of the POC flux at 400 m represents an extension of the ^{234}Th proxy because of the lower resolution at depth compared to the upper ocean, and thus because of the greater size of the integrated water column. There is thus a large uncertainty associated with the POC flux at 400 m and with T_{eff}. The highest transfer efficiencies were observed at Stations 26, 32, 38 and 64 where T_{eff} reached 75, 39, 65 and 78%, respectively. These results are in line with the important regional variability of the transfer efficiency reported elsewhere (Lam et al., 2011; Lutz et al., 2002). Due to the negative ^{234}Th and POC export fluxes estimated at 400 m of Stations 69 and 77, the transfer efficiency is null (0% of the surface export is transferred to depth). This is in agreement with the highest remineralization fluxes determined in this basin with the Ba_{xs} proxy (Lemaitre et al., in prep.).

At some stations, the high transfer efficiencies coincided with low POC attenuation relative to particulate ^{234}Th assessed by the b terms of the power law regressions of POC:^{234}Th ratios versus depth (Equation 3.6). Indeed, an inverse relationship between T_{eff} and b term was found (regression slope: -47.2; r^2: 68%; $p<0.05$; n=6) for Stations 1, 13, 21, 32, 38 and 51. The stations of the NAST province (Stations 1 and 13), as well as Station 21, were characterized by the lowest T_{eff} and by the highest b terms. Moreover, these stations were characterized by higher b terms for large than for small particles indicating that POC in large particles was attenuated at a stronger rate relative to ^{234}Th with depth than in small particles. The decrease of carbon content in large particles may be explained by an important bacterial activity, reinforced in warm waters (>13°C in the upper 100 m; Iversen and Ploug, 2013; Marsay et al., 2015; Rivkin and Legendre, 2001). This efficient recycling is characteristic of tightly coupled

and regeneration based microbial food webs of oligotrophic regimes (Karl, 1999; Thomalla et al., 2006), such as at Stations 1, 13 and, to a lesser extent, at Station 21. Efficient recycling also coincides with the significant attenuation of ^{234}Th fluxes between Eq and 400 m at these stations (Figure 3.5). In the Icelandic basin (Stations 32 and 38), the high T_{eff} and low b terms may be related to the important abundance of coccolithophorids (Figure 3.3.b), known to enhance the POC export flux to the deep ocean by ballast effect (Lam et al., 2011; François et al., 2002). Indeed, Bach et al. (2016) highlighted that a bloom of coccolithophorids can increase the transfer efficiency through the mesopelagic layer by 14-24%.

However, at Station 26 located in the NADR province and influenced by the sub-arctic front (SAF) and associated eddies, this relationship is invalid. This frontal zone was productive (PP reached 174 mmol.m-2.d^{-1} at Station 26) compared to adjacent waters due to the injection of nutrients into the euphotic layer (Lévy et al., 2012). In these nutrient rich fine scale filaments, large phytoplankton species usually dominate and can promote massive episodic particulate export fluxes (Guidi et al., 2007; Kemp et al., 2006; Rivière and Pondaven, 2006; Waite et al., 2016), which was the case at Station 26, dominated by micro-phytoplankton communities. These export fluxes can escape the heterotrophic degradation leading to high transfer efficiency. Indeed, Ragueneau et al. (2006) speculated that mesopelagic food webs might not be able to respond instantly to a sudden dramatic increase in food supply, thus allowing relatively more efficient transfer to depth.

In the Irminger Sea, Station 44 is characterized by a strong bloom and yet by the lowest T_{eff} of the study, probably because of the biomass accumulation in surface waters limiting the POC export fluxes (see section IV.2.a). The bloom structure appears thus to play an important role on the transfer efficiency and can explain its high temporal variability (Lam et al., 2011; Lutz et al., 2007).

In the Labrador Sea basin, Station 64 (high T_{eff} and moderate b term) was characterized by a strong increase of the pAl export fluxes between Eq and 400 m, suggesting an important lateral advection of lithogenic particles between both depths which likely ballast the POC export flux (Figure 3.**8**) and increase the transfer efficiency (Ternon et al., 2010).

These results suggest that $CaCO_3$ and lithogenic minerals induce higher mesopelagic transfer efficiencies than the BSi mineral, as already observed in other studies (Lam et al., 2011; François et al., 2002). Higher mesopelagic transfer efficiencies are also observed in frontal zones where sudden exports escape the heterotrophic respiration.

3.5. Conclusion

We investigated POC export fluxes in the North Atlantic during spring 2014 (GEOVIDE cruise) using the ^{234}Th-deficit approach. The carbon export fluxes varied by a factor ~ 9 along the transect indicating a high spatial variation. Our POC export estimates were similar or lower than other studies reported in the North Atlantic. The differences, up to a factor of 27 in only 1 month lag, confirm the high temporal variation of the POC export fluxes in this ocean.

We have investigated different control factors modifying the POC export fluxes regionally and temporally:

i) The magnitude of the POC export flux is directly related to the intensity and the stage of the bloom. During the bloom, an accumulation of biomass in surface water may induce a limitation of the POC export fluxes while exports can increase during the decline of the bloom, likely due to increasing numbers of rapidly sinking particles.

ii) The phytoplankton size structure might have influenced the magnitude of the POC export fluxes. Indeed, the only station characterized by pico-phytoplankton communities was characterized by one of the lowest POC export flux. However, the areas composed by nano- or micro-phytoplankton were both characterized by high POC export fluxes, indicating that the size structure was not the main factor influencing the fluxes during GEOVIDE.

iii) The ballast mineral effect plays a crucial role on the particulate sinking velocities and thus on the magnitude of the POC export fluxes. The highest POC export fluxes

were observed at stations where diatoms (Si ballast) and coccolithophorids ($CaCO_3$ ballast) dominated. Moreover, high POC export fluxes were observed near margins, probably due to the aggregation with lithogenic particles, also ballasting POC.

Finally, export efficiency was low (≤ 12% except at two stations where it reached 35 and 34%) and was inversely related to primary production, highlighting that the North Atlantic is not as efficient as previously thought. The highest transfer efficiencies appeared to be driven by sinking particles ballasted by calcite or lithogenic minerals, but also by the sub-mesoscale activities such as the sub-arctic front.

Acknowledgements

We would like to thank the captain and the crew of the R/V Pourquoi Pas?, as well as Fabien Perault and Emmanuel De Saint Léger from the CNRS DT-INSU for their help during the CTD and ISP deployments. Special thanks to Maxi Castrillejo (UAB, Spain), Yi Tang (Queens College, USA), Catherine Jeandel (LEGOS, France), Virginie Sanial (WHOI, USA), Raphaëlle Sauzède (LOV, France) and Lorna Foliot (LSCE, France) for their help at sea and for the pump coordination and collaboration. We would also like to thank Phoebe Lam for providing two modified McLane ISP. Laurence Monin (MRAC, Belgium), David Verstraeten, Claire Mourgues and Martine Leermarkers (VUB, Belgium) greatly helped during sampling processing and element analysis by ICP-MS and EA-IRMS. Satellite chlorophyll-a data and visualizations used in this study were produced with the Giovanni online data system, developed and maintained by the NASA GES DISC.

This work was funded by the Flanders Research Foundation (project G071512N), the Vrije Universiteit Brussel (Strategic Research Program, project SRP-2), the French ANR Blanc GEOVIDE (ANR-13-BS06-0014), ANR RPDOC BITMAP (ANR-12-PDOC-0025-01), IFREMER, CNRS-INSU (programme LEFE), INSU OPTIMISP and Labex-Mer (ANR-10-LABX-19).

Table S3.1: ^{238}U and total ^{234}Th activities in dpm.L^{-1} and resulting $^{234}Th/^{238}U$ ratios. ^{238}U activity is derived from salinity (see text).

Station	Depth	Temperature	Salinity	^{238}U			^{234}Th			$^{234}Th/^{238}U$
#	m	°C	psu	dpm.L^{-1}			dpm.L^{-1}			
#1 40.3°N / -10.0 °E	19	15.89	35.27	2.46	±	0.05	1.83	±	0.06	0.74
	39	14.93	35.55	2.48	±	0.05	1.69	±	0.05	0.68
	60	13.81	35.68	2.49	±	0.05	2.11	±	0.07	0.85
	79	13.44	35.71	2.49	±	0.05	2.39	±	0.07	0.96
	98	13.21	35.74	2.49	±	0.05	2.55	±	0.08	1.02
	119	13.02	35.73	2.49	±	0.05	2.50	±	0.08	1.00
	137	12.88	35.73	2.49	±	0.05	2.34	±	0.07	0.94
	158	12.73	35.71	2.49	±	0.05	2.44	±	0.08	0.98
	199	12.55	35.71	2.49	±	0.05	2.54	±	0.08	1.02
	246	12.29	35.69	2.49	±	0.05	2.60	±	0.08	1.05
	298	12.08	35.68	2.49	±	0.05	2.67	±	0.08	1.07
	396	11.69	35.65	2.49	±	0.05	2.59	±	0.08	1.04
	496	11.43	35.67	2.49	±	0.05	2.43	±	0.07	0.98
	589	11.41	35.77	2.50	±	0.05	2.61	±	0.08	1.05
	695	11.60	35.94	2.51	±	0.05	2.58	±	0.08	1.03
	791	11.72	36.07	2.52	±	0.05	2.90	±	0.09	1.15
	989	11.34	36.15	2.53	±	0.05	2.68	±	0.08	1.06
#13 41.4°N / -13.9 °E	20	15.49	35.85	2.50	±	0.05	1.75	±	0.05	0.70
	40	14.86	35.81	2.50	±	0.05	1.83	±	0.05	0.73
	60	13.30	35.76	2.50	±	0.05	2.23	±	0.07	0.90
	78	13.14	35.76	2.50	±	0.05	2.31	±	0.06	0.93
	99	12.99	35.75	2.49	±	0.05	2.26	±	0.07	0.91
	119	12.93	35.75	2.49	±	0.05	2.63	±	0.08	1.05
	139	12.88	35.75	2.49	±	0.05	2.82	±	0.07	1.13
	159	12.83	35.74	2.49	±	0.05	2.64	±	0.07	1.06
	197	12.64	35.71	2.49	±	0.05	2.52	±	0.07	1.01
	248	12.38	35.68	2.49	±	0.05	2.65	±	0.07	1.06
	298	12.20	35.66	2.49	±	0.05	2.50	±	0.07	1.00
	398	11.82	35.62	2.48	±	0.05	2.52	±	0.07	1.01
	496	11.59	35.62	2.48	±	0.05	2.66	±	0.08	1.07
	594	11.23	35.61	2.48	±	0.05	2.61	±	0.07	1.05
	693	10.66	35.57	2.48	±	0.05	2.55	±	0.08	1.03
	792	10.55	35.68	2.49	±	0.05	2.35	±	0.06	0.95
	990	9.33	35.65	2.49	±	0.05	2.63	±	0.08	1.06
	1485	6.73	35.45	2.47	±	0.05	2.48	±	0.07	1.00
#21 46.5°N / -19.7°E	10	14.44	35.68	2.49	±	0.05	1.41	±	0.05	0.57
	20	13.65	35.66	2.49	±	0.05	1.69	±	0.05	0.68
	39	12.79	35.64	2.49	±	0.05	1.79	±	0.05	0.72
	59	12.71	35.65	2.49	±	0.05	1.80	±	0.05	0.72
	76	12.63	35.67	2.49	±	0.05	2.07	±	0.06	0.83
	100	12.45	35.69	2.49	±	0.05	2.36	±	0.07	0.95
	119	12.36	35.68	2.49	±	0.05	2.62	±	0.07	1.05
	158	12.23	35.66	2.49	±	0.05	2.53	±	0.07	1.02
	198	12.08	35.64	2.49	±	0.05	2.70	±	0.07	1.09
	296	11.80	35.60	2.48	±	0.05	2.83	±	0.07	1.14
	396	11.38	35.55	2.48	±	0.05	2.61	±	0.07	1.05
	495	11.01	35.50	2.48	±	0.05	2.65	±	0.08	1.07
	594	10.74	35.47	2.47	±	0.05	2.52	±	0.07	1.02
	693	9.78	35.32	2.46	±	0.05	2.56	±	0.07	1.04
	792	8.77	35.29	2.46	±	0.05	2.69	±	0.08	1.09
	989	7.47	35.32	2.46	±	0.05	2.58	±	0.07	1.05
	1189	6.17	35.21	2.45	±	0.05	2.36	±	0.07	0.96

#26 50.3°N / -22.6°E	20	11.69	35.34	2.46	±	0.05	1.90	±	0.06	0.77
	49	9.77	35.19	2.45	±	0.05	1.90	±	0.06	0.77
	74	9.65	35.19	2.45	±	0.05	1.96	±	0.06	0.80
	99	9.40	35.16	2.45	±	0.05	2.07	±	0.07	0.85
	199	8.88	35.17	2.45	±	0.05	2.46	±	0.08	1.00
	297	8.17	35.07	2.44	±	0.05	2.36	±	0.07	0.97
	397	7.18	34.95	2.43	±	0.05	2.47	±	0.08	1.01
	593	5.97	35.00	2.44	±	0.05	2.59	±	0.08	1.07
	792	5.23	35.03	2.44	±	0.05	2.60	±	0.08	1.07
#32 55.5°N / -26.7°E	11	10.51	35.13	2.45	±	0.05	1.63	±	0.08	0.67
	20	10.48	35.13	2.45	±	0.05	1.58	±	0.06	0.65
	40	8.89	35.07	2.44	±	0.05	1.88	±	0.06	0.77
	60	8.60	35.08	2.44	±	0.05	1.87	±	0.05	0.77
	99	8.67	35.13	2.45	±	0.05	1.64	±	0.05	0.67
	119	8.08	35.04	2.44	±	0.05	2.32	±	0.06	0.95
	139	7.88	35.03	2.44	±	0.05	2.59	±	0.08	1.06
	160	8.23	35.12	2.45	±	0.05	2.48	±	0.07	1.01
	199	7.99	35.09	2.44	±	0.05	2.42	±	0.07	0.99
	298	7.05	34.98	2.43	±	0.05	2.48	±	0.07	1.02
	376	5.99	34.89	2.43	±	0.05	2.52	±	0.07	1.04
	446	6.36	35.04	2.44	±	0.05	2.47	±	0.07	1.01
	494	5.70	34.98	2.43	±	0.05	2.50	±	0.07	1.03
	593	5.15	34.98	2.43	±	0.05	2.52	±	0.08	1.04
	693	4.78	34.96	2.43	±	0.05	2.45	±	0.07	1.01
	792	4.48	34.94	2.43	±	0.05	2.29	±	0.06	0.94
#38 58.8°N / -31.3°E	10	9.30	35.06	2.44	±	0.05	1.23	±	0.04	0.50
	19	9.18	35.06	2.44	±	0.05	1.48	±	0.05	0.61
	39	8.22	35.08	2.44	±	0.05	2.12	±	0.07	0.87
	60	8.00	35.11	2.44	±	0.05	2.38	±	0.07	0.97
	78	7.73	35.11	2.44	±	0.05	2.45	±	0.07	1.00
	99	7.73	35.13	2.45	±	0.05	2.61	±	0.08	1.07
	118	7.68	35.14	2.45	±	0.05	2.61	±	0.08	1.07
	138	7.67	35.14	2.45	±	0.05	2.41	±	0.07	0.99
	158	7.62	35.14	2.45	±	0.05	2.43	±	0.07	0.99
	178	7.59	35.14	2.45	±	0.05	2.51	±	0.07	1.02
	198	7.60	35.15	2.45	±	0.05	2.46	±	0.07	1.01
	298	7.41	35.14	2.45	±	0.05	2.40	±	0.08	0.98
	396	7.21	35.13	2.45	±	0.05	2.50	±	0.09	1.02
	494	6.86	35.11	2.44	±	0.05	2.45	±	0.09	1.00
	593	6.32	35.09	2.44	±	0.05	2.48	±	0.08	1.01
	693	5.68	35.05	2.44	±	0.05	2.54	±	0.09	1.04
	791	5.00	35.01	2.44	±	0.05	2.51	±	0.09	1.03
#44 59.6°N / -38.9°E	9	6.83	34.85	2.42	±	0.05	1.91	±	0.06	0.79
	20	6.80	34.85	2.42	±	0.05	2.18	±	0.06	0.90
	40	5.07	34.89	2.43	±	0.05	2.42	±	0.07	1.00
	59	4.49	34.87	2.43	±	0.05	2.46	±	0.07	1.01
	79	4.33	34.90	2.43	±	0.05	2.31	±	0.06	0.95
	99	4.28	34.91	2.43	±	0.05	2.40	±	0.06	0.99
	118	4.12	34.89	2.43	±	0.05	2.44	±	0.07	1.00
	138	4.03	34.89	2.43	±	0.05	2.23	±	0.05	0.92
	158	4.04	34.89	2.43	±	0.05	2.42	±	0.07	1.00
	198	4.00	34.89	2.43	±	0.05	2.35	±	0.06	0.97
	297	3.92	34.89	2.43	±	0.05	2.56	±	0.06	1.05
	396	3.88	34.89	2.43	±	0.05	2.56	±	0.07	1.05
	495	3.79	34.88	2.43	±	0.05	2.38	±	0.06	0.98
	594	3.73	34.88	2.43	±	0.05	2.35	±	0.05	0.97
	692	3.63	34.87	2.43	±	0.05	2.62	±	0.06	1.08
	792	3.61	34.87	2.43	±	0.05	2.23	±	0.06	0.92
	1087	3.70	34.89	2.43	±	0.05	2.43	±	0.07	1.00

#51 59.8°N / -42.0°E	11	6.76	34.87	2.43	±	0.05	1.92	±	0.06	0.79
	19	6.65	34.88	2.43	±	0.05	1.89	±	0.05	0.78
	40	6.18	34.95	2.43	±	0.05	2.18	±	0.07	0.90
	60	5.96	34.97	2.43	±	0.05	2.07	±	0.06	0.85
	79	5.58	34.95	2.43	±	0.05	2.20	±	0.06	0.91
	100	5.51	34.95	2.43	±	0.05	2.44	±	0.07	1.00
	119	5.27	34.93	2.43	±	0.05	2.58	±	0.07	1.06
	139	5.13	34.92	2.43	±	0.05	2.42	±	0.07	1.00
	159	5.16	34.94	2.43	±	0.05	2.31	±	0.06	0.95
	178	4.93	34.92	2.43	±	0.05	2.44	±	0.07	1.01
	199	4.99	34.94	2.43	±	0.05	2.53	±	0.07	1.04
	298	4.97	34.96	2.43	±	0.05	2.51	±	0.07	1.03
	396	4.66	34.95	2.43	±	0.05	2.41	±	0.07	0.99
	495	4.51	34.94	2.43	±	0.05	2.26	±	0.06	0.93
	593	4.17	34.92	2.43	±	0.05	2.30	±	0.06	0.94
	692	4.05	34.91	2.43	±	0.05	2.49	±	0.07	1.02
	791	4.01	34.92	2.43	±	0.05	2.46	±	0.07	1.01
#64 59.1°N / -46.1°E	9	6.55	34.80	2.42	±	0.05	1.89	±	0.10	0.78
	20	6.04	34.85	2.42	±	0.05	2.00	±	0.07	0.83
	40	5.93	34.87	2.43	±	0.05	1.88	±	0.07	0.78
	79	5.37	34.95	2.43	±	0.05	2.46	±	0.09	1.01
	99	5.35	34.96	2.43	±	0.05	2.57	±	0.09	1.06
	139	5.17	34.96	2.43	±	0.05	2.43	±	0.09	1.00
	159	4.92	34.94	2.43	±	0.05	2.43	±	0.09	1.00
	197	4.78	34.93	2.43	±	0.05	2.31	±	0.08	0.95
	297	4.51	34.93	2.43	±	0.05	2.33	±	0.09	0.96
	396	4.35	34.93	2.43	±	0.05	2.45	±	0.09	1.01
	494	4.10	34.91	2.43	±	0.05	2.54	±	0.09	1.04
	594	3.97	34.90	2.43	±	0.05	2.52	±	0.09	1.04
	692	3.88	34.89	2.43	±	0.05	2.42	±	0.09	1.00
	792	3.71	34.88	2.43	±	0.05	2.46	±	0.09	1.01
	890	3.64	34.87	2.43	±	0.05	2.46	±	0.09	1.02
#69 55.8°N / -48.1°E	11	6.23	34.61	2.41	±	0.05	1.58	±	0.05	0.66
	20	6.15	34.61	2.41	±	0.05	1.84	±	0.05	0.77
	59	3.73	34.77	2.42	±	0.05	2.58	±	0.09	1.07
	80	3.92	34.83	2.42	±	0.05	2.52	±	0.08	1.04
	99	3.83	34.82	2.42	±	0.05	2.62	±	0.08	1.08
	119	3.95	34.85	2.42	±	0.05	2.55	±	0.08	1.05
	139	3.91	34.86	2.42	±	0.05	2.45	±	0.08	1.01
	159	3.83	34.86	2.42	±	0.05	2.41	±	0.07	0.99
	199	3.58	34.84	2.42	±	0.05	2.61	±	0.08	1.08
	298	3.54	34.85	2.42	±	0.05	2.56	±	0.08	1.05
	496	3.51	34.85	2.42	±	0.05	2.33	±	0.07	0.96
	595	3.48	34.85	2.42	±	0.05	2.50	±	0.08	1.03
	693	3.47	34.85	2.42	±	0.05	2.37	±	0.07	0.98
	792	3.48	34.85	2.42	±	0.05	2.53	±	0.08	1.04
	890	3.48	34.85	2.42	±	0.05	2.32	±	0.08	0.96
	990	3.46	34.85	2.42	±	0.05	2.36	±	0.07	0.98

#77 53.0°N / -51.1°E	10	6.92	34.49	2.40	±	0.05	1.80	±	0.07	0.75
	20	6.27	34.56	2.40	±	0.05	1.76	±	0.07	0.73
	39	5.11	34.64	2.41	±	0.05	2.12	±	0.08	0.88
	59	4.09	34.71	2.41	±	0.05	2.39	±	0.10	0.99
	79	3.60	34.74	2.42	±	0.05	2.27	±	0.07	0.94
	100	3.49	34.76	2.42	±	0.05	2.64	±	0.08	1.09
	119	3.44	34.77	2.42	±	0.05	2.52	±	0.08	1.04
	139	3.41	34.79	2.42	±	0.05	2.57	±	0.08	1.06
	159	3.43	34.81	2.42	±	0.05	2.64	±	0.08	1.09
	199	3.46	34.83	2.42	±	0.05	2.36	±	0.08	0.97
	298	3.53	34.85	2.42	±	0.05	2.57	±	0.09	1.06
	397	3.57	34.86	2.42	±	0.05	2.67	±	0.09	1.10
	495	3.52	34.86	2.42	±	0.05	2.60	±	0.09	1.07
	595	3.56	34.87	2.43	±	0.05	2.49	±	0.08	1.03
	693	3.49	34.86	2.43	±	0.05	2.69	±	0.08	1.11

Table S3.2: Particulate ^{234}Th activities and POC concentrations in the small (SSF; 1-53 µm) and large size fraction (LSF; >53 µm).

Station	Depth	1-53 µm (SSF)		>53 µm (LSF)	
		^{234}Th	POC	^{234}Th	POC
#	m	dpm.L^{-1}	µmol.L^{-1}	dpm.L^{-1}	µmol.L^{-1}
1 40.3°N -10.0 °E	30	0.163 ± 0.005	2.639 ± 0.099	0.021 ± 0.001	0.651 ± 0.009
	80	0.086 ± 0.003	0.208 ± 0.017	0.022 ± 0.001	0.357 ± 0.005
	120	0.188 ± 0.006	0.567 ± 0.035	0.021 ± 0.001	0.105 ± 0.005
	250	0.171 ± 0.004	0.428 ± 0.019	0.038 ± 0.001	0.068 ± 0.006
	550	0.123 ± 0.004	0.217 ± 0.016	0.014 ± 0.000	0.023 ± 0.002
	800	0.068 ± 0.003	0.035 ± 0.032	0.011 ± 0.001	0.024 ± 0.005
13 41.4°N -13.9 °E	30	0.456 ± 0.004	2.160 ± 0.035	0.028 ± 0.001	0.196 ± 0.005
	80	0.529 ± 0.004	1.170 ± 0.027	0.030 ± 0.001	0.080 ± 0.004
	120	0.431 ± 0.004	±	0.032 ± 0.001	0.039 ± 0.005
	250	0.210 ± 0.002	0.366 ± 0.021	0.020 ± 0.001	0.027 ± 0.003
	450	0.133 ± 0.001	0.266 ± 0.016	0.009 ± 0.000	0.018 ± 0.002
21 46.5°N -19.7°E	15	0.280 ± 0.009	6.053 ± 0.068	0.161 ± 0.003	4.747 ± 0.020
	60	0.775 ± 0.017	4.064 ± 0.105	0.243 ± 0.005	1.201 ± 0.031
	100	0.225 ± 0.005	0.545 ± 0.023	0.052 ± 0.001	0.133 ± 0.007
	200	0.122 ± 0.003	0.360 ± 0.021	0.038 ± 0.001	0.046 ± 0.002
	450	0.114 ± 0.003	0.234 ± 0.016	0.022 ± 0.000	0.023 ± 0.002
	800	0.108 ± 0.002	0.158 ± 0.013	0.014 ± 0.000	0.017 ± 0.001
26 50.3°N -22.6°E	30	0.279 ± 0.008	4.792 ± 0.059	0.206 ± 0.004	2.572 ± 0.017
	83	0.225 ± 0.005	0.848 ± 0.022	0.201 ± 0.002	0.877 ± 0.007
	153	0.131 ± 0.003	0.400 ± 0.021	0.030 ± 0.001	0.123 ± 0.003
	400	0.111 ± 0.005	0.240 ± 0.049	0.012 ± 0.001	0.035 ± 0.007
32 55.5°N -26.7°E	30	0.109 ± 0.003	5.830 ± 0.097	0.045 ± 0.002	0.292 ± 0.014
	60	0.359 ± 0.007	1.565 ± 0.027	0.027 ± 0.001	0.124 ± 0.004
	100	0.224 ± 0.005	0.887 ± 0.024	0.080 ± 0.002	0.338 ± 0.007
	200	0.121 ± 0.004	0.467 ± 0.022	0.010 ± 0.000	0.046 ± 0.003
	450	0.078 ± 0.002	0.240 ± 0.017	0.012 ± 0.000	0.037 ± 0.002
	800	0.084 ± 0.002	0.203 ± 0.015	0.010 ± 0.000	0.066 ± 0.002
38 58.8°N -31.3°E	20	0.239 ± 0.006	2.231 ± 0.041	0.028 ± 0.001	0.156 ± 0.004
	60	0.290 ± 0.006	1.273 ± 0.028	0.037 ± 0.001	0.128 ± 0.004
	109	0.143 ± 0.003	0.621 ± 0.018	0.043 ± 0.001	0.156 ± 0.005
	396	0.133 ± 0.004	0.292 ± 0.036	0.009 ± 0.000	0.030 ± 0.005
44 59.6°N -38.9°E	20	1.188 ± 0.020	16.736 ± 0.102	0.480 ± 0.007	3.965 ± 0.020
	40	0.474 ± 0.010	3.550 ± 0.056	0.041 ± 0.001	0.133 ± 0.013
	80	1.060 ± 0.028	6.736 ± 0.213	0.098 ± 0.004	0.306 ± 0.046
	150	0.116 ± 0.004	0.392 ± 0.041	0.005 ± 0.000	0.026 ± 0.009
	300	0.092 ± 0.003	0.334 ± 0.022	0.004 ± 0.000	0.022 ± 0.005
	500	0.067 ± 0.002	0.187 ± 0.016	0.005 ± 0.000	0.016 ± 0.004
51 59.8°N -42.0°E	8	0.183 ± 0.007	4.109 ± 0.064	0.230 ± 0.005	2.664 ± 0.017
	20	0.958 ± 0.025	8.974 ± 0.111		
	60	0.366 ± 0.009	2.154 ± 0.036	0.148 ± 0.003	0.554 ± 0.010
	70	0.451 ± 0.009	2.375 ± 0.034		
	100	0.179 ± 0.006	0.832 ± 0.032	0.052 ± 0.002	0.153 ± 0.007
	150	0.193 ± 0.006	0.747 ± 0.039		
	250	0.088 ± 0.003	0.328 ± 0.021	0.017 ± 0.001	0.076 ± 0.005

Station	Depth	1-53 µm (SSF)		>53 µm (LSF)	
		^{234}Th	POC	^{234}Th	POC
#	m	dpm.L^{-1}	µmol.L^{-1}	dpm.L^{-1}	µmol.L^{-1}
	30	0.024 ± 0.001	0.418 ± 0.009	0.026 ± 0.001	0.373 ± 0.002
64	60	0.174 ± 0.007	1.726 ± 0.054	0.015 ± 0.001	0.154 ± 0.012
59.1°N	100	0.162 ± 0.004	1.968 ± 0.028	0.030 ± 0.001	0.267 ± 0.006
-46.1°E	150	0.118 ± 0.005	0.189 ± 0.046	0.035 ± 0.002	0.208 ± 0.007
	400	0.113 ± 0.003	0.309 ± 0.019	0.010 ± 0.000	0.054 ± 0.004
	30	0.206 ± 0.007	4.130 ± 0.052	0.070 ± 0.002	1.077 ± 0.013
69	60	0.159 ± 0.005	1.958 ± 0.040	0.015 ± 0.001	0.172 ± 0.009
55.8°N	100	0.124 ± 0.004	1.655 ± 0.028	0.030 ± 0.001	0.299 ± 0.007
-48.1°E	150	0.097 ± 0.004	0.895 ± 0.039	0.010 ± 0.001	0.083 ± 0.009
	410	0.069 ± 0.002	0.313 ± 0.022	0.006 ± 0.000	0.075 ± 0.005
	10	0.313 ± 0.011	11.182 ± 0.098	0.206 ± 0.006	3.039 ± 0.021
77	50	0.447 ± 0.012	5.488 ± 0.067	0.057 ± 0.002	0.425 ± 0.016
53.0°N	80	0.150 ± 0.004	2.347 ± 0.028	0.039 ± 0.001	0.339 ± 0.007
-51.1°E	200	0.100 ± 0.004	0.533 ± 0.040	0.009 ± 0.000	0.081 ± 0.008
	460	0.069 ± 0.003	0.167 ± 0.017	0.011 ± 0.000	0.060 ± 0.004

Chapter 4

Particulate barium tracing significant mesopelagic carbon remineralization in the North Atlantic Ocean

This manuscript will be submitted in January 2017 to Biogeosciences (GEOVIDE special issue)

Abstract

The remineralization of sinking particles by heterotrophic activities is important for controlling oceanic carbon sequestration. Here, we report mesopelagic particulate organic carbon (POC) remineralization fluxes in the North Atlantic during the GEOTRACES GA01 cruise (GEOVIDE; May-June 2014) using the excess particulate biogenic barium (Ba_{xs}) proxy.

Mesopelagic remineralization fluxes varied from 8.0 $mmol.m^{-2}.d^{-1}$ in the NADR province up to 21 $mmol.m^{-2}.d^{-1}$ in the ARCT province. These important regional differences can be attributed to the intensity of past blooms, the phytoplankton size and community structure and the physical forcing, including downwelling. Indeed, the ARCT province was characterized by an intense bloom averaging 6 $mg.m^{-3}$ between January and June 2014 and by an intense 1500 m-deep convection in the central Labrador Sea during the winter preceding the sampling. This downwelling could have promoted a deepening of the bacterial activity, increasing the remineralization. In comparison, the NADR province was sampled during the bloom development, dominated by smaller and calcified cells which seem to be less affected by the remineralization. This is in line with the notion that calcite enhances the deep POC sequestration.

Interestingly, along the GEOVIDE section, mesopelagic POC remineralization fluxes were equaling or even exceeding upper ocean POC export fluxes. We explain this imbalance by the different integration timescales between production, export and remineralization. More importantly, our results highlight the important impact of the mesopelagic remineralization on the biological carbon pump with a near-zero, deep (> 1000 m) carbon sequestration efficiency in spring 2014.

4.1. Introduction

The oceanic biological carbon pump (BCP) controls the export of carbon and nutrients to the deep ocean, especially through the production of biogenic sinking particles.

Due to its strong spring bloom (Henson et al., 2009; Pommier et al., 2009), the North Atlantic has been identified as an efficient ocean to transport carbon to the deep ocean (Buesseler et al., 1992; Buesseler and Boyd, 2009; Herndl and Reinthaler, 2013; Honjo and Manganini, 1993; Le Moigne et al., 2013b) and estimated to contribute up to 18% of the BCP in the world's ocean (Sanders et al., 2014). However, the efficiency of this transfer depends on many processes including the remineralization intensity occurring within the mesopelagic zone (defined as the 100-1000 m depth layer of the ocean). In this layer, most of the particulate organic carbon (POC) exported from surface is released to the dissolved phase (Buesseler et al., 2007; Buesseler and Boyd, 2009; Burd et al., 2016; Herndl and Reinthaler, 2013; Lampitt and Antia, 1997; Martin et al., 1987). Mesopelagic remineralization has been often reported to exceed the carbon supplies (i.e. POC and dissolved organic carbon (DOC); Aristegui et al., 2009; Baltar et al., 2009; Burd et al., 2010; Collins et al., 2015; Fernández-castro et al., 2016; Giering et al., 2014; Reinthaler et al., 2006), highlighting the importance of the mesopelagic zone on the fate of the sinking POC, and occasionally questioning the efficiency of the North Atlantic to transfer POC to the deep ocean.

In this context, we examined mesopelagic POC remineralization along the GA01 GEOTRACES section GEOVIDE (15 May - 30 June, 2014; R/V Pourquoi Pas?) by assessing excess particulate biogenic barium (Ba_{xs}) contents. Earlier works have shown that accumulation of Ba_{xs} in the mesopelagic layer could have been related to the presence of barite ($BaSO_4$) crystals formed in surface waters by biota (Bishop, 1988; Dehairs et al., 1980). Recently, this association between phytoplankton organic matter and barite crystals has been demonstrated by coupling dissolved barium concentrations and stable isotopes (Cao et al., 2016; Horner et al., 2015). Most likely, these micro-sized crystals precipitate inside oversaturated micro-environments, mostly aggregates of organic material where bacterial activity is intense (Bishop, 1988; Collier and Edmond, 1984; Dehairs et al., 1980; Ganeshram

et al., 2003). Indeed, the precipitation of barite has been shown to be bacteria-mediated in culture experiments (Gonzalez-Munoz et al., 2003). Once these aggregates get remineralized, barite crystals are released within the mesopelagic zone. Excess barium content can then be related to oxygen consumption using an algorithm (Dehairs et al., 1997; Shopova et al., 1995) and converted to a remineralized POC flux in the mesopelagic zone (Dehairs et al., 1997). To our knowledge, the Ba_{xs} proxy has been used in the Southern (Cardinal et al., 2005; Jacquet et al., 2015, 2011, 2008a, 2008b; Planchon et al., 2013) and Pacific Oceans (Dehairs et al., 2008).

Therefore, this study is the first one to report the use of the Ba_{xs} proxy in the North Atlantic, allowing a comparison with other methods assessing mesopelagic remineralization fluxes, such as the oxygen utilization rate, incubations or moored sediment traps. Regional variations of the Ba_{xs} distributions along the biogeochemical provinces are discussed regarding the stage and intensity of the bloom, phytoplankton size and community structure and physical forcing. This, in combination with surface primary production (PP) and POC export estimates (Lemaitre et al., in prep.), was very useful to investigate the fate of POC to the deep ocean in order to better constrain the biological carbon pump and its efficiency in the North Atlantic.

4.2. Methods

4.2.1. Study area

The GEOVIDE section (15 May – 30 June 2014; R/V Pourquoi pas?) crossed different biogeochemical provinces in the North Atlantic including the North Atlantic subtropical gyre (NAST; Stations 1 and 13); the North Atlantic drift (NADR) covering the western European (Stations 21 and 26) and the Icelandic (Stations 32 and 38) basins; and the Atlantic Arctic (ARCT) divided between the Irminger Sea (Stations 44 and 51) and the Labrador Sea (Stations 64, 69 and 77) basins (Longhurst, 1995; Figures 4.1 and 4.2).

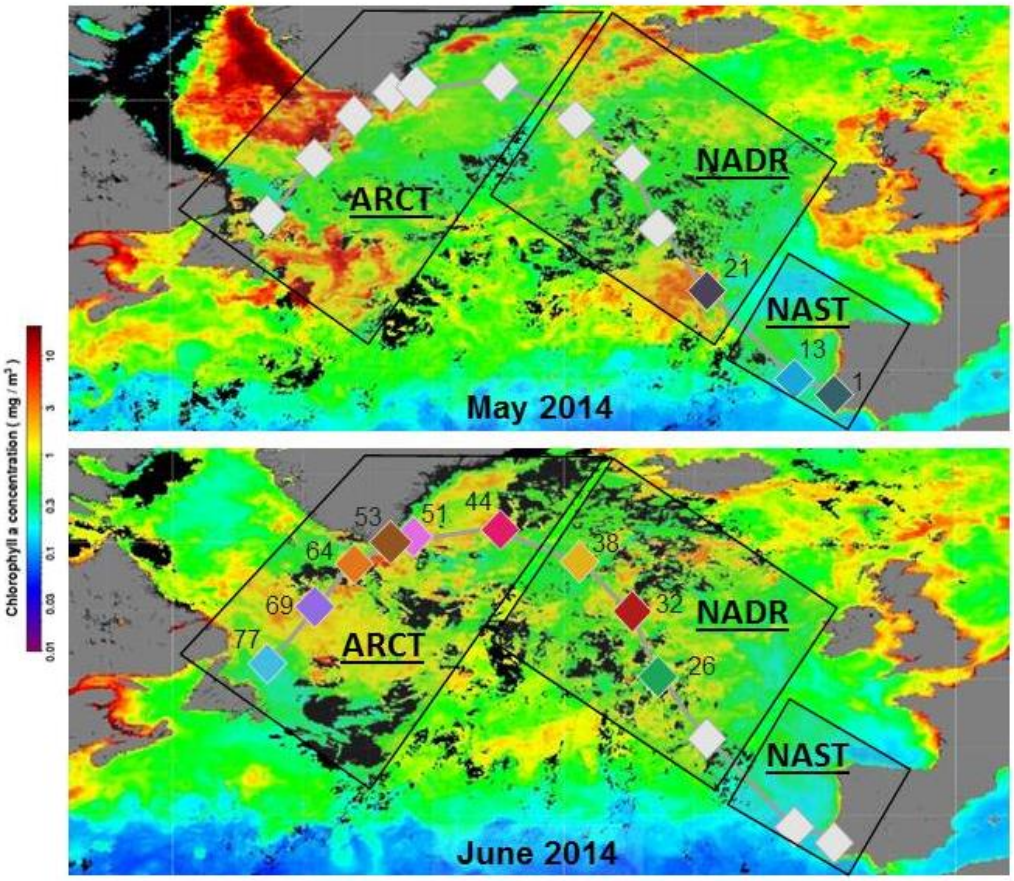

Figure 4.1: Satellite Chlorophyll-a concentrations (MODIS Aqua from http://oceancolor.gsfc.nasa.gov), in mg.m-3 during the GEOVIDE cruise (May and June 2014). Stations are indicated by the diamonds. Colored diamonds indicate the approximate time of sampling.

The evolution of chlorophyll-*a* (Chl-*a*) concentrations from satellite imagery (Figure 4.1) revealed the decline of the bloom in the NAST and Labrador Sea basins and the bloom period within the NADR province and the Irminger Sea basin (Lemaitre et al., in prep.). Indeed, the highest daily primary production rates (PP) were measured in the NADR and in the Irminger Sea basins (>150 mmol $C.m^{-2}.d^{-1}$; A. Roukaerts, D. Fonseca Batista and F. Deman, unpublished data). The phytoplankton community structure also varied regionally with diatoms dominating the ARCT province and the western European basin of the NADR, coccolithophorids dominating the Icelandic basin of the NADR and cyanobacteria in the NAST province. Finally, as specifically described elsewhere (Daniault et al., 2016; García-ibáñez et al., 2015; Kieke and Yashayaev, 2015), these provinces also differed in terms of their hydrographic features, in particular, the presence of the sub-arctic front (SAF; which during

GEOVIDE was located near Station 26), strong currents near the Greenland margin (probably influencing the Stations 51 and 64), and an intense 1500 m-deep convection in the central Labrador Sea (Station 69) due to the formation of the Labrador Sea Water (LSW) in winter. These features influenced the magnitude of the carbon export fluxes, as well as the export and transfer efficiencies along the transect (Lemaitre et al., in prep., Chapter 3). The highest POC export fluxes from the upper-ocean was observed in the NADR province and in the Labrador Sea basin, reaching 8.4 ± 0.5 and 10 ± 0.8 mmol $C.m^{-2}.d^{-1}$ at Stations 32 and 69, respectively. Export efficiencies (e.g. POC export flux divided by PP) were generally low (≤ 12%), except at Station 69 where it reached 30%. The transfer efficiencies (e.g. upper ocean POC export flux divided by POC export flux at 400 m) were more variable, ranging from 2% at Station 21 to 78% at Station 64 (Lemaitre et al., in prep.).

a)

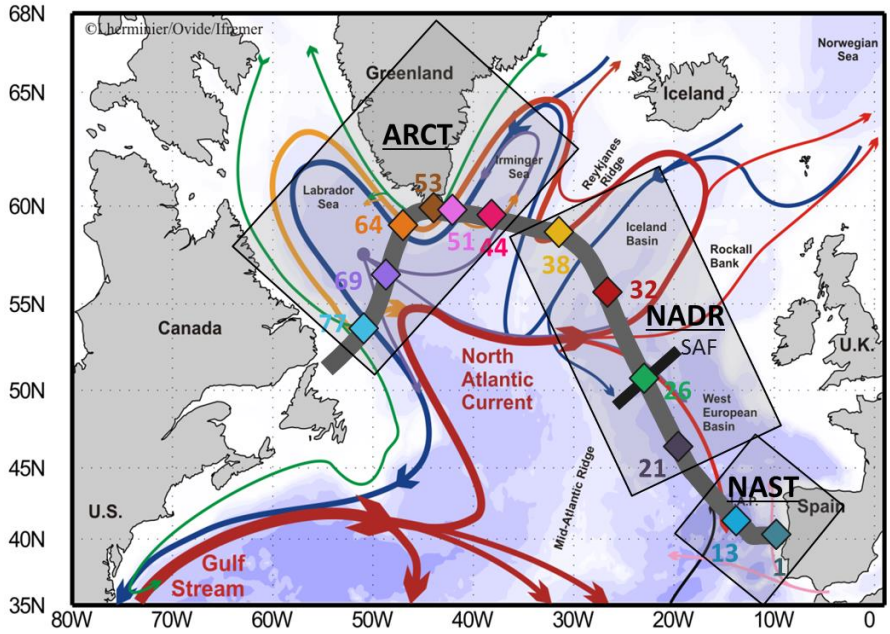

b)

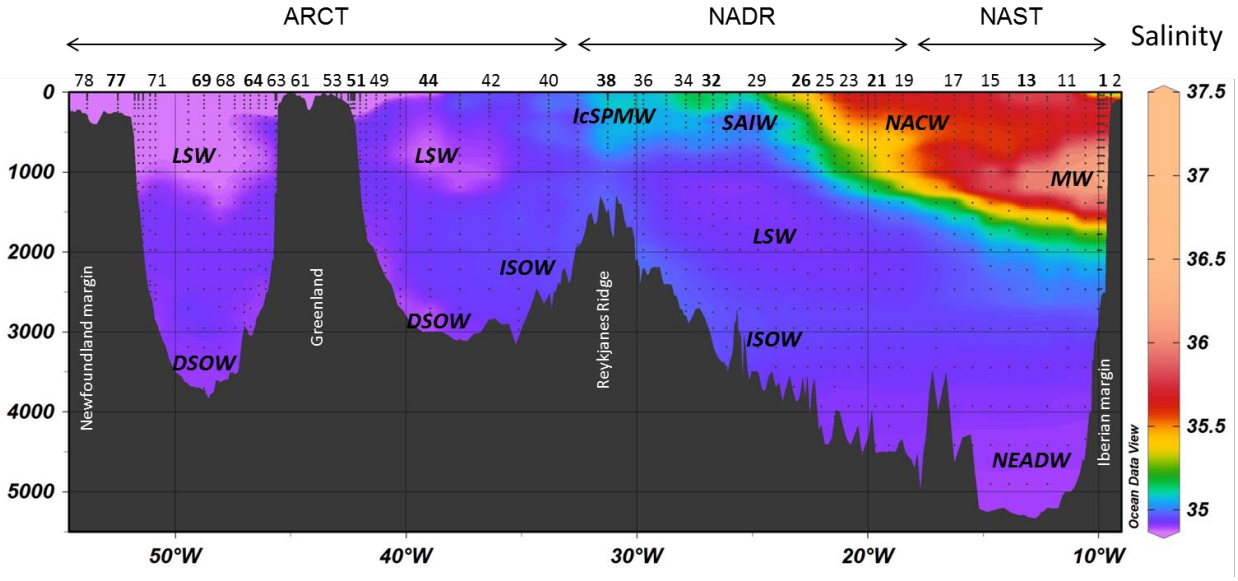

Figure 4.2: a) Schematic of the circulation features, adapted from Garcia-Ibanez et al., 2015. b) Salinity along the GEOVIDE section, and associated water masses: LSW: Labrador Seawater; ISOW: Iceland Scotland Overflow Water; IcSPMW: Iceland Subpolar Mode Water; SAIW: Sub Arctic Intermediate Water; NACW: North Atlantic Central Waters; MW: Mediterranean Water; DSOW: Danmark Strait Water; NEADW: North East Atlantic Deep Water. Stations in bold correspond to stations where detailed vertical Niskin profiles were collected.

4.2.2. Sampling and analyses

In this study, we present two datasets of Ba_{xs} concentrations:

1) Ba_{xs} concentrations deduced from samples collected using a standard CTD rosette equipped with 12L Niskin bottles. At most stations, 18 depths were sampled between surface and 1500 m in order to obtain a high depth resolution of the Ba_{xs} signal at stations where primary production and POC export fluxes were also determined (Table S4.1).

Four to eight liters of seawater were filtered on acid-cleaned polycarbonate membranes of 0.4 µm porosity (Nuclepore®, 47 or 90 mm diameter). Filter membranes were rinsed with Milli-Q water (18.2 MΩ·cm; ≤ 5 mL) to remove sea-salt, dried at ambient temperature under a laminar flow hood and finally stored in clean petri slides until analysis.

Back in the home-based laboratory, filters were totally digested with a concentrated tri-acid mixture (1.5 mL HCl – 1 mL HNO_3 – 0.5 mL HF; all Merck suprapur grades) in cleaned Teflon vials (Savillex®) on a hot plate at 90°C, overnight. Then, the acid solution was evaporated at 110°C until near dryness, and the residue was dissolved in 13 mL 0.32M HNO_3 (Merck; distilled Normapur). The solutions, in polypropylene tubes (VWR), were analyzed for Ba, Al and other major and minor elements using an inductively coupled plasma-quadrupole mass spectrometer (ICP-QMS; X Series 2 Thermo Fisher) equipped with a collision cell technology (CCT). We used a concentric quartz nebulizer (1 $mL.min^{-1}$) and nickel sample and skimmer cones. During the analyses, internal standards (Ru, In, Re and Bi) were added to samples in order to monitor and correct the instrumental drift and matrix-dependent sensitivity variations. Two multi-element artificial standard solutions were prepared for external calibration. The first contained major elements (Na, Mg, Al, Ca and Ti) and the second was prepared with minor elements (Sr, Ba, REEs, Th and U). Standards were prepared by dilution of the multi-element mixed standard stock solutions to span the expected range of sample concentrations, with concentrations in the standard curve spaced to cover potential sample variations.

The accuracy and precision of our analyses were assessed using the following Certified Reference Materials (CRM): BHVO-1, JB-3, JGb-1 and SLRS-5 (Table 4.1).

	Ba	Al
SLRS-5 (µg.kg^{-1})	13 ± 1	47 ± 2
n=4	***95%***	***95%***
BHVO-1 (µg.g^{-1})	129 ± 1	70118 ± 984
n=4	***93%***	***96%***
JB-3 (µg.g^{-1})	229 ± 13	92144 ± 1620
n=4	***94%***	***101%***
JGb-1 (µg.g^{-1})	68 ± 15	91491 ± 732
n=4	***106%***	***99%***

Table 4.1: Particulate barium (Ba) and aluminum (Al) concentrations and resulting recoveries (the bold and italic percentages) of the certified reference materials SLRS-5 (river water), BHVO-1 (basalt powder), JB-3 (basalt powder) and JGb-1 (gabbro powder).

The detailed procedure for sample preparation and analysis is given in Cardinal et al. (2001).

2) Ba_{xs} concentrations deduced from samples collected using the clean rosette, equipped with twenty-two 12L Go-Flo bottles at higher spatial resolution but with a lower vertical resolution in the mesopelagic zone. Indeed, the entire water column was sampled at 31 stations along the GEOVIDE transect. Details regarding filtration, sample processing and analyses can be found in Gourain et al. (in prep). Briefly, at each depth, two size fractions were investigated: 0.45-5 µm using polysulfone filters (Supor ®) and > 5 µm using mixed ester cellulose filters (MF, Millipore ®). Between 2 and 5L of seawater were filtered in surface and 10L below 100m. Back in the home-based laboratory, filters were digested with a solution 8M HNO_3 (Ultrapur grade, Merck) and 2.3M HF (Suprapur grade, Merck). Vials were then refluxed at 130°C on a hotplate during 4h. After a gentle evaporation, the residue was brought back into solution with 3% HNO_3 spiked with 1 µg.L^{-1} of Indium. Solutions, in acid cleaned 15 mL centrifuge tubes (Corning), were analyzed sing a SF-ICP-MS (Element 2, Thermo) following the method of Planquette and Sherrell (2012). Total Ba concentrations were deduced by adding the two size fractions, in order to compare both datasets.

For both datasets, the Ba_{xs} concentrations were calculated by subtracting the particulate lithogenic barium (pBa-litho) from the total particulate barium (pBa). The lithogenic fraction of

pBa was determined by multiplying the particulate aluminum (pAl) concentration by the upper continental crust (UCC) molar Ba:Al ratio (0.00135 $mol.mol^{-1}$; Taylor and Mclennan, 1985). Along GEOVIDE, pBa-litho represented less than 7% of the total barium, except at Stations 1 and 53 where pBa-litho accounted for 28 and 44%, respectively. Because of the rather large uncertainty associated with the UCC Ba:Al ratio and because of the strong lithogenic particle loads there, Stations 1 and 53 were not considered further in this study. Uncertainties on Ba_{xs} were estimated using error propagation and represented from 6 to 25% of the Ba_{xs} concentrations.

At stations where total pBa and pAl concentrations were available at a similar depth, the comparison between the Ba_{xs} concentrations obtained by two sampling and analytical methods was excellent (Figure 3, regression slope: 0.94; r^2: 64%; $p<0.01$; $n=85$).

In addition, analyses of filtered suspended matter were carried out using a Field Emission Scanning Electron Microscope (FE-SEM; JEOL JSM-7100F) in order to verify the relationship between Ba_{xs} and barite ($BaSO_4$) particles (see section 4.3.1). For seven samples, we analyzed a filter surface of 0.5 cm^2: 6 samples with high mesopelagic Ba_{xs} concentrations (Station 13 at 400 m; Station 38 at 300 m; Station 44 at 300 and 700 m; Station 69 at 600 m and Station 77 at 300 m) and one sample with high surface Ba_{xs} concentrations (Station 26, 50 m).

4.2.3. Determination of C remineralization fluxes

The mesopelagic carbon remineralization was estimated using Equation 1, which relates the accumulated mesopelagic Ba_{xs} inventories to the rate of oxygen consumption (Shopova et al., 1995; Dehairs et al., 1997):

$$JO_2 = (\text{mesopelagic } Ba_{xs} - Ba_{\text{residual}}) / 17200 \quad \text{(Equation 4.1)}$$

where JO_2 is the rate of oxygen consumption ($\mu mol.L^{-1}.d^{-1}$), *mesopelagic* Ba_{xs} is the depth-weighted average in the mesopelagic layer (DWA; $pmol.L^{-1}$), $Ba_{residual}$ is the deep ocean Ba_{xs} value observed at zero oxygen consumption (or Ba_{xs} background signal) which was determined to reach 180 $pmol.L^{-1}$ (Dehairs et al., 1997). Then, the oxygen consumption JO_2 can be converted into C remineralized by the following relationship:

$$\text{POC mesopelagic remineralization} = Z \times JO_2 \times (C{:}O_2)_{\text{Redfield Ratio}} \quad \text{(Equation 4.2)}$$

where the POC mesopelagic remineralization is in $mmol\ C.m^{-2}.d^{-1}$, Z is the thickness of the depth layer in which mesopelagic Ba_{xs} is calculated, JO_2 is given by the Equation 4.1 and $(C{:}O_2)_{Redfield\ Ratio}$ is the stoichiometric molar C to O_2 ratio (127/175).

4.3. Results

4.3.1. Barite is the main carrier of Ba_{xs}

Several barite particles were observed at proximity to biogenic fragments (Figure 4.3) suggesting the important role of the biogenic microenvironments in barite formation (Bishop, 1988; Dehairs et al., 1980; Stroobants et al., 1991). However, no barite crystals were observed in surface waters of Station 26 indicating different processes generating high Ba_{xs} concentrations between surface and mesopelagic samples. Indeed, the very high Ba_{xs} concentration in surface waters of Station 26 was not related to barite particles but more likely to Ba adsorption by biota, as reported for Sternberg et al. (2005) in culture experiments. This result fits in the concept of barite formation proposed by Stroobants et al. (1991). The authors show that the barium sulfate in biogenic aggregates of surface waters is not crystallized

whereas below this surface layer, when degradation occurs, the barite particles in aggregates are denser and acquire the typical crystal morphology.

We evaluated the contribution of the barite particles to Ba_{xs} for the sample collected at 600 m of Station 69 (we analyzed 0.003% of the total filter surface) which was selected because of its high mesopelagic Ba_{xs} content (Figure 4.5). Using the Field Emission Scanning Electron Microscope (FE-SEM), we detected all the barite particles present in this surface area and determined their volume. To this aim, each barite particle was pictured using a magnification setting between 12000 and 15000×. Images were then analyzed with the software ImageJ and, for each barite particle, the longest and shortest lengths were measured and converted from pixel to nanometers. Barite particles were then assimilated to ellipses to deduce their volume. Finally, the concentration of pBa in barite particles was calculated using the following equation:

$$\text{pBa in barite} = \Sigma \left[V \times \mu_{BaSO4} \times (M_{Ba} / M_{BaSO4}) \right] / V_{SW} \quad \text{(Equation 4.3)}$$

where V is the volume of each $BaSO_4$ particle (between 0.01 and 3.96 μm^3), μ_{BaSO4} is the density of barite (4.45 $g.cm^{-3}$), M_{Ba} / M_{BaSO4} is the molar proportion of barium in $BaSO_4$ (0.59) and V_{SW} is the volume of filtered seawater (equivalent to 0.2 mL through this portion of filter). Assuming that this filter piece is representative of the whole filter, the concentration deduced from the SEM reached 1260 $pmol.L^{-1}$. This is in the same order of magnitude that the concentration of total Ba_{xs} analyzed by ICP-MS (831 $pmol.L^{-1}$) on the whole filter of this sample. The similarity between both estimations is remarkable considering the limitations of the SEM procedure (i.e. the very small fraction of filtered seawater searched for barite). This also confirms that Ba_{xs} is carried by barite particles in the mesopelagic layer, as observed earlier (Dehairs et al., 1980).

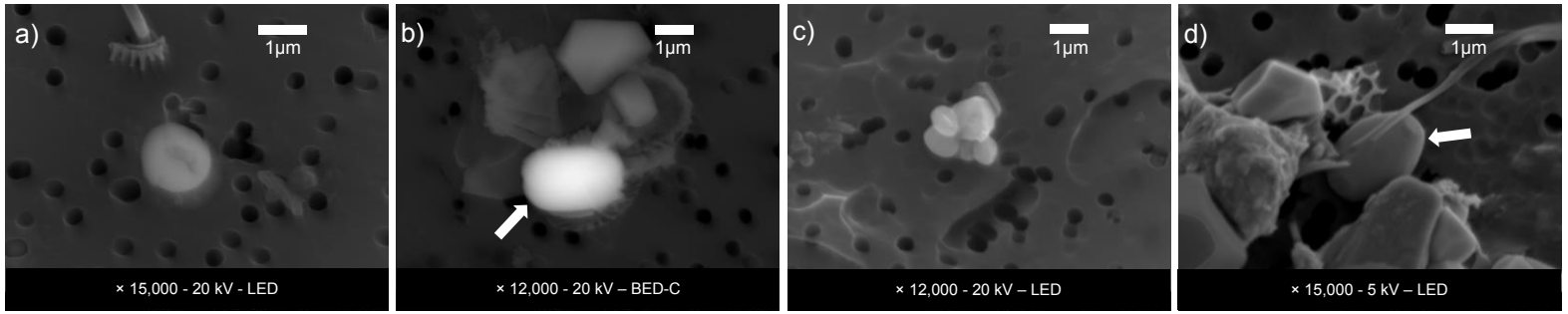

Figure 4.3: Barite particles observed by FE-SEM at a) Station 38 (300 m); b) Station 44 (700 m); c and d) Station 69 (600 m). The white arrows indicate the position of barite crystals.

4.3.2. Particulate biogenic Ba_{xs} profiles

4.3.2.1. Section overview

The high resolution section of Ba_{xs} concentrations (Figure 4.4) shows elevated concentrations in the mesopelagic zone across the section (Ba_{xs} (z between 100 and 1000 m) = 333±224 pmol.L^{-1}; median ± 1s.d.; n=209). In comparison, the surface ocean (z < 100 m) and the deep ocean (z > 1000 m) are characterized by lower median values (94 and 114 pmol.L^{-1}, n=113 and 199, respectively). Exceptions can be observed in the upper waters at Station 26 and close to the seafloor at Stations 29, 32, 36, 38 and 71 and may be attributed to Ba adsorption by phytoplankton (Station 26), and sediment resuspension (Stations 29, 32, 36, 38, 71; Gourain et al., in prep.). Concentrations ranged from 4 (Station 11, 55 m) to 24643 (Station 26, 35 m) pmol.L^{-1} in surface waters and from 7 (Station 71, 350 m) to 1388 (Station 15, 300 m) pmol.L^{-1} in the mesopelagic layer (100-1000 m) where the maximum concentrations were generally observed. In the mesopelagic layer, the highest Ba_{xs} concentration was determined in the NAST province, reaching 1388 pmol.L^{-1} at 300 m of Station 15. However, these important maxima are very local (in a layer of 100-300 m) while they are spread over larger depth intervals at other stations, in particular in the ARCT province (layer of the Ba_{xs} maxima: 1200 m at Station 69).

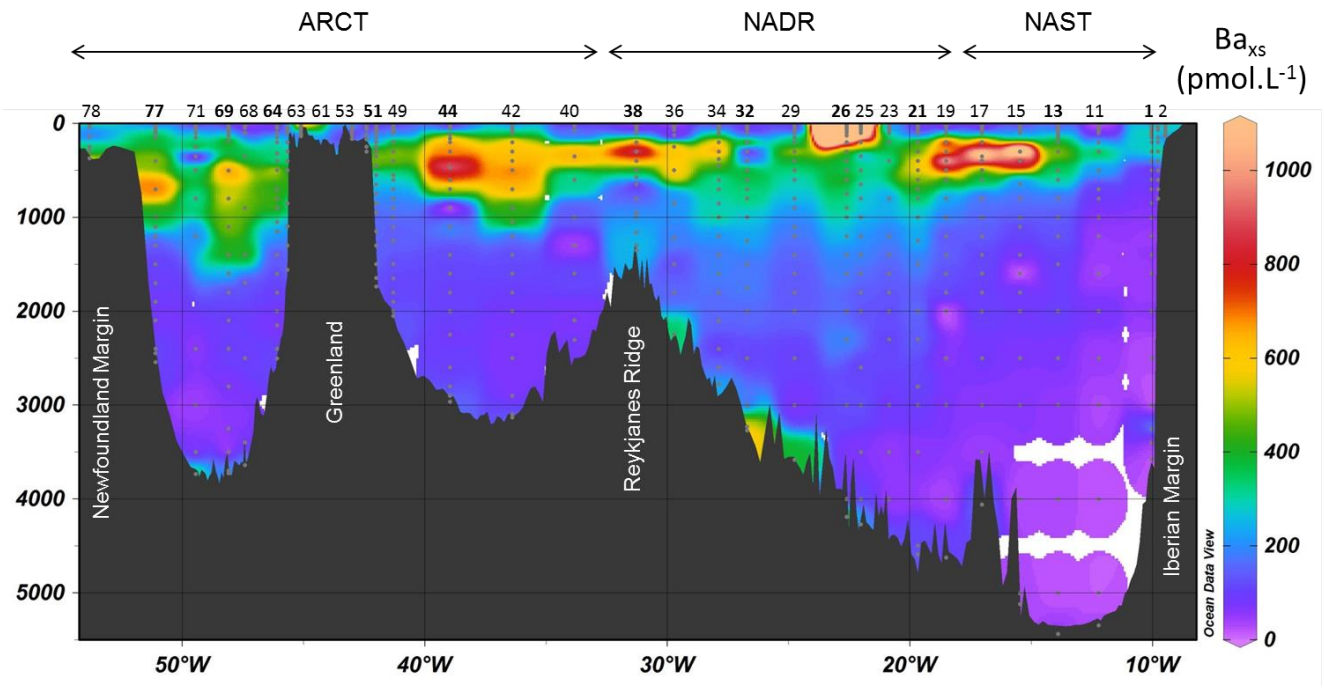

Figure 4.4: Section of the particulate biogenic barium (Baxs) in pmol.L^{-1} determined in samples collected with the Go-Flo bottles. Niskin detailed vertical profiles were determined at stations in bold.

4.3.2.2. Individual Profiles

In the following section, only the Ba_{xs} concentrations determined using Niskin bottles are described because of 1) the good comparison between both Niskin and Go-Flo dataset (regression slope: 0.94; r^2: 64%; $p<0.01$; n=85), 2) the better resolution in the 100-1000 m layer for Niskin bottles, and 3) the same cast between Niskin data and 234-Thorium data used for the determination of POC export. A comparison between primary production, POC export and POC remineralization is addressed in section IV.3.

The vertical profiles of Ba_{xs} concentrations at all stations are shown in Figure 4.5.

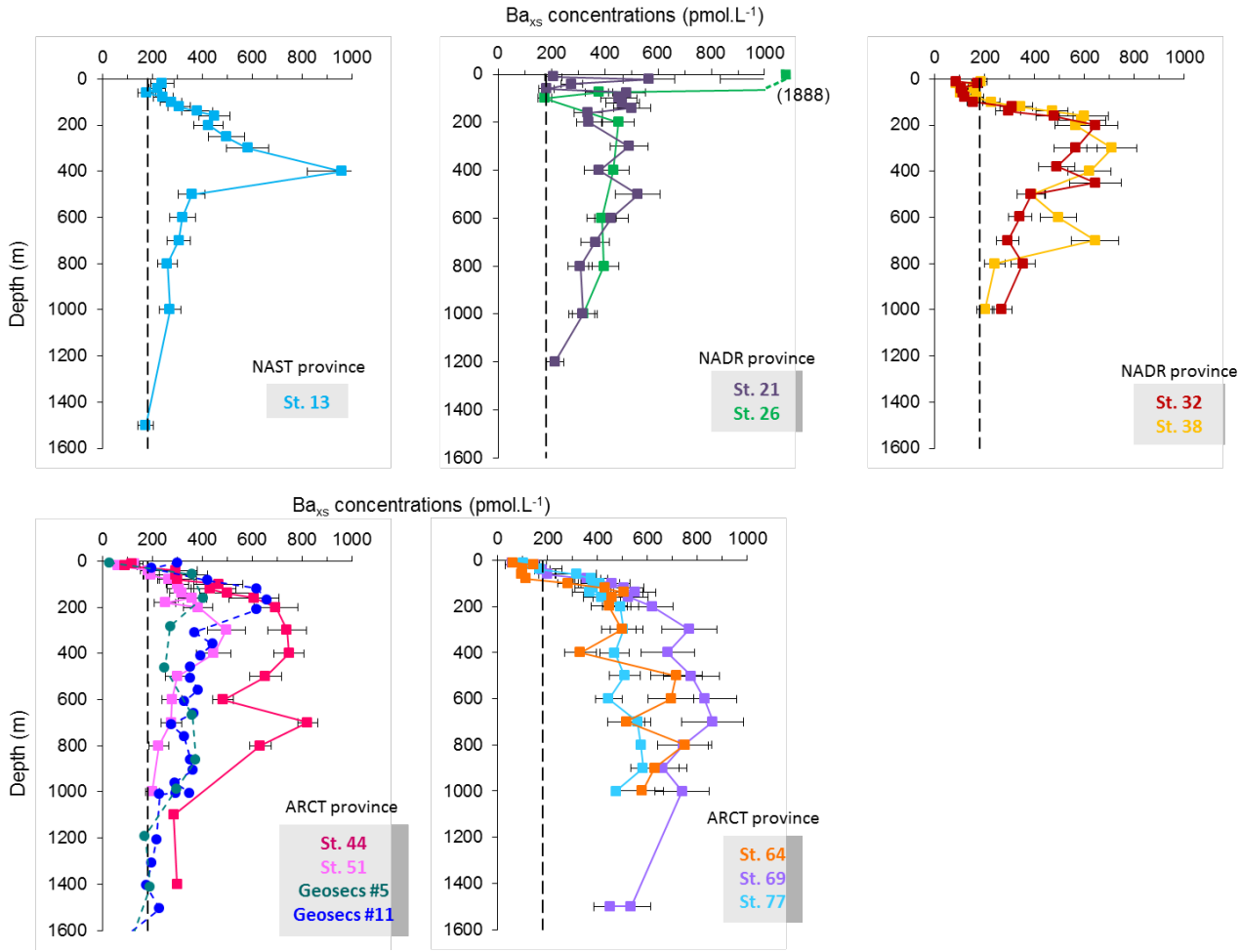

Figure 4.5: Individual profiles of Baxs concentrations (in pmol.L^{-1}) determined using Niskin bottles from GEOVIDE (squares) and GEOSECS (circles) cruises.

In the NAST province (Station 13), the Ba_{xs} concentrations steadily increased from the surface to 400 m, reaching 961 pmol.L^{-1} then decreased with depth, reaching the background level of 180 pmol.L^{-1} at 1500 m.

In the western European basin of the NADR province, vertical profiles of Ba_{xs} were similar at Station 21, yet concentrations in the mesopelagic layer were smaller, as the Ba_{xs} peaked only to 524 pmol.L^{-1}. Ba_{xs} concentrations returned to the background value at 1200 m. Ba_{xs} concentration in surface waters of Station 26 were the highest of the entire section, since surface Ba_{xs} reached 1888 pmol.L^{-1} at 50 m. Below this depth, Ba_{xs} concentrations decreased back to the background level at 100 m depth, then increased again, with a second peak of 451 pmol.L^{-1} measured at 200 m. In the Icelandic basin of the NADR province, Ba_{xs} concentrations

were relatively high, reaching 646 and 711 pmol.L^{-1} at 200 m of Station 32 and 300 m of Station 38, respectively. These stations were also characterized by Ba_{xs} profiles displaying a double peak at 200 and 450 m for Station 32, and at 300 and 700 m for Station 38. Below this second maximum, Ba_{xs} concentrations decreased to the background level at 1000 m for both stations. In the ARCT province, a similar double peak profile was observed at Station 44, in the Irminger Sea basin, with Ba_{xs} concentrations reaching 747 pmol.L^{-1} at 400 m and 823 pmol.L^{-1} at 700 m. Then, Ba_{xs} concentrations returned to the background value at 1100 m. Close to the Greenland Margin (Station 51), Ba_{xs} concentrations were lower than at other stations reaching 495 pmol.L^{-1} at 300 m, before to decrease until the background level at 1000 m.

The Ba_{xs} concentrations of Stations 44 and 51 were compared to those obtained at Station 11 (63.5°N – 324.8°E) and Station 5 (56.9°N – 317.2°E) of the GEOSECS cruise, in summer 1970 (Brewer et al., unpublished results). The Ba_{xs} concentrations obtained at GEOSECS Station 11 are in similar range as concentrations we measured at the GEOVIDE Station 44 (173-658 pmol.L^{-1} and 116-823 pmol.L^{-1}, respectively). Similar ranges were also observed between the GEOSECS Stations 5 and the GEOVIDE Station 51 (170-402 pmol.L^{-1} and 127-359 pmol.L^{-1}, respectively; Figure 4.5).

In the Labrador Sea basin (Stations 64, 69 and 77), high Ba_{xs} concentrations (> 450 pmol.L^{-1} and up to 863 pmol.L^{-1} at Station 69) were measured at greater depths than for other stations and Ba_{xs} concentrations did not return to the background level at 1000-1500 m as observed elsewhere in the section. Samples dedicated to trace metals (GO-FLO sampling) indicated that Ba_{xs} concentrations decreased to the background level (180 pmol.L^{-1}) at 1300, 1700 and 1200 m for Stations 64, 69 and 77, respectively.

4.3.3. Mesopelagic Ba_{xs} and bacterial abundance

The Ba_{xs} concentrations were integrated (trapezoidal integration) over two depth intervals of the mesopelagic zone (100-500 m and 100-1000 m; Table 4.2) to obtain a depth-weighted average (DWA) value. The DWA Ba_{xs} values between 100 and 500 m ranged from 399 to 672 pmol.L^{-1} and from 315 to 727 pmol.L^{-1} between 100 and 1000 m (Stations 51 and 69,

respectively). For both depth intervals, DWA Ba_{xs} values varied by less than a factor of 1.4 being larger for the 100-1000 m interval in the Labrador Sea basin (Stations 64, 69 and 77). The lowest median DWA Ba_{xs} was observed in the NADR province (403 ± 34 pmol.L^{-1} between 100 and 1000 m, n=4) while the highest median DWA Ba_{xs} was observed in the ARCT province (566 ± 155 pmol.L^{-1} between 100 and 1000 m, n=5).

Here, we take the opportunity to compare the upper mesopelagic (100-500 m) Ba_{xs} concentrations with the total bacterial abundance acquired by flow cytometry (Figure 4.6; J. Laroche, J. Ratten and R. Barkhouse, personal communication).

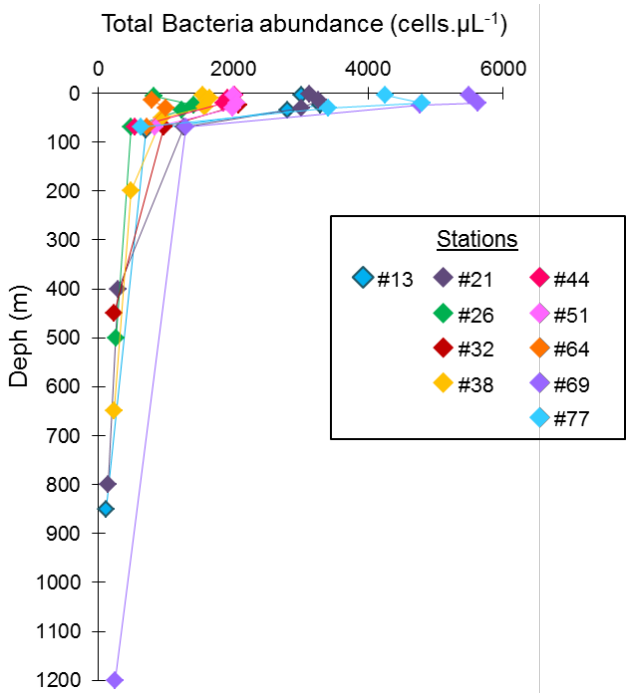

Figure 4.6: Total bacterial abundance (cells.µL^{-1}) measured by flow cytometry (J. Laroche, J. Ratten and R. Barkhouse, personal communication).

We compare both integrated values for the 100-500 m depth layer because of the better spatial resolution. Since the bacterial abundance was limited to the upper 100 m for Stations 44, 51, 64 and 77, these stations were not considered here. In Figure 4.7, the other stations are compared and the 100-500 m DWA Ba_{xs} appears to be correlated (r^2=0.48, n=6, p=0.13) with the 100-500 m integrated total bacterial abundance. This correlation between the DWA Ba_{xs}

values and the bacterial abundance agrees with the relationship between mesopelagic Ba_{xs} content and organic matter remineralization (Dehairs et al., 1980; Jacquet et al., 2008; 2015).

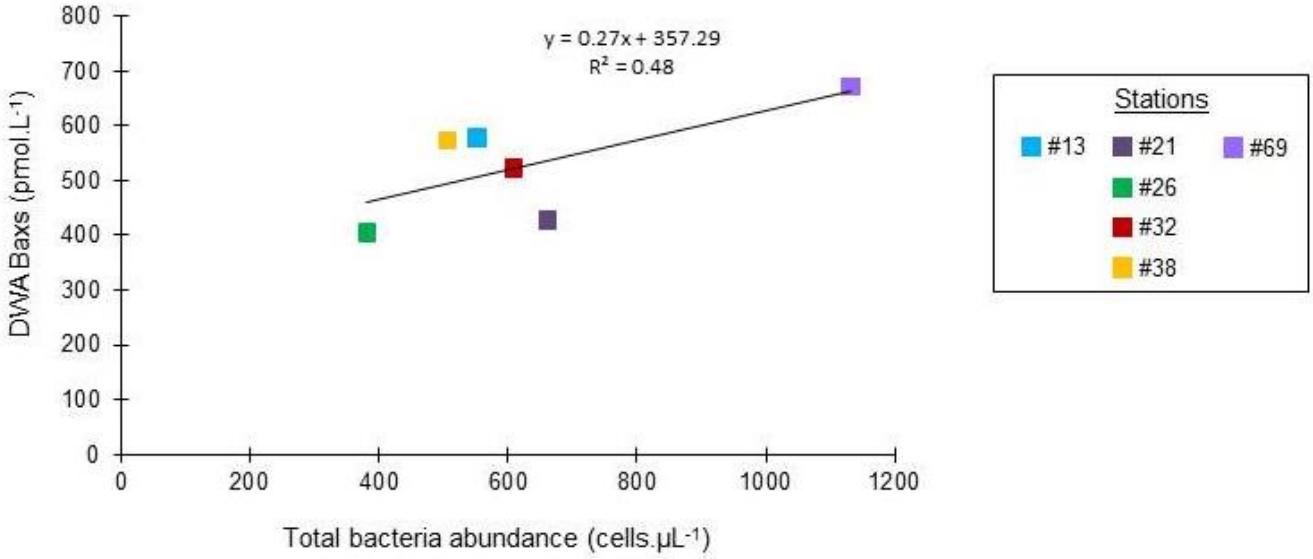

Figure 4.7: Regression of the 100-500 m integrated total bacterial abundance (cells.µL^{-1}) versus the 100-500 m DWA Baxs values (pmol.L^{-1}).

Province	Station	Latitude °N	Longitude °E	Time since bloom peak (weeks)	DWA Ba_{xs} 100-500m ($pmol.L^{-1}$)	DWA Ba_{xs} 100-1000m ($pmol.L^{-1}$)	MR 100-500m ($mmol.m^{-2}.d^{-1}$)	MR 100-1000m ($mmol.m^{-2}.d^{-1}$)
NAST	13	41.4	-13.9	8	578 ± 89	419 ± 71	6.7 ± 1.5	9.1 ± 2.7
NADR	21	46.5	-19.7	4	428 ± 69	394 ± 64	4.2 ± 1.2	8.1 ± 2.4
	26	50.3	-22.6	0.5	405 ± 59	391 ± 58	3.8 ± 1.0	8.0 ± 2.2
	32	55.5	-26.7	0	522 ± 81	413 ± 66	5.8 ± 1.4	8.9 ± 2.5
	38	58.8	-31.3	0	572 ± 86	465 ± 78	6.6 ± 1.5	11 ± 2.9
ARCT	44	59.6	-38.9	1	678 ± 104	633 ± 98	8.4 ± 1.8	17 ± 3.7
	51	59.8	-42.0	5	399 ± 72	315 ± 58	3.7 ± 1.2	5.1 ± 2.2
	64	59.1	-46.1	3	464 ± 95	566 ± 99	4.8 ± 1.6	15 ± 3.8
	69	55.8	-48.1	7	672 ± 111	727 ± 118	8.3 ± 1.9	21 ± 4.5
	77	53.0	-51.1	4	472 ± 80	505 ± 83	4.9 ± 1.4	12 ± 3.2

Table 4.2: Depth-weighted average (DWA) values of mesopelagic Baxs ($pmol.L^{-1}$) and resulting Baxs-based mesopelagic POC remineralization rates ($mmol\ C.m^{-2}.d^{-1}$) integrated between 100-500 m and 100-1000 m depths. The biogeochemical provinces defined by Longhurst et al. (1995) are also indicated: NAST: North Atlantic subtropical gyre; NADR: North Atlantic drift; ARCT: Atlantic Arctic.

4.3.4. Carbon remineralization fluxes

Despite the different depths to reach the background signal, we decided to integrate the carbon remineralization fluxes down to 1000 m in order to compare all stations. In few cases, such as the stations in the Labrador Sea basin where the background level is not reached at 1000 m, we estimated the mesopelagic carbon remineralization flux below 1000 m. However, this modification did not change significantly the magnitude of the remineralization fluxes. Indeed, the fluxed integrated over the 100-1300 m (Station 64), 100-1700 m (Station 69) and 100-1200 m (Station 77) were respectively only 1.5 folds lower, similar and 1.2 folds higher than the fluxes integrated over the 100-1000 m. At all stations, the mesopelagic remineralization fluxes integrated over 100-1000 m were greater than the fluxes integrated over 100-500 m. We thus considered the 100-1000 m depth interval as the interval representing the best the whole mesopelagic layer (Table 4.2, Figure 4.8).

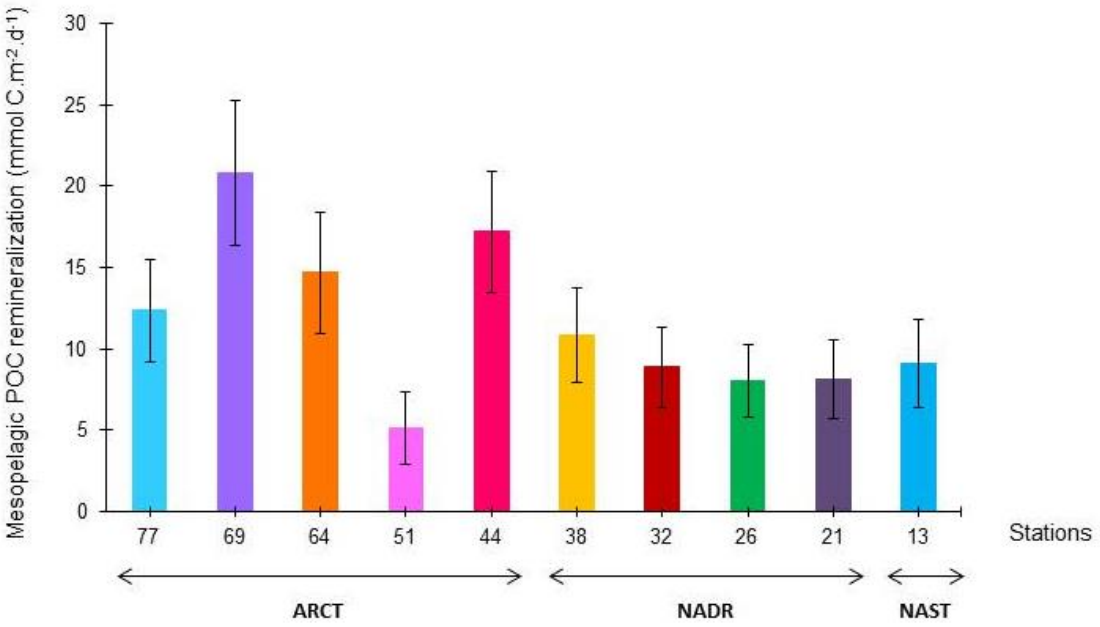

Figure 4.8: Carbon mesopelagic remineralization fluxes (in mmol $C.m^{-2}.d^{-1}$) at all stations sampled with Niskin bottles, between 100 - 1000 m. Provinces are indicated below the x-axis.

Similarly to DWA Ba_{xs} values, the lowest median mesopelagic remineralization flux was determined in the NADR province (8.5 ± 1.3 $mmol.m^{-2}.d^{-1}$, n=4) while the highest median was estimated in the ARCT province (14.7 ± 5.9 $mmol.m^{-2}.d^{-1}$, n=5). Station 13, in the NAST

province, was characterized by a similar mesopelagic remineralization flux than those of the NADR province, i.e. 9.1 mmol.m^{-2}.d^{-1}. In the ARCT province, mesopelagic remineralization fluxes were variable, ranging from 5.1 mmol.m^{-2}.d^{-1} at Station 51 to 21 mmol.m^{-2}.d^{-1} at Station 69 with a high mesopelagic remineralization flux of 17 mmol.m^{-2}.d^{-1} at Station 44.

These fluxes were compared to carbon mesopelagic remineralization fluxes determined with the Ba_{xs} method in the world's ocean (Table 4.3). Fluxes obtained during GEOVIDE were higher than other fluxes deduced by the Ba_{xs} proxy in the Southern and Pacific Oceans, highlighting an important remineralization in the North Atlantic compared to other oceans.

Cruise (season)	Location	Features	depth interval m	DWA Ba_{xs} $pmol.L^{-1}$	MR fluxes $mmol.m^{-2}.d^{-1}$	Reference
VERTIGO (summer)	Pacific Ocean	oligotrophic (Aloha) mesotrophic (K2)	150 - 500	157 - 205 367 - 713	1.0 - 3.0 2.7 - 8.8	Dehairs et al., 2008
CLIVAR SR3 - SAZ98 (spring/summer)	Southern Ocean	spring summer	150 - 400	235 - 554 296 - 353	0.3 - 3.0 0.2 - 3.4	Cardinal et al., 2005
EIFEX (summer)	Southern Ocean	Fe-fertilized (in patch) HNLC (out patch)	150 - 1000	273 - 415 233 - 423	2.6 - 7.7 1.2 - 8.0	Jacquet et al., 2008
KEOPS (summer)	Southern Ocean	Fe-fertilized (A3) HNLC (C11)	125 - 450	342 - 401 309 - 493	2.1 - 2.8 1.7 - 4.0	Jacquet et al., 2008
KEOPS 2 (spring)	Southern Ocean	Fe-fertilized (A3) HNLC (R2)	150 - 400	267 - 314 572	0.9 - 1.2 4.2	Jacquet et al., 2015
SAZ-SENSE (summer)	Southern Ocean	Fe-fertilized (SAZ east) HNLC (SAZ west)	100 - 600	244 - 395 199 - 249	3.0 - 6.1 2.1 - 3.1	Jacquet et al., 2011
Bonus GoodHope (summer)	Southern Ocean	North of PF South of PF	125 - 600	284 - 497 235 - 277	2.1 -6.4 1.1 - 1.9	Planchon et al., 2013
GEOSECS II (summer)	North Atlantic	NAST+NADR ARCT	100 - 1000	199 - 361 242 - 413	0.7 - 6.9 2.3 - 8.8	Brewer (unpublished values)
GEOVIDE (spring)	**North Atlantic**	**NAST+NADR** **ARCT**	**100 - 1000**	**272 - 465** **315 - 727**	**8.0 - 11** **5.1 - 21**	**this study**

Table 4.3: Comparison of the Baxs inventory ($pmol.L^{-1}$) and related-carbon mesopelagic remineralization fluxes ($mmol.m^{-2}.d^{-1}$) obtained in the world's ocean.

4.4. Discussion

4.4.1. Validation of the Ba_{xs} approach

4.4.1.1. Remineralization deduced from the Oxygen Utilization Rate (OUR)

Carbon remineralization fluxes were also estimated using the oxygen utilization rate (OUR) method, as used by Sonnerup et al. (2014) in the Pacific Ocean. The OUR ($\mu mol.kg^{-1}.yr^{-1}$) is determined by dividing apparent oxygen utilization (AOU, in $\mu mol.kg^{-1}$) by the water mass age. The OUR is then integrated over the layer associated with the water mass and converted into a remineralized carbon flux. In the North Atlantic, the mean age of the Labrador Seawater (LSW) has been estimated by Rhein et al. (2015) based on 25 years CFC contents. Since, we focus only on the upper 1500 m, we can only use data for the ARCT province (Stations 44, 51, 64, 69 and 77). For the areas corresponding to Stations 44, 51 and to Stations 64, 69, 77, Rhein et al. (2015) estimated a mean age of 6 and 4 years, respectively. Using these mean ages, the mesopelagic remineralization fluxes obtained with the OUR method were lower but in the same order of magnitude than those obtained with the Ba_{xs} method, with fluxes varying by a factor of 1.3 at Stations 44 and 69, 3.6 at Stations 51 and 77 and 14 at Station 64. The differences could result from an under-estimation of the respiration from the OUR method (Koeve and Kähler, 2016), or could be also due to the difficulty of estimating the age of the LSW. Indeed, the strong winter before the cruise (2013/2014) appeared to have strongly ventilated the LSW with a mixed layer depth exceeding 1700 m (Kieke and Yashayaev, 2015), indicating that the mean age estimated by Rhein et al. (2015) may have over-estimated the real LSW age (Lherminier et al., personal communication), leading to an under-estimation of the OUR. Moreover, in the Labrador Sea, the residence time of the LSW strongly varies between the central Labrador Sea (4-5 years) and the boundary currents off the Greenland and Newfoundland coasts (a few months; Deshayes et al., 2007; Straneo et al., 2003). This difference could explain the discordance between the OUR and Ba_{xs} methods, especially at Station 64, where the best correlation is obtained for an age of 4 months.

The overall good correlations between the two independent methods confirm the use of the Ba_{xs} proxy and our estimation of remineralization fluxes in the North Atlantic.

4.4.1.2. Remineralization deduced from direct measurements

In the North Atlantic, carbon respiration rates were also deduced by surface drifting sediment traps and associated-shipboard incubations. Collins et al. (2015) determined very high respiration rates reaching 39 and 72 mmol $C.m^{-2}.d^{-1}$ at sites located in the NADR and in the ARCT provinces, respectively. Nevertheless, these high fluxes were deduced in the upper mesopelagic zone (50-150 m) where respiration is greater compared to the lower mesopelagic zone (150-1000 m). This different depth interval could thus explain the greater integrated respiration rates determined in this study. Using a similar method supplemented by measurements of zooplankton respiration, Giering et al. (2014) determined respiration rates in the NADR province (PAP site) reaching 7.1 mmol $C.m^{-2}.d^{-1}$ during summer. This flux, determined over the 50-1000 m depth interval, is in the same order of magnitude than our estimates in the western European basin (Stations 21 or 26).

4.4.1.3. Remineralization from the deep sediment traps: Re-evaluating the integration time of the Ba_{xs} proxy approach

The remineralization flux in the mesopelagic layer can also be derived from the difference between a deep POC export flux and a surface POC export flux. Honjo et al. (2008) compiled deep POC export fluxes from moored and time-series sediment traps and calculated the corresponding export production (upper-ocean POC export flux) using an ecosystem model (Laws et al., 2000) for most world provinces. Then, by difference, the authors estimated an annual average of carbon remineralization fluxes in the mesopelagic layer, reaching after conversion into daily average fluxes of 34 mmol $C.m^{-2}.d^{-1}$ in the ARCT province, 9 mmol $C.m^{-2}.d^{-1}$ in the NADR province and 4 mmol $C.m^{-2}.d^{-1}$ in the NAST province. Noteworthy, the flux in the ARCT province was the highest mesopelagic remineralization flux estimated worldwide (with the region around Cape Verde), confirming the important remineralization in the North Atlantic compared to other oceans. The values published by Honjo et al. (2008) for the North Atlantic, are comparable to the median values obtained during GEOVIDE in each province.

Indeed, mesopelagic remineralization fluxes based on the Ba_{xs} proxy were 2.4 folds larger than the estimate deduced by Honjo et al. (2008) in the NAST province and 1.1 and 2.3 folds lower in the NADR and in the ARCT provinces.

Overall, the good comparison of our dataset with remineralization fluxes determined by other methods confirms the order of magnitude of the mesopelagic remineralization fluxes determined in this study of the North Atlantic and validates the Ba_{xs} proxy to estimate mesopelagic remineralization fluxes (Figure 4.9). Interestingly, the comparison with deep sediment traps highlights that the remineralization activity from the Ba_{xs} proxy may integrate over one complete season rather than several weeks as suggested in previous studies (Dehairs et al., 1997; Cardinal et al., 2005; Jacquet et al., 2015).

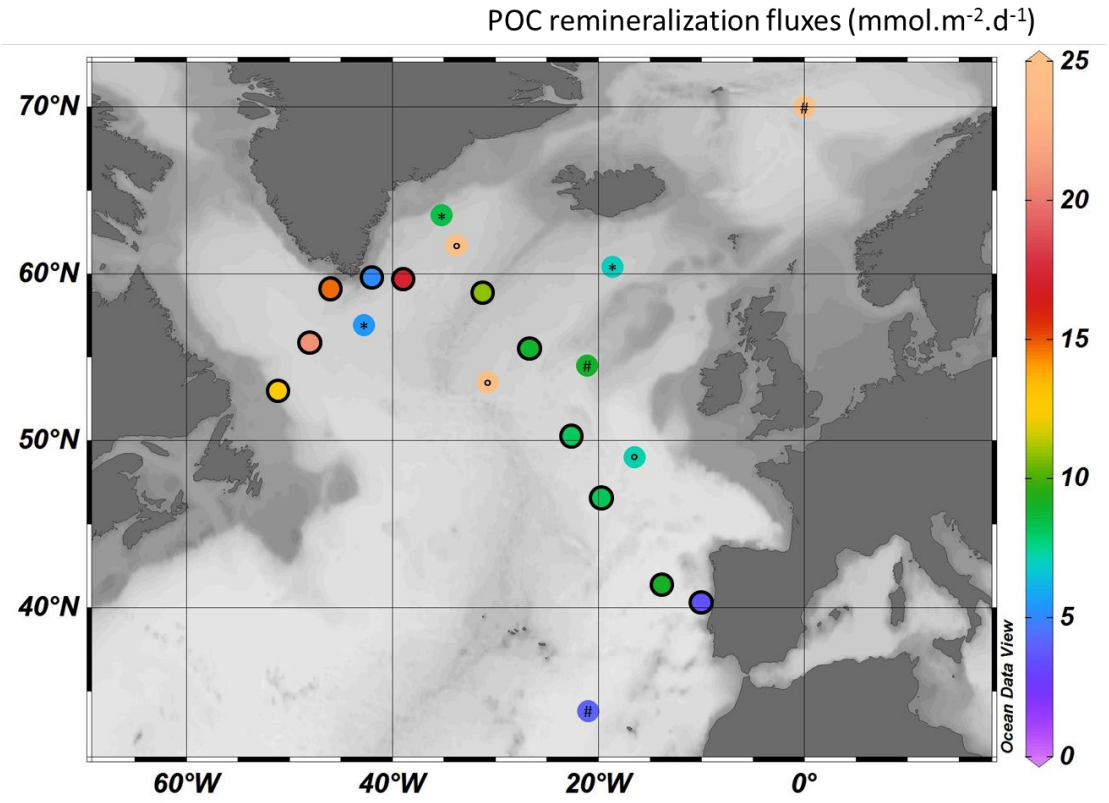

Figure 4.9: Comparison of POC remineralization fluxes from this study (circles lined in black) to remineralization fluxes from literature in the North Atlantic. Note that these studies used different methods for determining remineralization fluxes: moored sediment traps (# symbols, Honjo et al., 2008), onboard incubations (° symbols, Giering et al., 2014; Collins et al., 2015); excess barium proxy (* symbols, Brewer et al., unpublished results).

4.4.2. Factors influencing remineralization processes in the North Atlantic

The mesopelagic POC remineralization is known to vary regionally (Berelson, 2001; Buesseler et al., 2007; Guidi et al., 2015) and here we investigated this variability in function of different factors such as the intensity and the stage of the bloom, the phytoplankton size and community structure and the physical forcing.

4.4.2.1. Influence of the intensity and stage of the bloom

A high remineralization rate indicates a past production, together with an export event (Jacquet et al., 2015), as the mesopelagic Ba_{xs} signal builds up during the growth season (Dehairs et al., 1997; Cardinal et al., 2001; 2005). Assuming that the Ba_{xs} proxy integrates a full season, we compared our remineralization estimates with the averaged biomass development from January to June 2014 (Figure 4.10), which is the period integrating the complete bloom development in the North Atlantic.

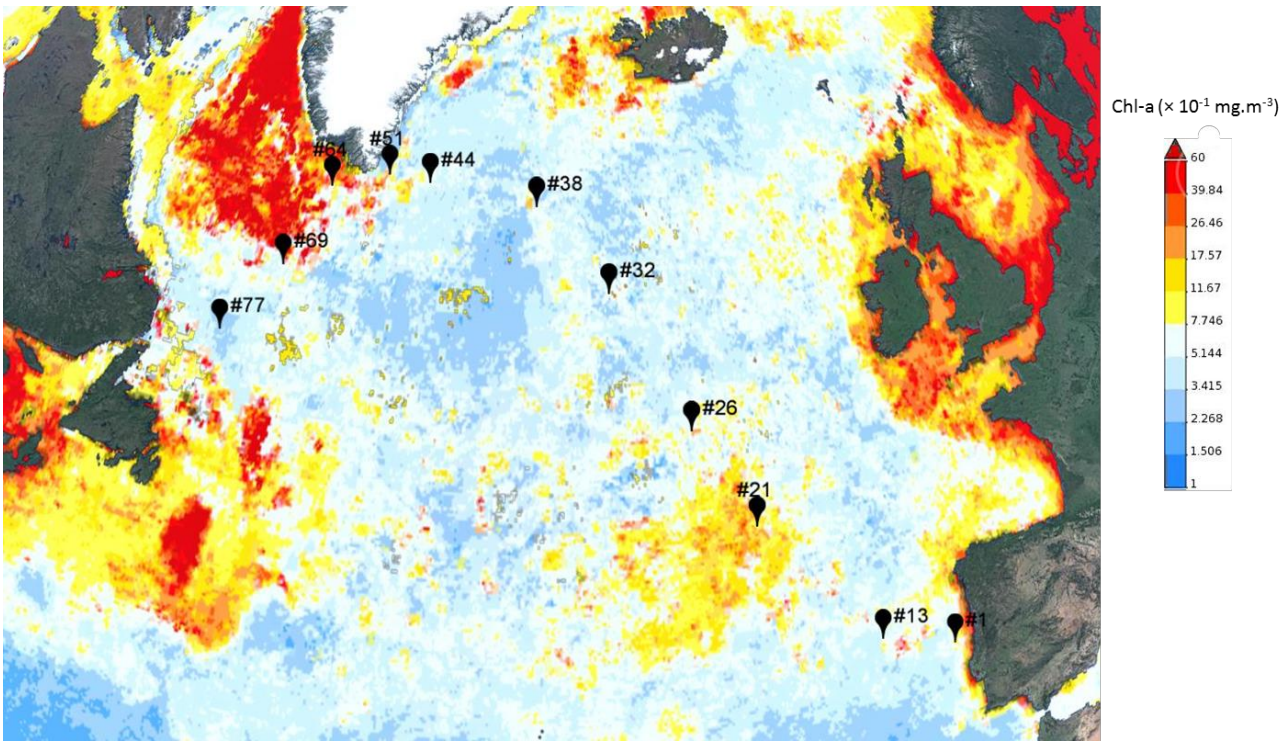

Figure 4.10: Time averaged map of Chlorophyll-a concentrations (mg.m-3) over January – June 2014 (monthly 4 km MODIS Aqua model; http://giovanni.sci.gsfc.nasa.gov/).

Along the GEOVIDE transect, the most productive area during this period was clearly the Labrador Sea basin of the ARCT province as Chl-*a* concentrations averaged 6 $mg.m^{-3}$ (Figure 4.10). This basin was sampled during the decline of the bloom (Figure 4.1; Chl-*a* concentration was > 3 $mg.m^{-3}$ one month before the sampling, and low PP and nutrient concentrations during sampling), which could explain the high mesopelagic remineralization fluxes observed in this area (Figure 4.8). To a lesser extent than the Labrador Sea basin, the western European basin of the NADR province, and in particular the area around Station 21, was characterized by an important biomass level between January and June (Figure 4.10). This bloom started in May (Figure 4.1; Chl-a concentration ≈ 3 $mg.m^{-3}$ one month before the sampling) but was still progressing during the sampling, as indicated by the high PP (135 $mmol.m^{-2}.d^{-1}$) during the sampling. These features can explain the lower mesopelagic remineralization fluxes observed at Station 21 (Figure 4.8) compared to the Labrador Sea basin. The other stations of the NADR (Stations 26, 32, 38) were sampled during the bloom development (Figure 4.1 and high PP reaching 174 at Station 26 during sampling) and were characterized by low mesopelagic remineralization fluxes compared to other stations, suggesting a time lag between production, export and remineralization. However, this was not the case for Station 44, in the Irminger Sea basin of the ARCT province, sampled during the bloom (high PP, high Chl-*a* and high nutrient concentrations during the sampling period) and characterized by one the highest mesopelagic remineralization flux. This high mesopelagic remineralization flux may reflect an important past bloom, as evidenced in fact by the satellite Chl-*a* data (see Table 2 or Figure 9 in Lemaitre et al., in prep.), highlighting the patchiness of the phytoplankton blooms in this area.

Overall, the large regional and temporal variability of the bloom development involves a large variability of POC remineralization in the North Atlantic.

4.4.2.2. Influence of the phytoplankton size and community structure

Together with grazing and bacterial activity (Burd et al., 2010; Steinberg et al., 2008), the size structure of the phytoplankton assemblage is one key component of the remineralization intensity in the mesopelagic layer (Boyd and Newton, 1999; Buesseler et al., 2007; Guidi et

al., 2015). Temperate and subpolar regions, dominated by large phytoplankton cells, are characterized by substantial surface POC export fluxes (Boyd and Newton, 1999) yet strongly attenuated with depth because of a high remineralization in the mesopelagic layer (Berelson et al., 2001; Guidi et al., 2009). Conversely, in tropical regions, small cells dominate surface waters, leading to lower POC export fluxes but also to lower flux attenuation in the mesopelagic layer (Guidi et al., 2009). Figure 4.11 shows that the remineralization flux increased with increasing abundance of micro-phytoplankton, relative to abundance of nano- and pico-phytoplankton (based on pigment data; Ras et al., 2008). It is particularly manifest in the ARCT province where the highest remineralization fluxes and micro-phytoplankton abundances were measured.

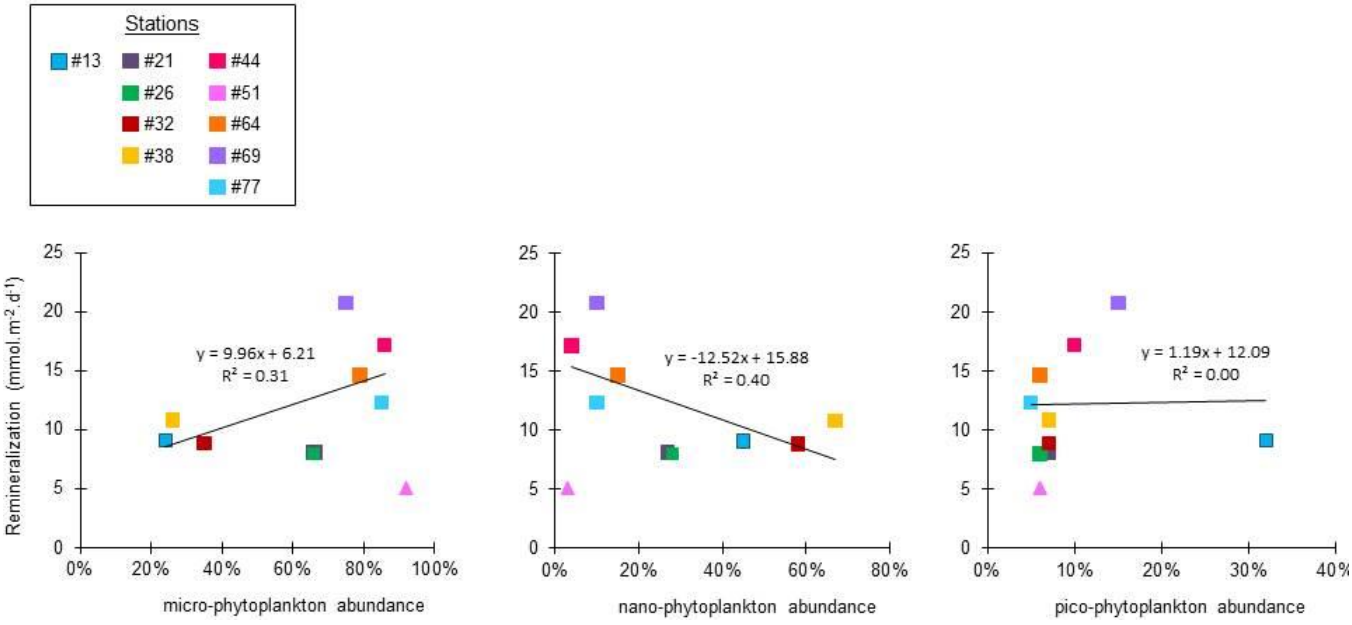

Figure 4.11: Mesopelagic remineralization fluxes (mmol.m-2.d-1) plotted as a function of the corresponding fractions of micro-, nano- and pico-phytoplankton. The black line corresponds to the linear regression between both parameters for all stations except Station 51 (pink triangle).

Phytoplankton community structure also influences the carbon remineralization in the mesopelagic layer by varying the sinking velocities of the particles through the biogenic minerals, such as biogenic silica or calcium carbonate, composing their shells (i.e., the ballast effect; Armstrong et al., 2002, 2009). In parallel to the phytoplankton size structure, high export

in mid- and high-latitudes are mediated by diatoms, that are usually rapidly recycled through the mesopelagic as the carbon associated to diatoms is more labile (Francois et al., 2002; Ragueneau et al., 2006). Indeed, the ARCT province was characterized by the highest mesopelagic remineralization fluxes and was dominated by diatoms (> 70%; Figure 4.12). Conversely, the lower mesopelagic remineralization fluxes, observed in the NAST and NADR provinces could be related to higher abundance of coccolithophorids (Figure 4.12). Indeed, calcifiers, such as coccolithophorids, have been shown to be more efficient in transferring carbon to the deep ocean compared to diatoms (Francois et al., 2002; Klaas and Archer, 2002; Lam et al., 2011). This difference could result from the low compaction or the high fluffiness of diatom aggregates, the high degree of degradability of organic compounds within diatom aggregates, the greater calcite density, the resistence of calcite to grazing and the more refractory nature of the exported organic matter associated to calcite (Bach et al., 2016; Francois et al., 2002; Klaas and Archer, 2002; Lam et al., 2011; Le Moigne et al., 2013a). Overall, the upper ocean ecosystem structure plays an important role on the POC sequestration and in the North Atlantic, the carbonate-dominated systems appear to resist more to remineralization through the mesopelagic layer than opal-dominated systems.

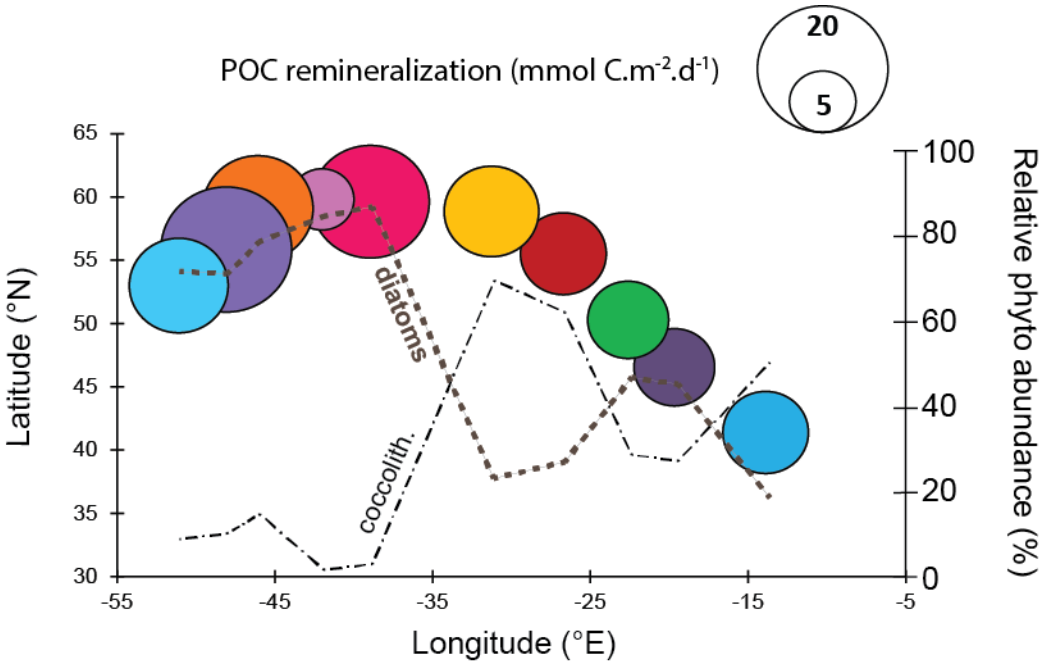

Figure 4.12: Bubble plot showing the mesopelagic remineralization flux (mmol.m-2.d-1) and the abundance of the two main phytoplankton communities (diatoms and coccolithophorids, in %) along the GEOVIDE transect. The size of the bubble is proportional to the magnitude of the flux.

4.4.2.3. Influence of water masses/physical forcing

The largest Ba_{xs} inventory and the highest mesopelagic remineralization flux were determined in the Labrador Sea basin (Stations 64, 69 and 77), characterized by the presence of the Labrador Sea Water in the upper 1500 m (LSW; potential temperature between 2.7 and 3.8°C and salinity below 34.9; Harvey, 1982; Yashayaev, 2007). The LSW formation takes place in the central Labrador Sea where the convection reached ~1700 m during the winter preceding GEOVIDE (Figure 4.2**;** Kieke and Yashayaev, 2015). The deepening of the mixed layer depth has been recently shown as a major source (from 23% to > 100% in high latitude regions) of organic carbon to the mesopelagic zone (Dall'Olmo et al., 2016), supporting the carbon demand of the mesopelagic food web (Burd et al., 2010; Aristegui et al., 2009). Moreover, the highest mesopelagic total bacterial abundance was observed in the central Labrador Sea (Station 69), reaching 896 cells.μL^{-1} at 500 m while the median for other stations, with available data in the mesopelagic zone (Stations 13, 21, 26, 32 and 38), was about 258 ± 60 cells.μL^{-1} at the same depth (Figure 4.6**;** J. Laroche, J. Ratten and R. Barkhouse, personal communication). Therefore, the subduction areas appear to reinforce the microbial loop by

increasing the layer in where the bacteria can thrive feeding on increasing food supplies. This condition consequently enhances the remineralization processes.

The LSW was also present in the Irminger Sea basin between 500 and 1000 m at Station 44 (Figure 4.2) where a second Ba_{xs} peak was observed (823 and 632 pmol.L^{-1} at 700 and 800 m; Figure 4.5). In the T-S plot, these high Ba_{xs} concentrations are clearly associated to the presence of the LSW (Figure 4.13.a), suggesting that this Ba_{xs} peak could represent an advected signal and thus reflecting remineralization of organic matter that occurred in another area. At Station 44, the contribution of the advected signal would be about 3 mmol C.m^{-2}.d^{-1} (19%) of the total signal, which is within the uncertainty of the flux. Similarly, a second Ba_{xs} peak was observed at 450 m of Station 32 (Figure 4.5) and the T-S plot (Figure 4.13.b) points out that this second peak was related to the presence of the Subarctic Intermediate water (SAIW; temperature at 5.6 ± 0.1°C and salinity at 34.70 ± 0.02; Alvarez et al., 2004), which contributes to 0.6 mmol C.m^{-2}.d^{-1} (7%) of the total signal.

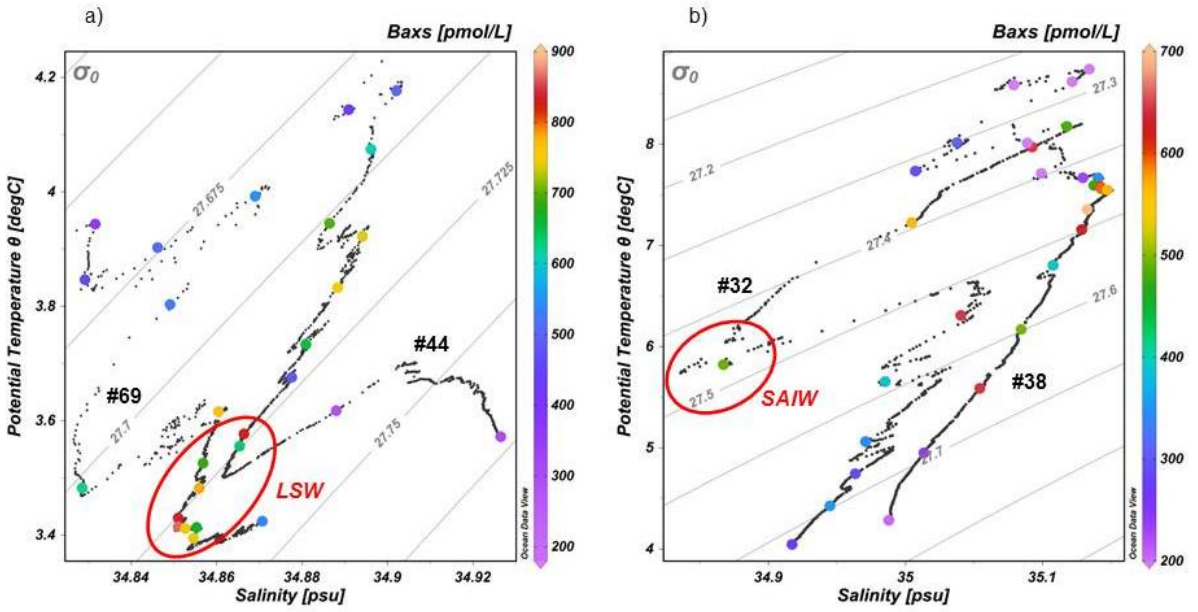

Figure 4.13: Potential temperature θ - salinity S plots and isopycnals for the Stations a) #44 and #69 and b) #32 and #38 of the GEOVIDE cruise focus on the 50-2000 m depth interval. The concentrations of Baxs are shown by the colored points. LSW: Labrador Sea water; SAIW: Subarctic Intermediate water.

The Station 38 was also characterized by a second Ba_{xs} peak at 700 m (Figure 4.5) but it is probably not related to a different water mass since there are no changes in the T-S plot (Figure 4.13.b). This second Ba_{xs} peak may represent a deeper remineralization generated by larger organic aggregates which would have sunk deeper. Similarly, the influence of water masses was not detected at the remaining stations. Overall, lateral transports influencing the Ba_{xs} distributions were observed at two stations during GEOVIDE but they did not modify significantly the magnitude of the remineralization fluxes. However, the subduction occurring in the Labrador Sea was related to a greater mesopelagic remineralization probably due to high POC export and associated bacterial activity in these areas.

4.4.3. Fate of the sinking POC in North Atlantic

In order to investigate the efficiency of the biological carbon pump in the North Atlantic, we examined the daily primary production (PP; A. Roukaerts, D. Fonseca Batista and F. Deman, unpublished data), the upper-ocean POC export (Lemaitre et al., in prep) and the POC remineralization in the mesopelagic layer (Table 4.4; Figure 4.14).

province	ARCT - *Labrador Sea*			ARCT - *Irminger Sea*		NADR				NAST
Station	77	69	64	51	44	38	32	26	21	13
PP [1]	95	31	67	165	137	68	142	174	135	80
Export [2]	6	10	8	3	1	5	8	7	5	2
Remineralization	12	21	15	5	14	11	8	8	8	9

Table 4.4: Comparison of the mesopelagic POC remineralization fluxes (Remineralization) with primary production (PP) and POC export fluxes in the upper water column (Export). All fluxes are expressed in mmol $C.m^{-2}.d^{-1}$. [1] PP data from A. Roukaerts, D. Fonseca Batista and F. Deman (unpublished data); [2] EP data from Lemaitre et al., in prep.

During GEOVIDE, low (≤ 12 %) export efficiencies (i.e., the ratio between PP and POC export) were observed at most stations indicating an accumulation of biomass in surface waters or a strong turn-over of the exported organic matter due to important remineralization occurring in the upper water column (< 100 m). Yet, high POC remineralization fluxes were also measured

in the mesopelagic layer, equaling or exceeding the POC export fluxes. This highlights a strong mesopelagic remineralization with little or no material left for export to the deep ocean, but above all, it involves an imbalance between carbon supplies and mesopelagic remineralization. This imbalance can be caused by the distinct time scales over which the PP, POC export and POC remineralization fluxes operate. Indeed, the measurements of PP represent a snapshot (24h incubations) while export (^{234}Th) and remineralization (Ba_{xs}) measurements integrate much longer time scales, in the order of several weeks and up to full season (see section IV.1.c), respectively. Moreover, previous studies in the Southern Ocean showed that mesopelagic processing of exported organic carbon, as reflected by Ba_{xs}, has a phase lag relative to the upper-ocean processes (Dehairs et al., 1997; Cardinal et al., 2005). Thus, we do not expect mesopelagic Ba_{xs} to be in phase with coinciding amplitude of PP and subsequent export. Because of the observed high remineralization fluxes relative to the export fluxes, we suppose that the surface particulate organic matter sank and accumulated in the mesopelagic layer in a period preceding the specific time windows for POC export and PP, leading to an important remineralization. This can be amplified by the spatial and temporal variability of the phytoplankton bloom in the North Atlantic, generating sudden high export events and associated remineralization. Therefore, the remineralization in the mesopelagic layer is an important process that needs to be taken into account as our results point to the poor ability of specific areas within the North Atlantic to sequester carbon at depth below 1000m in spring 2014.

Nevertheless, some authors reported POC export fluxes in the North Atlantic that were large enough to counterbalance our mesopelagic remineralization fluxes (NADR: 41 $mmol.m^{-2}.d^{-1}$, Buesseler et al., 1992; Irminger Sea: 36 $mmol.m^{-2}.d^{-1}$, Ceballos-romero et al., 2016; Labrador Sea: 47 $mmol.m^{-2}.d^{-1}$, Moran et al., 2003), confirming the large variability of production export in the North Atlantic. Considering the higher POC export estimations obtained in these studies, 20% of sinking POC would be remineralized in the NADR province, 36% in the Irminger Sea basin and 45% in the Labrador Sea basin.

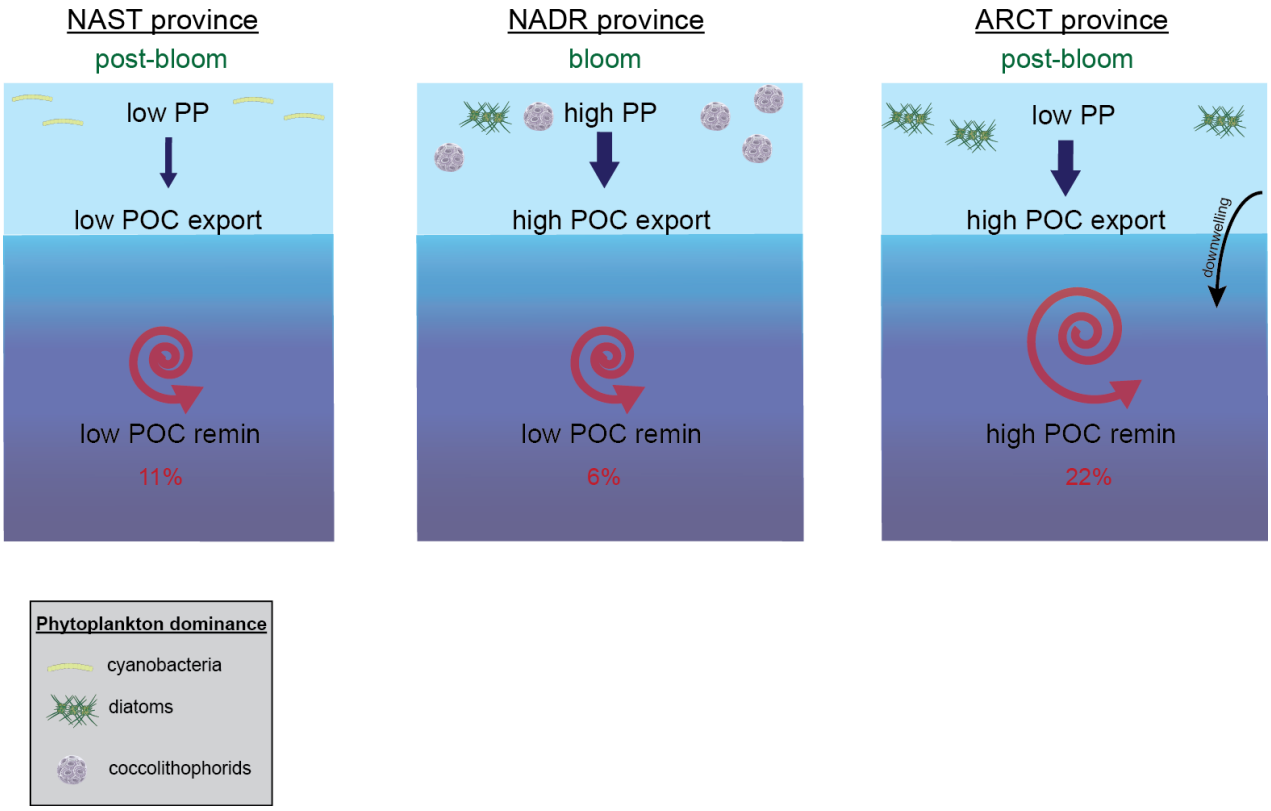

Figure 4.14: Global schematic of the biological carbon pump during GEOVIDE in the NAST, NADR and ARCT provinces. Primary production (PP) data from A. Roukaerts and D. Fonseca Batista; particulate organic carbon (POC) export fluxes from Lemaitre et al., in prep.; and POC remineralization fluxes from this study. The dominating phytoplanplankton communities and the stage of the bloom are also indicated. The red numbers are the ratio between PP and mesopelagic remineralization fluxes and indicate the proportion of PP remineralized through the mesopelagic layer.

4.5. Conclusion

We investigated mesopelagic carbon remineralization fluxes in the North Atlantic during the spring 2014 (GEOVIDE section) using the excess particulate biogenic barium (Ba_{xs}) approach for the first time in this area. This proxy approach provided similar estimations of remineralization fluxes obtained by independent methods (OUR, moored sediment traps, incubations).

The comparison with moored sediment traps highlights the fact that the Ba_{xs} proxy may integrate over a complete season while previous studies estimated its integration time to be only several weeks.

In the North Atlantic, remineralization was variable in the mesopelagic layer with the highest remineralization fluxes observed in the ARCT province, where high carbon production rates

were observed earlier in the season. The regional variations of remineralization fluxes can also be due to the different phytoplankton cell size and community composition encountered along this trans-Atlantic section. Lower remineralization fluxes were determined where the smaller calcified phytoplankton species dominated. Finally, the ARCT province was also characterized by an important water mass subduction, generating a larger transport of organic matter to the deep ocean, resulting to a larger remineralization.

In spring 2014, the remineralization in the North Atlantic was equal or larger than POC export, highlighting the important impact of the mesopelagic remineralization on the biological carbon pump and indicating that little to no particulate carbon was transferred below 1000 m.

Acknowledgements

We would like to thank the captain and the crew of the R/V Pourquoi Pas?, as well as Fabien Perault and Emmanuel De Saint Léger from the CNRS DT-INSU for their help during the CTD deployments. We acknowledge Lorna Foliot, Raphaëlle Sauzède, Joséphine Ras, Hervé Claustre and Céline Dimier for the sampling and analysis of pigments. Finally, we would like to thank the co-chief scientists Pascale Lherminier and Géraldine Sarthou. We also express our thanks to Monika Rhein, Julie Deshayes and Claude Talandier for providing useful help on the characteristics of the Labrador Sea water. Satellite chlorophyll-a data and visualizations used in this study were produced with the Giovanni and the Ocean Color (Ocean Biology Processing Group; OBPG) online data system, developed and maintained by the NASA.

This work was funded by the Flanders Research Foundation (project G071512N), the Vrije Universiteit Brussel (strategy research program: project SRP-2), the French ANR Blanc GEOVIDE (ANR-13-BS06-0014), ANR RPDOC BITMAP (ANR-12-PDOC-0025-01), IFREMER, CNRS-INSU (programme LEFE), INSU OPTIMISP and Labex-Mer (ANR-10-LABX-19).

Table S4.1: Excess particulate biogenic barium (Ba_{xs}) in $pmol.L^{-1}$ during GEOVIDE, obtained from Niskin bottles.

Station 1 (40.3 °N/-10.0 °E)				Station 13 (41.4°N/-13.9°E)				Station 21 (46.5°N/-19.7°E)				Station 26 (50.3°N/-22.6°E)			
Depth	Ba_{xs}			Depth	Ba_{xs}			Depth	Ba_{xs}			Depth	Ba_{xs}		
m	$pmol.L^{-1}$			m	$pmol.L^{-1}$			m	$pmol.L^{-1}$			m	$pmol.L^{-1}$		
20	126	±	19	20	239	±	53	10	207	±	36	20	1018	±	185
40	195	±	13	40	218	±	38	20	566	±	113	50	1888	±	314
60	214	±	17	60	177	±	42	40	276	±	45	75	378	±	54
79	363	±	35	78	242	±	48	60	181	±	35	99	174	±	29
98	412	±	80	100	274	±	50	76	483	±	79	200	451	±	64
119	291	±	67	120	306	±	50	100	453	±	73	400	433	±	63
139	288	±	64	140	379	±	71	120	467	±	66	599	388	±	60
160	241	±	54	160	449	±	70	140	502	±	74	800	396	±	61
200	340	±	88	200	425	±	64	160	338	±	56	1000	320	±	47
249	470	±	111	250	496	±	87	200	340	±	51				
299	310	±	101	300	582	±	90	300	491	±	76				
399	263	±	70	400	961	±	147	400	379	±	57				
499	286	±	86	500	357	±	62	500	524	±	91				
597	483	±	103	600	319	±	61	600	424	±	69				
702	156	±	95	700	305	±	54	700	364	±	59				
800	159	±	62	800	259	±	51	800	308	±	48				
1000	171	±	62	1000	270	±	49	1000	318	±	62				
1505	157	±	62	1501	172	±	43	1200	212	±	40				

Station 32 (55.5°N/-26.7°E)				Station 38 (58.8°N/-31.3°E)				Station 44 (59.6°N/-38.9°E)				Station 51 (59.8°N/-42.0°E)			
Depth	Ba_{xs}			Depth	Ba_{xs}			Depth	Ba_{xs}			Depth	Ba_{xs}		
m	$pmol.L^{-1}$			m	$pmol.L^{-1}$			m	$pmol.L^{-1}$			m	$pmol.L^{-1}$		
10	86	±	16	10	185	±	24	10	116	±	14	10	127	±	25
20	170	±	26	20	84	±	7	20	90	±	7	19	61	±	8
40	105	±	20	40	159	±	28	40	292	±	48	40	180	±	36
60	112	±	21	60	103	±	18	60	293	±	46	60	194	±	37
80	119	±	20	80	169	±	29	80	298	±	45	80	266	±	49
100	155	±	26	100	227	±	37	100	464	±	68	100	300	±	54
120	308	±	49	120	346	±	51	120	431	±	64	120	307	±	58
140	294	±	51	140	472	±	68	140	501	±	83	140	316	±	59
161	480	±	80	160	599	±	106	160	605	±	91	160	359	±	69
200	646	±	93	180	590	±	100	200	695	±	104	180	251	±	55
300	566	±	93	200	565	±	87	300	739	±	116	200	383	±	72
380	489	±	79	300	711	±	106	400	747	±	111	300	495	±	84
450	644	±	111	400	621	±	95	500	653	±	106	400	445	±	78
500	386	±	58	500	388	±	65	600	483	±	83	500	299	±	65
598	342	±	51	600	496	±	80	700	823	±	134	600	278	±	46
700	293	±	50	700	644	±	103	800	632	±	89	700	275	±	47
800	354	±	54	800	241	±	54	1100	284	±	54	800	225	±	47
1000	269	±	46	1000	202	±	48	1401	298	±	52	1000	199	±	34

Station 53 (59.9°N/-43.01°E)				Station 64 (59.1°N/-46.1°E)				Station 69 (55.8°N/-48.1°E)				Station 77 (53.0°N/51.1°E)			
Depth	Ba_{xs}			Depth	Ba_{xs}			Depth	Ba_{xs}			Depth	Ba_{xs}		
m	$pmol.L^{-1}$			m	$pmol.L^{-1}$			m	$pmol.L^{-1}$			m	$pmol.L^{-1}$		
10	295	±	122	10	61	±	13	11	58	±	13	10	104	±	6
20	203	±	133	20	143	±	32	20	148	±	11	20	113	±	9
40	137	±	80	40	99	±	22	41	178	±	40	39	170	±	16
60	98	±	75	60	97	±	22	60	198	±	46	60	316	±	57
80	100	±	98	80	112	±	23	80	358	±	72	80	374	±	63
100	218	±	114	100	282	±	47	100	459	±	89	100	411	±	71
120	284	±	113	120	432	±	77	120	505	±	96	120	381	±	68
140	129	±	143	140	506	±	86	140	550	±	102	140	369	±	61
				160	458	±	91	160	525	±	91	160	418	±	84
				199	447	±	89	200	619	±	97	200	493	±	87
				300	500	±	104	300	768	±	121	300	503	±	75
				400	332	±	82	400	682	±	119	401	470	±	80
				500	717	±	115	502	778	±	123	500	509	±	86
				600	696	±	100	601	831	±	135	601	445	±	73
				700	516	±	83	700	863	±	135	700	561	±	88
				800	750	±	121	802	744	±	113	800	575	±	101
				900	630	±	108	900	663	±	111	901	583	±	93
				1000	580	±	98	1001	741	±	119	1002	475	±	70
								1500	535	±	91				

Chapter 5

Biogenic trace element export fluxes in the North Atlantic Ocean

This chapter will serve as a basis for a manuscript in preparation for submission to Global Biogeochemical Cycles (March 2017).

Abstract

Trace elements (TEs) play an important role on the biological carbon pump, yet their biogeochemical cycles remain poorly constrained, in particular the magnitude of their vertical export through the sinking particles. In this study, particulate export fluxes of trace elements (Fe, Mn, Al, Co, Ni, Cu, Zn, Cd, P) were determined using the ^{234}Th-based approach in different biogeochemical provinces of the North Atlantic, as part of the GEOTRACES GA01 cruise (GEOVIDE; May-June 2014). Fluxes magnitude varied by one order of magnitude along the section, depending on the influence of lithogenic, oxide and biogenic particles, the highest trace element export fluxes being determined close to the margins. Near the Iberian margin, the TEs/Al export ratios were equal or relatively similar to the crustal ratio, highlighting the contribution of lithogenic particles in driving the export. Near the Greenland margin, the TEs/Al export ratios were close to ratios reported in Greenland sediments, which are rich in Fe and Mn oxides and sulphide minerals, suggesting that the high fluxes may be driven by a lateral advection of resuspended sedimentary particles.

Relatively high TEs export fluxes were also determined at open-ocean stations. Some stations had TEs/Al export ratios substantially in excess of crustal ratios and were characterized by high Mn and Fe fluxes indicating the potential contribution of Fe and Mn oxides to export the TEs. Moreover, at these same stations the TEs/POC and TEs/P export ratios were generally greater than intracellular quotas in phytoplankton.

In contrast, other stations were characterized by TEs/POC and TEs/P export ratios within the range observed in phytoplankton species highlighting that biogenic particles can also drive the TE export fluxes. The linear relationships between particulate TEs exports and BSi or $CaCO_3$ exports also showed the importance of diatoms and coccolithophorids in mediating the TEs vertical export.

5.1. Introduction

A range of bioactive trace elements (e.g. Fe, Cu, Zn, Co, Cd, Ni) are important in the regulation of the marine primary productivity (Morel, 2003), as they are essential nutrients for marine ecosystems. Trace elements are required for numerous metabolic processes (e.g. (Sunda, 1989; Twining and Baines, 2013) and their availability can strongly perturb the community structure, the phytoplankton production and the subsequent marine carbon cycle. As a result, the oceanic biogeochemical cycles of carbon and trace elements are intrinsically linked, and the quantification of the biogeochemical processes regulating the internal cycle of trace elements is essential to better understand the carbon cycle and in particular the biological carbon pump (BCP). Biogenic sinking particles, produced in the sunlit ocean, are one of the main vectors regulating the biogeochemical cycles as they transport the elements to the interior ocean. This process and the subsequent remineralization of biogenic particles influence indirectly the atmospheric CO_2 concentrations as the depths at which elements are remineralized affects the rates of their subsequent return to the surface (Kwon et al., 2009) and their bioavailability.

To date, little is known about the export of trace elements (Ellwood et al., 2014; Frew et al., 2006; Ho et al., 2010; Kuss et al., 2010; Kuss and Kremling, 1999; Lamborg et al., 2008; Lemaitre et al., 2016; Planquette et al., 2011; Stanley et al., 2004; Weinstein and Moran, 2005). One reason of the few number of studies is the difficulty to estimate trace element particulate fluxes, as trace elements are present at much lower concentrations in the ocean than macronutrients and are thus prone to contamination. Indeed, the direct measurement of particulate trace element fluxes using sediment traps can be biased because of the possible trace element contamination from the preservative solution, added in the cups to kill zooplankton swimmers (McDonnell et al., 2015). An alternative is to estimate indirectly the export fluxes by combining export fluxes of ^{234}Th with the trace element/^{234}Th ratio of sinking particles at the depth of export, using *in-situ* pumps that allow the clean collection of sufficient material (Planquette and Sherrell, 2012).

In the North Atlantic, the proximity of continental margins and the pronounced phytoplankton bloom (Henson et al., 2009) strongly affect the particulate trace element distribution (Kuss and Kremling, 1999; Ohnemus and Lam, 2014; Pohl et al., 2011; Saito et al., 2016; Weinstein and Moran, 2004). This region is also subjected sometimes to a lack of nutrients such as dissolved iron (dFe) (e.g. Nielsdottir et al., 2009), limiting the primary production development and thus the BCP (Achterberg et al., 2013; Blain et al., 2004; Le Moigne et al., 2014; Moore et al., 2013) but the role of export and remineralization on this limitation is poorly characterized. Indeed, large and fast sinking particles may sink efficiently and remove elements to deeper depths prior to remineralization. Some studies have revealed that particulate phosphorus (pP), nickel (pNi), zinc (pZn) and POC are remineralized faster than particulate iron (pFe) because of the strong scavenging of dFe onto sinking particles (Frew et al., 2006; Twining et al., 2014).

In this context, one of the objectives of the GEOTRACES section (GA01) GEOVIDE (15 May - 31 June, 2014; R/V Pourquoi Pas?) was to investigate the link between the trace elements and the production, export and remineralization of particulate organic matter. Using the terminology of Longhurst et al. (1995), the transect crossed different biogeochemical provinces including the North Atlantic Subtropical (NAST) province, the North Atlantic Drift (NADR) province and the Arctic (ARCT) province.

The NAST province is characterized by oligotrophic conditions leading to low primary production (Moore et al., 2008). As a consequence, low export fluxes of POC (Owens et al., 2014; Thomalla et al., 2006) and biogenic trace element (Kuss and Kremling, 1999a) have been reported. On the other hand, this province is sometimes under the influence of strong lithogenic inputs of refractory trace elements (Kuss and Kremling, 1999a; Kuss et al., 2010; Ohnemus and Lam, 2015) mainly originating from European and Saharan dusts (Jickells et al., 2005; Shelley et al., 2015). The presence of these lithogenic particles may ballast the particulate organic carbon (POC) and biogenic trace element to depth (Bressac et al., 2012; Klaas and Archer, 2002; Ye et al., 2011; Lemaitre et al., in prep.).

The NADR and ARCT provinces are characterized by lower lithogenic inputs because of the decreasing influence of the Saharan dust plume (Kuss and Kremling, 1999a). Nevertheless,

lateral supplies of lithogenic material from continental shelves have been reported to enhance the export fluxes in the ARCT province (Kuss et al., 2010; Weinstein and Moran, 2005). The export of POC (Lemaitre et al., in prep.; Antia et al., 2001; Billet et al., 1983; Henson et al., 2009; Lampitt et al., 2010; Peinert et al., 2001) and biogenic trace elements (Kuss et al., 2010) show episodic fluctuations along the season due to nutrient and/or light limitations.

It is therefore very important to consider the recycling and export patterns of bioavailable trace elements in order to better understand their distribution. This study investigates biogenic and lithogenic particulate trace element fluxes (Fe, Mn, Al, Co, Ni, Cu, Zn, Cd, P) using the ^{234}Th approach combined with data from bulk particulate material samples collected with *in-situ* pumps.

5.2. Methods

5.2.1. Sampling area

During the GEOVIDE cruise (May-June 2014; R/V Pourquoi Pas?), export fluxes were calculated at 11 stations across the three main biogeochemical provinces of the North Atlantic (Figure 5.1):

- the North Atlantic SubTropical (NAST) province (Stations 1 and 13) was sampled at the beginning of the cruise (19 and 24 of May, respectively) and was characterized by low nitrate (NO_3^-) and silicic acid ($Si(OH)_4$) concentrations (under 1 µmol.L^{-1} in in the upper 40m). In this province, dissolved iron (dFe) concentrations were non-limiting, with concentrations in surface waters varying between 0.15 and 1.08 nmol.L^{-1}. dFe concentrations were determined on samples collected using the trace metal clean rosette equipped with 12 L GO-FLO bottles (General Oceanics). Concentrations were determined by SF-ICP-MS coupled with a SeaFAST (Elemental Scientific) preconcentration system (Lagerström et al., 2013), and also by flow injection analysis (Tonnard et al., in prep.). Station 1 was sampled after the bloom period while Station 13 was sampled during the decline of the bloom (Lemaitre et al., in prep.), in line with

the low Chl-*a* concentrations (≤ 0.68 mg.m^{-3}) and low primary productivities (33 and 80 mmol C.m^{-2}.d^{-1} at Stations 1 and 13, respectively; A. Roukaerts, D. Fonseca Batista and F. Deman, unpublished data). The highest POC export was estimated at Station 1 (12 mmol.m^{-2}.d^{-1}), near the Iberian margin, probably due to the influence of lithogenic particles ballasting POC to depth, but Stations 13 was characterized by one of the lowest POC export (2.2 mmol.m^{-2}.d^{-1}), consistent with the low production in oligotrophic waters.

- the North Atlantic Drift (NADR) province, including the western European basin (Stations 21 and 26) and the Icelandic basin (Stations 32 and 38), was sampled from the 31st of May to the 10th of June. The surface waters had low $Si(OH)_4$ concentrations (≤ 1 µmol.L^{-1}), moderate dFe concentrations (Tonnard et al., in prep.), high NO_3^- concentrations (> 5 µmol.L^{-1}) except at Station 21 (NO_3^- concentrations below 1 µmol.L^{-1}). The NADR province was sampled during the bloom period and high Chl-*a* and PP were measured, reaching 1.2 mg.m^{-3} at Station 21 and 174 mmol C.m^{-2}.d^{-1} at Station 26. High POC exports were observed in this province and in particular at Station 32 (8.4 mmol.m^{-2}.d^{-1}).

- the Arctic (ARCT) province, including the Irminger Sea basin (Stations 44 and 51) and the Labrador Sea basin (Stations 64, 69 and 77) were sampled on the 13th and 16th of June and at the end of the cruise (19th, 22th and 26th of June), respectively. The Irminger Sea basin was characterized by high surface $Si(OH)_4$ and NO_3^- concentrations (> 6 µmol.L^{-1}) and moderate dFe concentrations (0.35-0.86 nmol.L^{-1}; Tonnard et al., in prep.). The surface waters of the Labrador Sea basin was characterized by low NO_3^- concentrations (< 1 µmol.L^{-1}) except at Station 64 (4.6 µmol.L^{-1}), high $Si(OH)_4$ concentrations (> 3.6 µmol.L^{-1}) except at Station 77 (~1 µmol.L^{-1}) and moderate to high dFe concentrations (from 0.75 nmol.L^{-1} at Station 64 to 2.5 nmol.L^{-1} above the Newfoundland Plateau; Tonnard et al., in prep.). Regarding the stage of the bloom, the province was divided between both basins with the Irminger Sea basin sampled during the bloom development and the Labrador Sea basin sampled during the decline of the bloom. Likewise, the median Chl-a concentration and PP data were higher in the Irminger Sea basin (2.5 mg.m^{-3} and 151 mmol C.m^{-2}.d^{-1}, respectively) compared to the Labrador Sea basin (1.0 mg.m^{-3} and 67 mmol C.m^{-2}.d^{-1}, respectively). The POC exports were also different

between both basins reaching 2.0±0.9 mmol.m^{-2}.d^{-1} in the Irminger Sea and 7.8±1.2 mmol.m^{-2}.d^{-1} in the Labrador Sea basin. This basin is also characterized by the subduction of the Labrador Seawater (LSW; Kieke and Yashayaev, 2015) which was particularly intense (1500m-deep convection) during the winter 2013-2014 (Lherminier, personal communication) and which may have induced an important POC remineralization in this area (Lemaitre et al., in prep.).

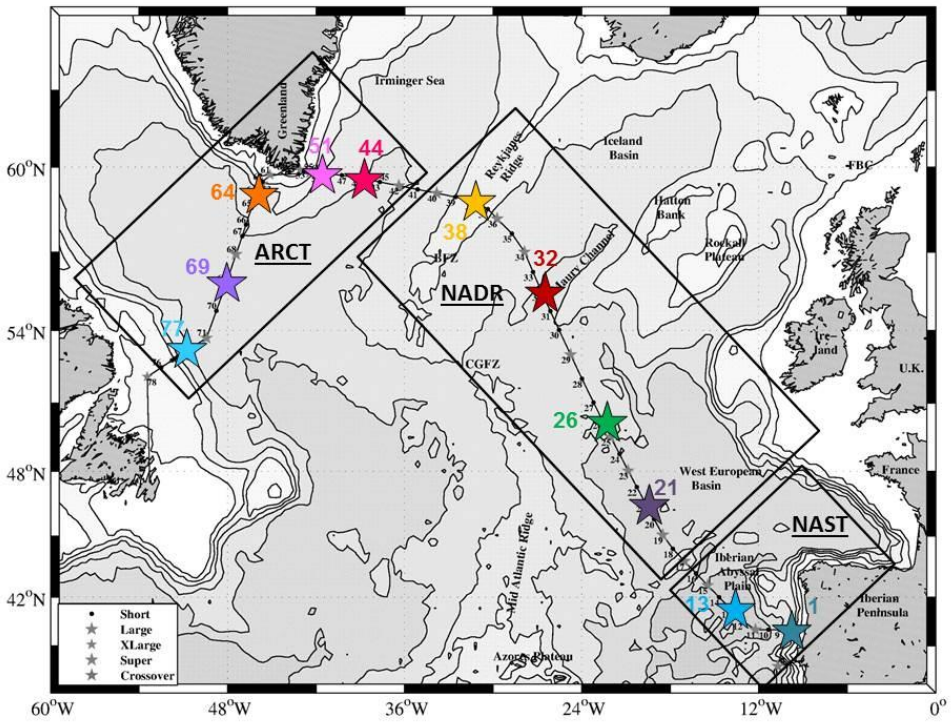

Figure 5.1: Map of the GEOVIDE section in the North Atlantic with the stations (stars) investigated within the North Atlantic Subtropical gyre (NAST) province, the North Atlantic Drift (NADR) province and the Arctic (ARCT) province (Longhurst, 1995).

5.2.2. Particle sampling

Particles were collected using *in-situ* large volume filtration systems (ISP hereafter) through paired 142 mm-diameter filters: a 53 µm mesh nylon screen (Petex; polyester) and a 0.8 µm polyestersulfone filter (Supor).

Before use, filters were placed in an acid cleaned containers containing 1.2M HCl (Suprapur grade, Merck). The containers were then double bagged in Ziploc bags and placed in an oven at 60°C overnight. After cooling, the acid solution was removed and filters were thoroughly

rinsed with Milli-Q water. Due to the slow release of acid from the filters, this rinsing step took days in order to reach a pH value slightly inferior to 7. Filters were then kept in the LDPE bottles filled with Milli-Q until use.

On board, filters were processed under a laminar flow unit within a customized clean “bubble” to prevent any contamination issues. Before and after the ISP recoveries, pump heads were also covered with plastic bags to minimize contamination. After pump recoveries, filter heads were dismantled and carried inside the clean bubble. Under the laminar flow hood, the 142 mm filters were then subsampled as follows: using a clean ceramic scalpel, one quarter of the PETEX, dedicated to ^{234}Th analyses in the large size fraction (LSF; >53 µm), was cut out. Then, particles were washed off this PETEX quarter using 0.45 µm filtered seawater (collected during the GEOVIDE cruise) through polyethersulfone filters (Supor®, porosity=0.45 µm, diameter=25 mm) mounted on a polysulfone filtration unit (Pall). Supor filters were then dried under the laminar flow unit and mounted on nylon holders, covered with Mylar and aluminum foil for analysis by Beta counting (low level beta counters, RISØ, Denmark). A second quarter of the PETEX which was dedicated to trace element analyses in the LSF was kept in a clean Petri slide (Millipore) at -20°C until sample processing and subsequent analysis in the home laboratory. The two remaining PETEX quarters were stored in clean Petri slides (Millipore) at -20°C for further analyses carried by other teams. The seawater volume filtered through a PETEX quarter was typically between 23 and 370 L (Tables S5.1 and S5.2). The 142 mm Supor filter was also subsampled for TE, major element and BSi analyses in the small size fraction (SSF; 1-53 µm), using a 13 mm diameter disposable skin biopsy Acupunch. The seawater volume filtered through these punches was typically between 1 and 13 L (Table S5.1). These punches were not Beta counted to avoid potential contamination of the samples and were directly stored in clean Petri slides double bagged in Ziploc bags and stored at -20°C until analysis.

5.2.3. Particle analyses

Sample handling, processing and preparation were performed in accordance with GEOTRACES recommendations (http://geotraces.org/images/stories/documents/intercalibration/Cookbook.pdf). Particles on the nylon screen were washed off the filter with 0.45 µm filtered surface seawater (sampled during the cruise at Station 77, 40m) and collected on acid cleaned 47 mm diameter mixed cellulose esters filters (MF-Millipore® filters, 0.8 µm), mounted on acid cleaned polysulfone filtration units (Nalgene®). This seawater has a dissolved iron (dFe) concentration of 0.102 ± 0.019 nmol.L^{-1} (Tonnard et al., in prep). The MF filter was then cut in two equal parts using an acid clean ceramic scalpel in order to digest totally the first half and to leach the second half (see below).

Under a Class-100 clean fume hood, one 13 mm punch of the Supor filter (SSF) or a half of the 47 mm MF filter (LSF) was placed along the wall of a 15 mL acid cleaned Teflon vial (Savillex). Then, 2 mL of a solution 8M HNO_3 (Ultrapur grade, Merck) and 2.3M HF (Suprapur grade, Merck) was added. Vials were then refluxed at 130°C on a hotplate during 4h. After gentle evaporation close to near dryness, 200 µL of concentrated HNO_3 (Ultrapur grade, Merck) was added in order to drive off the fluorides. The residue was brought back into solution with 3% HNO_3 spiked with 1 µg.L^{-1} of Indium and stored in acid cleaned 15 mL centrifuge tubes (Corning) until analysis for estimating the total particulate trace elements concentrations (Planquette and Sherrell, 2012).

All measurements for trace elements were performed using a SF-ICP-MS (Element 2, Thermo) following the method of Planquette and Sherrell (2012). Sample introduction system consisted of a FAST valve, a PFA nebulizer and a double stage spray chamber. Every 11 samples, a replicate analysis of a selected sample digest solution was made. The precision and the accuracy of our analyses were assessed by measuring replicates and the Certified Reference Materials (CRM) BCR-414, respectively (Table 5.1). External calibration curves were ran at the beginning, middle and end of the run.

	Certified/indicative* value (mg.kg^{-1})	Measured value (n=5; mg.kg^{-1})	Recovery (%)
Cd	0.383 ± 0.014	0.385 ± 0.020	101%
Al*	2154 ± 803 *	3112 ± 464	144%
P*	12840 ± 4978 *	15541 ± 3732	121%
Mn	299 ± 13	301 ± 42	101%
Fe*	1850 ± 190 *	1860 ± 230	101%
Co*	1.43 ± 0.06 *	1.44 ± 0.21	101%
Ni	18.8 ± 0.8	17.8 ± 2.91	95%
Cu	29.5 ± 1.3	29.7 ± 3.8	101%
Zn	111.6 ± 2.5	112.4 ± 18.8	101%

Table 5.1: Measured particulate trace element concentrations (in mg.kg^{-1}) and resulting recoveries (in %) of the certified reference material plankton BCR-414 compared to the certified or indicative (*) values (n=5).

Since then, other CRMs (sedimentary materials PACS-3 and MESS-4) have been digested using the same analytical method and good recoveries were achieved (between 92 and 108%; Gourain et al., in prep.).

5.2.4. Export fluxes

Trace element export fluxes were determined using the ^{234}Th-based approach by multiplying the ratio of the element of interest to ^{234}Th in particles with the total ^{234}Th export flux (presented in Lemaitre et al., in prep):

$$\text{Elemental export flux} = (\text{Element} : {}^{234}\text{Th})_{\text{particulate}} \times {}^{234}\text{Th flux} \quad \text{(Equation 5.1)}$$

Vertical export fluxes were determined at both the equilibrium depth (Eq hereafter) and 400 m. The Eq depth is where total ^{234}Th is back to equilibrium with ^{238}U. The ^{234}Th export at Eq represents the fully-integrated depletion of total ^{234}Th in the upper waters. In most cases, the depth resolution of *in-situ* pump sampling was lower than Niskin sampling, with the latter being used for assessing total ^{234}Th flux (Lemaitre et al., in prep.). The Element:^{234}Th ratios were calculated at Eq using a depth-weighted average (DWA; Element:^{234}Th=[Σ(Element$_i$ × Z_i) / $\Sigma(Z_i)$] / [Σ(^{234}Th$_i$ × Z_i) / $\Sigma(Z_i)$] where Z_i are the different depths sampled above Eq). Indeed, the

trace element to ^{234}Th ratios determined with the DWA method has been shown to better correspond to the ratio obtained in sediment traps (Lemaitre et al., 2016).

The Element:^{234}Th ratios were calculated at 400 m using a linear interpolation (Element:^{234}Th=a×Z+b where Z is the depth; a and b are the parameters obtained by a straight line fit between the upper and the lower data point bracketing the target depth, 400 m). The DWA method was not used at 400 m as it would give too much importance for the ratios in the upper water column and would not yield to a representative Element:^{234}Th ratio at 400 m.

Errors of the ratios were calculated using the partial derivative method in order to estimate the total error propagation. Finally, it was not possible to determine Element to ^{234}Th ratios in the SSF since particulate ^{234}Th could only be analyzed on QMA filters and not on the filters used for trace metal sampling. Hence, in the following, only results for the LSF will be presented and discussed.

5.3. Results

5.3.1. Distribution of particulate trace elements

Total particulate trace element concentrations are reported in Tables S5.1 and S5.2. A detailed description of the particulate trace element distribution along the GEOVIDE section can be found in Gourain et al. (in prep.). Good agreement between both datasets was achieved, and is presented in Chapter two.

In the large size fraction (LSF), pP, pFe, pMn, pZn, pNi, pCd, pCo and pCu concentrations spanned three orders of magnitude. The maximum pFe, pMn and pZn concentrations were determined at Station 1 and ranged from 0.02 nmol.L^{-1} (Station 16, 153 m) to 3.20 nmol.L^{-1} (Station 1, 550 m); from 0.1 pmol.L^{-1} (Station 77, 50 m) to 50 pmol.L^{-1} (Station 1, 550 m); from 0.001 nmol.L^{-1} (Station 13, 400 m) to 0.910 nmol.L^{-1} (Station 1, 550 m), respectively. The maximum pNi and pCo concentrations were determined in surface of Station 21 (15m) and ranged from 0.14 pmol.L^{-1} (Station 44, 300 m) to 70 pmol.L^{-1} (Station 21, 15 m) and from 0.04

(Station 38, 396 m) to 7.34 (Station 21, 15 m), respectively. The maximum concentrations of pCd and pCu were determined at Station 64 and ranged from 0.01 pmol.L^{-1} (Station 44, 300 m) to 7.08 pmol.L^{-1} (Station 64, 100 m) and from 0.66 pmol.L^{-1} (Station 44, 300 m) to 36 pmol.L^{-1} (Station 64, 100 m). Finally, pP concentrations ranged from 0.04 nmol.L^{-1} (Station 44, 300 m) to 24 nmol.L^{-1} (Station 51, 8 m).

As anticipated, trace elements concentrations were strongly enhanced close to the margins, including lithogenic prone elements such as pAl, for which the highest concentrations were measured at Station 1, particularly below 250 m (> 7 nmol.L^{-1}). Similarly, pFe, pMn, pZn, pNi, pCu, pCd and pCo concentrations increased below 250 m at this station, with concentrations at 550 m reaching 3.2 nmol.L^{-1}, 50 pmol.L^{-1}, 910 pmol.L^{-1}, 10.8 pmol.L^{-1}, 12.7 pmol.L^{-1}, 0.12 pmol.$L^{-1}$and 1.0 pmol.L^{-1}, respectively. Near the Greenland Margin, pAl concentrations were also high, reaching 1.3 and 2.5 nmol.L-1 at 60 and 100 m of Stations 51 and 64 respectively. Station 64 was also characterized by subsurface maxima of pP, pFe, pMn, pZn, pNi, pCu and pCd at 100 m depth.

Interestingly, at Station 26, high pMn concentrations were measured at 150 m, reaching 29 pmol.L^{-1}.

Overall, between surface and 100 m, the vertical distribution of particulate trace elements was rather similar to the one of particulate phosphorus (pP) concentrations, which could be used as an indicator of biomass in the open ocean (Collier and Edmond, 1984). Below 100 m, pP concentrations remained low and relatively constant, with median values of 0.21 nmol.L^{-1} (n=28).

5.3.2. Element to ^{234}Th ratios of particles

As stated above, Element to ^{234}Th ratios could only be determined for the LSF. The ratio magnitudes were very different among the elements and the provinces

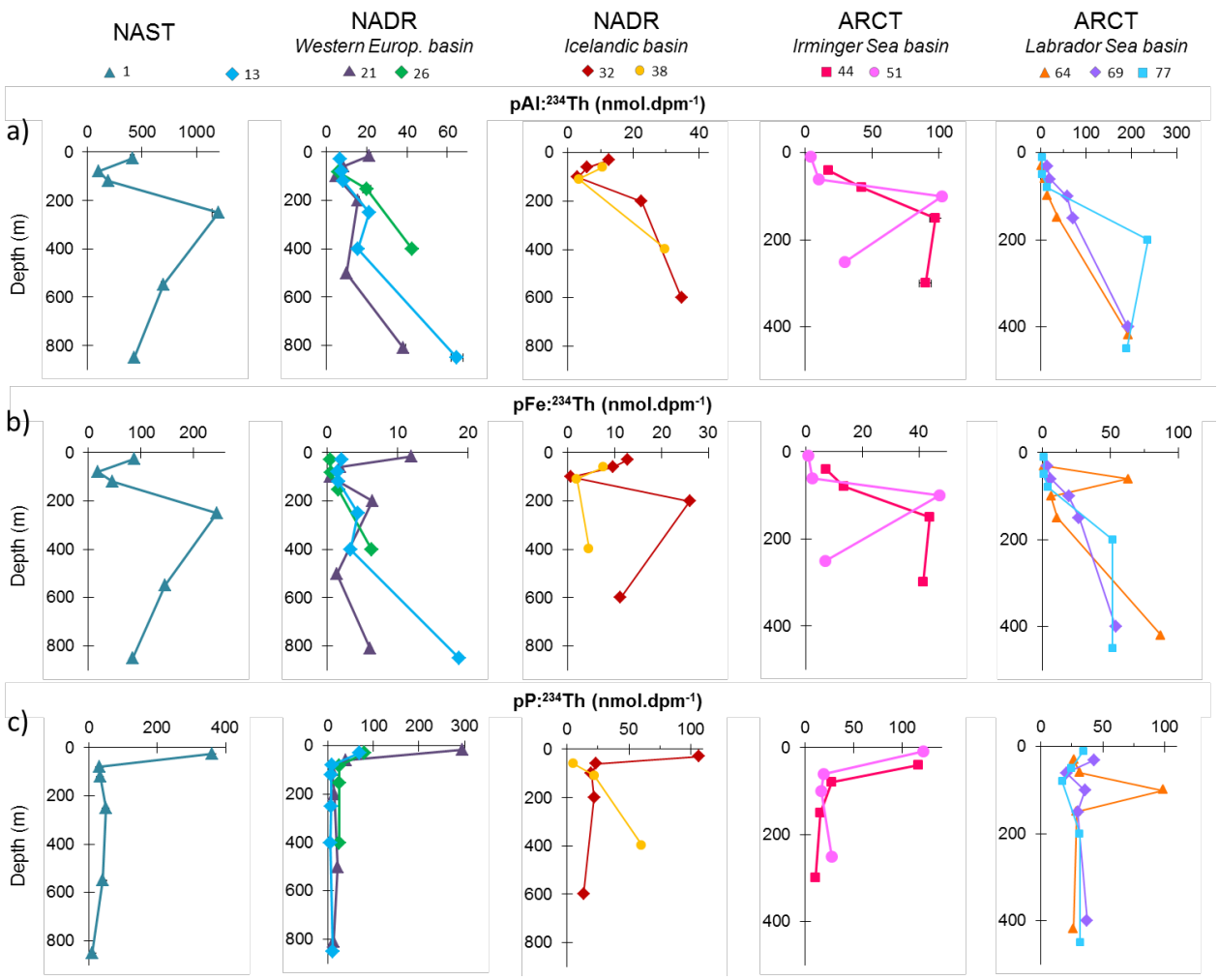
NAST
NADR
Western Europ. basin
NADR
Icelandic basin
ARCT
Irminger Sea basin
ARCT
Labrador Sea basin
1
13
21
26
32
38
44
51
64
69
77
a)
pAl:234Th (nmol.dpm-1)
b)
pFe:234Th (nmol.dpm-1)
c)
pP:234Th (nmol.dpm-1)
Depth (m)

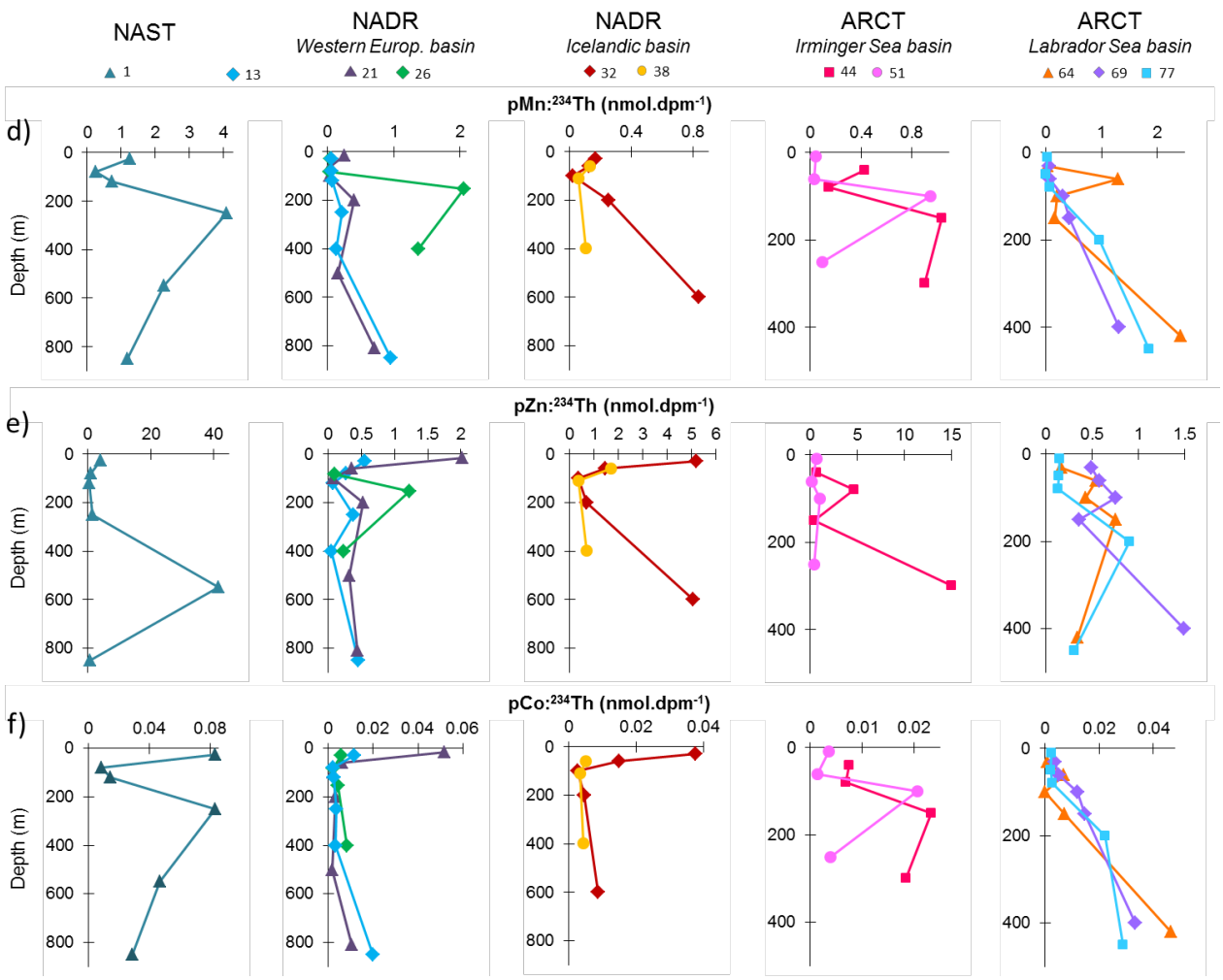
NAST
NADR
Western Europ. basin
NADR
Icelandic basin
ARCT
Irminger Sea basin
ARCT
Labrador Sea basin
1
13
21
26
32
38
44
51
64
69
77
d)
pMn:234Th (nmol.dpm-1)
e)
pZn:234Th (nmol.dpm-1)
f)
pCo:234Th (nmol.dpm-1)
Depth (m)

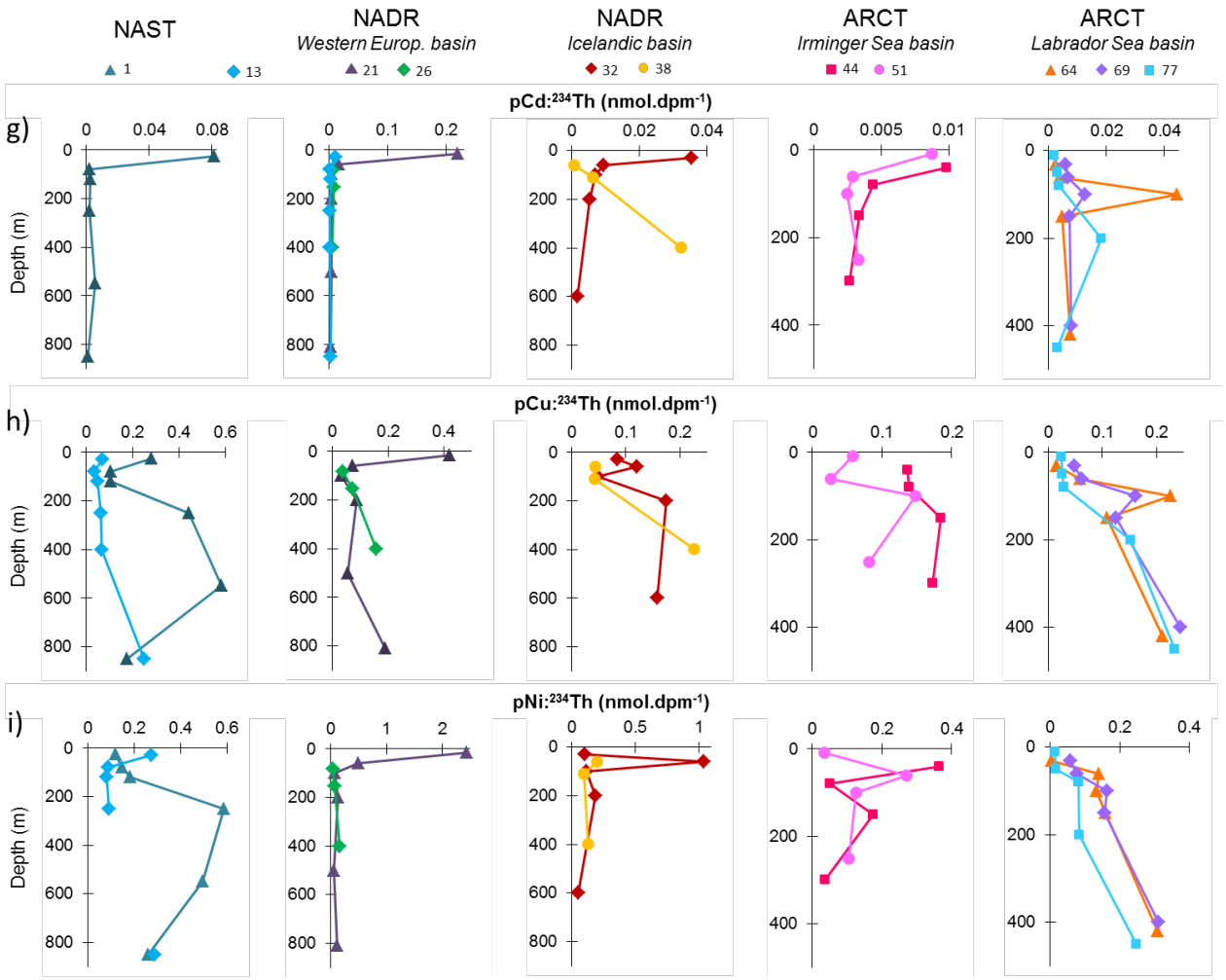

Figure 5.2: Particulate aluminum (pAl) (a); particulate iron (pFe) (b); particulate phosphorus (pP) (c); particulate manganese (pMn) (d); particulate zinc (pZn) (e); particulate cobalt (pCo) (f); particulate cadmium (pCd) (g); particulate cupper (pCu) (h); and particulate nickel (pNi) (i) to ^{234}Th ratios (nmol.dpm^{-1}) in the large size fraction (LSF; > 53 µm) along the GEOVIDE transect.

The pFe:^{234}Th, pMn:^{234}Th, pZn:^{234}Th and pCu:^{234}Th and ranged from 0.42 nmol.dpm^{-1} (Station 21, 100 m) to 245 nmol.dpm^{-1} (Station 1, 250 m); from 0.002 nmol.dpm^{-1} (Station 77, 50 m) to 4.11 nmol.dpm^{-1} (Station 1, 250 m); from 0.05 nmol.dpm^{-1} (Station 13, 400 m) to 42 nmol.dpm^{-1} (Station 1, 550 m) and from 0.02 nmol.dpm^{-1} (Station 77, 10 m) to 0.58 nmol.dpm^{-1} (Stations 1, 550 m) respectively. The highest pCd:^{234}Th, pCo:^{234}Th, pNi:^{234}Th ratios were observed in surface waters of Station 1 (reaching 0.08 for pCo:^{234}Th ratios) and Station 21 (reaching 2.44 and 0.22 nmol.dpm^{-1} for pNi and pCd:^{234}Th ratios).

Within the top 150 m, most trace Element to ^{234}Th ratios (Figure 5.2) tend to steadily decreased with depth, down to 150 m, then increased with depth. Interestingly, this trend was not

observed for pP, pCd and pNi:^{234}Th ratios, as the ratios decreased with depth similarly to POC:^{234}Th (Lemaitre et al., in prep.), then remained rather constant below 150 m. Elevated values of pP:^{234}Th were determined at at Station 1 and 21, reaching 360 and 296 nmol.dpm^{-1}. At other stations, pP:^{234}Th ratios were around 100 nmol.dpm^{-1} in surface waters, except in the Labrador Sea basin of the ARCT province where the ratios were lower (≈ 30 nmol.dpm^{-1}).

The highest pAl:^{234}Th, pFe:^{234}Th, pMn:^{234}Th, pZn:^{234}Th and pCu:^{234}Th ratios were determined at Station 1, located close to the Iberian Margin. High values were also determined in the vicinity of the Greenland margin, and in particular at Stations 51 (100 m) and 64 (60 m) reaching, for example, 47 and 63 nmol.dpm^{-1} for pFe:^{234}Th ratios, while noticeably, pZn:^{234}Th ratios were not really elevated., These results highlight the different influence of the margins on the distribution of the trace elements to ^{234}Th ratios, These differences will be specifically discussed in section 5.4.1.

5.3.3. Export fluxes

Export fluxes were calculated at Eq (the depth where ^{234}Th goes back to equilibrium with ^{238}U, between 40 and 200 m along the transect, median value of 90 m) and at 400 m. The results can be found in Table 5.2 and Figure 5.3.

5.3.3.1. Exports fluxes at Eq

The smallest export fluxes at Eq were determined at Station 77 reaching 2.8 µmol pAl.m^{-2}.d^{-1}, 1.1 µmol pFe.m^{-2}.d^{-1}, 0.02 µmol pMn.m^{-2}.d^{-1}, 0.02 µmol pNi.m^{-2}.d^{-1}, 0.02 µmol pCu.m^{-2}.d^{-1}, and 0.11 µmol pZn.m^{-2}.d^{-1}. The minimum pP and pCo export fluxes were observed at Stations 38 (8.6 µmol pP.m^{-2}.d^{-1}) and 64 (0.001 µmol pCo.m^{-2}.d^{-1}). The maximum export fluxes were determined at Station 1 reaching 341 µmol pAl.m^{-2}.d^{-1}, 70 µmol pFe.m^{-2}.d^{-1}, 1.0 µmol pMn.m^{-2}.d^{-1}, 263 µmol pP.m^{-2}.d^{-1} and 0.06 µmol pCo.m^{-2}.d^{-1}. The highest pNi, pCu and pZn export fluxes were observed at Stations 21 (1.64 µmol pNi.m^{-2}.d^{-1} and 0.28 µmol pCu.m^{-2}.d^{-1}) and 32

(6.23 µmol pZn.m^{-2}.d^{-1}). High pMn export fluxes were also determined at Eq of Stations 26 and 64, reaching respectively 2.97 and 2.79 µmol.m^{-2}.d^{-1}. Within the NADR province, the highest pP export fluxes were determined at Station 38, reaching 139 µmol.m^{-2}.d^{-1} at Eq of Station 32 and 59 µmol.m^{-2}.d^{-1}. Relatively high trace element export fluxes were also determined within this province, as pFe reached 16 µmol.m^{-2}.d^{-1}. Conversely, the fluxes in the ARCT province were low, averaging 2.32 µmol pFe.m^{-2}.d^{-1}, 0.04 µmol pMn.m^{-2}.d^{-1}, 0.26 µmol pZn.m^{-2}.d^{-1}, 0.06 µmol pNi.m^{-2}.d^{-1}, 0.04 µmol pCu.m^{-2}.d^{-1} (n=5, at Eq).

5.3.3.2. Export fluxes at 400 m

The export fluxes at 400 m were characterized by higher uncertainties and ranged from -31 (Station 69) to 116 (Station 1) mmol pFe.m^{-2}.d^{-1}, from -0.75 (Station 69) to 2.97 (Station 26) µmol pMn.m^{-2}.d^{-1}, and from -0.85 (Station 69) to 13 (Station 1) µmol pZn.m^{-2}.d^{-1}.

At 400 m, high pFe, pMn, pZn, pCo and pNi export fluxes were observed in proximity of the Iberian and Greenland margins, at Stations 1 and 64 respectively. The highest pFe, pZn, and pMn export fluxes at 400 m were determined at Station 1 (116 and 2.97 µmol.m^{-2}.d^{-1}). Similarly, the highest pAl flux was also determined at Station 1, reaching 565 µmol.m^{-2}.d^{-1}, while the median value of other stations was 11 µmol pAl.m^{-2}.d^{-1} (n=11). Relatively high pAl export fluxes were also determined in the NADR at Stations 26 and 64, reaching 92 and 225 µmol.m^{-2}.d^{-1}, respectively. This flux at Station 26 coincided with the highest pMn and pCu export fluxes calculated at 400 m and reaching 2.97 and 0.34 µmol.m^{-2}.d^{-1}, respectively.

At Station 32, relatively high pMn, pZn, pCd, pCo, pNi and pCu fluxes were determined at 400 m (reaching 0.22, 6.23, 0.05, 0.05, 0.39 and 016 µmol.m^{-2}.d^{-1}).

Finally, within the ARCT province, negative elemental export fluxes were determined at Stations 69 and 77 due to the excesses of ^{234}Th in depth inducing negative ^{234}Th export fluxes at 400 m.

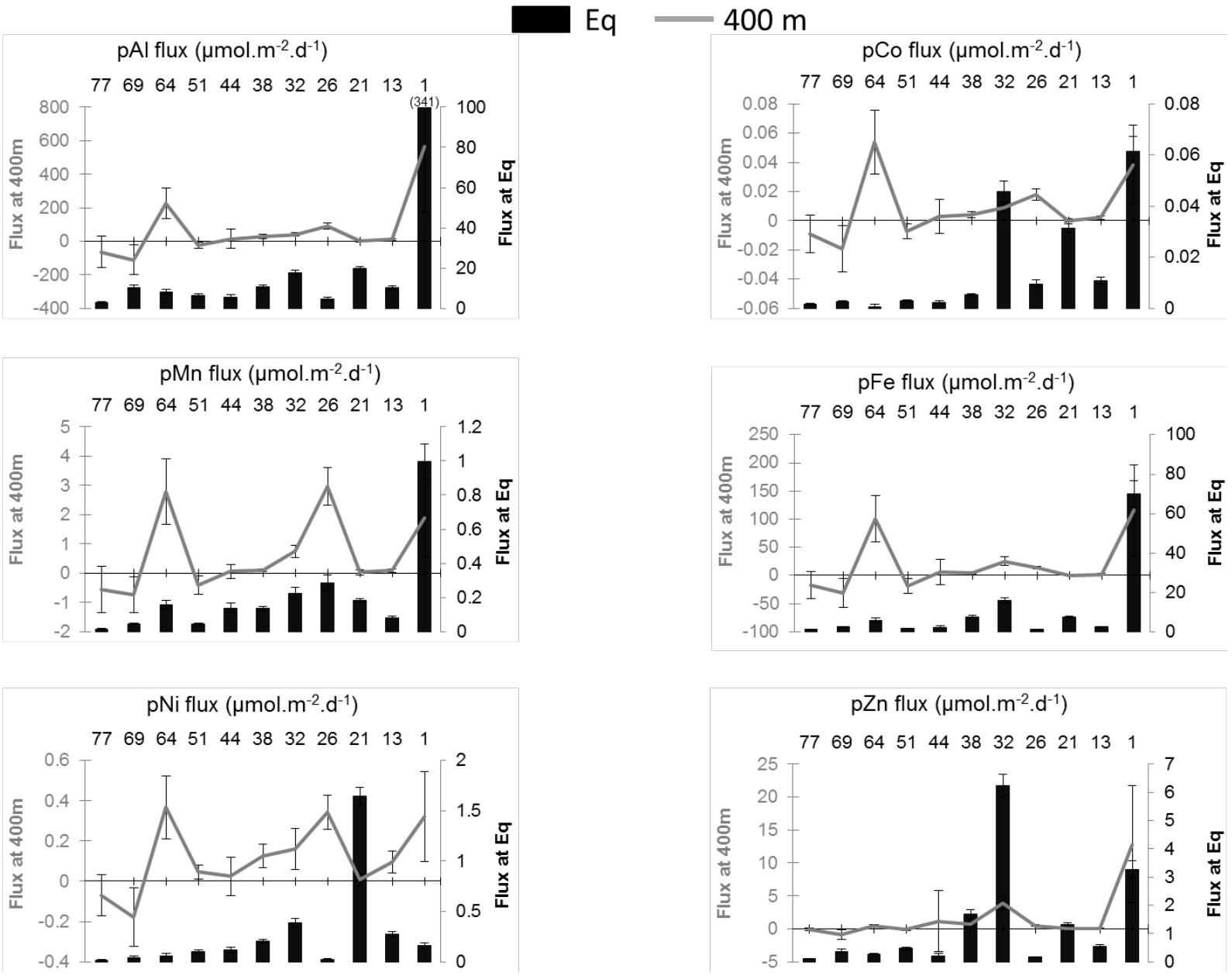
Eq
400 m
pAl flux (µmol.m-2.d-1)
77 69 64 51 44 38 32 26 21 13 1
(341)
Flux at 400m
Flux at Eq
pCo flux (µmol.m-2.d-1)
pMn flux (µmol.m-2.d-1)
pFe flux (µmol.m-2.d-1)
pNi flux (µmol.m-2.d-1)
pZn flux (µmol.m-2.d-1)

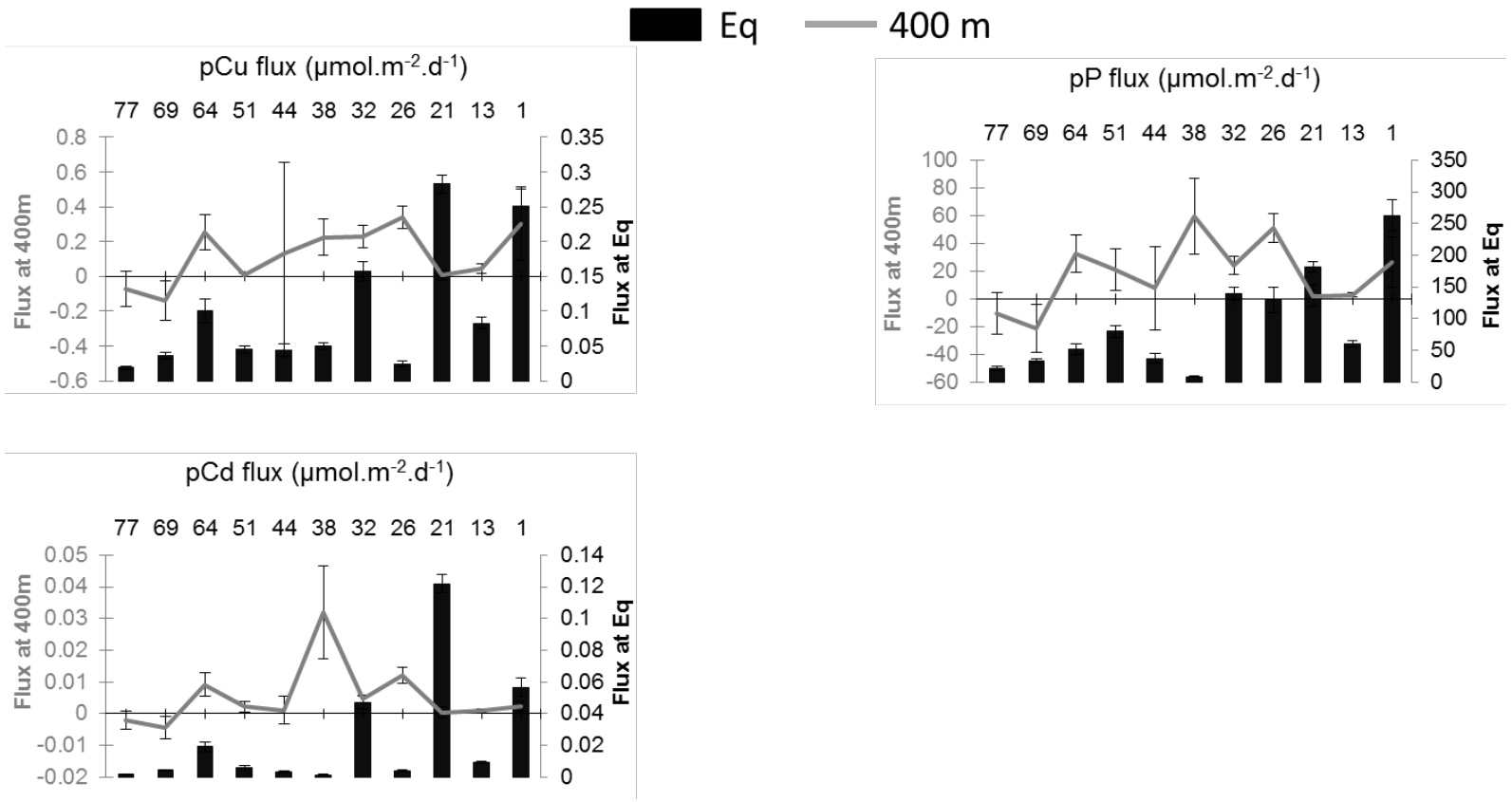

Figure 5.3: Particulate trace element export fluxes in µmol.m^{-2}.L^{-1} estimated in the large size fraction at the Eq depth (black bars) and at 400 m (grey line). Note the different y-axis scales.

Station #	Depth m	pFe flux µmol.m^{-2}.d^{-1}	pMn flux µmol.m^{-2}.d^{-1}	pCo flux nmol.m^{-2}.d^{-1}	pNi flux µmol.m^{-2}.d^{-1}	pCu flux µmol.m^{-2}.d^{-1}	pZn flux µmol.m^{-2}.d^{-1}	pCd flux nmol.m^{-2}.d^{-1}	pAl flux µmol.m^{-2}.d^{-1}	pP flux µmol.m^{-2}.d^{-1}
1	Eq	70.0 ± 6.5	1.00 ± 0.10	61.4 ± 5.7	0.16 ± 0.02	0.25 ± 0.03	3.27 ± 0.32	56.7 ± 5.7	341 ± 33	263 ± 24
	400	115.9 ± 80.7	1.89 ± 1.32	38.6 ± 26.9	0.32 ± 0.22	0.30 ± 0.21	12.78 ± 8.88	2.2 ± 1.6	565 ± 393	26 ± 18
13	Eq	2.5 ± 0.3	0.08 ± 0.01	10.9 ± 1.4	0.27 ± 0.03	0.08 ± 0.01	0.54 ± 0.05	9.2 ± 0.8	10 ± 1	60 ± 6
	400	2.2 ± 1.5	0.09 ± 0.06	2.1 ± 1.4	0.10 ± 0.06	0.04 ± 0.03	0.03 ± 0.03	0.9 ± 0.5	11 ± 6	3 ± 2
21	Eq	7.6 ± 0.4	0.18 ± 0.01	31.5 ± 1.8	1.64 ± 0.09	0.28 ± 0.01	1.32 ± 0.07	121.9 ± 6.0	20 ± 1	182 ± 9
	400	0.3 ± 1.3	0.02 ± 0.10	0.2 ± 1.0	0.01 ± 0.03	0.01 ± 0.03	0.04 ± 0.16	0.4 ± 1.6	1 ± 5	2 ± 8
26	Eq	1.1 ± 0.2	0.28 ± 0.05	9.6 ± 1.5	0.03 ± 0.01	0.02 ± 0.00	0.16 ± 0.03	4.1 ± 0.7	5 ± 1	129 ± 21
	400	13.7 ± 2.7	2.97 ± 0.64	17.9 ± 4.0	0.34 ± 0.08	0.34 ± 0.07	0.49 ± 0.16	12.0 ± 2.5	92 ± 18	51 ± 10
32	Eq	16.0 ± 1.2	0.22 ± 0.04	45.9 ± 4.1	0.39 ± 0.04	0.16 ± 0.01	6.23 ± 0.40	47.0 ± 3.9	17 ± 1	139 ± 10
	400	25.5 ± 7.1	0.74 ± 0.20	9.0 ± 2.4	0.16 ± 0.10	0.23 ± 0.06	3.95 ± 1.05	4.7 ± 1.3	39 ± 11	24 ± 7
38	Eq	7.7 ± 0.7	0.13 ± 0.01	5.3 ± 0.5	0.21 ± 0.02	0.05 ± 0.00	1.69 ± 0.15	1.6 ± 0.1	11 ± 1	9 ± 1
	400	4.4 ± 2.0	0.10 ± 0.05	4.3 ± 2.0	0.13 ± 0.06	0.22 ± 0.10	0.68 ± 0.32	31.8 ± 14.7	29 ± 14	59 ± 27
44	Eq	2.3 ± 0.5	0.14 ± 0.03	2.4 ± 0.5	0.12 ± 0.02	0.04 ± 0.01	0.22 ± 0.08	3.2 ± 0.7	6 ± 1	37 ± 8
	400	5.8 ± 22.7	0.06 ± 0.23	3.0 ± 11.9	0.02 ± 0.10	0.13 ± 0.52	1.17 ± 4.60	1.1 ± 4.5	15 ± 60	8 ± 30
51	Eq	1.7 ± 0.2	0.04 ± 0.01	2.8 ± 0.3	0.10 ± 0.01	0.05 ± 0.01	0.47 ± 0.06	6.3 ± 0.7	7 ± 1	80 ± 9
	400	-18.5 ± -13.5	-0.42 ± -0.31	-7.2 ± -5.2	0.05 ± 0.04	0.01 ± 0.01	-0.12 ± -0.10	2.3 ± 1.7	-23 ± -17	21 ± 15
64	Eq	5.8 ± 1.1	0.15 ± 0.03	0.7 ± 0.8	0.06 ± 0.02	0.10 ± 0.02	0.26 ± 0.04	19.1 ± 3.0	8 ± 1	52 ± 8
	400	100.7 ± 40.8	2.79 ± 1.13	53.8 ± 21.8	0.37 ± 0.16	0.25 ± 0.10	0.46 ± 0.20	9.1 ± 3.7	225 ± 91	33 ± 13
69	Eq	2.4 ± 0.2	0.04 ± 0.00	2.8 ± 0.3	0.04 ± 0.01	0.04 ± 0.00	0.37 ± 0.07	4.4 ± 0.4	10 ± 1	33 ± 4
	400	-30.9 ± -25.3	-0.75 ± -0.61	-19.1 ± -15.7	-0.18 ± -0.15	-0.14 ± -0.11	-0.85 ± -0.70	-4.4 ± -3.6	-110 ± -90	-21 ± -18
77	Eq	1.1 ± 0.3	0.02 ± 0.01	1.6 ± 0.3	0.02 ± 0.01	0.02 ± 0.00	0.11 ± 0.02	1.8 ± 0.3	3 ± 1	22 ± 3
	400	-16.9 ± -24.4	-0.55 ± -0.79	-9.0 ± -13.0	-0.07 ± -0.10	-0.07 ± -0.10	-0.14 ± -0.20	-2.0 ± -2.9	-65 ± -94	-10 ± -15

Table 5.2: pFe, pMn, pCo, pNi, pCu, pZn, pCd, pAl and pP export fluxes (in µmol.m^{-2}.d^{-1} or nmol.m^{-2}.d^{-1}) obtained by multiplying the ^{234}Th export flux with the Element to ^{234}Th ratio of large (>53 µm) particles. These fluxes were integrated between surface and Eq, where total ^{234}Th returns to equilibrium with ^{238}U, and at 400 m using a linear interpolation (see text for details).

Finally, despite large uncertainties at 400 m, it is interesting to compare elemental fluxes between Eq and 400 m in order to investigate the remineralization processes between both depths. Indeed, biogenic elements such as POC are known to be remineralized with depth (Marsay, 2012; Bruland and Lohan, 2003), leading to lower fluxes at 400m than Eq. This is mostly the case for pP fluxes (except at Station 38), pCd (except at stations 1, 26 and 38), pCo (except at stations 26 and 64) and pNi (except at stations 1, 26, and 64). On the contrary, higher pAl, pFe and pMn export fluxes at 400 m were observed except at stations 69 and 77 at which negative export fluxes were determined. Higher pCu export fluxes at 400m were mostly observed throughout the section, with the exceptions of Stations 13, 21, 51, 69 and 77. The increase of the flux with depth may indicate the authigenic formation of particle or scavenging of the element of interest by particles (Bruland and Lohan, 2003). These features are discussed in further details in sections 5.4.1 and 5.4.3.

5.3.3.3. PCA analysis

In order to have a better idea of the behavior of each elemental flux, a principal component analysis (PCA) of a larger multi-element dataset ($CaCO_3$, BSi, POC, pCd, pAl, pP, pTi, pMn, pFe, pCo, pNi, pCu and pZn) was performed (Figure 5.4). A first analysis was conducted including fluxes from all stations of the GEOVIDE transect and resulted in the fact that four principal components can explain 90% of the total dataset variance (Figure 5.4, Test 1). The first component (54% of the total variance) may indicate the lithogenic contribution for the fluxes as it describes 84% of pAl fluxes and 40% of pTi fluxes, both considered as lithogenic tracers. This component also explains > 60% of variances for pFe, pMn, pZn, pCu, pNi, pCo and pCd fluxes highlighting the strong influence of lithogenic materials on the export fluxes of these elements.

The second principal component (16 % of the total variance) probably describes the influence of diatoms on the fluxes, as it explains 70% of the variance of the biogenic silica (BSi) flux, constituent of the diatom frustules. This component is associated at 22% with pNi fluxes.

The third principal component (12% of the total variance) probably describes another influence of lithogenic materials as it explains 38% of the variance of pTi fluxes.

Finally, the fourth component (8% of the total variance) describes probably the influence of coccolithophorids on fluxes as it explains 66% of the variance for calcium carbonate ($CaCO_3$) flux, constituent of the coccolitophorid shells. The third component is associated at 14% with pCd fluxes.

In order to evaluate the biogenic influence on the trace element export fluxes, a second PCA analysis was ran without Station 1 (characterized by the highest or high particulate trace element fluxes; Figure 5.4, Test 2). Briefly, the same four components explain 91% of the total dataset variance. The lithogenic components (F1 and F3) are associated at > 77% with pAl, pFe, pMn, pCo, pNi, pCu and pZn. The BSi component (F2) does not describe significantly one elemental flux and the $CaCO_3$ component (F4) is associated at 33 and 13% with pCd and pMn fluxes.

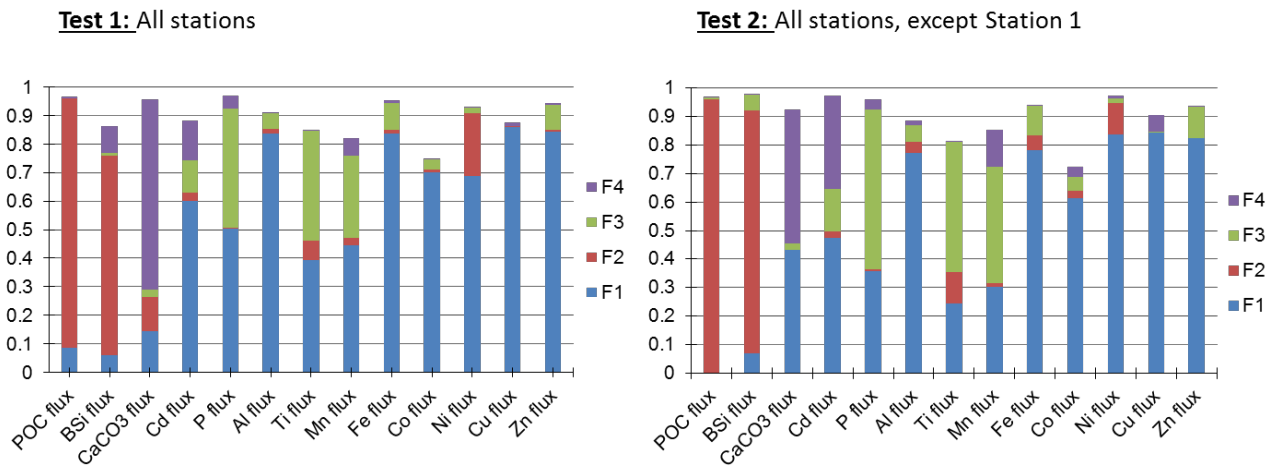

Figure 5.4: Variance of thirteen elemental fluxes determined at Eq at all stations (Test 1), at all stations except Station 1 (Test 2). The description of the components is provided in the text.

5.4. Discussion

5.4.1. The lithogenic contribution to fluxes

Possible candidates of lithogenic inputs include direct atmospheric inputs, glacial meltwater, advection of sediment-enriched water masses and lateral mixing with shallow coastal waters under continental influence.

Atmospheric deposition was specifically studied by (Shelley et al., 2016) who showed that atmospheric deposition was low throughout May-June 2014, and particularly in the Irminger and Labrador Seas, compared to southern regions under the influence of the Saharan dust plume (Shelley et al., 2015). Atmospheric deposition could have affected surface waters of Stations 1 and 51, but Gourain et al. (in prep.) show that atmospheric inputs are of low relative importance compared to lateral transports of lithogenic particles at considered stations. Therefore, in the following, the atmospheric contribution to fluxes is not considered any further.

Figure 5.5 presents the trace elements over Al flux ratios, determined at Eq, compared with the upper continental crust (UCC) ratio (Taylor and McLennan, 1985).

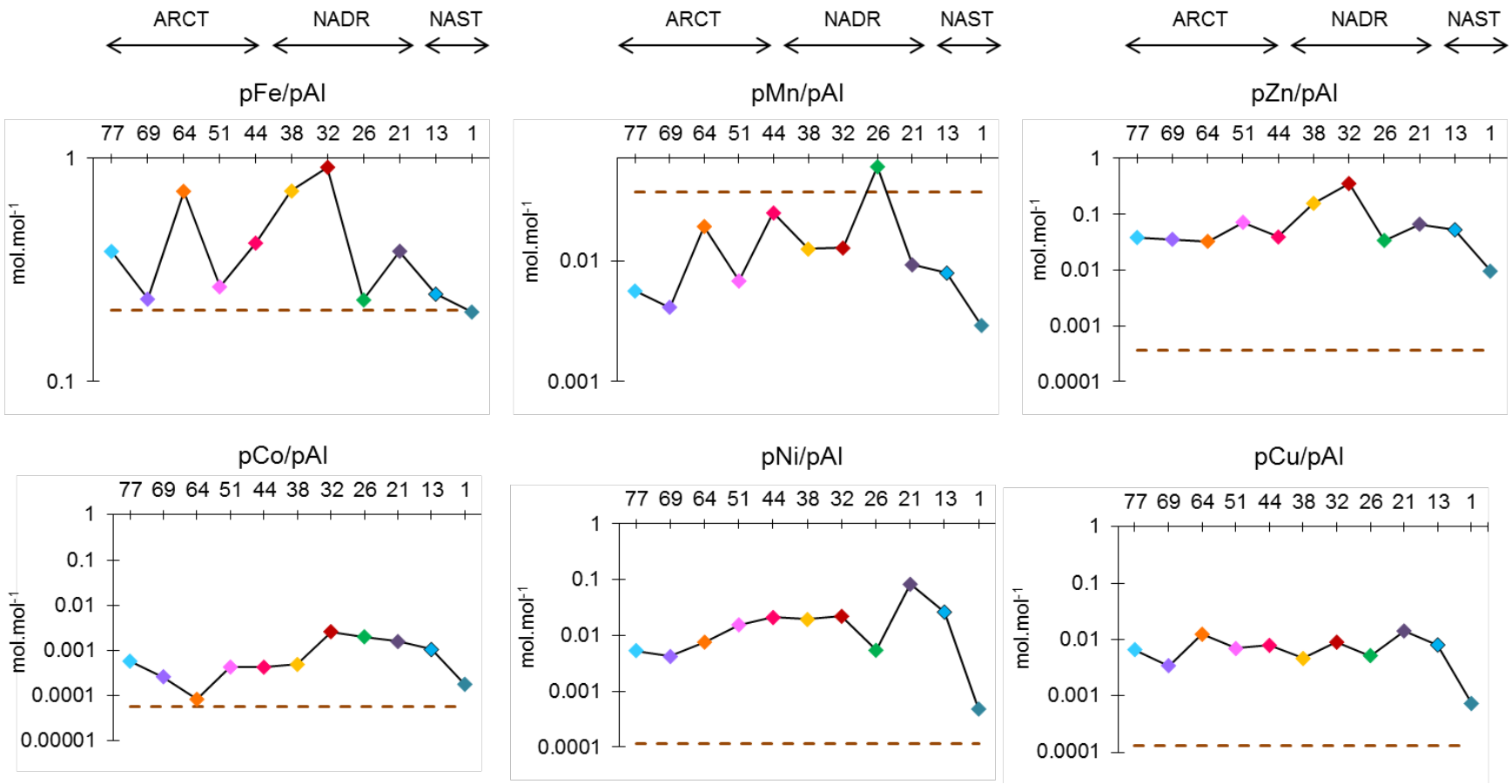

Figure 5.5: Molar ratios of the trace element over Al fluxes along the GEOVIDE transect determined at Eq. The brown horizontal dashed line represents the ratios determined in the upper continental crust (UCC) by Taylor and Mclennan (1985). Note that the y axis represents the values of the ratios in a logarithmic scale ($mol.mol^{-1}$).

It is possible to determine the contribution of lithogenic particles (derived from pAl fluxes), Fe oxyhydroxides (derived from Fe fluxes and using Al correction for lithogenic component) and Mn oxides (derived from Mn fluxes and using Al correction for lithogenic component), as proposed in Lam et al., 2015a (Figure 5.6). Al has the advantage that its concentration does not vary very much between upper continental crust (UCC Al = 8.04% by weight) and bulk continental crust (BCC Al = 8.41% by weight), so the estimate of lithogenic mass is not very sensitive to lithogenic source regions (Taylor and McLennan, 1995). Although Ti may be a better tracer for lithogenic Fe and Mn than Al as the ratios of Fe and Mn to Ti are less sensitive to source than ratios to Al (Lam et al., 2015a).

Lithogenic fluxes are therefore calculated using:

$$\text{Litho flux } (mg.m^{-2}.d^{-1}) = (\text{Al flux} \times 27 / 0.0804) / 1000 \quad \text{(Equation 5.3)}$$

where *Al flux* is the pAl flux in $\mu mol.m^{-2}.d^{-1}$; *0.0804* is the mass fraction of Al in the UCC.

Fe and Mn oxyhydroxides can be calculated by subtracting Fe and Mn associated with lithogenic material. Assuming that Fe oxyhydroxides are ferrihydrite and Mn oxyhydroxides to be birnessite, with formula weights 106.9 g $Fe(OH)_3$/mol Fe and 86.9 g MnO_2/mol Mn, it is possible to calculate:

$$Fe(OH)_3 \text{ flux } (mg.m^{-2}.d^{-1}) = ((\text{Fe flux} - (\text{Al flux} \times 0.21) \times 106.9) / 1000 \quad \text{(Equation 5.4)}$$

$$MnO_2 \text{ flux } (mg.m^{-2}.d^{-1}) = ((\text{Mn flux} - (\text{Al flux} \times 0.00367) \times 86.9) / 1000 \quad \text{(Equation 5.5)}$$

where *Fe flux*, *Al flux* and *Mn flux* are the fluxes in $\mu mol.m^{-2}.d^{-1}$

a) Fluxes at Eq

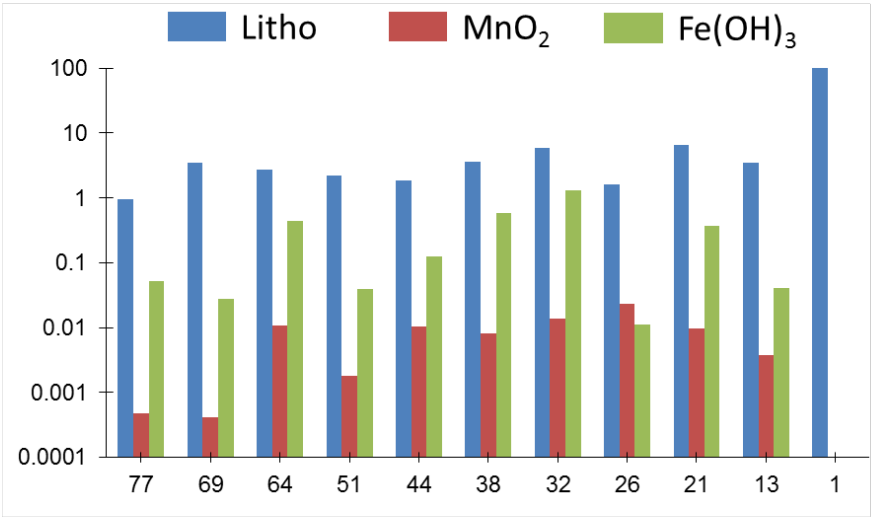

b) Fluxes at 400 m

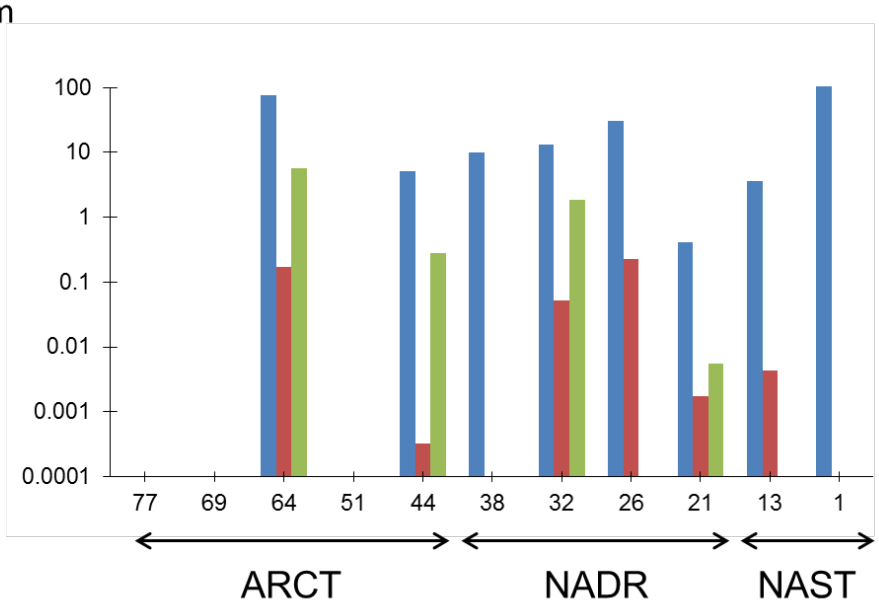

Figure 5.6: Export fluxes of lithogenic materials (Litho in mg.m^{-2}.d^{-1}), Mn oxides (MnO_2 in mg.m^{-2}.d^{-1}) and Fe oxides ($Fe(OH)_3$ in mg.m^{-2}.d^{-1}) determined at a) Eq and b) 400 m. Negative values have been set to zero.

Overall, lithogenic inputs are varying between 0.94 (Station 77) and 114 mg.m^{-2}.d^{-1} (Station 1) at Eq, and between 0 (Stations 77, 69, 51) and 189 mg.m^{-2}.d^{-1} (Station 1) at 400 m. Mn oxides were the highest at Station 26 (0.023 mg.m^{-2}.d^{-1} at Eq, and 0.229 mg.m^{-2}.d^{-1} at 400m) while Fe oxides ranged from 0 (Station 1) to 1.32 mg.m^{-2}.d^{-1} (Station 32) at Eq, and between 0 to 5.70 mg.m^{-2}.d^{-1} (Station 64) at 400 m. These different features are considered further below, with an emphasis on stations located close to margins (Stations 1 and 64), and where authigenic formation of Mn oxides can be considered (Station 26).

5.4.1.1. Margin inputs

High fluxes of trace elements were determined close to the Iberian and Greenland margins (Stations 1 and 64; Figure 5.3). These fluxes were associated with high beam attenuation (indicator of particle abundance, Figure 5.7) and low fluorescence signals between 120 and 350m for the Iberian Margin and between 80 and 200m for the Greenland Margin. However, export magnitudes as well as TE/Al ratios at Eq had different patterns between both margins.

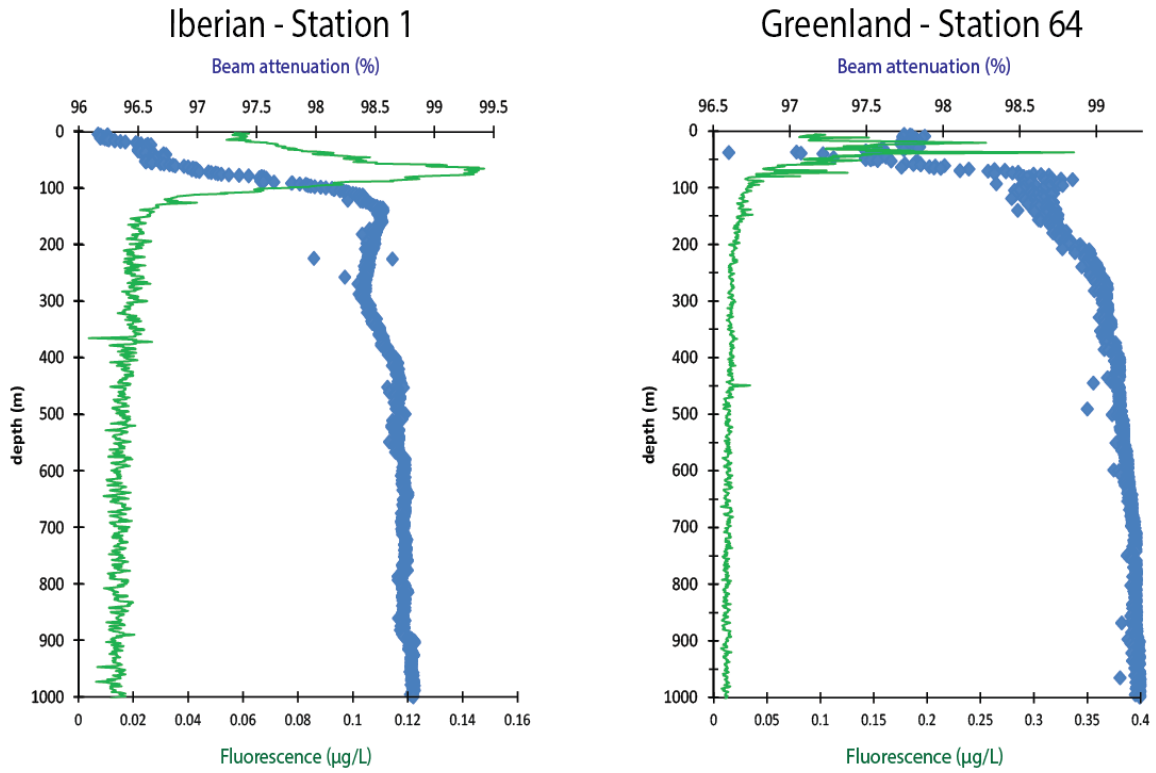

Figure 5.7: Beam attenuation (%; in blue) and fluorescence (µg.L^{-1}; in green) profiles of Stations 1 and 64, located near the Iberian and Greenland margins, respectively.

Close to the Iberian Margin all fluxes increased with depth, except Cd and P fluxes that decreased between Eq and 400 m, likely pointing out to a strong remineralization of these elements. Noteworthy, pFe/pAl and pCo/pAl molar ratios were equal to the upper continental crust (UCC) ratios of 0.21 mol.mol^{-1} and 0.057 mmol.mol^{-1} (Taylor and McLennan, 1985) at Eq, demonstrating the control of the pAl, pCo and pFe fluxes by lithogenic particles at this depth, and resulting in the highest lithogenic fluxes (115 mg.m^{-2}.d^{-1} and 190 mg.m^{-2}.d^{-1} at Eq) while the median value for other stations was about 3.1±1.8 mg.m^{-2}.d^{-1} (Figure 5.6). However,

this high lithogenic flux was not accompanied by any Mn or Fe oxide fluxes (negative values following Equations 5.4 and 5.5). Also, the pZn/pAl, pCu/pAl, pNi/pAl at Eq (9.6 $mmol.mol^{-1}$; 0.73 $mmol.mol^{-1}$; 0.48 $mmol.mol^{-1}$) were much higher than the UCC values (0.37 $mmol.mol^{-1}$; 0.13 $mmol.mol^{-1}$; 0.11 $mmol.mol^{-1}$; Taylor and McLennan, 1985), but the pCu/pZn (0.08 $mol.mol^{-1}$) and pNi/pZn (0.05 $mol.mol^{-1}$) ratios were close to those reported in sediment cores within the Tagus estuary (0.10 and 0.04 $mol.mol^{-1}$; Caçador et al., 1996), which is one of the largest estuaries of the European Atlantic coast (300 km^2). This estuary receives effluents from agricultural, industrial and urban sources that discharge important dissolved and particulate trace element concentrations (Cotté-Krief et al., 2000; Duarte et al., 2014; Duarte and Caçador, 2012), especially zinc (Cotté-Krief et al., 2000; Le Gall et al., 1999).

Therefore, these results strongly suggest that fluxes determined at Station 1 are under the anthropogenic influence of the Tagus estuary sediments that are laterally advected (Van Camp et al., 2000).

Near the Greenland Margin, at Station 64, particulate element fluxes increased with depth, with the exception of pP and pCd fluxes. At Eq, a low lithogenic flux (value 2.71 $mg.\ m^{-2}.d^{-1}$) was observed which is line with the greater values of the TE/Al ratios compared to the UCC ratios, except for Mn:Al which was below the UCC value (Figure 5.5). Indeed, the pFe/pAl, pZn/pAl and pCu/pAl ratios reached 0.71 $mol.mol^{-1}$, 33 $mmol.mol^{-1}$, 12 $mmol.mol^{-1}$.

However, pFe/pAl and pMn/pAl ratios were closer to those reported in Loring and Asmund (1996) in Greenland sediments (0.33 $mol.mol^{-1}$, 0.007 $mol.mol^{-1}$, respectively). Most of the elements in these sediments are associated to oxides and sulfide minerals (Loring and Asmund, 1995) which is confirmed by the high lithogenic, MnO_2 and $Fe(OH)_3$ fluxes observed at 400 m, reaching 76, 0.17 and 5.7 $mg.m^{-2}.d^{-1}$, respectively (Figure 5.6). The presence of these oxides could be also due to glacial meltwater inputs (e.g. Bhatia et al., 2013; Hawkings et al., 2014), although no decrease in salinity in surface waters could be detected.

Overall, high trace element fluxes at Station 64 might be partially explained by a lateral advection through the East Greenland Current of resuspended sediments.

5.4.1.2. Authigenic source and influence of Mn oxides

As seen in section IV.1.a, the stations described above were characterized by relatively high pMn export fluxes (1.89 and 2.79 µmol $pMn.m^{-2}.d^{-1}$ at Stations 1 and 64 at 400 m) but the highest pMn export flux was observed at Station 26 (2.97 µmol $pMn.m^{-2}.d^{-1}$; Figure 5.3), which was not located near a continental margin and which was not characterized by a high pAl export.

This interesting decoupling between high Mn and low Al fluxes has already been observed and was attributed to a distant shelf source of lithogenic particles (Lamborg et al., 2008). Indeed, the nepheloid layers sourced at the shelves loose particles by gravitational settling during the lateral advection but in the case of Mn, it has been shown that the dissolved Mn, remobilized from the shelf, oxidizes very slowly, enriching the particles during transport (Moffett and Ho, 1996). Long distance transport inducing a subsurface pMn maximum was also observed off California Coast (Lam and Bishop, 2008). Therefore, Station 26 could have been influenced by a strong lateral advection from the Eastern margins, loading pMn authigenically precipitated during the transport. This hypothesis is also in agreement with the highest MnO_2 flux observed at Station 26 reaching 0.023 and 0.229 $mg.m^{-2}.d^{-1}$ at Eq and 400 m.

At 400 m of Station 64, as stated in section 5.4.1.1, important pMn and MnO_2 fluxes were determined (2.79 µmol $pMn.m^{-2}.d^{-1}$; and 0.170 mg $MnO_2.m^{-2}.d^{-1}$; Figures 5.3 and 5.6) confirming the sediment inputs from the Greenland margin, that could have been laterally advected to this station (Bishop and Fleisher, 1987; Lam et al., 2006; Lam and Bishop, 2008).

Interestingly, these high Mn oxides fluxes determined at 400 m at Stations 26 and 64, and to a lesser extent at stations 13, 21 and 44 could have driven other TE fluxes. Indeed, Figure 5.8 confirmed the relationships between pCo, pCu, and pNi at 400 m (r^2 between 0.28 and 0.53, $p \leq 0.05$) highlighting that Mn oxides were probably involved in the scavenging of dissolved trace elements. Similarly, Fe oxides are associated with pCo and pNi fluxes at 400m (Figure 5.8, right), illustrating the strong scavenging of Co into Fe and Mn oxides, as evidenced recently by Saito et al. (2016) defining the Mn oxides as the responsible phase for the transport of Co in depth. However, at Eq depth, only pZn fluxes were correlated to pFe oxides fluxes (r^2=0.50, p=0.01)

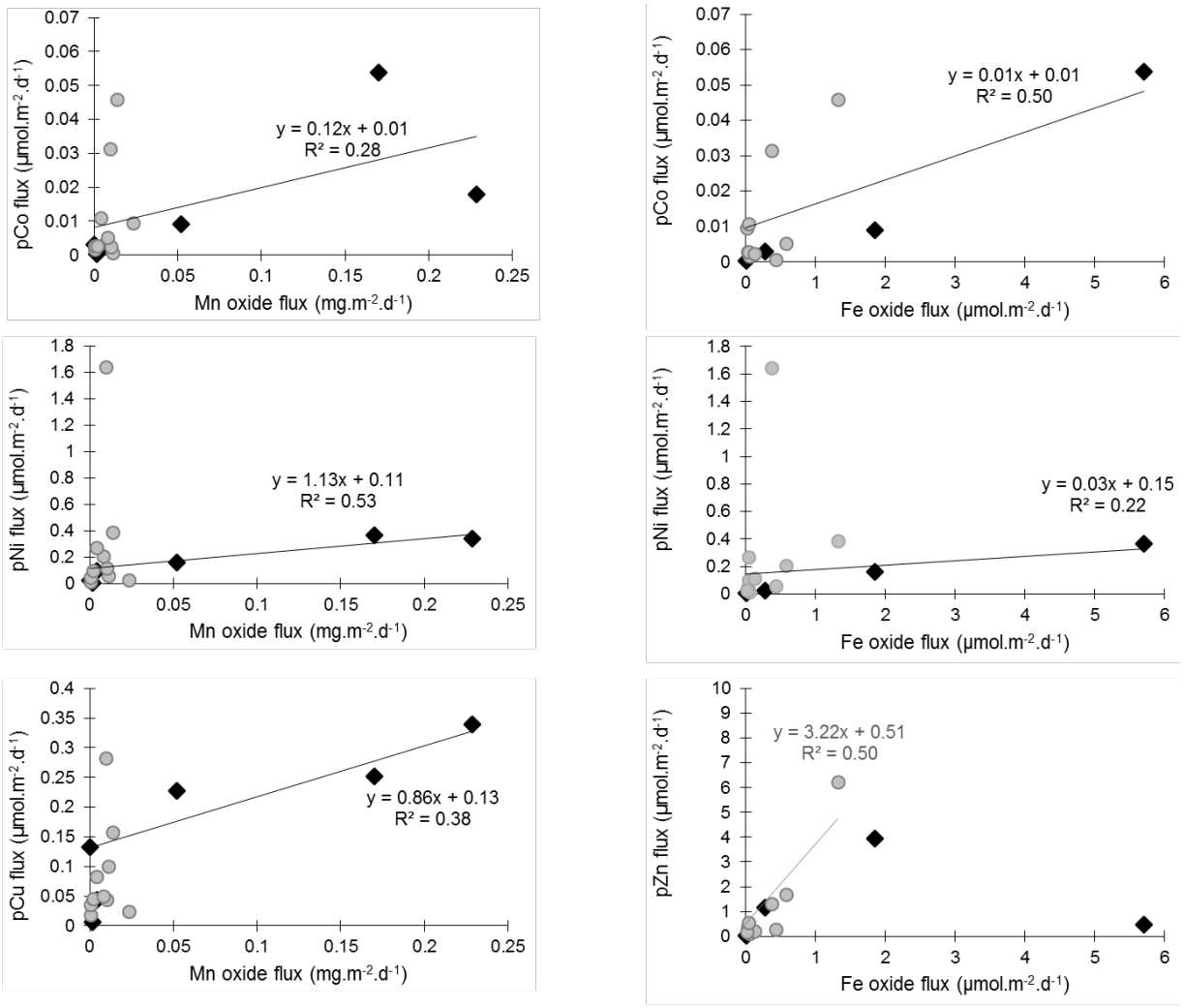

Figure 5.8: (left) Relationships between pCo, pNi and pCu fluxes versus Mn oxides fluxes (µmol.m^{-2}.d^{-1}), and (right) relationships between pCo, pNi and pZn fluxes versus Fe oxides fluxes. The grey circles and the black diamonds represent respectively the fluxes estimated at Eq and 400 m.

Overall, the lithogenic particles at stations close to the margins strongly participated to the export fluxes of TE, while high Mn fluxes were observed in the open ocean, probably due to authigenic formation of Mn oxides that are associated with pCo, pNi, and pCu fluxes at 400 m. Fe oxides seem to exert an influence on pZn fluxes at Eq and, on pCo and pNi fluxes at 400m.

5.4.2. The biogenic contribution to fluxes

5.4.2.1. Influence of bloom staging and remineralization processes

The GEOVIDE cruise was carried out in late spring (May-June), a period during which the bloom has already developed and incorporated nutrients, leading potentially to the export of biogenic elements.

In the subtropical and oligotrophic NAST province, Station 13 was sampled during the decline of the bloom (8 weeks after the bloom peak, see Figure 9 in Chapter 3). Moreover, the bloom intensity was low (< 0.7 mg Chl-*a*.m^{-3}) resulting in small POC fluxes (Lemaitre et al., in prep) and likely low trace elements export fluxes.

Higher TE export fluxes were determined within the NADR province, sampled from 0 to 4 weeks after the bloom peak. Interestingly, low TE export fluxes were determined in the ARCT province. This province was divided between the Labrador basin, sampled during the decline of the bloom (Station 69: 7 weeks after the bloom peak) and the Irminger Sea basin, sampled during the bloom development (Station 44: 1 week after the bloom peak).

Station 44, in the Irminger Sea, was characterized by high pP and pMn but, by low pFe and pZn export fluxes, highlighting a decoupling between these groups of elements. This station was also characterized by a low POC export which was related to an accumulation phase of biomass rather than an export phase (Lemaitre et al., a, in prep.). However, an important remineralization event in the mesopelagic layer was evidenced through the Ba_{xs} proxy at this station indicating a past production and export event (Lemaitre et al., in prep). Both results suggest either pFe and pZn were accumulated in surface waters unlike pP and pMn which

would be preferentially exported, or Fe and Zn were limiting during the sampling and thus non exported and recycled efficiently.

In the Labrador Sea, at Stations 69 and 77, negative fluxes at 400 m were determined, and are associated with deep remineralization fluxes (Lemaitre et al., in prep.) Interestingly, at Station 64, Ba_{xs} proxy indicated a strong POC remineralization flux, but higher TE fluxes at 400 m than Eq were determined. This feature could be related to the nutrient gradient observed in the Labrador Sea with NO_3^- decreasing from 4.55 to 0.33 µmol.L^{-1} and $Si(OH)_4$ decreasing from 4.50 to 1.10 µmol.L^{-1}, at Stations 64 and 77 respectively. This is in line with the different stage of the bloom sampled as Station 64 was sampled 3 weeks after the bloom peak and Stations 69 and 77 were sampled 7 and 4 weeks after the bloom peak. At station 64, nutrients such as PO_4^{3-}, dMn, dFe and dZn were probably less limiting than Station 77, which resulted to their greater export.

Interestingly the time lag of sampling seems to influence the different magnitude of the pMn fluxes at Eq as the stations sampled during the decline of the bloom were characterized by lower pMn fluxes (r^2=0.46 and $p<0.05$; n=10). However, no specific trends were observed for the other trace elements (pCo, pCd, pNi, pCu).

5.4.2.2. Importance of phytoplankton to the particulate element fluxes

Biogenic trace elements are required by phytoplankton communities for a number of intracellular functions (see Chapter 1). In order to investigate the biogenic contribution to export fluxes, trace element to carbon (pTE/POC) (Figure 5.9) and trace element to phosphorus (pTE/pP) (Figure 5.10) ratios for fluxes at Eq were compared to ratios of cultured phytoplankton cells, despite large uncertainties associated with this approach, as these published ratios correspond to intracellular quotas.

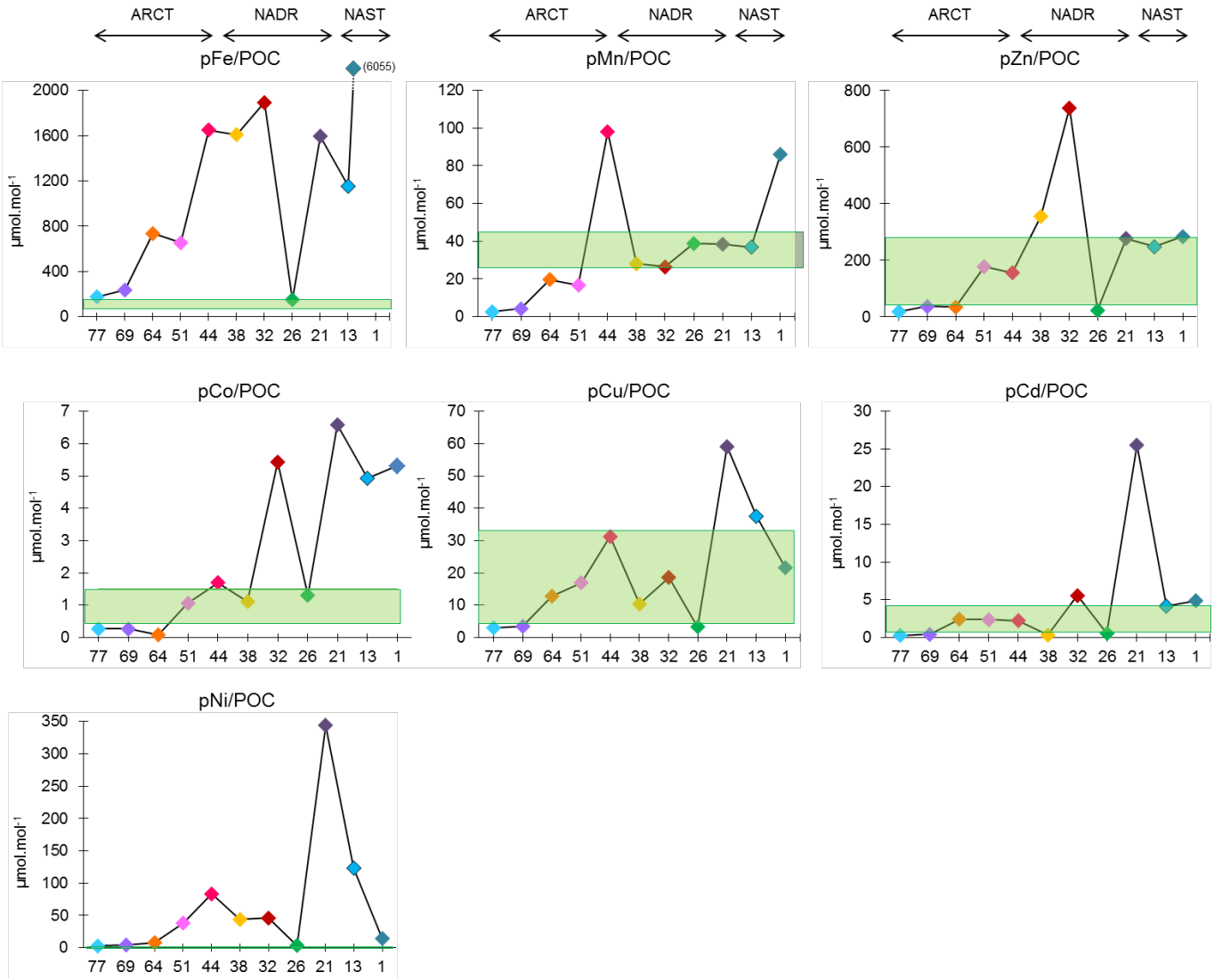

Figure 5.9: Carbon normalized Fe, Mn, Zn, Co, Cu, Cd and Ni molar ratios for export fluxes determined at Eq, from Station 1 (Iberian Margin; right) to Station 77 (Newfoundland Margin; left). The green rectangles indicate the range of intracellular metal stoichiometries presented by Twining et al. (2015), Muggli et al. (1996), Muggli and Harrison (1996) and Sunda and Huntsman (1995 a and b).

pZn/POC, pMn/POC, pCd/POC and pCu/POC flux ratios as pZn/pP, pMn/pP, pNi/pP, pCo/pP and pCd/pP at Eq were generally similar to cellular TE/C molar and TE/P ratios reported for phytoplankton cultures (Bruland et al., 1991; Muggli et al., 1996; Muggli and Harrison, 1996; Sunda and Huntsman, 1995; Sunda and Huntsman, 1995; Twining and Baines, 2012; Twining et al., 2015). Station 44 was sampled during the bloom (1 week after the peak bloom) and was characterized by greater pCo and pMn exports compared to POC, which is probably due to the fact that the POC export flux at this station was the lowest of the entire section (Lemaitre

et al., in prep., Chapter 4) indicating that export had not yet started. At this station, pZn/POC, pCu/POC and pCd/POC flux ratios were within the phytoplankton range indicating that the export of TEs was driven by phytoplankton particles.

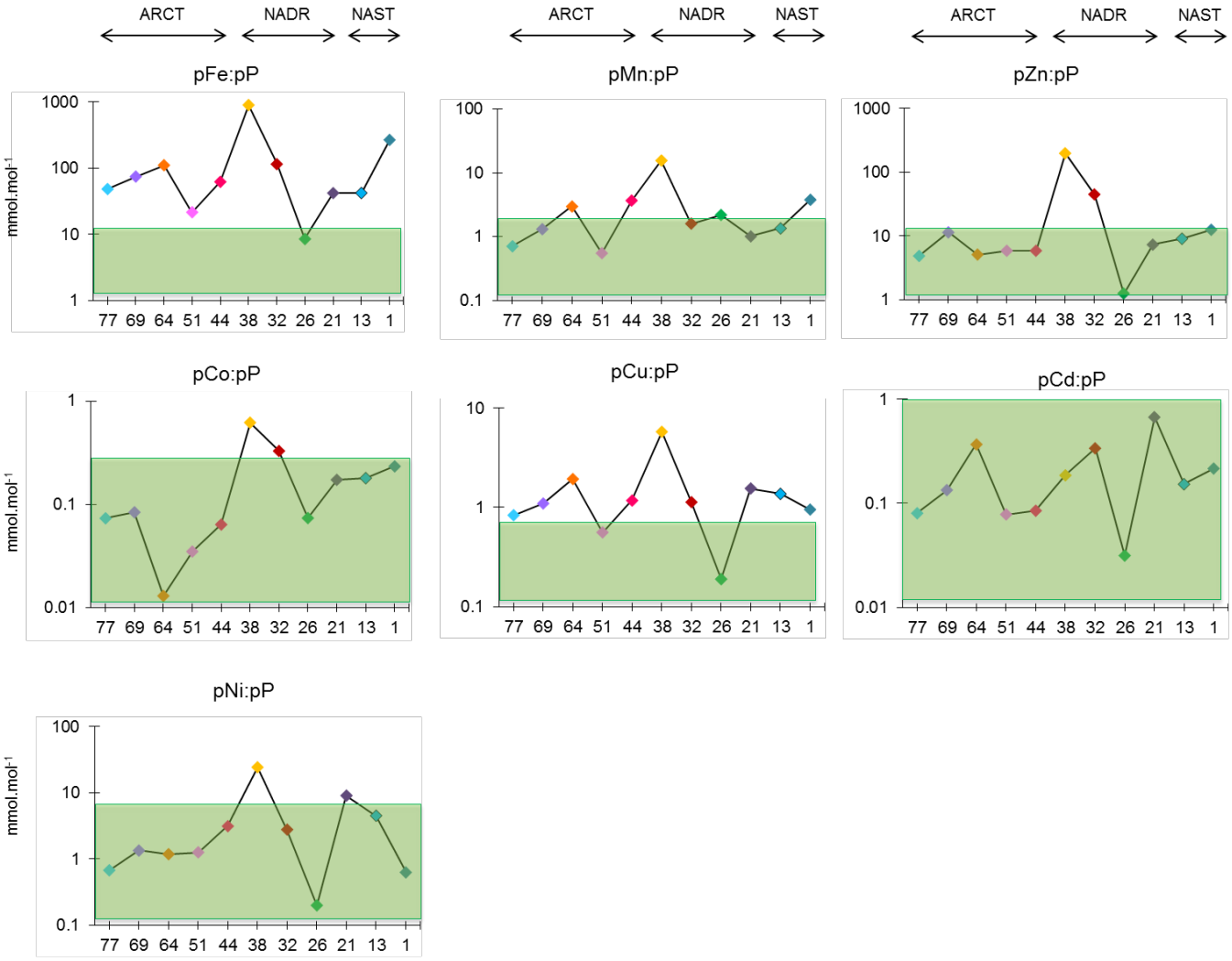

Figure 5.10: Phosphorus normalized Fe, Mn, Zn, Co, Cu, Cd and Ni molar ratios for export fluxes determined at Eq, from Station 1 (Iberian Margin; right) to Station 77 (Newfoundland Margin; left). The green rectangles indicate the range of intracellular metal stoichiometries presented by Twining and Baines (2013).

Interestingly pFe and pNi over C were higher than reported cell ratios at most stations except at Stations 26 and 77 that were characterized by Fe/C and Ni/C ratios similar to cell quotas. A similar observation can be made at Station 26 for Fe/P and Cu/P ratios. Fe and Ni are known to be scavenged onto particles with depth (Goldberg, 1954; Twining et al., 2015b) and it is

usual to observe an increase of the bulk quota ratios compared to the cellular quota ratio (Collier and Edmond, 1984; King et al., 2012; Twining et al., 2014). This can be caused by the inclusion of detrital, authigenic and lithogenic particles on the filters leading to an increase of the Fe/C and Ni/C ratio, as observed in Figure 5.9. Moreover, the intracellular Fe/C quota ranged usually between 30-160 μmol.mol^{-1} for diatoms and coccolithophorids (Muggli et al., 1996; Muggli and Harrison, 1996; Twining and Baines, 2013) but Sunda and Huntsman (1995) have measured a Fe/C ratio equal to 1700 μmol.mol^{-1} highlighting the high variation of the ratio and the difficulty to generalize the intracellular phytoplankton TE/C ratios as they vary between taxa and regions depending on the environmental conditions (e.g. nutrients, sunlight limitations; Twining and Baines, 2013).

Therefore, it is important to look at indicators of the phytoplankton community structure, varying along the GEOVIDE transect, as it may influence the different intracellular and export ratios.

5.4.2.2.1. Diatom dominated stations

The fucoxanthin pigment, can be linked to the presence of diatoms, prymnesiophytes, raphidophytes and chrysophytes (e.g. Wright and Jeffrey, 1987) and was detected all along the transect (see Figure 3 in Chapter 3). Within the NADR province, the fucoxanthin pigment accounted for 21±3% in the Icelandic basin (Stations 32 and 38), for 40±2% in the Western European basin and for 18±9% in the NAST province (Stations 1 and 13). Significant concentrations (77±8% of the total taxonomic pigments) were determined in the ARCT province (Stations 44, 51, 64, 69 and 77), and were associated with the highest BSi fluxes (Lemaitre et al., in prep.), likely pointing out to the export of diatoms.

The comparison between the intracellular and the export TE/POC ratios (Figure 5.9) highlighted that stations of the ARCT province were characterized by pMn/POC, pFe/POC, pZn/POC and pCu/POC flux ratios lower but relatively close to the diatom quota (45 μmol Mn.mol^{-1} C; 76 μmol Fe.mol^{-1} C; 42 μmol Zn.mol^{-1} C; and 4.2 μmol Cu.mol^{-1} C; Twining et al., 2015) suggesting that diatoms were contributing to the export of trace elements at Eq at these stations.

Moreover, a good correlation between the fluxes of Zn, known to be abundant in diatoms (Twining and Baines, 2013) and BSi has been demonstrated by Lamborg et al., (2008). In this study, two relationships were observed (Figure 5.11). Station 26 and the stations of the ARCT province were characterized by high BSi and low pZn export fluxes, while the other stations of the NADR province were characterized by higher pZn export fluxes. Interestingly, the Zn/Si ratio determined in phytoplankton cells by Twining et al. (2004, i.e. 2×10^{-4} $mol.mol^{-1}$) fits between the two slope values.

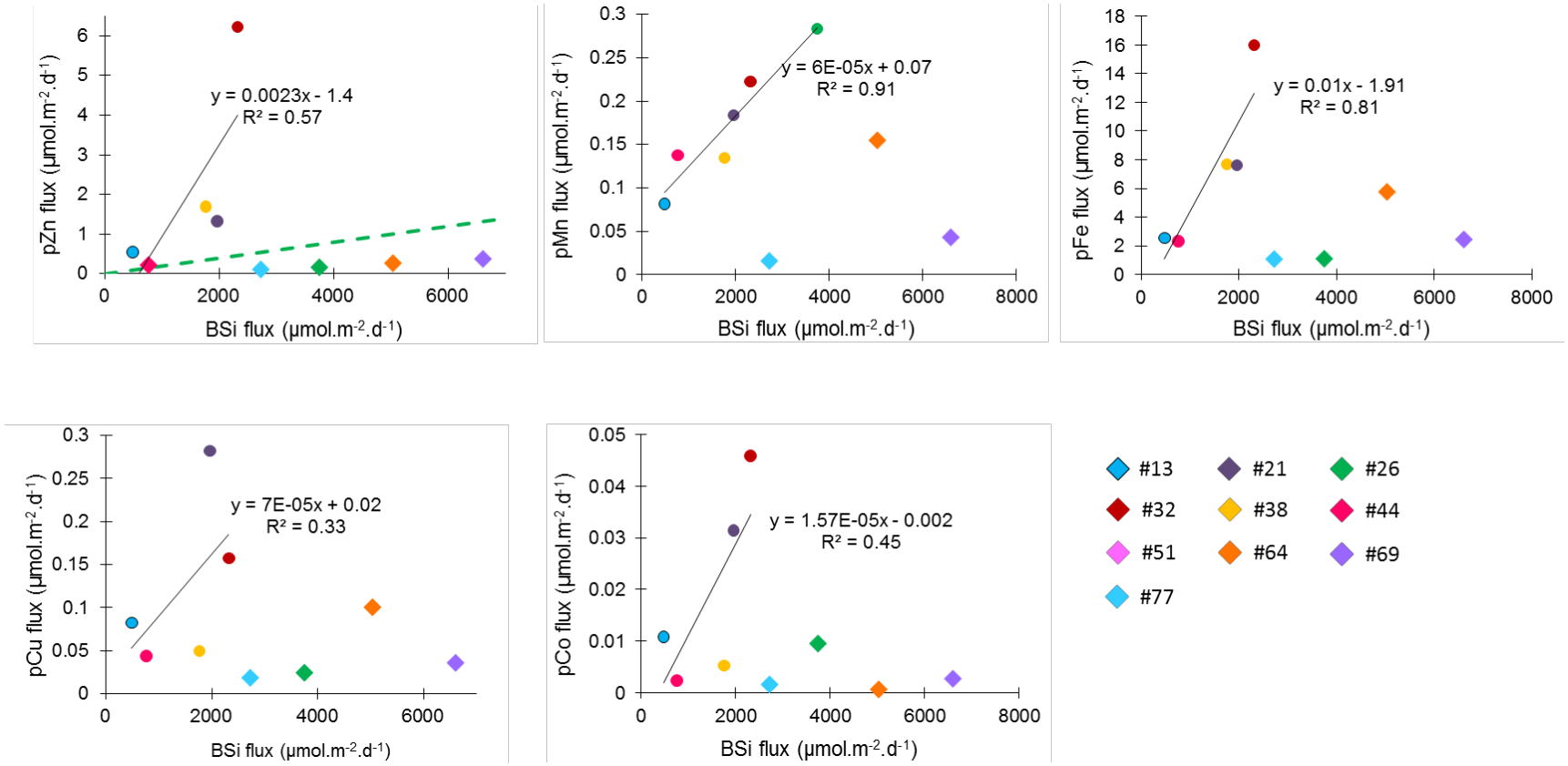

Figure 5.11: Relationships between pZn, pMn, pFe, pCu, pCo and BSi export fluxes at Eq. In the graph showing pZn and BSi exports, the green dashed line represents the averaged Zn/Si ratio measured in diatom phytoplankton cells (i.e. 2×10^{-4} mol.mol^{-1}; Twining et al., 2004).

Overall, diatoms drive biogenic TE fluxes in the ARCT province, as it was shown for POC along the same transect (Lemaitre et al., in prep.), and as shown by the PCA analysis, but this contribution was not homogeneous at other stations were diatoms were present, suggesting that environmental conditions, such as TE limitations in surface waters, limit the export to depth.

5.4.2.2.2. Coccolithophorids dominated stations

The highest concentration of the 19'Hexanoyloxyfucoxanthin pigment, a tracer of coccolithophorids was determined within the NADR province and in particular in the Icelandic basin (Stations 32 and 38, averaging 56±2% of the total pigments). This pigment was also detected in the western European basin and in the NAST province (25±1% and 31±0.3% of the total pigments, respectively) indicating the presence of coccolithophorids (see Figure 3 in Chapter 3).

At stations not influenced by margin inputs, the highest TE fluxes were observed within the NADR province (Figure 5.4), suggesting a contribution of coccoliphorids to the fluxes. Indeed, at these stations, $CaCO_3$ fluxes were the highest reaching 2.61±0.22 $mmol.m^{-2}.d^{-1}$ at Eq of Station 38.

Interestingly, the comparison between phytoplankton intracellular and export TE/POC ratios (Figure 5.9**)** highlighted that Stations 32 and 38 were characterized by pMn/POC flux ratios close to the coccolithophorid quota (26 µmol $Mn.mol^{-1}$ C; Twining et al., 2015) suggesting that coccolithophorids were indeed contributing to the export of Mn at Eq, as POC (Lemaitre et al., in prep). However, the pFe/POC, pZn/POC and pCo/POC flux ratios at these stations were greater than the intracellular quota, possibly due to adsorption of dissolved Fe, Zn and Co onto Mn and Fe oxides at this station (1.32 $mg.m^{-2}.d^{-1}$, the highest flux at Eq, Figure 5.6), often referred as scavengers of the sea (Goldberg, 1954).

Nevertheless, the contribution of coccolithophorids to export these trace elements was indicated by the relationship between the pFe (slope=3.13, r^2=0.40 and p=0.05), pMn

(slope=0.06, r^2=0.38 and p=0.06), pZn (slope=1.24, r^2=0.39 and p=0.05) and pCo (slope=0.01, r^2=0.22 and p=0.17) and $CaCO_3$ exports at Eq (Figure 5.12). Moreover, Stations 32 and 38, in the Icelandic basin, were characterized by pFe/pP flux ratios reaching 115 and 895 $mmol.mol^{-1}$ but also by high pFe:pAl flux ratios (0.91 and 0.72 $mol.mol^{-1}$) pointing out to an important contribution of biological particles to export Fe.

Finally, diatom-dominated stations (ARCT) have lower Fe/P quotas, as well as Mn/P, Co/P and Zn/P quotas, compared to coccolithophorids-dominated stations (e.g. station 38), which is in agreement with previous studies (Ho et al., 2003; Quigg et al., 2003; Twining and Baines, 2013).

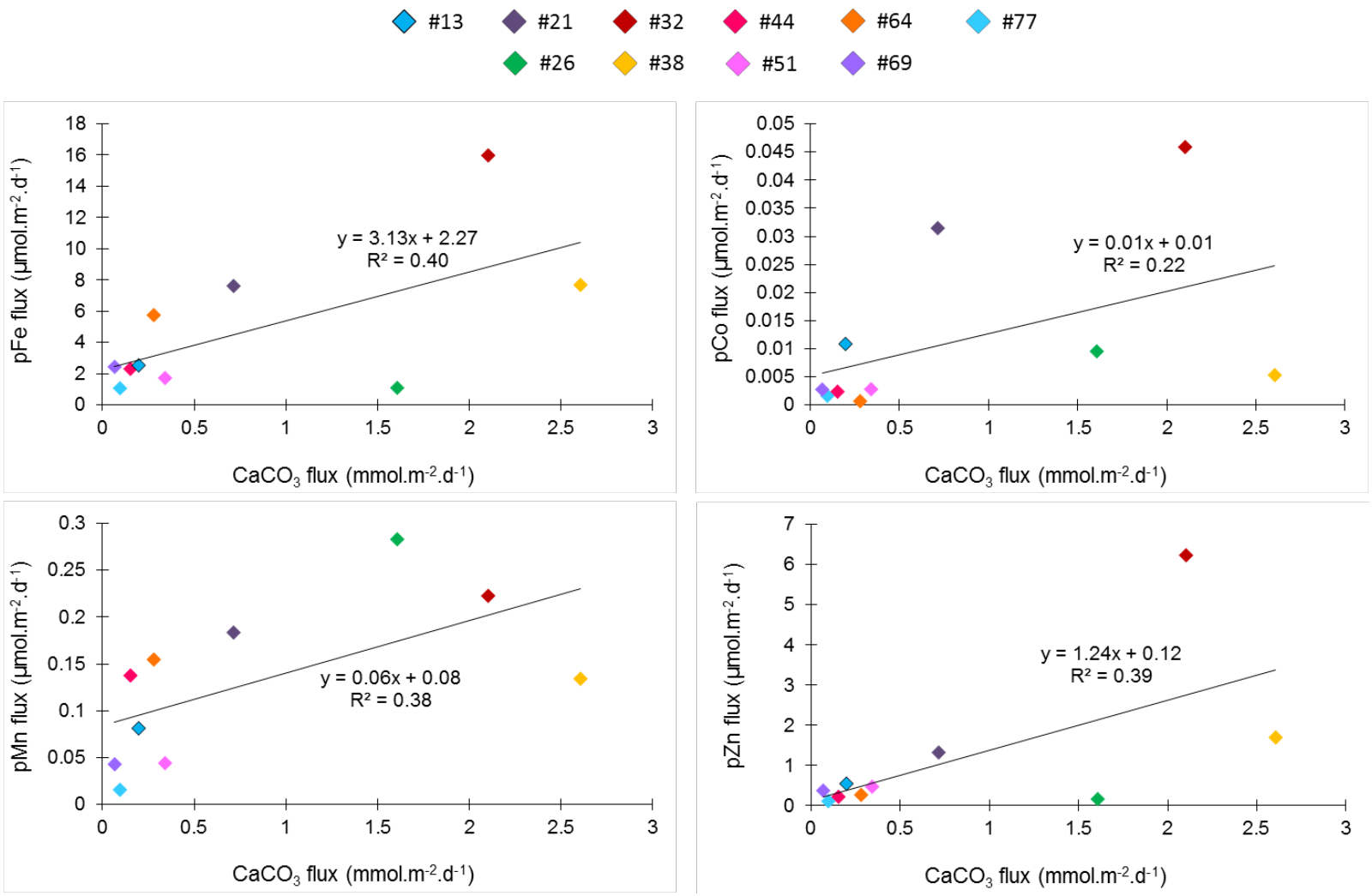

Figure 5.12: Relationship between pFe, pCo, pMn, pZn and $CaCO_3$ export fluxes at Eq.

Overall, diatom-dominated community in the ARCT province seems to drive pZn fluxes while coccolithophorid-dominated community drives pFe, pMn and pZn fluxes.

5.5. Conclusion

Using the ^{234}Th approach and the elemental composition of large, sinking particles, this study investigated the trace element export fluxes in the North Atlantic during the spring 2014 (GEOVIDE cruise). The export fluxes of trace elements appear to be controlled by a range of processes.

Lithogenic material is present everywhere in the section, but mainly controls the fluxes near the Iberian and Greenland margins, where the highest TE fluxes were determined. Close to the Iberian Margin, anthropogenic inputs may also enhance the TE fluxes, especially Zn. In the open ocean, authigenic formation of Mn oxides were associated with high pCu, pNi and pCo fluxes at 400m, while Fe oxides were influencing pZn fluxes at Eq, and pCo and pNi fluxes at 400m.

Diatoms in the ARCT province seem to export TE but at lower quota than the one measured in phytoplankton, possibly suggesting TE limitations in surface waters, in line with the decline of the bloom. In the NADR province, the $CaCO_3$ fluxes were correlated with the TE fluxes indicating that coccolithophorids enhanced the trace element export fluxes.

Acknowledgements

We are grateful to the helpful captain and crew of the R/V Pourquoi Pas?, as well as Fabien Perault and Emmanuel De Saint Léger from the CNRS DT-INSU who assisted to *in situ* pump deployments.

Special thanks to Maxi Castrillejo (UAB, Spain), Yi Tang (Queens College, USA), Catherine Jeandel (LEGOS, France), Virginie Sanial (WHOI, USA), Raphaëlle Sauzède (LOV, France) and Lorna Foliot (LSCE, France) for their help at sea and for the pump coordination and

collaboration. We would also like to thank Phoebe Lam for providing two modified McLane ISP. Claire Bollinger from the Pôle Spectrométrie Océan (PSO, Brest, France) greatly helped during the element analysis by ICP-MS. We acknowledge Y. Germain and M. Ponzevera for the use of the clean lab at IFREMER. Finally, we would like to thank the co-chief scientists Pascale Lherminier and Géraldine Sarthou. This work was funded by the Flanders Research Foundation (project G071512N), the Vrije Universiteit Brussel (Strategic Research Program, project SRP-2), the French ANR Blanc GEOVIDE (ANR-13-BS06-0014), ANR RPDOC BITMAP (ANR-12-PDOC-0025-01), IFREMER, CNRS-INSU (programme LEFE), INSU OPTIMISP and Labex-Mer (ANR-10-LABX-19).

Table S5.1: Particulate concentrations of pFe (nmol.L^{-1}), pMn(pmol.L^{-1}), pZn (pmol.L^{-1}), pCo (pmol.L^{-1}), pCd (pmol.L^{-1}), pCu (pmol.L^{-1}), pNi (pmol.L^{-1}), pP (nmol.L^{-1}), and pAl (nmol.L^{-1}) in the large size fraction (LSF; > 53 µm).

Station #	Lat °N	Long °E	Depth m	pFe nmol.L^{-1}	pMn pmol.L^{-1}	pZn pmol.L^{-1}	pCo pmol.L^{-1}	pCd pmol.L^{-1}	pCu pmol.L^{-1}	pNi pmol.L^{-1}	pP nmol.L^{-1}	pAl nmol.L^{-1}
1	40.333	-10.04	25	1.050 ± 0.001	15.0 ± 0.7	47 ± 1	0.993 ± 0.005	0.98 ± 0.04	3.3 ± 0.1	1.4 ± 0.2	4.307 ± 0.008	4.9 ± 0.1
1	40.333	-10.04	80	0.345 ± 0.009	4.8 ± 0.3	20 ± 1	0.16 ± 0.01	0.039 ± 0.006	2.0 ± 0.1	2.8 ± 0.3	0.60 ± 0.02	2.054 ± 0.009
1	40.333	-10.04	120	0.63 ± 0.04	10.1 ± 0.4	7.3 ± 0.2	0.20 ± 0.01	0.037 ± 0.001	1.43 ± 0.05	2.5 ± 0.1	0.435 ± 0.009	2.66 ± 0.06
1	40.333	-10.04	250	1.44 ± 0.03	24.2 ± 1.3	8.9 ± 0.3	0.49 ± 0.02	0.013 ± 0.000	2.59 ± 0.04	3.44 ± 0.09	0.283 ± 0.005	7.09 ± 0.05
1	40.333	-10.04	550	3.20 ± 0.05	49.8 ± 0.5	910 ± 12	1.028 ± 0.007	0.118 ± 0.002	12.7 ± 0.1	10.8 ± 0.2	0.893 ± 0.009	15.3 ± 0.2
1	40.333	-10.04	850	1.31 ± 0.01	18.4 ± 0.1	9.0 ± 0.7	0.438 ± 0.006	0.010 ± 0.000	2.7 ± 0.1	4.01 ± 0.06	0.135 ± 0.001	6.7 ± 0.1
13	41.383	-13.89	30	0.093 ± 0.006	2.5 ± 0.3	26 ± 1	0.54 ± 0.05	0.48 ± 0.02	3.3 ± 0.2	12.6 ± 0.5	3.2 ± 0.2	0.31 ± 0.02
13	41.383	-13.89	80	0.049 ± 0.004	1.8 ± 0.1	9.0 ± 0.7	0.07 ± 0.02	0.028 ± 0.003	1.14 ± 0.09	2.9 ± 0.2	0.273 ± 0.008	0.259 ± 0.005
13	41.383	-13.89	120	0.082 ± 0.004	3.8 ± 0.2	4.0 ± 0.4	0.14 ± 0.02	0.095 ± 0.002	2.6 ± 0.1	4.4 ± 0.4	0.34 ± 0.01	0.44 ± 0.01
13	41.383	-13.89	250	0.136 ± 0.007	6.8 ± 0.4	11.8 ± 0.3	0.11 ± 0.01	0.031 ± 0.001	1.89 ± 0.06	2.8 ± 0.3	0.213 ± 0.002	0.663 ± 0.003
13	41.383	-13.89	400	0.096 ± 0.007	3.8 ± 0.1	1.4 ± 0.4	0.09 ± 0.02	0.040 ± 0.002	1.90 ± 0.06		0.13 ± 0.01	0.46 ± 0.01
13	41.383	-13.89	850	0.116 ± 0.005	5.9 ± 0.1	2.8 ± 0.2	0.12 ± 0.01	0.014 ± 0.000	1.53 ± 0.03	1.8 ± 0.1	0.065 ± 0.005	0.40 ± 0.01
21	46.544	-19.67	15	0.343 ± 0.008	7.3 ± 0.2	58 ± 1	1.49 ± 0.04	6.29 ± 0.15	12.0 ± 0.1	70 ± 2	8.5 ± 0.1	0.609 ± 0.004
21	46.544	-19.67	60	0.16 ± 0.01	4.1 ± 0.3	29 ± 1	0.50 ± 0.03	1.34 ± 0.03	6.1 ± 0.3	42 ± 2	3.3 ± 0.1	0.69 ± 0.03
21	46.544	-19.67	100	0.024 ± 0.001	2.0 ± 0.1	4.0 ± 0.2	0.12 ± 0.01	0.192 ± 0.006	1.9 ± 0.1	4.0 ± 0.1	0.437 ± 0.007	0.271 ± 0.001
21	46.544	-19.67	200	0.157 ± 0.007	10 ± 1	13.1 ± 0.5	0.083 ± 0.003	0.099 ± 0.016	2.16 ± 0.06	3.0 ± 0.2	0.354 ± 0.007	0.389 ± 0.008
21	46.544	-19.67	500	0.034 ± 0.001	3.8 ± 0.07	7.9 ± 0.3	0.047 ± 0.003	0.095 ± 0.005	1.42 ± 0.06	1.2 ± 0.1	0.513 ± 0.005	0.255 ± 0.004
21	46.544	-19.67	810	0.056 ± 0.002	6.6 ± 0.2	4.0 ± 0.1	0.095 ± 0.003	0.016 ± 0.001	1.74 ± 0.09	1.07 ± 0.03	0.114 ± 0.002	0.350 ± 0.005
26	50.278	-22.6	30	0.063 ± 0.002	6.8 ± 0.1		0.76 ± 0.02				10.6 ± 0.3	
26	50.278	-22.6	83	0.053 ± 0.002	2.6 ± 0.2	8.8 ± 0.2	0.186 ± 0.000	0.65 ± 0.02	3.47 ± 0.05	3.8 ± 0.3	2.40 ± 0.04	0.555 ± 0.009
26	50.278	-22.6	153	0.023 ± 0.002	29 ± 1	17.5 ± 0.5	0.062 ± 0.002	0.120 ± 0.004	1.04 ± 0.02	1.00 ± 0.06	0.351 ± 0.003	0.287 ± 0.005
26	50.278	-22.6	400	0.053 ± 0.002	11.5 ± 0.6	1.9 ± 0.1	0.069 ± 0.007	0.046 ± 0.002	1.32 ± 0.01	1.3 ± 0.2	0.198 ± 0.004	0.356 ± 0.001
32	55.506	-26.71	30	0.41 ± 0.02	5.5 ± 0.8	170 ± 2	1.23 ± 0.07	1.16 ± 0.07	2.7 ± 0.2	3.4 ± 0.7	3.5 ± 0.1	0.41 ± 0.02
32	55.506	-26.71	60	0.134 ± 0.003	1.7 ± 0.09	20.2 ± 0.4	0.21 ± 0.02	0.132 ± 0.001	1.67 ± 0.05	14.5 ± 0.3	0.328 ± 0.002	0.084 ± 0.001
32	55.506	-26.71	100	0.046 ± 0.001	1.5 ± 0.2	24.3 ± 0.9	0.17 ± 0.02	0.47 ± 0.01	3.25 ± 0.09	7.7 ± 0.4	1.34 ± 0.02	0.198 ± 0.004
32	55.506	-26.71	200	0.229 ± 0.006	2.2 ± 0.1	6.2 ± 0.5	0.040 ± 0.004	0.046 ± 0.001	1.53 ± 0.06	1.6 ± 0.3	0.193 ± 0.004	0.198 ± 0.005
32	55.506	-26.71	600	0.052 ± 0.001	3.9 ± 0.3	23.7 ± 0.5	0.040 ± 0.002	0.007 ± 0.000	0.74 ± 0.05	0.22 ± 0.08	0.063 ± 0.002	0.163 ± 0.004
32	55.506	-26.71	850	0.107 ± 0.003	16.1 ± 0.4	7.6 ± 0.4	0.15 ± 0.01	0.038 ± 0.001	2.29 ± 0.07	1.85 ± 0.08	0.205 ± 0.005	0.52 ± 0.01
32	55.506	-26.71	1678	0.350 ± 0.011	28 ± 1	3.9 ± 0.3	0.40 ± 0.01	0.014 ± 0.002	5.17 ± 0.14	1.8 ± 0.1	0.134 ± 0.002	0.88 ± 0.03
38	58.843	-31.27	60	0.42 ± 0.01	7.1 ± 0.4	93 ± 3	0.27 ± 0.01	0.032 ± 0.000	2.4 ± 0.1	11.0 ± 0.1	0.282 ± 0.007	0.58 ± 0.01
38	58.843	-31.27	109	0.064 ± 0.002	1.9 ± 0.1	11.5 ± 0.4	0.11 ± 0.01	0.205 ± 0.003	1.37 ± 0.05	3.1 ± 0.1	0.72 ± 0.01	0.108 ± 0.005
38	58.843	-31.27	396	0.039 ± 0.004	0.9 ± 0.1	6.1 ± 0.3	0.038 ± 0.006	0.283 ± 0.002	1.98 ± 0.06	1.1 ± 0.1	0.53 ± 0.02	0.26 ± 0.01

Station #	Lat °N	Long °E	Depth m	pFe nmol.L^{-1}	pMn pmol.L^{-1}	pZn pmol.L^{-1}	pCo pmol.L^{-1}	pCd pmol.L^{-1}	pCu pmol.L^{-1}	pNi pmol.L^{-1}	pP nmol.L^{-1}	pAl nmol.L^{-1}
44	59.623	-38.95	40	0.159 ± 0.006	9.5 ± 0.3	15.0 ± 0.5	0.16 ± 0.01	0.218 ± 0.001	3.0 ± 0.1	8.0 ± 0.5	2.57 ± 0.07	0.382 ± 0.007
44	59.623	-38.95	80	0.088 ± 0.003	1.0 ± 0.03	30.0 ± 0.5	0.04 ± 0.01	0.029 ± 0.002	0.90 ± 0.05	0.33 ± 0.08	0.177 ± 0.004	0.275 ± 0.001
44	59.623	-38.95	150	0.196 ± 0.005	4.7 ± 0.1	1.9 ± 0.2	0.104 ± 0.003	0.015 ± 0.003	0.83 ± 0.01	0.8 ± 0.2	0.071 ± 0.003	0.438 ± 0.008
44	59.623	-38.95	300	0.161 ± 0.002	3.5 ± 0.3	57.7 ± 0.8	0.07 ± 0.01	0.010 ± 0.000	0.66 ± 0.03	0.14 ± 0.03	0.040 ± 0.002	0.347 ± 0.004
51	59.799	-42	8	0.175 ± 0.004	8.1 ± 0.2	133 ± 7	0.70 ± 0.02	1.73 ± 0.04	11 ± 1	6.6 ± 1.3	24.0 ± 0.3	0.75 ± 0.04
51	59.799	-42	60	0.28 ± 0.01	3.5 ± 0.5	18.3 ± 1.5	0.165 ± 0.002	0.36 ± 0.01	3.30 ± 0.08	33.2 ± 1.3	2.30 ± 0.07	1.28 ± 0.01
51	59.799	-42	100	0.285 ± 0.009	5.7 ± 0.4	6.1 ± 0.7	0.12 ± 0.02	0.015 ± 0.001	0.89 ± 0.02	0.8 ± 0.2	0.100 ± 0.005	0.61 ± 0.02
51	59.799	-42	250	0.26 ± 0.01	3.7 ± 0.3	15.1 ± 1.1	0.14 ± 0.01	0.124 ± 0.004	3.1 ± 0.1	4.0 ± 0.4	1.03 ± 0.05	1.12 ± 0.06
64	59.068	-46.08	30	0.065 ± 0.009	2.0 ± 0.2	11.8 ± 0.4	0.06 ± 0.01	0.18 ± 0.01	1.08 ± 0.06	0.3 ± 0.9	1.89 ± 0.04	0.23 ± 0.01
64	59.068	-46.08	60	1.52 ± 0.09	31 ± 1	13.1 ± 0.3	0.17 ± 0.04	0.091 ± 0.002	1.43 ± 0.02	3.4 ± 0.2	0.76 ± 0.02	0.231 ± 0.007
64	59.068	-46.083	100	1.0 ± 0.2	33 ± 3	68 ± 4		7.08 ± 0.02	36.2 ± 1.4	21 ± 6	15.76 ± 0.11	2.5 ± 0.2
64	59.068	-46.08	150	0.41 ± 0.01	6.1 ± 0.2	28.4 ± 0.6	0.270 ± 0.007	0.180 ± 0.005	4.09 ± 0.12	6.0 ± 0.2	1.09 ± 0.01	1.43 ± 0.03
64	59.068	-46.08	420	0.573 ± 0.008	15.9 ± 0.4	2.2 ± 0.4	0.31 ± 0.01	0.050 ± 0.002	1.39 ± 0.12	2.0 ± 0.4	0.172 ± 0.009	1.28 ± 0.04
69	55.842	-48.09	30	0.256 ± 0.003	4.5 ± 0.1	39 ± 1	0.288 ± 0.009	0.46 ± 0.01	3.76 ± 0.08	4.6 ± 0.3	3.43 ± 0.02	1.09 ± 0.02
69	55.842	-48.09	60	0.18 ± 0.01	2.2 ± 0.3	17.9 ± 0.8	0.15 ± 0.02	0.212 ± 0.008	1.9 ± 0.1	2.4 ± 0.3	0.646 ± 0.009	0.62 ± 0.01
69	55.842	-48.09	100	0.30 ± 0.01	4.7 ± 0.1	11.8 ± 0.2	0.190 ± 0.009	0.198 ± 0.004	2.54 ± 0.06	2.6 ± 0.1	0.56 ± 0.01	0.91 ± 0.02
69	55.842	-48.09	150	0.50 ± 0.01	7.9 ± 0.3	6.6 ± 0.1	0.27 ± 0.01	0.132 ± 0.006	2.32 ± 0.09	2.9 ± 0.3	0.55 ± 0.01	1.31 ± 0.04
69	55.842	-48.09	400	0.20 ± 0.01	4.8 ± 0.2	5.5 ± 0.3	0.123 ± 0.003	0.028 ± 0.001	0.90 ± 0.01	1.14 ± 0.06	0.137 ± 0.002	0.71 ± 0.02
77	52.989	-51.1	10	0.13 ± 0.04	2.3 ± 0.9	16 ± 2	0.24 ± 0.01	0.209 ± 0.005	2.5 ± 0.1	1.3 ± 1.1	3.60 ± 0.07	0.26 ± 0.05
77	52.989	-51.1	50	0.054 ± 0.003	0.1 ± 0.1	9.0 ± 0.3	0.12 ± 0.01	0.188 ± 0.002	1.66 ± 0.08	0.9 ± 0.3	1.59 ± 0.03	0.166 ± 0.002
77	52.989	-51.1	80	0.138 ± 0.003	2.2 ± 0.1	4.6 ± 0.1	0.088 ± 0.003	0.127 ± 0.003	1.00 ± 0.01	2.8 ± 0.1	0.607 ± 0.009	0.50 ± 0.01
77	52.989	-51.1	200	0.57 ± 0.04	11 ± 1	9.9 ± 0.4	0.24 ± 0.02	0.201 ± 0.002	1.67 ± 0.07	0.92 ± 0.01	0.346 ± 0.006	2.59 ± 0.04
77	52.989	-51.1	450	0.35 ± 0.02	12 ± 0	2.1 ± 0.1	0.195 ± 0.003	0.021 ± 0.001	1.6 ± 0.1	1.67 ± 0.07	0.215 ± 0.002	1.28 ± 0.02

Table S5.2: Particulate concentrations of pFe (nmol.L^{-1}), pMn(pmol.L^{-1}), pZn (pmol.L^{-1}), pCo (pmol.L^{-1}), pCd (pmol.L^{-1}), pCu (pmol.L^{-1}), pNi (pmol.L^{-1}), pP (nmol.L^{-1}), and pAl (nmol.L^{-1}) in the small size fraction (SSF; 1-53 µm).

Station #	Lat °N	Long °E	Depth m	pFe nmol.L^{-1}	pMn pmol.L^{-1}	pZn pmol.L^{-1}	pCo pmol.L^{-1}	pCd pmol.L^{-1}	pCu pmol.L^{-1}	pNi pmol.L^{-1}	pP nmol.L^{-1}	pAl nmol.L^{-1}
1	40.333	-10.036	25	0.26 ± 0.01	6.1 ± 0.2	35 ± 1	0.65 ± 0.03	0.27 ± 0.00	6.9 ± 0.3		2.65 ± 0.02	0.74 ± 0.01
1	40.333	-10.036	80	0.79 ± 0.03	30.3 ± 0.6	58 ± 4	2.08 ± 0.07	3.44 ± 0.05	27 ± 1		17.6 ± 0.1	2.82 ± 0.03
1	40.333	-10.036	120	0.16 ± 0.00	5.7 ± 0.2		0.12 ± 0.01	0.03 ± 0.00	0.89 ± 0.07	3.5 ± 0.3	0.10 ± 0.01	0.36 ± 0.01
1	40.333	-10.036	250	5.3 ± 0.1	165 ± 3	20.1 ± 0.8	1.8 ± 0.1	0.63 ± 0.01	19.8 ± 0.2	7.5 ± 0.8	2.68 ± 0.06	25.7 ± 0.3
1	40.333	-10.036	550	8.2 ± 0.1	199 ± 4	47 ± 4	3.7 ± 0.2	0.77 ± 0.00	37 ± 1	11 ± 1	2.74 ± 0.03	41.1 ± 0.3
1	40.333	-10.036	850	8.36 ± 0.09	227 ± 5	38 ± 2	3.19 ± 0.02	0.26 ± 0.00	27.1 ± 0.5	11 ± 1	1.80 ± 0.04	39.7 ± 0.5
13	41.383	-13.888	30	± 0.00	3.2 ± 0.3		1.12 ± 0.09	1.17 ± 0.03	6.1 ± 0.2		9.4 ± 0.1	
13	41.383	-13.888	80	0.04 ± 0.01	29 ± 2	29 ± 6	2.1 ± 0.2	6.33 ± 0.06	25 ± 1	14.6 ± 0.9	9.8 ± 0.1	0.26 ± 0.01
13	41.383	-13.888	120	0.23 ± 0.01	17.8 ± 0.5	2.8 ± 0.8	0.38 ± 0.03	0.97 ± 0.03	5.1 ± 0.1		1.13 ± 0.03	0.17 ± 0.00
13	41.383	-13.888	250	0.13 ± 0.01	73 ± 2	4.9 ± 0.9	0.67 ± 0.06	1.85 ± 0.02	15.5 ± 0.3		2.99 ± 0.04	0.62 ± 0.01
13	41.383	-13.888	400	1.07 ± 0.02	298 ± 10	66.4 ± 8.6	3.3 ± 0.2	2.96 ± 0.03	48 ± 2	2.70 ± 0.74	6.32 ± 0.03	4.11 ± 0.02
13	41.383	-13.888	850	0.57 ± 0.01	105.7 ± 0.5	8.2 ± 0.6	1.24 ± 0.05	0.28 ± 0.01	19.5 ± 0.4	1.05 ± 0.60	1.11 ± 0.03	2.11 ± 0.03
21	46.544	-19.672	15	0.08 ± 0.01	24 ± 1	50.7 ± 0.7	3.5 ± 0.3	7.4 ± 0.1	19.2 ± 0.5	13.5 ± 0.6	22.9 ± 0.2	0.01 ± 0.00
21	46.544	-19.672	60	0.04 ± 0.00	9.5 ± 0.4	18 ± 1	1.47 ± 0.07	5.27 ± 0.03	8.3 ± 0.3	47.8 ± 0.5	4.67 ± 0.04	0.18 ± 0.00
21	46.544	-19.672	100	0.25 ± 0.01	65 ± 1	67.3 ± 0.8	2.86 ± 0.02	6.17 ± 0.07	22.9 ± 0.3	28.3 ± 0.5	5.46 ± 0.04	0.83 ± 0.01
21	46.544	-19.672	150	0.11 ± 0.00	80 ± 1	27.1 ± 1.6	1.3 ± 0.1	2.87 ± 0.05	23 ± 1	12.2 ± 0.2	4.80 ± 0.02	1.28 ± 0.01
21	46.544	-19.672	200	0.13 ± 0.01	58.0 ± 0.8	36 ± 1	0.64 ± 0.02	1.63 ± 0.01	14.8 ± 0.5	5.8 ± 0.4	2.88 ± 0.04	0.55 ± 0.01
21	46.544	-19.672	300	0.12 ± 0.01	87 ± 1	32.6 ± 0.9	0.60 ± 0.04	0.99 ± 0.02	19.0 ± 0.7	4.4 ± 0.4	2.52 ± 0.05	1.07 ± 0.01
21	46.544	-19.672	500	0.17 ± 0.01	45 ± 1	29 ± 1	0.72 ± 0.02	0.95 ± 0.01	16.0 ± 0.6	6.20 ± 0.06	2.21 ± 0.03	0.78 ± 0.01
21	46.544	-19.672	810	0.31 ± 0.01	85.5 ± 0.5	14.7 ± 0.3	1.00 ± 0.09	0.41 ± 0.01	16.4 ± 0.4	5.1 ± 0.4	1.09 ± 0.02	1.25 ± 0.00
26	50.278	-22.605	30		19.7 ± 0.3	15.3 ± 0.7	0.69 ± 0.01	3.51 ± 0.02	4.2 ± 0.2	1.8 ± 0.3	7.36 ± 0.03	
26	50.278	-22.605	80		4.9 ± 0.1	5.7 ± 0.1	0.22 ± 0.01	2.30 ± 0.05	6.8 ± 0.3		3.69 ± 0.02	
26	50.278	-22.605	150	0.14 ± 0.01	53.5 ± 0.8	34.7 ± 0.1	0.55 ± 0.06	3.38 ± 0.07	13.1 ± 0.2	7.3 ± 0.6	3.45 ± 0.07	0.21 ± 0.00
26	50.278	-22.605	400	0.15 ± 0.00	102 ± 2	22 ± 1	0.38 ± 0.02	1.44 ± 0.03	16.9 ± 0.2		2.24 ± 0.02	0.56 ± 0.00
26	50.278	-22.605	2010	0.44 ± 0.01	63.9 ± 0.1	5.7 ± 0.4	0.49 ± 0.03	0.12 ± 0.00	8.1 ± 0.2	6.1 ± 0.2	0.44 ± 0.01	1.08 ± 0.01
26	50.278	-22.605	2800	1.17 ± 0.02	178 ± 2	2 ± 1	4.11 ± 0.09	0.28 ± 0.01	21.9 ± 0.7	6.4 ± 0.3	1.03 ± 0.02	3.33 ± 0.04
26	50.278	-22.605	3500	0.35 ± 0.01	36960 ± 292	56 ± 2	0.87 ± 0.02	0.19 ± 0.00	18.8 ± 0.3	6.1 ± 0.3	0.36 ± 0.01	0.80 ± 0.01
26	50.278	-22.605	3800	1.50 ± 0.07	499 ± 68	12.2 ± 0.9	1.40 ± 0.04	0.27 ± 0.02	17.6 ± 0.8		0.77 ± 0.04	6.3 ± 0.1
26	50.278	-22.605	4100	5.1 ± 0.1	1095 ± 37	31 ± 2	5.2 ± 0.2	0.55 ± 0.01	54 ± 2	9.9 ± 0.5	2.51 ± 0.08	23.7 ± 0.5
32	55.506	-26.71	20	1.09 ± 0.06	53 ± 2	170 ± 9	56 ± 2	46.8 ± 0.4	72 ± 1	152 ± 5	65.5 ± 0.6	
32	55.506	-26.71	30	0.28 ± 0.01	89 ± 2	354 ± 2	5.2 ± 0.2	32.4 ± 0.3	45.2 ± 0.5	9.2 ± 3.1	45.1 ± 0.3	
32	55.506	-26.71	60	0.18 ± 0.01	14 ± 1	97.8 ± 0.2	1.22 ± 0.02	9.4 ± 0.1	23.9 ± 0.5	12.3 ± 0.6	12.3 ± 0.2	0.08 ± 0.01
32	55.506	-26.71	100	0.14 ± 0.01	10 ± 1	63 ± 3	1.4 ± 0.2	7.3 ± 0.1	20.1 ± 0.6	13.0 ± 0.6	8.18 ± 0.05	0.05 ± 0.01
32	55.506	-26.71	150	0.49 ± 0.01	29.9 ± 0.7	66 ± 1	0.68 ± 0.04	7.01 ± 0.05	22.1 ± 1.1	3.9 ± 0.2	7.68 ± 0.04	1.44 ± 0.01
32	55.506	-26.71	200	0.09 ± 0.00	9.8 ± 0.4	35 ± 1	0.19 ± 0.03	4.48 ± 0.01	15.8 ± 0.0	0.0 ± 0.6	4.68 ± 0.03	0.40 ± 0.01
32	55.506	-26.71	380	0.38 ± 0.01	120.4 ± 0.8	22.8 ± 0.7	0.74 ± 0.05	2.90 ± 0.03	21.4 ± 0.2	2.6 ± 0.2	3.84 ± 0.05	1.91 ± 0.02
32	55.506	-26.71	600	0.50 ± 0.02	121.6 ± 2.8	36.9 ± 1.9	0.87 ± 0.02	1.99 ± 0.05	18.7 ± 0.2	7.1 ± 0.3	2.68 ± 0.05	2.02 ± 0.03
32	55.506	-26.71	850	0.18 ± 0.00	47.5 ± 0.3	8.0 ± 0.5	0.38 ± 0.01	0.57 ± 0.00	7.1 ± 0.2	0.31 ± 0.03	0.72 ± 0.01	0.68 ± 0.01

Station #	Lat °N	Long °E	Depth m	pFe nmol.L^{-1}	pMn pmol.L^{-1}	pZn pmol.L^{-1}	pCo pmol.L^{-1}	pCd pmol.L^{-1}	pCu pmol.L^{-1}	pNi pmol.L^{-1}	pP nmol.L^{-1}	pAl nmol.L^{-1}
38	58.843	-31.266	20	0.13 ± 0.02	51 ± 2	88 ± 5	4.6 ± 0.4	31.9 ± 0.3	46.7 ± 0.5	11.7 ± 2.7	45.2 ± 0.3	0.11 ± 0.03
38	58.843	-31.266	60	0.24 ± 0.00	22.6 ± 0.6	86 ± 2	1.5 ± 0.1	17.0 ± 0.3	31.4 ± 0.5	22.2 ± 1.5	12.2 ± 0.2	0.42 ± 0.01
38	58.843	-31.266	100	0.35 ± 0.02	18 ± 2	102 ± 3	0.87 ± 0.01	15.8 ± 0.4	42.0 ± 1.0	15.9 ± 0.5	7.6 ± 0.1	0.94 ± 0.01
38	58.843	-31.266	109	0.23 ± 0.01	12.9 ± 0.1	113 ± 2	0.92 ± 0.04	19.9 ± 0.2	27.6 ± 0.5	12.3 ± 0.6	6.50 ± 0.07	0.88 ± 0.01
38	58.843	-31.266	297	0.46 ± 0.01	27.7 ± 0.3	22.7 ± 0.5	0.32 ± 0.02	2.78 ± 0.02	17.1 ± 0.3	7.38 ± 0.20	3.19 ± 0.05	2.00 ± 0.03
38	58.843	-31.266	396	0.40 ± 0.01	31.3 ± 0.9	36 ± 1	0.26 ± 0.06	1.64 ± 0.04	13.1 ± 0.1	0.94 ± 0.20	2.27 ± 0.01	0.91 ± 0.01
38	58.843	-31.266	643	2.60 ± 0.07	126 ± 3	43 ± 1	2.55 ± 0.04	1.83 ± 0.05	22.2 ± 0.6	13.3 ± 0.8	2.88 ± 0.06	4.71 ± 0.05
38	58.843	-31.266	1087	11.5 ± 0.2	1221 ± 26	55 ± 4	5.2 ± 0.3	1.36 ± 0.02	28 ± 1	2.00 ± 0.76	2.41 ± 0.04	20.4 ± 0.4
38	58.843	-31.266	1316	23.6 ± 0.2	713 ± 3	52 ± 3	30.1 ± 0.4	1.59 ± 0.03	69.4 ± 0.3	1083 ± 3	3.18 ± 0.01	35.7 ± 0.5
44	59.623	-38.954	40	0.30 ± 0.01	16.1 ± 0.5	126 ± 1	0.82 ± 0.03	11.0 ± 0.4	31.9 ± 0.4	11 ± 2	26.8 ± 0.2	0.68 ± 0.10
44	59.623	-38.954	80	0.71 ± 0.01	26.2 ± 0.3	74 ± 2	0.60 ± 0.04	4.49 ± 0.07	23.4 ± 0.4	3.8 ± 0.4	7.04 ± 0.07	1.85 ± 0.03
44	59.623	-38.954	150	0.69 ± 0.01	32.5 ± 0.9	20 ± 2	0.42 ± 0.02	1.78 ± 0.01	11.1 ± 0.2		2.48 ± 0.03	1.58 ± 0.03
44	59.623	-38.954	300	1.11 ± 0.02	58 ± 3	57 ± 2	0.7 ± 0.1	2.63 ± 0.03	17.0 ± 0.4		3.06 ± 0.04	2.66 ± 0.04
44	59.623	-38.954	850		10.3 ± 0.8	29 ± 10		0.81 ± 0.06	8.3 ± 1.3		0.21 ± 0.03	
51	59.799	-42.013	8	0.14 ± 0.01	100 ± 2	124 ± 3	1.20 ± 0.06	18.0 ± 0.2	33.1 ± 1.5		57.1 ± 0.4	
51	59.799	-42.013	24	0.35 ± 0.01	22.4 ± 0.6	31 ± 2	0.48 ± 0.04	5.97 ± 0.06	10.9 ± 0.5		14.6 ± 0.2	0.22 ± 0.01
51	59.799	-42.003	60	0.41 ± 0.02	14.3 ± 0.5	104 ± 9	0.74 ± 0.05	94.4 ± 0.6	42.6 ± 1.7	8 ± 1	25.2 ± 0.2	1.68 ± 0.05
51	59.799	-42.003	100	0.91 ± 0.01	45.3 ± 0.8	7 ± 1	0.49 ± 0.05	339 ± 0.1	14.8 ± 0.5		2.59 ± 0.01	2.42 ± 0.08
51	59.799	-42.003	250	0.96 ± 0.02	22.7 ± 0.7	79 ± 2	0.60 ± 0.05	6.5 ± 0.2	42 ± 2	9.6 ± 0.9	12.6 ± 0.1	3.43 ± 0.11
51	59.799	-42.003	750	2.3 ± 0.1	177 ± 2	21 ± 3	1.7 ± 0.1	1.84 ± 0.05	25 ± 1	4 ± 1	2.34 ± 0.08	4.89 ± 0.11
51	59.799	-42.003	1190	5.5 ± 0.3	268 ± 7	13.0 ± 0.7	2.8 ± 0.1	0.98 ± 0.01	22.6 ± 0.4	5 ± 1	1.68 ± 0.04	12.4 ± 0.4
51	59.799	-42.003	1690	26 ± 1	735 ± 15	49 ± 2	12.2 ± 0.4	0.90 ± 0.04	46.0 ± 1.1	18 ± 2	3.11 ± 0.20	65.2 ± 1.9
64	59.068	-46.083	30	0.08 ± 0.01	4 ± 2	80 ± 4	0.2 ± 0.1	8.03 ± 0.14	20 ± 1		27.8 ± 0.05	
64	59.068	-46.083	60	0.51 ± 0.01	38.7 ± 0.3	532 ± 24	1.90 ± 0.01	50.5 ± 0.2	162 ± 7		75.1 ± 0.3	3.20 ± 0.34
64	59.068	-46.083	150	1.02 ± 0.01	38.2 ± 0.4	75 ± 3	0.83 ± 0.06	4.14 ± 0.05	22.6 ± 0.3	4.9 ± 0.9	7.77 ± 0.07	2.30 ± 0.02
64	59.068	-46.083	420	3.20 ± 0.09	145 ± 2	42.3 ± 0.9	1.6 ± 0.1	1.87 ± 0.04	16.1 ± 0.1		2.14 ± 0.06	6.62 ± 0.04
64	59.068	-46.083	630	2.02 ± 0.04	104 ± 2	47.7 ± 0.4	1.3 ± 0.1	2.13 ± 0.04	17.0 ± 0.7	1.72 ± 0.01	2.94 ± 0.08	4.6 ± 0.1
64	59.068	-46.083	900	1.48 ± 0.03	78 ± 1	17.4 ± 0.1	0.91 ± 0.05	1.49 ± 0.02	13.5 ± 0.1	2.0 ± 0.2	1.50 ± 0.03	3.56 ± 0.03
69	55.842	-48.093	30	0.56 ± 0.04	35 ± 1	104 ± 4	2.1 ± 0.1	13.3 ± 0.2	38.5 ± 0.8	48.7 ± 0.8	55.5 ± 0.2	1.82 ± 0.03
69	55.842	-48.093	60	1.19 ± 0.02	65.7 ± 0.7	73 ± 4	1.78 ± 0.04	15.3 ± 0.2	42.4 ± 0.4	17.1 ± 0.5	24.0 ± 0.1	3.96 ± 0.02
69	55.842	-48.093	100	1.10 ± 0.03	53 ± 1	65 ± 1	1.21 ± 0.04	8.05 ± 0.05	27.0 ± 0.7	7.5 ± 1.1	11.6 ± 0.04	3.35 ± 0.02
69	55.842	-48.093	150	1.59 ± 0.02	76 ± 2	56 ± 1	1.26 ± 0.07	5.49 ± 0.03	25.2 ± 0.3	2.32 ± 0.06	8.9 ± 0.1	4.28 ± 0.02
69	55.842	-48.093	400	0.96 ± 0.01	65 ± 1	22.8 ± 0.9	0.65 ± 0.03	2.59 ± 0.05	12.8 ± 0.4	1.9 ± 0.5	2.73 ± 0.04	2.70 ± 0.01
77	52.989	-51.095	10	0.68 ± 0.04	108 ± 3	184 ± 4	12.9 ± 0.3	48.8 ± 0.4	54 ± 1	76.2 ± 1.3	103 ± 1	0.22 ± 0.21
77	52.989	-51.095	50	0.54 ± 0.04	90 ± 8	200 ± 6	5.4 ± 0.1	49.5 ± 0.2	64 ± 2	63.7 ± 0.4	56.6 ± 0.3	1.52 ± 0.02
77	52.989	-51.095	80	1.76 ± 0.03	58 ± 1	106 ± 2	2.26 ± 0.04	14.4 ± 0.1	29.2 ± 0.2	9.86 ± 0.72	13.8 ± 0.1	5.62 ± 0.07
77	52.989	-51.095	200	2.97 ± 0.07	84.2 ± 0.9	57.9 ± 0.8	1.9 ± 0.1	4.68 ± 0.02	21.0 ± 0.1	6.70 ± 0.10	5.35 ± 0.03	8.7 ± 0.1
77	52.989	-51.095	450	1.45 ± 0.01	108.4 ± 2.0	13.2 ± 0.2	1.04 ± 0.05	1.92 ± 0.02	14.9 ± 0.5	5.73 ± 0.25	1.57 ± 0.01	4.49 ± 0.05

Chapter 6

Impact of the natural Fe-fertilization on the magnitude, stoichiometry and efficiency of particulate biogenic silica, nitrogen and iron export fluxes

This chapter has been published in Deep-Sea Research I in 2016:

N. Lemaitre, H. Planquette, F. Dehairs, P. Van der Merwe, A.R. Bowie, T.W. Trull, E.C. Laurenceau-Cornec, D. Davies, C. Bollinger, M. Le Goff, E. Grossteffan, F. Planchon (2016). Impact of the natural Fe-fertilization on the magnitude, stoichiometry and efficiency of BSi, PN and PFe export fluxes. Deep-Sea Research, 117, 11-27, doi:10.1016/j.dsr.2016.09.002

Abstract

The Kerguelen Plateau is characterized by a naturally Fe-fertilized phytoplankton bloom that extends more than 1000 km downstream in the Antarctic Circumpolar Current. During the KEOPS2 study, in austral spring, we measured particulate nitrogen (PN), biogenic silica (BSi) and particulate iron (PFe) export fluxes in order to investigate how the natural fertilization impacts the stoichiometry and the magnitude of export fluxes and therefore the efficiency of the biological carbon pump. At 9 stations, we estimated elemental export fluxes based on element concentration to ^{234}Th activity ratios for particulate material collected with *in-situ* pumps and ^{234}Th export fluxes (Planchon et al., 2015). This study revealed that the natural Fe-fertilization increased export fluxes but to variable degrees. Export fluxes for the bloom impacted area were compared with those of a high-nutrient, low-chlorophyll (HNLC), low-productive reference site located to the south-west of Kerguelen and which had the lowest BSi and PFe export fluxes (2.55 mmol BSi.m^{-2}.d^{-1} and 1.92 µmol PFe.m^{-2}.d^{-1}) and amongst the lowest PN export flux (0.73 mmol PN.m^{-2}.d^{-1}). The impact of the Fe fertilization was the greatest within a meander of the polar front (PF), to the east of Kerguelen, with fluxes reaching 1.26 mmol PN.m^{-2}.d^{-1}, 20.4 mmol BSi.m^{-2}.d^{-1}, and 22.4 µmol PFe.m^{-2}.d^{-1}. A highly productive site above the Kerguelen Plateau, on the contrary, was less impacted by the fertilization with export fluxes reaching 0.72 mmol PN.m^{-2}.d^{-1}; 4.50 mmol BSi.m^{-2}.d^{-1} and 21.4 µmol PFe.m^{-2}.d^{-1}. Our results suggest that ecosystem features (i.e. type of diatom community) could play an important role in setting the magnitude of export fluxes of these elements. Indeed, for the PF meander, the moderate productivity was sustained by the presence of large and strongly silicified diatom species while at the higher productivity sites, smaller and slightly silicified diatoms dominated. Interestingly, our results suggest that PFe export fluxes can be driven by the lithogenic pool of particles, especially over the Plateau where such inputs from the sediments are important. Finally, for the Plateau and the PF meander, the comparison between PFe export and the particulate PFe stock integrated over the mixed layer depth revealed an efficient PFe export out of the mixed layer at these sites. Export efficiencies (i.e.

the ratio between export and uptake) exhibit a very efficient silica pump especially at the HNLC reference station where heavily silicified diatoms were present. On the contrary, the increase with depth of the C:N ratio and the low nitrogen export efficiencies support the idea of a strong remineralization and nitrification activity.

6.1. Introduction

The oceanic biological pump transports carbon and other nutrient elements, like nitrogen, silicon and iron to the deep sea via the sinking of organic particles produced in surface waters from photosynthesis. The Southern Ocean is the largest HNLC (high-nutrient, low-chlorophyll) area and its potential to transfer these elements is usually limited by a lack of micronutrients (Martin, 1990). Among these micronutrients, iron is a crucial element which regulates the ocean biological productivity, as it is required by phytoplankton for many metabolic functions (e.g. Boyd and Ellwood, 2010; Sunda, 1989). Artificial iron fertilization experiments performed in the Southern Ocean (Boyd et al., 2007; de Baar, 2005) have confirmed that iron addition stimulates a significant air-sea CO_2 drawdown by phytoplankton. However, due to the limited extent and duration of the bloom induced during artificial fertilization experiments, the long-term fate of iron-induced particulate organic carbon (POC) export is difficult to determine (Gnanadesikan and Marinov, 2008; Smetacek and Naqvi, 2008).

An alternative way to study iron fertilization is to look at the large and persistent blooms occurring within natural iron fertilization areas of the Southern Ocean, where ecosystems are adapted to recurrent iron inputs (Charette et al., 2013). Morris and Charette (2013) reviewed different natural Fe-fertilization studies (KEOPS, CROZEX and BWZ) and reported that POC export within the naturally Fe-fertilized areas was ~3 times higher compared to Fe-limited sites. However, the impact of the fertilization on export of other elements has been less well studied. For example, silicon is a key element controlling export (Buesseler, 1998). It is essential for the construction of diatom frustules and can be limiting in surface waters (Mosseri et al., 2008) while nitrogen is a major macro-nutrient which does not limit productivity in Southern Ocean.

Several authors have highlighted surprisingly high nitrate stocks at the end of bloom periods due to a shallow remineralization of organic matter that reduces N export to the deep sea (Dehairs et al., 2015; Fripiat et al., 2015; Mosseri et al., 2008). Previous studies of naturally fertilized sites have documented that the relationship between production and export was not straightforward and that the pelagic food web structure impacted the retention and export of particulate matter. In that context, it appears important to consider elemental export fluxes other than carbon, such as macro (N, Si) and micro-nutrients (Fe; Jin et al., 2006; Le Moigne et al., 2014; Sarthou et al., 2005), in order to increase our understanding of ecological processes impacting the stoichiometry and the magnitude of these export fluxes and ultimately the efficiency of the biological carbon pump. Furthermore, the composition of the phytoplankton community plays an important role in the stoichiometric relationship between these elements. Depending on iron supplies and environmental conditions, different diatom species develop, driving a diverse range of biological answers affecting the stoichiometry of exports. Thin-shelled and fast-growing diatoms dominate the iron-fueled blooms and are characterized as carbon sinkers but they also undergo grazing which consume a large part of this carbon. Conversely, thick-shelled and slow-growing diatoms dominate the later phase of the bloom and are protected against grazing (Quéguiner, 2013). These heavily silicified diatoms are considered as preferential silica sinkers (Assmy et al., 2013; Boyd, 2013; Green and Sambrotto, 2006; Quéguiner, 2013)

Because of their key roles in the functioning of the biological carbon pump, we examined upper-ocean export fluxes of particulate nitrogen (PN), biogenic silica (BSi) and particulate iron (PFe) in the naturally Fe-fertilized area of the Kerguelen Plateau during the GEOTRACES process study “KEOPS2” (KErguelen Ocean and Plateau compared Study, October-November 2011, R/V Marion Dufresne). Upper-ocean export fluxes were deduced from vertical export fluxes of total ^{234}Th (Planchon et al., 2015). The settling of particles generates a deficit of ^{234}Th (characterized by a short half-life and a strongly particle-reactive behavior) with respect to ^{238}U (conservative in seawater) in the upper water column. This deficit is integrated over the upper column to yield a ^{234}Th flux (Coale and Bruland, 1985; Cochran and

Masqué, 2003; Savoye et al., 2006; Waples et al., 2006). Subsequently, the ^{234}Th flux is converted into an elemental flux by using the element:^{234}Th ratio of large (> 53 µm) sinking particles (^{234}Th:PN, ^{234}Th:BSi, ^{234}Th:PFe; Buesseler, 1998; Buesseler et al., 2006, 1992; Rutgers Van Der Loeff et al., 1997).

In this work, we use the biogeochemical export fluxes obtained in HNLC and Fe-enriched waters to assess the impact of the natural Fe-fertilization on the vertical transfer of PN, BSi and PFe. We further examine how phytoplankton community composition, lithogenic contribution and degradation of particles, influence the magnitude, efficiency and stoichiometry of the export fluxes.

6.2. Methods

6.2.1. Study area

The Kerguelen Plateau's complex shallow topography is characterized by sluggish circulation, which may precondition the development of a recurrent annual bloom (Park et al., 2008). The Kerguelen bloom is separated in two parts by the Polar Front (PF). The northern branch of the Kerguelen bloom extends northeast of the island to the north of the PF, while a larger bloom is located over the Plateau, bounded to the north by the PF and to the south by the Fawn Trough Current (FTC; Park et al., 2008; Figure 6.1).

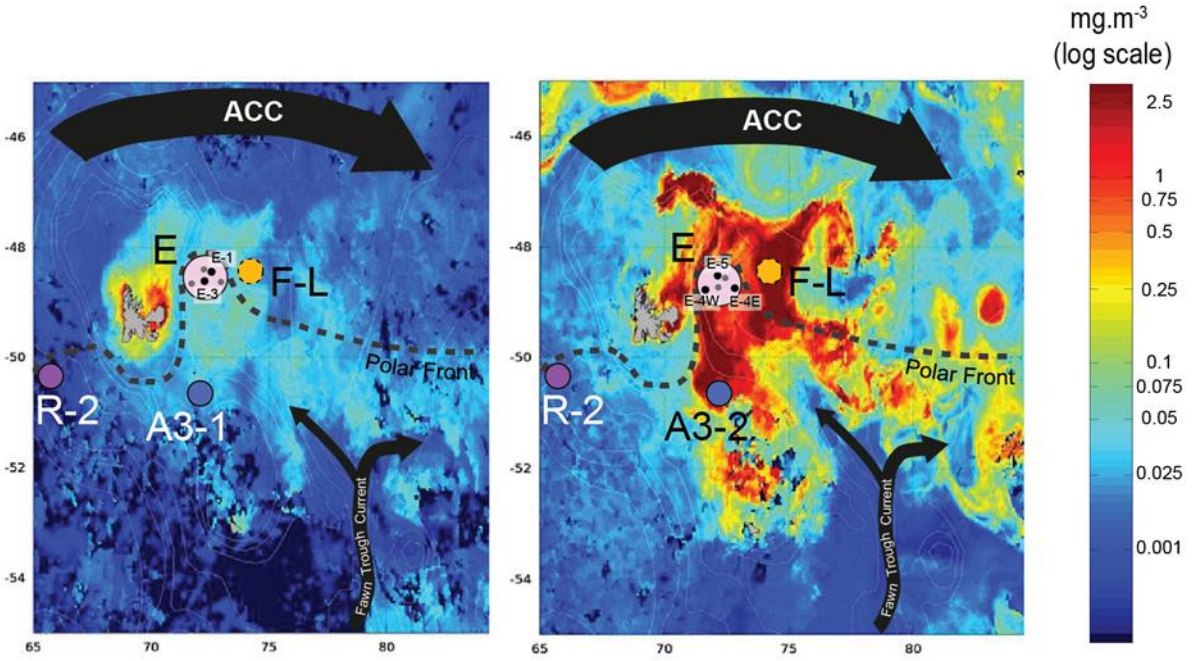

Figure 6.1: Surface Chlorophyll-a concentrations ($mg.m^{-3}$) at the beginning (19/10/2011) and at the end (17/11/2011) of the KEOPS2 cruise. Filled circles represent the location of stations. The station F-L, represented by a dotted circle, was sampled between these two dates (06/11/2011). The thick dotted line represents the approximate location of the Polar Front while the thick black arrows indicating the Antarctic Circumpolar Current (ACC) and the Fawn Trough Current (FTC; adapted from Park et al., 2008).

The productive period over the Kerguelen Plateau takes place from November to February (Blain et al., 2007). During KEOPS2, the bloom developed quickly but presented large spatio-temporal variations as shown by the satellite images of Chlorophyll *a* concentrations (Chl-*a* from 0.75 to 3 $\mu g.L^{-1}$ over the Plateau; Figure 6.1; Animation of the bloom can also be found in Supplement of Trull et al., 2015). Nine stations were investigated (Figure 6.1):

- a reference station in the HNLC area (R-2), upstream of the island, not impacted by lithogenic contributions, with low dissolved Fe concentrations (dFe < 0.1 $nmol.L^{-1}$; Quéroué et al., 2015), characterized by a low phytoplankton abundance (0.2 µg Chl-*a*.L^{-1}; Lasbleiz et al., 2014) and low net primary productivity (NPP=132 $mgC.m^{-2}.d^{-1}$; Cavagna et al., 2015).

- a station over the Plateau (A3) was sampled twice over a period of 27 days. Dissolved iron concentrations decreased from 0.28 $nmol.L^{-1}$ at A3-1 to 0.18 $nmol.L^{-1}$ at A3-2 in surface waters (Quéroué et al., 2015) due to a large diatom spring bloom development between both visits (from 0.2 to 1.3 µg Chl-*a*.L^{-1}; Lasbleiz et al., 2014). Sediments supplied large amounts of dFe

(Bowie et al., 2015) driving a relatively high NPP at A3-2 (2172 mgC.m^{-2}.d^{-1}; Cavagna et al., 2015).

- a station in a meander of the PF (E) was visited four times over a period of 19 days (E-1, E-3, E-4E, and E-5). Based on the trajectories of two surface drifters, stations E-1, E-3, E-4E, and E-5 were used to track the middle of a recirculation region and thus these stations are assumed to evolve in a pseudo-Lagrangian view (d'Ovidio et al., 2015; Zhou et al., 2014). Therefore, their succession in time can be considered as a time-series over 19.6 days during the bloom development. This area was fertilized by lateral Fe supply, coming from the Plateau or from glacial and fluvial sources (van der Merwe et al., 2015; Bowie et al., 2015). A drawdown of dFe concentrations was observed (from 0.38 to 0.06 nmol.L^{-1} in surface waters; Quéroué et al., 2015) along with the bloom development (from 0.3 µg Chl-*a*.L^{-1} at E-1 to 0.9 µg Chl-*a*.L^{-1} at E-5; Lasbleiz et al., 2014). Similarly, the NPP increased from 578 to 1064 mgC.m^{-2}.d^{-1} (Cavagna et al., 2015) from E-1 to E-5 stations respectively. A highly productive station (E-4W) located closer to the Kerguelen Plateau margin was also sampled but excluded from the time series, since being non-representative to trace the seasonal evolution in the less productive PF meander (Cavagna et al., 2015; Dehairs et al., 2015; Planchon et al., 2015).

- a station north of the PF (F-L) was sampled at mid-cruise and displayed moderate dFe concentrations in surface waters (0.26 nmol.L-1; Quéroué et al., 2015), the highest chlorophyll-*a* (3 µg.L-1; Lasbleiz et al., 2014) and NPP (3380 mgC.m^{-2}.d^{-1}; Cavagna et al., 2015) levels.

6.2.2. Sampling

In-situ pumps (Challenger Oceanics and McLane WTS6–1-142LV pumps, "ISP" hereafter) were deployed for a period of 4 hours, at depths ranging between 25 and 2000 meters. 500 to 2000 L of seawater were filtered through a 142mm diameter nylon pre-filter (Nytex, 53µm mesh size) superimposed on a quartz fiber filter (QMA, Sartorius, 1µm pore size). To limit elemental blanks, filters were acid-cleaned (H_2SO_4 5% v/v, Seastar Baseline^{TM}) and rinsed 3 times with Milli-Q water prior to sampling (Bowie et al., 2015; van der Merwe et al., 2015).

After collection, filters were subsampled on board under clean room conditions. Punches of 25 mm diameter were collected from the 142 mm QMA and dedicated to ^{234}Th, PN, POC (Planchon et al., 2015) and trace element (van der Merwe et al., 2015) analyses. One fourth of the 142 mm nylon screen was dedicated to ^{234}Th, PN and POC analyses (Planchon et al., 2015) while another quarter was dedicated to BSi and trace element determinations (TEs: only PFe and PAl data are presented in this work). This quarter was stored in acid-cleaned tubes and kept at ambient temperature until analysis.

In the home-based laboratory, handling of nylon screens dedicated to TEs and BSi measurements were carried out in trace metal clean conditions (Class-100). It was decided to remove the particles from the nylon screen for two main reasons: (i) high blanks for TEs have been reported from nylon screens (Weinstein and Moran, 2004), (ii) it is not possible to fully acid-digest the nylon screen. Therefore, the particles on the nylon screen were washed off with 0.22 µm filtered surface seawater collected during the KEOPS2 cruise (Station E5, 40m) onto acid cleaned 47 mm diameter polyestersulfone filters (Supor® filters, 0.8 µm), mounted on acid cleaned polysulfone filtration units (Nalgene®). This seawater had a dissolved iron (dFe) concentration of 0.08 ± 0.01 nM (Quéroué et al., 2015).

Finally, the Supor filters were cut in 4 equal parts using a ceramic blade. One quarter was dedicated to TEs analyses and another to BSi analyses. Filters were stored at -20°C in clean petri dishes until analyses.

It is important to note that ISP were not equipped with anti-washout baffles and thus a potential washout of the >53 µm particles upon pump retrieval may have biased the final concentrations (Bishop et al., 2012). Some loss could also have occurred during the resuspension of the >53 µm particles from the nylon screen and filtration on the Supor filter. To limit these effects, we focus on elemental ratios and element to ^{234}Th ratios, rather than on concentrations and activities.

6.2.3. Analytical methods

6.2.3.1. TEs analyses

All sample handling, processing and preparation was performed in accordance with GEOTRACES recommendations (http://geotraces.org/images/stories/documents/intercalibration/Cookbook.pdf) and specific procedures following Planquette and Sherrell (2012). Briefly, under a Class-100 clean hood, one quarter of a Supor filter was placed along the wall of a 15 mL clean Teflon vial. Then, 2 mL of a solution HNO_3 6.5M (Merck Ultrapur) + HF 2.3M (Merck Suprapur) was added. Vials were then refluxed at 130°C on a hotplate for 4h. After gentle evaporation, 200 µL of concentrated HNO_3 (Merck Ultrapur) was added in order to drive off the fluorides. The residue was brought back into solution with 3% HNO_3 spiked with 1 $\mu g.L^{-1}$ of Indium and stored in acid cleaned 15 mL centrifuge tubes until analysis.

All measurements were made by SF-ICP-MS (Element 2, ThermoFinnigan) following the method of Planquette and Sherrell (2012). Every 11 samples, a replicate analysis of a selected sample digest solution was made. The precision and the accuracy of our analyses were assessed by measuring replicates and the Certified Reference Materials (CRM) BCR-414, respectively (Table 6.1). Finally, in order to evaluate the origin of PFe pool in our samples, the PFe lithogenic contribution was estimated by multiplying the PFe:PAl molar ratio in Kerguelen basalt (0.43 $mol.mol^{-1}$; Gautier et al., 1990) with PAl concentration, whereby it is assumed that all PAl is of lithogenic origin. Then, subtracting the lithogenic Fe from total particulate Fe yields an estimation of the excess content which can be assimilated to biogenic iron (Table S6.1**;** Bowie et al., 2015; van der Merwe et al., 2015).

Lastly, trace elements in small particles (1-53 µm) were also analyzed, the results can be found in van der Merwe et al. (2015).

	Al*	Mn	Fe*
Certified/indicative* value (µg.g^{-1})	2154 ± 803	299 ± 13	1850 ± 190
Measured value (n=3; µg.g^{-1})	2393 ± 355	265 ± 43	1745 ± 279
Recovery (%)	111	89	94

Table 6.1: Determined concentrations (µg.g-1) and resulting recoveries (%) of the Certified Reference Material plankton BCR-414, compared to certified or indicative (*) values. Three replicates of BCR-414 were digested then analyzed during different ICP-MS sessions.

6.2.3.2. BSi analyses

All experiments were made using clean polymethylpentene and polypropylene centrifuge tubes. Silicate concentrations were determined using the automated acid/molybdate colorimetric method (Aminot and Kérouel, 2007), using an AutoAnalyzer3 Bran&Luebbe (precision: 0.01 µmol.L^{-1}) after an alkaline digestion of the filter (Ragueneau et al., 2005). Briefly, a quarter of the Supor filter was placed in a centrifuge tube and digested with a NaOH (Merck, pellets for analysis) 0.2M solution at 100°C during 40min in a hot bath. After cooling, the pH was neutralized by adding HCl 1M (Analar Normapur). Tubes were then centrifuged at ambient temperature for 10min at 4000 rpm (Thermo Scientific Multifuge 3S+/3SR+) and the supernatant was separated from the remaining suspended material. Finally 500 µL of supernatant was diluted 400 to 2000 times in Milli-Q water (18.2MΩ.cm) before analysis.

BSi concentration in small particles was not determined due to the impossibility to analyze this element on QMA filters.

6.2.3.3. Particulate ^{234}Th and PN analysis

Protocols and particulate ^{234}Th activity data are detailed in Planchon et al. (2015). Immediately after collection, particles from one quarter of the 142 mm nylon screen were re-suspended in filtered seawater and collected on 25 mm diameter silver filters (1.0 µm porosity) for particulate ^{234}Th, PN and POC analyses. Filters were counted on board for particulate ^{234}Th activity measurements via RISO low-beta counters. In the laboratory, PN and POC concentrations were measured via an elemental analyzer – isotope ratio mass spectrometer (EA-IRMS, Delta V Plus, Thermo Scientific). POC results have been presented by Planchon et al. (2015). Small particles, collected in the QMA filter, underwent the same procedure (Table S6.2). Acetanilide

standards were used for the calibration. N blanks were 0.08 µmol for Ag filters and 0.48 µmol for QMA filters.

6.2.3.4. Total ^{234}Th activities and ^{234}Th export fluxes

Total ^{234}Th activities were obtained from 4 L seawater samples collected from Niskin bottles. Seawater samples were processed for total ^{234}Th activity measurements following the double spike method (Pike et al., 2005). Details about methodology and ^{234}Th activity data can be found in Planchon et al. (2015). In this study, export fluxes of ^{234}Th were estimated using a 1-D box model (Savoye et al., 2006) under steady state assumptions and considering the physical terms as negligible. The calculation was extended down to a single export depth named Equilibrium depth (Eq hereafter), where total ^{234}Th was back to equilibrium with ^{238}U. The ^{234}Th export at this depth represents the fully-integrated depletion of total ^{234}Th in the upper waters.

6.2.4. Determination of particulate elemental fluxes

Particulate ^{234}Th activities and PN and PFe concentrations were obtained for two size-fractions of particles (PFe data for the 1-53 µm fraction are from van der Merwe et al., 2015) while BSi:^{234}Th ratios were obtained only for the large particles (>53 µm). In order to obtain biogeochemical (PN, BSi, PFe) export fluxes using the ^{234}Th-based approach, the element to ^{234}Th ratio of large (> 53 µm) particles, usually considered as representative of the sinking particulate matter, needs to be determined at the depth of export (Buesseler et al., 2006). The selection of the Element:^{234}Th ratio representative of sinking particles exiting the surface waters is decisive for the ^{234}Th proxy method. Several studies report that this ratio can vary spatially and temporally and is dependent on particle-size, plankton communities, food web dynamics, aggregation-disaggregation processes or sampling methods (Benitez-Nelson and Charette, 2004; Buesseler, 1991; Buesseler et al., 2006; Moran et al., 2003).

In most cases, the depth resolution of *in-situ* pump sampling was lower than Niskin sampling, with the latter used for assessing total ^{234}Th flux at Eq. This requires that Element:^{234}Th ratios of sinking particles at Eq be calculated from depths bracketing the Eq. In order to account for

the depth-related variations of element to ^{234}Th ratios, we decided to apply different interpolation/averaging methods to a range of estimates of this conversion factor at Eq, as follows:

- the linear interpolation at Eq:

Element:$^{234}Th=a\times Z+b$ where Z is the depth; a and b are the parameters obtained by a straight line fit between the upper and the lower data point bracketing the target depth, Eq.

- the average of the two ratios bracketing Eq:

Element:$^{234}Th=[(\text{Element:}^{234}Th)_{z-1}+(\text{Element:}^{234}Th)_{z+1}]/2$ where Z-1 and Z+1 are the depths immediately below and above Eq depth.

- the power law interpolation at Eq:

Element:$^{234}Th=a\times Z^{-b}$ where Z is the depth; a and b are the parameters obtained by an exponential fit performed on all or selected data points in order to obtain the best fit.

- the depth-weighted average Element:^{234}Th ratios in the water layer extending from surface to Eq:

Element:$^{234}Th=[\Sigma(\text{Element}_i \times Z_i) / \Sigma(Z_i)] / [\Sigma(^{234}Th_i \times Z_i) / \Sigma(Z_i)]$ where Z_i are the different depths sampled above Eq.

The choice of the interpolation method depends on how processes affect the element:^{234}Th ratios profile.

The linear interpolation between depths bracketing Eq, as well as taking the average of these depths, are appropriate calculations when the curve is monotonic but it can also yield over- or under-estimates if there is an important fluctuation at one of the depths bracketing Eq. The power law interpolation is only useful when the Element:^{234}Th ratios show a decrease with depth and generally fits well the vertical evolution of labile element (N, C) to ^{234}Th ratios. The depth-weighted average approach yields a ratio of all particles in the layer between surface and Eq thus potentially including living and non-sinking plankton cells which can affect the Element:^{234}Th ratio. However, this calculation seems particularly appropriate for the Fe:^{234}Th ratios increasing with depth.

Buesseler et al. (2006) also highlighted the temporal change of the ratio C:^{234}Th due to variations of biological communities in surface waters and thus variations of the particle size class and composition. Depending on the region, seasonal variations can impact the determination of the ratio. For example, in the Baltic Sea, the C:^{234}Th ratio varied by a factor of 10 over the year (see reference in Buesseler et al., 2006). In the present study, we assume that the particles collected for the determination of the element:^{234}Th ratio match with those that sank to create the ^{234}Th deficit. This assumption of steady state and the effect of temporal change of the ratio on the estimated flux will be discussed in section III.4.

We then compared the elemental export flux results based on these four techniques, calculated as:

$$\text{Elemental export flux} = (\text{Element} : {}^{234}\text{Th})_{particulate} \times {}^{234}\text{Th flux} \quad \text{(Equation 6.1)}$$

where *Elemental export flux* is the quantity of the element (in this study: PN, BSi or PFe) leaving the surface ocean (expressed in mmol.m^{-2}.d^{-1} or µmol.m^{-2}.d^{-1}) and calculated at Eq; $(Element : {}^{234}Th)_{particulate}$ is the ratio of the studied element to ^{234}Th on large particles calculated at Eq with one of the four different interpolation/averaging methods (expressed in µmol.dpm^{-1} or nmol.dpm^{-1}); and $^{234}Th\ flux$ is the integrated ^{234}Th flux (dpm.m^{-2}.d^{-1}) at Eq.

6.2.5. Determination of PN and BSi export efficiencies

The efficiency of export ($ThE_{element}$) can be estimated from the ratio of export flux to uptake flux (Buesseler, 1998). To determine the $ThE_{element}$ ratio, we used the relationship:

$$ThE_{element} = (\text{Elemental export flux} / \text{Elemental uptake flux}) \times 100 \quad \text{(Equation 6.2)}$$

where $ThE_{element}$ is the efficiency of the elemental flux expressed in %; the *Elemental export flux* is given by Equation 1; and the *Elemental uptake flux* is the water column integrated uptake from surface to 1% of surface Photosynthetically Active Radiation (PAR) determined via on-board incubation experiments (total N-uptake determined by Cavagna et al., 2015; net Si-uptake determined by Closset et al., 2014).

6.3. Results

6.3.1. Total ^{234}Th distribution and export fluxes

Total ^{234}Th activities are described and discussed in Planchon et al. (2015). At all sites, deficits of ^{234}Th relative to ^{238}U were observed, indicating the early export of particles in austral spring (Planchon et al., 2015). The ^{234}Th export fluxes were estimated with the steady state and the non-steady state models. The good agreement between the two models suggests that particle scavenging is at steady state, and thus that the export is constant at A3 and E stations. The estimated ^{234}Th fluxes at Eq ranged from 425 dpm.m^{-2}.d^{-1} at R-2 to 1995 dpm.m^{-2}.d^{-1} at E-3 (Table 6.2). In the Fe-fertilized area, the highest ^{234}Th export fluxes were found at E site (averaging 1823 ± 165 dpm.m^{-2}.d^{-1}) while lower ^{234}Th export fluxes were observed at highly-productive A3-2 and F-L sites (993 and 902 dpm.m^{-2}.d^{-1}, respectively). These two stations were visited only a few days after the start of the bloom and Planchon et al. (2015) hypothesized that these low ^{234}Th fluxes, as well as the high particulate ^{234}Th activities, were due to the fact that particles at these two stations were in accumulation phase rather than in export phase.

6.3.2. PN, BSi and PFe distributions

Concentrations of PN, BSi and PFe are shown in Figure 6.2 and in Table S6.1. The PN, BSi and PFe concentrations measured in surface waters of the HNLC area were the lowest (station R-2; 0.06 µmol.L^{-1}, 0.28 µmol.L^{-1} and 0.26 nmol.L^{-1}, respectively) while they were up to 10, 9 and 16 fold higher in surface waters of the Fe-fertilized area, respectively. The highest PN and BSi concentrations were observed at site E-5 (0.609 and 2.41 µmol.L^{-1}, respectively), and the highest PFe concentration was measured at station A3-2 (4.16 nmol.L^{-1}).

Two types of vertical distributions were encountered throughout the bloom duration:

- Before the bloom development (< 0.5 µg Chl-*a*.L^{-1}), in surface waters of R-2, A3-1, E-1 and E-3 stations, particulate concentrations did not exceed 0.2 µmol PN.L^{-1}, 0.5 µmol BSi.L^{-1} and 0.7 nmol PFe.L^{-1}. Similar concentrations were also found deeper in the water column except

for PFe at A3-1 and local maxima of PN, BSi and PFe concentrations measured at 130m of stations E-1 and E-3.

- While the bloom developed (> 0.5 µg Chl-*a*.L^{-1}), in surface waters of E-5, A3-2 and F-L stations, particulate concentrations were high reaching 0.61 µmol PN.L^{-1}, 2.41 µmol BSi.L^{-1} and 4.16 nmol PFe.L^{-1}. Concentrations decreased with depth reaching levels observed before the bloom.

However, PFe profiles did not follow exactly the same trend. PFe concentrations increased with depth at A3-1 station, ranging from 0.77 nmol.L^{-1} in surface waters to 2.16 nmol.L^{-1} at 440 m due to the presence of a nepheloid layer (van der Merwe et al., 2015). At A3-2, PFe concentrations decreased with depth from 4.16 nmol.L^{-1} in surface waters to 1.62 nmol.L^{-1} near the seafloor, but a local maximum was observed at 200 m reaching 3.3 nmol.L^{-1}. The shape of the vertical profiles at stations F-L and E-5 are similar except that concentrations were ~4 to ~5 fold lower than at A3-2.

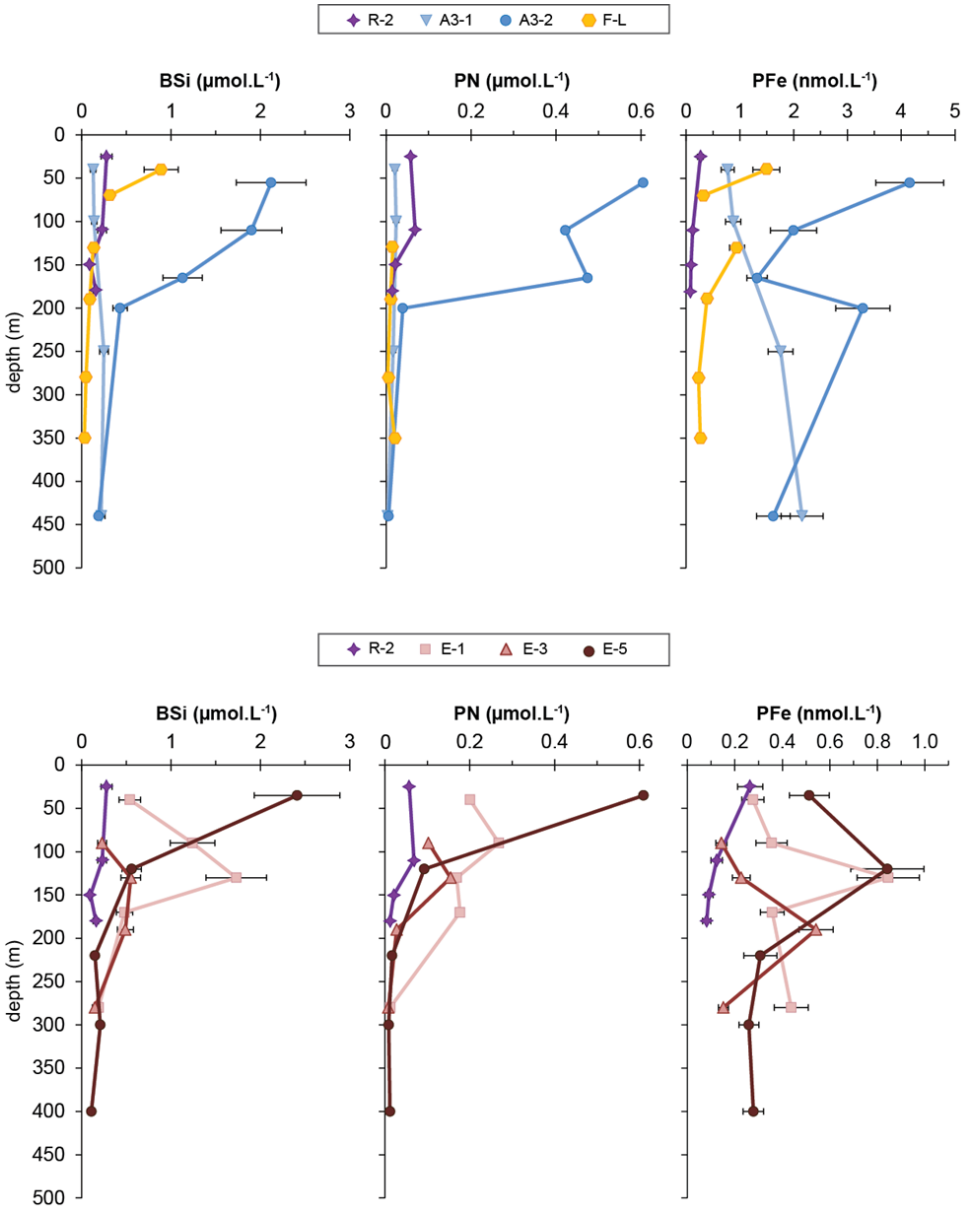

Figure 6.2: Vertical profiles of BSi, PN (µmol.L^{-1}) and PFe (nmol.L^{-1}) concentrations for the different stations.

6.3.3. Element to ^{234}Th ratio of particles

Profiles of Element:^{234}Th ratios are shown in Figure 6.3. For both particle sizes, PN:^{234}Th ratios were high in surface waters (0.98-2.67 µmol.dpm^{-1}), decreased by ~50 % in the upper 200 m and remained relatively constant below 200 m (0.32-0.88 µmol.dpm^{-1}).

Profiles of PFe:^{234}Th and BSi:^{234}Th ratios differed from those of PN:^{234}Th ratios (and POC:^{234}Th; Planchon et al., 2015) by exhibiting a general but variable increase with depth.

PFe:^{234}Th ratios at Eq were greater over the Plateau (36 nmol.dpm^{-1} at A3-2 and ~66 nmol.dpm^{-1} at A3-1) compared to other stations (from 3.2 nmol.dpm^{-1} at R-2 to 15 nmol.dpm^{-1} at E-4W). The highest PFe:^{234}Th ratios were measured at the first visit of the Plateau A3 site (A3-1), reaching 175 nmol.dpm^{-1} at 440 m, near the sea floor. In comparison, variations of BSi:^{234}Th ratios at Eq were smaller (from 2.40 µmol.dpm^{-1} at E-1 to 11.4 µmol.dpm^{-1} at E-3). Overall, PN and PFe to ^{234}Th ratios for the two size fractions (1-53 and > 53 µm) were comparable at Eq, except for a few cases. At A3-2 and E-1, PN:^{234}Th ratios in large particles were ~2 fold lower than ratios for small particles, and at E-3 and F-L, PFe:^{234}Th ratios for large particles were about a factor 2 larger than for small particles.

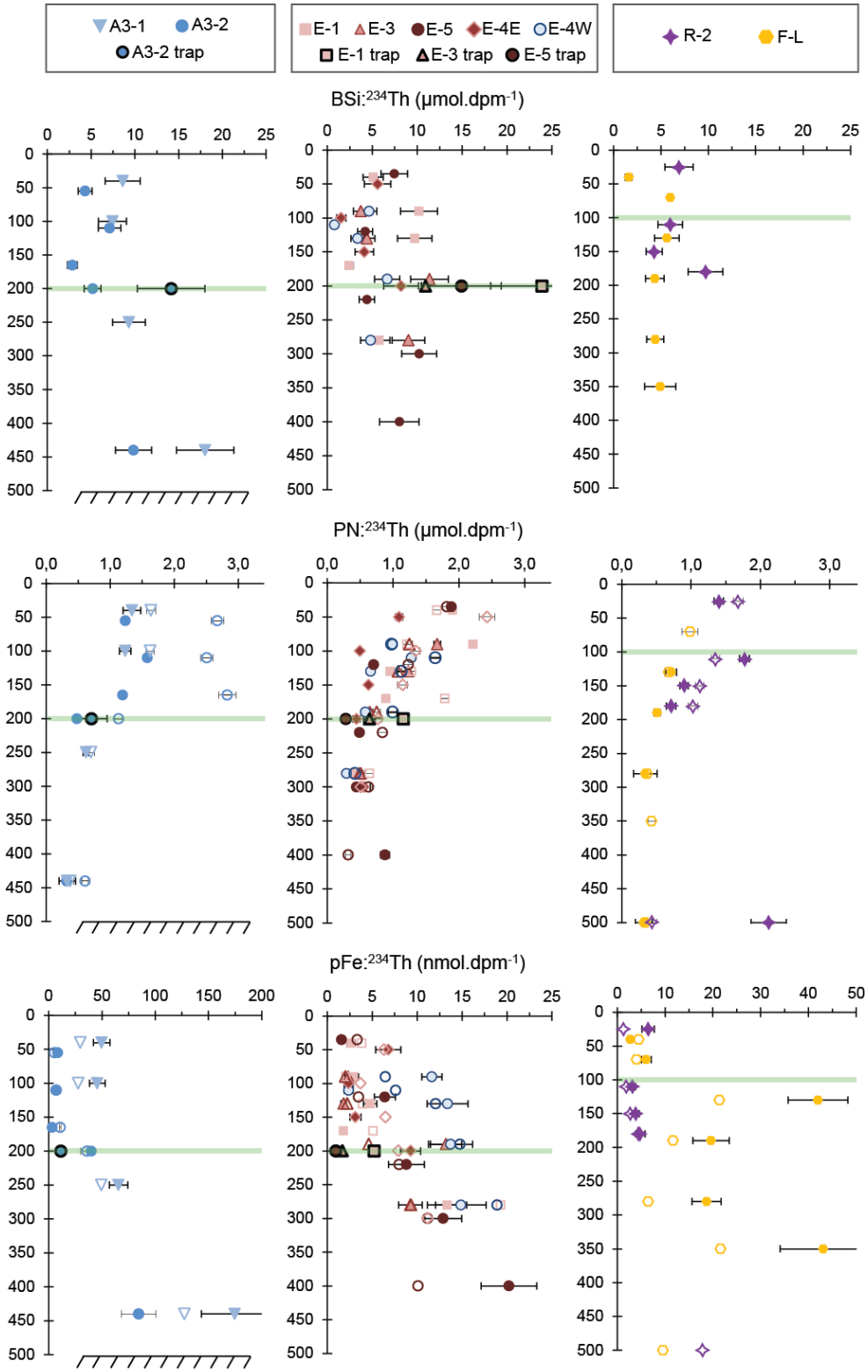

Figure 6.3: Vertical profiles of elemental ratios of a) BSi:^{234}Th, b) PN:^{234}Th, c) PFe:^{234}Th. Large (> 53 µm) particles are represented by filled symbols while small particles (1-53 µm) are represented by open symbols. PFe concentrations for small particles are discussed in van der Merwe et al. (2015), PN concentrations for small particles can be found in Table S2. Sediment trap ratios (from Laurenceau et al., 2015; Bowie et al., 2015) at 200 m are represented by thick black surrounded symbols. Bottom depths are indicated by the zebra lines and Eq depths are indicated by the light green lines.

6.3.4. Element to ^{234}Th ratio of sinking particles

In order to convert ^{234}Th fluxes into PN, BSi, PFe export fluxes, the PN; BSi; PFe to ^{234}Th ratios of the sinking particles at the export depth are required (Buesseler et al., 2006). The different interpolations, detailed in the methods section, were used to estimate the appropriate element:^{234}Th ratio at Eq and the range of the calculated ratios can be found in Table 6.2 and in Figure 6.4. The comparison of the different interpolation methods yields similar results but some disparities were observed especially between the linear interpolation and the depth weighted average methods. The values of PN:^{234}Th ratios derived from the linear interpolation were 1.6 and 2.3 fold lower at A3-2 and at F-L stations, respectively, than ratios calculated using other interpolation methods. On the contrary, the PFe:^{234}Th ratio at A3-2 calculated by linear interpolation was much larger than values estimated by other methods, due to an important local increase of the ratio between 110 and 200m (from 6.96 to 36.04 nmol.dpm^{-1}). The depth-weighted average method yielded the lowest BSi:^{234}Th ratios at E-3 and F-L stations (4.9 and 1.9 µmol.dpm^{-1} compared to average of 11 and 5.8 µmol.dpm^{-1}, respectively) due to low ratios in surface waters (3.73 µmol.dpm^{-1} at 90 m at E-3 and 1.60 µmol.dpm^{-1} at 40 m at F-L). Likewise, PFe:^{234}Th ratios estimated using the depth-weighted average were lower than those estimated by other interpolation methods (up to 8 fold at F-L) but they were similar to ratios obtained from free-floating sediment traps (“P-trap” hereafter; Bowie et al., 2015). Ratios determined by ISP and P-trap methods are in good agreement except for BSi:^{234}Th ratios that were from 1.2 to 5.4 fold higher in P-trap at E-3 and E-1, respectively (Table 6.2 and Figure 6.4). Disagreements in POC:^{234}Th ratios between P-trap and ISP methods have been observed elsewhere, with differences ranging between a factor 2 and 6 (Bacon et al., 1996; Benitez-Nelson et al., 2001; Buesseler et al., 1995, 1992; Lepore et al., 2009; Murray et al., 1996; Puigcorbé et al., 2015; Stewart et al., 2007). In this study, the largest difference between P-trap and ISP was observed at E-1 for BSi: ^{234}Th ratios (factor of 5.4). At all stations, lower BSi: ^{234}Th were measured in ISP compared to P-trap, suggesting that the use of ISP for the estimation of BSi export flux yields a lower limit.

Finally, elemental fluxes can be influenced by the temporal evolution of the Element to ^{234}Th ratio. The range of element:^{234}Th ratios for the different visits of the A3 and E sites somehow reflects the temporal changes in particle composition (Table 6.2, Figure 6.4). During the cruise, the BSi:^{234}Th and PFe:^{234}Th ratios significantly decreased over time by a factor of 1.9 and 2.6 at A3 and, 2.5 and 2.3 at E, respectively. A similar trend was observed at E station for the BSi:^{234}Th and PFe:^{234}Th ratios measured in the sediment traps decreasing by a factor of 2.2 and 5.5, respectively (Laurenceau-Cornec et al., 2015a; Bowie et al., 2015). These temporal evolutions are probably related to the bloom development, changing the biological and chemical conditions in the euphotic layer and thus influencing the particle size and composition. The dynamic shift of BSi:^{234}Th and PFe:^{234}Th ratios could lead to 2-3 fold changes in estimated BSi and PFe export fluxes, indicating the difficulty to estimate these export fluxes. Conversely, as the ratios PN:^{234}Th varied from less than a factor of 1.2 at both A3 and E stations, there seems to be no temporal effect of changing ratios on PN estimated fluxes.

The evolution of PN:^{234}Th ratios over time can also be studied over the growth season by comparing KEOPS2 (austral spring) with KEOPS1 (austral summer; Savoye et al., 2008) for the Plateau A3 site. Before the bloom in October (A3-1 station), PN:^{234}Th was equal to 0.83 ± 0.12 µmol.dpm^{-1} and decreased to 0.73 ± 0.18 µmol.dpm^{-1} in mid-November during the bloom development (A3-2 station). At the end of the productive period in February, as observed during KEOPS1, the PN:^{234}Th ratio reached 0.65 ± 0.28 µmol.dpm^{-1}. This comparison confirms the fairly constancy of the PN:^{234}Th ratio and thus the estimation of the PN export flux.

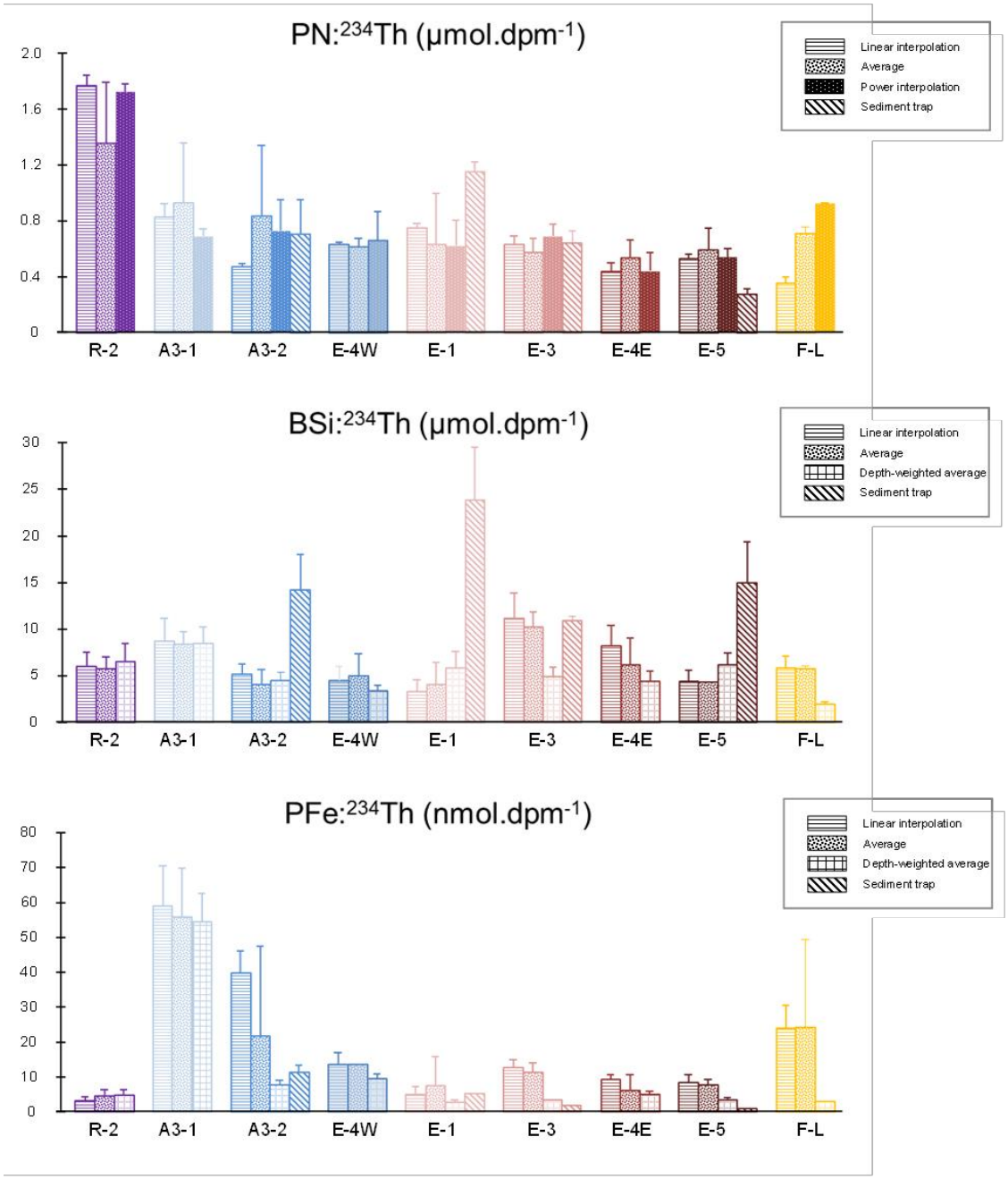

Figure 6.4: Elemental ratios of PN, BSi and PFe to ^{234}Th for the >53 µm size fraction calculated at the Eq depth using different interpolation/averaging methods being: linear interpolation; average around Eq; power interpolation; depth-weighted average. The ratios obtained from sediment traps are also indicated with the BSi:^{234}Th and PN:^{234}Th ratios from Laurenceau et al. (2015) and the PFe:^{234}Th ratios from Bowie et al. (2015).

	MLD m	Eq m	Th flux dpm.m^{-2}.d^{-1}	PN:^{234}Th µmol.dpm^{-1}	PN flux mmol.m-².d^{-1}	ThE PN %	BSi:^{234}Th µmol.dpm^{-1}	BSi flux mmol.m-².d^{-1}	ThE BSi %	PFe:^{234}Th nmol.dpm^{-1}	PFe flux µmol.m-².d^{-1}	POC:^{234}Th µmol.dpm^{-1}	POC flux mmol.m-².d^{-1}	ThE POC %
R-2	76	110	425 ± 134	1.4 - 1.8	0.58 - 0.75	7 - 9	5.73 - 6.46	2.44 - 2.75	79 - 89	3.20 - 4.87	1.36 - 2.07	8.0 - 9.8	3.4 - 4.2	30 - 37
med.				*1.7*	*0.73*	*9*	*5.99*	*2.55*	*82*	*4.5*	*1.92*	*9.5*	*4.1*	*36*
A3-1	123	200	776 ± 171	0.69 - 0.93	0.54 - 0.72		8.38 - 8.70	6.51 - 6.75		54.4 - 59.0	42.2 - 45.8	4.5 - 5.3	3.5 - 4.1	
med.				*0.83*	*0.64*		*8.43*	*6.54*		*55.7*	*43.2*	*4.8*	*3.7*	
A3-2	123	200	993 ± 200	0.48 - 0.84	0.47 - 0.83	1 - 2	4.01 - 5.19	3.99 - 5.15	8 - 11	7.66 - 39.9	7.60 - 36.9	3.1 - 5.6	3.1 - 5.5	2 - 3
med.				*0.73*	*0.72*	*2*	*4.54*	*4.50*	*9*	*21.6*	*21.4*	*5.2*	*5.1*	*3*
P-trap				0.71 ± 0.24	0.36 ± 0.14		14.2 ± 3.9	7.17 ± 2.24		11.4 ± 1.9	5.75 ± 1.20	4.4 ± 1.2	2.2 ± 0.68	
E-4W	55	150	1174 ± 168	0.62 - 0.66	0.73 - 0.77	2	3.37 - 5.01	3.95 - 5.89	12 - 19	9.55 - 13.5	11.2 - 15.9	3.8 - 4.4	4.5 - 5.1	2
med.				*0.63*	*0.74*	*2*	*4.46*	*5.24*	*16*	*13.5*	*15.8*	*3.9*	*4.5*	*2*
E-1	69	200	1665 ± 201	0.62 - 0.75	1.0 - 1.3	7 - 8	3.33 - 5.79	5.54 - 9.63	33 - 57	4.76 - 5.20	4.44 - 12.6	4.1 - 4.7	6.8 - 7.8	16 - 18
med.				*0.64*	*1.1*	*7*	*4.08*	*6.80*	*40*	*4.94*	*8.23*	*4.2*	*7.0*	*16*
P-trap				1.20 ± 0.07	1.0 ± 0.32		23.9 ± 5.7	21.0 ± 10.4		5.20 ± 0.23	4.58 ± 1.38	8.0 ± 0.5	7.0 ± 2.3	
E-3	35	200	1995 ± 176	0.58 - 0.69	1.2 - 1.4	7 - 8	4.91 - 11.1	9.80 - 22.2	93 - >100	3.37 - 12.8	9.80 - 25.5	3.9 - 4.4	7.7 - 8.8	13 - 15
med.				*0.63*	*1.3*	*7*	*10.2*	*20.4*	*> 100*	*11.2*	*22.4*	*4.1*	*8.2*	*14*
P-trap				0.64 ± 0.09	0.72 ± 0.21		10.9 ± 0.5	12.4 ± 2.48		1.67 ± 0.01	1.89 ± 0.29	4.3 ± 0.7	4.9 ± 1.5	
E-4E	80	200	1296 ± 193	0.44 - 0.54	0.57 - 0.69	3	4.91 - 10.2	5.67 - 10.6	27 - 51	4.88 - 9.27	6.33 - 12.0	2.9 - 3.5	3.8 - 4.5	5 - 6
med.				*0.44*	*0.57*	*3*	*8.21*	*7.99*	*38*	*6.20*	*8.03*	*2.9*	*3.8*	*5*
E-5	41	200	1810 ± 190	0.53 - 0.60	0.96 - 1.1	4 - 5	4.31 - 6.18	7.80 - 11.2	28 - 41	3.47 - 8.32	6.29 - 15.1	3.7 - 4.0	6.7 - 7.2	9
med.				*0.54*	*0.98*	*4*	*4.37*	*7.90*	*29*	*7.60*	*13.8*	*3.8*	*6.9*	*9*
P-trap				0.28 ± 0.03	0.27 ± 0.12		14.9 ± 4.5	14.3 ± 12.4		0.94 ± 0.16	0.90 ± 0.36	2.1 ± 0.2	2.0 ± 1.0	
F-L	47	100	902 ± 117	0.36 - 0.93	0.32 - 0.84	0.3 - 1	1.90 - 5.80	1.72 - 5.23	6 - 19	2.91 - 24.0	2.62 - 21.7	2.2 - 5.7	2.0 - 5.1	1 - 2
med.				*0.71*	*0.64*	*1*	*5.80*	*5.23*	*19*	*24.0*	*21.7*	*4.5*	*4.0*	*1*

Table 6.2: Mixed layer depth (MLD), depth of the maximal ^{234}Th export (i.e., "Eq"; Planchon et al., 2015), range of Element:^{234}Th ratios calculated with the different interpolation methods (µmol.dpm^{-1} for PN and BSi:^{234}Th; nmol.dpm^{-1} for PFe:^{234}Th) and corresponding ranges of elemental export fluxes estimated at Eq (mmol.m^{-2}.d^{-1} for PN and BSi fluxes; µmol.m^{-2}.d^{-1} for PFe fluxes). The median value (med.) is also indicated. Determination of BSi and PN export efficiencies were based on Si-uptake (Closset et al., 2014) and total N-uptake rates (Cavagna et al., 2015) in water column integrated from surface to 1% of surface Photosynthetically Active Radiation. Whenever possible, element:^{234}Th ratios and export fluxes are compared to fluxes estimated from sediment traps (P-trap; Laurenceau et al., 2015; Bowie et al., 2015). POC:^{234}Th ratios, POC export fluxes and efficiencies (from Planchon et al., 2015) are also indicated.

6.3.5. Elemental export fluxes

The elemental export fluxes at Eq are presented in Table 6.2 and Figure 6.5.

The highest PN and BSi fluxes were measured at station E-3 (median: 1.26 mmol $PN.m^{-2}.d^{-1}$ and 20.4 mmol $BSi.m^{-2}.d^{-1}$), while the highest PFe export flux was observed at A3-1 (median: 43.2 $\mu mol.m^{-2}.d^{-1}$).

The reference station R-2 was characterized by the lowest BSi and PFe fluxes (median values: 2.55 mmol $BSi.m^{-2}.d^{-1}$ and 1.92 $\mu mol\ PFe.m^{-2}.d^{-1}$). Regarding PN export fluxes, the lowest flux was estimated at E4-E (median value: 0.57 $mmol.m^{-2}.d^{-1}$) but the fluxes estimated at R-2, A3-1, A3-2, E-4W and F-L were not significantly different considering the error bars associated with the different interpolation methods (Figure 6.5). High export fluxes were observed at the moderately productive E site in the PF meander, reaching 1.26 mmol $PN.m^{-2}.d^{-1}$, 20.4 mmol $BSi.m^{-2}.d^{-1}$, 22.4 $\mu mol\ PFe.m^{-2}.d^{-1}$ at E-3, while the highly-productive stations (A3-2 and F-L stations) were characterized by lower fluxes, averaging 0.68 mmol $PN.m^{-2}.d^{-1}$, 4.87 mmol $BSi.m^{-2}.d^{-1}$, and 21.6 $\mu mol\ PFe.m^{-2}.d^{-1}$. Fluxes at F-L station are comparable to those estimated at the HNLC station R-2, and the A3-2 station was characterized by lower BSi and PFe export fluxes than during the early bloom condition prevailing at A3-1.

Lastly, the ranges of elemental fluxes estimated in this paper were in relatively good agreement with elemental fluxes measured with P-traps (Table 6.2, Figure 6.5; Bowie et al., 2015; Laurenceau-Cornec et al., 2015). Nevertheless, PN and PFe export fluxes measured with P-trap were lower or in the lower range of fluxes determined by ISP. In contrast, BSi export fluxes from the P-trap were higher than fluxes determined by ISP, except at station E-3 where both methods gave similar results.

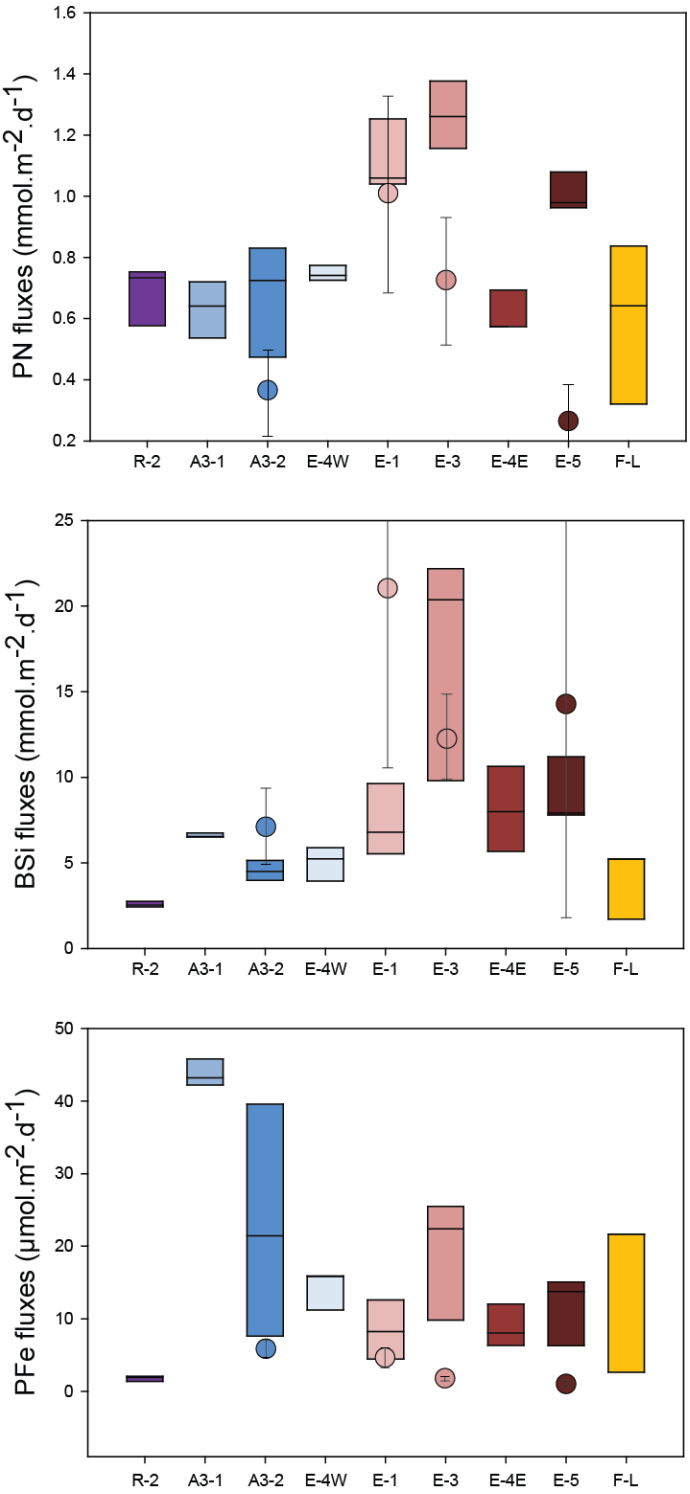

Figure 6.5: Range of calculated PN, BSi (mmol.m^{-2}.d^{-1}) and PFe (µmol.m^{-2}.d^{-1}) export fluxes at the Eq depth from in-situ pumps (box plots) and export fluxes obtained by sediment traps at 200 m (circles; Laurenceau et al., 2015 and Bowie et al., 2015) during KEOPS2. The heights of the boxes correspond to the lowest and the highest values determined by the 4 different interpolation/averaging methods. The plain line inside the box represents the median value.

6.4. Discussion

We will first briefly compare this data set to the existing literature before discussing the impact of the natural Fe-fertilization of the Kerguelen Plateau on the magnitude and stoichiometry of biogeochemical export fluxes. We look into the spatial and temporal variations of export magnitude and efficiency inside and outside of the fertilized area. Then, in order to explain these fluctuations, we consider several factors, such as the phytoplankton community structure, the ballast effects, and the degradation/dissolution processes of the sinking particles, which can all affect the transfer of particulate organic matter from the surface to the deep waters.

6.4.1. Comparison to previous studies

Particulate POC, PN, BSi, PFe concentrations and export fluxes in the Southern Ocean from existing literature are reported in Table 6.3. In particular, particulate concentrations and elemental export fluxes from this dataset are comparable with those of KEOPS1 and CROZEX.

During the bloom development, PN concentrations stayed quiet stable over time, from 0.61 $\mu mol.L^{-1}$ in November to 0.71 $\mu mol.L^{-1}$ in February over the Kerguelen Plateau while POC, BSi and PFe concentrations were roughly 2-fold, 10-fold and 3-fold higher during KEOPS1 and CROZEX, respectively (Mosseri et al., 2008; Planquette et al., 2009; Trull et al., 2008) in comparison to the KEOPS2 survey. The enhancement of the POC, BSi and PFe concentrations in the late season indicated a long retention time for nutrients which has been related to a shift of phytoplankton communities towards more heavily silicified diatoms in a deep chlorophyll maximum. Indeed, these diatoms are characterized by a slow growth and by a high iron storage capacity (Armand et al., 2008; Boyd, 2013; Lasbleiz et al., 2014; Mosseri et al., 2008; Uitz et al., 2009). Otherwise, the increase of PFe and PN concentrations during FeCycle II (austral spring) was related to a shoaling of the mixed layer (Ellwood et al., 2014).

Concerning the elemental export fluxes, PN, BSi and PFe export fluxes appear to be ~3-fold higher during austral summer (CROZEX, KEOPS1; Morris et al., 2007; Planquette et al., 2011;

Salter et al., 2007; Savoye et al., 2008) than in the present austral spring study. The comparison with other studies in the Southern Ocean shows that PN export fluxes were also 2.5-fold lower than fluxes measured during the austral summer artificial Fe fertilization experiment SOIREE, as well as during the austral spring natural Fe fertilization FeCyle II, unlike BSi and PFe export fluxes. These differences suggest an evolution over time of the parameters controlling the sinking particles and thus the export fluxes and they will be discussed in the following discussion.

Cruise	Season	Location	Method	Particle size	POC		PN		BSi		PFe		Reference
				µm	µmol.L^{-1}	mmol.m^{-2}.d^{-1}	µmol.L^{-1}	mmol.m^{-2}.d^{-1}	µmol.L^{-1}	mmol.m^{-2}.d^{-1}	nmol.L^{-1}	µmol.m^{-2}.d^{-1}	
CROZEX	Nov 2004 Jan 2005	Indian sector: Crozet Island	ISP	>53	0.30-0.86		0.05-0.13		0.12-1.1		0.15-13.2		Planquette et al., 2009
			ISP	>53								2.70-145	Planquette et al., 2011
			ISP	>53		5.30-25.8		1.1-4.2					Morris et al., 2007
			P-trap					0.16-2.3		0.80-60.9			Salter et al., 2007
SOFeX	Jan-Feb 2002	Pacific sector	ISP	>53					0.14-1.7				Lam and Bishop, 2007
			ISP	>53		1.20-12.3	0.11-0.45	0.4-1.7		0.10-1.30			Buesseler et al., 2005
SOIREE	Feb 1999	Indian sector	P-trap			5.70-17.0		1.1-3.6		3.15-6.73			Nodder and Waite, 2001
			estimations from P-trap									5.20	Bowie et al., 2001
US JGOFS AESOPS	Oct 1997 Mar 1998	Pacific sector	ISP	>70		5.50-44.4				1.40-11.0			Buesseler et al., 2001
FeCycle	Feb 2003	Pacific sector: southeast of New Zeland	P-trap			2.09-2.51		0.30		0.101-0.127	0.29-0.39	0.22-0.55	Frew et al., 2006
FeCycle 2	Sept-Oct 2008	Pacific sector: east of New Zealand	P-trap+ISP	>0.2	5.2-6.6	11.0-12.0	0.78-0.94	1.1-3.5		2.5-6.0	3.0-23.3	5.0-17.0	Ellwood et al., 2014
KEOPS1	Jan-Feb 2005	Indian sector: Kerguelen Island	filtration	>0.6					2.0-21				Mosseri et al., 2008
			P-trap+ISP	>1.2		10.3-24.5		1.6-4.8					Savoye et al., 2008
			filtration	>55	0.17-8.70		0.20-0.71						Trull et al., 2008
KEOPS2	Oct 2011-May 2012	Indian sector: Kerguelen Island	moored trap			0.04-1.60		0.01-0.23		0.03-2.60			Rembauville et al., 2015a
	Oct-Nov 2011		ISP	>53	0.11-3.9	2.50-10.8							Planchon et al., 2015
			ISP	>53			**0.02 - 0.61**	**0.32-1.4**	**0.13 - 2.4**	**1.72-22.2**	**0.51 - 4.2**	**1.36-45.8**	**this study**

Table 6.3: Comparison of reported ranges for particulate POC, PN, BSi, PFe concentrations and export fluxes in the Southern Ocean.

6.4.2. Impact of natural iron fertilization on export fluxes

The natural Fe fertilization of the Kerguelen Plateau induced an increase of export fluxes. POC export fluxes were higher at Fe-fertilized stations in comparison to the HNLC reference station. The greatest impact was at station E with a 2.9-4.5-fold higher carbon flux at 200m in comparison with the HNLC station (Planchon et al., 2015). Surprisingly, carbon export fluxes at high productivity stations were significantly less amplified (1.6-2.0-fold higher at A3-2, E-4W and F-L stations than at R-2 station; Planchon et al., 2015). Variations of export fluxes within the fertilized area thus appeared decoupled from the productivity, highlighting that other parameters influenced the magnitude and the efficiency of export fluxes during this early season period.

Similarly, BSi and PFe export fluxes at the HNLC reference site R-2 were the lowest, and, the PN flux was amongst the lowest observed in the whole area (Table 6.2, Figure 6.5), indirectly confirming that the natural Fe-fertilization positively enhanced PN, BSi and PFe export fluxes. However, despite the small fluxes; the export efficiencies at R-2 were high, as seen in the ThE_{BSi} value reaching 89% at R-2 and indicating a very efficient silica pump, even though the BSi export flux and the Si-uptake were low (Closset et al., 2014). Similarly, in Fe-limited seawaters of the EIFEX experiment, the Si sequestration was more efficient relative to other nutrients in the deep Southern Ocean (Assmy et al., 2013). These authors have also demonstrated that the POC export was enhanced in iron-replete seawaters. This result is not as evident in the Fe-replete seawaters of the Kerguelen Plateau. Although export fluxes were higher in the fertilized areas above the Plateau and downstream of the island, they did not increase with progress of the growth season. Indeed, the highly productive stations (A3-2 or E-5) were associated with similar or lower POC, PN, PFe and BSi export fluxes in comparison to the low to moderately productive stations (A3-1 or E-1 and E-3 stations; Figure 6.5). The sampling being done during the early stages of bloom development, it is likely that an accumulation of biomass in surface waters could limit the export (Jacquet et al., 2015; Planchon et al., 2015). Indeed, the lowest ThE_{PN} and ThE_{BSi} were recorded at A3-2, E-4W and

F-L stations, confirming that only a small fraction of the produced biomass was exported. In comparison, export fluxes measured during austral summer over the Plateau (using a moored sediment trap or ISP during KEOPS1), indicated that POC, PN and BSi export fluxes do increase during late season (Rembauville et al., 2015b; Savoye et al., 2008; Table 6.3). Clearly, the decline of the diatom bloom during summer, following the depletion of silicic acid (Boyd et al., 2004; Mosseri et al., 2008), triggered a diatom export. The high export fluxes in late season could also be supported by grazing pressures increasing over the season (Carlotti et al., 2015) and leading to the presence of strongly silicified, grazing-resistant and fast-sinking diatoms (Quéguiner, 2013; Pondaven et al., 2007). Similarly, higher POC, PN, BSi and PFe export fluxes were observed above the Crozet Plateau during mid to late season (November 2004 - January 2005; Morris et al., 2007; Planquette et al., 2011; Salter et al., 2007; Table 6.3). The highest PN and BSi export fluxes were measured at the moderately productive E station which was also characterized by the highest ThE_{PN} and ThE_{BSi} values for the Kerguelen area, indicating that elemental exports are not necessarily related to a high productivity (Table 6.2, Figure 6.8).

6.4.3. Importance of elemental composition on export fluxes

6.4.3.1. The silica ballast efficiency dependent on diatom communities

The relative contribution of each diatom is described with great detail by Lasbleiz et al. (submitted). Briefly, at the low and moderately productive stations (R-2 and E stations), the live cell abundance was dominated by large and highly silicified diatom species such as *Fragilariopsis kerguelensis* (18% at R-2 and E-1 and 6% at E-5) and *Thalassionema nitzschioides* (21% at R-2 and E-1 and 17% at E-5). On the contrary, at highly productive stations (A3-2 and F-L stations), small and lightly silicified diatom species such as *Chaetoceros* (*Hyalochaete*) spp. (87 and 31% respectively) and centrics spp. (<25 µm) like *Thalassiosira* spp (5 and 54% respectively) dominated. The different degrees of silicification could have induced different ballast efficiencies and therefore influenced the stoichiometry of export fluxes. In Figure 6.6, we examine the spatial distribution of the BSi:POC, BSi:PN and BSi:PFe

ratios in order to identify the different variations of stoichiometry. These ratios were investigated in the >53 µm bulk material collected via ISP (this study), material collected via P-trap (Laurenceau-Cornec et al., 2015) and for discrete diatom cells from surface waters (Lasbleiz, 2014). In all cases, the highest BSi:POC, BSi:PN and BSi:PFe ratios were measured at stations characterized by a low to moderate productivity (R-2, A3-1 and E stations). Several authors have documented that Si:C and Si:N ratios changed with light and nutrient limitations, grazing pressure, and varying composition of phytoplankton communities (Baines et al., 2010; Claquin et al., 2002; Franck et al., 2000; Hare et al., 2007; Hutchins and Bruland, 1998; Moore et al., 2007; Pondaven et al., 2007; Takeda, 1998). Moreover, it has been shown Si:C ratios tend to increase under Fe-stress conditions in comparison with Fe-replete conditions (Marchetti and Cassar, 2009). During KEOPS2, the Si:C ratios of diatoms confirm this trend, increasing from 0,25 and 0,71 at iron replete stations (F-L and A3-2 respectively) to 0,95 and 1,7 at Fe limited stations (E and R-2 respectively; Lasbleiz, 2014). In our study, BSi:POC, BSi:PN and BSi:PFe molar ratios, in the upper 150 m, varied between 0.54 and 1.29, 3.50 and 8.08, 0.14 and 1.00, respectively, at stations with slightly silicified diatoms (stations A3-2 and F-L), and between 0.40 and 1.71, 2.24 and 10.22, 0.16 and 4.70, respectively, where large and heavily silicified diatom communities dominated (stations R-2, A3-1 and E). The highest BSi:PN and BSi:POC ratios were related to the presence of heavily silicified diatoms dominant at stations where the mixed layer depth and light conditions varied over time (A3-1 and E stations), or where dFe concentrations were limiting (R-2 station). The variations of the BSi:PFe ratio were controlled by the BSi concentrations at E and R-2 stations where PFe concentrations did not vary more than 0.5 nmol.L^{-1} throughout the water column (Table S6.1). Over the Plateau at both visits and north of the PF, lower BSi:PFe ratios were observed due to higher PFe concentrations.

Therefore, the stoichiometry of the sinking particles seems to be related to the different diatom communities present in surface waters. Moreover, the comparison of the different elemental ratios between ISP and P-trap suggest that heavily silicified diatoms were an important contributor of the sinking flux (Figures 6.2 and 6.6). Indeed, BSi:^{234}Th ratios, as well as

BSi:POC, BSi:PN and BSi:PFe ratios, were higher in P-trap than ISP highlighting that the sinking flux was controlled by more heavily silicified diatoms than the standing stock, and/or by fecal pellets that had lost part of their N (or C), as a result of heterotrophic activity. As suggested by Rembauville et al. (2015a), the presence of empty diatom frustules could also control the export stoichiometry and increase the BSi:POC ratio. However, similar PN:^{234}Th (or POC: ^{234}Th) ratios were measured in P-trap and ISP, indicating that the high BSi proportion in particles was probably related to heavily silicified phytoplankton species and not to a loss of POC, PN or PFe.

The presence of these heavily silicified species might have promoted higher export fluxes by ballast, in particular at the low and moderately productive stations (R-2 and E stations) where the export efficiencies were the highest (Laurenceau-Cornec et al., 2015; Le Moigne et al., 2014).

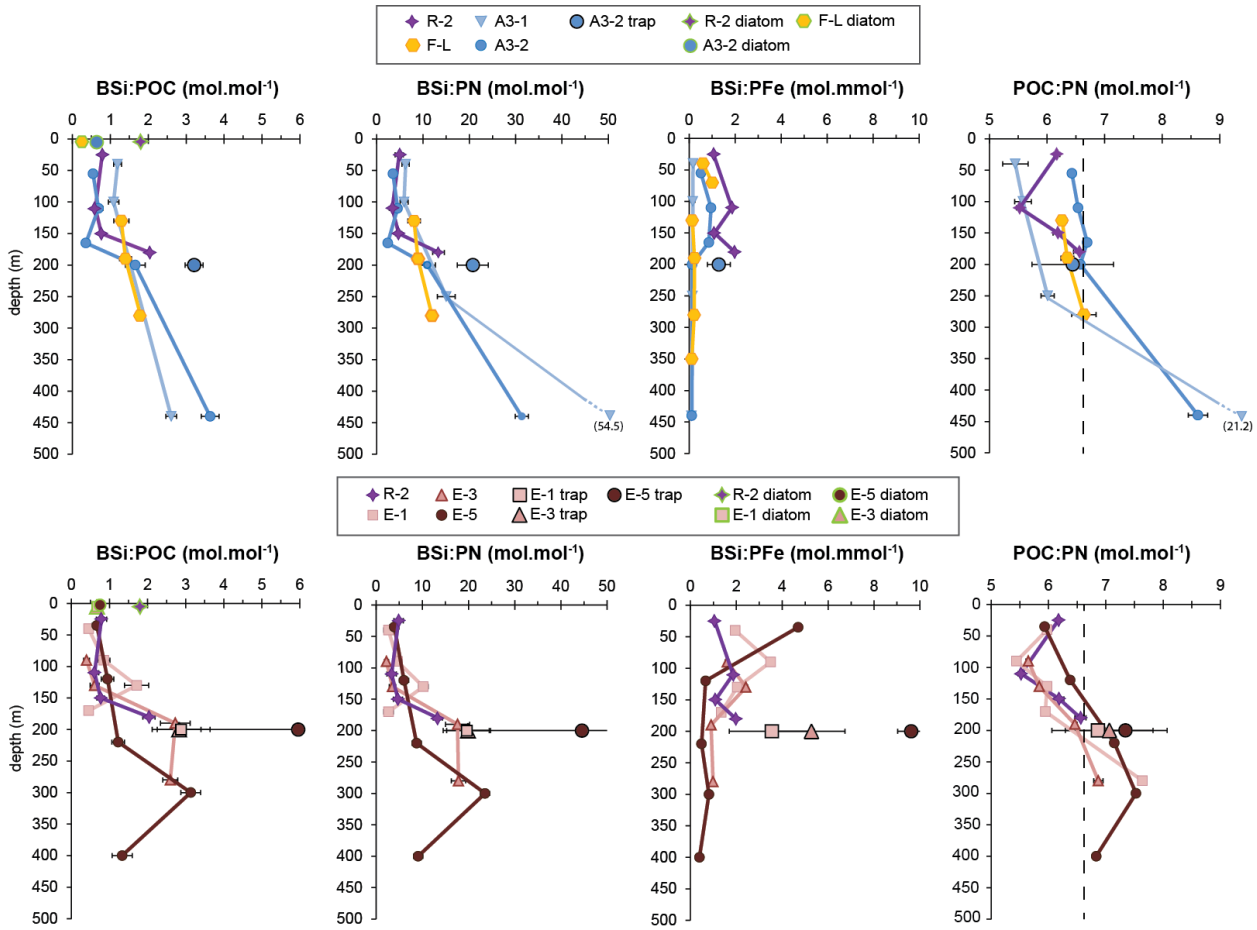

Figure 6.6: Vertical profiles of BSi:POC, BSi:PN, BSi:PFe and POC:PN molar ratios in large particles (> 53 µm) collected in the Kerguelen area. Close to the surface, green surrounded symbols represent Si:C ratios specific to diatoms as reported by Lasbleiz (2014). These ratios were obtained from the carbon biomass and the BSi concentration. The latter may be overestimated by taking into account the living and dead cells. At 200 m, ratios measured in sediment traps by Laurenceau et al. (2015) and Bowie et al. (2015) are represented by the black surrounded symbols. The dashed line represents the typical value of the C:N ratio (6.6) reported by Redfield et al. (1963).

6.4.3.2. PFe export fluxes: under biogenic and lithogenic influences

The highest total PFe export flux of the Kerguelen area was observed over the Plateau during the first visit (A3-1) where the lithogenic Fe fraction was larger than at other stations, with low percentages of biogenic PFe (4% in the upper 100 m at A3-1; Table S6.1). At the second visit, A3-2, the total PFe export flux decreased while the contribution of biogenic PFe increased, representing more than 60% between 110 and 165 m). The Fe retention by biology in surface waters can explain the lower export flux at station A3-2, as well as at E and F-L sites. Regarding small particles (1-53µm), van der Merwe et al. (2015) also observed a larger biogenic PFe pool

at A3-2, suggesting enhanced biological uptake at A3-2 compared to A3-1. Between both visits, the total PFe load shifted from small to large particles, with the 1-53 µm size fraction carrying 8.2 and 0.9 nmol.L^{-1} PFe (van der Merwe et al., 2015) and the >53 µm size fraction carrying 0.8 and 4.2 nmol.L^{-1} PFe (this study) in surface waters at A3-1 and A3-2 stations, respectively. The size partitioning was also investigated for particulate Th activities: 95% of the total particulate ^{234}Th activity was associated with 1-53 µm particles at A3-1 while only 26% was at A3-2 (Table S6.1). Thus, small particles at A3-1 composed largely of lithogenic material were likely responsible for the largest PFe export flux at this station. This corroborates the observations of Bowie et al. (2015) who showed a decrease of the lithogenic PFe stock over the mixed layer from A3-1 to A3-2 (from 892 to 265 µmol.m^{-2}, respectively) while the biogenic PFe stock remained constant between successive visits to the A3 site (from 13 to 14 µmol.m^{-2}). These results point to an important ballast effect of lithogenic particles that can influence the magnitude and the efficiency of the total PFe export flux. This is in line with Ellwood et al. (2014) who showed that the lithogenic PFe had a shorter residence time and was preferentially exported to depth.

Our dataset allows the comparison of vertical PFe export and the mixed layer PFe stock for the A3 and E sites. Bowie et al. (2015) estimated a PFe decrease of 991 and 56 µmol.m^{-2} PFe in the mixed layer over the time elapsed between A3-1 and A3-2 and between E-1 and E-5, respectively.

In order to investigate the temporal evolution, the ^{234}Th flux was calculated using the non-steady state (NSS) model at sites A3 (27 days between A3-1 and A3-2) and E (19 days between E-1 and E-5; Planchon et al., 2015). This ^{234}Th flux was then converted into PFe export fluxes using the average of all PFe:^{234}Th ratios obtained at A3 and E sites (A3-1 and A3-2, and then, E-1, E-3 and E-5 respectively). Over the Plateau, the NSS vertical PFe flux was 46.5 µmol.m^{-2}.d^{-1} which can be translated into an export of 1254 µmol.m^{-2} between A3-1 and A3-2. This value is of the same order of magnitude as the stock lost between the two visits, reported by Bowie et al. (2015), pointing to an efficient vertical transport of PFe. At E site, the NSS PFe flux was 17.7 µmol.m^{-2}.d^{-1} which is equivalent to 335 µmol.m^{-2} exported between E-

1 and E-5, so some 6-fold larger than the loss of PFe stock over the same period (Bowie et al., 2015). Since the E site was characterized by important mesoscale activity and by episodic lateral iron supplies (van der Merwe et al., 2015), the larger difference at this site could result from horizontal and vertical transport processes, other than export and which are not considered in our calculation. However, the PFe export flux through exceeding the PFe stock loss over time is of the same order of magnitude. Overall, the efficient vertical transport of PFe, mostly due to the presence of lithogenic particles, contributed strongly to the decrease of the Fe stock in surface waters (Bowie et al., 2015).

6.4.4. Fluxes and degradation of sinking particles

Ratios of POC over PN fluxes at the different stations was only slightly larger than the canonical Redfield ratio of 6.6 (7.1 mol.mol^{-1}, r²=0.95; n=9; Figure 6.7), indicating that both elements had a similar behavior and that the POC:PN ratio was generally not affected by iron limitation (Hoffmann et al., 2006; Price, 2005).

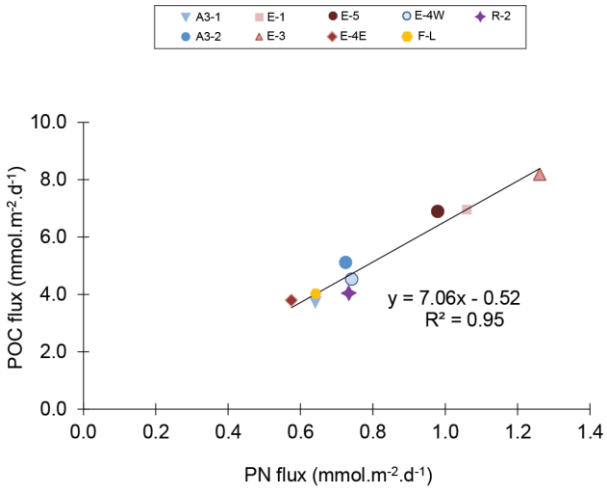

Figure 6.7: POC versus PN fluxes (mmol.m^{-2}.d^{-1}) for all stations.

However, a general increase of the POC:PN ratio with depth was observed for all stations (Figure 6.6). This change may be related to a decrease of PN content in sinking particles due to a preferential remineralization of PN relative to POC with depth, and resulting in nitrification during the bloom period Several authors have confirmed the significance of nitrification in the Kerguelen Plateau area, with nitrification equivalent to up to 47% of the nitrate uptake

(Cavagna et al., 2015; Dehairs et al., 2015; Fripiat et al., 2015). Other studies, investigating suspended particles in the subsurface ocean or particles from deep sediment traps, have generally found a more rapid remineralization of N than organic C (Boyd et al., 1999; Boyd and Trull, 2007; Schneider et al., 2003), consistent with the more labile nature of N (Gordon, 1971). The organic C content of sinking particulate matter is also impacted by remineralization (Jacquet et al., 2015). Using BSi:POC and BSi:PN ratios, the POC and PN degradation relative to BSi is reflected in the increase of ratios with depth (Figure 6.6). An increase of the Si:C ratio with depth is observed in all areas of the ocean and could be explained by zooplankton grazing leading to a preferential preservation of BSi in fecal pellets (Ragueneau et al., 2006, 2002). In particular, during KEOPS2, the highest mesozooplankton biomass was measured at A3-2 and F-L stations reaching 4 and 4.5 g $C.m^{-2}$ whereas it remained on average below 2 g $C.m^{-2}$ at the other stations (Carlotti et al., 2015). Similarly, the highest bacterial respiration rates were measured at the productive stations reaching 1.08, 1.73 and 1.82 µmol $C.L^{-1}.d^{-1}$ at A3-2, E-5 and F-L stations compared to rates on average equal to 0.66 µmol $C.L^{-1}.d^{-1}$ at other stations (Christaki et al., 2014). The high heterotrophic activities led to a reduction of the export fluxes and to low export efficiencies as observed in this study and also shown in Laurenceau-Cornec et al. (2015a).

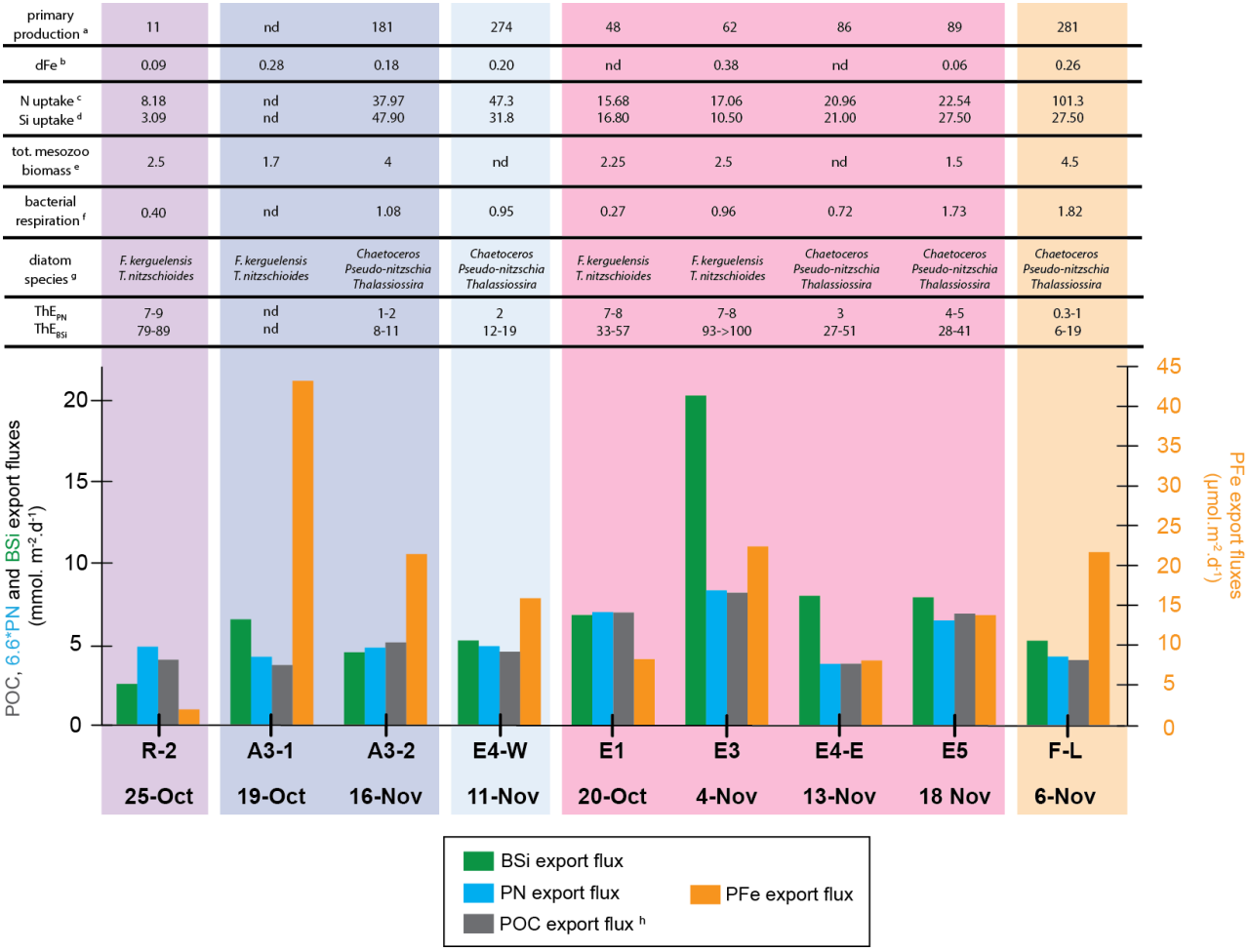

Figure 6.8: Schematic of the main variations of export fluxes determined in this study, in line with other parameters studied during KEOPS2 cruise, including ThE_{PN} , ThE_{BSi}, estimated POC (grey circles), PN (white squares), BSi (grey stars; $mmol.m^{-2}.d^{-1}$), and PFe (orange triangles; $\mu mol.m^{-2}.d^{-1}$) export fluxes. PN export fluxes are multiplied by 6.6 to examine directly the variations of the C:N Redfield ratio. [a] primary production data (mmol $C.m^{-2}.d^{-1}$) from Cavagna et al. (2015). [b] dFe concentrations ($nmol.L^{-1}$) from Quéroué et al. (2015). [c] N uptake data (mmol $N.m^{-2}.d^{-1}$) from Cavagna et al. (2015). [d] Si uptake data (mmol $Si.m^{-2}.d^{-1}$) from Closset et al. (2014). [e] total mesozooplankton biomass data (g $C.m^{-2}$) from Carlotti et al. (2015). [f] bacterial respiration rates ($\mu mol\ C.L^{-1}.d^{-1}$) from Christaki et al. (2014). [g] taxonomic data from Lasbleiz et al. (2016). [h] POC export fluxes ($mmol.m^{-2}.d^{-1}$) from Planchon et al. (2015).

6.5. Conclusion

We investigated PN, BSi and PFe export fluxes in the Kerguelen Plateau area (KEOPS2) using the ^{234}Th-based approach. One of the important issues in determining elemental export fluxes using the ^{234}Th-based approach, is estimating a representative element:^{234}Th ratio of sinking particles at the same depth horizon as the ^{234}Th flux (Buesseler et al., 1992). Due to practical issues related with the sampling of particulate ^{234}Th (need of ISP) compared to total ^{234}Th (CTD casts), it is, in most cases, not possible to obtain the same depth resolution for particulate as for total ^{234}Th. In order to account for the depth-related variations of element:^{234}Th ratios, we decided to apply different interpolation/averaging methods to obtain different estimates of the element to ^{234}Th ratio at the export depth. A range of fluxes was then calculated which highlighted several features of the naturally Fe-fertilized Kerguelen area:

i) At the HNLC site, low fluxes were observed, but BSi export efficiencies were high reaching 89% and suggesting an efficient silica pump.

ii) Low export fluxes were found at high productivity sites located on the Plateau (A3-2 station) and north of the Polar Front (F-L station) suggesting accumulation rather than export of biomass.

iii) Within the permanent meander of the PF (site E), the highest PN and BSi export fluxes were observed however productivity was relatively moderate and bloom development was delayed.

iv) The highest PFe export flux was estimated at the early bloom, low-productivity A3-1 station over the Plateau, largely sustained by Fe-rich lithogenic particles.

Overall, this study suggests that natural Fe-fertilization increased PN, BSi, PFe and POC export fluxes (Figure 6.8) and flux variations inside the fertilized area can be related to the phytoplankton community composition, highlighting a mosaic response to the fertilization. The high PN and BSi fluxes at E site can be driven by the presence of large and heavily silicified diatom communities increasing the proportion of BSi in the export flux via the silica ballast effect. Similarly, the lithogenic contribution could have ballasted PFe export fluxes during the early stages of the bloom, especially over the Plateau where resuspension of shelf-sediments

was important. Total PFe export efficiency was examined and our results were consistent with the data of Bowie et al. (2015) highlighting an efficient vertical transport of PFe particles outside the mixed layer. The degradation of particles was observed by the increase of the C:N ratio with depth, highlighting a preferential remineralization of PN over POC, and explaining the low magnitude and efficiencies of PN export fluxes measured during KEOPS2. The interactions between iron supply, the ecosystem development and export fluxes are complex and this work demonstrated the need to investigate the biogenic export fluxes, in addition to carbon, to obtain a more holistic understanding of the biological pump.

Acknowledgments

We would like to thank the captain, the crew, the scientific participants and chief scientists, Stéphane Blain and Bernard Quéguiner for their assistance at sea during the KEOPS2 expedition, onboard the R/V Marion Dufresne. We acknowledge P. Nonnotte, K. Quessette, M.L. Rouget and C. Liorzou (IUEM, France) for the use of the clean lab and F. Nenciolli (MIO, France) for the composite satellite image. The KEOPS project was supported by the French Agency of National Research (grant: ANR-10-BLAN-0614), the Program LEFE-CYBER of the Institut des Sciences de l'Univers (INSU) and the Institut Paul Emile Victor. Funding for this research was also obtained from Science Policy, Belgium (BELSPO, grant SD/CA/05A), Flanders Research Foundation (FWO, grant G071512N), Vrije Universiteit Brussel (Strategic Research Plan), the Antarctic Climate and Ecosystem Cooperative Research Center (ACE-CRC, Hobart, Australia). Finally, this work was funded by ANR grant BITMAP (ANR-12-PDOC-0025-01) to H. Planquette and by the "Laboratoire d'Excellence" LabexMer (ANR-10-LABX-19).

Table S6.1: Station details with corresponding sampling date, particulate 234Th activities, POC (from Planchon et al., 2015), PN, BSi (µmol.L-1), PAl and PFe (nmol.L-1) concentrations for the >53 µm size fraction. The percentage of biogenic particulate iron is also provided (see section II.3.a for details), and in case of negative values, the symbol "-" is used. Errors were calculated using the partial derivative method in order to estimate the total error propagation.

station	depth	^{234}Th	POC	PN	BSi	PAl	PFe	bio PFe
	m	dpm.L^{-1}	µmol.L^{-1}	µmol.L^{-1}	µmol.L^{-1}	nmol.L^{-1}	nmol.L^{-1}	%
R-2 50°23'S / 66°42'E 25-Oct-2011	25	0.041 ± 0.001	0.36 ± 0.02	0.058 ± 0.002	0.28 ± 0.06	0.30 ± 0.07	0.26 ± 0.05	51
	110	0.039 ± 0.001	0.38 ± 0.01	0.068 ± 0.002	0.23 ± 0.05	0.30 ± 0.06	0.12 ± 0.02	-
	150	0.024 ± 0.001	0.13 ± 0.01	0.021 ± 0.001	0.10 ± 0.02	0.24 ± 0.05	0.09 ± 0.02	-
	180	0.017 ± 0.001	0.08 ± 0.01	0.012 ± 0.001	0.16 ± 0.03	0.18 ± 0.04	0.08 ± 0.02	4
A3-1 50°38'S / 72°05'E 20-Oct-2011	40	0.016 ± 0.001	0.11 ± 0.02	0.021 ± 0.002	0.13 ± 0.03	1.91 ± 0.33	0.77 ± 0.12	-
	100	0.019 ± 0.001	0.13 ± 0.01	0.024 ± 0.002	0.14 ± 0.03	1.95 ± 0.29	0.88 ± 0.14	4
	250	0.027 ± 0.001	0.10 ± 0.01	0.017 ± 0.001	0.25 ± 0.05	3.12 ± 0.47	1.76 ± 0.23	24
	440	0.012 ± 0.000	0.09 ± 0.01	0.004 ± 0.002	0.22 ± 0.04	3.10 ± 0.45	2.16 ± 0.39	38
A3-2 50°37'S / 72°03'E 16-Nov-2011	55	0.490 ± 0.003	3.89 ± 0.03	0.605 ± 0.004	2.12 ± 0.39	9.08 ± 1.49	4.16 ± 0.63	6
	110	0.267 ± 0.002	2.76 ± 0.02	0.422 ± 0.002	1.90 ± 0.34	1.78 ± 0.26	2.00 ± 0.43	62
	165	0.397 ± 0.002	3.18 ± 0.03	0.474 ± 0.004	1.13 ± 0.22	1.15 ± 0.21	1.32 ± 0.19	63
	200	0.082 ± 0.001	0.26 ± 0.01	0.039 ± 0.001	0.43 ± 0.08	4.64 ± 0.68	3.29 ± 0.50	39
	440	0.019 ± 0.000	0.05 ± 0.01	0.006 ± 0.001	0.19 ± 0.04	2.97 ± 0.45	1.62 ± 0.31	21
E-4W 48°46'S / 71°26'E 11-Nov-2011	90	0.085 ± 0.002	0.50 ± 0.01	0.084 ± 0.002	0.39 ± 0.07	2.14 ± 0.18	0.98 ± 0.09	6
	110	0.212 ± 0.003	1.59 ± 0.01	0.271 ± 0.001	0.17 ± 0.04	1.31 ± 0.23	0.50 ± 0.10	-
	130	0.111 ± 0.002	0.44 ± 0.01	0.073 ± 0.001	0.37 ± 0.08	1.84 ± 0.28	1.48 ± 0.25	-
	190	0.072 ± 0.001	0.26 ± 0.01	0.041 ± 0.001	0.48 ± 0.10	0.78 ± 0.13	0.98 ± 0.18	66
	280	0.035 ± 0.001	0.07 ± 0.01	0.010 ± 0.001	0.17 ± 0.04	0.94 ± 0.14	0.52 ± 0.10	23
E-1 48°28'S / 72°12'E 30-Oct-2011	40	0.105 ± 0.002	1.20 ± 0.02	0.200 ± 0.003	0.54 ± 0.12	0.28 ± 0.08	0.28 ± 0.05	56
	90	0.121 ± 0.002	1.46 ± 0.01	0.269 ± 0.002	1.24 ± 0.25	0.78 ± 0.14	0.35 ± 0.07	5
	130	0.177 ± 0.002	1.01 ± 0.01	0.169 ± 0.001	1.73 ± 0.34	0.44 ± 0.10	0.85 ± 0.13	78
	170	0.198 ± 0.002	1.05 ± 0.01	0.177 ± 0.001	0.48 ± 0.09	0.80 ± 0.13	0.36 ± 0.05	4
	280	0.033 ± 0.001	0.10 ± 0.01	0.012 ± 0.001	0.19 ± 0.04	0.82 ± 0.13	0.44 ± 0.07	20
E-3 48°42'S / 71°56'E 3-Nov-2011	90	0.062 ± 0.001	0.58 ± 0.02	0.103 ± 0.002	0.23 ± 0.05	0.33 ± 0.06	0.14 ± 0.02	2
	130	0.126 ± 0.002	0.90 ± 0.01	0.155 ± 0.001	0.55 ± 0.11	0.53 ± 0.09	0.23 ± 0.04	1
	190	0.043 ± 0.001	0.18 ± 0.01	0.028 ± 0.001	0.49 ± 0.09	0.71 ± 0.12	0.54 ± 0.07	44
	280	0.016 ± 0.001	0.06 ± 0.01	0.008 ± 0.001	0.15 ± 0.03	0.37 ± 0.07	0.15 ± 0.02	-
E-4E 48°43'S / 72°34'E 13-Nov-2011	50	0.075 ± 0.002	0.52 ± 0.02	0.082 ± 0.003	0.42 ± 0.11	0.76 ± 0.15	0.51 ± 0.11	36
	100	0.057 ± 0.001	0.19 ± 0.01	0.028 ± 0.002	0.09 ± 0.03	0.22 ± 0.06	0.13 ± 0.03	29
	150	0.067 ± 0.001	0.27 ± 0.01	0.009 ± 0.001	0.28 ± 0.07	0.59 ± 0.10	0.21 ± 0.04	0
	200	0.020 ± 0.001	0.06 ± 0.01	0.007 ± 0.001	0.17 ± 0.04	0.37 ± 0.04	0.19 ± 0.02	15
E-5 48°25'S / 71°54'E 18-Nov-2011	35	0.323 ± 0.004	3.61 ± 0.03	0.609 ± 0.005	2.41 ± 0.48	0.46 ± 0.10	0.51 ± 0.08	62
	120	0.132 ± 0.001	0.59 ± 0.01	0.093 ± 0.002	0.56 ± 0.11	0.48 ± 0.09	0.84 ± 0.15	75
	220	0.035 ± 0.001	0.12 ± 0.01	0.017 ± 0.001	0.15 ± 0.03	0.81 ± 0.14	0.31 ± 0.07	-
	300	0.020 ± 0.001	0.07 ± 0.01	0.009 ± 0.001	0.21 ± 0.04	0.54 ± 0.09	0.26 ± 0.04	10
	400	0.014 ± 0.000	0.08 ± 0.01	0.012 ± 0.001	0.11 ± 0.03	0.53 ± 0.09	0.28 ± 0.04	18
F-L 48°31'S / 74°40'E 6-Nov-2011	40	0.558 ± 0.006	nd nd	nd nd	0.89 ± 0.19	1.58 ± 0.28	1.49 ± 0.25	55
	70	0.051 ± 0.001	nd nd	nd nd	0.31 ± 0.01	0.42 ± 0.06	0.31 ± 0.05	42
	130	0.023 ± 0.001	0.10 ± 0.01	0.016 ± 0.001	0.13 ± 0.03	1.43 ± 0.21	0.95 ± 0.14	35
	190	0.020 ± 0.001	0.06 ± 0.01	0.010 ± 0.001	0.09 ± 0.02	0.75 ± 0.11	0.39 ± 0.07	17
	280	0.012 ± 0.000	0.03 ± 0.01	0.004 ± 0.001	0.05 ± 0.01	0.53 ± 0.09	0.23 ± 0.04	1
	350	0.006 ± 0.000	nd nd	nd nd	0.03 ± 0.01	0.54 ± 0.11	0.27 ± 0.06	13

Table S6.2: Particulate ^{234}Th activities and Particulate Nitrogen (PN) concentrations in small (1-53 µm) and large (> 53 µm) particles collected with *in-situ* pumps during KEOPS2.

Station	Depth	1-53µm		>53µm	
		^{234}Th	PN	^{234}Th	PN
#	m	dpm.L^{-1}	µmol.L^{-1}	dpm.L^{-1}	µmol.L^{-1}
A3-1	40	0.276 ± 0.007	0.451 ± 0.016	0.016 ± 0.001	0.021 ± 0.002
50°38'S / 72°05'E	100	0.243 ± 0.006	0.395 ± 0.012	0.019 ± 0.001	0.024 ± 0.002
20-Oct-2011	250	0.168 ± 0.004	0.118 ± 0.009	0.027 ± 0.001	0.017 ± 0.001
	440	0.239 ± 0.006	0.089 ± 0.011	0.012 ± 0.000	0.004 ± 0.002
R-2	25	0.290 ± 0.008	0.488 ± 0.015	0.041 ± 0.001	0.058 ± 0.002
50°23'S / 66°42'E	110	0.273 ± 0.008	0.369 ± 0.013	0.039 ± 0.001	0.068 ± 0.002
25-Oct-2011	150	0.169 ± 0.005	0.190 ± 0.009	0.024 ± 0.001	0.021 ± 0.001
	180	0.142 ± 0.005	0.146 ± 0.008	0.017 ± 0.001	0.012 ± 0.001
	500	0.076 ± 0.002	0.033 ± 0.005	0.003 ± 0.000	0.006 ± 0.001
	700	0.076 ± 0.002	0.023 ± 0.004	0.004 ± 0.000	0.002 ± 0.001
	1020	0.072 ± 0.002	0.029 ± 0.009	0.003 ± 0.000	0.001 ± 0.001
	1800	0.090 ± 0.003	0.030 ± 0.009	0.002 ± 0.000	0.001 ± 0.001
	2380	nd nd	0.023 ± 0.009	0.003 ± 0.000	0.001 ± 0.001
E-1	40	0.397 ± 0.012	0.661 ± 0.019	0.105 ± 0.002	0.200 ± 0.003
48°28'S / 72°12'E	90	0.302 ± 0.006	0.366 ± 0.013	0.121 ± 0.002	0.269 ± 0.002
30-Oct-2011	130	0.158 ± 0.005	0.202 ± 0.010	0.177 ± 0.002	0.169 ± 0.001
	170	0.101 ± 0.003	0.180 ± 0.009	0.198 ± 0.002	0.177 ± 0.001
	280	0.103 ± 0.004	0.066 ± 0.011	0.033 ± 0.001	0.012 ± 0.001
	610	0.088 ± 0.002	0.030 ± 0.005	0.010 ± 0.000	0.004 ± 0.001
	960	0.059 ± 0.001	0.028 ± 0.004	0.006 ± 0.000	0.002 ± 0.001
	1460	0.065 ± 0.002	0.030 ± 0.007	0.003 ± 0.000	0.001 ± 0.001
	1760	nd nd	0.029 ± 0.007	nd nd	0.001 ± 0.001
	1990	0.041 ± 0.001	0.028 ± 0.007	0.007 ± 0.000	0.002 ± 0.001
E-3	90	0.363 ± 0.009	0.453 ± 0.015	0.062 ± 0.001	0.103 ± 0.002
48°42'S / 71°56'E	130	0.198 ± 0.005	0.214 ± 0.009	0.126 ± 0.002	0.155 ± 0.001
3-Nov-2011	190	0.141 ± 0.004	0.106 ± 0.007	0.043 ± 0.001	0.028 ± 0.001
	280	0.153 ± 0.004	0.076 ± 0.007	0.016 ± 0.001	0.008 ± 0.001
	600	0.098 ± 0.002	0.022 ± 0.005	0.009 ± 0.000	0.003 ± 0.001
	1180	0.109 ± 0.003	0.035 ± 0.007	0.006 ± 0.000	0.001 ± 0.001
	1480	0.095 ± 0.003	0.030 ± 0.007	0.006 ± 0.000	0.001 ± 0.001
	1800	0.074 ± 0.003	0.026 ± 0.007	0.008 ± 0.000	0.002 ± 0.001
F-L	40	0.344 ± 0.011	1.428 ± 0.023	0.558 ± 0.006	nd nd
48°31'S / 74°40'E	70	0.035 ± 0.002	0.034 ± 0.003	0.051 ± 0.001	nd nd
6-Nov-2011	130	0.143 ± 0.004	0.096 ± 0.007	0.023 ± 0.001	0.016 ± 0.001
	190	0.138 ± 0.003	0.071 ± 0.007	0.020 ± 0.001	0.010 ± 0.001
	280	0.130 ± 0.003	0.047 ± 0.007	0.012 ± 0.000	0.004 ± 0.001
	350	0.101 ± 0.003	0.043 ± 0.005	nd nd	nd nd
	500	0.142 ± 0.003	0.048 ± 0.007	0.006 ± 0.000	0.002 ± 0.001
	800	0.104 ± 0.002	0.043 ± 0.007	0.008 ± 0.000	0.002 ± 0.001
	1500	0.068 ± 0.002	0.027 ± 0.004	0.004 ± 0.000	0.001 ± 0.001
	2600	0.136 ± 0.004	0.063 ± 0.008	0.052 ± 0.001	0.010 ± 0.001
E-4W	90	0.262 ± 0.005	0.256 ± 0.012	0.085 ± 0.002	0.084 ± 0.002
48°46'S / 71°26'E	110	0.142 ± 0.003	0.233 ± 0.009	0.212 ± 0.003	0.271 ± 0.001
11-Nov-2011	130	0.142 ± 0.003	0.160 ± 0.008	0.111 ± 0.002	0.073 ± 0.001
	190	0.119 ± 0.003	0.118 ± 0.007	0.072 ± 0.001	0.041 ± 0.001
	280	0.166 ± 0.003	0.070 ± 0.007	0.035 ± 0.001	0.010 ± 0.001

E-4E	50	0.271 ± 0.009	0.658 ± 0.023	0.075 ± 0.002	0.082 ± 0.003
48°43'S / 72°34'E	100	0.222 ± 0.006	0.298 ± 0.013	0.057 ± 0.001	0.028 ± 0.002
13-Nov-2011	150	0.121 ± 0.004	0.139 ± 0.009	0.067 ± 0.001	0.042 ± 0.001
	200	0.131 ± 0.004	0.101 ± 0.008	0.020 ± 0.001	0.009 ± 0.001
	300	0.123 ± 0.004	0.063 ± 0.008	0.012 ± 0.000	0.007 ± 0.001
A3-2	55	0.172 ± 0.004	0.459 ± 0.013	0.490 ± 0.003	0.605 ± 0.004
50°37'S / 72°03'E	110	0.192 ± 0.004	0.482 ± 0.014	0.267 ± 0.002	0.422 ± 0.002
16-Nov-2011	165	0.093 ± 0.002	0.263 ± 0.011	0.397 ± 0.002	0.474 ± 0.004
	200	0.123 ± 0.003	0.139 ± 0.007	0.082 ± 0.001	0.039 ± 0.001
	440	0.148 ± 0.003	0.090 ± 0.007	0.019 ± 0.000	0.006 ± 0.001
E-5	35	0.385 ± 0.008	0.699 ± 0.020	0.323 ± 0.004	0.609 ± 0.005
48°25'S / 71°54'E	120	0.126 ± 0.003	0.155 ± 0.008	0.132 ± 0.001	0.093 ± 0.002
18-Nov-2011	220	0.117 ± 0.003	0.098 ± 0.007	0.035 ± 0.001	0.017 ± 0.001
	300	0.129 ± 0.004	0.081 ± 0.007	0.020 ± 0.001	0.009 ± 0.001
	400	0.142 ± 0.004	0.045 ± 0.006	0.014 ± 0.000	0.012 ± 0.001
	600	0.169 ± 0.005	0.039 ± 0.007	nd nd	0.001 ± 0.001
	900	0.113 ± 0.004	0.037 ± 0.007	0.004 ± 0.000	0.002 ± 0.001
	1200	0.042 ± 0.002	0.011 ± 0.004	nd nd	0.001 ± 0.001
	1850	0.123 ± 0.004	0.033 ± 0.007	0.008 ± 0.000	0.003 ± 0.001

Chapter 7

General conclusions and future directions

7.1. Major findings

The general objective of this work was to improve our understanding on the export and remineralization fluxes of carbon and nutrients (N, Si, trace elements) in two contrasting environments in terms of ecosystem, water masses and nutrient sources: the North Atlantic (GEOTRACES GA01 section) and the Kerguelen Island in the Southern Ocean (KEOPS2).

Chapter three highlighted the ***high regional and temporal variation of the POC export fluxes in the North Atlantic Ocean***, as carbon export fluxes varied by a factor ~ 9 across the east-west section (from 1.4 to 12 mmol $C.m^{-2}.d^{-1}$) and were similar or lower than other studies reported in the North Atlantic.

In line with other studies, this dataset revealed that the ***intensity and the stage of the bloom influenced the magnitude of the POC fluxes***. Indeed, the highest exports were observed at stations sampled during the decline of the bloom rather than at the bloom peak, when biomass was still accumulating in the surface waters. Low export fluxes were also observed at the subtropical site (Station 13), which also was sampled during the bloom decline but was characterized by Chl-*a* biomass development throughout the season.

Another finding of this study, and less anticipated, is that the ***community size structure was not the main factor influencing the fluxes***. While the lowest POC export flux (2.2 mmol $C.m^{-2}.d^{-1}$) was determined at the station where pico-phytoplankton communities dominated, POC export fluxes were high at other stations, regardless of nano- or microphytoplankton abundances.

This study also shows that ***the association of POC with minerals, usually called the ballast mineral effect, enhances the magnitude of the POC export fluxes***, probably by increasing the sinking velocities of the particles. The phytoplankton communities and in particular the diatoms and coccolithophorids, synthesizing SiO_2 and $CaCO_3$ shells, respectively, were demonstrated to ballast the POC export fluxes in the North Atlantic drift (NADR) and in the Arctic (ARCT) provinces, while aggregation of lithogenic particles enhanced POC fluxes at

ocean margins. The highest transfer efficiencies (deep POC export / upper POC export) appeared to be driven by sinking particles ballasted by calcite or lithogenic minerals, but also by the sub-mesoscale activities such as the sub-arctic front. Yet, export efficiency (upper POC export / primary production) was low (< 10% except at two stations where it reached 30 and 35%) and was inversely related to primary production, highlighting that ***the North Atlantic biological pump is not as efficient as previously thought, or at least during spring 2014.***

In **Chapter four**, the Ba_{xs} proxy is used to determine the POC mesopelagic remineralization fluxes along the same transect of the North Atlantic.

The reasonably good agreement between the remineralization based on mesopelagic Ba_{xs} inventories and other methods first confirms our estimations and points to the fact that ***the Ba_{xs} proxy may integrate the remineralization process over a complete season***.

As for POC export, ***remineralization fluxes were regionally variable in the mesopelagic layer*** and intensity of the past blooms and phytoplankton community composition have been identified as factors playing a role in these variations.

Lower remineralization fluxes were observed in case calcified phytoplankton dominated the phytoplankton communities, suggesting that ***carbonate-dominated aggregates resist more to remineralization during their transit through the mesopelagic layer compared to opal-dominated systems***.

This study also revealed ***the importance of the physical features such as the water mass subduction in the ARCT province in generating a larger transport of organic matter to the deep ocean and thus a greater remineralization flux.***

The comparison between Chapters three and four points to ***a balance or a slight excess of POC remineralization relative to POC export in the North Atlantic***. This surprising result highlights the important impact of the mesopelagic remineralization on the biological carbon pump and suggests that little to no particulate organic carbon was transferred below 1000 m.

In **Chapter five**, the vertical export fluxes of the trace elements (Fe, Mn, Al, Co, Ni, Cu, Zn, Cd, P) along the same transect in the North Atlantic are presented and discussed. To date, trace element export fluxes have never been investigated at this resolution anywhere else. The fluxes of trace elements are the net result of a range of processes and the principal component analysis highlighted that the ***lithogenic, BSi and $CaCO_3$ fluxes were the three main components describing the total variability of the trace element fluxes***, with an important regional variation.

The highest trace elements export fluxes were observed near the margins, in environments strongly influenced by lithogenic material. A strong, long-distance lateral transport of lithogenic particles from the Iberian margin was revealed by the presence of high pMn and Mn oxide fluxes at stations located further in the open ocean.

Phytoplankton community structure also influenced the magnitude of trace elements fluxes. The highest trace element fluxes observed in the NADR and the strong relationship between trace element and $CaCO_3$ fluxes suggests that coccolithophorids were important carriers of trace elements to the deep ocean. Diatoms were also driving the trace element fluxes, in particular pZn and pFe, but at diatom-dominated stations (ARCT province which was sampled during the decline of the bloom), these exports were rather low maybe due to a trace element limitation in surface waters or a more efficient recycling processes, limiting the export.

Finally **Chapter six** focused on pFe, BSi and PN export fluxes in the Kerguelen area (Southern Ocean) which is characterized by a naturally Fe-fertilized phytoplankton bloom that extends more than 1000 km downstream of Kerguelen Island (KEOPS2 cruise, austral spring 2011). Our study suggests that ***Fe-fertilization increased PN, BSi, pFe and POC export fluxes*** while flux variations inside the fertilized area could be related to the different diatom species. Indeed, higher elemental fluxes were observed at stations dominated by large and heavily silicified diatoms compared to stations dominated by small and slightly silicified diatoms. Moreover, our results suggest that ***pFe export fluxes could be driven by the lithogenic pool of particles***, especially over the Plateau where such inputs from the sediments are important.

7.2. Comparison of the two study areas

The North Atlantic and the Southern Ocean are two important systems controlling the Earth's climate. Both oceans are prone to strong convection forming deep water masses, such as the Labrador Sea Water (LSW) in the North Atlantic and the Antarctic Bottom Water (AABW) in the Southern Ocean. The formation of these deep water masses represents potentially an important CO_2 sink (Gruber et al., 2009).

The North Atlantic is characterized by one of the most productive phytoplankton bloom of the world's ocean (Longhurst, 2010) which is expected to sustain a strong biological carbon pump (BCP). In contrast, the Southern Ocean is the largest HNLC area of the global ocean where phytoplankton development is limited (a condition which is expected to lead to a weak BCP) except near the Subantarctic islands where natural fertilization feeds large blooms. Therefore, field work conducted in the North Atlantic and the Kerguelen Island area give a good opportunity to compare the biological carbon pump in different natural environments.

At both locations, the bloom development depends on different factors. The depth of the mixed layer and the light are important parameters for the bloom onset in the Kerguelen Island area and in the ARCT province of the North Atlantic (Lasbleiz et al., 2016; Riley et al., 2012). In the southern North Atlantic, especially the NAST province, nutrients usually limit the bloom development and HNLC conditions have been documented in this province (Blain et al., 2004; Moore et al., 2008; Nielsdottir et al., 2009). These different conditions lead to the dominance/succession of different phytoplankton communities. In the Kerguelen Island zone, diatoms dominated the production (Armand et al., 2008; Lasbleiz et al., 2016) yet appear to be smaller and less-silicified than the diatoms in unfavorable conditions (deep mixed layer depth or light limitation) or in Fe-limited waters of the Southern Ocean that are more resistant to grazing and sink efficiently (Quéguiner, 2013; Rembauville et al., 2016c; Salter et al., 2012). In the North Atlantic, diatoms also dominate the production (Martin, 2011; Pommier et al., 2009) but once silicic acid is exhausted an intense bloom of coccolithophorids takes over, persisting into late summer (Poulton et al., 2010). Coccolithophorid skeletons composed of

dense calcified shells are also known to sink efficiently (Bach et al., 2016; Francois et al., 2002; Lam et al., 2011; Salter et al., 2014).

All these regional and temporal differences have been shown to influence the POC export fluxes in both areas (see Chapter 3 for the North Atlantic and Planchon et al., 2015; Savoye et al., 2008 for the Kerguelen Island area).

Despite these differences in ecosystem functioning, the ***magnitude of the POC export fluxes between the North Atlantic*** (median value: 6.1 ± 3.3 mmol.m^{-2}.d^{-1}; n=11) ***and the Kerguelen Island*** (median value: 4.5 ± 1.7 mmol.m^{-2}.d^{-1}; n=9) ***is roughly similar***. ***Similar export efficiencies*** are also observed in both regions (Table 7.1).

Mesopelagic POC remineralization fluxes, on the contrary, are larger in the North Atlantic (median value: 5.4 ± 1.7 mmol.m^{-2}.d^{-1}; Table 7.1) compared to the Southern Ocean Kerguelen area (median during KEOPS2: 2.2 ± 1.1 mmol.m^{-2}.d^{-1}; and 2.8 mmol.m^{-2}.d^{-1} during KEOPS1; Table 7.1). The higher remineralization in the North Atlantic can be induced by higher zooplankton or bacterial activities, or by different sinking velocities of the particles as slower particles are more easily remineralized (Villa-Alfageme et al., 2016).

BSi fluxes in the Kerguelen Island area are larger than those determined in the North Atlantic (with maxima values reaching 20.4 and 6.6 mmol.m^{-2}.d^{-1} at KEOPS2 and GEOVIDE, respectively; Table 7.1). This suggests a larger flux of sinking diatoms around the Southern Ocean Island, probably ***due to the higher silicification of the diatoms and to the larger stock of available silicates***. Nevertheless, the Stations 64 and 69 in the Labrador Sea (GEOVIDE) are characterized by BSi export fluxes of similar magnitude as for Kerguelen area (5 and 6.6 mmol.m^{-2}.d^{-1}) suggesting the export of relatively highly silicified diatoms at these stations. Upper-ocean BSi fluxes are not available for KEOPS1 (summer) but deep BSi fluxes have been shown to increase with the progress of the season due to export of strongly silicified diatom resting spores (Rembauville et al., 2015a). These resting spores have also been described to enhance the POC export fluxes (Rembauville et al., 2016b; Salter et al., 2012) and may explain the increase between KEOPS1 and KEOPS2.

The highest pFe fluxes were observed close to the Iberian Margin (reaching 70 µmol.m^{-2}.d^{-1} at Station 1; Table 7.1) ***and above the Kerguelen Plateau*** (reaching 43 µmol.m^{-2}.d^{-1} at Station A3-1), both areas being characterized by high lithogenic inputs. ***Lithogenic particles thus represent important drivers for the export of Fe*** (and other trace elements, see Chapter 5). Higher pFe exports were determined within the Kerguelen Island area (18.6 ± 11 µmol.m^{-2}.d^{-1}; n=8) than in the North Atlantic (2.5 ± 4.7 µmol.m^{-2}.d^{-1}; n=10), suggesting probably a more efficient remineralization of the pFe in the North Atlantic. This may be due to a greater demand of Fe in the North Atlantic compared to the Kerguelen Island area which is not Fe-limited in surface waters because of the constant fueling of dissolved iron.

KEOPS1 **During or towards the decline of the bloom**

Stations	POC flux mmol/m²/d	ThE POC %	BSi flux mmol/m²/d	pFe flux µmol/m²/d	PP mmol/m²/d	POC Remin 150-450 m mmol/m²/d	POC Remin 150-800 m mmol/m²/d	Main characteristics	Main phytoplankton species
A3	22.0	28			156	2.8		fertilized station	large and heavily silicified
C11	9.5	58			32	1.7		non fertilized station	

KEOPS2 **Before - Beginning of the bloom**

Stations	POC flux mmol/m²/d	ThE POC %	BSi flux mmol/m²/d	pFe flux µmol/m²/d	PP mmol/m²/d	POC Remin 150-400 m mmol/m²/d	POC Remin 150-800 m mmol/m²/d	Main characteristics	Main phytoplankton species
R2	4.1	36	2.6	1.92	11	4.2	7.6	non fertilized station	large and heavily silicified
A3-1	3.7		6.5	43.2		1.2		MLD limitation-before the bloom	large and heavily silicified
A3-2	5.1	3	4.5	21.4	181	0.9		Beginning of the bloom	small and slightly silicified
E4W	4.5	2	5.2	15.8	274	3.0	6.3	Beginning of the bloom	small and slightly silicified
E1	7	16	6.8	8.23	48	2.2	4.0	MLD-light limitation	large and heavily silicified
E3	8.2	14	20.4	22.4	62	0.8	2.9	MLD-light limitation	large and heavily silicified
E4E	3.8	5	8.0	8.03	86	2.2	4.8	Beginning of the bloom	small and slightly silicified
E5	6.9	9	7.9	13.8	89	2.3	5.5	Beginning of the bloom	large and heavily silicified
FL	4	1	5.2	21.7	281	1.7	4.1	Beginning of the bloom	small and slightly silicified

GEOVIDE **During or or towards the decline of the bloom**

Stations	POC flux mmol/m²/d	ThE POC %	BSi flux mmol/m²/d	pFe flux (DWA) µmol/m²/d	PP mmol/m²/d	POC Remin 100-500m mmol/m²/d	POC Remin 100-1000m mmol/m²/d	Main characteristics	Main phytoplankton species
1	11.6	35	1.7	70.0	33		3	under lithogenic influence	mixed
13	2.2	3	0.5	2.5	80	6.7	9.1	end of the bloom - nutrient limitation	cyanobacteria
21	4.8	4	2.0	7.6	135	4.2	8.1	during the bloom	diatoms-dinoflagellates
26	7.3	4	3.8	1.1	174	3.8	8.0	during the bloom	diatoms-dinoflagellates
32	8.4	6	2.3	16.0	142	5.8	8.9	during the bloom	coccolithophorids
38	4.8	7	1.8	7.7	68	6.6	11	during the bloom	coccolithophorids
44	1.4	1	0.8	2.3	137	8.4	17	during the bloom	diatoms
51	2.7	2	1.6	1.7	165	3.7	5.1	during the bloom	diatoms
64	7.8	12	5.0	5.8	67	4.8	15	decline of the bloom	diatoms
69	10.4	34	6.6	2.4	31	8.3	21	decline of the bloom	diatoms
77	6.1	6	2.7	1.1	95	4.9	12	decline of the bloom	diatoms

Table 7.1: POC export fluxes and efficiencies (ThE POC), BSi and pFe export fluxes, primary production (PP), POC mesopelagic remineralization and the main biogeochemical features (bloom stage, limitation, phytoplankton communities) observed during KEOPS1 (Kerguelen Island, austral summer), KEOPS2 (Kerguelen Island, austral spring) and GEOVIDE (North Atlantic, boreal spring). Data from (Cavagna et al., 2015; Jacquet et al., 2015, 2008; Planchon et al., 2015; Savoye et al., 2008; A. Roukaerts, D. Fonseca Batista and F. Deman (unpublished data).

7.3. Perspectives

Several questions could not be addressed in the scope of this study, but the present thesis provides a solid basis for future investigations, including:

- ^{234}Th proxy: Particulate element to ^{234}Th ratio

The determination of the Element to ^{234}Th ratios has to be representative of the sinking particulate matter and needs to be determined at the depth of export (Buesseler et al., 2006). Thus, ***the selection of this ratio is crucial for the ^{234}Th proxy method***. Several studies, including this one, report that this ratio can vary spatially and temporally and is dependent on particle-size, plankton communities, food web dynamics, aggregation-disaggregation processes or sampling methods (Benitez-Nelson and Charette, 2004; Buesseler, 1991; Buesseler et al., 2006; Moran et al., 2003).

The ratio of the large (>53 µm) particles is usually considered as representative of the sinking particulate matter but ***recent studies highlighted that small particles (1-53 µm) can also participate to the export*** (Durkin et al., 2015; Puigcorbé et al., 2015). The comparison between both size fractions is thus highly recommended to evaluate the potential error induced when calculating the elemental flux based only on one size fraction. In Chapters 3 and 6, the Element to ^{234}Th ratios of small and large particles did not differ significantly, validating our estimations of the export fluxes as based only on ratios for large particles. However, in Chapter 5, the trace element to ^{234}Th ratios showed large variations depending on the element and the region. During GEOVIDE, the impossibility to compare these ratios with those determined via sediment trap sampling led us to discuss only elemental fluxes deduced from the large particles. Indeed, one problem emerging when taking the 1-53 µm in consideration is that their density, hence their sinking velocity is not constrained.

Another challenge concerns the mathematical method used to determine the Element to ^{234}Th ratios at the depth of export. In Chapter 6 (Kerguelen area, KEOPS2 study), we applied four different calculations (linear interpolation, average of the two ratios bracketing the specific

depth, power law interpolation and depth-weighted average) and significant differences between the estimations were observed depending on the depth-related variations of the element to ^{234}Th ratios. In this case, a good agreement with the element to ^{234}Th ratios in shallow surface tethered sediment traps confirmed the ratios determined for sinking particles. ***Therefore, the combination of in-situ pumps and sediment traps is highly recommended in future studies to confirm the estimation of the Element:^{234}Th ratios of the sinking particles and resolve the limitations*** when these approaches are used is stand-alone mode. Moreover, the relative abundance of smaller particles should increase with the global warming (Passow and Carlson, 2012), highlighting ***the necessity to investigate the contribution of the small particles in export***.

- Ba_{xs} proxy: Oxygen consumption in the mesopelagic

In Chapter 4, we investigated the Ba_{xs} distributions for the first time in the North Atlantic. Previously, this proxy has been mainly used in the Southern Ocean where a relationship between Ba_{xs} content and oxygen consumption was observed (Dehairs et al., 1997; Shopova et al., 1995). However this relationship has not been tested in other regions of the World's Ocean questioning the ubiquity of the Ba_{xs} content-oxygen consumption relationship in the global ocean. Nonetheless, in the North Atlantic, this proxy approach provided similar estimations of remineralization fluxes obtained by independent methods (OUR, moored sediment traps, incubations), confirming indirectly the relationship. ***More work on the Ba_{xs} proxy and on its relationship with the oxygen consumption in the mesopelagic layer would benefit the scientific community***.

Another great progress in the understanding of the Ba_{xs} proxy would be to ***evaluate its seasonal variability***. Indeed, the Ba_{xs} accumulation in the mesopelagic zone is thought to build-up along the growth season (Cardinal et al., 2005, 2001; Dehairs et al., 1997) but no study has verified that the Ba_{xs} content decreases to the background level after the productive period. Moreover, this investigation ***could also confirm the integration time of the proxy*** (in Chapter 4, we proposed a time integration of 1 year after the comparison with the deep

sediment traps). An ideal sampling scheme could be achieved by regular sampling every month at a fixed open-ocean station not influenced by strong lithogenic inputs, to limit the error induced by the lithogenic correction on the Ba_{xs} concentration, such as PAP (North Atlantic Ocean), BATS (North Atlantic Ocean), Aloha (Pacific Ocean) or Kerfix (Southern Ocean) stations.

- Formation and remineralization of particles

Our understanding on the exchanges between the particulate and dissolved pools is still to be improved as they are primordial to better understand the biological carbon pump.

Indeed, as seen in Chapter 5, the bulk particulate matter collected by sediment traps or *in-situ* pumps represents a large panel of particles that underwent different processes in the water column, such as authigenic mineral formation, dissolution, or enrichment through scavenging or lithogenic inputs, all these processes potentially hiding biological processes such as the uptake or the remineralization of trace metals (Twining et al., 2014).

To address the issues stated above, some new analytical techniques could be used.

The single-cell synchrotron x-ray fluorescence (SXRF) analysis allows the investigation of individual components of sinking material, such as specific phytoplankton communities (Lam et al., 2015b; Twining et al., 2015b, 2010).

Stable isotopes provide information on the relationship between the dissolved and particulate phases such as uptake, scavenging and remineralization as isotope fractionation is observed for each process. In surface waters, the increase of the isotopic signatures of dissolved compounds (NO_3^-, trace metals) can be related to the biological uptake of lighter isotopes while below the surface, the remineralization contributes to the lower isotopic signatures by releasing the lighter isotopes in solution (Hoefs, 2010).

In-situ systems equipped with imaging sensors present also some great advantages to observe the sinking particles and allow a better characterization of particles in terms of size, shape, morphology, abundance, depth distribution, which can help in distinguishing particles responsible of the export (such as aggregates, single cells or fecal pellets; Guidi et al., 2009),

and provide information on sinking speed. Also, at present, little is known on how the particle composition affects their sinking speed, and this point needs to be addressed too. As it will be discussed next Dec. 5th, 2016[2], existing “omic” and “trace elements” dataset acquired during the TARA and GEOTRACES programs could help to achieve this task.

Finally, the ongoing acquisition of the dissolved trace element concentrations (Fe, Mn, Cu, Co, Al) along the GEOVIDE transect will allow a better understanding of the interactions between particulate and dissolved pools and in particular of the processes affecting their concentrations, such as the scavenging and the remineralization.

7.4. The fate of the BCP with global warming

Levels of carbon dioxide (CO_2) gas have increased since preindustrial times due to the anthropogenic inputs such as combustion of fossil fuels. The ocean is the major carbon dioxide (CO_2) reservoir, which thus play an important role in setting the Earth’s climate (Sabine et al., 2004; Sarmiento, 2002). However, the consequences of the global warming on the biological carbon pump are difficult to evaluate, and the expected changes on the ocean biogeochemistry reported in this section are thus speculative.

The increase of oceanic CO_2 concentrations decreases the surface ocean pH (Wolf-gladrow et al., 1999). Such changes have been shown to slow down the calcification rate of corals, pteropods or coccolithophorids (Langdon et al., 2000; Riebesell et al., 2000). These changes of calcification rate may impact directly the biological carbon pump. As seen in Chapters 3 and 4, coccolithophorids, with their dense calcified shells, are important drivers of carbon to the deep ocean (Francois et al., 2002; Klaas and Archer, 2002; Lam et al., 2011; Salter et al., 2014).

The increase of the atmospheric CO_2 concentrations induces also an increase in atmospheric and sea surface temperature (IPCC, 2007). The ocean warming is likely to impact the biological carbon pump in different ways.

[2] http://geotraces.org/news-50/news/116-news/1325-first-geotraces-tara-meeting

First, the average cell size of phytoplankton is predicted to decrease with an elevation of sea-surface temperatures (Passow and Carlson, 2012). As seen in Chapter 3, the extent of small cells, such as pico-phytoplankton species may lead to less overall POC export, as smaller particles would sink slowly and would be prone to upper-remineralization (Villa-Alfageme et al., 2016). However, small particles are prone to lesser flux attenuation in the mesopelagic which would increase the export efficiency (Chapter 4; Guidi et al., 2009; Mouw et al., 2016).

Second, higher oceanic temperatures have been shown to reduce the POC remineralization depth (Marsay et al., 2015), which influence directly the air-sea carbon balance (Kwon et al., 2009).

In Chapter 3, we took the opportunity to compare the Ba_{xs}-based remineralization fluxes determined during GEOSECS and GEOVIDE cruises, 44 years later. No significant variation was observed between both studies with the mesopelagic remineralization flux varying from 5.4 to 5.1 mmol $C.m^{-2}.d^{-1}$ near Greenland, from 6.9 to 10.8 mmol $C.m^{-2}.d^{-1}$ in the Icelandic basin, during GEOSECS and GEOVIDE, respectively. However, remineralization fluxes up to 21 mmol $C.m^{-2}.d^{-1}$ were determined during GEOVIDE but the comparison with GEOSECS here is tricky as these high fluxes were related to the subduction of the Labrador Sea Water. Overall, in 44 years in the North Atlantic, the magnitude of the remineralization seems to be relatively constant.

Third, the increase of sea-surface temperatures may increase the stratification of the water column which would decrease the nutrient delivery into the euphotic zone from deeper ocean and thus decrease the productivity and the POC export (Laufkötter et al., 2016; Passow and Carlson, 2012). Conversely, the reduction of the mixed layer depth in the Southern Ocean may stabilize the water column and decrease the light limitations allowing the increase of the productivity in surface waters and thus the POC export.

Finally, the global warming may also induce a decline in oceanic dissolved oxygen concentrations (Falkowski et al., 2011; Matear and Hirst, 2003; Stramma et al., 2008). The expansion of these suboxic habitats may thus decrease the oxic remineralization by heterotrophs.

Overall, our ability to predict the future biological carbon pump in response to changing climate is limited, but the great effort which has been achieved in the last decades allows a better understanding on the different factors influencing carbon export and remineralization. The multiplication of these studies, in different specific environments, will help to improve the models at larger scales.

References

Achterberg, E.P., Moore, C.M., Henson, S.A., Steigenberger, S., Stohl, A., Eckhardt, S., Avendano, L.C., Cassidy, M., Hembury, D., Klar, J.K., Lucas, M.I., Macey, A.I., Marsay, C.M., Ryan-Keogh, T.J., 2013. Natural iron fertilization by the Eyjafjallajökull volcanic eruption. Geophys. Res. Lett. 40, 921–926. doi:10.1002/grl.50221

Alldredge, A.L., Silver, M.W., 1988. Characteristics, dynamics and significance of marine snow. Prog. Oceanogr. 20, 41–82.

Allredge, A.L., Jackson, G.A., 1995. Aggregation in Marine Systems. Deep Sea Res. Part II Top. Stud. Oceanogr. 42, 1–7. doi:10.1016/0967-0645(95)90003-9

Alvarez, M., Pérez, F., Bryden, H., Rios, A.F., 2004. Physical and biogeochemical transports structure in the North Atlantic subpolar gyre. J. Geophys. Res. 109, 1–21. doi:10.1029/2003JC002015

Aminot, A., Kérouel, R., 2007. Dosage automatique des nutriments dans les eaux marines: méthodes en flux continu, Ifremer-Qu. ed.

Antia, N., Peinert, R., Hebbeln, D., Bathmann, U., Fehner, U., Zeitzschel, B., 2001. Basin-wide particulate carbon flux in the Atlantic Ocean â€™ Regional export patterns and potential for atmospheric sequestration Avan Detlef TM Jan s Susanne regional differences in changes of the export ratio with depth are related to over the Atlantic Oc. Global Biogeochem. Cycles 15, 845–862. doi:10.1029/2000gb001376

Arístegui, J., Agustí, S., Middelburg, J.J., Duarte, C.M., 2005. Respiration in the mesopelagic and bathypelagic zones of the oceans, in: Del Giorgio, P.A., Williams, P.J. (Eds.), Respiration in Aquatic Ecosystems. pp. 182–206. doi:10.1093/acprof:oso/9780198527084.003.0010

Aristegui, J., Gasol, J.M., Duarte, C.M., Herndl, G.J., 2009. Microbial oceanography of the dark ocean' s pelagic realm. Limnol. Oceanogr. 54, 1501–1529.

Armand, L.K., Cornet-Barthaux, V., Mosseri, J., Quéguiner, B., 2008. Late summer diatom biomass and community structure on and around the naturally iron-fertilised Kerguelen Plateau in the Southern Ocean. Deep Sea Res. Part II Top. Stud. Oceanogr. 55, 653–676. doi:10.1016/j.dsr2.2007.12.031

Armstrong, R.A., Lee, C., Hedges, J.I., Honjo, S., Wakeham, S.G., 2002. A new, mechanistic model for organic carbon fluxes in the ocean based on the quantitative association of POC with ballast minerals. Deep Sea Res. Part II Top. Stud. Oceanogr. 49, 219–236. doi:10.1016/S0967-0645(01)00101-1

Armstrong, R. a., Peterson, M.L., Lee, C., Wakeham, S.G., 2009. Settling velocity spectra and the ballast ratio hypothesis. Deep Sea Res. Part II Top. Stud. Oceanogr. 56, 1470–1478. doi:10.1016/j.dsr2.2008.11.032

Assmy, P., Smetacek, V., Montresor, M., Klaas, C., Henjes, J., Strass, V.H., Arrieta, J.M., Bathmann, U., Berg, G.M., Breitbarth, E., Cisewski, B., Friedrichs, L., Fuchs, N., Herndl, G.J., Jansen, S., Kragefsky, S., Latasa, M., Peeken, I., Rottgers, R., Scharek, R., Schuller, S.E., Steigenberger, S., Webb, A., Wolf-Gladrow, D., 2013. Thick-shelled, grazer-protected diatoms decouple ocean carbon and silicon cycles in the iron-limited Antarctic Circumpolar Current. Proc. Natl. Acad. Sci. 110, 20633–20638. doi:10.1073/pnas.1309345110

Bach, L.T., Boxhammer, T., Larsen, A., Hildebrandt, N., Schulz, K.G., Riebesell, U., 2016.

Influence of plankton community structure on the sinking velocity of marine aggregates. Global Biogeochem. Cycles 30, 1145–1165. doi:10.1002/2016GB005372

Bacon, M.P., Anderson, R.F., 1982. Distribution of Thorium isotopes between dissolved and particulate forms in the deep sea. J. Geophys. Res. 87, 2045–2056.

Bacon, M.P., Cochran, J.K., Hirschberg, D., Fleer, A.P., Hammar, T.R., 1996. Export flux of carbon at the equator during the EqPac time-series cruises estimated from 234Th measurements. Deep Sea Res. Part II Top. Stud. Oceanogr. 43, 1133–1153.

Baines, S.B., Twining, B.S., Brzezinski, M.A., Nelson, D.M., Fisher, N.S., 2010. Causes and biogeochemical implications of regional differences in silicification of marine diatoms. Global Biogeochem. Cycles 24, 1–15. doi:10.1029/2010GB003856

Baltar, F., Aristegui, J., Gasol, J.M., Sintes, E., Herndl, G.J., 2009. Evidence of prokaryotic metabolism on suspended particulate organic matter in the dark waters of the subtropical North Atlantic. Limnol. Oceanogr. 54, 182–193.

Belcher, A., Iversen, M., Manno, C., Henson, S.A., Tarling, G.A., Sanders, R., 2016. The role of particle associated microbes in remineralization of fecal pellets in the upper mesopelagic of the Scotia Sea, Antarctica. Limnol. Oceanogr. 1049–1064. doi:10.1002/lno.10269

Benitez-Nelson, C., Buesseler, K.O., Karl, D.M., Andrews, J., 2001. A time-series study of particulate matter export in the North Pacific Subtropical Gyre based on 234 Th : 238 U disequilibrium. Deep Sea Res. Part I Oceanogr. Res. Pap. 48, 2595–2611.

Benitez-Nelson, C.R., Bidigare, R., Dickey, T.D., Landry, M.R., Leonard, C.L., Brown, S.L., Nencioli, F., Rii, Y.M., Maiti, K., Becker, J.W., Bibby, T.S., Black, W., Cai, W., Carlson, C.A., Chen, F., Kuwahara, V.S., Mahaffey, C., M., M.P., Quay, P.D., Rappé, M.S., Selph, K.E., Simmons, M.P., Yang, E.J., 2007. Mesoscale eddies drive increased silica export in the Subtropical Pacific Ocean. Science (80-.). 316, 1017–1022. doi:10.1126/science.1136221

Benitez-Nelson, C.R., Buesseler, K.O., Crossin, G., 2000. Upper ocean carbon export, horizontal transport, and vertical eddy diffusivity in the southwestern Gulf of Maine. Cont. Shelf Res. 20, 707–736. doi:10.1016/S0278-4343(99)00093-X

Benitez-Nelson, C.R., Charette, M.A., 2004. Uncertainty versus variability in upper ocean carbon flux estimates. Limnol. Oceanogr. 49, 1218–1220.

Berelson, W.M., 2001. The flux of particulate organic carbon into the ocean interior : A comparison of four U.S. JGOFS regional studies. Oceanography 14, 59–67.

Berner, R.A., 1980. Early diagenesis: A theoritical approach, Princeton. ed.

Bhat, S.G., Krishnaswanmy, S., Lal, D., Moore, W.S., 1969. 234Th/238U Ratios in the Ocean. Earth Planet. Sci. Lett. 5, 433–491.

Bhatia, M.P., Kujawinski, E.B., Das, S.B., Breier, C.F., Henderson, P.B., Charette, M.A., 2013. Greenland meltwater as a significant and potentially bioavailable source of iron to the ocean. Nat. Geosci. 6, 274–278. doi:10.1038/ngeo1746

Bidigare, R.R., Benitez-nelson, C., Leonard, C.L., Quay, P.D., Parsons, M.L., Foley, D.G., Seki, M.P., 2003. Influence of a cyclonic eddy on microheterotroph biomass and carbon export in the lee of Hawaii. Geophys. Res. Lett. 30, 1–4. doi:10.1029/2002GL016393

Bidle, K.D., Azam, F., 1999. Accelerated dissolution of diatom silica by marine bacterial assemblages. Nature 397, 508–512.

Billet, D.S.M., Lampitt, R.S., Rice, A.L., Mantoura, R.F.C., 1983. Seasonal sedimentation of phytoplankton to the deep-sea benthos. Nature 302.

Bishop, J.K.B., 1988. The barite-opal-organic carbon association in oceanic particulate matter.

Nature. doi:10.1038/332341a0

Bishop, J.K.B., Fleisher, M.Q., 1987. Particulate manganese dynamics in Gulf Stream warm-core rings and surrounding waters of the N.W. Atlantic. Geochim. Cosmochim. Acta 51, 2807–2825.

Bishop, J.K.B., Lam, P.J., Wood, T.J., 2012. Getting good particles: Accurate sampling of particles by large volume in-situ filtration. Limnol. Oceanogr. Methods 10, 681–710. doi:10.4319/lom.2012.10.681

Blain, S., Guieu, C., Claustre, H., Leblanc, K., Moutin, T., Guiner, B.Q., Ras, J., Sarthou, G., 2004. Availability of iron and major nutrients for phytoplankton in the north-east Atlantic Ocean. Limnol. Oceanogr. 49, 2095–2104. doi:10.4319/lo.2004.49.6.2095

Blain, S., Quéguiner, B., Armand, L.K., Belviso, S., Bombled, B., Bopp, L., Bowie, A.L., Brunet, C., Brussaard, C., Carlotti, F., Christaki, U., Corbière, A., Durand, I., Ebersbach, F., Fuda, J.L., Garcia, N., Gerringa, L., Griffiths, B., Guigue, C., Guillerm, C., Jacquet, S., Jeandel, C., Laan, P., Lefèvre, D., Lo Monaco, C., Malits, A., Mosseri, J., Obernosterer, I., Park, Y.H., Picheral, M., Pondaven, P., Remenyi, T., Sandroni, V., Sarthou, G., Savoye, N., Scouarnec, L., Souhaut, M., Thuiller, D., Timmermans, K., Trull, T., Uitz, J., van Beek, P., Veldhuis, M., Vincent, D., Viollier, E., Vong, L., Wagener, T., 2007. Effect of natural iron fertilization on carbon sequestration in the Southern Ocean. Nature 446, 1070–1074. doi:10.1038/nature05700

Boss, E., Guidi, L., Richardson, M.J., Stemmann, L., Gardner, W., Bishop, J.K.B., Anderson, R.F., Sherrell, R.M., 2015. Optical techniques for remote and in-situ characterization of particles pertinent to GEOTRACES. Prog. Oceanogr. 133, 43–54. doi:10.1016/j.pocean.2014.09.007

Bowie, A.R., Maldonado, M.T., Frew, R.D., Croot, P.L., Achterberg, E.P., Mantoura, R.F.C., Worsfold, P.J., Law, C.S., Boyd, P.W., 2001. The fate of added iron during a mesoscale fertilisation experiment in the Southern Ocean. Deep Sea Res. Part II Top. Stud. Oceanogr. 48, 2703–2743. doi:10.1016/S0967-0645(01)00015-7

Bowie, A.R., van der Merwe, P., Quéroué, F., Trull, T., Fourquez, M., Planchon, F., Sarthou, G., Chever, F., Townsend, A.T., Obernosterer, I., Sallée, J.-B., Blain, S., 2015. Iron budgets for three distinct biogeochemical sites around the Kerguelen archipelago (Southern Ocean) during the natural fertilisation experiment KEOPS-2. Biogeosciences 12, 4421–4445. doi:10.5194/bgd-12-4421-2015

Boyd, P.W., 2013. Diatom traits regulate Southern Ocean silica leakage. Proc. Natl. Acad. Sci. 110, 20358–20359. doi:10.1073/pnas.1320327110

Boyd, P.W., Ellwood, M.J., 2010. The biogeochemical cycle of iron in the ocean. Nat. Geosci. 3, 675–682. doi:10.1038/ngeo964

Boyd, P.W., Ibisanmi, E., Sander, S.G., Hunter, K.A., Jackson, G.A., 2010. Remineralization of upper ocean particles: Implications for iron biogeochemistry. Limnol. Oceanogr. 55, 1271–1288. doi:10.4319/lo.2010.55.3.1271

Boyd, P.W., Jickells, T., Law, C.S., Blain, S., Boyle, E.A., Buesseler, K.O., Coale, K.H., Cullen, J.J., de Baar, H.J.W., Follows, M., Harvey, M., Lancelot, C., Levasseur, M., Owens, N.P.J., Pollard, R., Rivkin, R.B., Sarmiento, J., Schoemann, V., Smetacek, V., Takeda, S., Tsuda, A., Turner, S., Watson, A.J., 2007. Mesoscale iron enrichment experiments 1993-2005: synthesis and future directions. Science (80-.). 315, 612–617. doi:10.1126/science.1131669

Boyd, P.W., Law, C.S., Wong, C.S., Nojiri, Y., Tsuda, A., Levasseur, M., Takeda, S., Rivkin, R., Harisson, P.J., Strzepek, R., Gower, J., McKay, R.M., Abraham, E., Arychuk, M., Barwell-Clarke, J., Crawford, W., Crawford, D., Hale, M., Harada, K., Johnson, K., Kiyosawa, H., Kudo, I., Marchetti, A., Miller, W., Needoba, J., Nishioka, J., Ogawa, H.,

Page, J., Robert, M., Saito, H., Sastri, A., Sherry, N., Soutar, T., Sutherland, N., Taira, Y., Whitney, F., Wong, S.-K.E., Yoshimura, T., 2004. The decline and fate of an iron-induced subarctic phytoplankton bloom. Nature 428, 549. doi:10.1029/2001JB001129

Boyd, P.W., Newton, P.P., 1999. Does planktonic community structure determine downward particulate organic carbon flux in different oceanic provinces ? Deep Sea Res. Part I Oceanogr. Res. Pap. 46, 63–91.

Boyd, P.W., Sherry, N.D., Berges, J. a., Bishop, J.K.B., Calvert, S.E., Charette, M. a., Giovannoni, S.J., Goldblatt, R., Harrison, P.J., Moran, S.B., Roy, S., Soon, M., Strom, S., Thibault, D., Vergin, K.L., Whitney, F. a., Wong, C.S., 1999. Transformations of biogenic particulates from the pelagic to the deep ocean realm. Deep Sea Res. Part II Top. Stud. Oceanogr. 46, 2761–2792. doi:10.1016/S0967-0645(99)00083-1

Boyd, P.W., Trull, T.W., 2007. Understanding the export of biogenic particles in oceanic waters: Is there consensus? Prog. Oceanogr. 72, 276–312. doi:10.1016/j.pocean.2006.10.007

Bressac, M., Guieu, C., Doxaran, D., Bourrin, F., Obolensky, G., Grisoni, J.-M., 2012. A mesocosm experiment coupled with optical measurements to assess the fate and sinking of atmospheric particles in clear oligotrophic waters. Geo-Marine Lett. 32, 153–164. doi:10.1007/s00367-011-0269-4

Brew, H.S., Moran, S.B., Lomas, M.W., Burd, A.B., 2009. Plankton community composition , organic carbon and thorium-234 particle size distributions , and particle export in the Sargasso Sea. J. Mar. Res. 67, 845–868.

Broecker, W.S., Peng, T.H., 1982. Tracers in the Sea, Lamont-Doh. ed.

Bruland, K.W., Donat, J.R., Hutchins, D. a., 1991. Interactive influences of bioactive trace metals on biological production in oceanic waters. Limnol. Oceanogr. 36, 1555–1577. doi:10.4319/lo.1991.36.8.1555

Bruland, K.W., Lohan, M.C., 2008. Elevated Fe (II) and dissolved Fe in hypoxic shelf waters off Oregon and Washington : An enhanced source of iron to coastal upwelling regimes. Environ. Sci. Technol. 42, 6462–6468. doi:10.1021/es800144j

Bruland, K.W., Lohan, M.C., 2003. Controls of trace metals in seawater, in: Elderfield, H. (Ed.), The Oceans and Marine Geochemistry. pp. 23–47.

Buesseler, K.O., 1998. The decoupling of production and particulate export in the surface ocean. Global Biogeochem. Cycles 12, 297. doi:10.1029/97GB03366

Buesseler, K.O., 1991. Do upper-ocean sediment traps provide an accurate record of particle flux? Nature. doi:10.1038/353420a0

Buesseler, K.O., Andrews, J.A., Hartman, M.C., Belastock, R., Chai, F., 1995. Regional estimates of the export flux of particulate organic carbon derived from thorium-234 during the JGOFS EqPac program. Deep Sea Res. Part II Top. Stud. Oceanogr. 42, 777–804. doi:10.1016/0967-0645(95)00043-P

Buesseler, K.O., Andrews, J.E., Pike, S., Charette, M.A., 2005. Particle export during the Southern Ocean Iron Experiment (SOFeX). Limnol. Oceanogr. 50, 311–327. doi:10.4319/lo.2005.50.1.0311

Buesseler, K.O., Antia, A.N., Chen, M., Fowler, S.W., Gardner, W.D., Gustafsson, O., Harada, K., Michaels, A.F., Rutgers van der Loeff, M., Sarin, M., Steinberg, D.K., Trull, T., 2007. An assessment of the use of sediment traps for estimating upper ocean particle fluxes. J. Mar. Res. 65, 345–416. doi:10.1357/002224007781567621

Buesseler, K.O., Bacon, M.P., Kirk Cochran, J., Livingston, H.D., 1992. Carbon and nitrogen export during the JGOFS North Atlantic Bloom experiment estimated from 234Th: 238U disequilibria. Deep Sea Res. Part A. Oceanogr. Res. Pap. 39, 1115–1137. doi:10.1016/0198-0149(92)90060-7

Buesseler, K.O., Ball, L., Andrews, J., Cochran, J.K., Hirschberg, D.J., Bacon, M.P., Fleer, A., Brzezinski, M., 2001. Upper ocean export of particulate organic carbon and biogenic silica in the Southern Ocean along 170W. Deep Sea Res. Part II Top. Stud. Oceanogr. 48, 4275–4297. doi:10.1016/S0967-0645(01)00089-3

Buesseler, K.O., Benitez-Nelson, C.R., Moran, S.B., Burd, a., Charette, M., Cochran, J.K., Coppola, L., Fisher, N.S., Fowler, S.W., Gardner, W.D., Guo, L.D., Gustafsson, Ö., Lamborg, C., Masque, P., Miquel, J.C., Passow, U., Santschi, P.H., Savoye, N., Stewart, G., Trull, T., 2006. An assessment of particulate organic carbon to thorium-234 ratios in the ocean and their impact on the application of 234Th as a POC flux proxy. Mar. Chem. 100, 213–233. doi:10.1016/j.marchem.2005.10.013

Buesseler, K.O., Boyd, P.W., 2009. Shedding light on processes that control particle export and flux attenuation in the twilight zone of the open ocean. Limnol. Oceanogr. 54, 1210–1232. doi:10.4319/lo.2009.54.4.1210

Buesseler, K.O., Lamborg, C.H., Boyd, P.W., Lam, P.J., Trull, T.W., Bidigare, R.R., Bishop, J.K.B., Casciotti, K.L., Dehairs, F., Elskens, M., Honda, M., Karl, D.M., Siegel, D. a, Silver, M.W., Steinberg, D.K., Valdes, J., Mooy, B. Van, Wilson, S., 2007. Revisiting Carbon Flux Through the Ocean ' s Twilight Zone. Science (80-.). 316, 567–570. doi:10.1126/science.1137959

Burd, A.B., Buchan, A., Church, M., Landry, M.R., McDonnell, A.M.P., Passow, U., Steinberg, D.K., Benway, H., 2016. Towards a transformative understanding of the ocean' s biological pump: Priorities for future research. Rep. NSF Biol. Biol. Pump Work. doi:10.1575/1912/8263

Burd, A.B., Hansell, D.A., Steinberg, D.K., Anderson, T.R., Ar??stegui, J., Baltar, F., Beaupr??, S.R., Buesseler, K.O., DeHairs, F., Jackson, G.A., Kadko, D.C., Koppelmann, R., Lampitt, R.S., Nagata, T., Reinthaler, T., Robinson, C., Robison, B.H., Tamburini, C., Tanaka, T., 2010. Assessing the apparent imbalance between geochemical and biochemical indicators of meso- and bathypelagic biological activity: What the @$#! is wrong with present calculations of carbon budgets? Deep Sea Res. Part II Top. Stud. Oceanogr. 57, 1557–1571. doi:10.1016/j.dsr2.2010.02.022

Caçador, I., Vale, C., Catarino, F., 1996. Accumulation of Zn, Pb, Cu, Cr and Ni in sediments between roots of the Tagus estuary salt marshes, Portugal. Estuar. Coast. Shelf Sci. 42, 393–403.

Caldeira, K., Wickett, M.E., 2003. Anthropogenic carbon and ocean pH. Nature 425, 365. doi:10.1038/425365a

Cao, Z., Siebert, C., Hathorne, E.C., Dai, M., Frank, M., 2016. Constraining the oceanic barium cycle with stable barium isotopes. Earth Planet. Sci. Lett. 434, 1–9. doi:10.1016/j.epsl.2015.11.017

Capone, D.G., Burns, J.A., Montoya, J.P., Subramaniam, A., Mahaffey, C., Gunderson, T., Michaels, A.F., Carpenter, E.J., 2005. Nitrogen fixation by Trichodesmium spp .: An important source of new nitrogen to the tropical and subtropical North Atlantic Ocean. Global Biogeochem. Cycles 19, 1–17. doi:10.1029/2004GB002331

Capone, D.G., Zehr, J.P., Paerl, H.W., Bergman, B., Carpenter, E.J., 1997. Trichodesmium, a globally significant marine cyanobacterium. Science (80-.). 276, 1221–1229. doi:10.1126/science.276.5316.1221

Cardinal, D., Dehairs, F., Cattaldo, T., André, L., 2001. Geochemistry of suspended particles in the Subantarctic and Polar Frontal zones south of Australia: Constraints on export and advection processes. J. Geophys. Res. 106, 31637. doi:10.1029/2000JC000251

Cardinal, D., Savoye, N., Trull, T.W., André, L., Kopczynska, E.E., Dehairs, F., 2005. Variations of carbon remineralisation in the Southern Ocean illustrated by the Baxs proxy. Deep Sea

Res. Part I Oceanogr. Res. Pap. 52, 355–370. doi:10.1016/j.dsr.2004.10.002

Carlotti, F., Jouandet, M.-P., Nowaczyk, A., Harmelin-Vivien, M., Lefèvre, D., Richard, P., Zhu, Y., Zhou, M., 2015. Mesozooplankton structure and functioning during the onset of the Kerguelen phytoplankton bloom during the KEOPS2 survey. Biogeosciences 12, 4543–4563. doi:10.5194/bg-12-4543-2015

Carlson, C.A., Hansell, D.A., Nelson, N.B., Siegel, D.A., Smethie, W.M., Khatiwala, S., Meyers, M.M., Halewood, E., 2010. Dissolved organic carbon export and subsequent remineralization in the mesopelagic and bathypelagic realms of the North Atlantic basin. Deep Sea Res. Part II Top. Stud. Oceanogr. 57, 1433–1445. doi:10.1016/j.dsr2.2010.02.013

Carpenter, E.J., Montoya, J.P., Burns, J., Mulholland, M.R., Subramaniam, A., Capone, D.G., 1999. association in the tropical Atlantic Ocean. Mar. Ecol. Prog. Ser. 185, 273–283.

Cavagna, A.J., Fripiat, F., Elskens, M., Dehairs, F., Mangion, P., Chirurgien, L., Closset, I., Lasbleiz, M., Flores–Leiva, L., Cardinal, D., Leblanc, K., Fernandez, C., Lefèvre, D., Oriol, L., Blain, S., Quéguiner, B., 2015. Biological productivity regime and associated N cycling in the vicinity of Kerguelen Island area, Southern Ocean. Biogeosciences 12, 6515–6528. doi:10.5194/bgd-12-6515-2015

Cavan, E.L., Le Moigne, F.A.C., Poulton, A.J., Tarling, G.A., Ward, P., Daniels, C.J., Fragoso, G.M., Sanders, R.J., 2015. Attenuation of particulate organic carbon flux in the Scotia Sea, Southern Ocean, is controlled by zooplankton fecal pellets. Geophys. Res. Lett. 42, 821–830. doi:10.1002/2014GL062744.Received

Ceballos-romero, E., Le Moigne, F.A.C., Henson, S., Marsay, C.M., Sanders, R.J., García-Tenorio, R., Villa-Alfageme, M., 2016. Influence of bloom dynamics on particle export efficiency in the North Atlantic: a comparative study of radioanalytical techniques and sediment traps. Mar. Chem. 186, 198–210. doi:10.1016/j.marchem.2016.10.001

Charette, M.A., Gille, S.T., Sanders, R.J., Zhou, M., 2013. Southern Ocean natural iron fertilization. Deep Sea Res. Part II Top. Stud. Oceanogr. 90, 1–3. doi:10.1016/j.dsr2.2013.04.014

Christaki, U., Lefèvre, D., Georges, C., Colombet, J., Catala, P., Courties, C., Sime-Ngando, T., Blain, S., Obernosterer, I., 2014. Microbial food web dynamics during spring phytoplankton blooms in the naturally iron-fertilized Kerguelen area (Southern Ocean). Biogeosciences 11, 6739–6753. doi:10.5194/bg-11-6739-2014

Church, T., 1970. Marine barite. PhD thesis. University of California, San Diego. pp. 100.

Claquin, P., Martin-Jézéquel, V., Kromkamp, J.C., Veldhuis, M.J.W., Kraay, G.W., 2002. Uncoupling of silicon compared with carbon and nitrogen metabolisms and the role of the cell cycle in continuous cultures of Thalassiosira pseudonana (Bacillariophyceae) under light, nitrogen, and phosphorus control. J. Phycol. 38, 922–930. doi:10.1046/j.1529-8817.2002.t01-1-01220.x

Clark, L.L., Ingall, E.D., 1998. Marine phosphorus is selectively remineralized. Nature 393, 426. doi:10.1038/30881

Closset, I., Lasbleiz, M., Leblanc, K., Quéguiner, B., Cavagna, A.-J., Elskens, M., Navez, J., Cardinal, D., 2014. Seasonal evolution of net and regenerated silica production around a natural Fe-fertilized area in the Southern Ocean estimated with Si isotopic approaches. Biogeosciences 11, 5827–5846. doi:10.5194/bg-11-5827-2014

Coale, K.H., Bruland, K.W., 1985. Thorium-234:uranium-238 disequilibria within the California Current. Limnol. Oceanogr. 30, 22–33. doi:10.4319/lo.1985.30.1.0022

Cochran, J.K., Masqué, P., 2003. Short-lived U/Th series radionuclides in the ocean: Tracers for scavenging rates, export fluxes and particle dynamics. Rev. Mineral. Geochemistry

52, 461–492. doi:10.2113/0520461

Collier, R., Edmond, J., 1984. The trace element geochemistry of marine biogenic particulate matter. Prog. Oceanogr. 13, 113–199.

Collins, J.R., Edwards, B.R., Thamatrakoln, K., Ossolinski, J.E., Ditullio, G.R., Bidle, K.D., Doney, S.C., Mooy, B.A.S. Van, 2015. The multiple fates of sinking particles in the North Atlantic Ocean. Global Biogeochem. Cycles 29, 1471–1494. doi:10.1002/2014GB005037.Received

Copin-Montégut, G., 1996. Chimie de l'eau de mer.

Costa Goela, P., Cordeiro, C., Danchenko, S., Icely, J., Cristina, S., Newton, A., 2016. Time series analysis of data for sea surface temperature and upwelling components from the southwest coast of Portugal. J. Mar. Syst. 163, 12–22. doi:10.1016/j.jmarsys.2016.06.002

Cotté-Krief, M.-H., Guieu, C., Thomas, A.J., Martin, J.-M., 2000. Sources of Cd, Cu, Ni and Zn in Portuguese coastal waters. Mar. Chem. 71, 199–214.

Cox, P.M., Betts, R.A., Jones, C.D., Spall, S.A., Totterdell, I.J., 2000. Acceleration of global warming due to carbon-cycle feedbacks in a coupled climate model. Nature 408, 184–187.

Crowley, T.J., 2010. Causes of climate change over the past 1000 years. Science (80-.). 289. doi:10.1126/science.289.5477.270

d'Ovidio, F., Della Penna, A., Trull, T.W., Nencioli, F., Pujol, M.I., Rio, M.H., Park, Y.H., Cotté, C., Zhou, M., Blain, S., 2015. The biogeochemical structuring role of horizontal stirring: Lagrangian perspectives on iron delivery downstream of the Kerguelen Plateau. Biogeosciences 12, 5567–5581. doi:10.5194/bg-12-5567-2015

Dalbec, A. a., Twining, B.S., 2009. Remineralization of bioavailable iron by a heterotrophic dinoflagellate. Aquat. Microb. Ecol. 54, 279–290. doi:10.3354/ame01270

Dall'Olmo, G., Dingle, J., Polimene, L., Brewin, R.J.W., Claustre, H., 2016. Substantial energy input to the mesopelagic ecosystem from the seasonal mixed-layer pump. Nat. Geosci. 1, 1–6. doi:10.1038/NGEO2818

Dall'Olmo, G., Mork, K.A., 2014. Carbon export by small particles in the Norwegian Sea. Geophys. Res. Lett. 41, 2921–2927. doi:10.1002/2014GL059244.1.

Daniault, N., Mercier, H., Lherminier, P., Sarafanov, A., Falina, A., Zunino, P., Pérez, F.F., Ríos, A.F., Ferron, B., Huck, T., Thierry, V., Gladyshev, S., 2016. The northern North Atlantic Ocean mean circulation in the early 21st century. Prog. Oceanogr. 146, 142–158. doi:10.1016/j.pocean.2016.06.007

de Baar, H.J.W., 2005. Synthesis of iron fertilization experiments: from the iron age in the age of enlightenment. J. Geophys. Res. 110, C09S16. doi:10.1029/2004JC002601

de Baar, H.J.W., Jong, J.T., 2001. Distributions, sources and sinks of iron in seawater. IUPAC Ser. analyitical Phys. Chem. Environ. Syst. 7, 123–254.

De La Rocha, C.L., Passow, U., 2007. Factors influencing the sinking of POC and the efficiency of the biological carbon pump. Deep Sea Res. Part II Top. Stud. Oceanogr. 54, 639–658. doi:10.1016/j.dsr2.2007.01.004

de Lavergne, C., Palter, J.B., Galbraith, E.D., Bernardello, R., Marinov, I., 2014. Cessation of deep convection in the open Southern Ocean under anthropogenic climate change. Nat. Clim. Chang. 4, 278–282. doi:10.1038/nclimate2132

Dehairs, F., Chesselet, R., Jedwab, J., 1980. Discrete suspended particles of barite and the barium cycle in the open ocean. Earth Planet. Sci. Lett. 49, 528–550.

Dehairs, F., Fripiat, F., Cavagna, A.J., Trull, T.W., Fernandez, C., Davies, D., Roukaerts, A.,

Fonseca Batista, D., Planchon, F., Elskens, M., 2015. Nitrogen cycling in the Southern Ocean Kerguelen Plateau area: Evidence for significant surface nitrification from nitrate isotopic compositions. Biogeosciences 12, 1459–1482. doi:10.5194/bg-12-1459-2015

Dehairs, F., Jacquet, S., Savoye, N., Van Mooy, B. a S., Buesseler, K.O., Bishop, J.K.B., Lamborg, C.H., Elskens, M., Baeyens, W., Boyd, P.W., Casciotti, K.L., Monnin, C., 2008. Barium in twilight zone suspended matter as a potential proxy for particulate organic carbon remineralization: Results for the North Pacific. Deep Sea Res. Part II Top. Stud. Oceanogr. 55, 1673–1683. doi:10.1016/j.dsr2.2008.04.020

Dehairs, F., Shopova, D., Ober, S., Veth, C., Goeyens, L., 1997. Particulate barium stocks and oxygen consumption in the Southern Ocean mesopelagic water column during spring and early summer: Relationship with export production. Deep Sea Res. Part II Top. Stud. Oceanogr. 44, 497–516. doi:10.1016/S0967-0645(96)00072-0

Dehairs, F., Stroobants, N., Goeyens, L., 1991. Suspended barite as a tracer of biological activity in the Southern Ocean. Mar. Chem. 35, 399–410. doi:10.1016/S0304-4203(09)90032-9

Deshayes, J., Frankignoul, C., Drange, H., 2007. Formation and export of deep water in the Labrador and Irminger Seas in a GCM. Deep Sea Res. Part I Oceanogr. Res. Pap. 54, 510–532. doi:10.1016/j.dsr.2006.12.014

Dickson, B., Yashayaev, I., Meincke, J., Turrell, B., Dye, S., Holfort, J., 2002. Rapid freshening of the deep North Atlantic Ocean over the past four decades. Nature 416, 832–836.

Dortch, Q., Packard, T.T., 1989. Differences in biomass structure between oligotrophic and eutrophic marine ecosystems. Deep Sea Res. Part A. Oceanogr. Res. Pap. 36, 223–240.

Duarte, B., Caçador, I., 2012. Particulate metal distribution in Tagus estuary (Portugal) during a flood episode. Mar. Pollut. Bull. 64, 2109–2116. doi:10.1016/j.marpolbul.2012.07.016

Duarte, B., Silva, G., Lino, J., Paulo, J., Azeda, C., Sá, E., Metelo, I., José, M., Caçador, I., 2014. Heavy metal distribution and partitioning in the vicinity of the discharge areas of Lisbon drainage basins (Tagus Estuary , Portugal). J. Sea Res. 93, 101–111. doi:10.1016/j.seares.2014.01.003

Dugdale, R.C., Goering, J.J., 1967. Uptake of new and regenerated forms of nitrogen in primary productivity. Limnol. Oceanogr. 12, 196–206. doi:10.4319/lo.1967.12.2.0196

Durkin, C.A., Estapa, M.L., Buesseler, K.O., 2015. Observations of carbon export by small sinking particles in the upper mesopelagic. Mar. Chem. 175, 72–81. doi:10.1016/j.marchem.2015.02.011

Dymond, J., Collier, R., 1996. Particulate barium fluxes and their relationships to biological productivity. Deep Sea Res. Part II Top. Stud. Oceanogr. 43, 1283–1308. doi:10.1016/0967-0645(96)00011-2

Eagle, M., Paytan, A., Arrigo, K., van Dijken, G., Murray, R.W., 2003. A comparison between excess barium and barite as indicators of carbon export. Paleoceanography 18, 1–13. doi:10.1029/2002PA000793

Ebersbach, F., Trull, T.W., 2008. Sinking particle properties from polyacrylamide gels during the KErguelen Ocean and Plateau compared Study (KEOPS): Zooplankton control of carbon export in an area of persistent natural iron inputs in the Southern Ocean. Limnol. Oceanogr. 53, 212–224. doi:10.4319/lo.2008.53.1.0212

Ellwood, M.J., Nodder, S.D., King, A.L., Hutchins, D.A., Wilhelm, S.W., Boyd, P.W., 2014. Pelagic iron cycling during the subtropical spring bloom, east of New Zealand. Mar. Chem. 160, 18–33. doi:10.1016/j.marchem.2014.01.004

Elrod, V.A., Berelson, W.M., Coale, K.H., Johnson, K.S., 2004. The flux of iron from continental shelf sediments: A missing source for global budgets. Geophys. Res. Lett. 31, 2–5.

doi:10.1029/2004GL020216

Emilio, F., Boyd, P., Holligan, P.M., Derek, S.H., 1993. Production of organic and inorganic carbon within a large-scale coccolithophore bloom in the northeast Atlantic Ocean. Mar. Ecol. Prog. Ser. 97, 271–285.

Eppley, R.W., 1989. New Production: history, methods, and problems, in: Berger, W.H., Smetacek, V.S., Wefer, G. (Eds.), Productivity of the Ocean: Present and Past. John Wiley & Sons, New York, pp. 85–97.

Eppley, R.W., Peterson, B.J., 1979. Particulate organic matter flux and planktonic new production in the deep ocean. Nature 282, 677–680. doi:10.1038/282677a0

Esaias, W.E., Feldman, G.C., MnClain, C.R., Elrod, J.A., 1986. Monthly satellite-derived phytoplankton pigment distribution for the North Atlantic basin. Ocenaography Rep. 67, 835–837.

Falkowski, P.G., Algeo, T., Codispoti, L., Deutsch, C., Emerson, S., Hales, B., Huey, R.B., Jenkins, W.J., Kump, L.R., Levin, L.A., Lyons, T.W., Nelson, N.B., Schofield, O.S., Summons, R., Talley, L.D., Thomas, E., Whitney, F., Pilcher, C.B., 2011. Ocean deoxygenation: Past, Present, and Future. Am. Geophys. Union 92, 409–420.

Feely, R.A., Sabine, C.L., Schlitzer, R., Bullister, J.L., Mecking, S., Greeley, D., 2004. Oxygen utilization and organic carbon remineralization in the upper water column of the Pacific Ocean. J. Oceanogr. 60, 45–52.

Fernández-castro, B., Arístegui, J., Anderson, L., Montero, M.F., Hernández-León, S., Maranon, E., Mourino-Carballido, B., 2016. Mesopelagic respiration near the ESTOC (European Station for Time-Series in the Ocean, 15.5°W, 29.1°N) site inferred from a tracer conservation model. Deep Sea Res. Part I Oceanogr. Res. Pap. 115, 63–73. doi:10.1016/j.dsr.2016.05.010

Ferron, B., Kokoszka, F., Mercier, H., Lherminier, P., 2014. Dissipation rate estimates from microstructure and finescale internal wave observations along the A25 Greenland-Portugal OVIDE line. J. Atmos. Ocean. Technol. 31, 2530–2543. doi:10.1175/JTECH-D-14-00036.1

Foster, R.A., Subramaniam, A., Mahaffey, C., Carpenter, E.J., Capone, D.G., Zehr, J.P., 2007. Influence of the Amazon River plume on distributions of free-living and symbiotic cyanobacteria in the western tropical north Atlantic Ocean. Limnol. Oceanogr. 52, 517–532. doi:10.4319/lo.2007.52.2.0517

Foster, R.A., Zehr, J.P., 2006. Characterization of diatom-cyanobacteria symbioses on the basis of nifH, hetR and 16S rRNA sequences. Environ. Microbiol. 8, 1913–1925. doi:10.1111/j.1462-2920.2006.01068.x

Franck, V., Brzezinski, M.A., Coale, K.H., Nelson, D.M., 2000. Iron and silicic acid concentrations regulate Si uptake north and south of the Polar Frontal Zone in the Pacific Sector of the Southern Ocean. Deep Sea Res. Part II Top. Stud. Oceanogr. 47, 3315–3338. doi:10.1016/S0967-0645(00)00070-9

Francois, R., Honjo, S., Krishfield, R., Manganini, S., 2002. Factors controlling the flux of organic carbon to the bathypelagic zone of the ocean. Global Biogeochem. Cycles 16, 1–20. doi:10.1029/2001GB001722

Francois, R., Honjo, S., Manganini, J., Ravizza, E., 1995. Biogenic barium fluxes to the deep sea: Implications for paleoproductivity reconstruction. Global Biogeochem. Cycles 9, 289–303.

Frankignoulle, M., Canon, C., Gattuso, J.-P., 1993. Marine calcification as a source of carbon dioxide: Positive feedback of increasing atmospheric CO2. Limnol. Oceanogr. 39, 458–462.

Frew, R.D., Hutchins, D.A., Nodder, S., Sanudo-Wilhelmy, S., Tovar-Sanchez, A., Leblanc, K., Hare, C.E., Boyd, P.W., 2006. Particulate iron dynamics during FeCycle in subantarctic waters southeast of New Zealand. Global Biogeochem. Cycles 20, 1–15. doi:10.1029/2005GB002558

Fripiat, F., Elskens, M., Trull, T.W., Blain, S., Cavagna, A.J., Fernandez, C., Fonseca Batista, D., Planchon, F., Raimbault, P., Roukaerts, A., Dehairs, F., 2015. Significant mixed layer nitrification in natural iron-fertilized bloom of the Southern Ocean. Global Biogeochem. Cycles 29. doi:10.1002/2014GB005051

Galloway, J.N., Dentener, F.J., Capone, D.G., Boyer, E.W., Howarth, R.W., Seitzinger, S.P., Asner, G.P., Cleveland, C.C., Green, P.A., Holland, E.A., Karl, D.M., Michaels, A.F., Porter, J.H., Townsend, A.R., Vörösmarty, C.J., 2004. Nitrogen cycles : past , present , and future. Biogeochemistry 70, 153–226. doi:10.1007/s10533-004-0370-0

Ganeshram, R.S., François, R., Commeau, J., Brown-Leger, S.L., 2003. An experimental investigation of barite formation in seawater. Geochim. Cosmochim. Acta 67, 2599–2605. doi:10.1016/S0016-7037(03)00164-9

Gao, X., Zhou, F., A., C.C.T., 2014. Pollution status of the Bohai Sea: an overview of the environmental quality assessment related trace metals. Environ. Int. 62, 12–30. doi:10.1016/j.envint.2013.09.019

García-ibáñez, M.I., Pardo, P.C., Carracedo, L.I., Mercier, H., Lherminier, P., Ríos, A.F., Pérez, F.F., 2015. The water mass structure and transports in the Atlantic Subpolar Gyre. Prog. Oceanogr. 135, 18–36. doi:10.1016/j.pocean.2015.03.009

Gardner, W.D., Richardson, M.J., Carlson, C.A., Hansell, D., Mishonov, A. V., 2003. Determining true particulate organic carbon: Bottles, pumps and methodologies. Deep Sea Res. Part II Top. Stud. Oceanogr. 50, 655–674. doi:10.1016/S0967-0645(02)00589-1

Gautier, I., Weis, D., Mennessier, J.-P., Vidal, P., Giret, A., Loubet, M., 1990. Petrology and geochemistry of the Kerguelen Archipelago basalts (South Indian Ocean)" evolution of the mantle sources from ridge to intraplate position. Earth Planet. Sci. Lett. 100, 59–76.

Giering, S.L.C., Sanders, R., Lampitt, R.S., Anderson, T.R., Tamburini, C., Boutrif, M., Zubkov, M. V., Marsay, C.M., Henson, S.A., Saw, K., Cook, K., Mayor, D.J., 2014. Reconciliation of the carbon budget in the ocean's twilight zone. Nature 507, 480–483. doi:10.1038/nature13123

Giering, S.L.C., Sanders, R., Martin, A.P., Lindemann, C., Möller, K.O., Daniels, C.J., Mayor, D.J., St. John, M.A., 2016. High export via small particles before the onset of the Nort Atlantic spring bloom. J. Geophys. Res. 121, 1–17. doi:10.1002/2016JC012048.Received

Giering, S.L.C., Steigenberger, S., Achterberg, E.P., Sanders, R., Mayor, D.J., 2012. Elevated iron to nitrogen recycling by mesozooplankton in the Northeast Atlantic Ocean. Geophys. Res. Lett. 39, 3–7. doi:10.1029/2012GL051776

Gledhill, M., Buck, K.N., 2012. The organic complexation of iron in the marine environment: a review. Front. Microbiol. 3, 1–17. doi:10.3389/fmicb.2012.00069

Gnanadesikan, A., Marinov, I., 2008. Export is not enough: Nutrient cycling and carbon sequestration. Mar. Ecol. Prog. Ser. 364, 289–294. doi:10.3354/meps07550

Goldberg, E.D., 1954. Chemical ccavengers of the sea. Chigaco Journals 62, 249–265.

Gonzalez-Munoz, M.T., Fernandez-Luque, B., Martínez-Ruiz, F., Chekroun, K. Ben, Arias, J.M., Rodríguez-Gallego, M., Martínez-Canamero, M., de Linares, C., Paytan, A., 2003. Precipitation of barite by Myxococcus xanthus: possible implications for the biogeochemical cycle of barium. Appl. Environ. Microbiol. 69, 5722–5725. doi:10.1128/AEM.69.9.5722

Gordon, D.C., 1971. Distribution of particulate organic carbon and nitrogen at an oceanic station in the central Pacific. Deep Sea Res. Part A, Oceanogr. Res. Pap. 18, 1127–1134. doi:10.1016/0011-7471(71)90098-2

Green, S.E., Sambrotto, R.N., 2006. Plankton community structure and export of C, N, P and Si in the Antarctic Circumpolar Current. Deep Sea Res. Part II Top. Stud. Oceanogr. 53, 620–643. doi:10.1016/j.dsr2.2006.01.022

Gruber, N., 2008. The Marine Nitrogen Cycle, in: Nitrogen in the Marine Environment. pp. 1–50. doi:10.1016/B978-0-12-372522-6.00001-3

Gruber, N., 2004. The dynamics of the marine nitrogen cycle and its influence on atmospheric CO2 variations, in: The Ocean Carbon Cycle and Climate. pp. 97–148.

Gruber, N., Gloor, M., Mikaloff Fletcher, S.E., Doney, S.C., Dutkiewicz, S., Follows, M.J., Gerber, M., Jacobson, A.R., Joos, F., Lindsay, K., Menemenlis, D., Mouchet, A., Müller, S.A., Sarmiento, J.L., Takahashi, T., 2009. Oceanic sources, sinks, and transport of atmospheric CO2. Global Biogeochem. Cycles 23, 1–21. doi:10.1029/2008GB003349

Guidi, L., Legendre, L., Reygondeau, G., Uitz, J., Stemmann, L., Henson, S.A., 2015. A new look at ocean carbon remineralization for estimating deepwater sequestration. Glob. Planet. Change 29, 1044–1059. doi:10.1002/2014GB005063.Received

Guidi, L., Stemmann, L., Jackson, G.A., Ibanez, F., Claustre, H., Legendre, L., Picheral, M., Gorsky, G., 2009. Effects of phytoplankton community on production , size and export of large aggregates : A world-ocean analysis. Limnol. Oceanogr. 54, 1951–1963.

Guidi, L., Stemmann, L., Legendre, L., Picheral, M., Prieur, L., Gorsky, G., 2007. Vertical distribution of aggregates (>110 µm) and mesoscale activity in the northeastern Atlantic: Effects on the deep vertical export of surface carbon. Limnol. Oceanogr. 52, 7–18.

Guieu, C., Leblond, N., Jeandel, C., Souhaut, M., Cann, B. Le, Dufour, A., Bournot, C., 2005. Vertical particle flux in the northeast Atlantic Ocean (POMME experiment). J. Geophys. Res. 110, 1–21. doi:10.1029/2004JC002672

Hagstrom, G.I., Levin, S.A., Martiny, A.C., 2016. Resource ratios determine nutrient limitation of primary productivity in the ocean. bioRxiv 1–20. doi:10.1101/064543

Hama, T., Miyazaki, T., Ogawa, Y., Iwakuma, T., Takahashi, M., Otsuki, A., Ichimura, S., 1983. Mesurement of photosynthtic production of a marine phytoplankton population using a stable 13C isotope. Mar. Biol. 73, 31–36.

Hansell, D.A., Carlson, C.A., Repeta, D.J., Schlitzer, R., 2009. Dissolved organic matter in the ocean. A Controv. Stimul. new insights.

Hare, C.E., DiTullio, G.R., Riseman, S.F., Crossley, A.C., Popels, L.C., Sedwick, P.N., Hutchins, D.A., 2007. Effects of changing continuous iron input rates on a Southern Ocean algal assemblage. Deep Sea Res. Part I Oceanogr. Res. Pap. 54, 732–746. doi:10.1016/j.dsr.2007.02.001

Harvey, J., 1982. 0-S relationships and water masses in the eastern North Atlantic. Deep Sea Res. Part A. Oceanogr. Res. Pap. 29, 1021–1033.

Hawkings, J., Wadham, J., Tranter, M., Telling, J., Bagshaw, E., Beaton, A., Simmons, S.-L., Chandler, D., Tedstone, A., Nienow, P., 2016. The Greenland Ice Sheet as a hot spot of phosphorus weathering and export in the Arctic. Global Biogeochem. Cycles 30, 191–210. doi:10.1016/S0074-6142(08)62690-X

Hawkings, J.R., Wadham, J.L., Tranter, M., Raiswell, R., Benning, L.G., Statham, P.J., Tedstone, A., Nienow, P., Lee, K., Telling, J., 2014. Ice sheets as a significant source of highly reactive nanoparticulate iron to the oceans. Nat. Commun. 5, 1–8. doi:10.1038/ncomms4929

Heinze, C., Meyer, S., Goris, N., Anderson, L., Steinfeldt, R., Chang, N., Le Qu??r??, C., Bakker, D.C.E., 2015. The ocean carbon sink - Impacts, vulnerabilities and challenges. Earth Syst. Dyn. 6, 327–358. doi:10.5194/esd-6-327-2015

Henson, S.A., Dunne, J.P., Sarmiento, J.L., 2009. Decadal variability in North Atlantic phytoplankton blooms. J. Geophys. Res. 114, C04013. doi:10.1029/2008JC005139

Henson, S.A., Sanders, R., Holeton, C., Allen, J.T., 2006. Timing of nutrient depletion, diatom dominance and a lower-boundary estimate of export production for Irminger Basin, North Atlantic. Mar. Ecol. Prog. Ser. 313, 73–84.

Henson, S.A., Yool, A., Sanders, R., 2015. Variability in efficiency of particulate organic carbon export: a model study. Global Biogeochem. Cycles 29, 33–45. doi:10.1002/2014GB004965.Received

Herndl, G.J., Reinthaler, T., 2013. Microbial control of the dark end of the biological pump. Nat. Geosci. 6, 718–724. doi:10.1038/ngeo1921

Ho, T., Chou, W., Wei, C., Lin, F., Wong, G.T.F., Lin, H.-L., 2010. Trace metal cycling in the surface water of the South China Sea: Vertical fluxes, composition, and sources. Limnol. Oceanogr. 55, 1807–1820. doi:10.4319/lo.2010.55.5.1807

Hoefs, J., 2010. Stable isotope geochemistry - 6th Edition, Springer. ed.

Hoffmann, L.J., Peeken, I., Lochte, K., Assmy, P., Veldhuis, M., 2006. Different reactions of Southern Ocean phytoplankton size classes to iron fertilization. Limnol. Oceanogr. 51, 1217–1229. doi:10.4319/lo.2006.51.3.1217

Honjo, S., 1996. Fluxes of particles to the interior of the open oceans, in: Particle Flux in the Ocean. pp. 91–254.

Honjo, S., Eglinton, T.I., Taylor, C.D., Ulmer, K.M., Sievert, S.M., Bracher, A., German, C.R., Edgcomb, V., Francois, R., Iglesias-Rodriguez, M.D., van Mooy, B., Repeta, D.J., 2014. Understanding the role of the biological pump in the global carbon cycle. Oceanography 27, 10–16. doi:10.5670/oceanog.2014.78

Honjo, S., Manganini, S.J., 1993. Annual biogenic particle fluxes to the interior of the North Atlantic Ocean; studied at 34°N 21°W and 48°N 21°W. Deep Sea Res. Part I Oceanogr. Res. Pap. 40, 587–607.

Honjo, S., Manganini, S.J., Krishfield, R.A., Francois, R., 2008. Particulate organic carbon fluxes to the ocean interior and factors controlling the biological pump: A synthesis of global sediment trap programs since 1983. Prog. Oceanogr. 76, 217–285. doi:10.1016/j.pocean.2007.11.003

Horner, T.J., Kinsley, C.W., Nielsen, S.G., 2015. Barium-isotopic fractionation in seawater mediated by barite cycling and oceanic circulation. Earth Planet. Sci. Lett. 430, 511–522. doi:10.1016/j.epsl.2015.07.027

Hutchins, D.A., Bruland, K.W., 1998. Iron-limited diatom growth and Si : N uptake ratios in a coastal upwelling regime. Nature 393, 561–564. doi:Doi 10.1038/31203

Irvine, U.C., 2007. GEOTRACES - An international study of the global marine biogeochemical cycles of trace elements and their isotopes. Chemie der Erde - Geochemistry 67, 85–131. doi:10.1016/j.chemer.2007.02.001

Iversen, M.H., Ploug, H., 2013. Temperature effects on carbon-specific respiration rate and sinking velocity of diatom aggregates – potential implications for deep ocean export processes. Biogeosciences 10, 4073–4085. doi:10.5194/bg-10-4073-2013

Jacquet, S.H.M., Dehairs, F., Cavagna, A.J., Planchon, F., Monin, L., André, L., Closset, I., Cardinal, D., 2015. Early season mesopelagic carbon remineralization and transfer efficiency in the naturally iron-fertilized Kerguelen area. Biogeosciences 12, 1713–1731.

doi:10.5194/bg-12-1713-2015

Jacquet, S.H.M., Dehairs, F., Dumont, I., Becquevort, S., Cavagna, A.-J., Cardinal, D., 2011. Twilight zone organic carbon remineralization in the Polar Front Zone and Subantarctic Zone south of Tasmania. Deep Sea Res. Part II Top. Stud. Oceanogr. 58, 2222–2234. doi:10.1016/j.dsr2.2011.05.029

Jacquet, S.H.M., Dehairs, F., Savoye, N., Obernosterer, I., Christaki, U., Monnin, C., Cardinal, D., 2008a. Mesopelagic organic carbon remineralization in the Kerguelen Plateau region tracked by biogenic particulate Ba. Deep Sea Res. Part II Top. Stud. Oceanogr. 55, 868–879. doi:10.1016/j.dsr2.2007.12.038

Jacquet, S.H.M., Savoye, N., Dehairs, F., Strass, V.H., Cardinal, D., 2008b. Mesopelagic carbon remineralization during the European Iron Fertilization Experiment. Global Biogeochem. Cycles 22, n/a-n/a. doi:10.1029/2006GB002902

Jeandel, C., Tachikawa, K., Bory, A., Dehairs, F., 2000. Biogenic barium in suspended and trapped material as a tracer of export production in the tropical NE Atlantic (EUMELI sites). Mar. Chem. 71, 125–142. doi:10.1016/S0304-4203(00)00045-1

Jenkins, W.J., 1982. Oxygen utilization rates in North Atlantic subtropical gyre and primary production in oligotrophic systems. Nature 300, 246–248. doi:10.1038/300246a0

Jiao, N., Herndl, G.J., Hansell, D. a., Benner, R., Kattner, G., Wilhelm, S.W., Kirchman, D.L., Weinbauer, M.G., Luo, T., Chen, F., Azam, F., 2010. Microbial production of recalcitrant dissolved organic matter: long-term carbon storage in the global ocean. Nat. Rev. Microbiol. 8, 593–599. doi:10.1038/nrmicro2386

Jickells, T.D., An, Z.S., Andersen, K.K., Baker, A.R., Bergametti, G., Brooks, N., Cao, J.J., Boyd, P.W., Duce, R.A., Hunter, K.A., Kawahata, H., Kubilay, N., LaRoche, J., Liss, P.S., Mahowald, N., Prospero, J.M., Ridgwell, A.J., Tegen, I., Torres, R., 2005. Global Iron Connections Between Desert Dust, Ocean Biogeochemistry, and Climate. Science (80-.). 308, 67–71. doi:10.1126/science.1105959

Jickells, T.D., Newton, P.P., King, P., Lampitt, R.S., Boutle, C., 1996. A comparison of sediment trap records of particle fluxes from 19 to 48°N in the northeast Atlantic and their relation to surface water productivity. Deep Sea Res. Part I Oceanogr. Res. Pap. 43, 971–986.

Jin, X., Gruber, N., Dunne, J.P., Sarmiento, J.L., Armstrong, R.A., 2006. Diagnosing the contribution of phytoplankton functional groups to the production and export of particulate organic carbon, CaCO 3 , and opal from global nutrient and alkalinity distributions. Global Biogeochem. Cycles 20. doi:10.1029/2005GB002532

Johnson, G.C., 2008. Quantifying Antarctic Bottom Water and North Atlantic Deep Water volumes. J. Geophys. Res. Ocean. 113, 1–13. doi:10.1029/2007JC004477

Johnson, S., 2001. Iron supply and demand in the upper ocean: Is extraterrestrial dust a significant source of bioavailable iron ? Global Biogeochem. Cycles 15, 61–63.

Joos, F., Spahni, R., 2008. Rates of change in natural and anthropogenic radiative forcing over the past 20,000 years. Proc. Natl. Acad. Sci. 105, 1425–1430. doi:10.1073/pnas.0707386105

Karl, D.M., 1999. A Sea of change: Biogeochemical variability in the North Pacific Subtropical Gyre. Ecosystems 2, 181–214.

Kaufman, A., Li, Y.-H., Turekian, K.K., 1981. The removal rates of 234Th and 228Th from waters of the New York Bight. Earth Planet. Sci. Lett. 54, 385–392.

Kemp, A.E.S., Pearce, R.B., Grigorov, I., Rance, J., Lange, C.B., Quilty, P., Salter, I., 2006. Production of giant marine diatoms and their export at oceanic frontal zones: Implications for Si and C flux from stratified oceans. Global Biogeochem. Cycles 20, 1–13.

doi:10.1029/2006GB002698

Kieke, D., Yashayaev, I., 2015. Studies of Labrador Sea Water formation and variability in the subpolar North Atlantic in the light of international partnership and collaboration. Prog. Oceanogr. 132, 220–232. doi:10.1016/j.pocean.2014.12.010

King, a. L., Sañudo-Wilhelmy, S. a., Boyd, P.W., Twining, B.S., Wilhelm, S.W., Breene, C., Ellwood, M.J., Hutchins, D. a., 2012. A comparison of biogenic iron quotas during a diatom spring bloom using multiple approaches. Biogeosciences 9, 667–687. doi:10.5194/bg-9-667-2012

Klaas, C., Archer, D.E., 2002. Association of sinking organic matter with various types of mineral ballast in the deep sea: Implications for the rain ratio. Global Biogeochem. Cycles 16, 1–14. doi:10.1029/2001GB001765

Koeve, W., Kähler, P., 2016. Oxygen utilization rate (OUR) underestimates ocean respiration: a model study. Global Biogeochem. Cycles 30, 1166–1182. doi:10.1002/2015GB005354.Received

Kuhlbrodt, T., Griesel, A., Montoya, M., Levermann, A., Hofmann, M., Rahmstorf, S., 2007. On the driving processes of the Atlantic meridional overturning circulation. Rev. Geophys. 45, 1–32. doi:10.1029/2004RG000166

Kuss, J., Kremling, K., 1999. Particulate trace element fluxes in the deep northeast Atlantic Ocean. Deep Sea Res. Part I Oceanogr. Res. Pap. 46, 149–169. doi:10.1016/S0967-0637(98)00059-4

Kuss, J., Kremling, K., 1999. Spatial variability of particle associated trace elements in near-surface waters of the North Atlantic (30 degrees N/60 degrees W to 60 degrees N/2 degrees W), derived by large-volume sampling. Mar. Chem. 68, 71–86. doi:Doi 10.1016/S0304-4203(99)00066-3

Kuss, J., Waniek, J.J., Kremling, K., Schulz-bull, D.E., 2010. Seasonality of particle-associated trace element fluxes in the deep northeast Atlantic Ocean. Deep Sea Res. Part I Oceanogr. Res. Pap. 57, 785–796. doi:10.1016/j.dsr.2010.04.002

Kwon, E.Y., Primeau, F., Sarmiento, J.L., 2009. The impact of remineralization depth on the air–sea carbon balance. Nat. Geosci. 2, 630–635. doi:10.1038/ngeo612

Lagerström, M.E., Field, M.P., Séguret, M., Fischer, L., Hann, S., Sherrell, R.M., 2013. Automated on-line flow-injection ICP-MS determination of trace metals (Mn, Fe, Co, Ni, Cu and Zn) in open ocean seawater: Application to the GEOTRACES program. Mar. Chem. 155, 71–80. doi:10.1016/j.marchem.2013.06.001

Lalande, C., Moran, S.B., Wassmann, P., Grebmeier, J.M., Cooper, L.W., 2008. 234Th-derived particulate organic carbon fluxes in the northern Barents Sea with comparison to drifting sediment trap fluxes. J. Mar. Syst. 73, 103–113. doi:10.1016/j.jmarsys.2007.09.004

Lam, P.J., Bishop, J.K.B., 2008. The continental margin is a key source of iron to the HNLC North Pacific Ocean. Geophys. Res. Lett. 35, 1–5. doi:10.1029/2008GL033294

Lam, P.J., Bishop, J.K.B., 2007. High biomass, low export regimes in the Southern Ocean. Deep Sea Res. Part II Top. Stud. Oceanogr. 54, 601–638. doi:10.1016/j.dsr2.2007.01.013

Lam, P.J., Bishop, J.K.B., Henning, C.C., Marcus, M.A., Waychunas, G.A., Fung, I.Y., 2006. Wintertime phytoplankton bloom in the subarctic Pacific supported by continental margin iron. Global Biogeochem. Cycles 20, n/a-n/a. doi:10.1029/2005GB002557

Lam, P.J., Doney, S.C., Bishop, J.K.B., 2011. The dynamic ocean biological pump: Insights from a global compilation of particulate organic carbon, CaCO 3, and opal concentration profiles from the mesopelagic. Global Biogeochem. Cycles 25, 1–14. doi:10.1029/2010GB003868

Lam, P.J., Ohnemus, D.C., Auro, M.E., 2015a. Size-fractionated major particle composition and concentrations from the US GEOTRACES North Atlantic Zonal Transect. Deep Sea Res. Part II Top. Stud. Oceanogr. 116, 303–320. doi:10.1016/j.dsr2.2014.11.020

Lam, P.J., Twining, B.S., Jeandel, C., Roychoudhury, A., Resing, J.A., Santschi, P.H., Anderson, R.F., 2015b. Methods for analyzing the concentration and speciation of major and trace elements in marine particles. Prog. Oceanogr. 133, 32–42. doi:10.1016/j.pocean.2015.01.005

Lamborg, C.H., Buesseler, K.O., Lam, P.J., 2008. Sinking fluxes of minor and trace elements in the North Pacific Ocean measured during the VERTIGO program. Deep Sea Res. Part II Top. Stud. Oceanogr. 55, 1564–1577. doi:10.1016/j.dsr2.2008.04.012

Lampitt, R.S., Antia, A.N., 1997. Particle flux in deep seas: Regional characteristics and temporal variability. Deep Sea Res. Part I Oceanogr. Res. Pap. 44, 1377–1403.

Lampitt, R.S., Bett, B.J., Kiriakoulakis, K., Popova, E.E., Ragueneau, O., Vangriesheim, A., Wolff, G.A., 2001. Material supply to the abyssal seafloor in the Northeast Atlantic. Prog. Oceanogr. 50, 27–63.

Lampitt, R.S., Boorman, B., Brown, L., Lucas, M., Salter, I., Sanders, R., Saw, K., Seeyave, S., Thomalla, S.J., Turnewitsch, R., 2008. Particle export from the euphotic zone: Estimates using a novel drifting sediment trap, 234Th and new production. Deep Sea Res. Part I Oceanogr. Res. Pap. 55, 1484–1502. doi:10.1016/j.dsr.2008.07.002

Lampitt, R.S., Salter, I., de Cuevas, B.A., Hartman, S., Larkin, K.E., Pebody, C.A., 2010. Long-term variability of downward particle flux in the deep northeast Atlantic: Causes and trends. Deep Sea Res. Part II Top. Stud. Oceanogr. 57, 1346–1361. doi:10.1016/j.dsr2.2010.01.011

Langdon, C., Takahashi, T., Sweeney, C., Chipman, D., Atkinson, J., 2000. Effect of calcium carbonate saturation state on the calcification rate of an experimental coral reef. Global Biogeochem. Cycles 14, 639–654. doi:10.1029/1999GB001195

Lannuzel, D., Bowie, A.R., van der Merwe, P.C., Townsend, A.T., Schoemann, V., 2011. Distribution of dissolved and particulate metals in Antarctic sea ice. Mar. Chem. 124, 134–146. doi:10.1016/j.marchem.2011.01.004

Lasbleiz, M., 2014. Cycles biogéochimiques (Si, C, N, P) en lien avec la dynamique nutritionnelle du phytoplancton dans la région naturellement fertilisée des Kerguelen. PhD thesis. Mediterranean Institute of Oceanography. pp 313.

Lasbleiz, M., Leblanc, K., Armand, L.K., Christaki, U., Georges, C., Obernosterer, I., Qu??guiner, B., 2016. Composition of diatom communities and their contribution to plankton biomass in the naturally iron-fertilized region of Kerguelen in the Southern Ocean. FEMS Microbiol. Ecol. 92, 1–16. doi:10.1093/femsec/iw171

Lasbleiz, M., Leblanc, K., Bowie, a. R., Ras, J., Cornet-Barthaux, V., Hélias Nunige, S., Quéguiner, B., 2014. Pigments, elemental composition (C, N, P, Si) and stoichiometry of particulate matter, in the naturally iron fertilized region of Kerguelen in the Southern Ocean. Biogeosciences 11, 5931–5955. doi:10.5194/bg-11-5931-2015

Laufkötter, C., Vogt, M., Gruber, N., Aumont, O., Bopp, L., Doney, S.C., Dunne, J.P., Hauck, J., John, J.G., Lima, I.D., Seferian, R., Völker, C., 2016. Projected decreases in future marine export production: The role of the carbon flux through the upper ocean ecosystem. Biogeosciences 13, 4023–4047. doi:10.5194/bg-13-4023-2016

Laurenceau-Cornec, E.C., Trull, T.W., Davies, D.M., Bray, S.G., Doran, J., Planchon, F., Carlotti, F., Jouandet, M.P., Cavagna, A.J., Waite, A.M., Blain, S., 2015a. The relative importance of phytoplankton aggregates and zooplankton fecal pellets to carbon export: insights from free-drifting sediment trap deployments in naturally iron-fertilised waters near the Kerguelen Plateau. Biogeosciences 12, 1007–1027. doi:10.5194/bg-12-1007-

2015

Laurenceau-Cornec, E.C., Trull, T.W., Davies, D.M., De La Rocha, C.L., Blain, S., 2015b. Phytoplankton morphology controls on marine snow sinking velocity. Mar. Ecol. Prog. Ser. 520, 35–56. doi:10.3354/meps11116

Laws, E.A., Ducklow, H., McCarthy, J.J., 2000. Temperature effects on export production in the open ocean. Global Biogeochem. Cycles 14, 1231–1246. doi:10.1029/1999GB001229

Le Gall, A.C., Statham, P.J., Morley, N.J., Hydes, D.J., Hunt, C.H., 1999. Processes influencing distributions and concentrations of Cd, Cu, Mn and Ni at the North West European shelf break. Mar. Chem. 68, 97–115.

Le Moigne, F.A.C., Gallinari, M., Laurenceau, E., De La Rocha, C.L., 2013a. Enhanced rates of particulate organic matter remineralization by microzooplankton are diminished by added ballast minerals. Biogeosciences 10, 5755–5765. doi:10.5194/bg-10-5755-2013

Le Moigne, F.A.C., Henson, S.A., Cavan, E.L., Georges, C., Pabortsava, K., Achterberg, E.P., Ceballos-romero, E., Zubkov, M., 2016. What causes the inverse relationship between primary production and export efficiency in the Southern Ocean? Geophys. Res. Lett. 43, 1–10. doi:10.1002/2016GL068480.Received

Le Moigne, F.A.C., Moore, M.C., Sanders, R.J., Villa-Alfageme, M., Steigenberger, S., Achterberg, E.P., 2014. Sequestration efficiency in the iron-limited North Atlantic: Implications for iron supply mode to fertilized blooms. Geophys. Res. Lett. 41, 4619–4627. doi:10.1002/2014GL060308

Le Moigne, F.A.C., Pabortsava, K., Marcinko, C.L.J., Martin, P., Sanders, R.J., 2014. Where is mineral ballast important for surface export of particulate organic carbon in the ocean? Geophys. Res. Lett. 41, 8460–8468. doi:10.1002/2014GL061678

Le Moigne, F.A.C., Sanders, R.J., Villa-Alfageme, M., Martin, A.P., Pabortsava, K., Planquette, H., Morris, P.J., Thomalla, S.J., 2012. On the proportion of ballast versus non-ballast associated carbon export in the surface ocean. Geophys. Res. Lett. 39, L15610. doi:10.1029/2012GL052980

Le Moigne, F.A.C., Villa-Alfageme, M., Sanders, R.J., Marsay, C., Henson, S., García-Tenorio, R., 2013b. Export of organic carbon and biominerals derived from 234Th and 210Po at the Porcupine Abyssal Plain. Deep Sea Res. Part I Oceanogr. Res. Pap. 72, 88–101. doi:10.1016/j.dsr.2012.10.010

Le Quéré, C., Moriarty, R., Andrew, R.M., Canadell, J.G., Sitch, S., Korsbakken, J.I., Friedlingstein, P., Peters, G.P., Andres, R.J., Boden, T.A., Houghton, R.A., House, J.I., Keeling, R.F., Tans, P., Arneth, A., Bakker, D.C.E., Barbero, L., Bopp, L., Chang, J., Chevallier, F., Chini, L.P., Ciais, P., Fader, M., Feely, R.A., Gkritzalis, T., Harris, I., Hauck, J., Ilyina, T., Jain, A.K., Kato, E., Kitidis, V., Klein Goldewijk, K., Koven, C., Landsch??tzer, P., Lauvset, S.K., Lefèvre, N., Lenton, A., Lima, I.D., Metzl, N., Millero, F., Munro, D.R., Murata, A., S. Nabel, J.E.M., Nakaoka, S., Nojiri, Y., O'Brien, K., Olsen, A., Ono, T., P??rez, F.F., Pfeil, B., Pierrot, D., Poulter, B., Rehder, G., Rödenbeck, C., Saito, S., Schuster, U., Schwinger, J., Séférian, R., Steinhoff, T., Stocker, B.D., Sutton, A.J., Takahashi, T., Tilbrook, B., Van Der Laan-Luijkx, I.T., Van Der Werf, G.R., Van Heuven, S., Vandemark, D., Viovy, N., Wiltshire, A., Zaehle, S., Zeng, N., 2015. Global Carbon Budget 2015. Earth Syst. Sci. Data 7, 349–396. doi:10.5194/essd-7-349-2015

Le Quéré, C., Raupach, M.R., Canadell, J.G., Al., G.M., 2009. Trends in the sources and sinks of carbon dioxide. Nat. Geosci. 2, 831–836. doi:10.1038/ngeo689

Le Quéré, C., Rödenbeck, C., Buitenhuis, E.T., Conway, T.J., Langenfelds, R., Gomez, A., Labuschagne, C., Ramonet, M., Nakazawa, T., Metzl, N., Gillett, N., Heimann, M., 2007. Sink Due to Recent Climate Change. Science (80-.). 316, 1735–1738.

Lee, C., Hedges, J.I., Wakeham, S.G., Zhu, N., 1992. Effectiveness of various treatments in retarding microbial activity in sediment trap material and their effects on the collection of swimmers. Limnol. Oceanogr. 37, 117–130.

Lee B, G., Fisher, N., 1992. Decomposition and release of elements from zooplankton debris. Mar. Ecol. Prog. Ser. 88, 117–128. doi:10.3354/meps088117

Lefèvre, D., Guigue, C., Obernosterer, I., 2008. The metabolic balance at two contrasting sites in the Southern Ocean: The iron-fertilized Kerguelen area and HNLC waters. Deep Sea Res. Part II Top. Stud. Oceanogr. 55, 766–776. doi:10.1016/j.dsr2.2007.12.006

Legendre, L., Rivkin, R.B., Weinbauer, M.G., Guidi, L., Uitz, J., 2015. The microbial carbon pump concept: Potential biogeochemical significance in the globally changing ocean. Prog. Oceanogr. 134, 432–450. doi:10.1016/j.pocean.2015.01.008

Lemaitre, N., Bayon, G., Ondréas, H., Caprais, J.-C., Freslon, N., Bollinger, C., Rouget, M.-L., de Prunelé, A., Ruffine, L., Olu-Le Roy, K., Sarthou, G., 2014. Trace element behaviour at cold seeps and the potential export of dissolved iron to the ocean. Earth Planet. Sci. Lett. 404, 376–388. doi:10.1016/j.epsl.2014.08.014

Lemaitre, N., Planquette, H., Dehairs, F., van der Merwe, P., Bowie, A.R., Trull, T.W., Laurenceau-Cornec, E.C., Davies, D., Bollinger, C., Le Goff, M., Grossteffan, E., Planchon, F., 2016. Impact of the natural Fe-fertilization on the magnitude, stoichiometry and efficiency of particulate biogenic silica, nitrogen and iron export fluxes. Deep Sea Res. Part I Oceanogr. Res. Pap. 117, 11–27. doi:10.1016/j.dsr.2016.09.002

Lenton, A., Tilbrook, B., Law, R.M., Bakker, D., Doney, S.C., Gruber, N., Ishii, M., Hoppema, M., Lovenduski, N.S., Matear, R.J., McNeil, B.I., Metzl, N., Mikaloff Fletcher, S.E., Monteiro, P.M.S., Rödenbeck, C., Sweeney, C., Takahashi, T., 2013. Sea-air CO2 fluxes in the Southern Ocean for the period 1990-2009. Biogeosciences 10, 4037–4054. doi:10.5194/bg-10-4037-2013

Lepore, K., Moran, S.B., Burd, A.B., Jackson, G.A., Smith, J.N., Kelly, R.P., Kaberi, H., Stavrakakis, S., Assimakopoulou, G., 2009. Deep-Sea Research I Sediment trap and in-situ pump size-fractionated POC / 234 Th ratios in the Mediterranean Sea and Northwest Atlantic : Implications for POC export. Deep Sea Res. Part I Oceanogr. Res. Pap. 56, 599–613. doi:10.1016/j.dsr.2008.11.004

Levitus, S., Antonov, J., Boyer, T., 2005. Warming of the world ocean, 1955-2003. Geophys. Res. Lett. 32, 1–4. doi:10.1029/2004GL021592

Levy, M., Bopp, L., Karleskind, P., Resplandy, L., Ethe, C., Pinsard, F., 2013. Physical pathways for carbon transfers between the surface mixed layer and the ocean interior. Global Biogeochem. Cycles 27, 1001–1012. doi:10.1002/gbc.20092

Lévy, M., Iovino, D., Resplandy, L., Klein, P., Madec, G., Tréguier, A.M., Masson, S., Takahashi, K., 2012. Large-scale impacts of submesoscale dynamics on phytoplankton: Local and remote effects. Ocean Model. 43–44, 77–93. doi:10.1016/j.ocemod.2011.12.003

Liu, Z., Lee, C., Wakeham, S.G., 2006. Effects of mercuric chloride and protease inhibitors on degradation of particulate organic matter from the diatom Thalassiosira pseudonana. Org. Geochem. 37, 1003–1018. doi:10.1016/j.orggeochem.2006.05.013

Liu, Z., Stewart, G., Cochran, J.K., Lee, C., Armstrong, R.A., Hirschberg, D.J., Gasser, B., Miquel, J.C., 2005. Why do POC concentrations measured using Niskin bottle collections sometimes differ from those using in-situ pumps? Deep. Res. Part I Oceanogr. Res. Pap. 52, 1324–1344. doi:10.1016/j.dsr.2005.02.005

Longhurst, A., 1995. Seasonal cycles of pelagic production and consumption. Prog. Oceanogr. 36, 77–167.

Longhurst, A.R., 2010. Ecological geography of the sea, Academic P. ed. San Diego.

Longhurst, A.R., Glen Harrison, W., 1988. Vertical nitrogen flux from the oceanic photic zone by diel migrant zooplankton and nekton. Deep Sea Res. Part A, Oceanogr. Res. Pap. 35, 881–889. doi:10.1016/0198-0149(88)90065-9

Loring, D.H., Asmund, G., 1996. Geochemical factors controlling accumulation of major and trace elements in Greenland coastal and fjord sediments. Environ. Geol. 28, 2–11.

Lutz, M., Dunbar, R., Caldeira, K., 2002. Regional variability in the vertical flux of particulate organic carbon in the ocean interior. Global Biogeochem. Cycles 16, 1–15. doi:10.1029/2000GB001383

Lutz, M.J., Caldeira, K., Dunbar, R.B., Behrenfeld, M.J., 2007. Seasonal rhythms of net primary production and particulate organic carbon flux to depth describe the efficiency of biological pump in the global ocean. J. Geophys. Res. 112, 1–26. doi:10.1029/2006JC003706

Mahadevan, a., D'Asaro, E., Lee, C., Perry, M.J., 2012. Eddy-Driven Stratification Initiates North Atlantic Spring Phytoplankton Blooms. Science (80-.). 337, 54–58. doi:10.1126/science.1218740

Maiti, K., Charette, M.A., Buesseler, K.O., Kahru, M., 2013. An inverse relationship between production and export efficiency in the Southern Ocean. Geophys. Res. Lett. 40, 1557–1561. doi:10.1002/grl.50219

Marchetti, A., Cassar, N., 2009. Diatom elemental and morphological changes in response to iron limitation: a brief review with potential paleoceanographic applications. Geobiology 7, 419–431. doi:10.1111/j.1472-4669.2009.00207.x

Margalef, R., 1978. Life-forms of phytoplankton as survival alternatives in an unstable environment. Oceanol. Acta 1, 493–509. doi:10.1007/BF00202661

Marinov, I., Gnanadesikan, A., Toggweiler, J.R., Sarmiento, J.L., 2006. The Southern Ocean biogeochemical divide. Nature 441, 964–967. doi:10.1038/nature04883

Marra, J.F., Lance, V.P., Vaillancourt, R.D., Hargreaves, B.R., 2014. Resolving the ocean's euphotic zone. Deep Sea Res. Part I Oceanogr. Res. Pap. 83, 45–50. doi:10.1016/j.dsr.2013.09.005

Marsay, C.M., Sanders, R.J., Henson, S.A., Pabortsava, K., Achterberg, E.P., Lampitt, R.S., 2015. Attenuation of sinking particulate organic carbon flux through the mesopelagic ocean. Proc. Natl. Acad. Sci. U. S. A. 112, 1089–94. doi:10.1073/pnas.1415311112

Martin, J.H., 1990. Glacial-interglacial CO2 change: the iron hypothesis. Paleoceanography 5, 1–13.

Martin, J.H., Knauer, G. a., Karl, D.M., Broenkow, W.W., 1987. VERTEX: carbon cycling in the northeast Pacific. Deep Sea Res. Part A. Oceanogr. Res. Pap. 34, 267–285. doi:10.1016/0198-0149(87)90086-0

Martin, P., 2011. Particle export and flux through the mesopelagic in the high-latitude North and South Atlantic. PhD thesis, Univ. Southampt. 168.

Martin, P., Lampitt, R.S., Jane Perry, M., Sanders, R., Lee, C., D'Asaro, E., 2011. Export and mesopelagic particle flux during a North Atlantic spring diatom bloom. Deep Sea Res. Part I Oceanogr. Res. Pap. 58, 338–349. doi:10.1016/j.dsr.2011.01.006

Martiny, A.C., Pham, C.T.A., Primeau, F.W., Vrugt, J.A., Moore, J.K., Levin, S.A., Lomas, M.W., 2013. Strong latitudinal patterns in the elemental ratios of marine plankton and organic matter. Nat. Geosci. 6, 279–283. doi:10.1038/ngeo1757

Matear, R.J., Hirst, A.C., 2003. Long-term changes in dissolved oxygen concentrations in the ocean caused by protracted global warming. Global Biogeochem. Cycles 17, 1–17. doi:10.1029/2002GB001997

McDonnell, A.M.P., Lam, P.J., Lamborg, C.H., Buesseler, K.O., Sanders, R., Riley, J.S., Marsay, C., Smith, H.E.K., Sargent, E.C., Lampitt, R.S., Bishop, J.K.B., 2015. The oceanographic toolbox for the collection of sinking and suspended marine particles. Prog. Oceanogr. 133, 17–31. doi:10.1016/j.pocean.2015.01.007

McGillicuddy, D.J., Robinson, a R., 1997. Eddy induced nutrient supply and new production in the Sargasso Sea. Deep Sea Res. Part I Oceanogr. Res. Pap. 44, 1427–1450. doi:10.1016/S0967-0637(97)00024-1

Meire, L., Meire, P., Struyf, E., Krawczyk, D.W., Arendt, K.E., Yde, J.C., Juul Pederson, T., Hopwood, M.J., Rysgaard, S., Meysman, F.J.R., 2016. High export of dissolved silica from the Greenland Ice Sheet. Geophys. Res. Lett. 43, 9173–9182. doi:10.1002/2016GL070191

Mercier, H., Lherminier, P., Sarafanov, A., Gaillard, F., Daniault, N., Desbruyères, D., Falina, A., Ferron, B., Gourcuff, C., Huck, T., Thierry, V., 2015. Variability of the meridional overturning circulation at the Greenland-Portugal OVIDE section from 1993 to 2010. Prog. Oceanogr. 132, 250–261. doi:10.1016/j.pocean.2013.11.001

Michaels, A.F., Silver, M.W., 1988. Primary production, sinking fluxes and the microbial food web. Deep Sea Res. Part A. Oceanogr. Res. Pap. 35, 473–490.

Moffett, J.W., Ho, J., 1996. Oxidation of cobalt and manganese in seawater via a common microbially catalyzed pathway. Geochim. Cosmochim. Acta 60, 3415–3424.

Moore, C.M., Hickman, A.E., Poulton, A.J., Seeyave, S., Lucas, M.I., 2007. Iron–light interactions during the CROZet natural iron bloom and EXport experiment (CROZEX): II—Taxonomic responses and elemental stoichiometry. Deep Sea Res. Part II Top. Stud. Oceanogr. 54, 2066–2084. doi:10.1016/j.dsr2.2007.06.015

Moore, C.M., Lucas, M.I., Sanders, R., Davidson, R., 2005. Basin-scale variability of phytoplankton bio-optical characteristics in relation to bloom state and community structure in the Northeast Atlantic. Deep Sea Res. Part I Oceanogr. Res. Pap. 52, 401–419. doi:10.1016/j.dsr.2004.09.003

Moore, C.M., Mills, M.M., Arrigo, K.R., Berman-Frank, I., Bopp, L., Boyd, P.W., Galbraith, E.D., Geider, R.J., Guieu, C., Jaccard, S.L., Jickells, T.D., La Roche, J., Lenton, T.M., Mahowald, N.M., Maranon, E., Marinov, I., Moore, J.K., Nakatsuka, T., Oschlies, A., Saito, M.A., Thingstad, T.F., Tsuda, A., Ulloa, O., 2013. Processes and patterns of oceanic nutrient limitation. Nat. Geosci. 6, 701–710. doi:10.1038/ngeo1765

Moore, C.M., Mills, M.M., Langlois, R., Milne, A., Achterberg, E.P., Roche, J. La, Geider, R.J., 2008. Relative influence of nitrogen and phosphorus availability on phytoplankton physiology and productivity in the oligotrophic sub-tropical North Atlantic Ocean. Limnol. Oceanogr. 53, 291–305.

Moore, C.M., Mills, M.M., Milne, A., Langlois, R., Achterberg, E.P., Lochte, K., Geider, R.J., La Roche, J., 2006. Iron limits primary productivity during spring bloom development in the central North Atlantic. Glob. Chang. Biol. 12, 626–634. doi:10.1111/j.1365-2486.2006.01122.x

Moore, L.R., Post, A.F., Rocap, G., Chisholm, S.W., 2002. Utilization of different nitrogen sources by the marine cyanobacteria Prochlorococcus and Synechococcus. Limnol. Oceanogr. 47, 989–996. doi:10.4319/lo.2002.47.4.0989

Moran, S.B., Charette, M.A., Pike, S.M., Wicklund, C.A., 1999. Differences in seawater particulate organic carbon concentration in samples collected using small- and large-volume methods: The importance of DOC adsorption to the filter blank. Mar. Chem. 67, 33–42. doi:10.1016/S0304-4203(99)00047-X

Moran, S.B., Weinstein, S.E., Edmonds, H.N., Smith, J.N., Kelly, R.P., Pilson, M.E.Q., Harrison, W.G., 2003. Does 234Th/238U disequilibrium provide an accurate record of the

export flux of particulate organic carbon from the upper ocean? Limnol. Oceanogr. 48, 1018–1029. doi:10.4319/lo.2003.48.3.1018

Morel, F.M.M., 2003. The Biogeochemical Cycles of Trace Metals in the Oceans. Science (80-.). 300, 944–947. doi:10.1126/science.1083545

Morris, P.J., Charette, M. a., 2013. A synthesis of upper ocean carbon and dissolved iron budgets for Southern Ocean natural iron fertilisation studies. Deep Sea Res. Part II Top. Stud. Oceanogr. 90, 147–157. doi:10.1016/j.dsr2.2013.02.001

Morris, P.J., Sanders, R., Turnewitsch, R., Thomalla, S., 2007. Th-234-derived particulate organic carbon export from an island-induced phytoplankton bloom in the Southern Ocean. Deep Sea Res. Part II Top. Stud. Oceanogr. 54, 2208–2232. doi:DOI 10.1016/j.dsr2.2007.06.002

Mosseri, J., Quéguiner, B., Armand, L., Cornet-Barthaux, V., 2008. Impact of iron on silicon utilization by diatoms in the Southern Ocean: A case study of Si/N cycle decoupling in a naturally iron-enriched area. Deep Sea Res. Part II Top. Stud. Oceanogr. 55, 801–819. doi:10.1016/j.dsr2.2007.12.003

Mouw, C.B., Barnett, A., Mckinley, G.A., Gloege, L., Pilcher, D., 2016. Phytoplankton size impact on export flux in the global Ocean. Global Biogeochem. Cycles 30, 1542–1562. doi:10.1002/2015GB005355

Muggli, D.L., Harrison, P.J., 1996. Effects of nitrogen source on the physiology and metal nutrition of Emiliania huxleyi grown under different iron and light conditions. Mar. Ecol. Prog. Ser. 130, 255–267.

Muggli, D.L., Lecourt, M., Harrison, P.J., 1996. Effects of iron and nitrogen source on the sinking rate , physiology and metal composition of an oceanic diatom from the subarctic Pacific. Mar. Ecol. Prog. Ser. 132, 215–227.

Murray, J.W., Young, J., Newton, J.A.N., Dunne, J., Chapin, T., Paul, B., McCarthys, J.J., 1996. Export flux of particulate organic carbon from the central equatorial Pacific determined using a combined drifting trap-234Th approach. Deep Sea Res. Part II Top. Stud. Oceanogr. 43, 1095–1132.

Nelson, D.M., Brzezinski, M.A., 1997. Diatom growth and productivity in an oligotrophic midocean gyre : A 3-yr record from the Sargasso Sea near Bermuda. Limnol. Oceanogr. 42, 473–486.

Nielsdottir, M.C., Moore, C.M., Sanders, R., Hinz, D.J., Achterberg, E.P., 2009. Iron limitation of the postbloom phytoplankton communities in the Iceland Basin. Global Biogeochem. Cycles 23, 1–13. doi:10.1029/2008GB003410

Nightingale, D., Malin, G., Law, C.S., Watson, J., Liss, S., Liddicoat, I., 2000. In situ evaluation of air-sea gas exchange parameterizations using novel conservtauve and volatile tracers. Global Biogeochem. Cycles 14, 373–387. doi:10.1029/1999GB900091

Nodder, S.D., Waite, A.M., 2001. Is Southern Ocean organic carbon and biogenic silica export enhanced by iron-stimulated increases in biological production? Sediment trap results from SOIREE. Deep Sea Res. Part II Top. Stud. Oceanogr. 48, 2681–2701. doi:10.1016/S0967-0645(01)00014-5

Nuester, J., Shema, S., Vermont, A., Fields, D.M., Twining, B.S., 2014. The regeneration of highly bioavailable iron by meso- and microzooplankton. Limnol. Oceanogr. 59, 1399–1409. doi:10.4319/lo.2014.59.4.1399

Ohnemus, D.C., Lam, P.J., 2014. Cycling of Lithogenic Marine Particulates in the US GEOTRACES North Atlantic Transect. Deep Sea Res. Part II Top. Stud. Oceanogr. In Press, 283–302. doi:http://dx.doi.org/10.1016/j.dsr2.2014.11.019

Omand, M.M., D'Asaro, E.A., Lee, C.M., Perry, M.J., Briggs, N., Cetinić, I., Mahadevan, A.,

Sanders, R., Henson, S.A., Koski, M., Rocha, C.L.D. La, Painter, S.C., Poulton, A.J., Riley, J., Salihoglu, B., Visser, A., Yool, A., Bellerby, R., Martin, A.P., Körtzinger, A., Send, U., Lampitt, R.S., Hartman, S., Wallace, D.W.R., Karstensen, J., Villagarcia, M.G., Llinás, O., DeGrandpre, M.D., Sabine, C.L., Feely, R.A., Gruber, N., Key, R.M., Lee, K., Bullister, J.L., Wanninkhof, R., Wong, C.S., Wallace, D.W., Tilbrook, B., Millero, F.J., Peng, T.H., Kozyr, A., Ono, T., Rios, A.F., Follows, M.J., Williams, R.G., Marshall, J.C., Gardner, W.D., Chung, S.P., Richardson, M.J., Walsh, I.D., Sverdrup, H.U., Mahadevan, A., D'Asaro, E., Lee, C., Perry, M.J., Taylor, J., Ferrari, R., Ducklow, H.W., Harris, R.P., Sallée, J.B., Matear, R.J., Rintoul, S.R., Lenton, A., Barth, J.A., Karleskind, P., Lévy, M., Memery, L., Mahadevan, A., Mahadevan, A., Tandon, A., Spall, M.A., Lee, M., Nurser, A., McWilliams, J.C., Colas, F., Molemaker, M.J., Lévy, M., Klein, P., Treguier, A.M., Pollard, R., Regier, L., Fielding, S., Crisp, N., Allen, J.T., Hartman, M.C., Rabe, B., Roe, H.S.J., Briggs, N., Perry, M.J., Cetinić, I., Lee, C., D'Asaro, E., Gray, A.M., Rehm, E., Rynearson, T., Richardson, K., Lampitt, R.S., Sieracki, M.E., Poulton, A.J., Lyngsgaard, M.M., Perry, M.J., Alkire, M.B., D'Asaro, E., Lee, C., Perry, M.J., Gray, A., Cetinić, I., Briggs, N., Rehm, E., Kallin, E., Kaiser, J., González-Posada, A., Palter, J.B., Lozier, M.S., Barber, R.T., Mahadevan, A., Oliger, J., Street, R., Bagniewski, W., Fennel, K., Perry, M.J., D'Asaro, E.A., Johnston, T., Cheriton, O., Pennington, J.T., Chavez, F.P., Held, I., Schneider, T., Fox-Kemper, B., Ferrari, R., Hallberg, R., Mahadevan, A., Tandon, A., Ferrari, R., Martin, P., Lampitt, R.S., Perry, M.J., Sanders, R., Lee, C., D'Asaro, E., Buesseler, K.O., Bacon, M.P., Cochran, J.K., Livingston, H.D., Siegel, D.A., Buesseler, K.O., Doney, S.C., Sailley, S.F., Behrenfeld, M.J., Boyd, P.W., Steinberg, D., Mooy, B.A.S. Van, Buesseler, K.O., Boyd, P.W., Kobari, T., Karl, D.M., Burd, A., Hansell, D.A., Steinberg, D.K., Anderson, T.R., Arístegui, J., Baltar, F., Beaupré, S.R., Buesseler, K.O., DeHairs, F., Jackson, G.A., Kadko, D.C., Koppelmann, R., Lampitt, R.S., Nagata, T., Reinthaler, T., Robinson, C., Robison, B.H., Tamburini, C., Tanaka, T., Giering, S.L., Sanders, R., Lampitt, R.S., Anderson, T.R., Tamburini, C., Boutrif, M., Zubkov, M. V., Marsay, C.M., Henson, S.A., Saw, K., Cook, K., Mayor, D.J., Dall'Olmo, G., Mork, K.A., Richardson, T.L., Jackson, G.A., Eriksen, C.C., Osse, T.J., Light, R.D., Wen, T., Lehman, T.W., Sabin, P.L., Ballard, J.W., Chiodi, A.M., Cetinić, I., Perry, M.J., Briggs, N.T., Kallin, E., D'Asaro, E.A., Lee, C.M., Bretherton, F., Davis, R.E., Fandry, C.B., Rudnick, D.L., Ferrari, R., Hodges, B., Rudnick, D., Flament, P., D'Asaro, E.A., Boccaletti, G., Ferrari, R., Fox-Kemper, B., Stone, P.H., Fox-Kemper, B., Danabasoglu, G., Ferrari, R., Griffies, S.M., Hallberg, R.W., Holland, M.M., Maltrud, M.E., Peacock, S., Samuels, B.L., Tandon, A., Garrett, C., Martin, J.H., Fitzwater, S.E., Gordon, R.M., Hunter, C.N., Tanner, S.J., 2015. Eddy-driven subduction exports particulate organic carbon from the spring bloom. Science (80-.). 348, 222–5. doi:10.1126/science.1260062

Orsi, A.H., Jacobs, S.S., Gordon, A.L., Visbeck, M., 2001. Cooling and ventilating the abyssal ocean. Geophys. Res. Lett. 28, 2923–2926. doi:10.1029/2001GL012830

Owens, S.A., Buesseler, K.O., Sims, K.W.W., 2011. Re-evaluating the 238U-salinity relationship in seawater: Implications for the 238U-234Th disequilibrium method. Mar. Chem. 127, 31–39. doi:10.1016/j.marchem.2011.07.005

Owens, S.A., Pike, S., Buesseler, K.O., 2014. Thorium-234 as a tracer of particle dynamics and upper ocean export in the Atlantic Ocean. Deep Sea Res. Part II Top. Stud. Oceanogr. 116, 42–59. doi:10.1016/j.dsr2.2014.11.010

Park, Y.-H., Roquet, F., Durand, I., Fuda, J.-L., 2008. Large-scale circulation over and around the Northern Kerguelen Plateau. Deep Sea Res. Part II Top. Stud. Oceanogr. 55, 566–581. doi:10.1016/j.dsr2.2007.12.030

Passow, U., 2002. Transparent Exopolymer Particles in Aquatic Environments. Prog. Oceanogr. 55, 287–333. doi:10.1016/S0079-6611(02)00138-6

Passow, U., Carlson, C.A., 2012. The biological pump in a high CO2 world. Mar. Ecol. Prog. Ser. 470, 249–271. doi:10.3354/meps09985

Paytan, A., Griffith, E.M., 2007. Marine barite: Recorder of variations in ocean. Deep Sea Res. Part II Top. Stud. Oceanogr. 54, 687–705. doi:10.1016/j.dsr2.2007.01.007

Paytan, A., McLaughlin, K., 2007. The oceanic phosphorus cycle. Chem. Rev. 107, 563–576. doi:10.1021/cr0503613

Paytan, A., Moore, W.S., Kastner, M., 1996. Sedimentation rate as determined by 226Ra activity in marine barite. Geochim. Cosmochim. Acta 60, 4313–4319.

Peinert, R., Antia, A.N., Bauerfeind, E., v. Bodungen, B., Haupt, O., Krumbholz, M., Peeken, I., Ramseier, R.O., Voss, M., Zeitzschel, B., 2001. Particle Flux Variability in the Polar and Atlantie Biogeoehemieal Provinees of the Nordie Seas. North. North Atl. 53–68.

Pérez, F.F., Mercier, H., Vázquez-rodríguez, M., Lherminier, P., Velo, A., Pardo, P.C., Rosón, G., Ríos, A.F., 2013. Atlantic Ocean CO2 uptake reduced by weakening of the meridional overturning circulation. Nat. Geosci. 6, 146–152. doi:10.1038/ngeo1680

Pickart, R.S., Torres, D., Clarke, R.A., 2002. Hydrography of the Labrador Sea during active convection. J. Phys. Oceanogr. 32, 428–457.

Pike, S., Buesseler, K.O., Andrews, J., Savoye, N., 2005. Quantification of 234Th recovery in small volume seawater samples by Inductively Coupled Plasma Mass Spectrometry. J. Radioanal. Nucl. Chem. 263, 355–360.

Planchon, F., Ballas, D., Cavagna, A.-J., Bowie, A.R., Davies, D.M., Trull, T., Laurenceau, E.C., van der Merwe, P., Dehairs, F., 2015. Carbon export in the naturally iron-fertilized Kerguelen area of the Southern Ocean based on the 234 Th approach. Biogeosciences 12, 3831–3848. doi:10.5194/bgd-12-3831-2015

Planchon, F., Cavagna, A.-J., Cardinal, D., André, L., Dehairs, F., 2013. Late summer particulate organic carbon export and twilight zone remineralisation in the Atlantic sector of the Southern Ocean. Biogeosciences 10, 803–820. doi:10.5194/bg-10-803-2013

Planquette, H., Fones, G.R., Statham, P.J., Morris, P.J., 2009. Origin of iron and aluminium in large particles (> 53 μm) in the Crozet region, Southern Ocean. Mar. Chem. 115, 31–42. doi:DOI 10.1016/j.marchem.2009.06.002

Planquette, H., Sanders, R., Statham, P.J., Morris, P.J., Fones, G.R., 2011. Fluxes of particulate iron from the upper ocean around the Crozet Islands: A naturally iron-fertilized environment in the Southern Ocean. Global Biogeochem. Cycles 25, 1–12. doi:10.1029/2010GB003789

Planquette, H., Sherrell, R.M., 2012. Sampling for particulate trace element determination using water sampling bottles: methodology and comparison to in situ pumps. Limnol. Oceanogr. Methods 10, 367–388. doi:10.4319/lom.2012.10.367

Pohl, C., Croot, P.L., Hennings, U., Daberkow, T., Budeus, G., Rutgers van der Loeff, M.M., 2011. Synoptic transects on the distribution of trace elements (Hg, Pb, Cd, Cu, Ni, Zn, Co, Mn, Fe, and Al) in surface waters of the Northern- and Southern East Atlantic. J. Mar. Syst. 84, 28–41. doi:10.1016/j.jmarsys.2010.08.003

Pollard, R., Sanders, R., Lucas, M., Statham, P., 2007. The Crozet Natural Iron Bloom and Export Experiment (CROZEX). Deep Sea Res. Part II Top. Stud. Oceanogr. 54, 1905–1914. doi:10.1016/j.dsr2.2007.07.023

Pollard, R.T., Salter, I., Sanders, R.J., Lucas, M.I., Moore, C.M., Mills, R. a, Statham, P.J., Allen, J.T., Baker, A.R., Bakker, D.C.E., Charette, M. a, Fielding, S., Fones, G.R., French, M., Hickman, A.E., Holland, R.J., Hughes, J.A., Jickells, T.D., Lampitt, R.S., Morris, P.J., Nédélec, F.H., Nielsdóttir, M., Planquette, H., Popova, E.E., Poulton, A.J., Read, J.F., Seeyave, S., Smith, T., Stinchcombe, M., Taylor, S., Thomalla, S., Venables, H.J., Williamson, R., Zubkov, M. V, 2009. Southern Ocean deep-water carbon export enhanced by natural iron fertilization. Nature 457, 577–580. doi:10.1038/nature07716

Pommier, J., Gosselin, M., Michel, C., 2009. Size-fractionated phytoplankton production and biomass during the decline of the northwest Atlantic spring bloom. J. Plankton Res. 31, 429–446. doi:10.1093/plankt/fbn127

Pondaven, P., Gallinari, M., Chollet, S., Bucciarelli, E., Sarthou, G., Schultes, S., Jean, F., 2007. Grazing-induced Changes in Cell Wall Silicification in a Marine Diatom. Protist 158, 21–28. doi:10.1016/j.protis.2006.09.002

Poulton, A.J., Charalampopoulou, A., Young, J.R., Tarran, G.A., Lucas, M.I., Quartly, G.D., 2010. Coccolithophore dynamics in non-bloom conditions during late summer in the central Iceland Basin (July-August 2007). Limnol. Oceanogr. 55, 1601–1613. doi:10.4319/lo.2010.55.4.1601

Price, N.M., 2005. The elemental stoichiometry and composition of an iron-limited diatom. Limnol. Oceanogr. 50, 1159–1171. doi:10.4319/lo.2005.50.4.1159

Puigcorbé, V., Benitez-Nelson, C.R., Masque, P., Verdeny, E., White, A., Popp, B.N., Prahl, F.G., Lam, P.J., 2015. Small phytoplankton drive high summertime carbon and nutrient export in the Gulf of California and Eastern Tropical North Pacific. Glob. Planet. Change 29. doi:10.1002/2015GB005134

Quéguiner, B., 2013. Iron fertilization and the structure of planktonic communities in high nutrient regions of the Southern Ocean. Deep Sea Res. Part II Top. Stud. Oceanogr. 90, 43–54. doi:10.1016/j.dsr2.2012.07.024

Quéroué, F., Sarthou, G., Planquette, H.F., Bucciarelli, E., Chever, F., van der Merwe, P., Lannuzel, D., Townsend, a. T., Cheize, M., Blain, S., D'Ovidio, F., Bowie, a. R., 2015. High variability of dissolved iron concentrations in the vicinity of Kerguelen Island (Southern Ocean). Biogeosciences 12, 3869–3883. doi:10.5194/bg-12-3869-2015

Ragueneau, O., Dittert, N., Pondaven, P., Treguer, P., Corrin, L., 2002. Si/C decoupling in the world ocean: is the Southern Ocean different? Deep Sea Res. Part II Top. Stud. Oceanogr. 49, 3127–3154. doi:10.1016/S0967-0645(02)00075-9

Ragueneau, O., Savoye, N., Del Amo, Y., Cotten, J., Tardiveau, B., Leynaert, A., 2005. A new method for the measurement of biogenic silica in suspended matter of coastal waters: using Si:Al ratios to correct for the mineral interference. Cont. Shelf Res. 25, 697–710. doi:10.1016/j.csr.2004.09.017

Ragueneau, O., Schultes, S., Bidle, K., Claquin, P., Moriceau, B., 2006. Si and C interactions in the world ocean: Importance of ecological processes and implications for the role of diatoms in the biological pump. Global Biogeochem. Cycles 20, n/a-n/a. doi:10.1029/2006GB002688

Raitsos, D.E., Lavender, S.J., Pradhan, Y., Tyrrell, T., Reid, P.C., Edwards, M., 2006. Coccolithophore bloom size variation in response to the regional environment of the subarctic North Atlantic. Limnol. Oceanogr. 51, 2122–2130.

Ras, J., Claustre, H., Uitz, J., 2008. Spatial variability of phytoplankton pigment distributions in the Subtropical South Pacific Ocean: comparison between in situ and predicted data. Biogeosciences 5, 353–369.

Redfield, A.C., Ketchum, B.H., Richards, F.A., 1963. The influence of organisms on the composition of the sea water, in: Hill, M.N. (Ed.), The Sea. pp. 26–77.

Reinthaler, T., van Aken, H., Veth, C., Aristegui, J., Robinson, C., Williams, P.J.B., Lebaron, P., Herndl, G.J., 2006. Prokaryotic respiration and production in the meso- and bathypelagic realm of the eastern and western North Atlantic basin. Limnol. Oceanogr. 51, 1262–1273.

Rembauville, M., Blain, S., Armand, L., Quéguiner, B., Salter, I., 2015a. Export fluxes in a naturally iron-fertilized area of the Southern Ocean – Part 2: Importance of diatom resting

spores and faecal pellets for export. Biogeosciences 12, 3171–3195. doi:10.5194/bg-12-3171-2015

Rembauville, M., Blain, S., Caparros, J., Salter, I., 2016a. Particulate matter stoichiometry driven by microplankton community structure in summer in the Indian sector of the Southern Ocean. Limnol. Oceanogr. 61, 1301–1321. doi:10.1002/lno.10291

Rembauville, M., Manno, C., Tarling, G.A., Blain, S., Salter, I., 2016b. Strong contribution of diatom resting spores to deep-sea carbon transfer in naturally iron-fertilized waters downstream of South. Deep Sea Res. Part I Oceanogr. Res. Pap. 115, 22–35. doi:10.1016/j.dsr.2016.05.002

Rembauville, M., Meilland, J., Ziveri, P., Schiebel, R., Blain, S., Salter, I., 2016c. Planktic foraminifer and coccolith contribution to carbonate export fluxes over the central Kerguelen Plateau. Deep Sea Res. Part I Oceanogr. Res. Pap. 111, 91–101. doi:10.1016/j.dsr.2016.02.017

Rembauville, M., Salter, I., Leblond, N., Gueneugues, A., Blain, S., 2015b. Export fluxes in a naturally iron-fertilized area of the Southern Ocean – Part 1: Seasonal dynamics of particulate organic carbon export from a moored sediment trap. Biogeosciences 12, 3153–3170. doi:10.5194/bg-12-3153-2015

Report, I., 2007. Climate Change 2007: An assessment of the Intergovernmental Panel on Climate Change.

Resplandy, L., Martin, A.P., Le Moigne, F., Martin, P., Aquilina, A., M??mery, L., L??vy, M., Sanders, R., 2012. How does dynamical spatial variability impact 234Th-derived estimates of organic export? Deep Sea Res. Part I Oceanogr. Res. Pap. 68, 24–45. doi:10.1016/j.dsr.2012.05.015

Reverdin, G., Niiler, P.P., Valdimarsson, H., 2003. North Atlantic Ocean surface currents. J. Geophys. Res. 108, 1–21. doi:10.1029/2001JC001020

Rhein, M., Kieke, D., Steinfeldt, R., 2015. Advection of North Atlantic Deep Water from the Labrador Sea to the southern hemisphere. J. Geophys. Res. 120, 2471–2487. doi:10.1002/2014JC010605.Received

Riebesell, U., Zondervan, I., Rost, B., Tortell, P.D., Zeebe, R.E., Morel, F.M.M., 2000. Reduced calcification of marine plankton in response to increased atmospheric CO2. Nature 407, 364–367.

Riley, G., 1957. Phytoplankton of the North Central Sargasso Sea, 1950-52. Limnol. Oceanogr. 2, 252–270. doi:10.1002/lno.1957.2.3.0252

Riley, J.S., Sanders, R., Marsay, C., Le Moigne, F.A.C., Achterberg, E.P., Poulton, A.J., 2012. The relative contribution of fast and slow sinking particles to ocean carbon export. Global Biogeochem. Cycles 26, 1–10. doi:10.1029/2011GB004085

Rivière, P., Pondaven, P., 2006. Phytoplankton size classes competitions at sub-mesoscale in a frontal oceanic region. J. Mar. Syst. 60, 345–364. doi:10.1016/j.jmarsys.2006.02.005

Rivkin, R.B., Legendre, L., 2001. Biogenic carbon cycling in the upper ocean: Effects of microbial respiration. Science (80-.). 291, 2398–2400.

Robert, A., 2012. Mineralisation in-situ de la matiere organique le long de la colonne d'eau: application sur une station eulerienne. PhD thesis. Mediterranean Institute of Oceanography. pp 189.

Roca-Marti, M., Puigcorbé, V., Iversen, M.H., van der Loeff, M.R., Klaas, C., Cheah, W., Bracher, A., Masqué, P., 2016a. High particulate organic carbon export during the decline of a vast diatom bloom in the Atlantic sector of the Southern Ocean. Deep Sea Res. Part II Top. Stud. Oceanogr. doi:10.1016/j.dsr2.2015.12.007

Roca-Marti, M., Puigcorbé, V., van der Loeff, M.R., Katlein, C., Fernandez-Mendez, M., Peeken, I., Masqué, P., 2016b. Carbon export fluxes and export efficiency in the central Arctic during the record sea-ice minimum in 2012: a joint 234Th/238U and 210Po/210Pb study. J. Geophys. Res. 121, 1–20. doi:10.1002/2016JC011816.Received

Rue, E.L., Bruland, K.W., 1995. Complexation of Fe(III) by natural organic ligands in the Central North Pacific as determined by a new competitive ligand equilibration/adsorptive cathodic stripping voltammetric method. Mar. Chem. 50, 117–138.

Rutgers van der Loeff, M.M., Buesseler, K., Bathmann, U., Hense, I., Andrews, J., 2002. Comparison of carbon and opal export rates between summer and spring bloom periods in the region of the Antarctic Polar Front, SE Atlantic. Deep Sea Res. Part II Top. Stud. Oceanogr. 49, 3849–3869. doi:10.1016/S0967-0645(02)00114-5

Rutgers van der Loeff, M.M., Friedrich, J., Bathmann, U. V., 1997. Carbon export during the Spring Bloom at the Antarctic Polar Front, determined with the natural tracer 234Th. Deep Sea Res. Part II Top. Stud. Oceanogr. 44, 457–478. doi:10.1016/S0967-0645(96)00067-7

Rynearson, T.A., Richardson, K., Lampitt, R.S., Sieracki, M.E., Poulton, A.J., Lyngsgaard, M.M., Perry, M.J., 2013. Major contribution of diatom resting spores to vertical flux in the sub-polar North Atlantic. Deep. Res. Part I 82, 60–71. doi:10.1016/j.dsr.2013.07.013

Sabine, C.L., Feely, R.A., 2007. The oceanic sink for carbon dioxide, in: Reay, D., Hewitt, C.N., Smith, K., Grace, J. (Eds.), Greenhouse Gas Sinks. pp. 31–48.

Sabine, C.L., Feely, R.A., Gruber, N., Key, R.M., Lee, K., Bullister, J.L., Wanninkhof, R., Wong, C.S., Wallace, D.W.R., Tilbrook, B., Millero, F.J., Peng, T., Kozyr, A., Ono, T., Rios, A.F., 2004. The Oceanic Sink for Anthropogenic CO2. Science (80-.). 305, 367–371. doi:10.1126/science.1097403

Saito, M.A., Noble, A.E., Hawco, N., Twining, B.S., Ohnemus, D.C., John, S.G., Lam, P., Conway, T.M., Johnson, R., Moran, D., Mcilvin, M., 2016. The acceleration of dissolved cobalt's ecological stoichiometry due to biological uptake, remineralization, and scavenging in the Atlantic Ocean. Biogeosciences Discuss. 1–43. doi:10.5194/bg-2016-511

Salter, I., Kemp, A.E.S., Lampitt, R.S., Gledhill, M., 2010. The association between biogenic and inorganic minerals and the amino acid composition of settling particles. Limnol. Oceanogr. 55, 2207–2218. doi:10.4319/lo.2010.55.5.2207

Salter, I., Kemp, A.E.S., Moore, C.M., Lampitt, R.S., Wolff, G.A., Holtvoeth, J., 2012. Diatom resting spore ecology drives enhanced carbon export from a naturally iron-fertilized bloom in the Southern Ocean. Glob. Planet. Change 26, 1–17. doi:10.1029/2010GB003977

Salter, I., Lampitt, R.S., Sanders, R., Poulton, A., Kemp, A.E.S., Boorman, B., Saw, K., Pearce, R., 2007. Estimating carbon, silica and diatom export from a naturally fertilised phytoplankton bloom in the Southern Ocean using PELAGRA: A novel drifting sediment trap. Deep Sea Res. Part II Top. Stud. Oceanogr. 54, 2233–2259. doi:10.1016/j.dsr2.2007.06.008

Salter, I., Schiebel, R., Ziveri, P., Movellan, A., Lampitt, R., Wol, G. a, 2014. Carbonate counter pump stimulated by natural iron fertilization in the Polar Frontal Zone. Nat. Geosci. 7, 885–889. doi:10.1038/NGEO2285

Sanders, R., Brown, L., Henson, S., Lucas, M., 2005. New production in the Irminger Basin during 2002. J. Mar. Syst. 55, 291–310. doi:10.1016/j.jmarsys.2004.09.002

Sanders, R., Henson, S.A., Koski, M., La, C.L. De, Painter, S.C., Poulton, A.J., Riley, J., Salihoglu, B., Visser, A., Yool, A., Bellerby, R., Martin, A.P., 2014. The Biological Carbon Pump in the North Atlantic. Prog. Oceanogr. 129, 200–218. doi:10.1016/j.pocean.2014.05.005

Sanders, R., Morris, P.J., Poulton, A.J., Stinchcombe, M.C., Charalampopoulou, A., Lucas, M.I., Thomalla, S.J., 2010. Does a ballast effect occur in the surface ocean ? Geophys. Res. Lett. 37, 1–5. doi:10.1029/2010GL042574

Santschi, P.H., Li, Y., Bell, J.O.Y., 1979. Natural radionuclides in the water of narragansett bay. Earth Planet. Sci. Lett. 45, 201–213.

Sarmiento, J.L., Gruber, N., 2006. Ocean biogeochemical dynamics. Princeton University Press.

Sarmiento, J.L.G., 2002. Sinks for Anthropogenic Carbon. Phys. Today 55, 30. doi:10.1063/1.1510279

Sarthou, G., Timmermans, K.R., Blain, S., Tréguer, P., 2005. Growth physiology and fate of diatoms in the ocean: a review. J. Sea Res. 53, 25–42. doi:10.1016/j.seares.2004.01.007

Sarthou, G., Vincent, D., Christaki, U., Obernosterer, I., Timmermans, K.R., Brussaard, C., 2008. The fate of biogenic iron during a phytoplankton bloom induced by natural fertilisation: Impact of copepod grazing. Deep Sea Res. Part II Top. Stud. Oceanogr. 55, 734–751. doi:10.1016/j.dsr2.2007.12.033

Savoye, N., Benitez-Nelson, C., Burd, A.B., Cochran, J.K., Charette, M., Buesseler, K.O., Jackson, G.A., Roy-Barman, M., Schmidt, S., Elskens, M., 2006. 234Th sorption and export models in the water column: A review. Mar. Chem. 100, 234–249. doi:10.1016/j.marchem.2005.10.014

Savoye, N., Trull, T.W., Jacquet, S.H.M., Navez, J., Dehairs, F., 2008. 234Th-based export fluxes during a natural iron fertilization experiment in the Southern Ocean (KEOPS). Deep Sea Res. Part II Top. Stud. Oceanogr. 55, 841–855. doi:10.1016/j.dsr2.2007.12.036

Schneider, B., Schlitzer, R., Fischer, G., Nothig, E.M., 2003. Depth-dependent elemental compositions of particulate organic matter (POM) in the ocean. Global Biogeochem. Cycles 17, 1032. doi:10.1029/2002GB001871

Schuster, U., Watson, A.J., 2007. A variable and decreasing sink for atmospheric CO2 in the North Atlantic. J. Geophys. Res. Ocean. 112, 1–10. doi:10.1029/2006JC003941

Seager, R., Battisti, D.S., Yin, J., Gordon, N., Naik, N., Clement, A.C., Cane, M.A., 2002. Is the Gulf Stream responsible for Europe's mild winters? Quartely J. R. Meteorol. Soc. 128, 2563–2586. doi:10.1256/qj.01.128

Shelley, R.U., Morton, P.L., Landing, W.M., 2015. Elemental ratios and enrichment factors in aerosols from the US-GEOTRACES North Atlantic transects. Deep Sea Res. Part II Top. Stud. Oceanogr. 116, 262–272. doi:10.1016/j.dsr2.2014.12.005

Shelley, R.U., Roca-Martí, M., Castrillejo, M., Masqué, P., Landing, W.M., Planquette, H., Sarthou, G., 2016. Quantification of trace element atmospheric deposition fluxes to the Atlantic Ocean (>40°N; GEOVIDE, GEOTRACES GA01) during spring 2014. Deep Sea Res. Part I Oceanogr. Res. Pap. doi:10.1016/j.dsr.2016.11.010

Shopova, D., Dehairs, F., Baeyens, W., 1995. A simple model of biogeochemical element distribution in the oceanic water column. J. Mar. Syst. 6, 331–344.

Shutler, J.D., Land, P.E., Piolle, J.-F., Woolf, D.K., Goddijn-Murphy, L., Paul, F., Girard-Ardhuin, F., Chapron, B., Donlon, C., 2016. FluxEngine: A flexible processing system for calculating atmosphere-ocean carbon dioxide gas fluxes and climatologies. J. Atmos. Ocean. Technol. 33, 741–756. doi:10.1175/JTECH-D-14-00204.1

Siegel, D.A., Buesseler, K.O., Doney, S.C., Sailley, S.F., Behrenfeld, M.J., Boyd, P.W., 2014. Global assessment of ocean carbon export by combining satellite observations and food-web models. Global Biogeochem. Cycles 28, 181–196. doi:10.1002/2013GB004743

Sigman, D., Karsh, K., Casciotti, K., 2009. Ocean Process Tracers: Nitrogen Isotopes in the

Ocean. Encycl. Ocean Sci. 4138–4153. doi:10.1006/rwos.2001.0172

Sigman, D.M., Boyle, E.A., 2000. Glacial/interglacial variations in atmospheric carbon dioxide. Nature 407, 859–869.

Sigman, D.M., Hain, M.P., 2012. The Biological Productivity of the Ocean. Nat. Educ. 3, 1–16.

Silver, M.W., Gowing, M.M., 1991. The “particle” flux: Origins and biological components. Prog. Oceanogr. 26, 75–113. doi:10.1016/0079-6611(91)90007-9

Simon, M., Grossart, H.P., Schweitzer, B., Ploug, H., 2002. Microbial ecology of organic aggregates in aquatic ecosystems. Aquat. Microb. Ecol. 28, 175–211. doi:10.3354/ame028175

Smetacek, V., Naqvi, S.W.A., 2008. The next generation of iron fertilization experiments in the Southern Ocean. Philos. Trans. R. Soc. A 366, 3947–3967. doi:10.1098/rsta.2008.0144

Sonnerup, R.E., Mecking, S., Bullister, J.L., Warner, M.J., 2014. Transit time distributions and oxygen utilization rates from chlorofluorocarbons and sulfur hexafluoride in the Southeast Pacific Ocean. J. Geophys. Res. 120, 3761–3776. doi:10.1002/2015JC010781

Stanley, R.H.R., Buesseler, K.O., Manganini, S.J., Steinberg, D.K., Valdes, J.R., 2004. A comparison of major and minor elemental fluxes collected in neutrally buoyant and surface-tethered sediment traps. Deep Sea Res. Part I Oceanogr. Res. Pap. 51, 1387–1395. doi:10.1016/j.dsr.2004.05.010

Steinberg, D.K., Carlson, C.A., Bates, N.R., Goldthwait, S.A., Madin, L.P., Michaels, A.F., 2000. Zooplankton vertical migration and the active transport of dissolved organic and inorganic carbon in the Sargasso Sea. Deep Sea Res. Part I Oceanogr. Res. Pap. 47, 137–158.

Steinberg, D.K., Carlson, C.A., Bates, N.R., Johnson, R.J., Michaels, A.F., Knap, A.H., 2001. Overview of the US JGOFS Bermuda Atlantic Time-series Study (BATS): a decade-scale look at ocean biology and biogeochemistry. Deep Sea Res. Part II Top. Stud. Oceanogr. 48, 1405–1447.

Steinberg, D.K., Van Mooy, B.A.S., Buesseler, K.O., Boyd, P.W., Kobari, T., Karl, D.M., 2008. Bacterial vs. zooplankton control of sinking particle flux in the ocean’s twilight zone. Limnol. Oceanogr. 53, 1327–1338. doi:10.4319/lo.2008.53.4.1327

Sternberg, E., Tang, D., Ho, T.Y., Jeandel, C., Morel, F.M.M., 2005. Barium uptake and adsorption in diatoms. Geochim. Cosmochim. Acta 69, 2745–2752. doi:10.1016/j.gca.2004.11.026

Stewart, G., Cochran, J.K., Miquel, J.C., Masqué, P., Szlosek, J., Rodriguez y Baena, A.M., Fowler, S.W., Gasser, B., Hirschberg, D.J., 2007. Comparing POC export from 234 Th / 238 U and 210 Po / 210 Pb disequilibria with estimates from sediment traps in the northwest Mediterranean. Deep Sea Res. Part I Oceanogr. Res. Pap. 54, 1549–1570. doi:10.1016/j.dsr.2007.06.005

Stramma, L., Johnson, G.C., Sprintall, J., Mohrholz, V., 2008. Expanding Oxygen-Minimum Zones in the tropical oceans. Science (80-.). 320, 655–658. doi:10.1126/science.1153847

Straneo, F., Pickart, R.S., Lavender, K., 2003. Spreading of Labrador sea water: an advective-diffusive study based on Lagrangian data. Deep Sea Res. Part A. Oceanogr. Res. Pap. 50, 701–719. doi:10.1016/S0967-0637(03)00057-8

Stroobants, N., Dehairs, F., Goeyens, L., Vanderheijden, N., Van Grieken, R., 1991. Barite formation in the Southern Ocean water. Mar. Chem. 35, 411–421. doi:10.1016/S0304-4203(09)90033-0

Strzepek, R.F., Maldonado, M.T., Higgins, J.L., Hall, J., Safi, K., Wilhelm, S.W., Boyd, P.W.,

2005. Spinning the “Ferrous Wheel”: The importance of the microbial community in an iron budget during the FeCycle experiment. Global Biogeochem. Cycles 19, n/a-n/a. doi:10.1029/2005GB002490

Sugie, K., Kuma, K., 2008. Resting spore formation in the marine diatom Thalassiosira nordenskioeldii under iron- and nitrogen-limited conditions. J. Plankton Res. 30, 1245–1255. doi:10.1093/plankt/fbn080

Sunda, W., 1989. Trace metal interactions with marine phytoplankton. Biol. Oceanogr. 6, 411–442. doi:10.1080/01965581.1988.10749543

Sunda, W.G., Huntsman, S.A., 1995. Cobalt and zinc interreplacement in marine phytoplankton: Biological and geochemical implications. Limnol. Oceanogr. 40, 1404–1417.

Sunda, W.G., Huntsman, S.A., 1995. Iron uptake and growth limitation in oceanic and coastal phytoplankton. Mar. Chem. 50, 189–206.

Swift, D.G., 1981. Vitamin levels in the Gulf of Maine and ecological significance of vitamin B12 there. J. Mar. Res. 39, 375–403.

Tagliabue, A., Bopp, L., Dutay, J.-C., Bowie, A.R., Chever, F., Jean-Baptiste, P., Bucciarelli, E., Lannuzel, D., Remenyi, T., Sarthou, G., Aumont, O., Gehlen, M., Jeandel, C., 2010. Hydrothermal contribution to the oceanic dissolved iron inventory. Nat. Geosci. 3, 252–256. doi:10.1038/ngeo818

Takeda, S., 1998. Influence of iron availability on nutrient consumption ratio of diatoms in oceanic waters. Nature 393, 774–777. doi:10.1038/31674

Tarling, G.A., Ward, P., Atkinson, A., Collins, M.A., Murphy, E.J., 2012. DISCOVERY 2010: Spatial and temporal variability in a dynamic polar ecosystem. Deep. Res. Part II Top. Stud. Oceanogr. 59–60, 1–13. doi:10.1016/j.dsr2.2011.10.001

Taylor, S.R., Mclennan, S.M., 1985. The continental crust: its composition and evolution, Blackwells. ed.

Teng, Y.-C., Primeau, F.W., Moore, J.K., Lomas, M.W., Martiny, A.C., 2014. Global-scale variations of the ratios of carbon to phosphorus in exported marine organic matter. Nat. Geosci. 7, 895–898. doi:10.1038/NGEO2303

Ternon, E., Guieu, C., Löye-Pilot, M.-D., Leblond, N., Bose, E., Gasser, B., Miquel, J.-C., Martin, J., 2010. The impact of Saharan dust on the particulate export in the water column of the North Western Mediterranean Sea. Biogeosciences 7, 809–826.

Thomalla, S., Turnewitsch, R., Lucas, M., Poulton, A., 2006. Particulate organic carbon export from the North and South Atlantic gyres: The 234Th/238U disequilibrium approach. Deep Sea Res. Part II Top. Stud. Oceanogr. 53, 1629–1648. doi:10.1016/j.dsr2.2006.05.018

Thomalla, S.J., Poulton, A.J., Sanders, R., Turnewitsch, R., Holligan, P.M., Lucas, M.I., 2008. Variable export fluxes and efficiencies for calcite, opal, and organic carbon in the Atlantic Ocean: A ballast effect in action ? Global Biogeochem. Cycles 22, 1–10. doi:10.1029/2007GB002982

Tréguer, P., Nelson, D.M., Van Bennekom, a J., Demaster, D.J., Leynaert, A., Quéguiner, B., 1995. The silica balance in the world ocean: a reestimate. Science (80-.). 268, 375–379. doi:10.1126/science.268.5209.375

Tréguer, P.J., De La Rocha, C.L., 2013. The world ocean silica cycle. Ann. Rev. Mar. Sci. 5, 477–501. doi:10.1146/annurev-marine-121211-172346

Trezzi, G., Garcia-orellana, J., Santos-echeandia, J., Rodellas, V., Garcia-solsona, E., 2016. The in fluence of a metal-enriched mining waste deposit on submarine groundwater discharge to the coastal sea. Mar. Chem. 178, 35–45.

doi:10.1016/j.marchem.2015.12.004

Trull, T., Davies, D.M., Dehairs, F., Cavagna, A.-J., Lasbleiz, M., Laurenceau, E.C., d'Ovidio, F., Planchon, F., Queguiner, B., Blain, S., 2015. Chemometric perspectives on plankton community responses to natural iron fertilization over and downstream of the Kerguelen plateau in the Southern Ocean. Biogeosciences 12, 1029–1056. doi:10.5194/bg-12-1029-2015

Trull, T.W., Davies, D., Casciotti, K., 2008. Insights into nutrient assimilation and export in naturally iron-fertilized waters of the Southern Ocean from nitrogen, carbon and oxygen isotopes. Deep Sea Res. Part II Top. Stud. Oceanogr. 55, 820–840. doi:10.1016/j.dsr2.2007.12.035

Turekian, K.K., Tausch, E.H., 1964. Barium in deep-sea sediments of the Atlantic Ocean. Nature 201, 696–697.

Turner, A., Millward, G.., 2002. Suspended Particles: Their Role in Estuarine Biogeochemical Cycles. Estuar. Coast. Shelf Sci. 55, 857–883. doi:10.1006/ecss.2002.1033

Turner, J.T., 2015. Zooplankton fecal pellets, marine snow, phytodetritus and the ocean's biological pump. Prog. Oceanogr. 130, 205–248. doi:10.1016/j.pocean.2014.08.005

Twining, B.S., Baines, S.B., 2013. The trace metal composition of marine phytoplankton. Ann. Rev. Mar. Sci. 5, 191–215. doi:10.1146/annurev-marine-121211-172322

Twining, B.S., Baines, S.B., Fisher, N.S., 2004. Element stoichiometries of individual plankton cells collected during the Southern Ocean Iron Experiment (SOFeX). Limnol. Oceanogr. 49, 2115–2128. doi:10.4319/lo.2004.49.6.2115

Twining, B.S., Nodder, S.D., King, A.L., Hutchins, D.A., LeCleir, G.R., DeBruyn, J.M., Maas, E.W., Vogt, S., Wilhelm, S.W., Boyd, P.W., 2014. Differential remineralization of major and trace elements in sinking diatoms. Limnol. Oceanogr. 59, 689–704. doi:10.4319/lo.2014.59.3.0689

Twining, B.S., Nun, D., Vogt, S., Johnson, R.S., Sedwick, P.N., 2010. Variations in Synechococcus cell quotas of phosphorus, sulfur, manganese, iron, nickel, and zinc within mesoscale eddies in the Sargasso Sea. Limnol. Oceanogr. 55, 492–506.

Twining, B.S., Rauschenberg, S., Morton, P.L., Ohnemus, D.C., Lam, P.J., 2015a. Comparison of particulate trace element concentrations in the North Atlantic Ocean as determined with discrete bottle sampling and in situ pumping. Deep Sea Res. Part II Top. Stud. Oceanogr. 116, 273–282. doi:10.1016/j.dsr2.2014.11.005

Twining, B.S., Rauschenberg, S., Morton, P.L., Vogt, S., 2015b. Metal contents of phytoplankton and labile particulate material in the North Atlantic Ocean. Prog. Oceanogr. 137, 261–283. doi:10.1016/j.pocean.2015.07.001

Uitz, J., Claustre, H., Griffiths, F.B., Ras, J., Garcia, N., Sandroni, V., 2009. A phytoplankton class-specific primary production model applied to the Kerguelen Islands region (Southern Ocean). Deep Sea Res. Part I Oceanogr. Res. Pap. 56, 541–560. doi:10.1016/j.dsr.2008.11.006

Uitz, J., Claustre, H., Morel, A., Hooker, S.B., 2006. Vertical distribution of phytoplankton communities in open ocean: An assessment based on surface chlorophyll. J. Geophys. Res. 111, 1–23. doi:10.1029/2005JC003207

Usbeck, R., 2002. Shallow remineralization in the Weddell Gyre. Geochemistry Geophys. Geosystems 3. doi:10.1029/2001GC000182

Van Camp, L., Nykjaer, L., Mittelstaedt, E., Schlittenhardt, P., 2000. Upwelling and boundary circulation off Northwest Africa as depicted by infrared and visible satellite observations. Prog. Oceanogr. 26, 357–402.

van der Loeff, M.R., Sarin, M.M., Baskaran, M., Benitez-Nelson, C., Buesseler, K.O., Charette, M., Dai, M., Gustafsson, Ö., Masque, P., Morris, P.J., Orlandini, K., Rodriguez y Baena, A., Savoye, N., Schmidt, S., Turnewitsch, R., Vöge, I., Waples, J.T., 2006. A review of present techniques and methodological advances in analyzing 234Th in aquatic systems. Mar. Chem. 100, 190–212. doi:10.1016/j.marchem.2005.10.012

van der Merwe, P., Bowie, A.R., Quéroué, F., Armand, L., Blain, S., Chever, F., Davies, D.M., Dehairs, F., Planchon, F., Sarthou, G., Townsend, a T., Trull, T., 2015. Sourcing the iron in the naturally-fertilised bloom around the Kerguelen Plateau: particulate trace metal dynamics. Biogeosciences 12, 739–755. doi:10.5194/bg-12-739-2015

van Weering, T.C.E., de Stigter, H.C., Boer, W., de Haas, H., 2002. Recent sediment transport and accumulation on the NW Iberian margin. Prog. Earth Planet. Sci. 52, 349–371.

Vellinga, M., Wood, R.A., 2002. Global climatic impacts of a collapse of the Atlantic thermohaline circulation. Clim. Chang. 54, 251–267.

Villa-Alfageme, M., Soto, F.C., Ceballos, E., Giering, S.L.C., Le Moigne, F.A.C., Henson, S., Mas, J.L., Sanders, R.J., 2016. Geographical, seasonal and depth variation in sinking particle speeds in the North Atlantic. Geophys. Res. Lett. 43, 8609–8616. doi:10.1002/2016GL069233.Received

Volk, T., Hoffert, M.I., 1985. Ocean carbon pumps: analysis of relative strengths and efficiencies in ocean-driven atmospheric CO2 changes, in: The Carbon Cycle and Atmospheric CO2: Natural Variations Archean to Present. pp. 99–110.

Waite, A.M., Stemmann, L., Guidi, L., Calili, P.H.R., Hogg, A.M.C., Feng, M., Thompson, P.A., Picheral, M., Gorsky, G., 2016. The wineglass effect shapes particle export to the deep ocean in mesoscale eddies. Geophys. Res. Lett. 43, 1–10. doi:10.1002/2015GL066463.Received

Wanninkhof, R., McGillis, W.R., 1999. A cubic relationship between air-sea CO2 exchange and wind speed. Geophys. Res. Lett. 26, 1889–1892. doi:10.1029/1999GL900363

Waples, J.T., Benitez-Nelson, C., Savoye, N., Rutgers van der Loeff, M., Baskaran, M., Gustafsson, Ö., 2006. An introduction to the application and future use of 234Th in aquatic systems. Mar. Chem. 100, 166–189. doi:10.1016/j.marchem.2005.10.011

Watson, A.J., Schuster, U., Bakker, D.C.E., Bates, N.R., Corbière, A., González-Dávila, M., Friedrich, T., Hauck, J., Heinze, C., Johannessen, T., Körtzinger, A., Metzl, N., Olafsson, J., Olsen, A., Oschlies, A., Padin, X.A., Pfeil, B., Santana-Casiano, J.M., Steinhoff, T., Telszewski, M., Rios, A.F., Wallace, D.W.R., Wanninkhof, R., 2009. Tracking the variable North Atlantic sink for atmospheric CO2. Science (80-.). 326, 1391–1393. doi:10.1126/science.1177394

Weber, T.S., Deutsch, C., 2010. Ocean nutrient ratios governed by plankton biogeography. Nature 467, 550–554. doi:10.1038/nature09403

Weinstein, S.E., Moran, S.B., 2005. Vertical flux of particulate Al, Fe, Pb, and Ba from the upper ocean estimated from 234Th/238U disequilibria. Deep Sea Res. Part I Oceanogr. Res. Pap. 52, 1477–1488. doi:http://dx.doi.org/10.1016/j.dsr.2005.03.008

Weinstein, S.E., Moran, S.B., 2004. Distribution of size-fractionated particulate trace metals collected by bottles and in-situ pumps in the Gulf of Maine-Scotian Shelf and Labrador Sea. Mar. Chem. 87, 121–135. doi:10.1016/j.marchem.2004.02.004

Wolf-gladrow, D.A., Riebesell, U., Burkhardt, S., Bijma, J., 1999. Direct effects of CO2 concentration on growth and isotopic composition of marine plankton. Tellus 51, 461–476.

Wright, S.W., Jeffrey, S.W., 1987. Fucoxanthin pigment markers of marine phytoplankton analysed by HPLC and HPTLC. Mar. Ecol. Prog. Ser. 38, 259–266.

Wright, S.W., van den Enden, R.L., Pearce, I., Davidson, A.T., Scott, F.J., Westwood, K.J., 2010. Phytoplankton community structure and stocks in the Southern Ocean (30-80°E) determined by CHEMTAX analysis of HPLC pigment signatures. Deep Sea Res. Part II Top. Stud. Oceanogr. 57, 758–778. doi:10.1016/j.dsr2.2009.06.015

Wu, J., Sunda, W., Boyle, E. a, Karl, D.M., 2000. Phosphate depletion in the western North Atlantic Ocean. Science (80-.). 289, 759–762. doi:10.1126/science.289.5480.759

Yashayaev, I., 2007. Hydrographic changes in the Labrador Sea, 1960-2005. Prog. Oceanogr. 73, 242–276. doi:10.1016/j.pocean.2007.04.015

Ye, Y., Wagener, T., Völker, C., Guieu, C., Wolf-Gladrow, D.A., 2011. Dust deposition: iron source or sink ? A case study. Biogeosciences 8, 2107–2124. doi:10.5194/bg-8-2107-2011

Zeebe, R.E., 2012. History of seawater carbonate chemistry, atmospheric CO2, and ocean acidification. Ann. Rev. Mar. Sci. 40, 141–165. doi:10.1146/annurev-earth-042711-105521

Zehr, J.P., Mellon, M.T., Zani, S., 1998. New nitrogen-fixing microorganisms detected in oligotrophic oceans by amplification of nitrogenase (nifH) genes. Appl. Environ. Microbiol. 64, 3444–3450. doi:PMC106745

Zehr, J.P., Ward, B.B., 2002. Nitrogen Cycling in the Ocean : New Perspectives on Processes and Paradigms MINIREVIEW Nitrogen Cycling in the Ocean : New Perspectives on Processes and Paradigms. Appl. Environ. Microbiol. 68, 1015–1024. doi:10.1128/AEM.68.3.1015

Zehr, J.P., Waterbury, J.B., Turner, P.J., Montoya, J.P., Omoregie, E., Steward, G.F., Hansen, A., Karl, D.M., 2001. Unicellular cyanobacteria fix N2 in the subtropical North Pacific Ocean. Nature 412, 635–638. doi:10.1038/35088063

Zhou, K., Maiti, K., Dai, M., Kao, S.J.K., Buesseler, K.O., 2016. Does adsorption of dissolved organic carbon and thorium onto membrane filters affect the carbon to thorium ratios , a primary parameter in estimating export carbon flux ? Mar. Chem. 184, 1–10. doi:10.1016/j.marchem.2016.06.004

Zhou, M., Zhu, Y., d'Ovidio, F., Park, Y.-H., Durand, I., Kestenare, E., Sanial, V., van Beek, P., Queguiner, B., Carlotti, F., Bowie, A.R., 2014. Surface currents and upwelling in Kerguelen Plateau regions. Biogeosciences Discuss. 11, 6845–6876. doi:10.5194/bgd-11-6845-2014

Zúñiga, D., Villacieros-Robineau, N., Salgueiro, E., Alonso-Pérez, F., Rosón, G., Abrantes, F., Castro, C.G., 2016. Particle fluxes in the NW Iberian coastal upwelling system: Hydrodynamical and biological control. Cont. Shelf Res. 123, 89–98. doi:10.1016/j.csr.2016.04.008

Approche multi-proxy (Thorium-234, Baryum en excès) des flux d'export et de reminéralisation du carbone et des éléments nutritifs associés à la pompe biologique océanique.

Résumé : L'objectif principal de cette thèse est de mieux comprendre les différents facteurs contrôlant la pompe biologique de carbone en Atlantique Nord et dans l'Océan Austral, à proximité des îles Kerguelen, en utilisant notamment deux approches: le Thorium-234 (^{234}Th) et le baryum biogénique (Ba_{xs}).
En Atlantique Nord, les flux d'export de carbone organique particulaire (POC) augmentent lorsqu'ils sont associés à des minéraux biogéniques (silice biogénique et carbonate de calcium) et lithogènes, capable de lester les particules. L'efficacité d'export, généralement plus faible que précédemment supposé (< 10%), est inversement corrélée à la production, soulignant un décalage temporel entre production et export. La plus forte efficacité de transfert, i.e. la fraction de POC atteignant 400m, est reliée à des particules lestées par du carbonate de calcium ou des minéraux lithogènes.
Les flux de reminéralisation mésopélagique sont similaires ou parfois supérieurs aux flux d'exports et dépendent de l'intensité du développement phytoplanctonique, de la structure en taille, des communautés phytoplanctoniques et des processus physiques (advection verticale).
Comme observé pour le POC, l'export des éléments traces est influencé par les particules lithogènes provenant des marges océaniques, mais aussi des différentes espèces phytoplanctoniques.
Dans l'Océan Austral, la zone à proximité de l'île de Kerguelen est naturellement fertilisée en fer, augmentant les flux d'export de fer, d'azote et de silice biogénique. Il a été démontré que la variabilité des flux dépendait des communautés phytoplanctoniques dans la zone fertilisée.

Mots clés : pompe biologique océanique, export, reminéralisation, carbone, éléments traces, silice biogénique, carbonate de calcium.

Multi-proxy approach (Thorium-234, excess Barium) of export and remineralization fluxes of carbon and biogenic elements associated with the oceanic biological pump

Abstract : The main objective of this thesis is to improve our understanding of the different controls that affect the oceanic biological carbon pump. Particulate export and remineralization fluxes were investigated using the thorium-234 (^{234}Th) and biogenic barium (Ba_{xs}) proxies.
In the North Atlantic, the highest particulate organic carbon (POC) export fluxes were associated to biogenic (biogenic silica or calcium carbonate) and lithogenic minerals, ballasting the particles. Export efficiency was generally low (< 10%) and inversely related to primary production, highlighting a phase lag between production and export. The highest transfer efficiencies, i.e. the fraction of POC that reached 400m, were driven by sinking particles ballasted by calcite or lithogenic minerals.
The regional variation of mesopelagic remineralization was attributed to changes in bloom intensity, phytoplankton cell size, community structure and physical forcing (downwelling). Carbon remineralization balanced, or even exceeded, POC export, highlighting the impact of mesopelagic remineralization on the biological pump with a near-zero, deep carbon sequestration for spring 2014.
Export of trace metals appeared strongly influenced by lithogenic material advected from the margins. However, at open ocean stations not influenced by lithogenic matter, trace metal export rather depended on phytoplankton activity and biomass.
A last part of this work focused on export of biogenic silica, particulate nitrogen and iron near the Kerguelen Island. This area is characterized by a natural iron-fertilization that increases export fluxes. Inside the fertilized area, flux variability is related to phytoplankton community composition.

Key words : oceanic biological pump, export, remineralization, carbon, trace elements, biogenic silica, calcium carbonate